DISSERTATION

MODIFYING ELECTRONIC AND SOLID-STATE PROPERTIES OF FULLERENES, POLYCYCLIC AROMATIC HYDROCARBONS, AND PERYLENE DIIMIDES

Submitted by

Tyler T. Clikeman

Department of Chemistry

In partial fulfillment of the requirements

For the Degree of Doctor of Philosophy

Colorado State University

Fort Collins, Colorado

Fall 2015

Doctoral Committee:

Advisor: Steven H. Strauss
Co-Advisor: Garry Rumbles

Matt P. Shores
` Eugene Y.-X. Chen
Travis Bailey
Jim Sites

ABSTRACT

MODIFYING ELECTRONIC AND SOLID-STATE PROPERTIES OF FULLERENES, POLYCYCLIC AROMATIC HYDROCARBONS, AND PERYLENE DIIMIDES

The growing world energy demand necessitates the development of novel, cheap, and efficient energy sources and low energy consumption electronics devices. Organic photovoltaics, transistors, and light-emitting diodes are actively being developed as replacements for traditional energy sources and electronic devices. Strong electron acceptors are required to increase the efficiency and air stability for many of these applications. Studying how the incremental introduction of strong electron-accepting moieties onto electron-accepting substrates can affect performance is essential for systematically developing new devices. Furthermore, synthetic methodologies and characterization of these molecules are essential before incorporation into real world applications. This dissertation focuses on synthesizing families of strong electron acceptors via modification with strong perfluoroalkyl or cyano electron-withdrawing groups for fundamental studies in the development of advanced electronics.

The first chapter focuses on the synthesis and characterization of new trifluoromethylfullerene derivatives. Synthetic methods for adding CF_3 groups to C_{60}, C_{70}, and $M_3N@C_{80}$ are discussed and new CF_3 addition patterns are revealed by single crystal XRD. Then the addition of electrophiles, nucleophiles, and cycloadducts to these trifluoromethylfullerene derivatives are discussed. Adding single nucleophiles and electrophiles to the cages along with collaborative DFT studies show which cage carbon atoms are most susceptible towards

additional attack. The variations in electron accepting behavior were studied by adding a combination of electron-withdrawing and electron-donating groups at these specific locations on the fullerene cage. The studies revealed that these groups can modify electronic behaviors incrementally and somewhat unexpectedly by disrupting the fullerene π system. Understanding where and why new groups add to the fullerene cages and how they affect electronic behaviors could be used as the foundation for synthesizing new fullerene molecules to be used in advanced electronic devices.

The second chapter concentrates on substituting electron-withdrawing fluorinated groups onto polycyclic aromatic hydrocarbon substrates. A family of poly(trifluoromethyl)azulene derivatives was synthesized and characterized for the first time. Trifluoromethylation of azulene systematically increases the electron-withdrawing strength and affects solid-state packing motifs. The molecular structures and solid-state packing of four other families of fluorine-modified polycyclic aromatic hydrocarbon substrates, corannulene, phenazine, triphenylene, and anthracene, were studied using single crystal XRD. Not only did XRD reveal previously unknown substitution patterns, but it was able to show where close π- π interactions existed within the packing structure, which could be extrapolated to solid-state charge transport in future applications.

The third chapter focuses on developing a new series of perylene diimide acceptors and their use in organic photovoltaic active layers. Perylene diimides with previously unknown substitution patterns were synthesized with CF_3 and CN groups and then isolated to isomeric purity using HPLC. Substituting with these strong electron-withdrawing groups at specific positions modified absorption, emission, solid-state packing, and solution- and gas-phase electron-accepting strength. These properties were compared within the entire series and solution

reduction potentials were compared with a comprehensive list of literature reported perylene diimide acceptors. It was found that these properties were dependent on position and were not constant for each substituent. The series of poly(trifluoromethyl)perylene diimides were then blended with polymer donors and tested in photovoltaic active layer films. The systematic tuning of electron-withdrawing strength was used as a handle for fundamental studies on how increased electron affinity and fluorination affect charge transfer in the solid-state. All of the perylene diimides were able to accept charge from the polymer donors, but increasing the electron-withdrawing strength by introducing more fluorine atoms did not improve the charge separation yield.

ACKNOWLEDGMENTS

I would like to thank my parents, Jim and Lori Clikeman, for always supporting me throughout graduate school, the 17 years of school leading up to graduate school, and all of the support and advice outside of school. I would not be anywhere near where I am today if they hadn't raised me so well. I would like to thank my siblings, Sam and Nicole Clikeman, for encouraging me and accepting me for being a weird science nerd. My girlfriend, Tianna Hurtado, has been there for me throughout my grad school troubles and has motivated me to write this dissertation so that I can graduate and get a real job, thank you. The rest of my family and friends that have always supported me and at least feigned interest when asking me the details of my chemistry research are too numerous to list here, so thank you all.

To all past and present Strauss group members, especially Eric Bukovsky and Long San who have been there the entire time with me, who have helped me with chemistry questions, laboratory techniques, computer problems, seminar practices, editing papers, and making sure I fill out forms correctly and don't miss deadlines, thank you. Thank you to all of the Rumbles group members, Bryon Larson, Nikos Kopidakis, and other NREL employees who have helped me learn new concepts and techniques at NREL that were far from what I was used to at CSU. Yu-Sheng Chen has been a big support while learning crystallography and never fails in providing a good laugh at the end of a 24-hour APS shift. Andreas Hirsch and his research group were very supportive when letting a peculiar foreigner who didn't speak any German into their lab and taught me a lot about culture and chemistry. Collaborators, Xue-Bin Wang and Alexey Popov, provided a wealth of electron affinity and DFT data that helped make this dissertation possible.

Lastly, I would like to thank my advisors, Steve Strauss, Garry Rumbles, and Olga Boltalina, for all of the scientific insight, research and collaboration opportunities, travel and conference opportunities, and flexibility with my various research projects.

TABLE OF CONTENTS

INTRODUCTION

New energy solutions will be necessary to meet the growing energy demand as the world population continues to increase at an aggressive rate. Among alternative energy sources, solar energy is one of the most abundant and viable options that could easily exceed the world's current and future energy demands. For example, the energy that the earth absorbs in one hour of solar radiation is more than the world's energy consumption every year.[1] If new, efficient, and cheap devices could collect just a small fraction of this energy throughout the entire year, then providing energy for a growing world population becomes more likely. Among solar energy conversion devices, organic photovoltaics (OPVs) are regarded as commercially viable renewable energy sources that have already achieved efficiencies over 10% by utilizing conducting polymers and fullerenes as electron-donors and electron-acceptors, respectively.[2] OPV devices have the potential to be easily fabricated into lightweight, flexible, and cheap electricity sources.[3] New donor and acceptor materials must first be developed to help understand and gain insight into how OPVs function in order to develop a highly functioning OPV device that will help provide energy at low costs.

Derivatization of donor and acceptor molecules, such as fullerenes or polycyclic aromatic hydrocarbons (PAHs), is directly involved in the preparation of new materials for OPV and a wide variety of other applications.[4] Introduction of electron-withdrawing groups (EWGs) into organic molecules is known to generally enhance their electron acceptor properties, and this approach has been actively used to design new *n*-type organic semiconductor materials.[5,6] Energy level engineering of donor-acceptor pairs directly affects the optimal driving force for maximum charge transfer in OPV active layers.[7] As new low-band-gap polymers are

synthesized, new acceptor molecules with increased electron accepting strength (higher electron affinity (EA), or lower LUMO levels) must follow in order to match the frontier orbitals of the donor and achieve the optimal driving force for maximizing charge transfer. Synthetically introducing strong electron accepting CF_3 and CN groups presents one method of increasing the electron accepting strength of molecular substrates. Furthermore, vast families of electron acceptors based on one set of substrates can be synthesized by only changing the amount of CF_3 or CN groups. These families of molecules often exhibit similar physicochemical properties such as size, solubility, absorption, etc. while major differences in electron accepting strength and solid-state packing are observed.[8] The availability of such families allows for fundamental studies of molecular interactions in advanced electronics over a wide range of acceptor strength while keeping most other properties constant.

Perfluoroalkylfullerenes (PFAFs) are promising starting materials in this regard because they constitute one of the most diverse classes of derivatized fullerenes that exhibit high stability in air and in solution, thermal stability at elevated temperatures, and excellent solubility in organic solvents.[8-16] For example, there are more than 130 well-characterized fullerene$(CF_3)_n$ compounds, including more than 30 $C_{60}(CF_3)_n$ derivatives.[9] PFAFs have already been used for fundamental studies in regards to fullerene reactivity,[17-19] intermolecular charge transfer in OPV active layers,[7] and accepting strength of perfluoroalkyl groups based on the same substrate.[20] The success of these studies has prompted further research on new fullerene reactions, charge transfer with new electron donors in OPV active layers, and determining the accepting strength of other electron accepting addends.

Synthetically pure fullerenes can be expensive and difficult to purify, so non-fullerene acceptors are actively being researched as fullerene replacements in OPV active layers, field-

effect transistors (FETs), and other advanced electronics.[21-24] PAH acceptors can be highly tunable,[25] have high charge-carrier mobilities,[26,27] and offer low-cost advantages over fullerene derivatives. Modifying the electronic properties of these more planar PAH systems with electron accepting substituents is similarly tunable and more predictable than fullerenes since the overall π-systems do not change as significantly as fullerene derivatives.[25] Developing new families of PAH acceptors is essential towards fundamental understanding of charge transfer based on amount, placement, and type of EWG.

Extrapolating the knowledge gained from fundamental studies based on large families of similarly modified substrates can result in the systematic development of new molecules for advanced electronics. Understanding how subtle, systematic changes in molecular properties in these families impacts overall performance in various phases will enable optimized parameters to be utilized for commercial applications.

This thesis involves the synthesis and characterization of electron-accepting families of molecules based on various carbon-rich substrates. New synthetic approaches are developed to synthesize new derivatives and understand specific reactivity. The charge transfer characteristics in solid, liquid, and gas states are investigated. Crystallographic packing motifs are studied to predict possible charge transfer pathways in the solid state.

CHAPTER 1. Fullerene Reactions and Electronic Properties in Solution and Gas Phase for Select Fullerene Derivatives

1.1 Introduction

Recent advances in synthetic methods and separation techniques have resulted in the availability of 100+ mg quantities of several PFAFs.[9,28] Rational, selective, and general further elaboration of PFAFs would allow for modified electronic levels, increased solubility, or covalent linkages to other materials to afford supramolecular assemblies. However, the current arsenal of PFAF derivatizations consists of only a few examples of two types of regioselective reactions: (i) cycloadditions to the C11–C29 bond in C_s-p^7-$C_{70}(CF_3)_8$ (**70-8-1**)[29] and the C33–C34 bond in C_1-p^7mp-$C_{70}(CF_3)_{10}$ (**70-10-1**);[17-19] and (ii) the addition of two Cl atoms to **70-8-1**[30] and 12 Cl atoms to S_6-$C_{60}(CF_3)_{12}$[31]. Except for the 12-Cl-atom addition, these reactions allow (i) a single substituent (the exocyclic moiety) or (ii) two *identical* radical substituents to be added to a particular C=C bond (i.e., to adjacent C atoms). A third reaction type, as yet unexplored for PFAFs, would consist of sequential additions of *different* substituents in a single reaction vessel: the addition of an anionic nucleophile followed by the addition of a cationic electrophile. These separate additions might not be to adjacent C atoms, which is commonly observed in cycloaddition reactions. To make the characterization of products and the determination of regioselectivity as straightforward as possible, an initial study of sequential nucleophile/electrophile additions to PFAFs with simple nucleophiles and with simple electrophiles was initiated in this work (for simplicity, two of the electrophiles, CN^+ and CH_3^+, have the same atomic composition as the two nucleophiles). Furthermore, introduction of CN moieties is expected to enhance the electron accepting strength, which was also explored.

This work explores the addition of nucleophiles and subsequent regioselective addition of electrophiles to a variety of PFAFs with the intention of understanding regioselectivity of specific carbon atoms while also synthesizing fullerenes with new electron accepting capabilities for use in advanced electronics. PFAFs are advantageous for such a study because, in many cases, the addition patterns of PFAFs and their derivatives can be readily determined by ^{19}F NMR spectroscopy by virtue of through-space $^{5,6,7}J_{FF}$ spin-spin coupling between proximate CF_3 groups and 2D ^{19}F COSY correlations.[10,32-34] No other addend X gives rise to multiple fullerene$(X)_n$ compositions and isomers that has this advantage. Unlike previous studies that determined the C=C bonds most susceptible to cycloaddition for C_{60} *derivatives*[35-37] and for higher fullerenes,[36-39] this work focused on the reactivity of *individual* cage C atoms to nucleophilic and to electrophilic attack. Would these C atoms belong to the most reactive C=C bonds? Even if they would, which of the two C=C atoms would react preferentially with the nucleophile? Would the electrophile then add to the second C atom of the original C=C bond or to a different cage C atom? And if it were possible to add two nucleophiles at the same time, where would the second nucleophile go? Presumably this would not be the second C atom of the original C=C bond. The seminal work of Wudl et al. and Peel et al., which demonstrated that the strong nucleophile CN^- adds to C_{60} and to $C_{60}(CN)_2$ in solution[40,41] and to C_{60}, C_{70}, and a variety of higher fullerenes in the gas phase[42-44] and that *p*-TsCN reacts with $C_{60}(CN)_n^-$ to form $C_{60}(CN)_{n+1}$ (n = 1, 3),[40,41] provided the stimulation for this study.

Modification of fullerene core with EWGs has been widely used to tune E_{LUMO} levels and achieve better OPV performance. For example, $C_{60}(CF_3)_{2,}$[45] and $C_{60}(CN)_2$[46] were reported as favorable alternatives to PCBM and C_{60}(indene) fullerene cycloadducts in certain active layer formulations. Furthermore, an electron-withdrawing CN moiety was intentionally attached to the

acceptor, C_{60}(indene), to match the orbital energies of a low-band-gap polymer, and power conversion efficiency in OPV devices showed improvements compared to underivatized C_{60}(indene).[47] Understanding the electron-withdrawing strength of new derivatives is paramount when designing new electron acceptors before using them in OPV devices. However, it has been recognized that derivatization has a complex influence on the electron-accepting properties of fullerenes. On one hand, saturation of the fullerene π-system that occurs upon addition of functional groups destabilizes the LUMO and hence decreases electron affinity (EA). On the other hand, EWGs tend to increase EA.

Recent experimental and theoretical studies of the gas-phase EAs and reduction potentials of PFAFs showed that for n = 6, 8, 10, or 12, the first reduction potentials for isomers of $C_{60}(CF_3)_n$ vary by 0.33, 0.39, 0.50, or 0.48 V, respectively.[20,48] This wealth of structure/property information led to a detailed understanding of how different addition patterns affect the locations, shapes, and energies of fullerene-derivative frontier orbitals, and therefore how addition patterns affect, or might affect, physicochemical properties (an illustrative example is that two isomers of $C_{60}(CF_3)_{10}$ that differ in the placement of only one CF_3 group have first reduction potentials that differ by 0.40 V).[20,48] Another even more striking example worth mentioning concerns two isomers of $C_{60}(CF_3)_6$; one isomer (C_1 symmetry, Schlegel diagram in Figure 1.1, left) is 0.26 V easier to reduce than C_{60}, whereas the other isomer (C_s symmetry, Schlegel diagram in Figure 1.1, right) is a weaker acceptor than C_{60} (−0.07 V vs. the $C_{60}^{0/-}$ couple) according to cyclic voltammetry.[48] This result might be erroneously interpreted as CF_3 groups having opposing electronic effects in these two isomers: it appears that CF_3 groups exhibit electron withdrawing effects in C_1-$C_{60}(CF_3)_6$ isomer, whereas CF_3 groups have electron donating effects in the C_s isomer. In fact, the reason for such a different electrochemical behavior

lies in the LUMO distributions on these fullerenes: the LUMO in the C_1 isomer is localized in the proximity of the electron withdrawing groups (EWGs), whereas the LUMO in the C_s isomer is located on the opposite side of the sphere, as shown on Figure 1.1.

Electronic properties of C_{70} TMFs were previously studied by cyclic voltammetry and theoretically using DFT, see Figure 1.2 for DFT calculated E_{LUMO} for $C_{70}(CF_3)_n$.[49] These studies revealed that all but one of $C_{70}(CF_3)_n$ molecules have significantly lower-lying LUMOs than the parent C_{70}, with $0.218 < \Delta E_{LUMO}$, vs. $C_{70} < 0.514$, and thus are much better acceptors than the parent C_{70}. The exception, an E_{LUMO} shift of only 0.036 eV was calculated for the most abundant isomer of $C_{70}(CF_3)_{10}$ (**70-10-1**). Such an unexpected result was in line with the observed small negative shift in $E_{1/2}$ vs. C_{70}. In case of all the other $C_{70}(CF_3)_n$ compounds, large positive shifts in $E_{1/2}$ vs. C_{70} were measured, and up to three quasi-reversible reductions were recorded. It was found that **70-8-2** had the highest positive shift in $E_{1/2}$ as well as the lowest-lying LUMO in the entire series (Figure 1.2).[49]

What if the addition pattern of a fullerene derivative remains constant, while the nature of the substituents vary (e.g., EWG vs. electron donating group (EDG), or different strength EWGs)? The Strauss/Boltalina group recently showed that it is possible to determine relative electron-withdrawing effects of R_F substituents in a series of 1,4-$C_{60}(R_F)_2$.[20] Direct comparison of electron-withdrawing effects of CF_3 and CN groups on E_{LUMO} in the isostructural compounds revealed that cyanation is stronger than trifluoromethylation.[48] The newly synthesized $C_{70}(CF_3)_n(CN)_m$ fullerene acceptors developed as part of this work offer a way to study electronic properties of each addend using LT PES and DFT calculations and compare with previously studied C_{60} derivatives. Theoretical E_{LUMO} predictions[48] as well as experimental evidence for cyanated C_{60} derivatives indicated that a considerable enhancement of acceptor properties

occurs when CN groups are attached to a parent C_{60}, $C_{60}(CF_3)_{2n}$ or C_{60}(indene).[50] [40,47] Furthermore, gas-phase studies of $C_{70}(CN)_n$ species by electrospray mass spectrometry accompanied by semi-empirical theoretical analysis demonstrated the propensity of C_{70} to form stable singly- and doubly-charged $C_{70}(CN)_n$ anions, where n = 1–6.[43] No bulk samples of $C_{70}(CN)_n$ compounds have been reported in the literature, so this new family of $C_{70}(CF_3)_n(CN)_m$ fullerene acceptors is the first of its kind for such a study. The family of $C_{70}(CF_3)_n$ compounds that were chosen as substrates for cyanation in this study currently includes dozens of structurally and spectroscopically characterized molecules, some of which can be prepared selectively and in large quantities.[49,51] Contrary to cyanated C_{60} derivatives, several cyanated C_{70} derivatives studied in this work exhibited an opposite effect on EA upon addition of CN groups. Therefore, one cannot consider cyanation as a general and straightforward approach for boosting acceptor properties in fullerenes and their derivatives.

Synthetically modifying PFAFs is interesting for application as materials for OPVs and also to be covalently linked to other functional molecules to afford supramolecular assemblies for other applications. Organic transistors have recently received considerable research attention due to the possibility to fabricate low-cost, printable, and flexible devices.[52] One-dimensional metal oxide (MO_x) nanostructures show promise as new components in high-tech electronics.[53] However, MO_x nanostructures suffer from substandard charge transfer across the particle/particle interfaces, so mainstream application has yet to be achieved. Tunable electron acceptors have been attached to ZnO nanorods in the form of self-assembled monolayers (SAMs) in order to tune the electrical properties of the ZnO nanostructures.[54-56] The Hirsch group from Friedrich-Alexander-Universität in Erlangen, Germany has shown that a SAM with C_{60}-acceptor units can accept and accumulate electronic charges when incorporated into organic thin-film memory

transistors.[55] The Hirsch group used C_{60} derivatives that differed by alkyl linkers of different chain lengths and formed SAMs on the surface of ZnO nanorods with different insulating properties to tune the electrical properties of ZnO nanorods.[56] The electron withdrawing C_{60} moiety was able to electronically couple with ZnO and as a result, the electrical performance of ZnO nanorods was improved. Further performance optimizations on SAM modified ZnO nanorods, and other MO_x such as AlO_x, require more efficient electron transfer and longer lifetimes of the reduced C_{60} moiety. SAMs consisting of PFAFs, which are superior electron acceptors to C_{60}, could ease the transfer of electrons and increase the lifetimes of the charged state (Figure 1.3). A variety of PFAFs could be tested to discover the optimal electron-withdrawing strength and degree of fluorine insulation.

Fullerenes can also be modified with polymerizable groups as another way for incorporation into supramolecular assemblies.[36] Specifically, endometallofullerenes could be incorporated into polymer beads that are used as tagging markers for cancer cells. Increased solubility and insulation from trifluoromethylation makes perfluoroalkyl endometallofullerenes (EMPFAFs) excellent candidates for inclusion into tagging beads. EMPFAFs with different metals could be attached in various ratios to polymer beads specific for different cancer types. Then the tagging markers could be analyzed by flow-cytometry inductively-coupled-plasma mass to determine which cancer cells are present based on the detection of specific metal-tagged polymer beads. In theory, thousands of specific markers could be synthesized by only using a few types of EMPFAFs in different ratios. The first proof-of-concept study of derivatization of EMPFAFs with polymerizable groups was undertaken in this work.

This chapter involves work that has been reproduced from *Chem. Eur. J.* **2013**, *19*, 5070-5080, *Chem. Eur. J.* **2013**, *19*, 15404-15409, *Phys. Chem. Chem. Phys*. **2015**, *17*, 551-556, and

Analyst **2015**, DOI: 10.1039/C5AN01129A with permission from John Wiley and Sons and The Royal Society of Chemistry. DFT calculations were performed by Alex Popov and coworkers, LT PES experiments were performed by Xue-Bin Wang and coworkers, collection and refinement of single crystal XRD structures of cyano modified fullerenes were performed by Natalia Shustova and Brian Newell, initial cyanide addition reactions were performed with help from Igor Kuvychko, FET measurements were performed by Thomas Schmaltz and Marcus Halik, EMPFAF syntheses were performed with Igor Kuvychko and James Whitaker, and cyclic voltammetry measurements were performed with the help of James Whitaker or by Popov and coworkers in the case of 70-10-1. Tyler Clikeman primarily performed the synthesis and characterization experiments, PES and DFT data interpretation, and collection and refinement of the other fullerene crystal structures.

1.2 Synthesis of $C_{60}(CF_3)_n$, $C_{70}(CF_3)_n$, and $M_3N@C_{80}(CF_3)_n$

Research interest in PFAFs began in 1991 shortly after the discovery of fullerene reactions and have received steady synthetic interest ever since.[8] As such, many synthetic methods to synthesize $C_{60}(CF_3)_n$ and $C_{70}(CF_3)_n$ have already been developed. Some of the more recent and large scale methods were used in this body of work in order to have ample starting material for additional derivatization, which will be briefly described below.

The GTGS reactor that was developed in the Strauss/Boltalina lab was used for the syntheses of $C_{60}(CF_3)_n$.[28] This reaction method was chosen because of its more selective synthesis of $C_{60}(CF_3)_n$ with low *n* values and reduces the ratio of **60-4-2(O)** to **60-4-2** compared to other synthetic methods, such as flow tube syntheses. In a typical reaction, C_{60} (500 mg) was loaded into the large GTGS thimble and the atmosphere was evacuated under dynamic vacuum while heating. The vacuum was removed and CF_3I (120 torr) was added when the hot plate

temperature reached 610 °C (note that the reaction temperature is ca. 500 °C). The thimble and cold finger began to immediately fill with brown, red, and black solid, indicating the reaction was in progress. The thimble was evacuated and filled with additional CF_3I (120 torr) every two hours and then the heat and all volatiles were removed after eight hours. Soluble products along with starting C_{60} were collected in toluene. Residual I_2 was removed before HPLC separation. This can be done by successively removing toluene/I_2 with a rotovap and adding/removing toluene until no I_2 is observed in the receiving flask. A faster and more efficient method is to remove I_2 by mixing the toluene solution with a saturated aqueous solution of sodium thiosulfate and collecting the organic layer. After I_2 removal, major products were then separated by one stage of HPLC (Figure 1.4) and the more minor and less easily separable products were combined for later separation in solvent mixtures with increased heptane that yield longer retention times. An ^{19}F NMR spectrum of the crude reaction mixture before HPLC separation is shown in Figure 1.5.

Utilizing a Buckyprep-M column for multiple stage HPLC separations of $C_{60}(CF_3)_n$ will typically yield higher purity derivatives with shorter retention times than when using a Buckyprep column. These separations were extensively explored by Bryon Larson and are described in his dissertation. Repetitive separations by Larson and I resulted in high-purity PFAFs that were suitable for single-crystal XRD experiments performed by myself. These XRD experiments were essential to confirm the unique CF_3 addition patterns that could not be confidently determined by ^{19}F NMR. Single-crystals of **60-8-3** were grown from the slow evaporation of a dichloromethane solution and crystallized in the monoclinic *Cc* space group with one dichloromethane molecule per fullerene, see Figure 1.6. In this case, the CF_3 addition pattern is the same as what was predicted by NMR experiments.[48]

In two other cases, spectroscopic experiments were not enough to ascertain the CF_3 addition pattern for PFAFs and the precise addition patterns of **60-10-14** and **60-12-X** were only determined after XRD experiments, see Figure 1.5 for ^{19}F NMR spectra. Diffraction quality single-crystals of **60-10-14** were grown by Bryon Larson via slow evaporation from solvent and it crystallized in the $P2_1/c$ space group without solvent inclusion. The CF_3 groups added in a ribbon of 8 hexagons plus an isolated hexagon as shown in Figure 1.6. This ribbon position was predicted from ^{19}F NMR spectra, but the two additions at the isolated hexagon were predicted to be at different carbon atoms of the same hexagon. The additions at the isolated hexagon are significantly far from the ribbon CF_3 groups, so that there is no F−F coupling, which makes the placement of the isolated hexagon difficult to predict without XRD. In the case of **60-12-X**, the CF_3 groups are in such close proximity that significant F−F coupling makes predicting the addition pattern difficult to interpret. Diffraction quality single-crystals of **60-12-X** were grown by Bryon Larson via the slow evaporation from solvent and it crystallized in the $P\bar{1}$ space group without solvent inclusion. The CF_3 groups add in a continuous ribbon in such a way that two CF_3 groups add to one C_{60} pentagon and only one cage pentagon is free of CF_3 additions (Figure 1.6).

For cyanation studies of C_{70} TMFs, two $C_{70}(CF_3)_n$ substrates were chosen, C_s-$C_{70}(CF_3)_8$ (**70-8-1)** and C_1-$C_{70}(CF_3)_{10}$ (**70-10-1**). Both compounds represent the most thermodynamically stable isomers among respective compositions and they form most abundantly in high-temperature syntheses. Notably, **70-10-1** contains a subset of the addition pattern of **70-8-1** plus the addition of 2 CF_3 groups (see Figure 1.19 for Schlegel diagrams). These derivatives can be readily prepared and isolated in practical amounts following previously reported literature procedures.[49,51] In a typical reaction, C_{70} (20 mg) and Cu (300 mg) powders were mixed and loaded in the center of a flow-tube that was placed in a furnace at room temperature. The tube

was evacuated under vacuum and then CF_3I was allowed to flow over the C_{70}/Cu mixture at ambient pressure. The temperature was increased to 560 °C and the reaction proceeded for two hours before heat and CF_3I flow were removed. The toluene soluble mixture was combined with similarly small-scale reactions for one large HPLC separation and the desired products were isolated in two stages (Figure 1.7).

The EMFs, $M_3N@C_{80}$ (M = Sc or Lu), were also decorated with trifluoromethyl groups using the specialized GTGS reactor. The cheaper and more abundant $Sc_3N@C_{80}$ was used first to perfect the reaction and work up procedure with the expectation that the more expensive and less abundant EMF would behave similarly. Previously optimized conditions described above to make $C_{60}(CF_3)_n$ (n < 12) were first explored. Low values for n were desired in order to not overcrowd the cage so that further derivatization may be sterically facilitated. Briefly, the EMF (4.0 mg) was heated to 550 °C under vacuum in the GTGS reactor and then charged with 600 torr of CF_3I gas for 5 hours. Upon cooling and removal of excess volatiles (I_2, CF_3I, etc.), the remaining dark solid was dissolved in toluene and analyzed by HPLC, see Figure 1.8. All of the solid appeared to dissolve and was a mixture of $Sc_3N@C_{80}(CF_3)_n$ (n = 0-18) with ca. 60 % conversion of starting EMF, according to HPLC integration. Unreacted $Sc_3N@C_{80}$ could be recycled after HPLC separation and re-used for derivatization.

The same optimized conditions for the synthesis of $Sc_3N@C_{80}(CF_3)_n$ were then used as a starting point for similar reactions with $Lu_3N@C_{80}$. Unlike the previous $Sc_3N@C_{80}(CF_3)_n$ reaction, a substantial portion of this product mixture was poorly soluble in toluene. The toluene insoluble material was recovered with *o*-DCB and was mostly unreacted $Lu_3N@C_{80}$. The toluene soluble material made a brown orange solution that was analyzed by HPLC. The HPLC analysis

showed that many products were formed and that most of the soluble material (> 80 %) was unreacted $Lu_3N@C_{80}$.

Several more conditions were attempted in order to increase conversion and optimize the conditions. First, an experiment was performed by Igor Kuvychko with excess copper and more CF_3I, which resulted in outstanding conversion but a high number of additions ($Lu_3N@C_{80}(CF_3)_{16\text{-}20}$). This sample was found to have poor incorporation into polymer beads, so the attempt to make derivatives with low CF_3 additions continued. Five more reactions were performed using a total of 30.5 mg $Lu_3N@C_{80}$ with CF_3I pressure of 580–650 torr, T_{HP} = 575–650 °C, and 0.5–1.5 h reaction time. The best combination of conversion to products with low CF_3 additions and low degree of insoluble material was found with high temperatures (~650 °C), high pressure of CF_3I (> 600 torr), and short reaction times (0.5 – 1.5 h). These conditions were far from optimized, but led to some conversion into the desired low CF_3 addition products. These products were separated as a whole from unreacted $Lu_3N@C_{80}$ by HPLC in toluene (Figure 1.9). The best separation used the semi-preparative Buckyprep-M column because retention times were about half as long as when using the semi-preparative Buckyprep column. The separated, unreacted $Lu_3N@C_{80}$ was combined with the *o*-DCB soluble material and used for additional GTGS reactions by either James Whitaker or myself. The desired HPLC separated material was combined and either sent to collaborators in Toronto for polymer incorporation or used for additional reactions described later in this chapter. The composition was determined only by mass spectrometry and HPLC because only low ^{19}F signal was observed in NMR spectra, possibly due to the presence of multiple products with low symmetry.

1.3 Cyanation of $C_{60}(CF_3)_n$: Synthesis and Characterization

1.3.1 Tetraethylammonium Cyanide Reactions with 60-2-1

Reactions of NEt_4CN with **60-2-1** vary greatly depending on the solvent choice. The addition of a colorless acetonitrile solution of NEt_4CN to a brown $C_6D_6/PhCH_3$ solution of **60-2-1** produces one predominant isomer of ***C*$_1$-(60-2-1)(CN)$^-$**, but only after several hours or days of reaction, depending on the amount of NEt_4CN added. The ^{19}F NMR singlet from the two CF_3 groups on **60-2-1** instantly disappears upon NEt_4CN addition and several new singlets and broad, unrefined multiplets appear over time (Figure 1.10). The two quartets that correspond to the predominant isomer of ***C*$_1$-(60-2-1)(CN)$^-$** become more refined after one hour and do not achieve maximum sharpness and intensity for seven hours when one equivalent of NEt_4CN is used. If only half an equivalent of NEt_4CN is used, then the two quartets do not reach maximum sharpness for at least two days. In either case, the resulting ^{19}F NMR spectrum of the mixture exhibits two predominant quartets from asymmetric ***C*$_1$-(60-2-1)(CN)$^-$**, two singlets which are assumed to arise from different, symmetric isomers of **(60-2-1)(CN)$^-$**, and no singlet from **60-2-1** itself. The lack of ^{19}F NMR signal from **60-2-1**, even when only half an equivalent of NEt_4CN is used, indicates that some fast exchange between **60-2-1** and the other species must occur. Furthermore, the two sharp quartets disappear or become too broad to be observed in the NMR experiment when excess NEt_4CN is added after the 1:1 mixture has reached the slow exchange conditions. The excess free CN^- must allow exchange between **60-2-1**, ***C*$_1$-(60-2-1)(CN)$^-$**, and free CN^- to be constant. It appears that the stable isomer cannot persist because free CN^- is able to interact with the PFAF species and cause indefinite rapid exchange.

The reaction conditions drastically improve when the reaction is performed in DCM instead of the previous solvent mixture. The two quartets corresponding to asymmetric ***C*$_1$-(60-2-**

1)(CN)⁻ instantly appear in the ^{19}F NMR spectrum when one or more equivalents of NEt_4CN are added to **60-2-1** (Figure 1.11B). The two quartets comprise ≥ 95 % of the signal intensities and only a small singlet from another minor isomer is also observed. A sharp singlet from **60-2-1** and the two predominant quartets from ***C*$_1$-(60-2-1)(CN)⁻** were also instantly observed when a deficiency of NEt_4CN was added, indicating that the previously observed fast exchange regime does not occur in DCM.

The appearance of two quartets indicates that the addition of CN^- breaks the symmetry of **60-2-1** and forms a ***C*$_1$-(60-2-1)(CN)⁻** species that is consistent with C_1 symmetry. DFT calculations performed by Alex Popov suggest that ***C*$_1$-(60-2-1)(CN)⁻** has the p^2 addition pattern shown in Figure 1.11B. All 31 possible isomers of ***C*$_1$-(60-2-1)(CN)⁻** were calculated. Their relative energies range from 0.0 to 54.5 kJ mol^{-1} where the lowest energy isomer is more than 13 kJ mol^{-1} lower in energy than all other isomers. If the p^2 addition were true, this would indicate thermodynamic control for the nearly regiospecific addition of CN^- to **60-2-1**. The LUMO diagram shown in Figure 1.12 also clearly shows that the kinetically favored positions for the addition of a nucleophile the size of CN^- are C10, C11, and C28 if C8 is too sterically congested for facile cyanide addition (symmetry-related C atoms are omitted). Therefore, formation of the p^2 intermediate shown in Figure 1.11B appears to be kinetically and thermodynamically favored.

1.3.2 Addition of Electrophiles to $C_{60}(CF_3)_2(CN)^-$

Subsequent addition of the electrophiles CH_3^+ or H^+ led cleanly to only two isomers of ***C*$_1$-(60-2-1)(CN)(X)** in ca. 3:2 (X = CH_3) or ca. 1:1 (X = H) mole ratios, respectively (Figure 1.11). According to the ESP calculated for **(60-2-1)(CN)⁻**, the most likely carbon atoms susceptible to electrophilic attack are C8 and C10. However, as shown in Figure 1.12 and in Table 1.1, electrophilic attack at these two sites led to *ortho-meta-para* (*omp*) products, for X =

CH_3, that differ in relative energy by 19.1 kJ mol^{-1}. Furthermore, there are two p^3 product isomers that are within 2.6 kJ mol^{-1} of the 19.1 kJ mol^{-1} *omp* product (also for X = CH_3).

The effects of sterics on the relative stabilities of the ***C*$_1$-(60-2-1)(CN)(X)** compositions was examined by calculating the ΔE values for the X = H isomers. The p^3 isomers are predicted to be less stable than the *omp* isomers by $\geq$ 32 kJ mol^{-1} for X = H but by only $\leq$ 22 kJ mol^{-1} for X = CH_3, and, significantly, the two *omp* isomers differ by only 0.4 kJ mol^{-1} for X = H but by 19.1 kJ mol^{-1} for X = CH_3. Therefore, for two reasons, it appears that the electrophilic addition of CH_3^+ or H^+ to ***p*^{2}-(60-2-1)(CN)$^-$** must be under kinetic control: (i) two isomers are formed for X = CH_3 even though the DFT-predicted second most stable isomer is nearly 20 kJ mol^{-1} higher in energy than the most stable isomer; (ii) the same two predominant isomers appear to be formed for electrophiles of different size, X = H or CH_3 (based on their ^{19}F NMR spectra), in approximately the same relative amounts, despite the fact that the difference in energy for the two most-stable isomers is less than 1 kJ mol^{-1} for X = H but 19.1 kJ mol^{-1} for X = CH_3.

An additional piece of relevant evidence is shown in the ^{19}F NMR spectrum, in Figure 1.11E, produced by the addition of *p*-TsCN to ***C*$_1$-(60-2-1)(CN)$^-$**. Only *one* predominant isomer was formed, which is *asymmetric*, and all multiplets have very different δ values than the quartets for either of the X = CH_3 or H products. The spectrum in Figure 1.11 also exhibits two, much less intense, singlets which must arise from symmetric isomers of **(60-2-1)(CN)$_2$**. If this is the **(60-2-1)(10,11-CN)$_2$** isomer, then there must be an explanation for the absence of a second predominant isomer of this composition. If the predominant isomer is **(60-2-1)(11,27-CN)$_2$**, possibly for steric reasons because the electrophilic reagent *p*-TsCN is sterically more demanding than either CH_3OTf or CF_3COOH, then the absence of symmetric **(60-2-1)(11,24-CN)$_2$** as a second *predominant* isomer must be explained, since the environment of C24 is

sterically similar to that of C27. One tentative hypothesis is that the electrophilic reagent is attracted to the site of greatest negative charge on the surface of the **(60-2-1)(11-CN)**$^-$ intermediate, which is the cyano N atom, and from there the incipient electrophile adds to the *closest*, sterically-accessible cage C atom with substantial negative charge, either C27 in the case of *p*-TsCN or both C10 and C27 in the case of either CH_3OTf or CF_3COOH. However, without confirmation by X-ray crystallography, at this time, the most-likely addition patterns for the predominant isomers of **(60-2-1)(CN)(CH_3)**, **(60-2-1)(CN)(H)**, or **(60-2-1)($CN)_2$** cannot be confidently predicted.

There is also a possibility that *p*-TsCN is not what is directly reacting with ***C*$_1$-(60-2-1)(CN)$^-$**. The addition of excess *p*-TsCN to ***C*$_1$-(60-2-1)(CN)$^-$** in DCM led to the formation of one major isomer of ***C*$_1$-(60-2-1)($CN)_2$** within five hours (compared to several days). Presumably, the excess NEt_4CN reacts with *p*-TsCN to form $(CN)_2$ and then $(CN)_2$ reacts with ***C*$_1$-(60-2-1)(CN)$^-$** faster and more selectively than *p*-TsCN. The reaction proceeds much slower and less selective when no free NEt_4CN is present. In either case, the ^{19}F signals (Figure 1.14) from the dicyano products have very different chemical shifts than products from the previous two electrophiles, so it appears to be adding to a completely different carbon. This difference is probably due to $(CN)_2$ being less attracted to the site of greatest negative charge or simply the smaller size of $(CN)_2$ compared to the other electrophilic reagents.

1.3.3 Addition of Other Nucleophiles to 60-2-1

An attempt to generate the "opposite isomer" of ***C*$_1$-(60-2-1)(CN)(CH_3)** was explored by first adding CH_3^- as a nucleophile and quenching with electrophilic CN. An Et_2O solution of $LiCH_3$ (ca. one equivalent) was added to a brown, toluene solution of **60-2-1**. The solution appeared to become darker brown and formed brown precipitates. The ^{19}F NMR spectrum of the

solution containing brown precipitates showed a singlet from **60-2-1** along with two quartets (ca. 6%). A significant amount of brown solid precipitated immediately after adding one more equivalent of $LiCH_3$ (ca. two total equivalents). The resulting ^{19}F NMR spectrum showed no peak from unreacted **60-2-1**, but still had a small signal from the two quartets. Apparently all **60-2-1** reacted to form mostly insoluble **(60-2-1)$(CH_3)_n^{n-}$**. The solution was light brown with a lot of dark brown precipitate. Subsequent addition of *p*-TsCN in toluene (2 equivalents) resulted in a brown solution and no remaining solids after 2 days. The ^{19}F singlet from **60-2-1** returned upon dissolution and no new peaks in the ^{19}F NMR spectrum appeared. It appears that *p*-TsCN was able to extract CH_3^- from insoluble (**60-2-1)$(CH_3)^-$** and reverse the reaction to form starting **60-2-1** instead of desired ***C*$_1$-(60-2-1)(CH_3)(CN)**.

In related experiments, solutions of tetrabutylammonium azide in DCM and tetrabutylammonium thiocyanate in acetone were each added to a solution of **60-2-1** in DCM (11 equivalents of nucleophile). In both cases, the ^{19}F NMR indicated that no reaction had occurred even after 24 h since the only observable peaks were from **60-2-1** and no solids were observed. Perhaps the reagents are too bulky for the nucleophilic additions to occur readily in DCM or N_3^- and SCN^- are not strong enough nucleophiles to add to **60-2-1**.

1.3.4 Tetraethylammonium Cyanide Reactions with 60-4-2

Similar to reactions with **60-2-1**, choosing the correct solvent mixture was essential when adding CN^- to **60-4-2**, see Figure 1.15 for molecular diagram. Cyanation proceeded slowly and required > 10 equivalents NEt_4CN when **60-4-2** was dissolved in $CDCl_3$ and NEt_4CN was added as a CH_3CN solution. However, the reaction proceeded almost instantaneously and only required 1 equivalent of NEt_4CN when all reactants were added via DCM. The addition of a DCM solution of NEt_4CN to a brown DCM solution of **60-4-2** yielded a brown soluble material, **(60-4-**

2)(CN)$^-$ which exhibited an ^{19}F NMR spectrum with only two predominant CF_3 multiplets, as shown in Figure 1.15. The two predominant multiplets were also observed in the original $CDCl_3/CH_3CN$ mixture, but other minor multiplets were also present in significant amounts. Interestingly, in either solvent mixture, the multiplets corresponding to **(60-4-2)O** remain unchanged. This indicates that the 54 sp^2-C atoms of **(60-4-2)O** are relatively unreactive and demonstrates the stability of **(60-4-2)O** towards nucleophilic attack. On the other hand, **60-4-2** has a particularly reactive and short double exocyclic bond in the fulvene fragment on the cage in the proximity of CF_3 groups. This is the same bond that completely and selectively forms **(60-4-2)O** upon oxidation. It is clear that one carbon atom along this double bond must be the predominant site for CN^- addition, since only one multiplet pattern of **(60-4-2)(CN)$^-$** dominates the ^{19}F NMR spectrum. The $C_{60}X_5$ addition pattern arising from addition of CN^- at the end of the fulvene fragment is very common among $C_{60}X_5$ derivatives.[57-61] This particular addition pattern creates a stabilizing effect of the aromatic cyclopentadiene anion moiety on the central pentagon. Cyanide addition to this carbon atom is also predicted to be most favorable by DFT calculations performed by Alex Popov, so it is the most likely site for CN^- addition.

1.3.5 Addition of an Electrophile to (60-4-2)(CN)$^-$

The most likely site for electrophilic addition of H^+ would appear to be at the C atom on the cyclopentadiene ring adjacent to CN^-. Experimental and DFT experiments indicate that this is not the case. Subsequent addition of CF_3COOH to **(60-4-2)(CN)$^-$** resulted in the immediate formation of an orange compound (**(60-4-2)(CN)H**) that was readily purified by HPLC. Interestingly, the two unresolved multiplets from the four CF_3 groups in **(60-4-2)(CN)$^-$** became four well resolved multiplets upon H^+ addition (two quartets and two apparent septets, Figure 1.16). The asymmetry of the CF_3 multiplets illustrates that H^+ does not add to the carbon atom

located in the *ortho* position with respect to the carbon atom bonded to the CN group. However, the UV-Vis spectrum of **(60-4-2)(CN)H** resembles the spectrum of **(60-4-2)O** and **60-6-2**.[48,62] Notably, the distinctive peak near 385 nm is present in all three cases and the broad peaks that are only present for starting **60-4-2 (**between 450–500 and 550–700 nm) are absent in the spectrum of **(60-4-2)(CN)H**. This similarity in UV-Vis spectra suggests that H^+ added to a C atom on the central cyclopentadiene (**(60-4-2)(CN)H-1**, **(60-4-2)(CN)H-2**, and **(60-4-2)(CN)H-3** shown in Figure 1.15), but the asymmetric nature in the ^{19}F NMR spectrum suggests that isomer 3 is not possible. Note that the fullerene π system is identical for all three isomers.

The DFT-derived gas-phase energies of three possible isomers with different positions of H atoms in **(60-4-2)(CN)H** (structures **(60-4-2)(CN)H-1**, **(60-4-2)(CN)H-2**, and **(60-4-2)(CN)H-3** on Figure 1.14) are very close at the PBE/TZ2P level, but the isomer with the H attached near the "internal" CF_3 (structure (**60-4-2)(CN)H-1**) is lower than the asymmetric (**60-4-2)(CN)H-2** and symmetric (**60-4-2)(CN)H-3** in energy by 4.5 kJ mol^- and 4.9 kJ mol^-, respectively. A similar DFT result was obtained for the hypothetical compound **(60-4-2)H_2**, i.e., the isomer with the same addition pattern as (**60-4-2)(CN)H-1,** was 6.4 kJ mol^{-1} lower in energy than an isomer with the same addition pattern as (**60-4-2)(CN)H-2.** In view of this small energy difference, computations at the B3LYP-D3/def2-TZVP level (with dispersion correction) were also performed and virtually the same values in the gas phase (within 1 kJ mol^{-1}) were found. Solvation energy corrections (computed for DCM using C-PCM model at the B3LYP/6-311G** level) further destabilized the isomer (**60-4-2)(CN)H-3** (ΔE = 16.9 kJ mol^{-1}) with respect to the isomer (**60-4-2)(CN)H-1**, however the isomer **(60-4-2)H** became 0.8 kJ mol^{-1} more stable than the latter. The barriers of the interconversion between **(60-4-2)(CN)H-1**, **(60-4-2)(CN)H-2**, and **(60-4-2)(CN)H-3** all exceed 110-130 kJ mol^{-1}, such interconversion is not to be expected at

room temperature. So far, it is not possible to distinguish between **(60-4-2)(CN)H-1** and **(60-4-2)(CN)H-2** based on these computational data.

The product compositions after the first and second reaction steps were determined by mass spectrometry as $C_{60}(CF_3)_4(CN)^-$ and $C_{60}(CF_3)_4(CN)H$, respectively (Figure 1.17). Partial dehydrogenation of $C_{60}(CF_3)_4(CN)H$ was observed during the mass spectrometry analysis, even under mild NI-APCI and NI-ESI MS conditions, as followed from the isotopic distribution analysis of its peak, leading to the generation of $C_{60}(CF_3)_4(CN)^-$. Complete dehydrogenation was observed in the ESI ion source during LT PES measurements, which will be discussed in section 1.6.

1.3.6 Stability of (60-4-2)(CN)⁻ and (60-4-2)(CN)H in Air

The stabilities of **(60-4-2)(CN)H** and $(NEt_4)^+$ salt of **(60-4-2)(CN)⁻** were determined in solution under ambient and anaerobic conditions prior to photoelectron spectroscopy studies that will be described in section 1.6. **(60-4-2)(CN)H** is stable for weeks as a solid under ambient conditions and compound **NEt_4^+(60-4-2)(CN)⁻** is relatively stable in aerobic solution for days, as confirmed by ^{19}F NMR. Compound **NEt_4^+(60-4-2)(CN)⁻** remains stable for days as a brown DCM solution under anaerobic conditions, and only shows minor degradation under ambient conditions when a slight excess of NEt_4CN is present (Figure 1.18). After the ^{19}F NMR spectrum of **NEt_4^+(60-4-2)(CN)⁻** was obtained in anaerobic conditions, the solution was exposed to air and a small amount of brown precipitates immediately formed along with small peaks in the ^{19}F NMR spectrum. The ^{19}F NMR spectrum remained the same in appearance for 6 days (Figure 1.18) confirming that the degradation reaction for **NEt_4^+(60-4-2)(CN)⁻** is slow, even in ambient conditions. The stability of this fullerene anion under ambient conditions opens new venues for design of air-stable molecular complexes. Conversion of **(60-4-2)(CN)H** back into **(60-4-**

2)(CN)$^-$ can be easily realized by removal of proton upon the addition of proton sponge in anaerobic conditions, as shown in the ^{19}F NMR spectrum in Figure 1.16. A large excess of proton sponge was added to ca. 0.3 mg HPLC purified **(60-4-2)(CN)H** in 0.8 mL DCM and the color remained yellow the entire time. The two multiplets in the ^{19}F NMR spectrum shown in Figure 1.16 have slightly different chemical shifts from **NEt_4^+(60-4-2)(CN)$^-$**, which is probably due to differences in ion-pairing from the different solvent environment (i.e. DCM enriched with proton sponge) and the different cation (proton sponge(H)$^+$ vs. NEt_4^+). The spectrum stayed the same for six days even when it was exposed to air (Figure 1.18). The salt complex is not stable on silica gel. The mixture was passed through a silica gel column to remove proton sponge. Not too surprisingly, the bare anion degrades quickly on silica gel when the proton sponge is removed, as indicated by the resulting ^{19}F NMR spectrum.

1.4 Cyanation of $C_{70}(CF_3)_n$: Synthesis and Characterization

1.4.1 Tetraethylammonium Cyanide Reactions with 70-8-1

Adding ten substituents to C_{70} often results in the formation of the p^9o(loop) addition pattern which was first observed crystallographically for $C_{70}Br_{10}$.[63] The addition pattern has not been observed for $C_{70}(CF_3)_{10}$ isomers, presumably due to the steric hindrance of the rather bulky CF_3 groups. However, this addition pattern has been observed in TMF derivatives, specifically **(70-8-1)Cl_2**[30] and **[70-8-1]$_2$**.[29] These two TMF derivatives also represent two of the few examples of regioselective additions to **70-8-1**. The work discussed below represents another class of regioselective addition to **70-8-1**; nucleophilic addition of cyanide followed by the addition of an electrophile.[64]

Working with dilute solutions of **70-8-1** is best in order to avoid the loss of **70-8-1** to dimerization.[29] Dimerization across the C11–C29 bond of **70-8-1** causes an insoluble yellow

solid to crash out of concentrated solutions. Therefore, the addition of a colorless solution of NEt_4CN in MeCN was added to a dilute solution of **70-8-1** in toluene resulting in the immediate formation of a greyish-blue solution. The ^{19}F NMR spectrum of the new solution contains eight multiplets that were assigned to $\boldsymbol{C_1}$**-(70-8-1)(CN)$^-$**, indicating that the original C_s symmetry of **70-8-1** was broken by the addition of CN^- (Figure 1.20). In some cases, a second set of eight multiplets was observed, indicating that another minor isomer of $\boldsymbol{C_1}$**-(70-8-1)(CN)$^-$** was formed. In either case, the subsequent addition of a colorless solution of *p*-TsCN in toluene resulted in a light brown solution containing an abundant derivative, $\boldsymbol{C_s}$**-(70-8-1)(CN)$_2$** (90+ mol% regioselectivity), that exhibited an ^{19}F NMR spectrum with only four multiplets, indicating reestablishment of C_s symmetry. A minor isomer, $\boldsymbol{C_1}$**-(70-8-1)(CN)$_2$**, was present in approximately 10 mol% yield based on ^{19}F NMR spectroscopy and exhibited an eight-multiplet containing spectrum, which indicated C_1 symmetry. HPLC was used to purify the major isomer, $\boldsymbol{C_s}$**-(70-8-1)(CN)$_2$**, and minor isomer, $\boldsymbol{C_1}$**-(70-8-1)(CN)$_2$**, from unreacted **70-8-1** and small amounts of other unknown compositions.

X-ray crystallography revealed that $\boldsymbol{C_s}$**-(70-8-1)(CN)$_2$** has the C_s-p^9o(loop) addition pattern shown in Figure 1.21. The p^9o(loop) addition pattern was recently observed for $C_{70}(CF_3)_8Cl_2$ (**C_s-(70-8-1)(Cl)$_2$**).[30] In these derivatives, the C11–C29 bond (the only cage $C(sp^3)$–$C(sp^3)$ bond) is long. It is 1.656(8), 1.63(1), and 1.59(2) Å in **C_s-(70-8-1)(CN)$_2$**, **C_s-(70-8-1)(Cl)$_2$**, and $C_{70}Br_{10}$, respectively. The C_{70} cage centroids, ⊙, form rigorously planar pseudo-hexagonal arrays in crystallographic *ab* planes with ⊙···⊙ distances within each layer that range from 10.49 to 12.26 Å (Figure 1.21). These layers are stacked in the crystallographic *c* direction with 13.17 Å spacings, resulting in pseudo-HCP packing. Within each layer the molecular DFT-predicted

dipole vectors have the same *b* component, and alternate strongly-dipolar layers have their resultant dipole vectors in the +*b* or −*b* direction.

Figure 1.22 shows the IUPAC numbering for C_{70}, the DFT-predicted LUMO of **70-8-1**, and a DFT-predicted ESP diagram for the **(70-8-1)(CN)**$^-$ isomer with its CN group on C11. It is virtually certain that the predominant **(70-8-1)(CN)**$^-$ isomer is the 11-CN isomer because the predominant product, **(70-8-1)(CN)$_2$**, has CN groups on C11 and C29 (note that C11 and C29 are symmetry related in **70-8-1**). The DFT calculations listed in Table 1.2 show that the 11-CN anion is favored by 7.6 kJ mol^{-1} over the next most stable isomer, which has the CN group on C25. In addition, nucleophilic attack on C11 in **70-8-1** is also favored due to the large contributions of p-π orbitals on C11 (and C29) to the LUMO of **70-8-1**. The PFAF **70-8-1**, with its C_s-p^7 addition pattern, is unusual in that the addition of two Cl atoms initiated by ICl electrophilic (or radical) attack, *and* the addition of two CN groups initiated by CN$^-$ nucleophilic attack, *both* lead to a C_s-p^9o(loop) isomer as the abundant product. This is because *both* the HOMO and the LUMO of **70-8-1** have large contributions from the p-π orbitals on C11 and C29.

The ESP for the 11-CN isomer of **(70-8-1)(CN)**$^-$, mapped onto its van der Waals surface, indicates that the cage C atoms with the greatest negative charge are C29 and C31, which should be the two sites favored for electrophilic attack by *p*-TsCN. Combined with the results in Table 1.2, CN$^+$ addition to C29 is favored relative to any other cage C atom. This explains the formation of the major C_s isomer, ***C*$_s$-(70-8-1)(CN)$_2$**. If minor isomer ***C*$_1$-(70-8-1)(CN)$_2$** is formed from the minor 25-CN isomer of **(70-8-1)(CN)**$^-$ (7.6 kJ mol^{-1} less stable than the 11-CN isomer), then the most likely addition pattern of ***C*$_1$-(70-8-1)(CN)$_2$** is the C_1-p^7mp addition pattern (i. e. the same addition pattern observed in **70-10-1**), with CN groups on C10 and C25. Interestingly, **70-10-1**, the lowest energy isomer of $C_{70}(CF_3)_{10}$, is predicted to be only 12.4 kJ mol^{-1} lower in

energy than the putative isomer C_s-p^9o(loop)-$C_{70}(CF_3)_{10}$, while ***C*$_s$-(70-8-1)(CN)$_2$** is predicted to be 42.6 kJ mol^{-1} lower in energy than C_1-p^7mp-$C_{70}(CF_3)_8(CN)_2$. The small difference in DFT-predicted energies for **70-10-1** and C_s-p^9o(loop)-$C_{70}(CF_3)_{10}$ is clearly due to the large size of CF_3 substituents, since the hypothetical isomer C_s-p^9o(loop)-$C_{70}H_{10}$ is 47.1 kJ mol^{-1} lower in energy than the hypothetical isomer C_1-p^7mp-$C_{70}H_{10}$.

Another possibility is that the minor isomer derives from CN^+ addition to C31 of the 11-CN isomer of **(70-8-1)(CN)$^-$**. This would produce a C_1-p^9-isomer of **(70-8-1)(CN)$_2$**, an addition pattern known for two symmetric $C_{70}X_{10}$ compounds, C_2-p^9-$C_{70}(CF_3)_{10}$[49] and C_2-p^9-C_{70}(*t*BuOO)$_{10}$.[65] However, the UV-Vis spectrum of the minor isomer is nearly congruent with the spectrum of **70-10-1** and significantly different than the spectrum of C_2-p^9-$C_{70}(CF_3)_{10}$ (Figure 1.23). Therefore, the minor isomer is most likely ***C*$_1$-*p*^{7}*mp*-(70-8-1)(CN)$_2$**, formed from the 25-CN minor isomer of **(70-8-1)(CN)$^-$**. Note that this is an example of a pair of substituents being added to the *para* positions of a cage hexagon instead of a cage C=C bond, even though the addition of the same substituents to a cage C=C is possible (and in fact, in this case, represents the more abundant product).

1.4.2 Addition of Other Nucleophiles to 70-8-1

Nucleophilic additions of N_3 and SCN were attempted in similar reactions to the attempted **60-2-1** reactions described in Section 1.3.3. Solutions of tetrabutylammonium azide in DCM and tetrabutylammonium thiocyanate in acetone were each added to a solution of **70-8-1** in DCM (22 equivalents of nucleophile). In both cases, the ^{19}F NMR spectra indicated that no reaction had occurred even after 24 h since the only observable peaks were from the **70-8-1**. Solids were formed in both cases which are most likely from dimer formation and may or may not be influenced by the addition of the TBA reagents. Perhaps the reagents are too bulky for the

nucleophilic additions to occur readily in DCM or N_3 and SCN are not strong enough nucleophiles to add to **70-8-1**. Since these reactions failed with **60-2-1** and **70-8-1** they were not attempted with any other PFAF.

1.4.3 Tetraethylammonium Cyanide Reactions with 70-10-1

Another C_{70} TMF was used to study the versatility of cyanide reactions, *C_1-p^7mp*-$C_{70}(CF_3)_{10}$, **70-10-1**. This asymmetric compound has 60 unique C(sp^2) atoms to which a nucleophile might add. The C33–C34 bond has been shown to be reactive towards cycloadditions,[36-39] but never has an experiment showed which specific atom is more reactive. A single nucleophilic addition to asymmetric **70-10-1** could reveal which C(sp^2) atom of the double bond is more reactive; it is even possible that one of the other 58 C(sp^2) atoms apart from the C33–C34 is actually more susceptible towards nucleophilic attack.

Addition of a colorless solution of NEt_4CN in MeCN to a yellow solution of **70-10-1** in C_6D_6/toluene resulted in the immediate formation of a green species with a new set of 10 CF_3 multiplets in the ^{19}F NMR spectrum (Figure 1.24). Subsequent addition of an excess of CH_3OTf or CF_3COOH resulted in the immediate formation of yellow solutions containing, in both cases, one major product. These were each purified by HPLC and exhibited nearly identical ^{19}F NMR spectra, suggesting that CH_3^+ and H^+ add to the same C atom.

As shown earlier, the solvent choice for nucleophilic CN^- was very important in **60-2-1** and **60-4-2** reactions. Performing the nucleophilic cyanation reaction with **70-10-1** in toluene, benzene, dichloromethane, chloroform, acetonitrile, or various mixtures of the solvents did not significantly affect the rate or selectivity of the reaction. The immediate formation of **(70-10-1)(CN)$^-$** was observed in all reaction conditions when one or two equivalents of NEt_4CN versus

70-10-1 were used. On the other hand, a large excess of electrophile was necessary to push the reaction to completion. Deficient amounts of electrophile resulted in the reverse reaction and recovery of **70-10-1**. A large excess of electrophile is required to push the reaction to completion. In various solvent mixtures, the reaction reverts back to 100% **70-10-1** when less than 10 equivalents MeOTf are added to the cyano anion, produces 100% **(70-10-1)(CN)(CH_3)** when more than 30 equivalents are added, and produces a mixture of **70-10-1** and **(70-10-1)(CN)(CH_3)** when intermediate ratios are used. In an NMR experiment, one equivalent of Et_4NCN was reacted with one equivalent of **70-10-1** in CD_2Cl_2 with *p*-trifluoromethyl benzene as an internal standard. This internal standard was used so that the fluorine:hydrogen ratio in the reaction mixture could be calculated. Upon the addition of MeOTf (ca. 5 equiv.) the ^{19}F NMR spectrum only exhibited multiplets from **70-10-1** and a singlet for CH_3CN appeared in the ^{1}H NMR spectrum. More CH_3CN formed when an additional equivalent of Et_4NCN was added to the mixture and no multiplets for **(70-10-1)(CN)$^-$** or **(70-10-1)(CN)(CH_3)** were observed in the ^{19}F NMR spectrum. This demonstrates that the cyanide has some lability and can react with CH_3^+ to produce acetonitrile. The CH_3^+ electrophile has a higher affinity towards the cyano anion than for the cyanofullerene anion. Any free cyanide will quickly react with a methyl cation to produce acetonitrile, so if the cyanide on the PFAF has any lability it will quickly be consumed by methyl cations. Similar results were observed when less than an excess of *p*-TsCN was added to **(70-10-1)(CN)$^-$**.

NMR and NI-APCI MS spectra indicate the successful additions of CN^- and CH_3^+ to **70-10-1**, but they cannot determine which carbon atom reacts with each moiety. Absorption spectra of known $C_{70}(CF_3)_{10}$ compounds were compared with **(70-10-1)(CN)(CH_3)** to determine the addition pattern. Cycloadducts across the C33–C34 bond sufficiently disrupted the pi system of

70-10-1 and Ovchinnikova et al. were able to observe new absorption peaks in **(70-10-1)[C($CO_2Et)_2$]** compared with starting **70-10-1**.[17] In the case of **(70-10-1)(CN)(CH_3)**, the absorption spectrum looks strikingly similar to **70-10-1**, so DFT calculations were used to determine which C atoms are most reactive.

DFT calculations performed by Alex Popov suggest that the **(70-10-1)(CN)**$^-$ intermediate probably has its CN group on C34, as shown in Table 1.3 and Figure 1.25, although the preference for this site is only 6.6 kJ mol^{-1}. Based on the p-π orbital contributions to the LUMO and LUMO+1 of **70-10-1**, the sites favored for nucleophilic attack by CN^- on **70-10-1** may be C33 and C34, followed by C29 and C11 (which are sterically crowded because they share a pentagon or a pentagon *and* a hexagon, respectively, with CF_3 groups). The LUMO in Figure 1.26 is based on figures published in 2008.[17,49] Although LUMO+2 is only 0.04 eV above LUMO+1, it is not shown because the same cage C atoms are involved. Therefore, the remarkably selective nucleophilic addition of CN^- to **70-10-1** may be under kinetic as well as thermodynamic control, because all of the other low-energy CN^- addition sites (except C33), not just C11 and C29, share a pentagon or a pentagon and a hexagon with bulky CF_3 groups.

If the CN group is indeed on C34 in **(70-10-1)(CN)**$^-$, then the product with its CH_3 group on C33 (i.e., **(70-10-1)(34-CN)(33-CH_3)**) may also be kinetically and thermodynamically favored: kinetically according to the ESP for **(70-10-1)(CN)**$^-$ shown in Figure 1.26 as well as the fact that all other cage C atoms share a pentagon with a CF_3 group, and thermodynamically by more than 46 kJ mol^{-1}. Note that there is only a 1.0 kJ mol^{-1} difference in the DFT-predicted energies of **(70-10-1)(34-CN)(33-CH_3)** and **(70-10-1)(33-CN)(34-CH_3)**.

The **(70-10-1)(44-CN)(23-CH_3)** isomer can be dismissed as a candidate for the predominant isomer despite the fact that the X-ray structure of **(70-10-1)$(CH_3)_2(CN)_2$**, which will be discussed below, shows that a nucleophile/electrophile pair can add to C44 and C23, respectively, on **70-10-1** (note that these cage C atoms are *para* to one another on a hexagon near the C_{70} equator, whereas the C33–C34 bond is near one of the C_{70} poles). The DFT-predicted energies of **(70-10-1)(44-CN)$^-$** and **(70-10-1)(44-CN)(23-CH_3)** are 15.1 and 12.0 kJ mol^{-1} higher, respectively, than the corresponding lowest energy isomers. In addition to the steric hindrance at C44 relative to C34, the ^{19}F NMR spectrum of the 95+ mol% regioselective product does not exhibit *a pair* of multiplets with $-\delta$ values $\leq$ 60, which suggests that the added substituents have *not* affected the conformations of the CF_3 groups relative to the conformations observed for **70-10-1** and therefore are remote from the CF_3 groups.[10,32,66] Considering all of the experimental and DFT results, it appears that the predominant products formed by treating **70-10-1** first with NEt_4CN and then with either CH_3OTf or CF_3COOH are, respectively, **(70-10-1)(34-CN)(33-CH_3)** and **(70-10-1)(34-CN)(33-H)**.

Another compound, C_1-$C_{70}(CF_3)_{10}(CN)_2$ (**(70-10-1)(CN_2)**), was then prepared from **70-10-1** according to a similar procedure. The predominant isomer of ***C_1*-(70-10-1)(CN)$^-$** was quenched with *p*-TsCN to produce one predominant product, **(70-10-1)$(CN)_2$**. The ^{19}F NMR spectrum of this new fullerene exhibited ten CF_3 multipets that differ from the ten multiplets of **70-10-1** as shown in Figure 1.25, and practically identical to the ^{19}F NMR spectra of ***C_1*-(70-10-1)(CN)(CH_3)**. Therefore, the new derivative most likely has the same addition pattern as the latter, where two cyano groups are both added to the most reactive cage carbon atoms (C33 and C34), as shown on Figure 1.25.

The possibility of generating the "opposite isomer" of **(70-10-1)(34-CN)(33-CH_3)**, **(70-10-1)(34-CH_3)(33-CN)** by first adding CH_3^- followed by *p*-TsCN was also explored. Presumably, the nucleophilic reagent, whether CH_3^- or CN^-, would attack the same C atom and allow for the "opposite isomer" to be generated. In one experiment, a solution of MeMgBr in Et_2O (16 equiv.) was added to a yellow solution of **70-10-1** toluene and the solution became brown within ten minutes. Fluorine-19 NMR spectra of the green-brown solution showed the complete loss of **70-10-1** multiplets and 10 new multiplets appeared, presumably **(70-10-1)(CH_3)$^-$**. This new set of peaks is more similar to the 10 multiplet pattern of **(70-10-1)(CN)$^-$** than of **70-10-1** despite differences in the solvent mixtures used for the NMR experiments. A toluene solution of *p*-TsCN (16 equiv.) was then added and the solution instantly became cloudy yellow. The solution was then exposed to air, the solvent was removed, and then the solid was all dissolved in C_6D_6. Fluorine-19 NMR revealed that ca. 50% of the mixture reverted back to **70-10-1** and ten new multiplets indicated that a predominate product was formed with ca. 40% yield. The product was separated by HPLC and APCI mass spec indicated that **(70-10-1)(CH_3)(CN)** was formed. The 10 multiplets of **(70-10-1)(CH_3)(CN)** are more similar to the 10 multiplets of **(70-10-1)(CN)(CH_3)** formed from the cyano anion than the multiplets from **70-10-1**, so it is very likely that the opposite isomer was indeed formed (Figure 1.27). The reappearance of **70-10-1** in the reaction mixture revealed the reversibility of the reaction in agreement with the reversibility of **(70-10-1)(CN)$^-$** reactions with MeOTf described above. In some attempts to form **(70-10-1)(CH_3)(CN)**, all of the methyl anion reverted back to **70-10-1** and no product was formed. The possibility of adding a large excess of *p*-TsCN to quickly quench the reaction was never explored. Perhaps a large excess will push the reaction towards the desired product similar

to adding a large excess of MeOTf to **(70-10-1)(CN)$^-$**. However, this reaction could be limited by the solubility of *p*-TsCN in the chosen reaction mixture.

Perhaps the use of a different counter ion with **(70-10-1)(CH$_3$)$^-$** could help push the reaction towards the desired product. A solution of $LiCH_3$ in Et_2O was added to a yellow solution of **70-10-1** in toluene and a green precipitate immediately formed. When only one or two equivalents of the methylating agent were added, an ^{19}F NMR spectrum indicated that some amount of **70-10-1** was still present in solution. Four equivalents of $LiCH_3$ were required to cause the complete conversion of yellow, soluble **70-10-1** into the green precipitate, presumably the lithium salt of **(70-10-1)(CH$_3$)$_n^{n-}$** anions. A noisy spectrum with very few discernable peaks indicated that nearly all of the fluorine atoms were in the green solid (Figure 1.28). The formation of the green precipitate is in contrast to the green, soluble **NEt$_4^+$(70-10-1)(CN)$^-$** and green-brown **MgBr$^+$(70-10-1)(CH$_3$)$^-$** described earlier. Subsequent addition of four equivalents of a toluene solution of *p*-TsCN caused the immediate conversion of the green precipitate into a yellow solution.

The ^{19}F NMR spectrum of the yellow solution (Figure 1.28D) indicated the absence of **70-10-1** and the presence of two principal products, one of them more abundant than the other. The success of this reaction is in contrast to similar *p*-TsCN reactions with **60-2-1(CN$_3$)$^-$** described earlier. The two predominate products were purified by HPLC (confirming their different relative abundances) and exhibited the NMR spectra shown in Figure 1.28. Mass spectra showed that they were isomers of the composition **(70-10-1)(CH$_3$)$_2$(CN)$_2$.** It is unlikely that the green precipitate only contained the **(70-10-1)(CH$_3$)**$^-$ monoanion and that the excess $LiCH_3$ present in solution added to **(70-10-1)(CH$_3$)(CN)** as it formed from the green solid when *p*-TsCN was added, because free $LiCH_3$ reacts extremely rapidly with *p*-TsCN to form CH_3CN

(i.e., there would be little or no remaining $LiCH_3$ to react with the putative intermediate **(70-10-1)(CH_3)(CN)**). Therefore, the green precipitate likely contains two (or more) isomers of the lithium salt of the **(70-10-1)(CH_3)$_2$**$^{2-}$ dianion, namely the dianions that form the major and minor isomers of **(70-10-1)(CH_3)$_2$(CN)$_2$**.

The minor isomer formed crystals suitable for X-ray diffraction via slow evaporation from DCM, and its structure is shown in Figure 1.29. (The structure is of poor quality, with an R_w value of 0.21, but there is no doubt about its addition pattern) The two CH_3 groups have been added to C33 and C44 and the two CN groups have been added to C34 and C23. It was expected that a nucleophile/electrophile pair would add to the C33–C34 bond (although in this isomer the two groups are switched from the proposed, lowest-energy isomer **(70-10-1)(34-CN)(33-CH_3)**. The other nucleophile/electrophile pair added to the *para* positions of a hexagon near the C_{70} equator. The presence of both ***C$_s$*-(70-8-1)(CN)$_2$** and ***C*$_1$-(70-8-1)(CN)$_2$** resulting from the addition of CN^- and CN^+ to **70-8-1** showed that a nucleophile/electrophile pair can add to a cage C=C bond *or* to the *para* positions of a cage hexagon. The formation of **(70-10-1)(33,44-CH_3)$_2$(23,34-CN)$_2$** shows that *both* types of addition can occur simultaneously on the same substrate molecule.

It is likely that the minor isomer characterized by X-ray diffraction was formed by the addition of two CN^+ moieties to the **(70-10-1)(33,44-CH_3)$_2$**$^{2-}$ dianion. DFT calculations, listed in Table 1.4, predict that this isomer is 4.1 kJ mol^{-1} less stable than the corresponding **(70-10-1)(34,44-CH_3)$_2$** dianion. Based on the DFT predictions, and the near congruence of the ^{19}F NMR spectra of the major and minor isomers (Figure 1.28), it seems likely that the major isomer was formed from the **(70-10-1)(34,44-CH_3)$_2$**$^{2-}$ dianion and is ***C*$_1$-(70-10-1)(34,44-CH_3)$_2$(23,33-CN)$_2$**. (Note that both isomers exhibit two multiplets with $-\delta$ values ≤ 60, indicating that the added

substituents have affected the conformation of one CF_3 group relative to its conformation in **70-10-1**. Both the X-ray structure and the DFT-optimized structure of the minor isomer show that the 23-CN and 44-CH_3 substituents are in close proximity to two CF_3 groups and one CF_3 group, respectively. The multiplet at δ −61.6 in the spectrum of **70-10-1** belongs to the CF_3 group closest to the CH_3 group on C44.[67] It is sensible that this multiplet would be the one to shift to ca. δ −58 in the spectra of **(70-10-1)(CH$_3$)$_2$(CN)$_2$**. Furthermore, note that the quartet at δ −70.9 in the spectrum of **70-10-1** also experiences a large shift. This is because the terminal CF_3 group on C25 in **70-10-1** is no longer terminal in **(70-10-1)(CH$_3$)$_2$(CN)$_2$**; it is *para* to the CF_3 group on C10 and *meta* to the CN group on C23.

Interestingly, the minor isomer is predicted to be marginally *more* stable than the major isomer. The DFT calculations by Alex Popov also predict that the addition of one of the two CH_3^- nucleophiles to C23, or the addition of both of them to C33 and C34, are unlikely. An ESP diagram of the **(70-10-1)(33,44-CH$_3$)$_2^{2-}$** dianion shows that the addition of CN^+ electrophiles to C34 and C23 may be kinetically controlled as well as thermodynamically favored. In addition, **(70-10-1)(33,44-CH$_3$)$_2$(34-CN)$^-$** and **(70-10-1)(33,44-CH$_3$)$_2$(23-CN)$^-$** DFT calculated ESP diagrams of monoanions show that the addition of CN^+ to C23 or C34, respectively, may also be kinetically controlled.

1.5 Tetraethylammonium Cyanide Reactions with Other PFAFs

The reactions described above demonstrated the versatility of nucleophilic cyano addition to two $C_{60}(CF_3)_n$ and two $C_{70}(CF_3)_n$ derivatives. Preliminary NEt_4CN reactions with other PFAFs were explored in order to demonstrate the universal nature of this reaction for a greater variety of fullerene derivatives. Addition of NEt_4CN to a brown solution of *o*-$C_{60}(CF_2C_6F_5)_2$ resulted in a brown solution with two new sets of ^{19}F resonances indicating that two isomers of

$C_{60}(CF_2C_6F_5)_2(CN)^-$ were formed. Subsequent addition of benzyl bromide resulted in two new sets of ^{19}F resonances. The products of this reaction were not further characterized because precipitates formed over time with the final products and with the $C_{60}(CF_2C_6F_5)_2(CN)^-$ mixture. Addition of NEt_4CN to a brown solution to a mixture of **60-4-1**>**60-2-1**>**60-6-1** resulted in a brown solution that exhibited entirely new ^{19}F multiplets. This reaction was not further characterized, but it did indicate that the three PFAFs readily react with NEt_4CN. Addition of NEt_4CN to a dark brown solution of **60-10-1** immediately resulted in a dark green solution. This reaction did not appear to be very selective by ^{19}F NMR since the ten-multiplet spectrum of **60-10-1** changed to > 30 new multiplets. The ^{19}F NMR spectrum of this anion mixture remained unchanged for two days in anaerobic conditions indicating that this reaction happens very quickly and does not undergo further rearrangements or reactions with CN^-. Subsequent addition of MeOTf to this reaction mixture converted some of the anion into three predominant products and some reverted back to **60-10-1** as confirmed by a combination of ^{19}F NMR and HPLC. The composition of one fraction from HPLC contained $C_{60}(CF_3)_{10}(CN)(CH_3)$ with a small amount of $C_{60}(CF_3)_{12}(CN)(CH_3)$ (due to $C_{60}(CF_3)_{12}$ impurity in the starting material) as confirmed by APCI-MS. Addition of NEt_4CN to a yellow solution of $C_{60}F_{18}$ resulted in a dark green solution that exhibited new singlets in its ^{19}F NMR spectrum, but the resulting mixture precipitated out of solution over time. These preliminary experiments have demonstrated that CN^- will add to PFAFs but does not always result in a regioselective addition with stable products.

Traditionally, $C_{60}(CF_3)_n$ derivatives with n>10 are difficult or impossible to separate by HPLC using the Cosmosil Buckyprep column. The highly fluorinated species have very little interaction with the aromatic stationary phase of the column and typically elute at dead volume. In most cases involving cyano modified PFAFs described above, the newly synthesized cyano

PFAFs eluted later in the HPLC experiments than the parent PFAFs. The new addends caused the molecule to interact with the column to a greater extent and could be separated at later elution times. Perhaps, similar modifications to mixtures of highly trifluoromethylated $C_{60}(CF_3)_n$ and $C_{70}(CF_3)_n$ could cause the molecules to interact more readily with the stationary phase and could then be isolated at longer retention times. This notion was explored with inseparable mixtures of $C_{60}(CF_3)_{12}$ and $C_{70}(CF_3)_{12}$ with the intention to isolate fullerenes with previously unknown addition patterns.

Many addition patterns of $C_{60}(CF_3)_{12}$ and $C_{70}(CF_3)_{12}$ are not known because they cannot be isolated from other isomers. It is thermodynamically more favorable for a CF_3 addition to occur on one of the 12 pentagons of the fullerene cage, so it is reasonable to suggest that, in most cases, all 12 pentagons of the cages contain a CF_3 group. The next addition to $C_{60}(CF_3)_{12}$ would have to share a pentagon with one CF_3 group, which could be sterically hindered due to the close proximity of the bulky CF_3 addends. Additions to $C_{70}(CF_3)_{12}$ could also occur on a shared pentagon or on a triple-hexagon junction. In either case, CN^- addition is likely unfavorable thermodynamically. On the other hand, CN^- benefits by being sterically small compared to CF_3 groups.

Toluene was added to a mixture of $C_{60}(CF_3)_{12}$ and ca. half of the fullerenes appeared to dissolve, forming a red-orange solution. Addition of NEt_4CN instantly formed a dark green solution and most of the solid appeared to dissolve. Aliquots of this $C_{60}(CF_3)_{12}(CN)^-$ anion mixture were then reacted with a large excess of MeOTf or a small excess of *p*-TsCN and each solution became yellow-brown over time. After washing each solution with H_2O and drying with $MgSO_4$ the solutions were analyzed by ^{19}F NMR and separated by HPLC, see Figure 1.30. The reaction with a large excess of MeOTf converted almost the entire starting fullerene into new

products. These products were isolated by HPLC to varying degrees of purity and all of them exhibited 12 multiplet ^{19}F NMR spectra. APCI-MS of these fractions confirmed the formation of $C_{60}(CF_3)_{12}(CN)(CH_3)$ and also the presence of a small amount of $C_{60}(CF_3)_{14}$ that was present in the starting material.

Some $C_{60}(CF_3)_{12}(CN)^-$ converted back to starting $C_{60}(CF_3)_{12}$ and some formed $C_{60}(CF_3)_{12}(CN)_2$ products in the reaction with a small excess of *p*-TsCN. Two predominant products of $C_{60}(CF_3)_{12}(CN)_2$ were isolated by HPLC (Figure 1.30) in 100% hexanes at 6.7 and 7.3 minutes and the composition was confirmed by APCI-MS. A small signal from $C_{60}(CF_3)_{14}(CN)_2$ was observed in MS experiments with each fraction. The remaining peaks from HPLC were collected as one fraction. The APCI-MS of this fraction confirmed that most of the mixture was still $C_{60}(CF_3)_{12}$ while a small amount could be associated with $C_{60}(CF_3)_{12}(CN)_2$ that eluted at or near the same retention time as the starting materials. Attempts at crystallizing purified fractions from each experiment to elucidate the CF_3 addition pattern of $C_{60}(CF_3)_{12}$ isomers were unsuccessful and no 2D-NMR experiments were attempted as an alternative. The versatile cyanation of PFAFs that was originally used as a way to determine which C atoms of the cage were the most active can now be utilized to isolate previously inseparable PFAFs. However, the addition pattern of these newly isolated $C_{60}(CF_3)_{12}$ derivatives remain unknown until suitable crystals are formed.

Successful isolation of $C_{60}(CF_3)_{12}(CN)(CH_3)$ derivatives prompted similar experiments with mixtures of $C_{70}(CF_3)_{12}$. A mixture of $C_{70}(CF_3)_{12}$ isomers containing a small amount of $C_{70}(CF_3)_{14,16}$ was dissolved in toluene to form a dark orange solution. Upon reaction with Et_4NCN the mixture became dark green and remained stable in anaerobic conditions for at least one day. The ^{19}F NMR spectrum of the green solution revealed that most of the multiplets from

the starting material had shifted, confirming the addition of CN^-. Subsequent addition of a very large excess of MeOTf created a yellow solution. Analysis of the resulting ^{19}F NMR spectrum, APCI-MS, and HPLC chromatogram of the worked up yellow solution revealed that most of the $C_{70}(CF_3)_{12}(CN)^-$ reverted back to starting material upon addition of MeOTf. Only a small fraction of the material converted to the desired product (confirmed by MS) which could not be isolated by HPLC in 100% hexane with a Buckyprep column. Efforts to optimize this reaction with the unknown mixture of $C_{70}(CF_3)_{12}$ isomers were not pursued further.

1.6 Electrochemistry and Electron Affinity of Cyanated $C_{60}(CF_3)_n$ and $C_{70}(CF_3)_n$

In the research community developing OPV materials and optimizing device performance, strong electron acceptors are commonly referred to as materials with low-lying LUMO levels. The quantitative value of LUMO energy has been conveniently (but not always consistently and correctly)[68] derived from the measured reversible first reduction potential ($E_{1/2}^{0/-}$ value) using cyclic voltammetry with typical uncertainties of 10-20 mV. Determination of solid-state EA of organic materials is now becoming available via IPES, but with lower precision and accuracy; errors as high as 300 meV are typically reported.[69,70] Gas-phase EA measured by LT PES represents the most fundamental intrinsic measure of a molecule's ability to accept electrons, and uncertainties as low as 5-10 meV can be readily achieved in modern state-of-the-art instruments, allowing for reliable comparisons of compounds even with very small differences in EA, for example C_{60} and C_{70}.[71,72] This method is indispensable when organic acceptors do not exhibit reversible electrochemical behavior in solution, and when the amounts of materials are too small to be used for IPES which is frequently the case at the exploratory stage of research. Since sharp peaks are often resolved in the threshold region of photoelectron spectra of fullerene related anions, the accuracy of EA measurements is around 10 meV,

comparable to the best cyclic voltammetry experiments. The LT PES technique was performed by collaborators at PNNL to elucidate electron accepting properties of many C_{60} and C_{70} cyano modified PFAFs, since electrochemical irreversibility was so prevalent. A short discussion on cyclic voltammetry measurements will be followed by the electrochemical behavior of C_{60} derivatives from LT PES and then the more peculiar and less predictable results from the C_{70} derivatives will be described.

1.6.1 Electronic Properties of p^3-$C_{60}(CF_3)_4$ (60-4-2) and $C_{60}(CF_4)_4(CN)(H)$ ((60-4-2)(CN)H).

In this section, the electronic effects of functional groups in the most common type of hexa-substituted C_{60} fullerenes, containing the SPP addition pattern (Schlegel diagram is shown on Figure 1.15) will be addressed. Several isostructural penta-substituted derivatives of C_{60} (in radical and anionic forms) C_5-$C_{60}X_5$, where X is either an EWG, EDG, or both were studied. Such penta-substituted species were observed as chemical intermediates on the way to the neutral hexa-substituted compounds with the SPP addition pattern. Versatility of the C_5-$C_{60}X_5$ motif in the organic and organometallic chemistry of fullerenes and importance of related fullerene materials in practical applications necessitate a knowledge and better understanding of the influence of different functional groups on the electron-accepting properties of such derivatives.[73-82]

Cyclic voltammetry of **60-4-2** and **(60-4-2)(CN)H** revealed that reduction processes were irreversible, which was in sharp contrast to the previously observed three or four reversible reductions for the majority of TMFs, including *pmp*-$C_{60}(CF_3)_4$ (**60-4-1**) and SPP-$C_{60}(CF_3)_6$ (**60-6-2**).[48] The most likely explanation for such a drastic difference in the electrochemical properties is the high chemical reactivity of **60-4-2** and **(60-4-2)(CN)H** in reduced forms. In the former case, a reactive double bond can be attacked by nucleophiles from solution (e.g., OH^- or CN^-); in

the case of **(60-4-2)(CN)H**, hydrogen can be easily removed under electrochemical experiment conditions, causing **60-4-2(CN)$^-$** to undergo further chemical transformations, and thus yielding electrochemically irreversible processes. Consequently, it is not possible to use cyclic voltammetry for reliable estimations of redox properties of these compounds.

The LT PES method was used for the experimental determination of gas-phase electron affinity of **60-4-2** and **(60-4-2)(CN)H**. Preliminary APCI mass spectrometry studies of the acetonitrile solutions of **60-4-2** and **(60-4-2)(CN)H** indicated that corresponding molecular anionic species can be readily generated, see section 1.3.5. Noteworthy, in the ESI source of the mass spectrometer, **(60-4-2)(CN)H** was observed only as fully deprotonated species **(60-4-2)(CN)$^-$** (see Figure 1.17). The EA measurements at 266 nm (4.661 eV) were carried out for acetonitrile solutions of **60-4-2** and **(60-4-2)(CN)H** mixed with appropriate donors using a magnetic-bottle time-of-flight PES coupled with an ESI source and a cryogenic ion-trap for size-selected anions as described elsewhere and performed by collaborators at PNNL.[83]

Interestingly, the photoelectron spectrum of the anion produced from **60-4-2** consists of two features, one at 3.21±0.01 eV, and the second one, more pronounced, at 3.96 ±0.01 eV which indicates that two anionic species with considerably different electron affinities contribute to the photoelectron detachment process (Figure 1.31). It is reasonable to suggest that the peak observed at 3.21 eV is due to the parent molecular $C_{60}(CF_3)_4^-$ anion, whereas the peak at 3.96 eV is likely to be due to a hydrogenated anion, $C_{60}(CF_3)_4H^-$ (structure **(60-4-2)H$^-$**, Figure 1.15) based on the observed ion signal width. The most likely explanation for the formation of the penta-substituted anion is a very high reactivity of the anionic form of **60-4-2** in solution that leads to hydrogen abstraction from the solvent (not thoroughly dry) or from the ESI process which occurred at the ambient environment with a certain amount of water vapor and formation

of the particularly stable anion (**60-4-2**$^-$ + H), **(60-4-2)H**$^-$, bearing an aromatic cyclopentadiene moiety. Within the current instrumental mass resolution, it is difficult to separate anionic beams with *m/z* 996 (**60-4-2**$^-$) and 997 (**(60-4-2)H**$^-$), but there was a change of spectral area ratio of the low and high binding energy features corresponding to these two species ranging from 0.039 to 0.089 in five different LT PES studies by selecting different portions of the ion clouds containing both m/z 996 (**60-4-2**$^-$) (minor) and 997 (**(60-4-2)H**$^-$) (majority). Note that these ratios cannot be directly translated into the ion population of **60-4-2**$^-$ over **(60-4-2)H**$^-$ because the detachment cross sections of these two anionic species may not be the same. The formation of **(60-4-2)H**$^-$ occurring after mass selection can be safely ruled out because of the absence of a hydrogen atom source: only N_2 molecules constitute the background gas in the PES instrument (at vacuum as high as 10^{-8} torr). This interpretation of the LT PES spectrum of **60-4-2** is strongly supported by the theoretical calculations from Popov. The DFT-derived EA of **60-4-2** is 3.10 eV, whereas the EA value of **(60-4-2)H** was calculated as 3.73 eV. Such a considerable difference between the EAs of the two species is explained by two factors: (i) EA of the open shell molecular species is known to be higher than that of closed-shell species,[84] and (ii) addition of H atom to **60-4-2**$^-$ leads to a significant stabilization of the structure due to the formation of an aromatic moiety as shown in Figure 1.15 for **(60-4-2)H**$^-$.

The LT PES spectrum of **(60-4-2)(CN)H** consists of only one strong peak at 4.28 eV. Slightly different mass selection for the ion beam generated from a solution of **(60-4-2)(CN)H** has been also carried out, which indicated that only one ion species existed, **(60-4-2)(CN)**$^-$, a product of complete deprotonation of **(60-4-2)(CN)H** under applied experimental conditions, in agreement with the preliminary ESI MS results for **(60-4-2)(CN)H** discussed in Section 1.3.5.

Therefore, the EA of **(60-4-2)(CN)** was measured from the first resolved peak to be 4.28 ± 0.01 eV.

Table 1.5 contains adiabatic EA value for **60-4-2** and, for comparison, earlier reported EAs of some closed-shell TMFs and C_{60}, and the DFT-calculated EA, $E_{1/2}$, and E_{LUMO} values. Importantly, relative trends in electron acceptor strength for the listed compounds based either on their EAs, $E_{1/2}$ or E_{LUMO} are in qualitative agreement, meaning that acceptor strength increases in the row: **60-4-2** > **60-4-1** > **60-2-1** > C_{60} > S_6-$C_{60}(CF_3)_{12}$.

The EA of the isomerically pure TMF, **60-4-2**, is the first value for a TMF with more than two CF_3 groups measured with the high precision of 0.01 eV, compare with the error of 0.17 eV reported for S_6-$C_{60}(CF_3)_{12}$.[85] Also note that the EA data for $C_{60}(CF_3)_{10}$ were obtained using a sample comprised of a mixture of isomers with unknown composition and with higher uncertainty of ca. 0.2 eV[86,87,85] and hence they were not used in this data analysis. The EA value of 3.21 eV measured for **60-4-2** in this work is 0.37 eV higher than measured for C_{60};[88] this confirms the predicted high electron affinity for the p^3 addition pattern in C_{60} made in earlier studies and serves as good validation of the DFT method used.[48] Experimental EA values for **(60-4-2)H** and **(60-4-2)(CN)** are also reliably reproduced by the results of DFT calculations (Table 1.6). While the absolute EAs are systematically underestimated by ca. 0.2 eV, the difference between **(60-4-2)H** and **(60-4-2)(CN)** is predicted with very high precision (ΔEA_{DFT} = 0.34 eV vs. ΔEA_{exp} = 0.32 eV).

Currently, there are only a few examples when the effect of different functional groups could be determined experimentally from the measurements of reduction potentials or EAs of fullerene derivatives with the same addition pattern.[20,40] For example, Wudl and coworkers have

shown that $C_{60}(CN)_2$ is easier to reduce in solution than isostructural $C_{60}H(CN)$ by 0.07–0.12 V.[40,41] For $C_{60}(CN)_4$ and $C_{60}H(CN)_3$, the same authors reported a difference of 0.15 V, however, the measurements were performed for mixtures of isomers.[41] Results from this current study show that the difference of EA values of $C_{60}(CF_3)_4CN$ and $C_{60}(CF_3)_4H$ radicals can be as high as 0.32 eV! The electrochemical data on the effect of the substituents in the fullerene derivatives with the SPP-structures are even more scarce,[73] despite abundance of such structures among the synthesized organic derivatives.

After validation of the DFT calculations of EA values discussed above, an extended analysis of EAs of the $C_{60}X_5$ compounds with different addends based on the DFT-computed data (Table 1.6) was performed. Computations show that depending on the addend, EA of $C_{60}X_5$ radical can vary within the range of 1.71 eV, from 2.76 eV for X = CH_3 to exceptionally high value of 4.47 eV for X = CN. When X = H, EA increases by only 0.02 eV vs. $C_{60}(CH_3)_5$, whereas EA of $C_{60}(Ph)_5$ is increased to 3.07 eV. Note that the DFT-computed EA of C_{60} is 2.64 eV, and hence the difference of computed EA values of C_{60} and $C_{60}(Ph)_5$, 0.43 eV, is very close to the experimentally measured difference of their reduction potentials in THF.[73] $C_{60}(CF_3)_5$ and $C_{60}(C_2F_5)_5$ exhibit almost identical values of 3.99 and 4.02 eV, respectively. Interestingly, the difference between these two values, 0.03 eV, is the same as the difference between the experimentally determined EAs of $C_{60}(CF_3)_2$ and $C_{60}(C_2F_5)_2$[20] and thus it confirms that the electron withdrawing effect of R_F groups increases slightly in going to higher R_F homologues. Importantly, one fifth of the difference between EAs of $C_{60}H_5$ and $C_{60}(CN)_5$, 0.34 eV, is equal to the H-to-CN increment found for the EAs of the $C_{60}(CF_3)_4X$ (X = H, CN) pair.

One of the factors resulting in the high electron affinity of $C_{60}X_5$ radicals is the formation of the aromatic cyclopentadiene anion. In the earlier theoretical considerations, it was

hypothesized that high EA of highly fluorinated fullerene, $C_{60}F_{34}$ could be due to the presence of two cyclopentadiene moieties in its structure.[89] In this work, in order to analyze if there is a correlation between the addend X and aromaticity, NICS at several points of $C_{60}X_5^-$ anions were computed by Alex Popov, namely at the center of the cyclopentadiene ring, at the center of the opposite cage ring, and the center of C_{60} cage. These calculations showed that, as anticipated, the cylopentadiene ring is aromatic with NICS values of −5 to −13 ppm, whereas the opposite pentagon is always antiaromatic (positive NICS values of 10–12 ppm). Interestingly, NICS values in the center of the cage are even more negative than in the center of the cyclopentadiene ring. Moreover, they exhibit a perfectly linear correlation with the EA values showing that the "bulk" aromaticity of the cage is related to the addend in the same way as EA (i. e., the higher EA, the more negative NICS). At the same time, the values in the center of the cyclopentadiene ring are less correlated with EA (presumably due to the local shielding effects of the addends).

The rare representative of a fullerene derivative prepared in this work, **(60-4-2)(CN)H** with the SPP addition pattern in which five substituents are strong electron withdrawing groups was an extraordinary compound for LT PES and DFT studies. This type of SPP derivative possesses good air stability, in contrast to the counterparts with electron donating groups, and exceptionally high electron affinity of the respective radicals, and hence, high thermodynamic stability of the anions. Due to these unique properties, such SPP derivatives of TMFs may become increasingly important building blocks in the molecular and supramolecular designs of electroactive functional materials.

1.6.2 Electrochemistry and Electron Affinity of $C_{70}(CF_3)_8$ and $C_{70}(CF_3)_{10}$

While investigating the irreversible electrochemical behavior of **70-10-1**, Popov and co-workers revealed some rather unique behavior of electrochemically reduced **70-10-1** with ESR,

Vis-NIR, and ^{19}F NMR spectroelectrochemistry experiments.[90] To summarize, the combined spectroelectrochemical studies by Popov and coworkers of the **70-10-1** reduction mechanism showed that (a) **70-10-1** reduction is irreversible at slow scan rates (< 1 $V \cdot s^{-1}$) and only shows reversibility at faster scan rates (500 $V \cdot s^{-1}$); (b) the process is chemically reversible, *i.e.* pristine **70-10-1** is fully recovered after electrochemical re-oxidation; (c) the first reduction produces both diamagnetic and paramagnetic species in ca 9:1 ratio; (d) in the diamagnetic reduction product, the CF_3 addition pattern is similar to that of **70-10-1**. These experimental data, along with DFT calculations, suggest that the most probable follow-up reaction is a reversible dimerization of **70-10-1**$^-$ with formation of the single-bonded diamagnetic dimer **(70-10-1**$^-$**)$_2$**.

In order to gain insight in the mechanism of reduction, I chemically reduced **70-10-1** with cobaltacene. Two equivalents of cobaltacene were necessary to fully reduce a solution of **70-10-1**. The solution changed from yellow to green and the multiplets in the resultant ^{19}F NMR spectrum shifted upon reduction. Multiplets from parent **70-10**-1 were still present when using less than two equivalents of cobaltacene. The ^{19}F NMR spectrum from the chemically reduced species was identical to the electrochemically reduced species. Interestingly, the shifts in multiplet positions in the ^{19}F NMR spectrum of **70-10-1** were nearly the same as the shifts induced by addition of CN^- group upon formation of the **(70-10-1)(CN)**$^-$ anion described in Section 1.4.3 (see Figure 1.32 for the comparison). It appears that the same C atom of **70-10-1** is reactive in all three reduction methods since the ^{19}F NMR spectra were so similar. DFT calculations by Alex Popov revealed that the most likely product upon reduction was a **70-10-1** dimer that was bonded across C34 of each monomer subunit. This is consistent with the calculations described above for CN^- attack and is consistent with the similar features in NMR spectra.

The presence of a dimeric species was experimentally determined from the NI-APCI mass-spectra of $Co(Cp)_2$-reduced **70-10-1** (Figure 1.33). The dimer and monomer anions were easily oxidized by the traces of air from the CH_3CN carrier which lead to strong signals from the various oxidized species. The low dimer signal compared to the monomer signal is another indication of the lower stability of dimeric species in the gas phase. An analogous study of pristine **70-10-1** did not show dimeric or oxidized species. All attempts to grow X-ray quality single crystals of $Co(Cp)_2$-reduced **70-10-1** in order to confirm dimerization between the C34 atoms were unsuccessful.

These experiments showed that the less stable dimer is easily attacked by oxygen in mass spectrometry conditions whereas **70-10-1** is stable towards residual oxygen. Such a dimer is also not stable after electrochemical re-oxidation, and hence **70-10-1** is restored at the end of the cyclic voltammetry cycle. If the unpaired electron spins in the dimer couple in an antiferromagnetic fashion, then the dimer is diamagnetic and hence accessible by NMR. If the bond between two monomer units is formed via the same carbon atom, which is functionalized in **(70-10-1)(CN)**$^-$ anion, the similarity of the their NMR spectra can be explained.

Cyclic voltammetry measurements were also attempted on several cyano modified PFAFs in this work with minimal success. Most attempts used 0.1 M $TBABF_4$ in *o*-DCB and used $Fe(Cp)_2$ as an internal standard only after reversible voltammograms were first obtained without internal $Fe(Cp)_2$. A pseudo-reversible first reduction of **(70-10-1)(CN)$_2$** was obtained by cyclic voltammetry and was determined to be −1.11 V vs. $Fe(Cp)_2^{+/0}$. On the other hand, **(70-10-1)(CN)(CH$_3$)** and the other **70-10-1** cyano derivatives with CH_3 or H addends were irreversible. It is possible that dimerization reactions also interfere with **70-10-1** cyano derivatives. Consequently C34 is where one CN is predicted to bond in **(70-10-1)(CN)$_2$** which presumably

prevents dimerization and allows for the pseudo-reversible first reduction of **(70-10-1)(CN)$_2$** to be observed at moderate scan rates. The CH_3 or H groups on other cyano modified **70-10-1** derivatives could be more labile than the CN or CF_3 groups, which could explain why electrochemical reductions of other derivatives are less reversible than **(70-10-1)(CN)$_2$.**

In some cases, such as with ***C$_s$*-(70-8-1)(CN)$_2$**, the fullerene would react with $TBABF_4$ electrolyte before the experiment could begin. Changing the electrolyte to TBAP from $TBABF_4$ did not help in the case of ***C$_s$*-(70-8-1)(CN)$_2$** because the first and second reductions were both irreversible. Irreversibility of ***C$_s$*-(70-8-1)(CN)$_2$** was unexpected since **70-8-1** and similar fullerene derivatives have exhibited reversible first reductions.[40,49] Irreversible cyclic voltammograms were also observed with ***C$_1$*-(70-8-1)(CN)$_2$** and **(60-2-1)(CN)(CH$_3$)**.

The irreversible nature of **70-10-1** and cyano modified **70-8-1** and **70-10-1** derivatives prompted EA and DFT experiments in order to compare electron accepting abilities of the new derivatives. First, LT PES experiments were performed by collaborators at PNNL to determine gas-phase EAs of **70-8-1** and **70-10-1**. Figure 1.34 (bottom panel) and Figure 1.35 (bottom panel) show the photoelectron spectra of the mono-anions of **70-8-1** and **70-10-1,** respectively, recorded at 266 nm (4.661 eV) using acetonitrile solutions of each fullerene mixed with appropriate donors using a magnetic-bottle time-of-flight PES coupled with an ESI source and a cryogenic ion-trap for size-selected anions as described previously.[83]

The experimentally determined adiabatic EA of **70-8-1** is 3.08(1) eV which is 0.315 eV higher than the EA value of parent C_{70} measured using the PES technique,[72] whereas the EA value measured here for **70-10-1** is only 2.93(1) eV (see Table 1.7 for all experimental and calculated EA values). A 150 meV decrease in EA of **70-10-1** compared to **70-8-1** is likely

caused by destabilization of the fullerene π system due to the introduction of two additional CF_3 groups to **70-8-1** structure, and it is not compensated by the electron-withdrawing effect of the CF_3 groups. These measured EA values are in qualitative agreement with the previously calculated E_{LUMO} for these molecules, i.e., **70-8-1** was predicted to have a 0.204 eV lower-lying LUMO than **70-10-1**. Their EA values were also calculated by DFT for this work, which agree well with the experiment: the relative differences in EA between **70-8-1** and **70-10-1** are ΔEA_{DFT} = 0.202 eV. This validation of the DFT-derived EA values was further used for the comparison of the electronic properties for the pair of C_2-$C_{70}(CF_3)_8$ (**70-8-2**) and C_2-$C_{70}(CF_3)_{10}$ (**70-10-2**) compounds, the latter has the **70-8-2** substructure in its addition pattern as shown on the Schlegel diagrams in Figure 1.19. The **70-8-2** molecule was predicted to be a stronger acceptor than **70-10-2** based on E_{LUMO} values and reduction potentials,[49] which is now supported by comparing their new DFT data for EAs: EA_{DFT}(**70-8-2**) = 3.224 eV, which is 0.272 eV higher than that of **70-10-2**. Remarkably, **70-8-2** appears to even be a stronger acceptor than F4-TCNQ,[91] and comparable to fluorinated fullerenes, $C_{60}F_{18}$ and $C_{60}F_{36}$,[92] the latter has been widely used as a *p*-dopant in organic electronics,[93-95] and for enhancement of diamond surface conductivity.[96] These new results make **70-8-2** a promising alternative to a fluorofullerene for doping applications, not only due to comparable EA values, but also because it is chemically more inert towards hydrolysis.[97,98]

1.6.3 Electron Affinity of Cyanated $C_{70}(CF_3)_8$

Investigating if the destabilization resulting from two CF_3 additions to **70-8-1** as observed in **70-10-1** could be overcome by adding stronger electron-accepting groups than CF_3, and whether the locations of these EWGs on the cage influence the EAs, was performed next. Two products from the cyanation of **70-8-1** were prepared for this work as described in Section

1.4.1,[64] ***C*$_s$-(70-8-1)(CN)$_2$** and ***C*$_1$-(70-8-1)(CN)$_2$**. They were studied by LT PES, and the resulting spectra, together with the Schlegel diagrams, are shown in Figure 1.34. These results reveal that introducing two CN groups to **70-8-1** does not actually increase the EA in these two cyanated derivatives, as one might expect, but it even results in slight decreases of 10-20 meV. The strong electron-withdrawing nature of CN groups was not enough to overcome destabilization caused by the changed π system for these two isomers. These slight decreases in EA compared to parent **70-8-1** were confirmed by DFT calculated EA values as shown in Table 1.7.

To examine if placing CN group(s) on different cage carbon atoms in **70-8-1** may cause an opposite effect and lead to an increased EA value, DFT was used to study a theoretical isomer of $C_{70}(CF_3)_8(CN)_2$ (***C*$_1$-(70-8-1)(CN)$_2$-th**) that has the same addition pattern as **70-10-2** and only differs from ***C*$_s$-(70-8-1)(CN)$_2$** by the location of one CN moiety (see Figure 1.19). Indeed, this minimal change in addition pattern leads to a large increase in EA of 0.213 eV compared to **70-8-1** (Table 1.7). Thus, the introduction of two CN groups to **70-8-1** can either increase or decrease EA based on addition pattern. The calculated EA of three isomers of $C_{70}(CF_3)_8(CN)_2$ differ by as much as 0.255 eV, which manifests strong dependence of electronic properties on the location of each addend on fullerene cores. In contrast, small-molecule acceptors with polycyclic aromatic cores exhibit linear incremental dependence on the number of EWGs, and isomeric molecules within the same composition have very similar EAs.[25,99]

These results indicate that the relative electron-withdrawing effect of a CN group is larger than that of a CF_3 group when *ipso*-substitution of a CF_3 group takes place. For pairs of isostructural $C_{70}(CF_3)_8(CN)_2$ and $C_{70}(CF_3)_{10}$ with the **70-10-1** and **70-10-2** addition patterns, incremental increase in DFT-calculated EA (per one CN group) is ca. 90 meV and 100 meV,

respectively, which is in agreement with the incremental EA value of 80 meV per one CN group for the isostructural pair of $C_{60}(CF_3)_5$ and $C_{60}(CF_3)_4CN$ species described in Section 1.6.1.[50] Experimental data from photoelectron spectroscopy reported here provide unequivocal support for these conclusions derived from the DFT data: the measured EA of ***C*$_1$-(70-8-1)(CN)$_2$** is 140 meV higher than that of **70-10-1**, indicating that substituting CF_3 for CN results in an increase of EA by 70 meV per substitution. Furthermore, the $C_{70}(CF_3)_8(CN)_2$ and $C_{70}(CF_3)_{10}$ isomers with the **70-10-2** addition pattern have an increased EA over the **70-10-1** pattern by 238 meV and 220 meV, respectively.

1.6.4 Electron Affinity of Cyanated $C_{70}(CF_3)_{10}$

The electronic properties of the three cyano derivatives of **70-10-1** were also studied by LT PES and DFT. Two isomers of *C*$_1$-$C_{70}(CF_3)_{10}(CH_3)_2(CN)_2$ (**(70-10-1)(34,44-CH$_3$)$_2$(23,33-CN)$_2$** and **(70-10-1)(33,44-CH$_3$)$_2$(23,34-CN)$_2$**) and **(70-10-1)(CN)$_2$** were synthesized using the method described in Section 1.4.3.[64] The gas-phase EA of **(70-10-1)(CN)$_2$** was determined by LT PES and compared to **70-10-1**. Cyanation of **70-10-1** resulted in a 210 meV increase of EA. Remarkably, comparison of **70-10-1** and the two isomers of **(70-10-1)(CH$_3$)$_2$(CN)$_2$** shows slightly higher EA values for the latter despite the presence of two electron-donating CH_3 groups in their structures and decreased π-system of C_{70} core. The measured EA values of both **(70-10-1)(CH$_3$)$_2$(CN)$_2$** isomers are virtually the same: apparently, difference in relative positions of CN and CH_3 do not have a significant effect on their electronic properties. DFT calculations confirm the observed trend of increasing EA from **70-10-1** to **(70-10-1)(CH$_3$)$_2$(CN)$_2$** to **(70-10-1)(CN)$_2$** (Table 1.7 and Figure 1.35). In contrast to the unanticipated trends in electronic properties of cyanated $C_{70}(CF_3)_8$ compounds described above, these three examples of chemical modifications

of **70-10-1** appear to follow the expected trend where electron-withdrawing CN groups increase EA and electron-donating CH_3 groups decrease EA.

1.7 Addition of Polymerizable Groups to Fullerene Derivatives

A method was developed to decorate EMFs with a polymerizable group with the desire that they would then incorporate more readily into polymer beads for cancer targets than mixtures of EMFs with no polymerizable group (see Section 1.2). The reaction conditions were first confirmed on a mixture of cheaper and more abundant $C_{70}(CF_3)_{10,12}$. When the conditions were successful with the hollow fullerenes they were next tested on mixtures $Sc_3N@C_{80}(CF_3)_n$ and then other available $M_3N@C_{80}(CF_3)_n$ mixtures. Two reaction conditions that were successful on $C_{70}(CF_3)_{10,12}$ were attempted on EMF derivatives and will be described below; the Prato reaction and the Bingel reaction. Less successful attempts with $C_{70}(CF_3)_{10,12}$ will be described first.

One approach to add a polymerizable group was attempted utilizing cyano fullerene anions. The experiments described in Section 1.3 involved the simple synthesis of cyano fullerene anions and quenching with electrophiles to produce neutral PFAF(CN)(electrophile) derivatives. Perhaps the electrophile could have a polymerizable functional group attached. Mixtures of $C_{70}(CF_3)_{10,12}$ were used to initially explore this reaction. A solution of Et_4NCN was added to a red-brown solution of $C_{70}(CF_3)_{10,12}$ and the solution instantly became dark green indicating the formation of $C_{70}(CF_3)_{10,12}(CN)^-$. A large excess of vinylbenzyl chloride was added and the solution remained the same color for six days. It appeared that the vinylbenzyl group was not a strong enough electrophile to quench the $C_{70}(CF_3)_{10,12}(CN)^-$ anions. Previous experiments using strong electrophiles like MeOTf, trifluoroacetic acid, and *p*-TsCN were able to quench the cyano anions rather quickly, so perhaps weak electrophiles cannot be used. In the next

experiments, vinylbenzyl chloride was reacted with AgOTf in order to make an electrophile with a better leaving group. Addition of 1.3 equivalents vinylbenzyl chloride to AgOTf in toluene resulted in a clear solution with white precipitates. Presumably the white precipitates were AgCl and the solution contained vinylbenzylOTf. A portion of this solution was added to a mixture of $C_{70}(CF_3)_{10,12}(CN)^-$ and the solution instantly turned orange. Analysis by APCI-MS revealed that the reaction reverted back to starting $C_{70}(CF_3)_{10,12}$. Possibly the electrophile, including any Ag^+ still present in the vinylbenzylOTf, could quench the cyano derivatives resulting in the reverse reaction to starting $C_{70}(CF_3)_n$. This could be possibly be overcome by using a larger excess of electrophile like in the **70-10-1** reactions described above.

The next attempts at adding a polymerizable group involved the incorporation of an allyl group to the core. Lithium reactants are known to readily add to C_{60} and PFAFs, so it is feasible that allyllithium could be generated in situ and added directly to EMFs. An excess of allylbromide (3.5 equiv.) was added to *t*-BuLi in pentane at −72°C. This mixture was added in large excess (ca. 700 equiv.) to a mixture of $C_{70}(CF_3)_n$ and the fullerene solution became brown after warming to room temperature. This reaction mixture was then quenched with trifluoroacetic acid. The reaction mixture was analyzed by APCI-MS after removing the solvent, exposing to air, and then filtering in DCM. Peaks arising from $C_{70}(CF_3)_{10,12}$, $C_{70}(CF_3)_{10,12}(Bu)_{1,2}$, and $C_{70}(CF_3)_{10,12}(Bu)_{1,2}(allyl)_1$ were present. Butyl groups most likely add to $C_{70}(CF_3)_{10,12}$ before allyl groups since no peaks arising from $C_{70}(CF_3)_{10,12}(allyl)$ were observed. This method appeared to successfully add an allyl group, but also contained many unfavorable butyl additions. The next experiments were done with cyano anions to avoid using highly reactive *t*-BuLi and avoid unfavorable butyl additions. A green solution of $C_{70}(CF_3)_n(CN)^-$ was quenched with a very large excess of allylbromide and the solution turned yellow after several hours. After

removing the solvent and excess allylbromide by vacuum the ^{1}H NMR revealed that no excess allylbromide remained. Initial injections into APCI-MS revealed peaks corresponding to $C_{70}(CF_3)_{10,12}(CN)(allyl)^-$ that quickly disappeared and were dominated by $C_{70}(CF_3)_{10,12}^-$ peaks. It was difficult to determine the yield of products with the small scale that these allyl reactions were performed and the mixtures of fullerenes used, but it was apparent that allyl groups could be added.

A modified Prato reaction to add a vinylic group was next performed based on a previously reported reaction with C_{60}.[100] An excess of sarcosine and 10-undecenal were heated with a toluene solution of $C_{70}(CF_3)_{10,12}$. The fullerene reaction mixture was then separated by column chromatography on silica gel from unreacted sarcosine and 10-undecenal and then analyzed by mass spectrometry. The mass spectrometry indicated that at least two successful ylide additions to $C_{70}(CF_3)_{10}$ and one addition to $C_{70}(CF_3)_{12}$ occurred (Figure 1.36). Higher additions were not detected due to instrument dynamic range limitations. These successful additions were followed by similar success with mixtures of $Sc_3N@C_{80}(CF_3)_{12}$ or $Sc_3N@C_{80}(CF_3)_{12\text{-}18}$ using nearly identical reaction conditions. Peaks in the mass spectra were observed for mono- and bis- ylide additions to $Sc_3N@C_{80}(CF_3)_{12\text{-}16}$, but not the more heavily decorated $Sc_3N@C_{80}(CF_3)_{18}$ (Figures 1.37 and 1.38). For this reason, EMPFAFs with lower amounts of CF_3 additions were desired as described in Section 1.2.

The successful Prato reaction conditions were then used with ca. 1.5 mg samples of $Lu_3N@C_{80}(CF_3)_{8\text{-}10}$, $Lu_3N@C_{80}(CF_3)_n$, and $Y_3N@C_{80}(CF_3)_{14\text{-}18}$. No ylide products were observed by APCI mass spectrometry. In the case of $Lu_3N@C_{80}(CF_3)_{8\text{-}10}$, multiple matrices were used in MALDI mass spectrometry and still no products could be identified. This could be

because products were not formed in substantial amounts or because the products did not ionize as easily.

A new method, a modified Bingel reaction, was next developed since the modified Prato reaction was unsuccessful with $Lu_3N@C_{80}(CF_3)_n$ or $Y_3N@C_{80}(CF_3)_{14\text{-}18}$. A malonate containing two styrene groups was synthesized from malonyl chloride and vinyl benzyl chloride according to standard literature procedures.[54-56] The malonate was then used in standard Bingel conditions with easily available $C_{70}(CF_3)_{10,12}$ to confirm the validity of the reaction. Toluene solutions of the malonate, I_2, and DBU (2 equiv. each) were added to a toluene solution of $C_{70}(CF_3)_{10,12}$ and stirred overnight. The fullerene products were separated from excess reagents using flash chromatography on silica and analyzed by APCI mass spectrometry (Figure 1.39). The mass spectrometry conditions could not physically measure malonate additions to $C_{70}(CF_3)_{12}$ due to *m/z* limitations, but the monoaddition to $C_{70}(CF_3)_{10}$ was observed so the reaction was deemed successful.

The modified Bingel reaction was then used with a mixture of $Sc_3N@C_{80}(CF_3)_{0\text{-}18}$ which unfortunately contained a small amount of $C_{60}(CF_3)_{10,12}$. TMFs of C_{60} ionize much more readily than those of $Sc_3N@C_{80}$, so the small impurity suppressed the signals from the latter in the mass spectrometry analysis. No peaks that definitively corresponded to the malonate addition to $Sc_3N@C_{80}(CF_3)_{0\text{-}18}$ were identified due to some overlap from the $C_{60}(CF_3)_{10,12}$ peaks. Fortunately, mono- and bis-malonate additions to $C_{60}(CF_3)_{10,12}$ were observed, so this reaction demonstrated that this particular malonate also adds readily to heavily decorated C_{60} TMFs. The reaction was then attempted on two other EMF samples that did not contain $C_{60}(CF_3)_{10,12}$ impurities (first a mixture of $Sc_3N@C_{80}(CF_3)_{12}$ isomers and then pure $Sc_3N@C_{80}$). The conditions described above were used for $Sc_3N@C_{80}(CF_3)_{12}$, but no products were observed by

APCI mass spectrometry. The reaction with $Sc_3N@C_{80}$ included a more polar solvent (DMF) and more equivalents of DBU, malonate, and I_2. This reaction was slightly modified since literature reports show that a more polar solvent and a larger excess of reagents are necessary for the Bingel reaction to occur with $Sc_3N@C_{80}$.[101] As in the case with the other two EMF reactions, no products were observed by APCI mass spec.

The synthesis of EMFs with polymerizable groups proved challenging despite developing multiple methods that could successfully add polymerizable groups to C_{60} and C_{70} TMFs. The low availability and high cost of starting EMF materials was another bottle-neck when trying to optimize reaction conditions. Furthermore, traditional spectroscopic techniques for analyzing C_{60} and C_{70} TMFs (NMR, mass spectrometry, etc.) were not as effective when analyzing EMF reactions.

1.8 Addition of Phosphonic Acids to $C_{60}(CF_3)_n$

Earlier reactions with PFAFs containing varying amounts of trifluoromethyl groups have shown that nucleophilic addition CN^- were regioselective.[50,64,102] However, it was found in the work described below that the selectivity of a Bingel-Hirsch reaction with phosphonic acid malonatic ester greatly depended on the PFAF substrate. The synthesis of 11-(diethoxyphosphoryl)undecyl methyl malonate and subsequent Bingle-Hirsch reactions were carried out according to modified literature procedures (Scheme 1.1).[54-56] The amount of phosphonic ester (PE) additions and isomers formed can be large or small depending on the PFAF. In general, the derivatives with more CF_3 groups, $C_{60}(CF_3)_{10}$ isomers, were more selective than derivatives with two or four CF_3 groups. Reactions with **60-2-1** and **60-4-1** resulted in far too many products that were inseparable by combinations of flash chromatography and HPLC. The product mixtures exhibited complex and broad ^{19}F signals which indicated the formation of

many products. Furthermore, a significant amount of insoluble products were formed during the reactions, which were more than expected for a typical Bingel-Hirsch reaction. On the other hand, Bingel-Hirsch reactions with **60-10-3**, **60-10-5**, and **60-10-6** were much more selective and did not produce as many undesirable and insoluble materials. It appears that the abundance of CF_3 groups help direct the malonate additions to the more scarce and unsubstituted cage pentagons present in $C_{60}(CF_3)_{10}$ isomers compared to the less substituted TMFs. Monoadducts were separated from bis- and trisadducts by flash chromatography with toluene/methanol mixtures and then the major monoadducts were further purified with HPLC in toluene.

A single, predominant isomer of **(60-10-3)(PE)** was isolated by HPLC in toluene using a Buckyprep column. The ^{19}F NMR spectrum of this product exhibited a ten multiplet spectrum with similar chemical shifts to parent **60-10-3**, indicating that the addition pattern of the ten CF_3 groups remained unchanged upon phosphonic ester addition (Figure 1.40). A peak at 1748 *m/z* in the MALDI mass spectrum corresponded to $C_{60}(CF_3)_9(PE)H^-$ and confirmed the addition of a single malonate to the fullerene core along with analysis of the ^1H and ^{31}P NMR spectrum. A Bingel-Hirsch reaction with **60-10-5** and malonate phosphonic ester produced a yellow solution with two predominant isomers of **(60-10-5)(PE)** as determined by ^{19}F NMR (Figure 1.41). The two isomers were produced in relatively equal amounts according to ^{19}F and ^{31}P analyses and could not be separated by HPLC using a Buckyprep column. The reaction with **60-10-6** was the least selective of the $C_{60}(CF_3)_{10}$ reactions investigated. At least six isomers of **(60-10-6)(PE)** (see Figure 1.42) were produced that could not be separated by HPLC in 100% toluene using a Buckyprep column, so the product mixture was not used for further reactions.

The phosphonic ester moieties on one isomer of **(60-10-3)(PE)** and the mixture of two isomers of **(60-10-5)(PE)** were then converted to phosphonic acids, $C_{60}(CF_3)_{10}(PA)$. Phosphonic

esters do not bind to MO_x as strongly as phosphonic acids, so the acid derivatives were desired for SAM formation. The phosphonic acid was synthesized by performing several steps of the reported literature procedure.[54-56] Each phosphonic ester was dissolved in dry dichloromethane with excess $BrSiMe_3$ for 1 to 3 days before the solvent was removed and MeOH and HCl were added. This procedure was repeated several times to maximize acid formation. The solubility of the product mixtures were much lower than the starting phosphonic ester derivatives; this was also observed with other C_{60}(PA) derivatives.[54-56] Solubility of the product mixtures decrease in the series of chloroform/methanol, chloroform, toluene, toluene/methanol, DCM, DCM/methanol, methanol, and CS_2. A decrease in the ^1H NMR signals of the ester moiety relative to other ^1H signals indicated a loss of phosphonic ester. Broadening of the CF_3 multiplets in ^{19}F NMR spectra were observed with no shifts in peak positions. Mass spectra (ESI and MALDI in positive and negative mode) showed peaks from the formation of the phosphonic acid and partially reacted ester products. Complete conversion to the phosphonic acid is not essential, since the partial and full esters will not bind as strongly when forming the SAM and can be washed away to leave a pure monolayer of the $C_{60}(CF_3)_{10}$(phosphonic acid) derivatives.

The successfully synthesized **(60-10-3)(PA)** sample was sent to the Marcus Halik research group in Erlangen, Germany for SAMFET measurements performed by Thomas Schmaltz. In brief, SAMs were formed when FET substrates (atomic layer deposited (ALD) AlO_x on Si substrate) were immersed in **(60-10-3)(PA)** solution. Monolayers of **(60-10-3)(PA)** binded to the AlO_x surface while weakly bound excess layers and **(60-10-3)(PE)** were washed away with solvent, which left a single monolayer denoted as **(60-10-3)(PA)**-SAM. In some cases mixed monolayers were formed starting with $C_{10}F_{17}$-(carboxylic acid) SAMFETs that were exchanged with a solution of **(60-10-3)(PA)**-SAM.

Confirmation of SAM formation was obtained by static contact angle (SCA), X-ray reflectivity (XRR) measurements, and grazing incidence X-ray diffraction (GID). The SCA of **(60-10-3)(PA)**-SAMs with water were 101.0° ± 0.7° which is indicative of a hydrophobic surface. In comparison, similarly fabricated non-fluorinated C_{60}-SAMs showed contact angle values < 90°. The vertical electron density profile from XRR shows that the **(60-10-3)(PA)** molecules arrange preferentially with the fullerene moieties on top of the SAM (Figure 1.43). GID measurements of **(60-10-3)(PA)**-SAMs exhibited no diffraction peaks, which indicated that the SAM was (predominantly) amorphous. In comparison, the non-fluorinated C_{60}-SAMs showed a hexagonal crystalline order.

FET devices using **(60-10-3)(PA)**-SAMs were tested (Figure 1.44). Several different transistor setups and layouts (top contact, bottom contact, patterned by photolithography/e-beam lithography, and shadow masks) were fabricated, but in all cases the drain current across the transistor channel did not exceed the leakage current through the SAM. In case of the shadow mask patterned devices during the gold evaporation for the source/drain electrodes, some gold leached into the transistor channel leading to an Ohmic part of the current-voltage curve. Due to this leach, the drain current was lifted above the leakage current level and a current modulation with the gate voltage could be observed. This demonstrates that, in general, the devices worked. However, the charge transport in the SAM layer was so poor that it was hidden behind the leakage current in all other devices. Some charge carrier mobility of approximately 10^{-7} $cm^2/(Vs)$ (approximately two orders of magnitude lower than in the non-fluorinated C_{60}-SAMs) could be extracted. However, the devices with gold in the channel cannot really be considered FETs and none of the other devices worked. Various experiments to increase the thickness of the dielectric were attempted in order to reduce the leakage current, but did not improve device performance.

1.9 Conclusions

The predominant sites of anionic nucleophile addition to several PFAFs (primarily **60-2-1, 60-4-2, 70-8-1, and 70-10-1**) were probed and the predominant sites of subsequent cationic electrophile addition to the anionic PFAF-derived intermediates were determined. For nucleophilic and electrophilic addition, and with two nucleophiles and three electrophiles, the regioselectivity for the predominant isomer or pair of isomers was >50 mol% for $C_{70}(CF_3)_{10}(CH_3)_2(CN)_2$ and 90+ mol% for the other reactions. In the case of **60-2-1**, the addition of the nucleophile/electrophile pairs led to one or two predominant isomers, at least one of which could not have been formed by addition to a cage C=C bond. Electrophilic attack on **(60-4-2)(CN)**$^-$ results in an asymmetric product that is not part of the previously-identified most-reactive C=C bond. The product, **(60-4-2)(CN)H**, is a rare representative of a fullerene derivative with the SPP addition pattern in which five substituents are strong electron withdrawing groups. This type of SPP derivative possesses good air stability, in contrast to the counterparts with electron donating groups. In the case of **70-8-1**, the sites of nucleophilic and electrophilic attack are the symmetry-related cage C atoms that comprise the previously-identified most-reactive C=C bond. In the case of a single nucleophile addition to **70-10-1**, these sites also comprise the previously-identified most-reactive C=C bond, but these results demonstrate for the first time that only one of these two unique C(sp^2) atoms is, almost exclusively, the site of nucleophilic attack. In the case of a double nucleophile addition to **70-10-1**, the one nucleophile was added to either of the two most-reactive C=C bond C(sp^2) atoms and another nucleophile added to a C(sp^2) atom far removed from the first site, and "its" electrophile added to a C(sp^2) atom *para* to it and not to a neighboring C atom (i.e., the concept of a second-most-reactive C=C bond in **70-10-1** is invalid). The experimental results are supported by DFT calculations, which indicate that some of the electrophile additions may be kinetically controlled rather than thermodynamically

controlled. Taken together, this work goes beyond the chemistry of PFAFs and suggests that the sequential one-pot addition of different types of substituents to specific cage C atoms of fullerene derivatives could lead to the design of even more elaborate derivatives using DFT as a guide, instead of merely discovering new derivatives by trial and error.

The effects of trifluoromethylation and cyanation on the electron affinity of eight C_{60} and seven C_{70} fullerene derivatives were studied using LT PES and DFT. In some cases, the addition of electron-withdrawing CF_3 or CN groups leads to the improvement of electron accepting properties, whereas in the several other cases cyanation led to decreased EA. The SPP derivatives stemming from **60-4-2** exhibited exceptionally high electron affinity of the respective radicals, and hence, high thermodynamic stability of its anions. In the case of two fullerene derivatives with the same addition pattern, CN substitution of CF_3 results in an EA increase of 70 meV per substitution, as determined experimentally, and an increase of 90-100 meV was predicted by DFT. DFT calculations on two different **(70-8-1)(CN)$_2$** isomers demonstrated that the difference in location of only one CN group can change the EA by 255 meV. Overall, excellent correlation between the experimentally determined and DFT calculated EA values (with systematic underestimation of DFT values of ca. 150 meV) were observed for seven studied C_{70} fullerenes (Figure 1.45). These results highlight the usefulness of the validated theoretical analysis of electronic properties prior to practical synthesis of new acceptor materials where design is based solely on the chemical intuition. Complex and mutually cancelling effects of the electron-withdrawing functional groups, saturation of the fullerene π system and addition pattern type are difficult to predict empirically, whereas modern DFT theory allows for reliable, if not quantitative, data and trends to be revealed for these classes of molecules. Due to these

unique properties, such derivatives of PFAFs may become increasingly important building blocks in the molecular and supramolecular designs of the electroactive functional materials.

EMFs and their TMF derivatives have very different chemical reactivity from each other and from hollow cage fullerenes. This different reactivity proved to make the synthesis and isolation of desired EMF products much more complicated than anticipated and optimized conditions for hollow fullerenes and some EMFs did not translate to all EMFs and EMF derivatives. Small amounts of $Lu_3N@C_{80}(CF_3)_n$ (n < 12) could be made with low yields, but were not successfully modified with a polymerizable group. The standard Bingel reaction conditions used were not successful with EMFs, but several conditions could still be changed in order to optimize the reaction. The addition of a more polar solvent (DMF), heat, a different base (NaH instead of DBU), or a different halogen reagent (CBr_4 instead of I_2) are all simple changes that could possible improve the reaction. It appears that the reaction conditions do not simply translate from using hollow cage TMFs to EMFs, so new reaction conditions must first be developed to synthesize $M_3N@C_{80}(CF_3)_n$ compounds in more quantitative amounts.

A phosphonic ester malonate was readily added to several PFAFs and the PFAFs containing ten CF_3 groups were able to direct the malonate to more regioselective cage locations than PFAFs with two or four CF_3 groups. Successfully isolated **60-10-3(PE)** was sufficiently converted into a phosphonic acid that was able to strongly bind to AlO_x and form SAMs that were used in FET measurements. The SAMs were more hydrophobic and less crystalline than similar non-fluorinated C_{60}-SAMs. Charges were observed with FET measurements. However, the strong electron-withdrawing nature of the **60-10-3** moiety was not enough to overcome inferior morphology that ultimately lead to high leakage current and low charge carrier mobility compared to non-fluorinated C_{60}-SAMs.

1.10 Experimental Section

General information: All reagents and solvents were reagent grade or better. ACS Grade dichloromethane (Fisher Scientific), HPLC Grade acetonitrile (Fisher Scientific), ACS Grade hexanes (Fisher Scientific), sodium thiosulfate crystals (Mallinckrodt), trifluoromethyl iodide (Synquest Labs), chloroform-D (Cambridge Isotopes Laboratories), hexafluorobenzene (Oakwood Products), NEt_4CN (Sigma-Aldrich), *p*-TsCN(Sigma-Aldrich), MeOTf (Sigma-Aldrich), and CF_3COOH (Sigma-Aldrich) were used as received. Proton sponge (Sigma Aldrich) was sublimed prior to use. All manipulations of $PFAF(CN)^-$ solutions were carried out under an atmosphere of purified dinitrogen using either glovebox or Schlenk techniques and solvents that were dried with 3 Å molecular seives. HPLC analyses and purifications were carried out using Shimadzu HPLC instrumentation (CBM-20A control module, SPD-20A UV-detector set to 300 nm, LC-6AD pump, manual injector valve) equipped with a semi-preparative 10 mm I.D. × 250 mm or a preparative 25 mm I.D. × 250 mm Cosmosil Buckyprep column (Nacalai Tesque, Inc.) or a semi-preparative 10 mm I.D. × 250 Cosmosil Buckyprep-M column (Nacalai Tesque, Inc.). Fluorine-19 NMR spectra were recorded using a Varian 400 spectrometer operating at 376.5 MHz (C_6F_6 internal standard, δ −164.9). Negative-ion APCI mass spectra were recorded using a Finnigan 2000 LCQ-DUO spectrometer. The samples were injected as ca. 50:50 v:v $PhCH_3$:ACN solutions; the mobile phase was ACN. Electronic spectra recorded using a Cary 500 spectrophotometer with a resolution of 1 nm. Cyclic voltammetry measurements were carried out on PAR 263 potentiostat/galvanostat in anaerobic conditions; platinum working and counter electrodes; silver wire quasi-reference electrode; 0.1 M $TBABF_4$ in *o*-DCB; ferrocene internal standard. PES measurements: the spectroscopy and procedures used were described previously.[83] Anions of C_{70} fullerene derivatives were generated by electrospraying a 0.1 mM acetonitrile solution of each fullerene mixed with TDAE donors. Anions generated were transported by RF

ion guides into a cryogenic ion trap, where they were accumulated and cooled to 12 K, before being pulsed out at 10 Hz into an extraction zone of a time-of-flight (TOF) mass spectrometer. Mass-selected anions were first maximally decelerated and then intersected by 266 nm (4.661 eV) photons from a Nd:YAG laser in the photodetachment zone. The laser was operated at a 20 Hz repetition rate with ion beam off at alternating shots, enabling shot-by-shot background subtraction. Photoelectrons were collected at nearly 100% efficiency using the magnetic-bottle and analyzed in a 5.2 m long photoelectron flight tube. The TOF photoelectron spectrum was converted to the kinetic energy spectrum, calibrated by the known I^- and ClO_2^- spectra. The binding energy spectra were obtained by subtracting the kinetic energy spectra from the photon energy used. The gas-phase EA of each compound was determined from the 0-0 transition in the 12 K LT-PES spectrum of each radical anion with an accuracy of 10 meV.

Single-Crystal XRD Experiments: Data for **60-8-3** were collected during the 2014 American Crystallographic Association Summer Course in Chemical Crystallography at the University of Notre Dame. Data for ***C*$_1$-C$_{70}$(CF$_3$)$_{10}$(33,44-CH$_3$)$_2$(23,34-CN)$_2$** were collected at CSU by Brian Newell. These data were collected using a Bruker Kappa APEX II CCD diffractometer employing $Mo_{K\alpha}$ radiation and a graphite monochromator. Data for **60-10-14, 60-12-X**, ***C*$_s$-(70-8-1)(CN)$_2$** were collected on the Advanced Photon Source synchrotron instrument at Argonne National Laboratory, Argonne IL, on beamline 15ID-B with a wavelength of 0.41328 Å, employing a diamond(111) monochromator and Bruker D8 goniometer.

Unit cell parameters were obtained from least-squares fits to the angular coordinates of all reflections, and intensities were integrated from a series of frames (ω and ϕ rotation) covering more than a hemisphere of reciprocal space. Absorption and other corrections were applied using SCALE.[103] The structures were solved using direct methods and refined (on F^2, using all data) by

a full-matrix, weighted least-squares process. Standard Bruker control and integration software (APEX II) was employed,[104] and Bruker SHELXTL software was used with Olex2 for structure solution, refinement, and molecular graphics.[105,106] More data can be found in Tables 1.8 and 1.9.

Generation of NEt_4[*C*$_1$-$C_{60}(CF_3)_2(CN)$], two isomers each of *C*$_1$-$C_{60}(CF_3)_2(CN)$-(CH_3) and *C*$_1$-$C_{60}(CF_3)_2(CN)H$, and a single isomer of *C*$_1$-$C_{60}(CF_3)_2(CN)_2$ in solution. In a typical preparation, the ***C*$_1$-(60-2-1)$(CN)^-$** anion was generated by adding an aliquot of an 11.4 mM CH_2Cl_2 solution of NEt_4CN (0.11 mL, 0.0013 mmol CN^-) to a brown CD_2Cl_2 solution of **60-2-1** (1.1 mg, 0.0013 mmol) at 23(2) °C (CN^-:**60-2-1** mol ratio = 1.0). The reaction mixture became dark brown. After five min, NMR scale aliquots were treated with an excess of CH_3OTf, CF_3COOH, or *p*-TsCN. In all three cases a yellow solution was formed immediately. These solutions were exposed to air, washed three times with water, and dried with $MgSO_4$. The solvent was removed and the remaining solids were analyzed by HPLC and mass spectrometry (see Figures 1.46 and 1.47 for examples). Colorless CH_2Cl_2 solutions of NEt_4CN became yellow after one day; therefore fresh solutions were used for each reaction.

Spectroscopic data for NEt_4[*C*$_1$-$C_{60}(CF_3)_2(CN)$]. ^{19}F NMR (376.5 MHz; CD_2Cl_2; δ(C_6F_6) = −164.9): δ −71.8 (q, int. 1.0, *J*FF = 13(1) Hz), −72.6 (q, int. 1.0, *J*FF = 14(1) Hz).

Spectroscopic data for the *C*$_1$-$C_{60}(CF_3)_2(CN)(CH_3)$ reaction mixture. ^{19}F NMR (376.5 MHz; CD_2Cl_2; δ(C_6F_6) = −164.9): δ −70.9 (q, int. 0.97, 3F, *J*FF = 14(1) Hz), −71.2 (q, int. 0.66, 3F, *J*FF = 12(1) Hz), −72.0 (q, int. 1.00, 3F, *J*FF = 14(1) Hz), −73.6 (q, int. 0.63, 3F, *J*FF = 12(1) Hz).

Spectroscopic data for the *C*$_1$-$C_{60}(CF_3)_2(CN)(H)$ reaction mixture. ^{19}F NMR (376.5 MHz; CD_2Cl_2; δ(C_6F_6) = −164.9): δ −70.9 (q, int. 0.99, 3F, *J*FF = 14(1) Hz), −71.1 (q, int. 0.43, 3F,

*J*FF = 12(1) Hz), −72.0 (q, int. 1.00, 3F, *J*FF = 14(1) Hz), −73.6 (q, int. 0.53, 3F, *J*FF = 12(1) Hz).

Spectroscopic data for the C_1-$C_{60}(CF_3)_2(CN)_2$ reaction mixture. ^{19}F NMR (376.5 MHz; CD_2Cl_2; δ(C_6F_6) = −164.9): δ −68.7 (q, int. 1.0, 3 F, *J*FF = 14(1) Hz), −71.1 (q, int. 1.0, 3 F, *J*FF = 14(1) Hz).

Synthesis and isolation of p^3-$C_{60}(CF_3)_4$, (60-4-2): In a typical reaction, C_{60} (550 mg, 0.76 mmol) was ground into a fine powder and placed into the homemade GTGS reactor as reported elsewhere.[28] The reactor was put under dynamic vacuum and quickly heated to 600 °C within about 20 min. The reactor was then charged with 120 mtorr CF_3I and sublimed product was observed on the cold finger. The gas was removed every two hours with dynamic vacuum and fresh CF_3I (120 mtorr) was added. After 8 hours the heat was turned off and the gas was removed with vacuum. The crude solid contained a mixture of unreacted C_{60}, one isomer of $C_{60}(CF_3)_2$, two isomers of $C_{60}(CF_3)_4$, one major isomer of $C_{60}(CF_3)_6$, and minor products of $C_{60}(CF_3)_{6\text{-}10}$. Polar solvents and light were avoided in order to suppress oxidation of **60-4-2**. The crude solid was dissolved in toluene and then the solvent and I_2 were removed via rotovap. The rotovap procedure was repeated until all traces of I_2 were removed. Then **60-4-2** was separated from the reaction mixture by two-stage HPLC (first stage: toluene/heptane = 1:1, 10 mm I.D. × 250 mm Cosmosil Buckyprep-M column (Nacalai Tesque, inc), 5 mL min^{-1}, retention time = 9.5 min.; second stage: toluene/heptane =2:3, 5 mL min^{-1}, retention time = 14 min.). ^{19}F NMR (CD_2Cl_2): δ −69.98 (unresolved multiplet (um), int. 6), −70.11 (um, int. 6).

Generation of NEt_4[C_s-$C_{60}(CF_3)_4(CN)$] in solution and the isolation of C_1-$C_{60}(CF_3)_4(CN)H$: Under an atmosphere of purified N_2, the C_s-$C_{60}(CF_3)_4(CN)^-$ anion was generated by adding an

aliquot of a colorless 25.8 mM DCM solution of NEt_4CN (1.10 mL, 7.1 µmol CN^-) to a brown solution of **60-4-2** (7.1 mg, 7.1 µmol) in dry DCM (8.3 mL) at 23(2) °C and the color remained brown. After 20 min. an excess of trifluoroacetic acid (~1000 equiv.) was added dropwise and the solution immediately turned orange. The reaction mixture was then exposed to air, passed through silica gel in DCM, and the solvent was removed. The brown solid was then purified by HPLC (Figure 1.48, semi-preparative 10 mm I.D. × 250 mm Cosmosil Buckyprep column (Nacalai Tesque, Inc.), toluene/heptane = 4 : 1, 5 mL min^{-1}, retention time = 10.9 min.). ^{19}F NMR (CD_2Cl_2) δ −69.2 (apparent septet (as), int. 3), −69.9 (q, int. 3, J_{FF} = 11(1) Hz), −72.2 (q, int. 3, J_{FF} = 11(1) Hz), −72.5 (as, int. 3). Note that colorless DCM solutions of NEt_4CN become yellow after one day, so fresh solutions were prepared for the reaction.

Generation of $NEt_4[C_1$-$C_{70}(CF_3)_8(CN)]$ in solution and the isolation of C_s- and C_1-$C_{70}(CF_3)_8(CN)_2$. In a typical preparation, the C_1-$C_{70}(CF_3)_8(CN)^-$ anion was generated by adding an aliquot of a colorless 6.41 mM ACN solution of NEt_4CN (1.63 mL, 0.0104 mmol CN^-) to a yellow solution of **70-8-1** (9.67 mg, 0.00695 mmol) in $PhCH_3$ (10 mL) at 23(2) °C (CN^-:**70-8-1** mol ratio = 1.50; in some preparations C_6D_6 was used instead of $PhCH_3$). (CAUTION: salts of the cyanide anion are toxic and should be handled by trained personnel wearing protective clothing; any waste must be handled carefully, especially solutions to which acid has been added, because HCN is volatile as well as toxic.) The reaction mixture became greyish-blue within seconds and remained the same color for 2 h, at which point an aliquot of a 9.40 mM $PhCH_3$ solution of *p*-TsCN was added (7.20 mL, 0.0677 mmol "CN^+", 9.73 equiv based on **70-8-1**), creating a light-brown solution. After another 2 h, the solution was exposed to air, washed three times with water, and dried with $MgSO_4$. The solvent was removed under vacuum, leaving

yellow solids that were purified by HPLC. Compositions were confirmed by APCI-MS (Figures 1.49 and 1.50) the compounds were analyzed by ^{19}F NMR and UV-Vis (Figure 1.51).

Spectroscopic data for C_1-p^8-$C_{70}(CF_3)_8(CN)^-$. ^{19}F NMR (376.5 MHz; 7:1 C_6D_6:ACN; δ(C_6F_6) = −164.9): δ −61.4 (apparent septet (as), int. 3), −62.2 (as, int. 3), −62.3 (as, int. 3), −62.9 (as), int. 3), −61.1 (as, int. 3), −64.8 (as, int. 3), −66.7 (q, int. 3, J_{FF} = 12(1) Hz), −70.7 (q, int. 3, J_{FF} = 11(1) Hz).

Spectroscopic data for C_s-p^9o(loop)-$C_{70}(CF_3)_8(CN)_2$ (the major isomer). ^{19}F NMR (376.5 MHz; $CDCl_3$; δ(C_6F_6) = −164.9): δ −63.1 (as, int. 6), −63.4 (unresolved multiplet (um), int. 6), −63.6 (um, int. 6), −66.4 (q, int. 6, J_{FF} = 13(1) Hz). The structure of C_s-p^9o(loop)-$C_{70}(CF_3)_8(CN)_2$ determined by X-ray crystallography is named 11,29-dicyano-1,4,19,41,49,60,66,69-octakis(trifluoromethyl)-1,4,11,19,29,41,49,60,66,69-decahydro(C_{70}-D_{5h})[5,6]fullerene.

Spectroscopic data for C_1-$C_{70}(CF_3)_8(CN)_2$ (minor isomer). ^{19}F NMR (376.5 MHz; $CDCl_3$; δ(C_6F_6) = −164.9): δ −63.1 (as, int. 3), −63.3 (um, int. 3), −63.60 (as, int. 3),−63.4 (as, int. 3), −63.7 (as, int. 3), −64.1 (as, int. 3), −65.5 (q, int. 3, J_{FF} = 13(1) Hz), −68.7 (q, int. 3, J_{FF} = 12(1) Hz).

Generation of NEt_4[C_1-$C_{70}(CF_3)_{10}(CN)$] and C_1-$C_{70}(CF_3)_{10}(CN)(H)$ in solution, and the isolation of C_1-$C_{70}(CF_3)_{10}(CN)(CH_3)$. In a typical preparation, the **(70-10-1)(CN)$^-$** anion was generated by adding an aliquot of a 6.41 mM ACN solution of NEt_4CN (3.04 mL, 0.0195 mmol CN^-) to a yellow solution of **70-10-1** (20.0 mg, 0.0131 mmol) in $PhCH_3$ (10 mL) at 23(2) °C (CN^-:**70-10-1** mol ratio = 1.50; in some preparations C_6D_6 was used instead of $PhCH_3$). The reaction mixture became green within seconds and remained the same color for 1 day, at which point a large excess of CH_3OTf was added, instantly creating a yellow solution. (CAUTION:

CH_3OTf is volatile, toxic, and a suspected carcinogen and should only be handled by trained personnel wearing protective clothing.) After 12 h, the solution was exposed to air, filtered through silica gel, and the solvent was removed under flowed air. The remaining yellow solid was purified by HPLC (Figure 1.52). At 1 day, an NMR scale aliquot of the **(70-10-1)(CN)**$^-$ anion was also quenched with a large excess of CF_3COOH, immediately creating a yellow solution. After 1 day, the solution was exposed to air, washed three times with water, and dried with $MgSO_4$. The solvent was removed and the remaining solid was purified by HPLC and then analyzed by ^{19}F NMR and UV-Vis (Figure 1.53).

Synthesis of (70-10-1)(CN)$_2$: The $C_{70}(CF_3)_{10}(CN)^-$ anion was generated by adding an aliquot of a 6.41 mM ACN solution of NEt_4CN (5.20 mL, 33.3 µmol CN^-) to a yellow solution of **10-1** (25.7 mg, 16.8 µmol) in toluene (15 mL) at 23(2) °C (CN^-:**70-10-1** mol ratio = 2.00). The reaction mixture immediately became dark green. An aliquot of the solution (10.1 mL, 8.4 µmol **(70-10-1)(CN)**$^-$) was reacted with a 75 mM toluene solution of *p*-TsCN (5 mL, 376 µmol "CN^+", 45 equiv.) and the solution became yellow after 3 h. The solution was exposed to air, washed four times with water, and dried with $MgSO_4$. The solvent was removed and the remaining solids were analyzed by ^{19}F NMR and separated by HPLC: Cosmosil Buckyprep semi-preparative column, toluene/heptane = 60/40 mobile phase, 5 mL min^{-1}, 300 nm detection, retention time = 3.2 minutes. NI-APCI-MS: calculated 1581.96, observed 1582.07 *m/z*.

Generation of $Li_2C_{70}(CF_3)_{10}(CH_3)_2$ as a green precipitate and the isolation of two isomers of C_1-$C_{70}(CF_3)_{10}(CH_3)_2(CN)_2$. Four equivalents of $LiCH_3$ in Et_2O were added to a yellow solution of **70-10-1** in toluene, causing the immediate formation of a green precipitate and the disappearance of the ^{19}F NMR multiplets belonging to **70-10-1**. Addition of four equivalents of *p*-TsCN resulted in the rapid formation of a golden-yellow solution and the complete

disappearance of the precipitate. The reaction mixture was pre-purified by flash chromatography to remove Li(*p*-Ts). The two predominant products were purified by HPLC and compositions were confirmed with APCI-MS (Figures 1.54-1.56). The minor isomer afforded crystals suitable for X-ray diffraction.

Spectroscopic data for C_1-$C_{70}(CF_3)_{10}(CN)^-$. ^{19}F NMR (376.5 MHz; 2:2:1 C_6D_6:$PhCH_3$:ACN; $\delta(C_6F_6) = -164.9$): δ −60.2 (as, int. 3), −62.1 (as, int. 3), −63.2 (as, int. 3),−62.6 (as, int. 3), −62.7 (as, int. 3), −62.8 (as, int. 3), −63.6 (um, int. 3), −64.7 (um, int. 3), −68.7 (q, int. 3, J_{FF} = 12(1) Hz), −71.0 (q, int. 3, J_{FF} = 10(1) Hz).

Spectroscopic data for C_1-$C_{70}(CF_3)_{10}(CN)(CH_3)$. ^{19}F NMR (376.5 MHz; 2:2:1 C_6D_6:$PhCH_3$:ACN; $\delta(C_6F_6) = -164.9$): δ −60.0 (um, int. 3), −61.7 (um, int. 6), −62.3 (as, int. 3),−62.8 (um, int. 6), −63.5 (um, int. 3), −64.5 (um, int. 3), −68.0 (q, int. 3, J_{FF} = 14(1) Hz), −70.5 (q, int. 3, J_{FF} = 10(1) Hz). ^{19}F NMR (376.5 MHz; $CDCl_3$; $\delta(C_6F_6) = -164.9$): δ −59.8 (um, int. 3), −61.7 (as, int. 3), −62.1 (as, int. 3),−62.6 (as, int. 3), −62.9 (as, int. 3), −63.2 (as, int. 3), −63.7 (as, int. 3), −64.7 (um, int. 3), −68.4 (q, int. 3, J_{FF} = 13(1) Hz), −70.7 (q, int. 3, J_{FF} = 10(1) Hz).

Spectroscopic data for C_1-$C_{70}(CF_3)_{10}(CN)(H)$. ^{19}F NMR (376.5 MHz; 2:2:1 C_6D_6:$PhCH_3$:ACN; $\delta(C_6F_6) = -164.9$): δ −60.0 (um, int. 3), −61.7 (um, int. 6), −62.3 (as, int. 3),−62.8 (um, int. 6), −63.5 (um, int. 3), −64.5 (um, int. 3), −68.0 (q, int. 3, J_{FF} = 14(1) Hz), −70.5 (q, int. 3, J_{FF} = 10(1) Hz).

Synthesis of 11-(tetrahydropyranyloxy)-1-bromoundecane: PPTS (0.230 g, 0.907 mmol) and DHP (0.52 mL, 5.7 mmol) were added to 11-bromo-1-undecenol (1.14 g, 4.54 mmol) in DCM (100 mL). After 16 h the reaction mixture was washed with a saturated $NaHCO_3$ solution (300

mL) and separated. The aqueous layer was washed with additional DCM (100 mL). The two organic solutions were combined and washed with a saturated NaCl solution (200 mL) then dried over Na_2SO_4. The solvent was removed by rotovap and the product was obtained as a colorless oily liquid. Yield: 1.55 g, 100%.

Synthesis of diethyl [18-(tetrahydropyranyloxy)undecyl] phosphonate: A yellow mixture of 11-(tetrahydropyranyloxy)-1-bromoundecane (1.07 g, 3.19 mmol) and triethylphosphite (5.46 mL, 31.9 mmol, 10 equiv.) was refluxed for 6 hours (oil bath temperature = 170 °C). The excess triethylphosphite was removed by vacuum at 165 °C and a yellow-orange, oily liquid remained. The crude product was used in the next step without further purification and isolation.

Synthesis of 11-(diethoxyphosphoryl)-1-undecanol: A mixture of diethyl [18-(tetrahydropyranyloxy)undecyl] phosphonate (assume 3.19 mmol), ethanol (140 mL), and PPTS (86.1 mg, 0.343 mmol) were refluxed for 3 hours (oil bath temperature = 100 °C). The solvent was removed by rotovap and a yellow, oily liquid remained. The reaction mixture still contained unreacted PPTS which was removed on a small silica gel column. The product was purified by flash-chromatography on silica gel with ethyl acetate. Yield 0.435 g, 1.41 mmol, 44 % yield from 11-(tetrahydropyranyloxy)-1-bromoundecane.

Synthesis of 11-(diethoxyphosphoryl)undecyl methyl malonate: A solution of methylmalonyl chloride (0.23 mL in 30 mL DCM, 2.11 mmol, 1.5 equiv.) was added dropwise over the course of 30 min. to a solution of 11-(diethoxyphosphoryl)-1-undecanol (0.435 g, 1.41 mmol) and Et_3N (0.30 mL, 2.11 mmol, 1.5 equiv.) in DCM (80 mL) at 0 °C. The solution was stirred for 2 h at 0 °C then for 20 h at room temperature. The solvent was removed by rotovap and a yellow oil remained. The oil was dissolved in ethyl acetate and purified by flash-chromatography on silica

with ethyl acetate and methanol. The product was collected as a colorless, oily liquid. Yield: 0.147 g, 0.375 mmol, 25.5 %.

Synthesis of (60-10-3)(phosphonic ester): Under nitrogen and exclusion of light, **60-10-3** (35.7 mg, 25.3 mmol) was dissolved in degassed toluene (18 mL) at room temperature. Subequently, 11-(diethoxyphosphoryl)undecyl methyl malonate (0.20 mL, 0.60 equiv.) and I_2 (1.80 , 0.76 equiv.) were added. A solution of DBU in toluene (0.79 equiv.) was added dropwise over the course of seven minutes. The reaction was monitored by TLC and was stopped after 20 h when unreacted **60-10-3** was no longer observed. White precipitate was filtered from a dark brown solution and the solution was subjected to flash chromatography on silica with toluene and toluene/methanol mixtures. The fractions containing **(60-10-3)(phosphonic ester)** monoadducts were further purified by HPLC in toluene. The product was analyzed by ^{1}H, ^{19}F, and ^{31}P NMR and MALDI mass spectrometry. Two peaks were present in the mass spectrum; 1830 m/z is 14 more than desired product and unknown, 1748 m/z is $C_{60}(CF_3)_9$(malonate/phosphonic ester) + 1, which corresponds to the loss of one CF_3 group in the mass spec experiment. Yield: 14.7 mg, 32% yield based on starting **60-10-3**.

Synthesis of (60-10-3)(phosphonic acid): A dry dichloromethane solution (5 mL) of **(60-10-3)(phosphonic ester)** (11.7 mg, 6.44 mmol) was cooled in an ice bath and $BrSiMe_3$ (0.1 mL, 38 mmol, 5.9 equiv.) was slowly added. The ice bath was removed after 2 hours and the soluiton was stirred for an additional 19 hours. Toluene, hexamethyldisiloxane and the excess of bromotrimethysilane were removed under vacuum. To remove any remaining traces of reagents, dry toluene (5.0 mL) was added and subsequently removed under vacuum. The residue was dissolved in $CHCl_3$ (5 mL) and then MeOH (5 mL) and H_2O (1 mL) were added at room temperature and stirred for 2 hours. The solvents, except for H_2O, were removed under vacuum.

Acetone was added and the acetone/H_2O azeotrope was removed under vacuum. The solid was dissolved in $CHCl_3$, dried over Na_2SO_4, and then filtered. This entire reaction scheme was repeated several times. In some cases, $HCl_{(aq)}$ was substituted for H_2O or mixtures of $CHCl_3$/MeOH were used for final collection. The product was analyzed by ^{1}H, ^{19}F, and ^{31}P NMR and MALDI mass spectrometry. The peaks in NMR have the same chemical shifts as starting **(60-10-3)(phosphonic ester)**, but are more broadened. Proton peaks corresponding to the ester moiety were reduced. MALDI mass spectra indicated that there was a mixture of partially converted products, unreacted **(60-10-3)(phosphonic ester)**, and **(60-10-3)(phosphonic acid)**. This mixture was used for SAM formation, since only the completely converted products form strong bonds and the esters and half esters can be washed away from the strongly bound SAM.

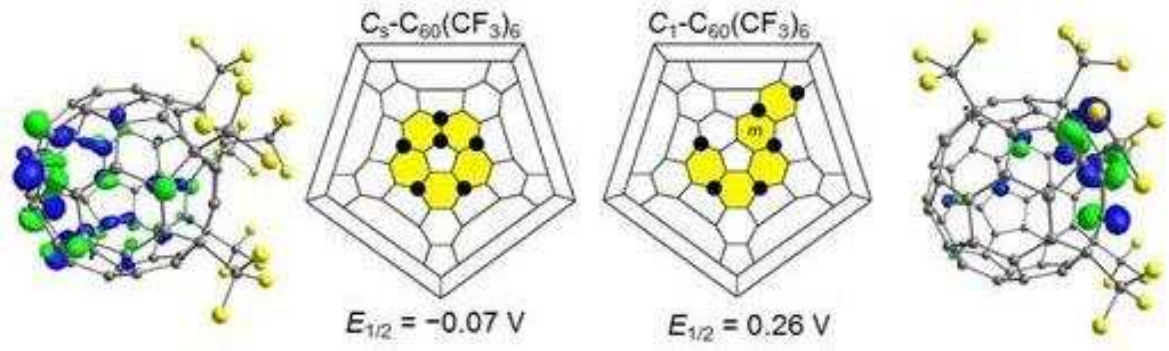

Figure 1.1. Schlegel diagrams and the DFT-predicted cage carbon atom contributions to the LUMO (blue and green orbitals) of C_1-$C_{60}(CF_3)_6$ (left) and C_s-$C_{60}(CF_3)_6$ (right). The black circles indicate the cage carbon atoms to which the CF_3 groups are attached. The ribbon of edge-sharing *m*- and *p*-$C_6(CF_3)_2$ hexagons are highlighted in yellow.

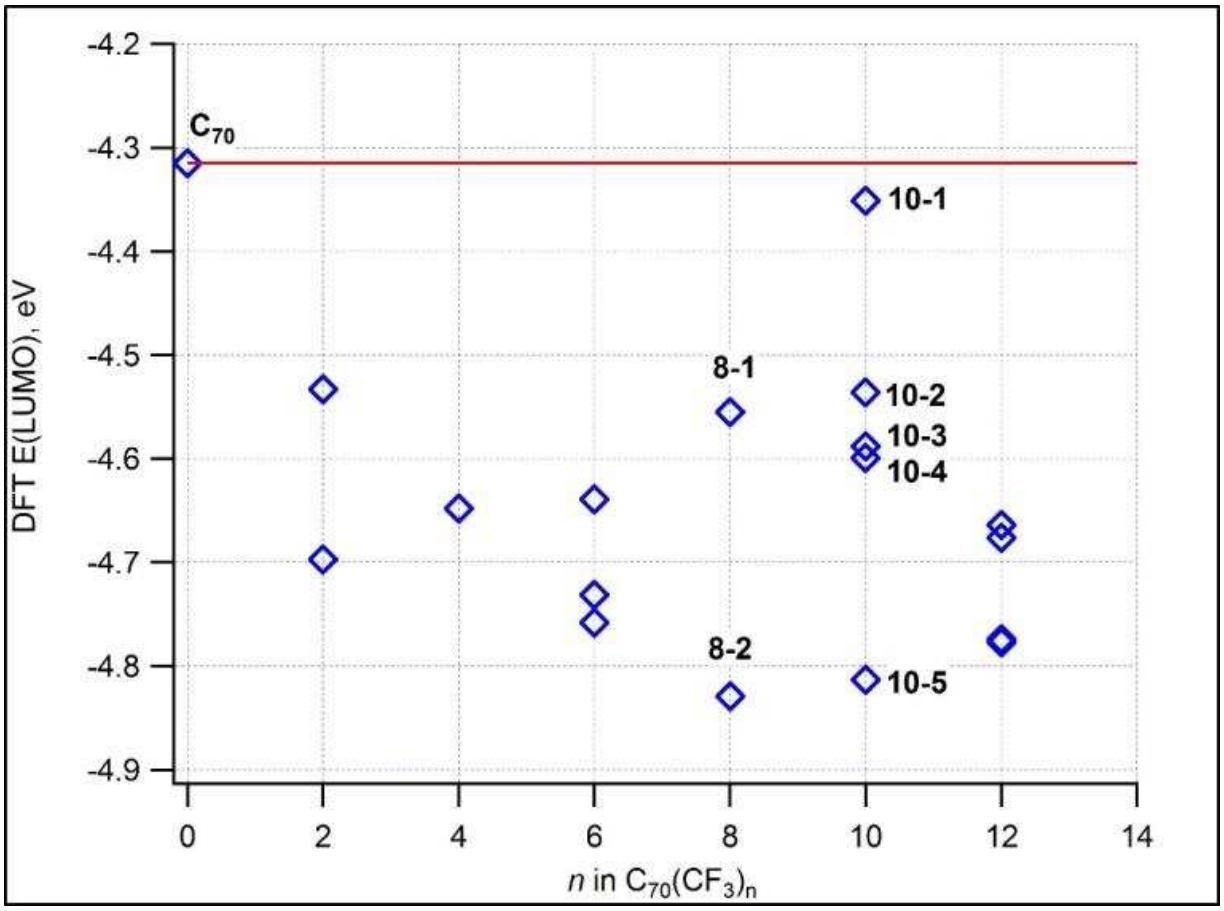

Figure 1.2. DFT calculated E_{LUMO} for known $C_{70}(CF_3)_n$ (n = 0-12) compounds.[49]

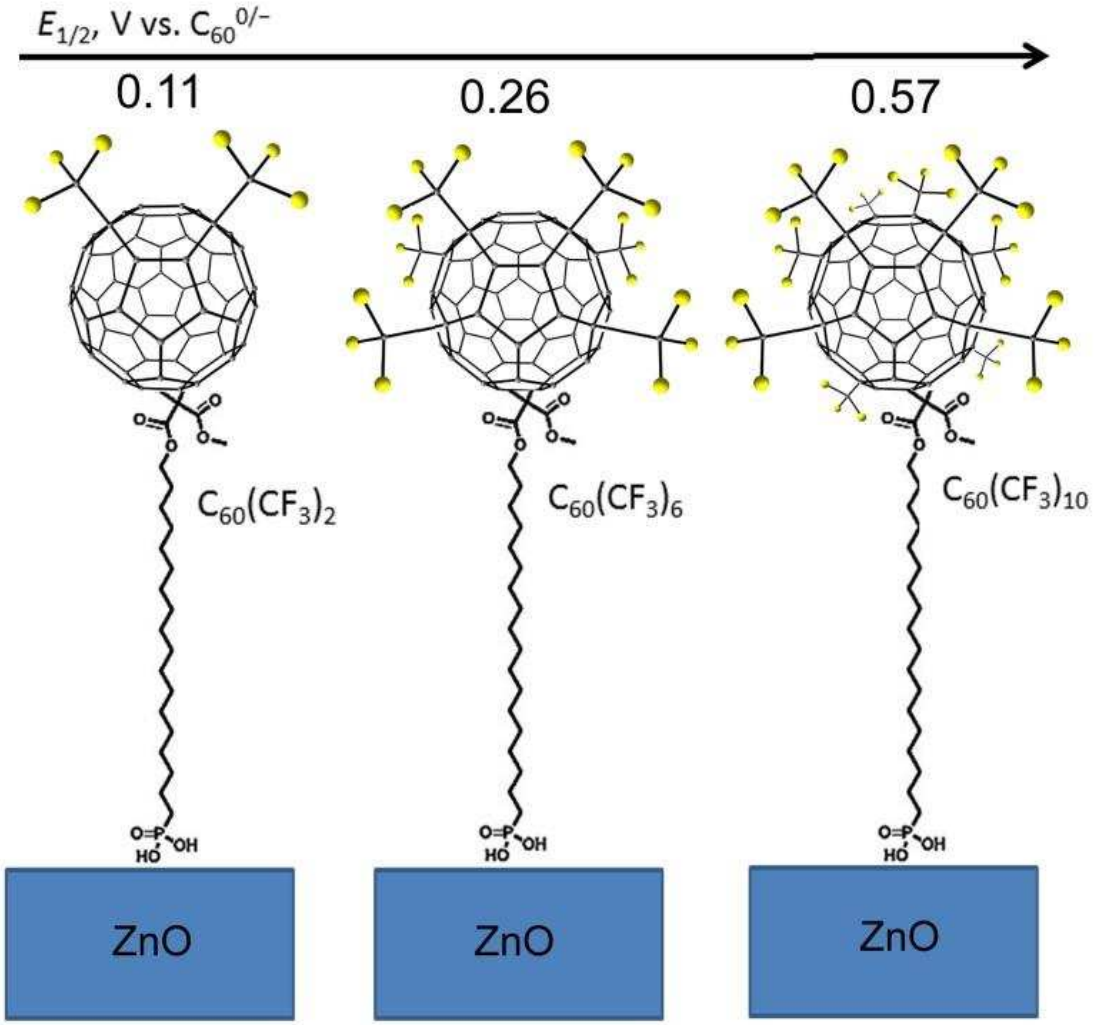

Figure 1.3. Schematic representation of ZnO nanorods coated with SAMs using different PFAFs. Reduction potentials of PFAFs without phosphonic acid linkages are shown.

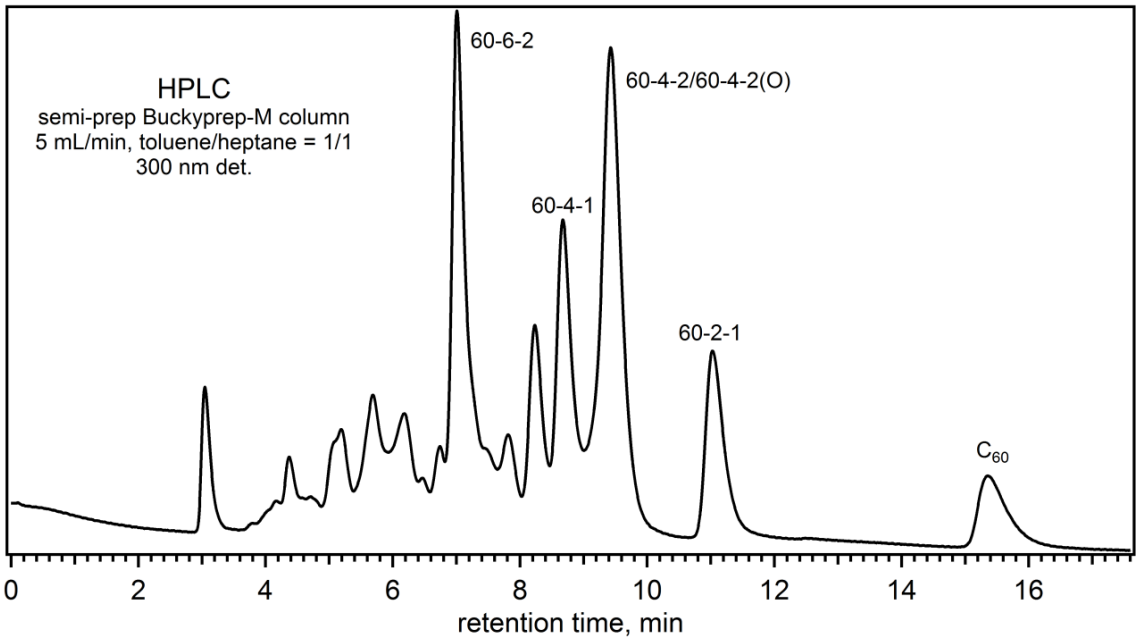

Figure 1.4. HPLC spectrum of crude $C_{60}(CF_3)_n$ from a typical GTGS reaction. Some of the major and more easily separable products are labeled for reference.

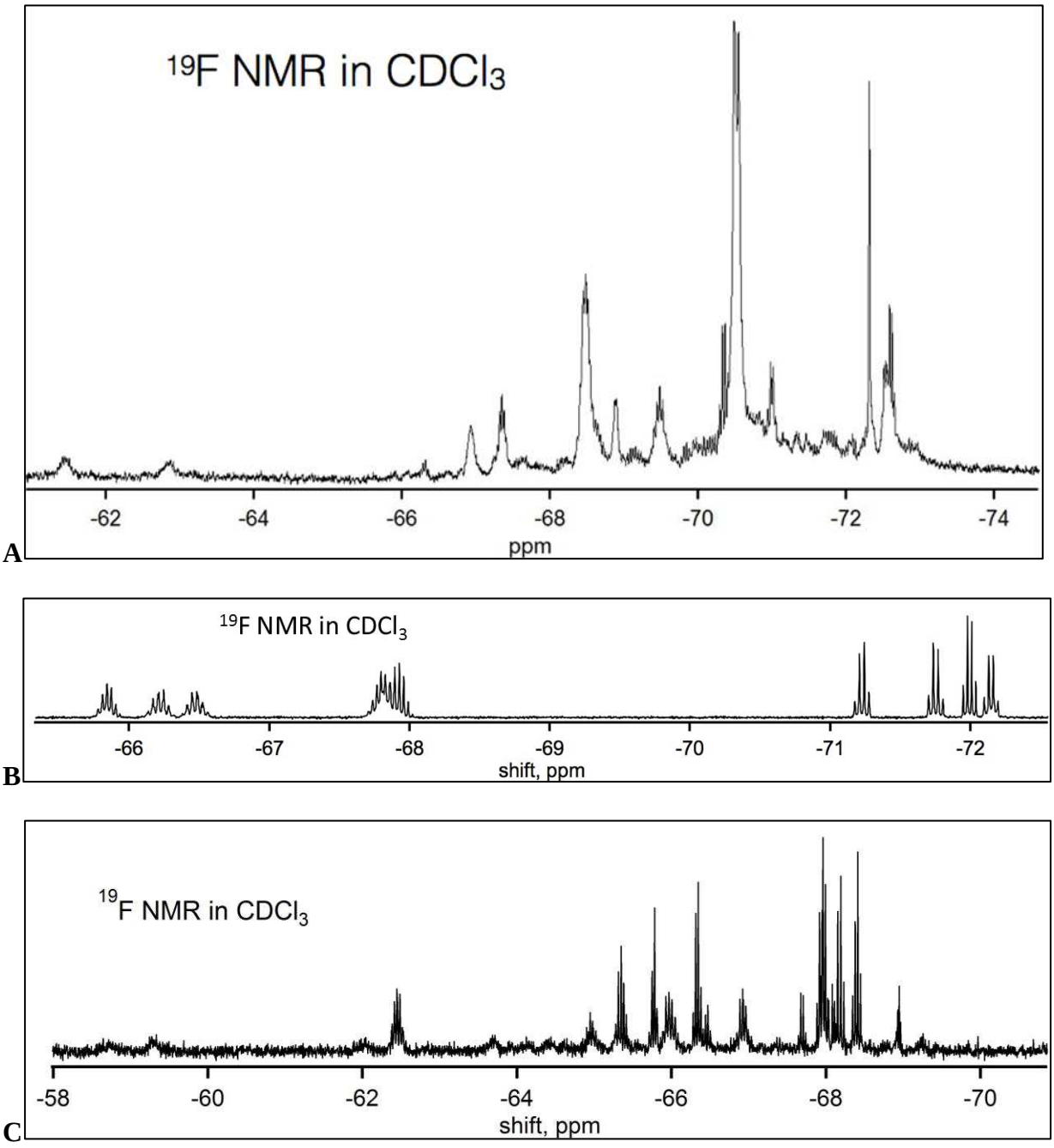

Figure 1.5. Fluorine–19 NMR spectra of (A) a typical GTGS reaction mixture, (B) **60-10-14**, and (C) **60-12-X** in $CDCl_3$.

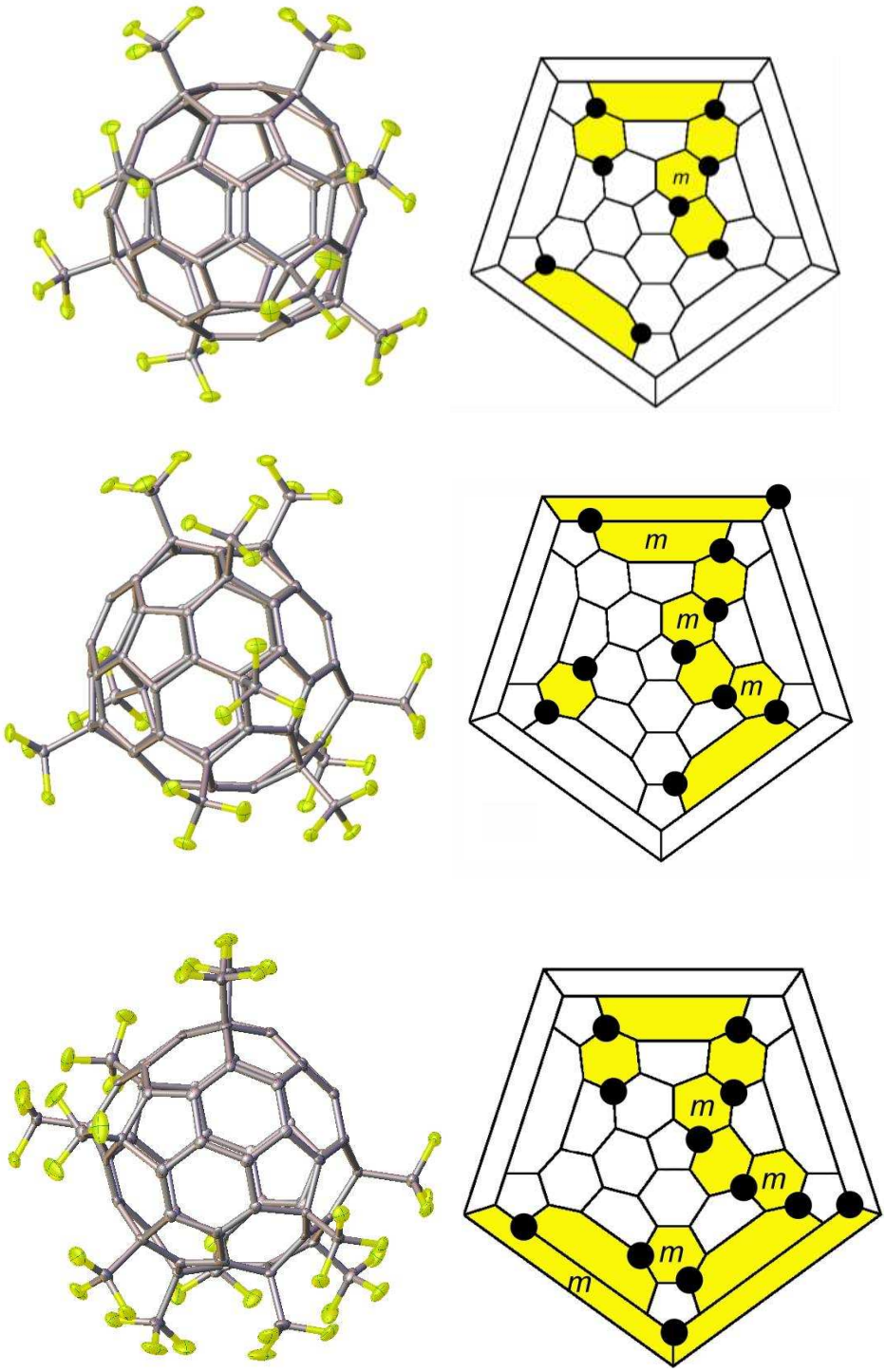

Figure 1.6. Thermal ellipsoid plots and corresponding Schlegel diagrams of **60-8-3** (top) **60-10-14** (middle) and **60-12-X** (bottom). For **60-8-3**: dichloromethane molecules were removed for clarity and only one enantiomer is shown, but both enantiomers were present in the crystal structure.

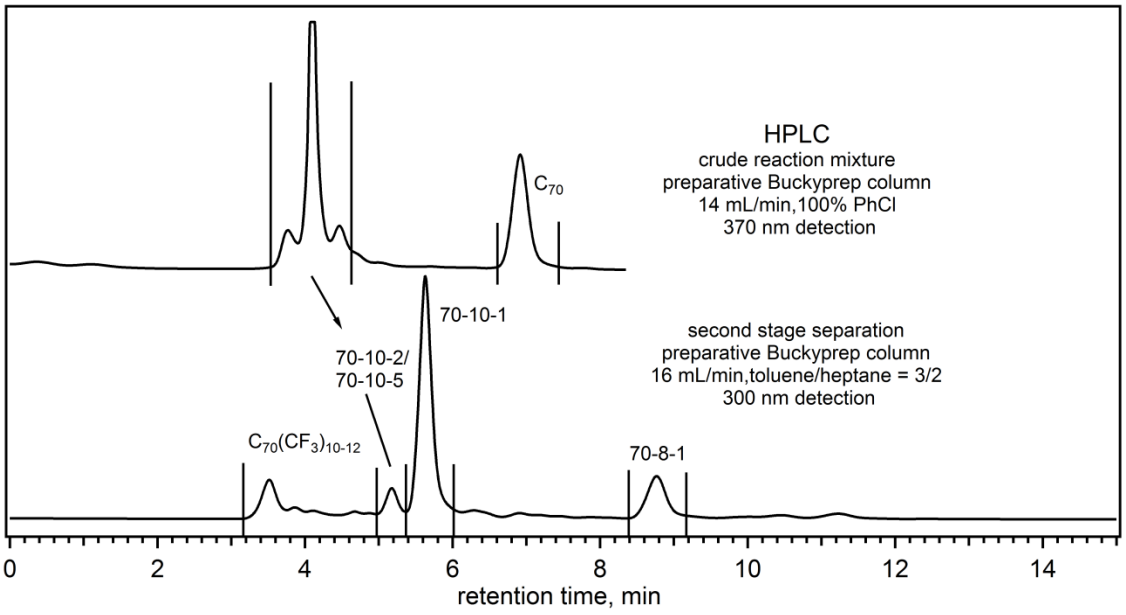

Figure 1.7. HPLC spectra of the two stage isolation of **70-8-1** and **70-10-1** from a typical $C_{70}(CF_3)_n$ flow-tube reaction.

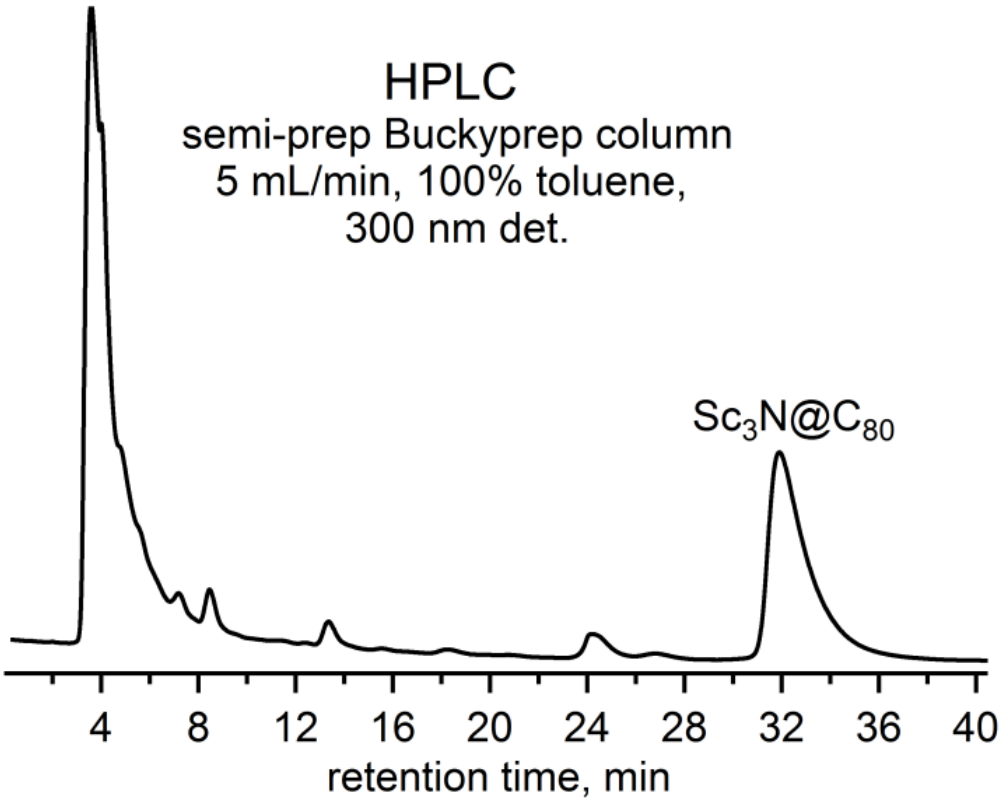

Figure 1.8. HPLC of $Sc_3N@C_{80}(CF_3)_n$ (n = 0-18). All peaks eluting before 30 min correspond to $Sc_3N@C_{80}(CF_3)_n$ (n = 2-18).

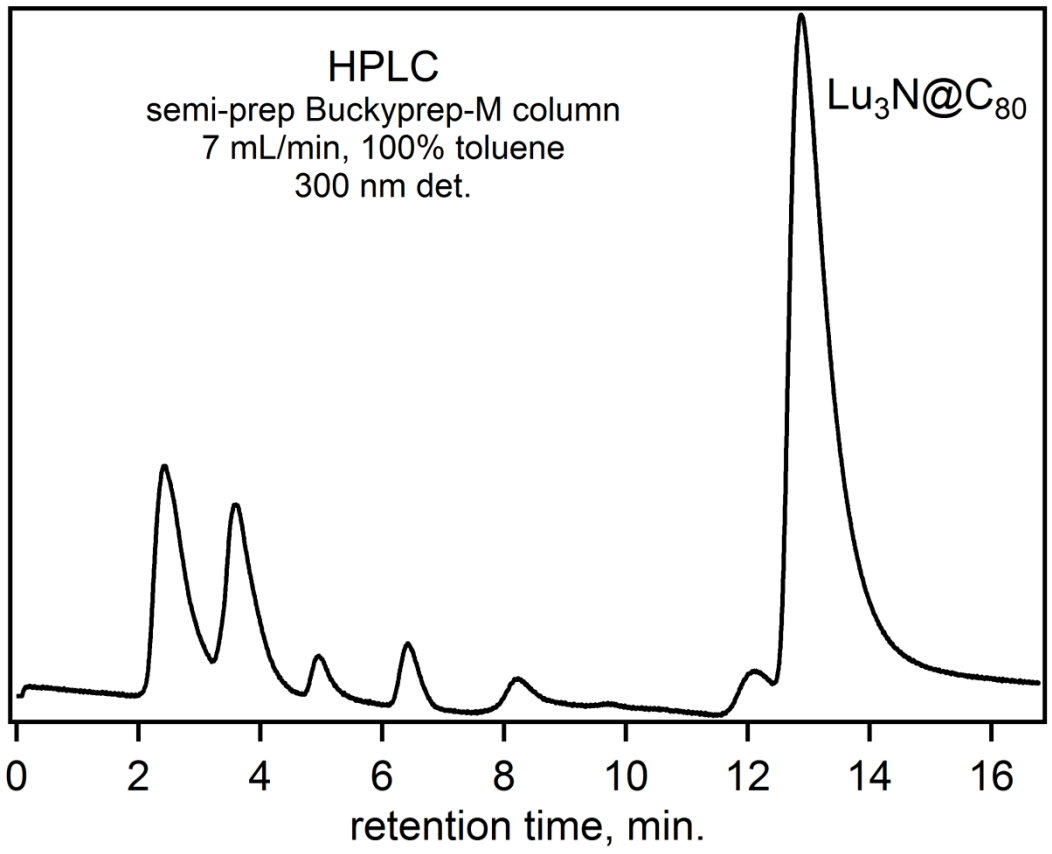

Figure 1.9. HPLC of $Lu_3N@C_{80}(CF_3)_n$ reaction. All peaks eluting before 11 min correspond to $Lu_3N@C_{80}(CF_3)_n$ and were collected together. GTGS reaction conditions: 5.2 mg $Lu_3N@C_{80}$, 630 torr CF_3I, T_{HP} = 650 °C, 0.5 h.

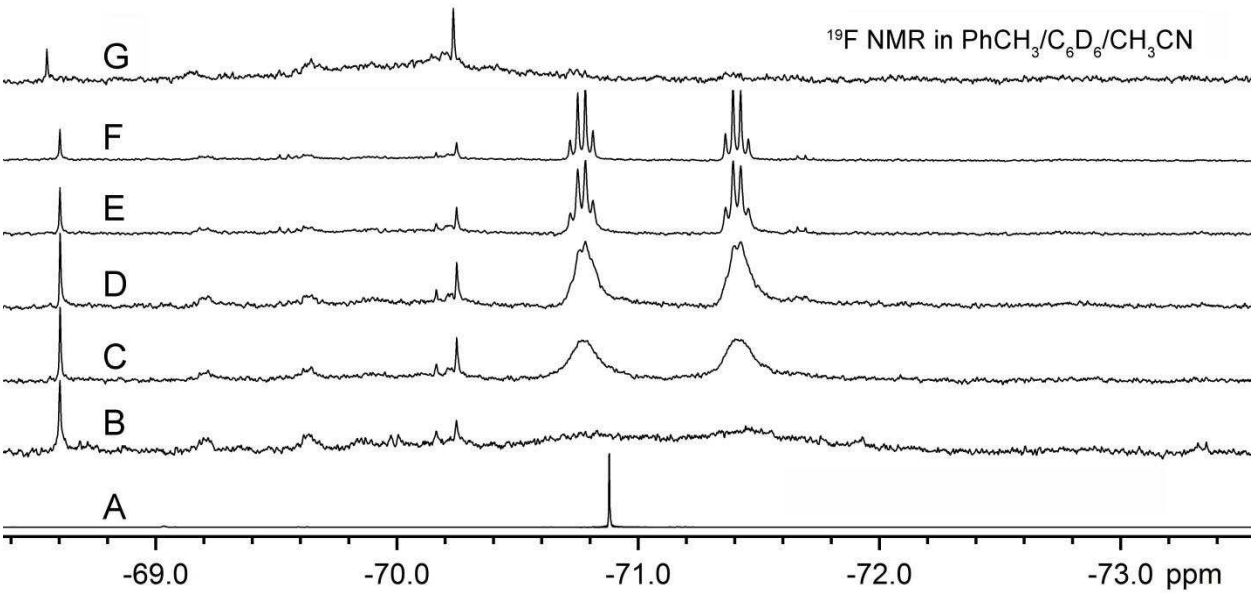

Figure 1.10. Fluorine-19 NMR spectra in toluene/C_6D_6/CH_3CN = 1.2/1.2/1.0 v/v/v showing: A) singlet from **60-2-1**, B) fast exchange limit 25 minutes after 1 equiv. CN^- is added, C) 2 h after CN^- addition, D) 3 h after CN^- addition, E) 4.5 h after CN^- addition, F) 7 h after CN^- addition, and G) the perpetual fast exchange limit when excess CN^- is added after establishment of the slow exchange limit in spectrum F.

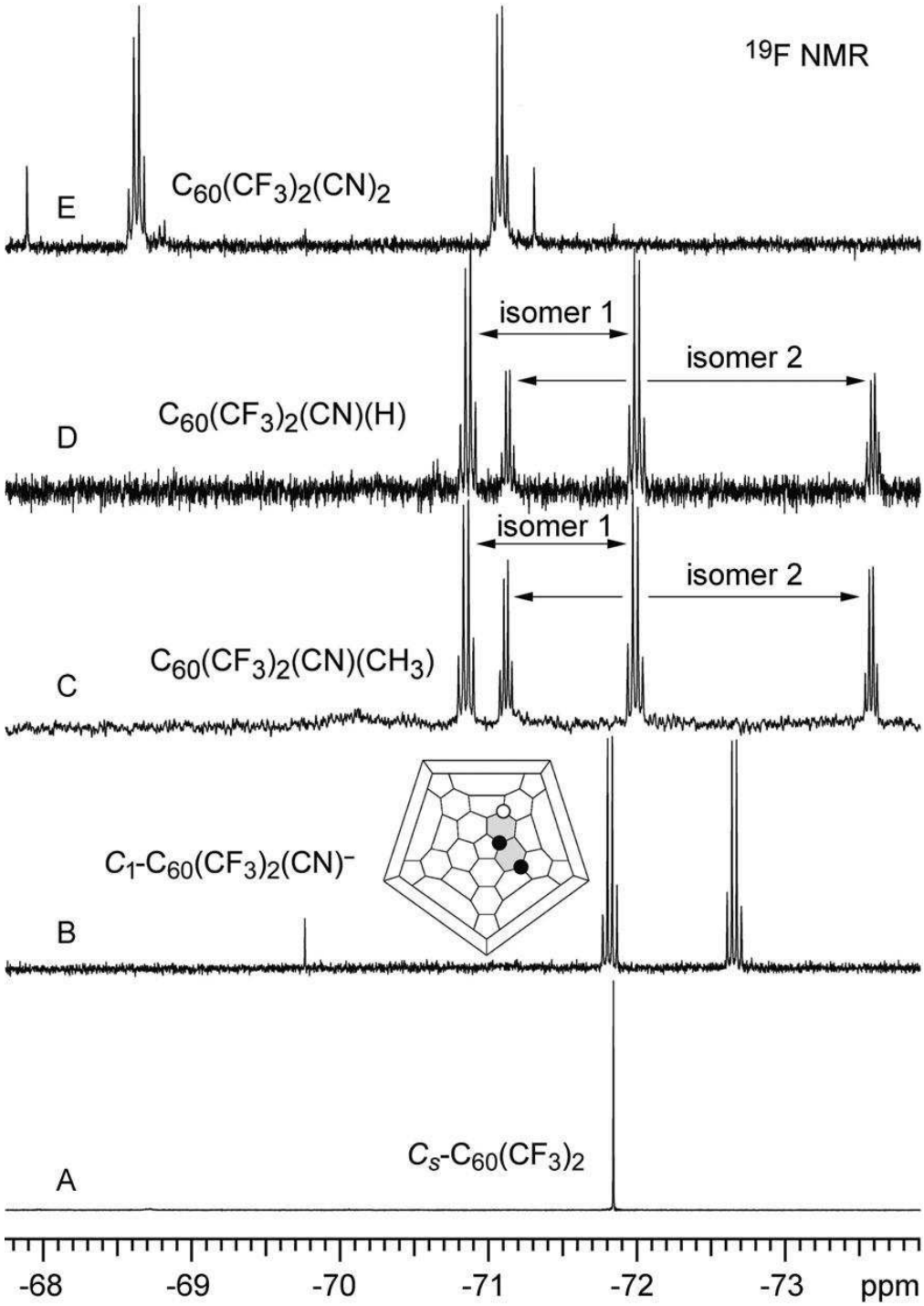

Figure 1.11. ^{19}F NMR spectra (376.5 MHz; CD_2Cl_2 ; $\delta(C_6F_6) = -164.9$ ppm) showing A) the singlet of III, B) the two-quartet pattern of ***C*$_1$-(60-2-1)(CN)$^-$**, the two-quartet patterns for the two predominant isomers of C) ***C*$_1$-(60-2-1)(CN)(CH$_3$)** and D) ***C*$_1$-(60-2-1)(CN)(H)**, and E) the two-quartet pattern for the predominant isomer of ***C*$_1$-(60-2-1) (CN)$_2$**. A Schlegel diagram showing the DFT-predicted lowest-energy isomer of ***C*$_1$-(60-2-1)(CN)$^-$** is also shown.

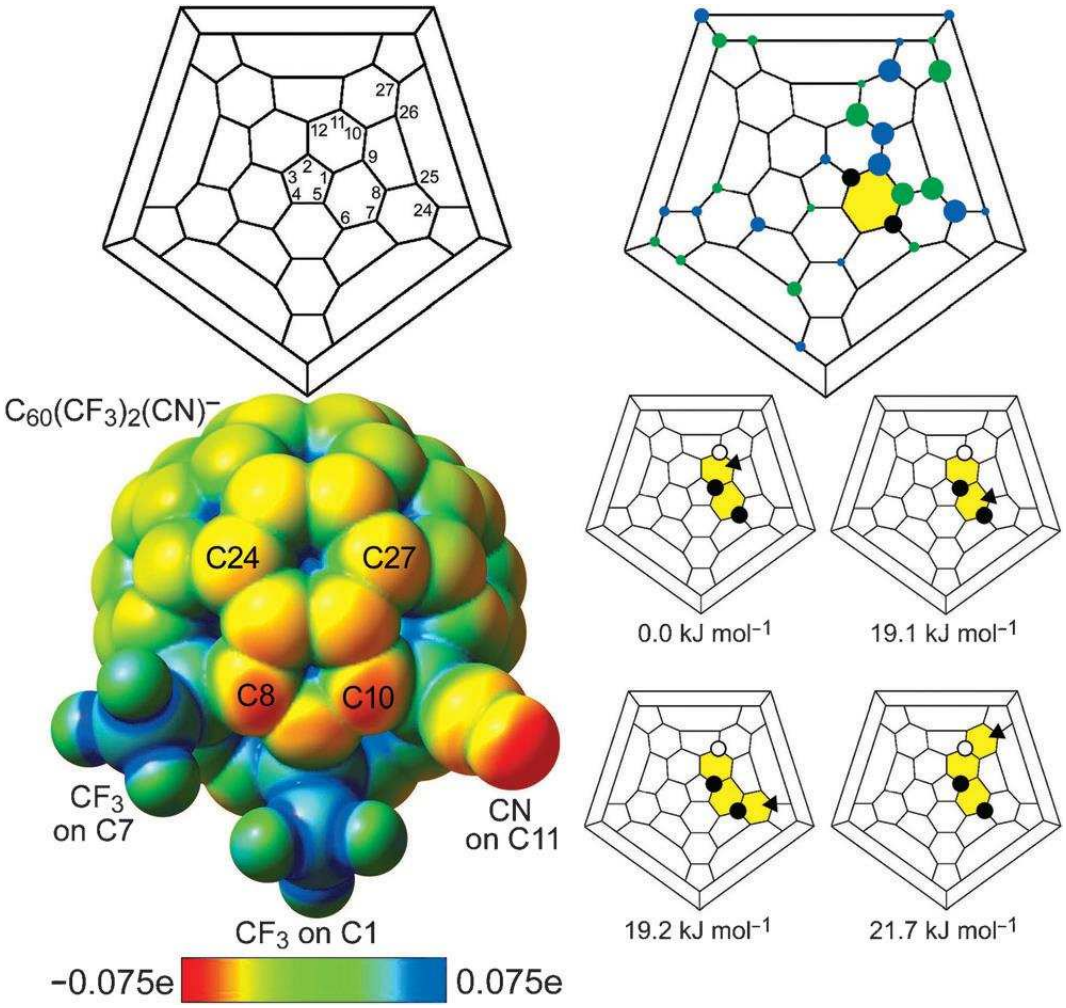

Figure 1.12. Schlegel diagrams showing the IUPAC numbering for C_{60} (top left), the DFT-predicted LUMO for *C_s-p*-$C_{60}(CF_3)_2$ (**60-2-1**, top right), a DFT-predicted ESP diagram for ***C_1*-(60-2-1)$(CN)^-$**, and Schlegel diagrams for the lowest energy and most likely isomers of ***C_1*-(60-2-1)(CN)(CH_3)**.

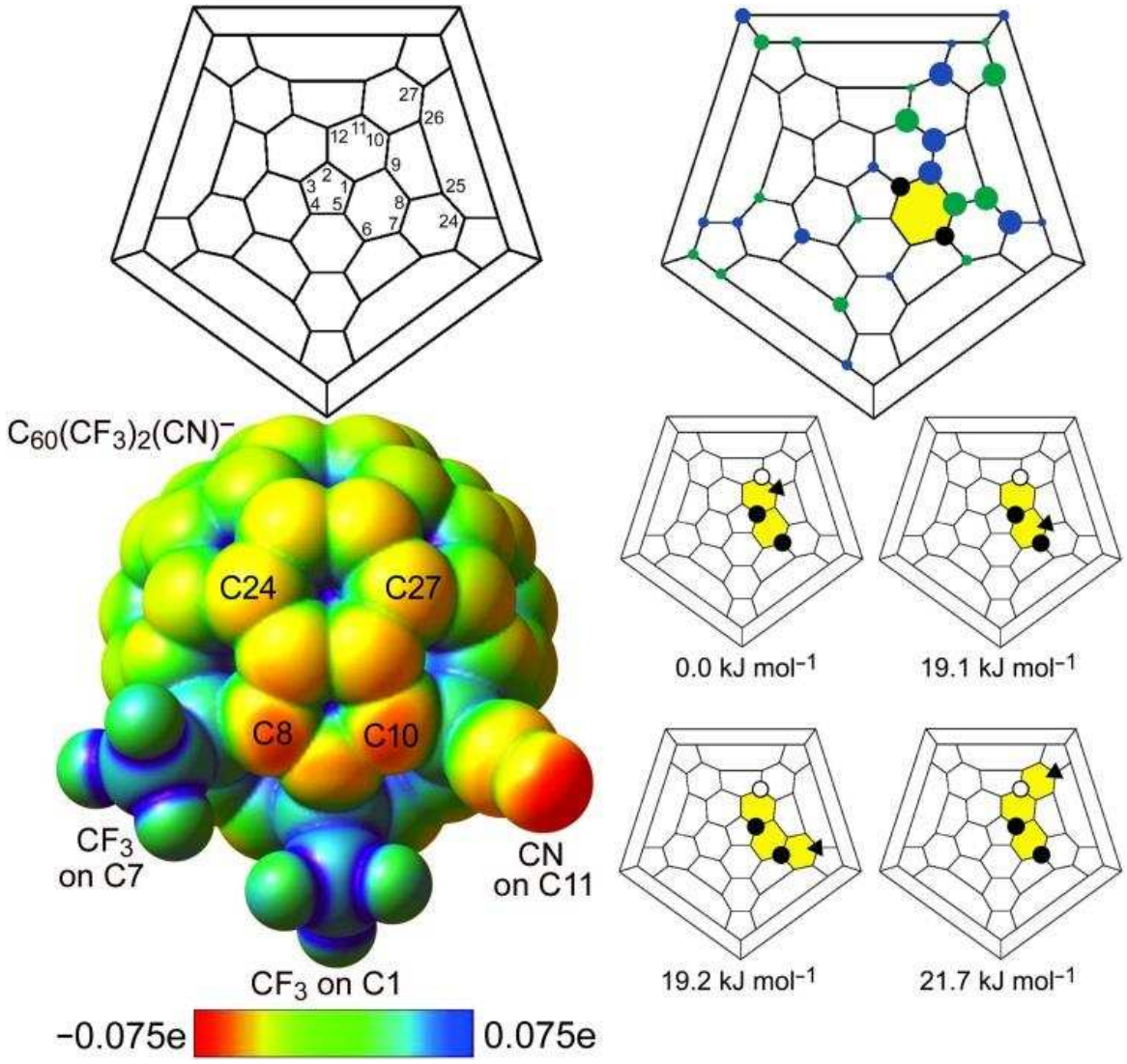

Figure 1.13. Schlegel diagrams showing the IUPAC numbering for C_{60} (top left), the DFT-predicted LUMO for **60-2-1**, a DFT-predicted ESP diagram for ***C*$_1$-(60-2-1)(CN)$^-$**, and Schlegel diagrams for the lowest energy and most-likely isomers of **(60-2-1)(CN)(CH$_3$)**.

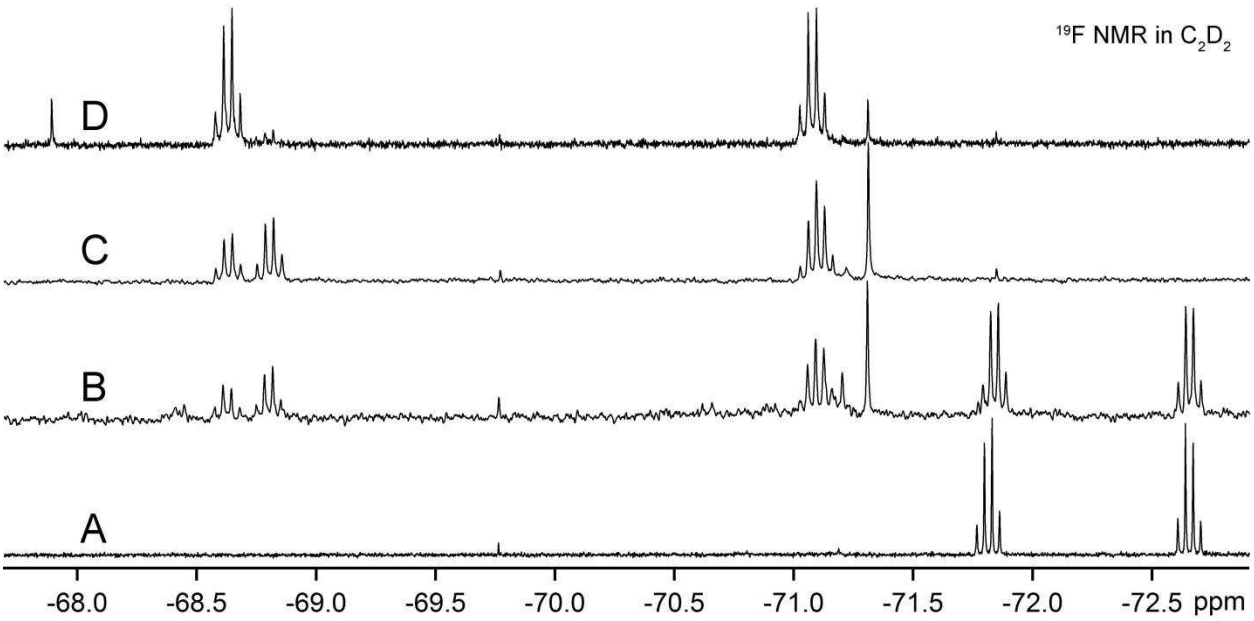

Figure 1.14. Fluorine-19 NMR spectra in C_2D_2 showing: A) the two quartets for ***C*$_1$-(60-2-1)(CN)$^-$**, B) the reaction mixture 5 hours after CN^+ addition, which still has a significant amount of unreacted ***C*$_1$-(60-2-1)(CN)$^-$**, C) the reaction mixture after several days of reaction, D) the reaction mixture 5 hours after CN^+ addition when excess NEt_4CN is present.

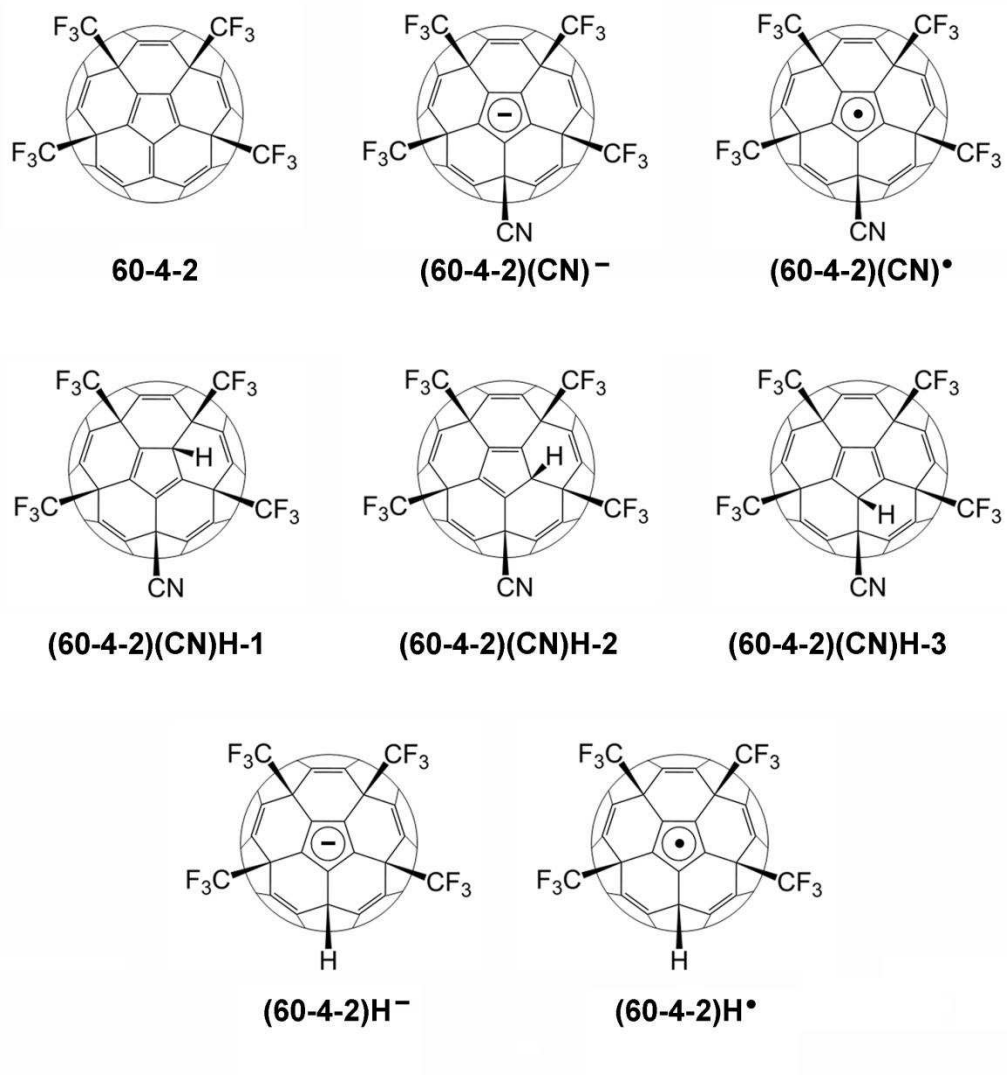

Figure 1.15. Drawings of molecular structures of **60-4-2** derivatives from this work.

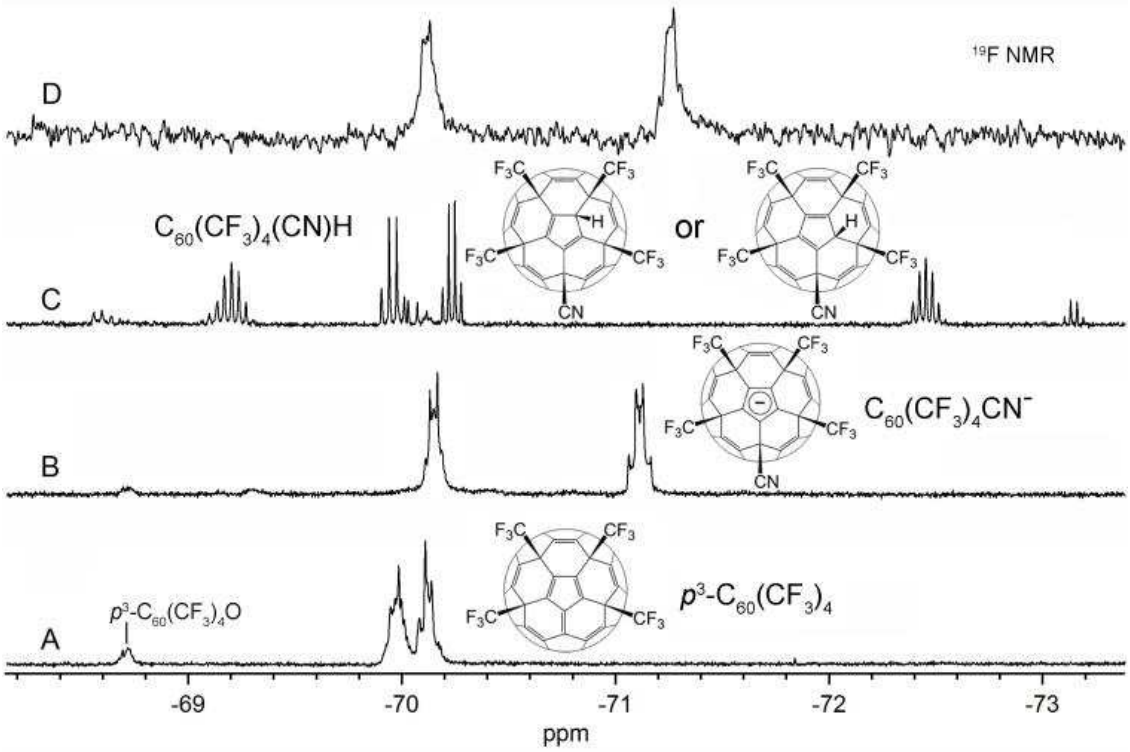

Figure 1.16. Fluorine-19 NMR spectra (CD_2Cl_2; δ(C_6F_6) −164.9) showing: the multiplets for **60-4-2** including a small amount of (**60-4-2)O** (δ = −68.7) (A), crude **(60-4-2)(CN)⁻** (B), **(60-4-2)(CN)H** (C), and **(60-4-2)(CN)⁻** after treatment of **(60-4-2)(CN)H** with proton-sponge® (D).

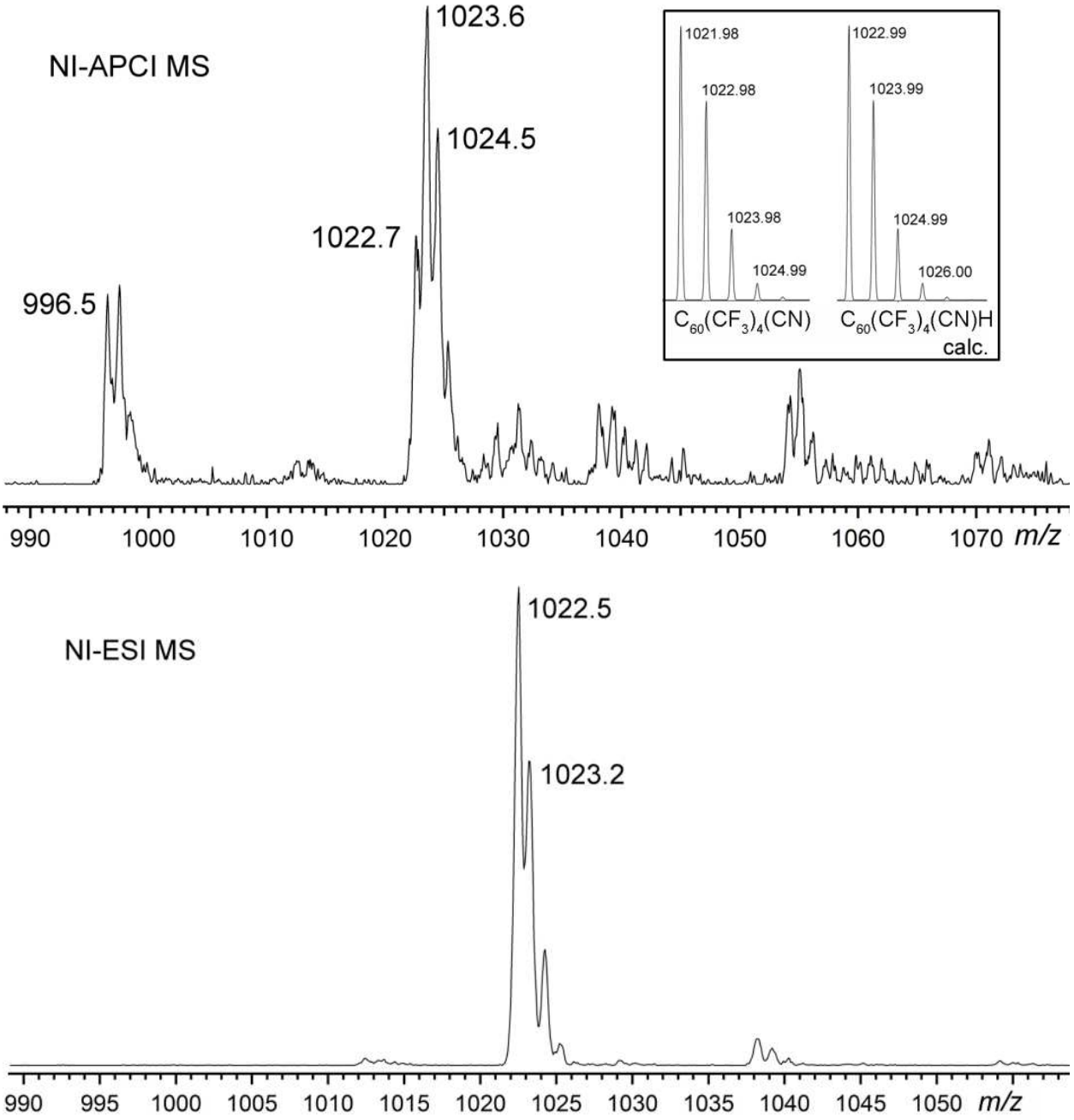

Figure 1.17. Negative ion mass spectra of $C_{60}(CF_3)_4(CN)H^-$ (**(60-4-2)(CN)H$^-$**) and $C_{60}(CF_3)_4(CN)^-$ (**(60-4-2)(CN)$^-$**): APCI (top), ESI (bottom), and calculated isotopic peak distribution (inset). The masses on the experimental spectra are systematically shifted +0.5 Da compared to the calculated masses.

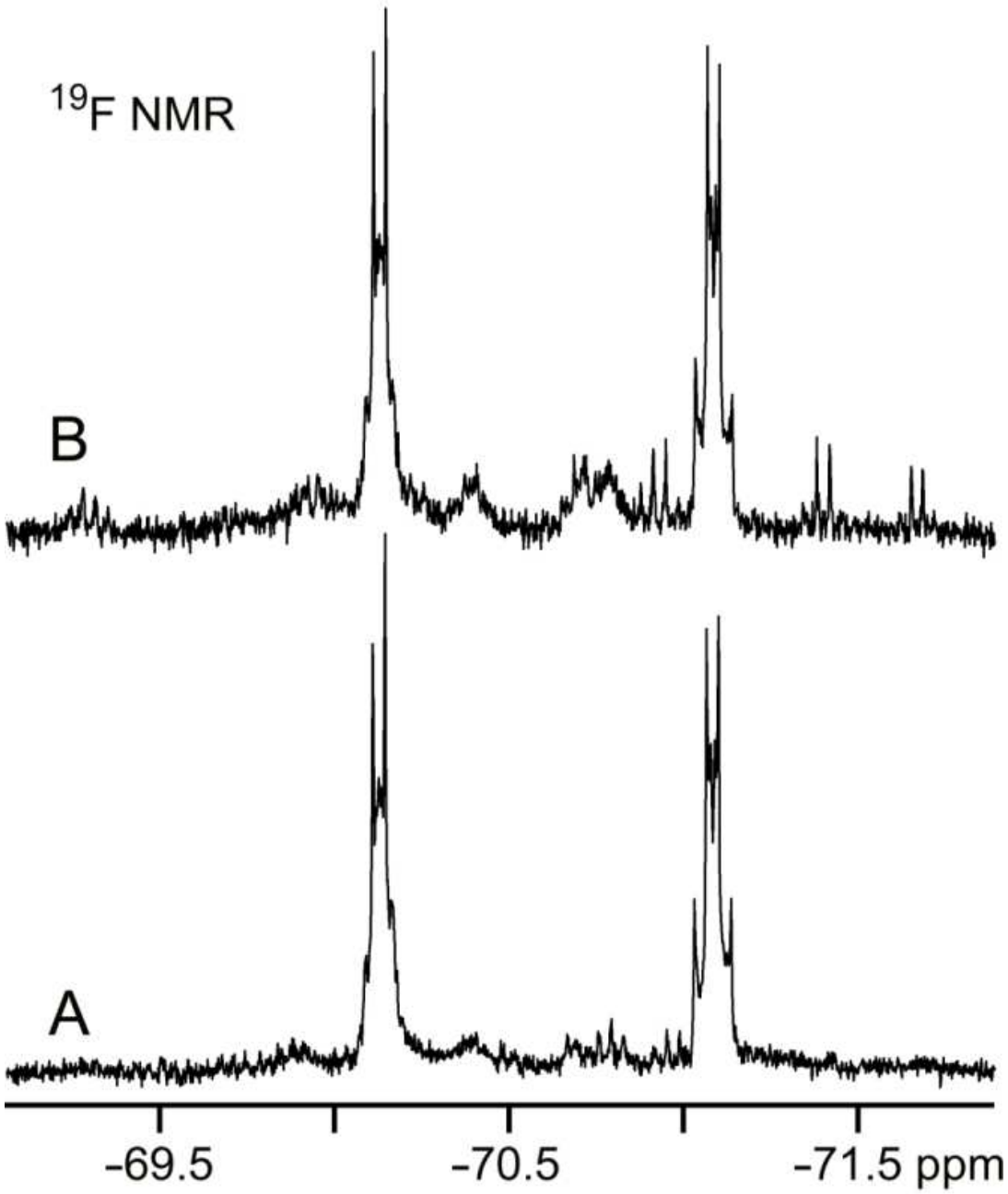

Figure 1.18. Fluorine-19 NMR spectra showing the two multiplets from $[C_{60}(CF_4)_4(CN)^-(NEt_4)^+]$ (**(60-4-2)(CN)$^-$**). A) anaerobic conditions; B) 6 days after exposure to air.

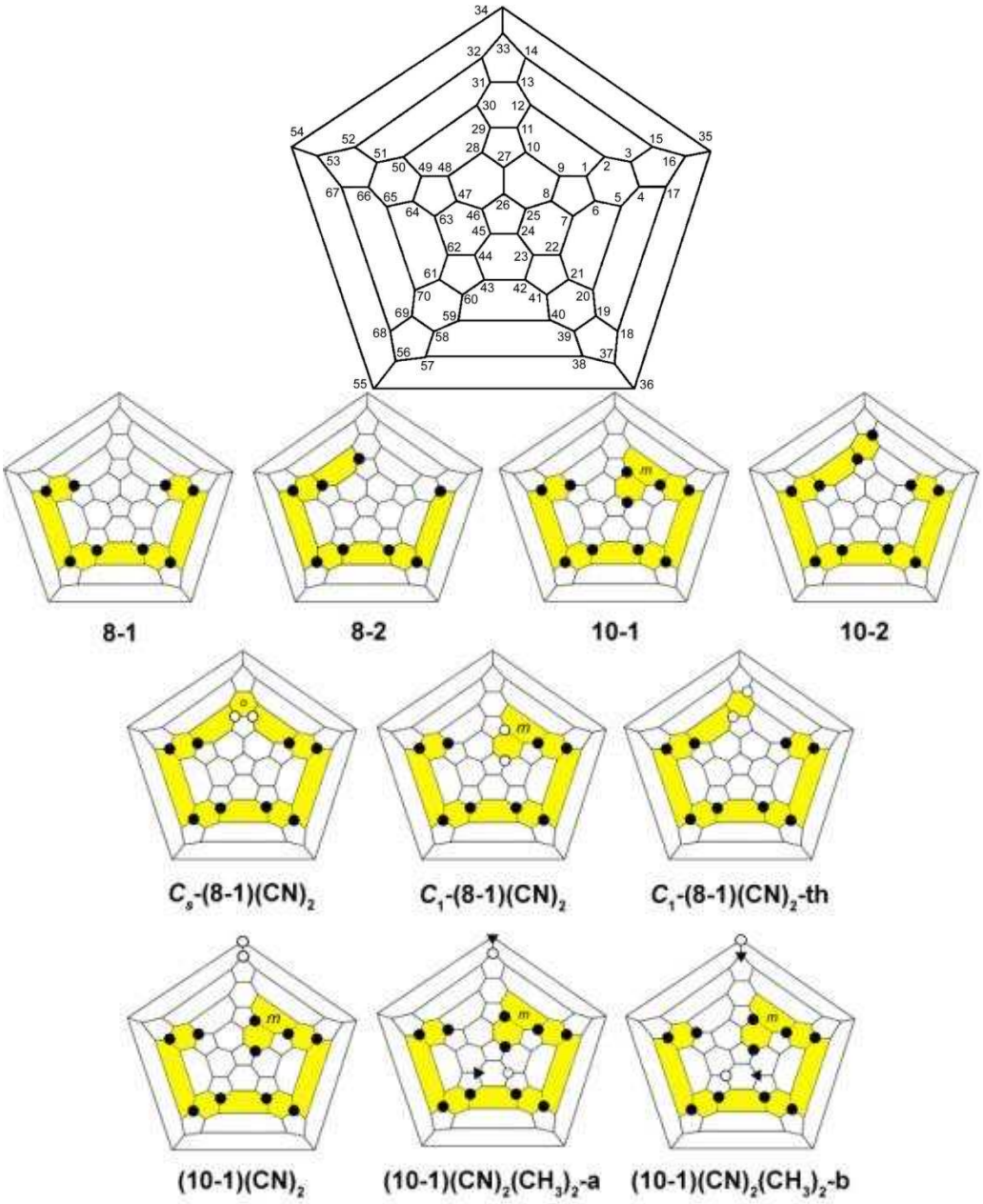

Figure 1.19. Schlegel diagrams of C_{70} TMFs, their cyanated derivatives, and the numbering of each C atom in C_{70}. Filled and open circles represent cage carbon atoms of bonded CF_3 and CN, respectively, triangles represent location of CH_3 additions. Yellow indicates continuous ribbon of edge sharing *p*-, *m*-, and *o*-C_6X_2 hexagons. Meta and ortho C_6X_2 hexagons are labeled with *m* and *o*, respectively.

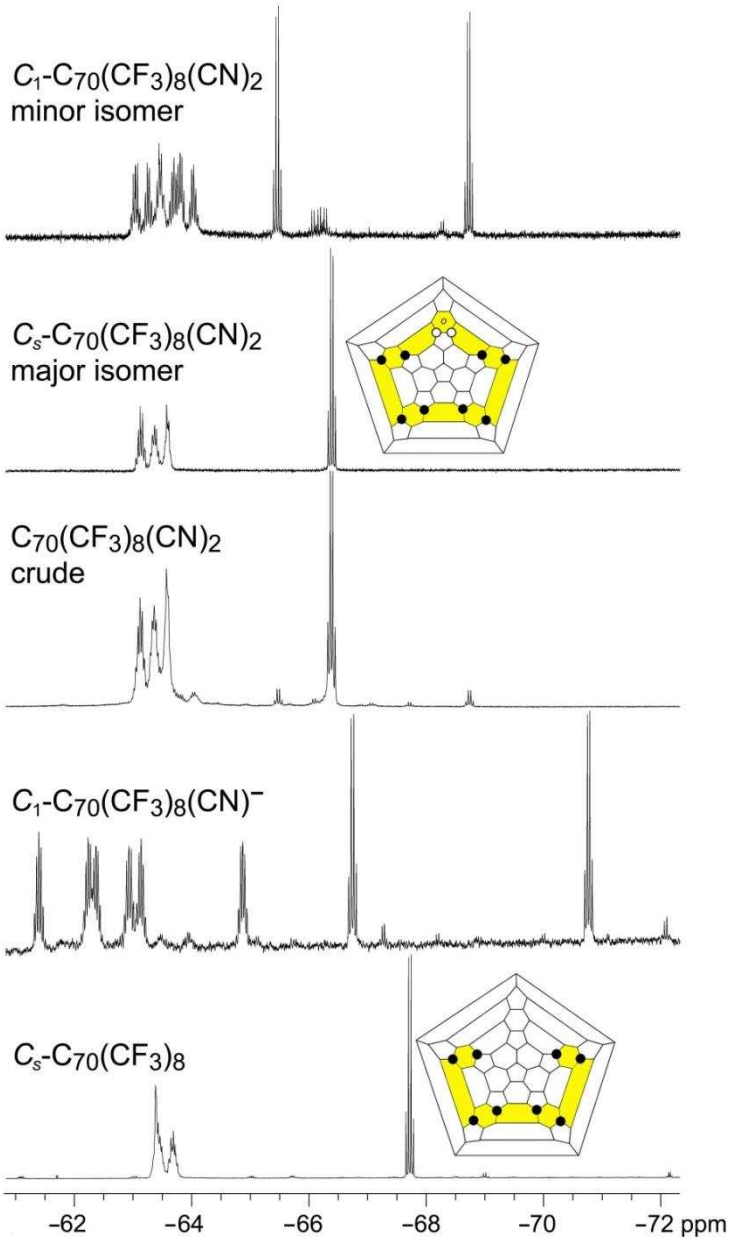

Figure 1.20. Fluorine-19 NMR spectra (376.5 MHz; δ(C_6F_6) −164.9) showing (from bottom to top) the four multipets and Schlegel diagram of **70-8-1** (95+ mol% purity; $CDCl_3$), the eight prominent multiplets of a single isomer of ***C*$_1$-(70-8-1)(CN)$^-$** (7:1 C_6D_6:ACN; 90+ mol% regioselectivity), the crude $C_{70}(CF_3)_8(CN)_2$ product mixture, showing major (ca. 90 mol%) and minor (ca. 10 mol%) isomers of $C_{70}(CF_3)_8(CN)_2$, the four multiplets and Schlegel diagram of HPLC purified ***C*$_s$-(70-8-1)(CN)$_2$** (major isomer; $CDCl_3$), and the eight multiplets of HPLC purified ***C*$_1$-(70-8-1)(CN)$_2$** (minor isomer; $CDCl_3$).

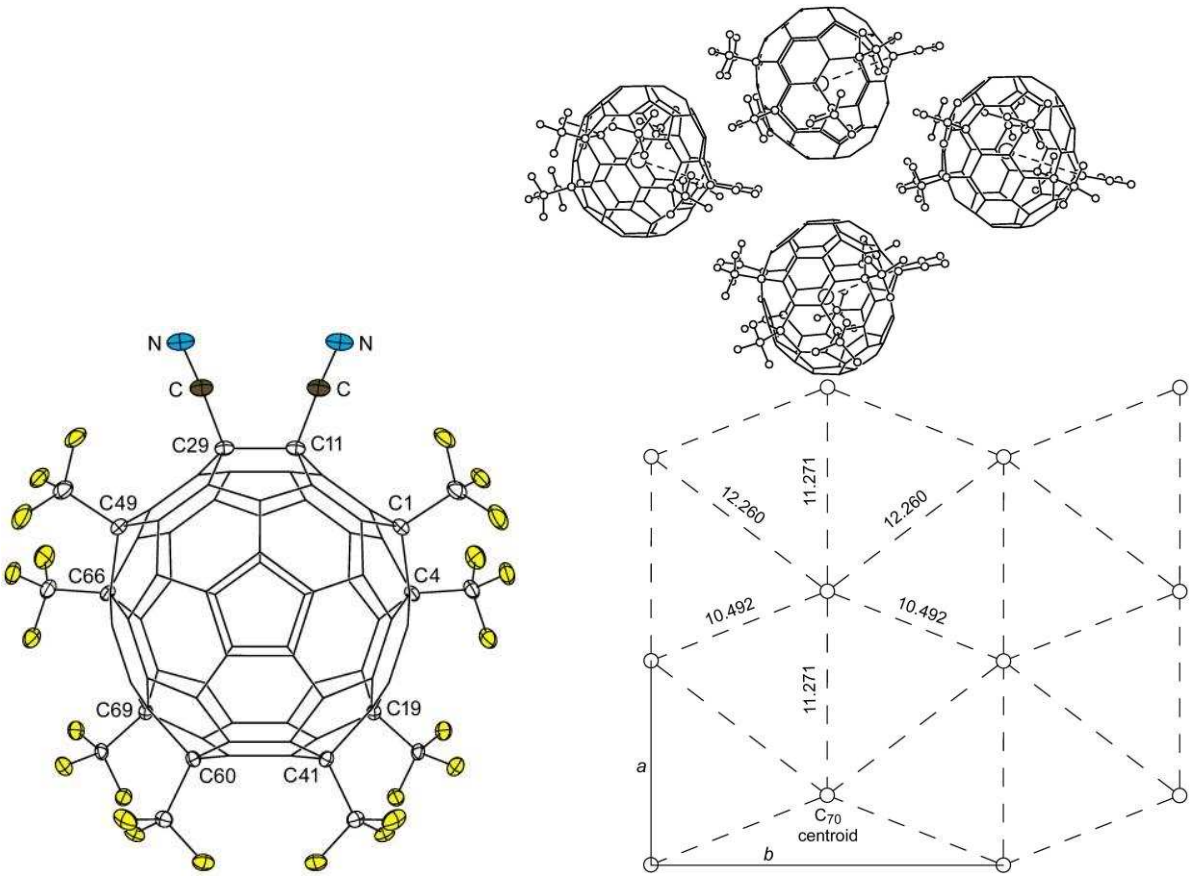

Figure 1.21. Left) The structure of C_s-p^9o(loop)-$C_{70}(CF_3)_8(CN)_2$ (***C*$_s$*-(70-8-1)(CN)$_2$**), showing 50% ellipsoids for the ten substituents and the cage C atoms to which they are attached (disordered $CHCl_3/CH_2Cl_2$ molecules are omitted; only half of the molecule is unique (i.e., C29 = C11'; C49 = C1'; etc.)). Selected distances (Å) and angles (deg): C11–CN, 1.476(5); C–N, 1.145(5); C11–C29, 1.658(8); C11–C–N, 177.0(4); C11–C29–C, 110.7(2). Right) The packing of molecules of in rigorously-planar pseudo-hexagonal layers of C_{70} centroids (⊙, large circles, this is the crystallographic *ab* plane). The ⊙···⊙ distances shown in the lower drawing are in Å. The dotted lines in the upper drawing, which is shown in the same orientation as the lower drawing, connect the C_{70} centroids with the centroids of the C11–C29 bonds, which are approximately the same as the directions of the molecular dipole vectors. The dipole vectors have the same crystallographic *b* components, with offsetting components along the crystallographic *a* axis.

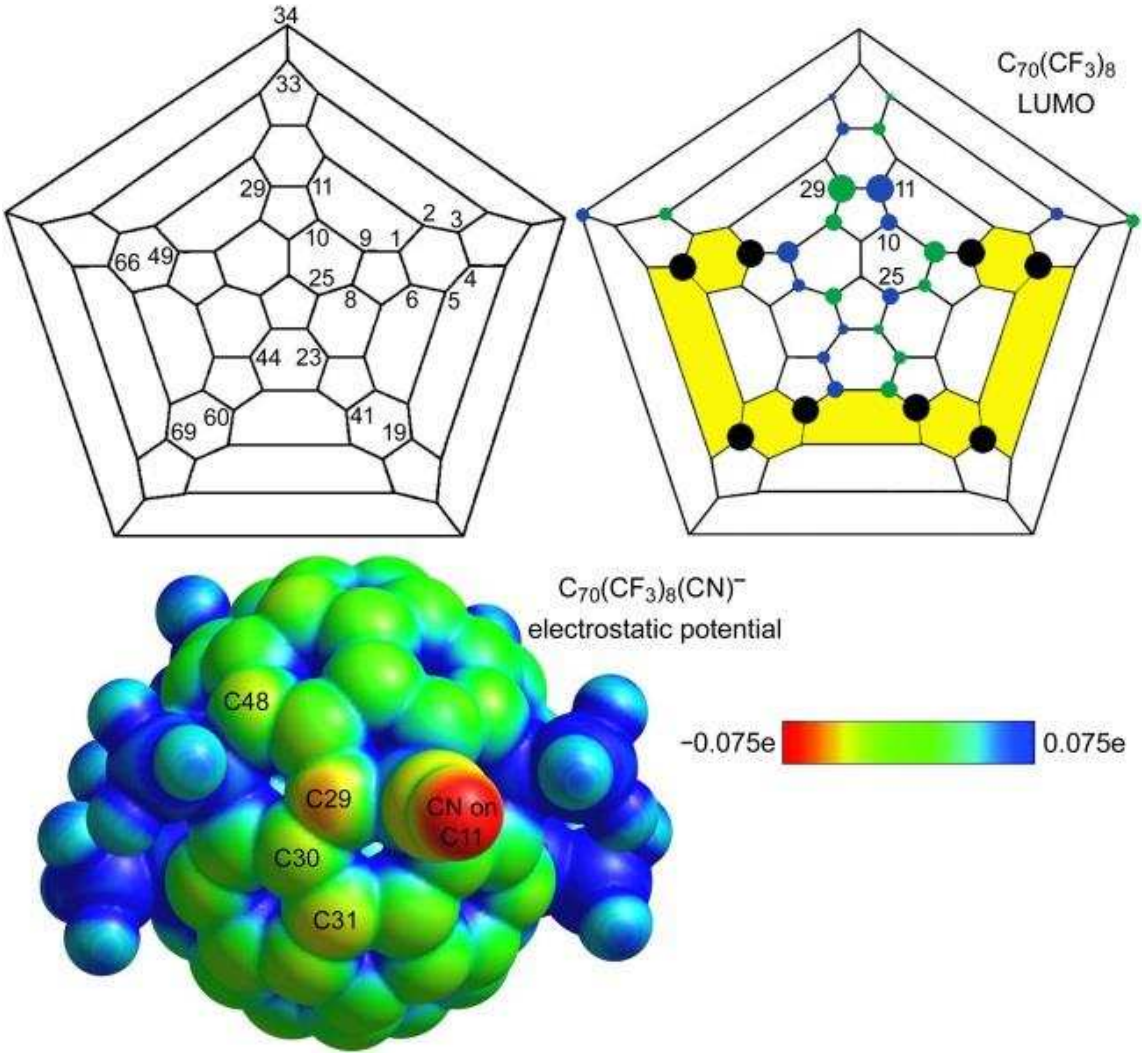

Figure 1.22. The IUPAC numbering for C_{70}, the DFT-predicted LUMO for **70-8-1**, and a DFT-predicted ESP diagram for ***C*$_s$-(70-8-1)(CN)$^-$**. The p-π orbital contributions to the LUMO, shown as green or blue circles, are approximately proportional in size to their relative contributions to the orbital.

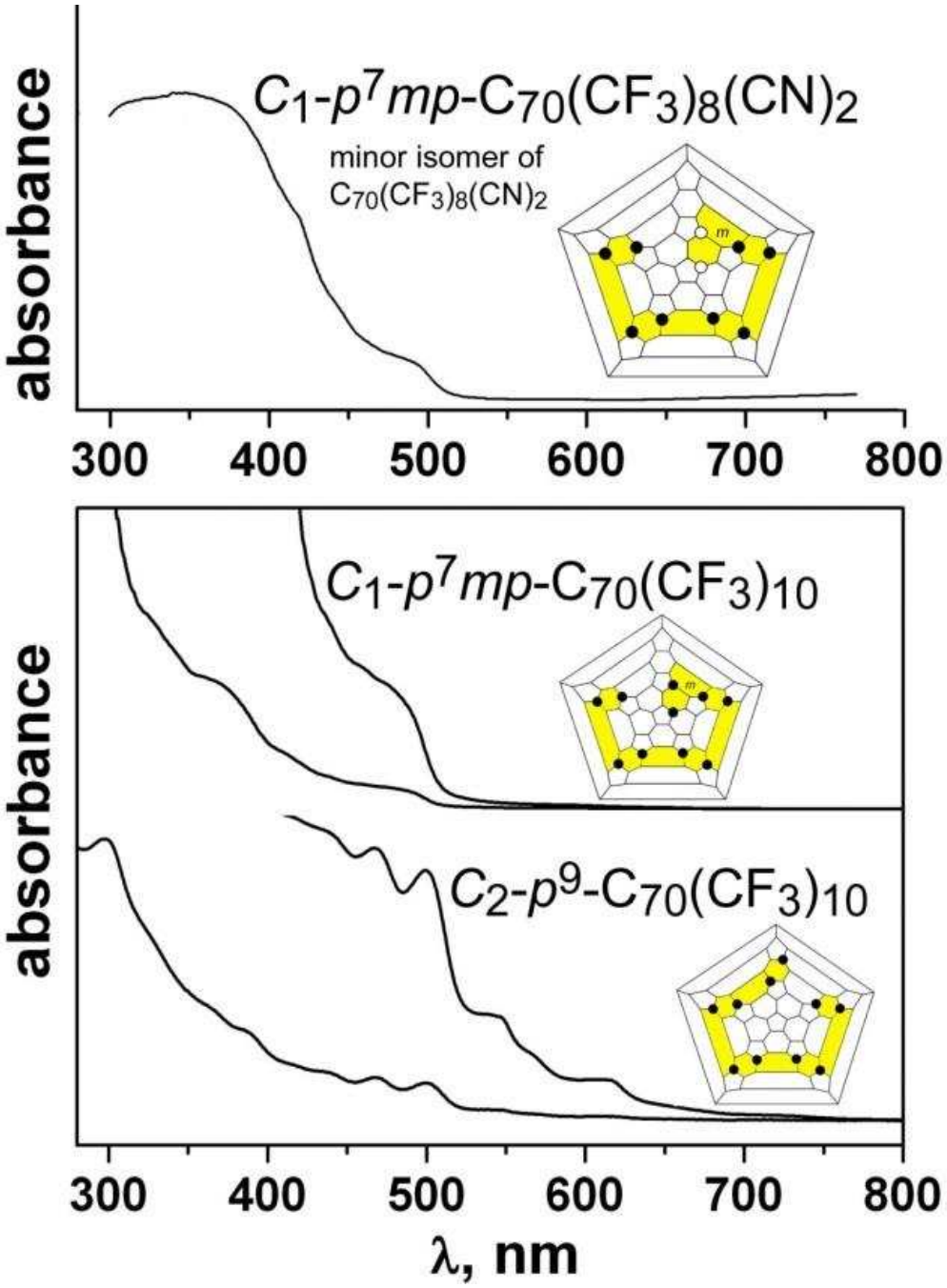

Figure 1.23. Comparison of the electronic spectrum of the minor, asymmetric $C_{70}(CF_3)_8(CN)_2$ isomer with those of p^7mp-$C_{70}(CF_3)_{10}$ and p^9-$C_{70}(CF_3)_{10}$. On the basis of these spectra, the minor $C_{70}(CF_3)_8(CN)_2$ isomer was determined to have the p^7mp addition pattern.

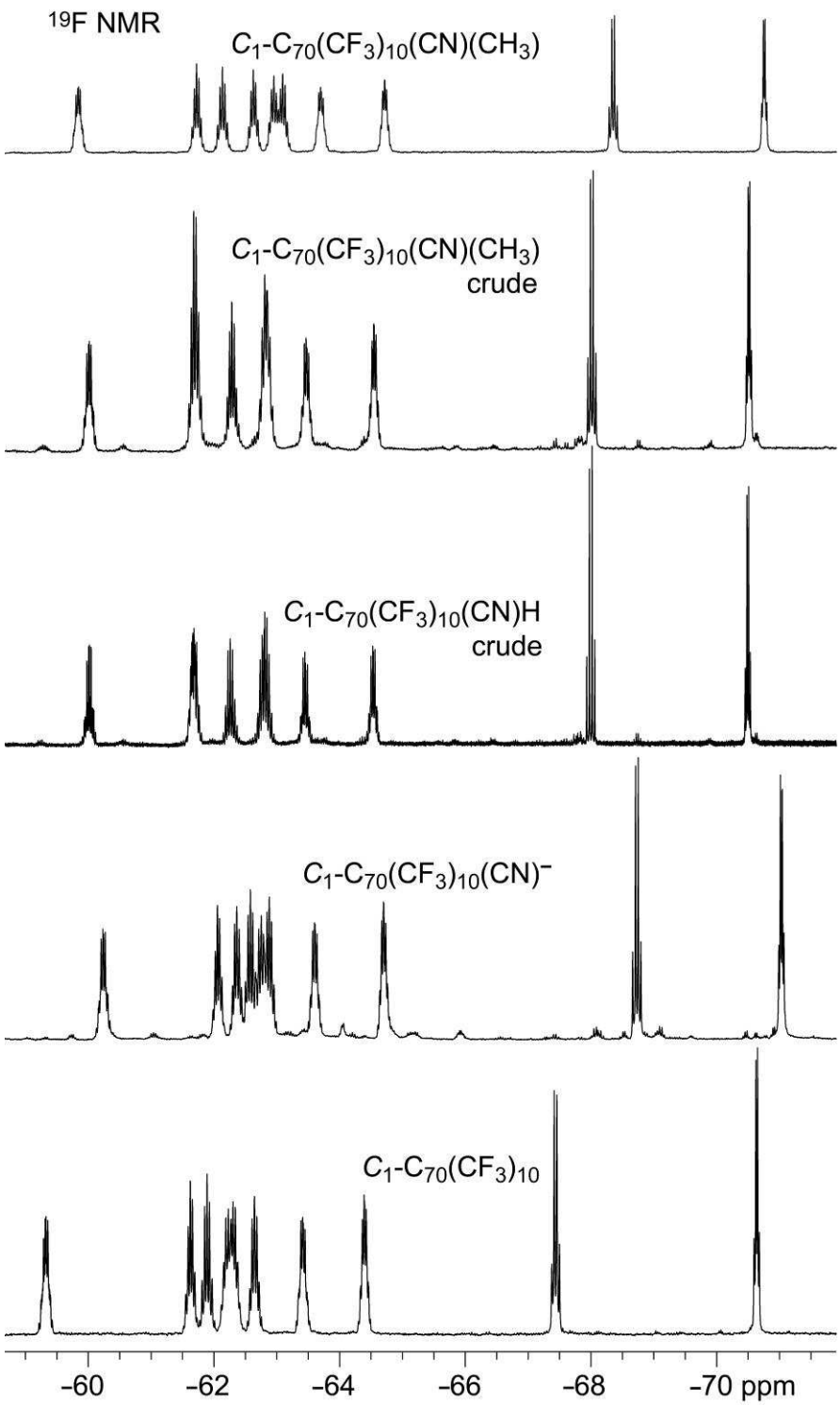

Figure 1.24. Fluorine-19 NMR spectra (2:2:1 C_6D_6:$PhCH_3$:ACN; 376.5 MHz; δ(C_6F_6) −164.9) showing (bottom to top) the ten multiplets for **70-10-1**, **(70-10-1)(CN)**$^-$ (95+ mol% regioselectivity), **(70-10-1)(CN)(H)** and **(70-10-1)(CN)(CH_3)** crude reaction products (both with 90+ mol% regioselectivity), and HPLC purified **(70-10-1)(CN)(CH_3)** in $CDCl_3$.

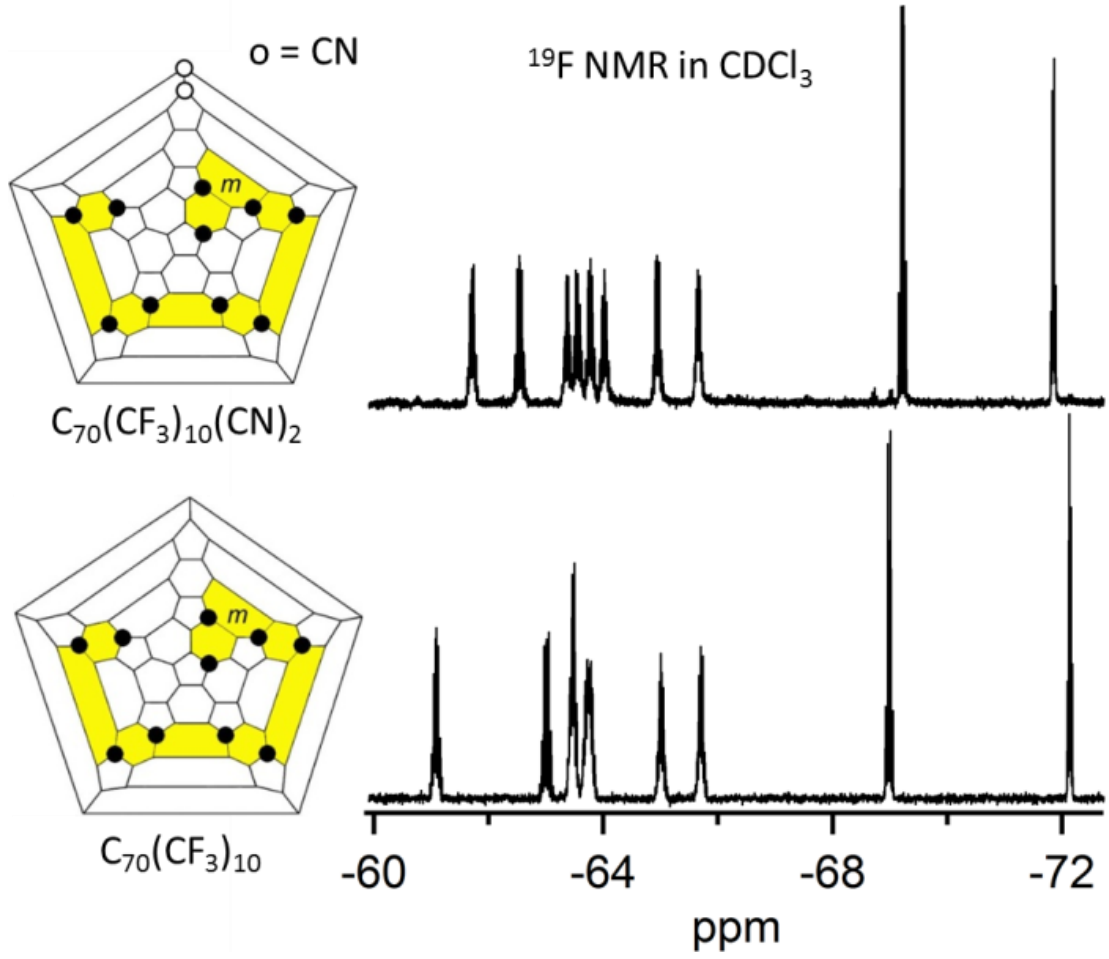

Figure 1.25. Fluorine-19 NMR spectra of **70-10-1** and **(70-10-1)(CN)$_2$** in $CDCl_3$ and corresponding Schlegel diagrams.

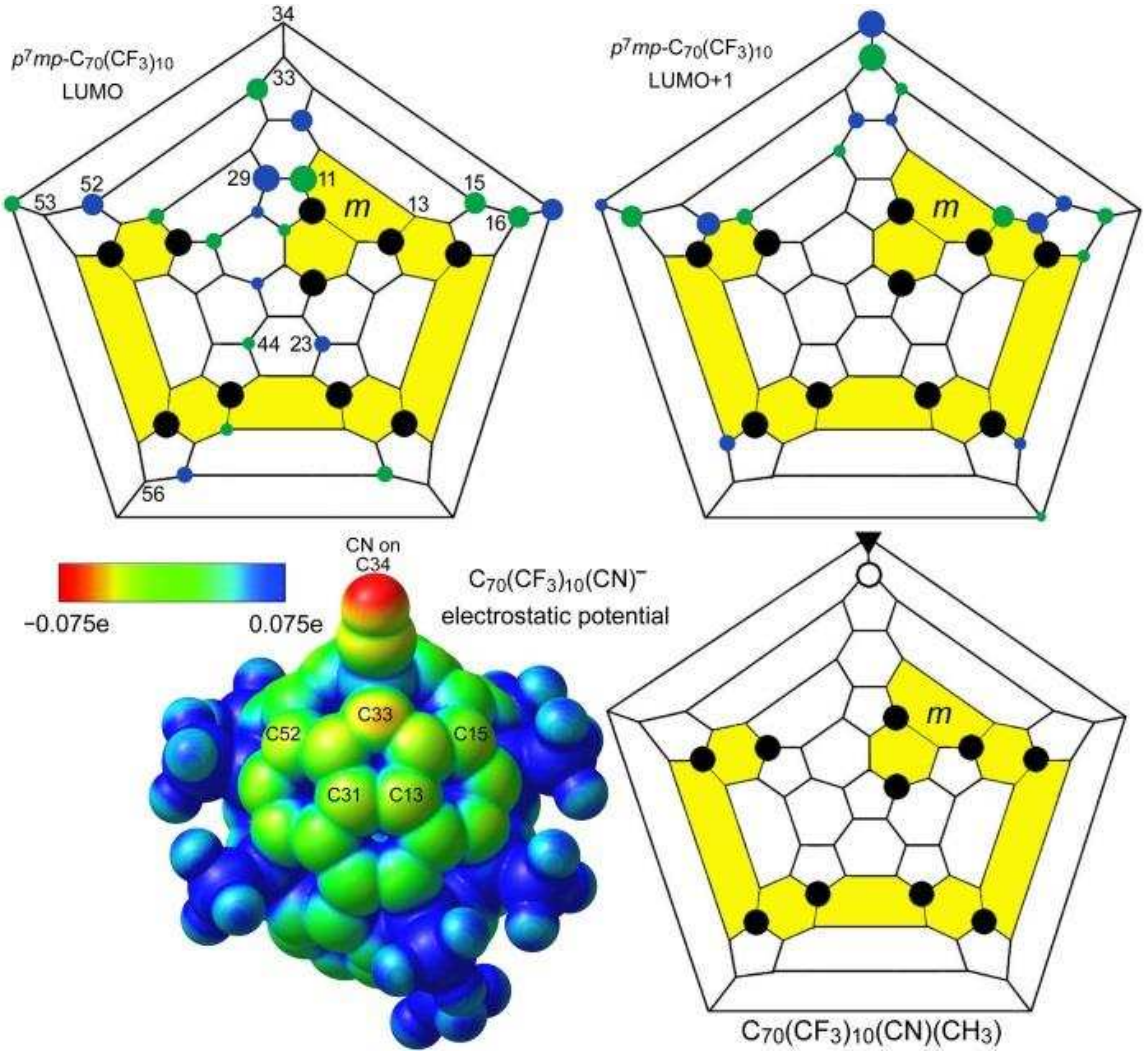

Figure 1.26. Schlegel diagrams showing the DFT-predicted LUMO and LUMO+1 for **70-10-1**, a DFT-predicted ESP diagram for ***C*$_1$-(70-10-1)(CN)$^-$**, and the Schlegel diagram for the most likely isomer of ***C*$_1$-(70-10-1)(CN)(CH$_3$)** with its CN group (open circle) and CH_3 group (solid triangle) on C34 and C33, respectively.

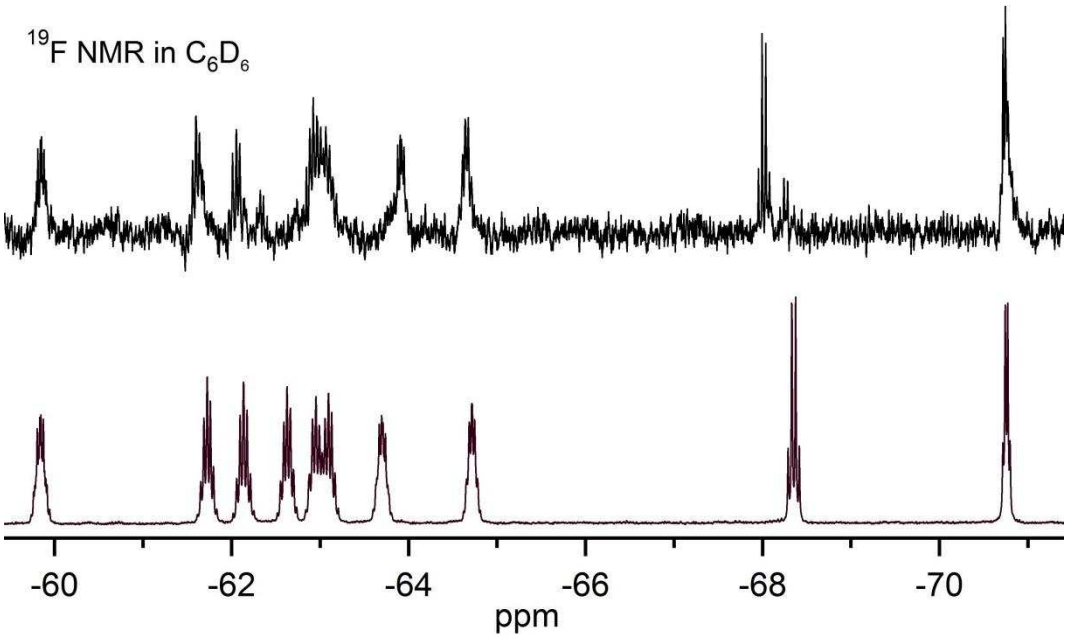

Figure 1.27. Fluorine-19 NMR of **(70-10-1)(CH_3)(CN)** (top) and **(70-10-1)(CN)(CH_3)** (bottom) in C_6D_6 after HPLC purification.

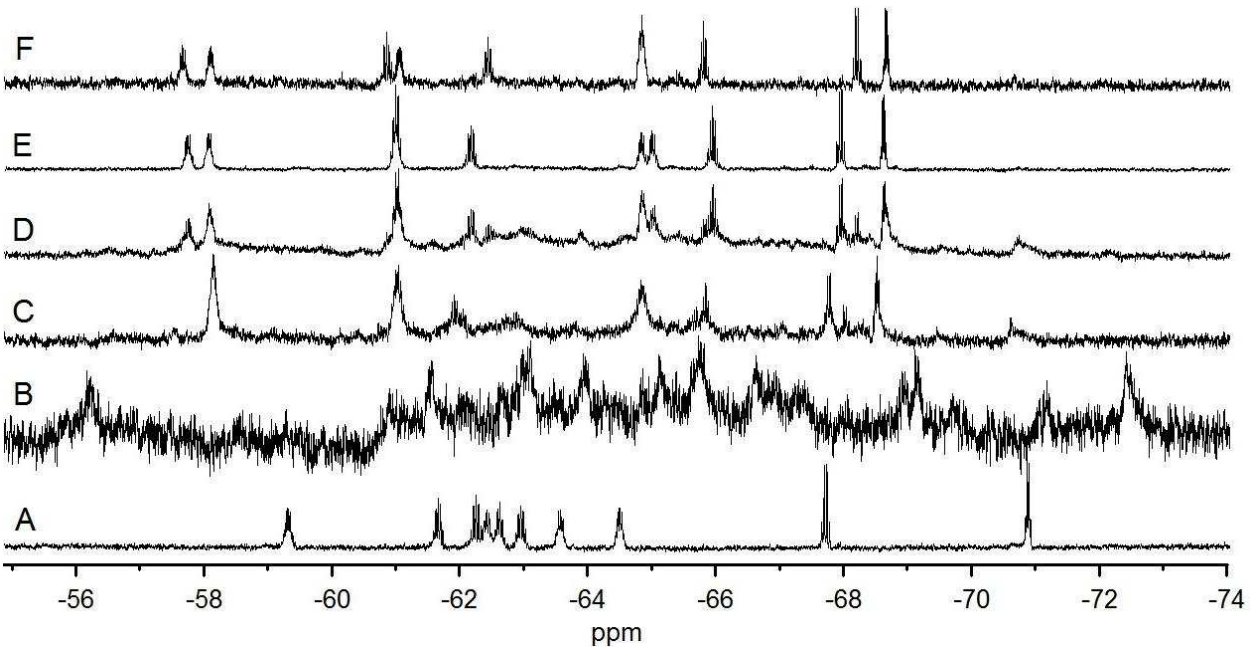

Figure 1.28. Fluorine-19 NMR spectra (376.5 MHz; δ(C_6F_6) −164.9) showing ten multiplets for **70-10-1** (A, 4:1 toluene:ether), **(70-10-1)$(CH_3)_n^{n-}$** after 4 equiv. $LiCH_3$ (B, 4:1 toluene:ether; note that most of this species was in the form of a green precipitate as a lithium salt), crude **(70-10-1)$(CH_3)_2(CN)_2$** (C, 6:1 toluene:ether and D, C_6D_6), the major (70-10-1)$(CH_3)_2(CN)_2$ isomer (***C*$_1$-$C_{70}(CF_3)_{10}$(34,44-$CH_3)_2$(23,33-$CN)_2$**, E, C_6D_6), and the minor (70-10-1)$(CH_3)_2(CN)_2$ isomer (***C*$_1$-$C_{70}(CF_3)_{10}$(33,44-$CH_3)_2$(23,34-$CN)_2$**; F, C_6D_6).

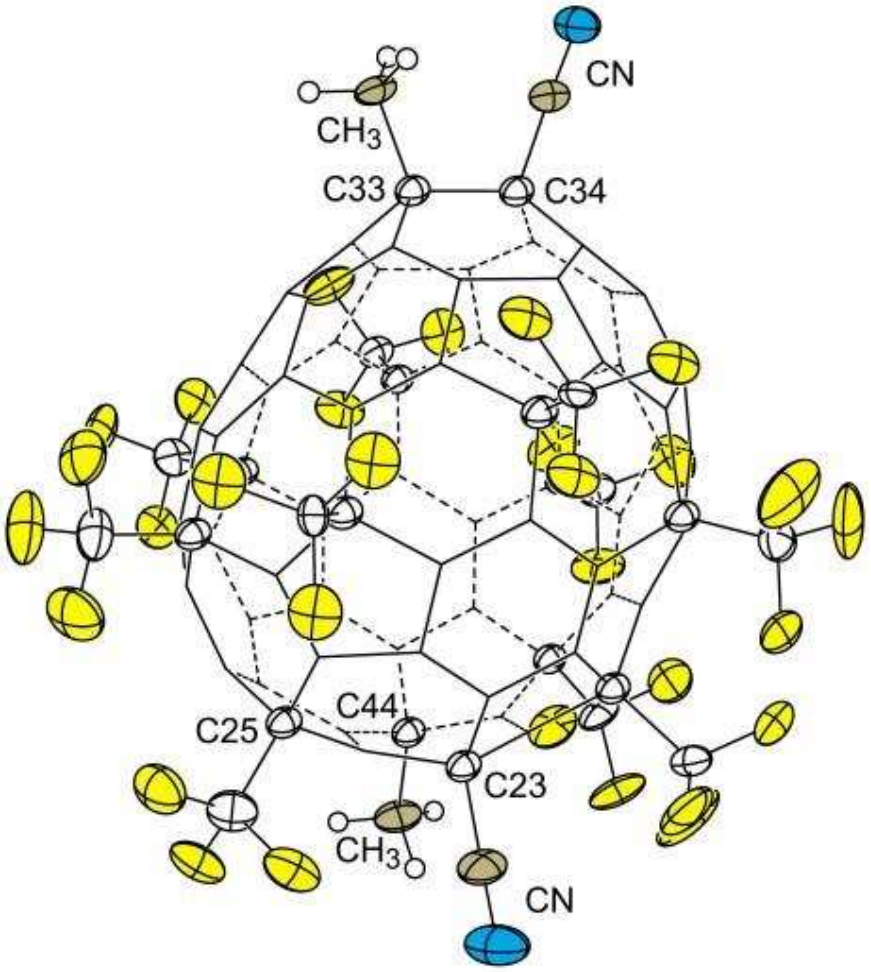

Figure 1.29. The structure of minor isomer C_1-$C_{70}(CF_3)_{10}$(33,44-CH_3)$_2$(23,34-CN)$_2$ (50% probability ellipsoids for the 14 substituents and the C atoms to which they are attached; H atoms shown as spheres of arbitrary size; CH_2Cl_2 solvent omitted for clarity). For Schlegel diagram, see Figure 1.19.

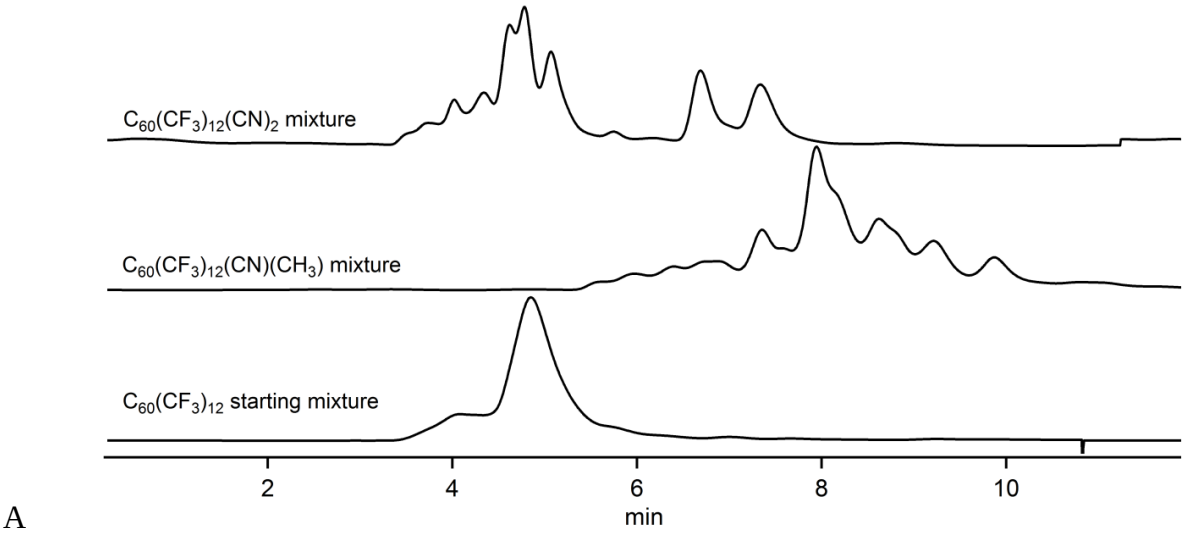

A

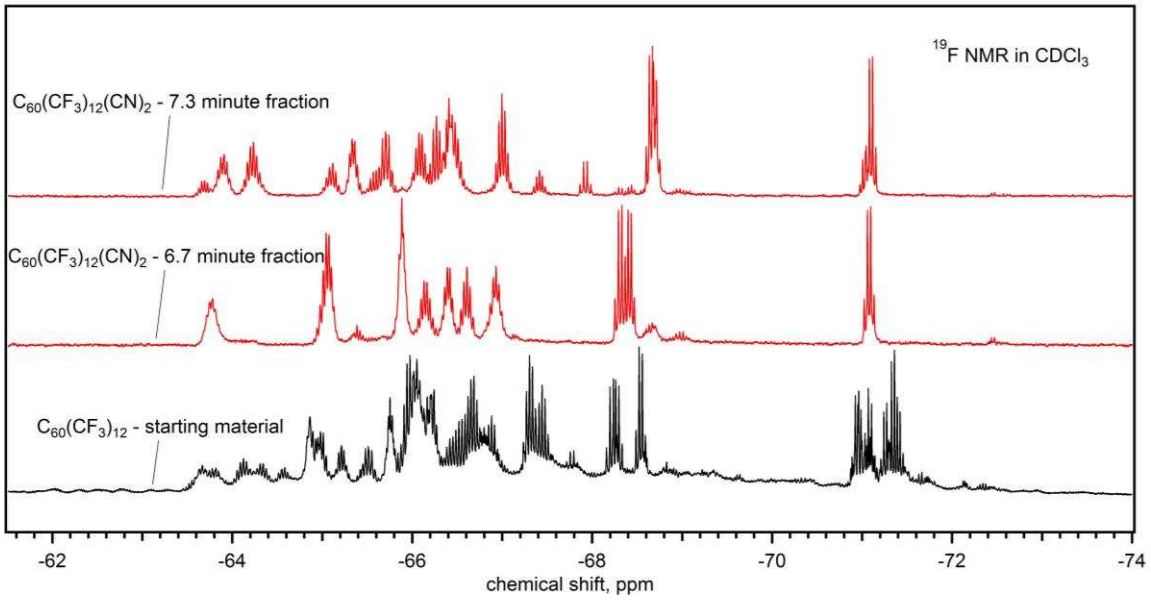

B

Figure 1.30. A) HPLC of a mixture of $C_{60}(CF_3)_{12}$ isomers (bottom), after the mixture was reacted with CN^- and CH_3^+ (middle) and after the mixture was reacted with CN^- and CN^+ (top) using 100% hexane with Buckyprep columns. B) ^{19}F NMR spectra of starting $C_{60}(CF_3)_{12}$ mixture and two fractions from the $C_{60}(CF_3)_{12}(CN)_2$ reaction.

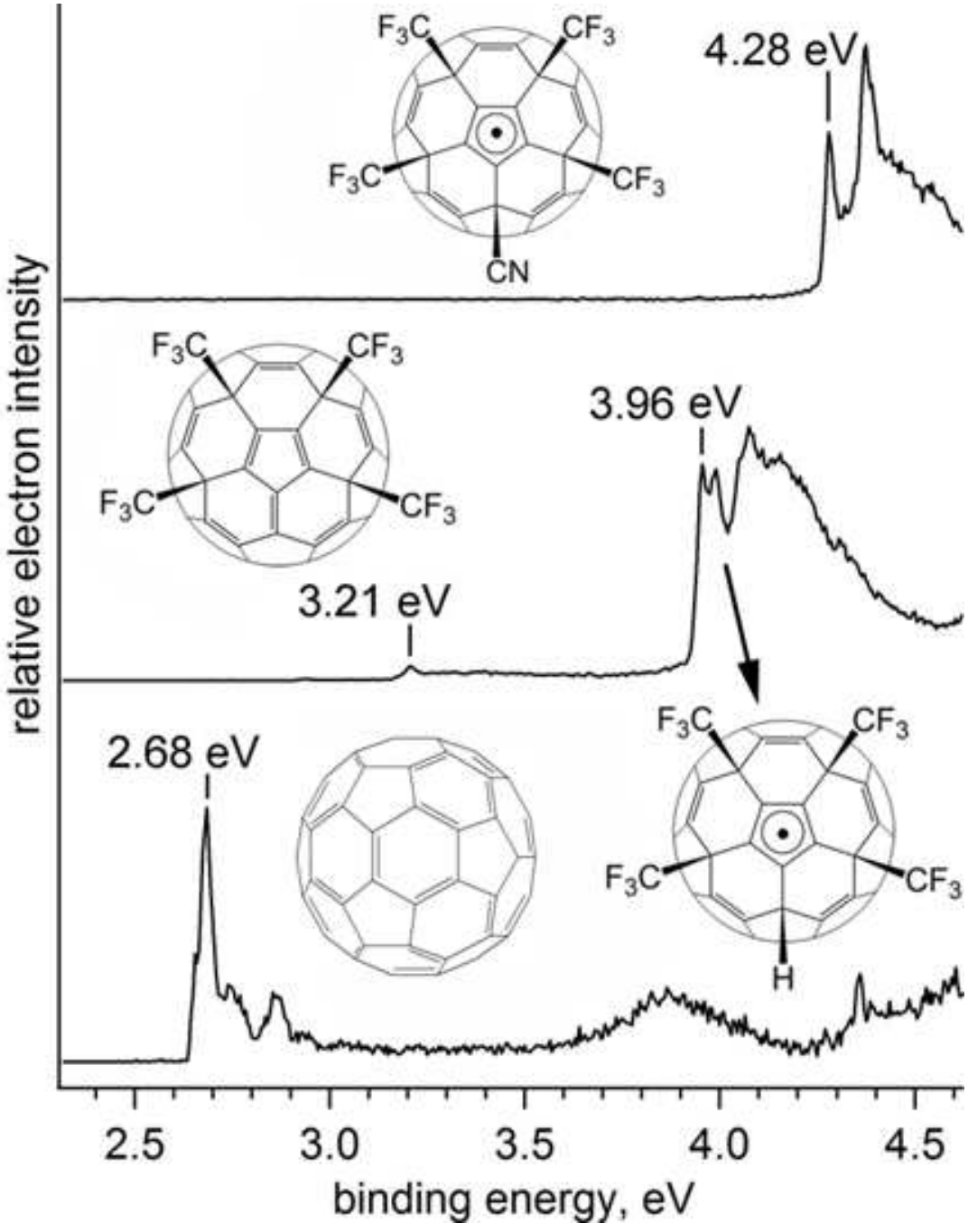

Figure 1.31. The low temperature (12 K) photoelectron spectrum at 266 nm of $C_{60}(CF_3)_4(CN)^-$ (**(60-4-2)(CN)$^-$,** top), $C_{60}(CF_3)_4^-$ and $C_{60}(CF_3)_4H^-$ (**60-4-2$^-$** and **(60-4-2)H$^-$,** middle); and C_{60} (at 68 K) (bottom, first reported in ref.[88])

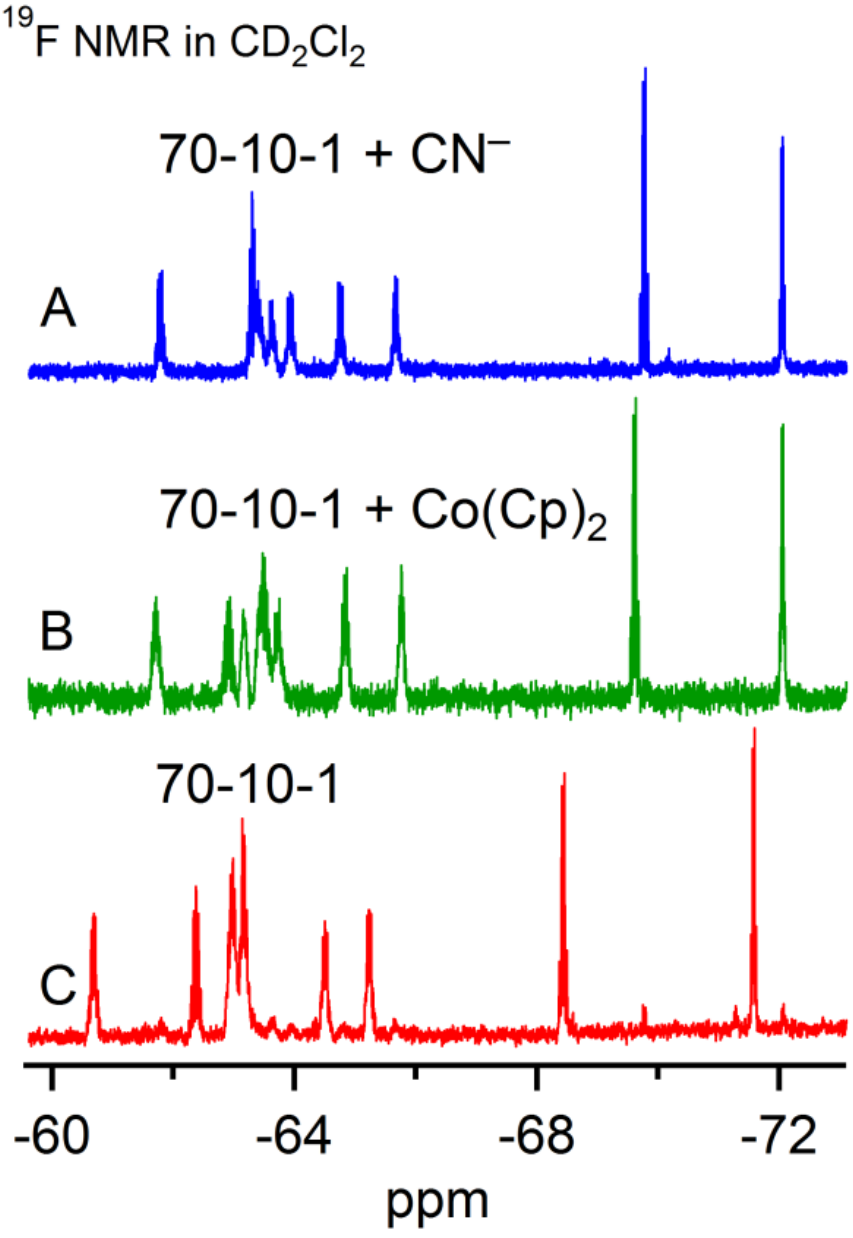

Figure 1.32. ^{19}F NMR spectra of **70-10-1**, its anionic adduct with CN and its dianionic dimer **(70-10-1^{-})$_2$** obtained by the reaction of **70-10-1** with $CoCp_2$ (376.5 MHz, CD_2Cl_2, 298 K, $\delta(C_6F_6) = -164.9$)

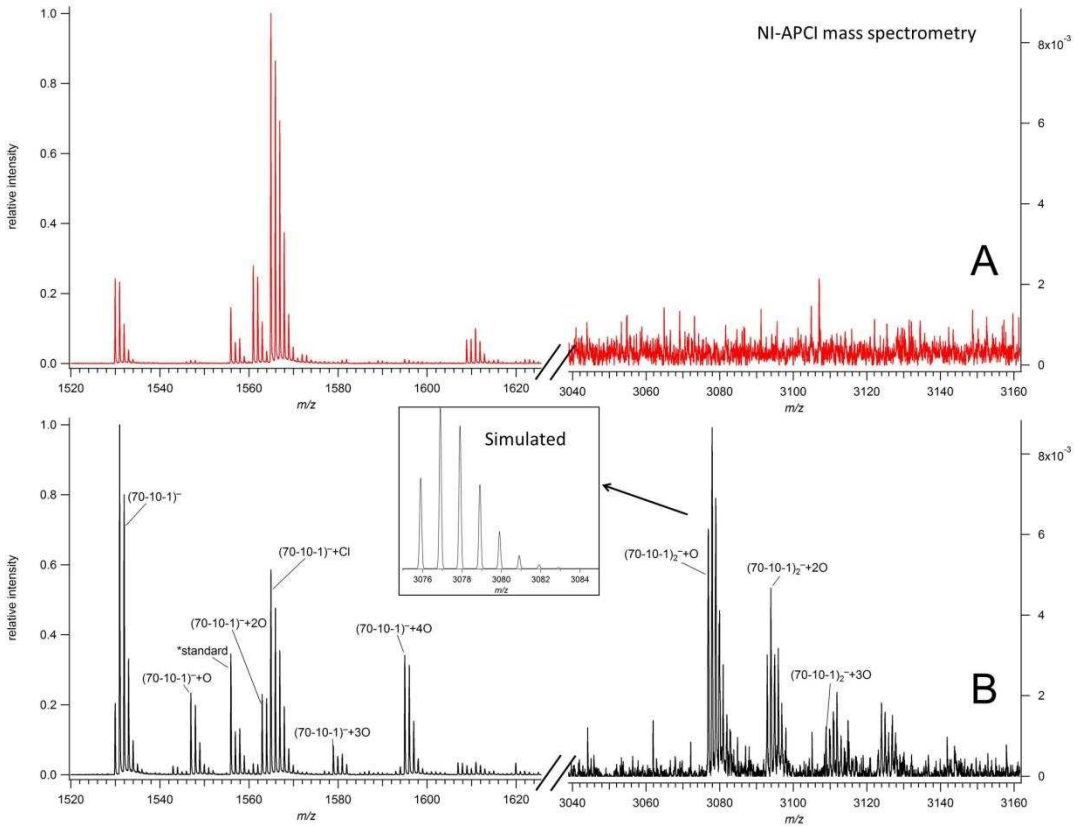

Figure 1.33. NI-APCI mass spectra of **70-10-1** (upper panel) and **70-10-1** reduced with $CoCp_2$ (lower panel) recorded using an Agilent Technologies Model 6210 TOF spectrometer. Dichloromethane solutions were injected with acetonitrile mobile phase.

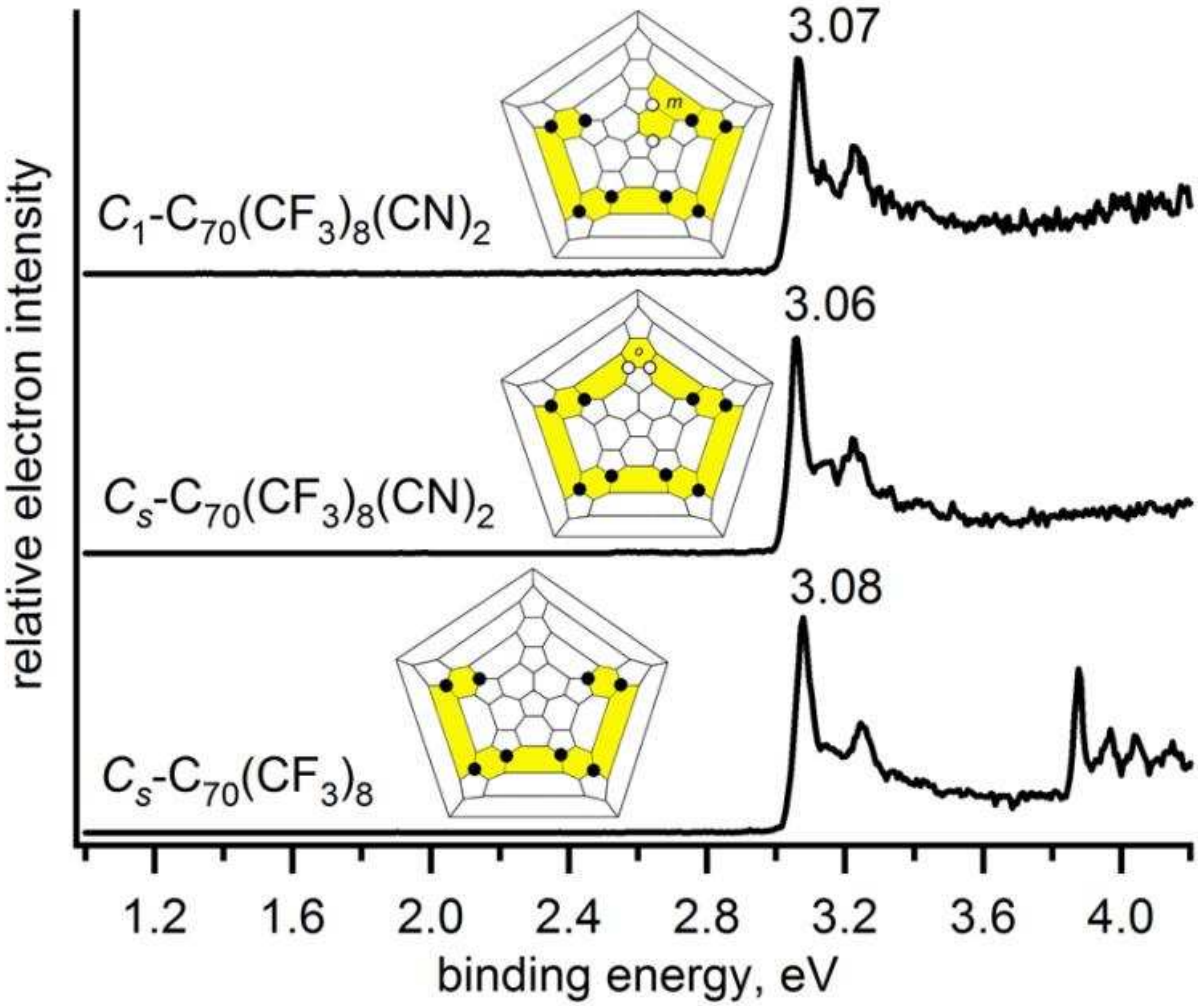

Figure 1.34. The low temperature (12K) photoelectron spectra at 266 nm of C_s-$C_{70}(CF_3)_8$ (**70-8-1**), C_s-$C_{70}(CF_3)_8(CN)_2$ (***C*$_s$-(70-8-1)(CN)$_2$**), and C_1-$C_{70}(CF_3)_8(CN)_2$ (***C*$_1$-(70-8-1)(CN)$_2$**).

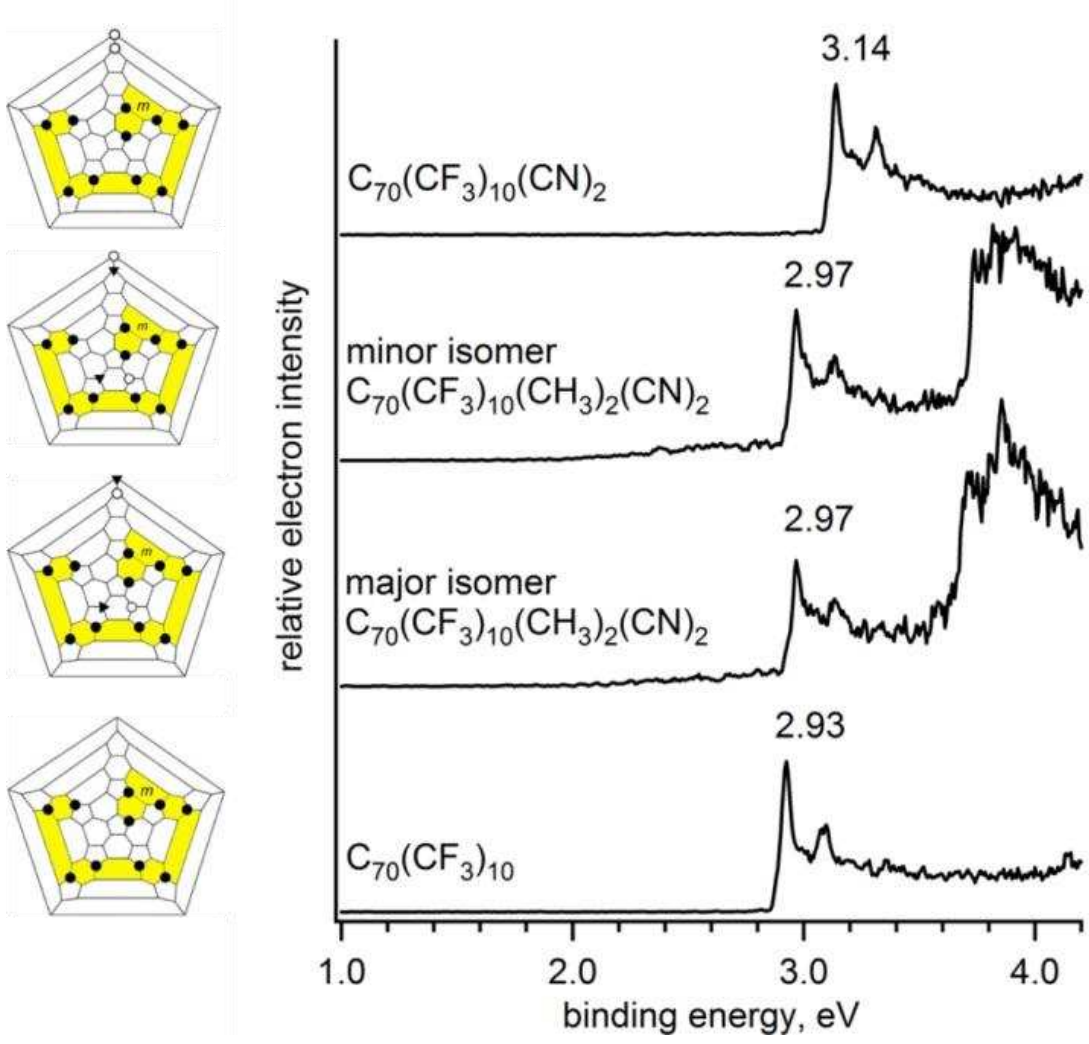

Figure 1.35. Photoelectron spectra of cyanated derivatives of **70-10-1** and corresponding Schlegel diagrams. Major isomer = ***C*$_1$-C$_{70}$(CF$_3$)$_{10}$(34,44-CH$_3$)$_2$(23,33-CN)$_2$** and minor isomer = ***C*$_1$-C$_{70}$(CF$_3$)$_{10}$(33,44-CH$_3$)$_2$(23,34-CN)$_2$**.

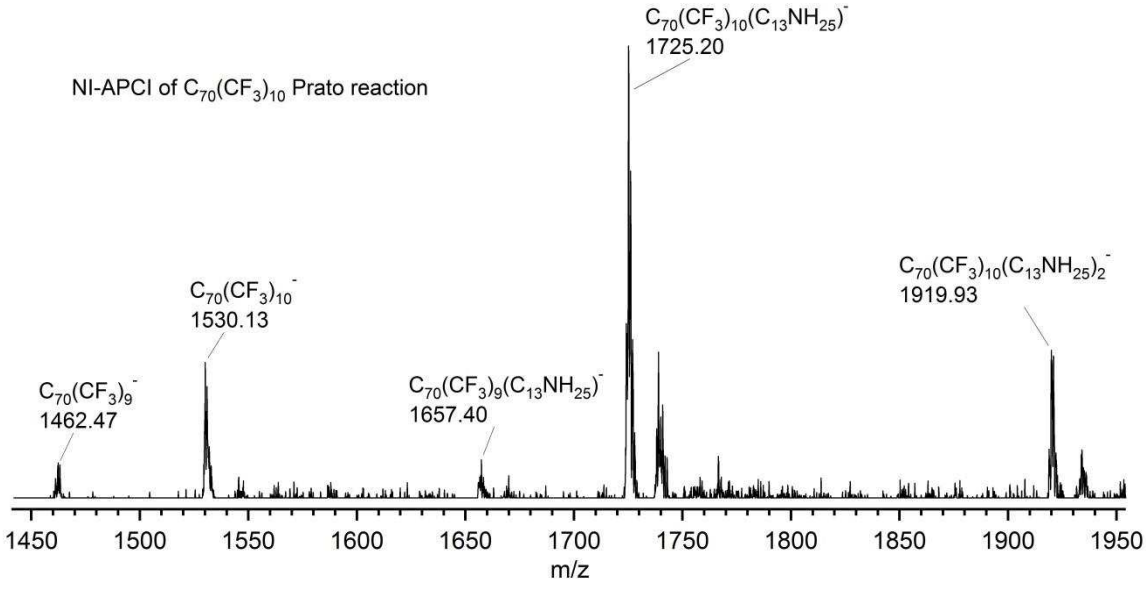

Figure 1.36. NI-APCI mass spectrum of the modified Prato reaction with $C_{70}(CF_3)_{10}$. The peaks at 1725.20 and 1919.93 m/z correspond to mono- and bis- ylide additions to $C_{70}(CF_3)_{10}$, respectively.

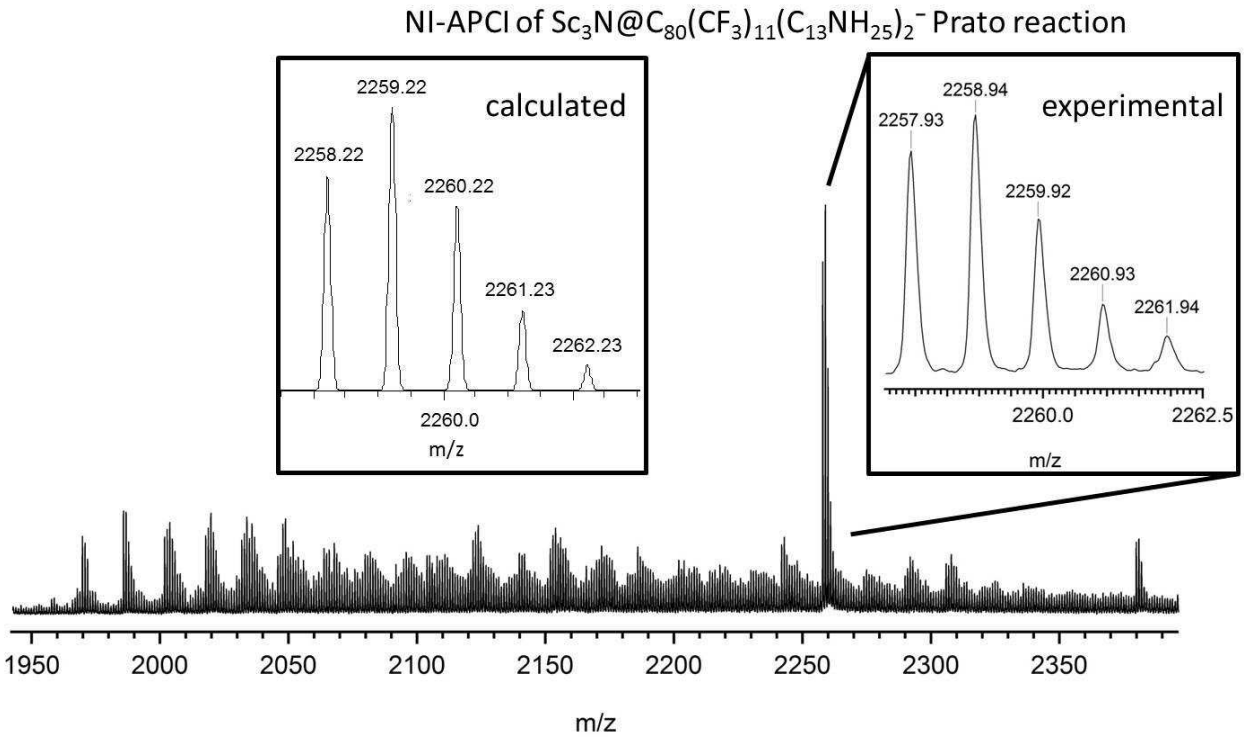

Figure 1.37. Experimental and calculated NI-APCI mass spectra of $Sc_3N@C_{80}(CF_3)_{11}(C_{13}NH_{25})_2^-$ which must come from the loss of $C_{13}NH_{25}$ from $Sc_3N@C_{80}(CF_3)_{12}(C_{13}NH_{25})_2^-$.

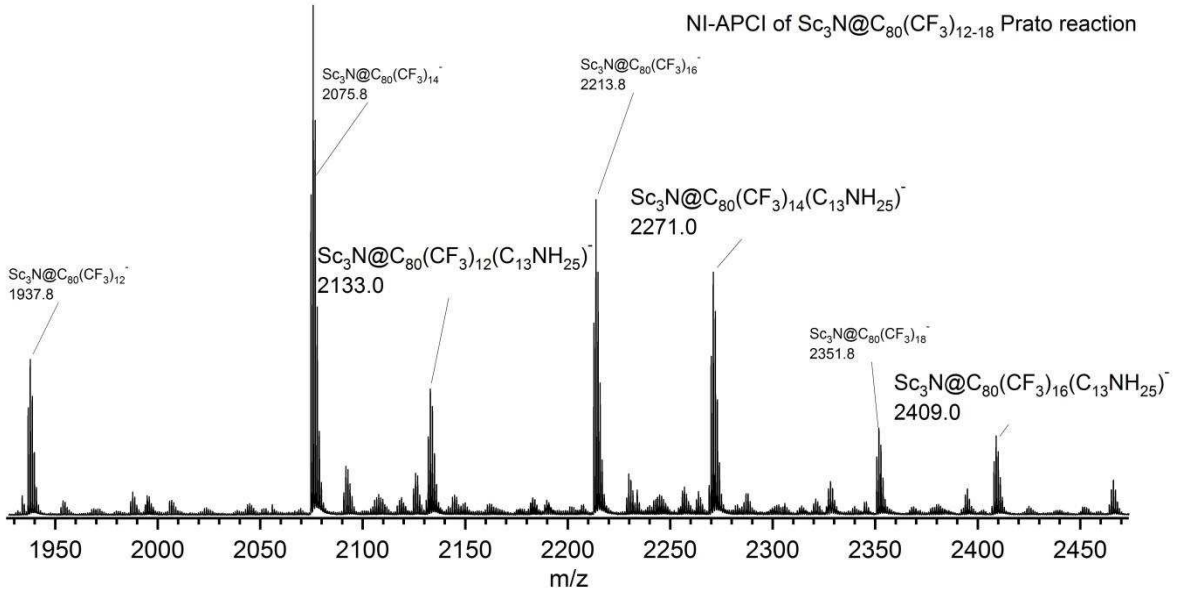

Figure 1.38. NI-APCI mass spectrum of the modified Prato reaction with $Sc_3N@C_{80}(CF_3)_{12\text{-}18}$. There are no peaks at 2547 m/z which would correspond to $Sc_3N@C_{80}(CF_3)_{18}(C_{13}NH_{25})^-$.

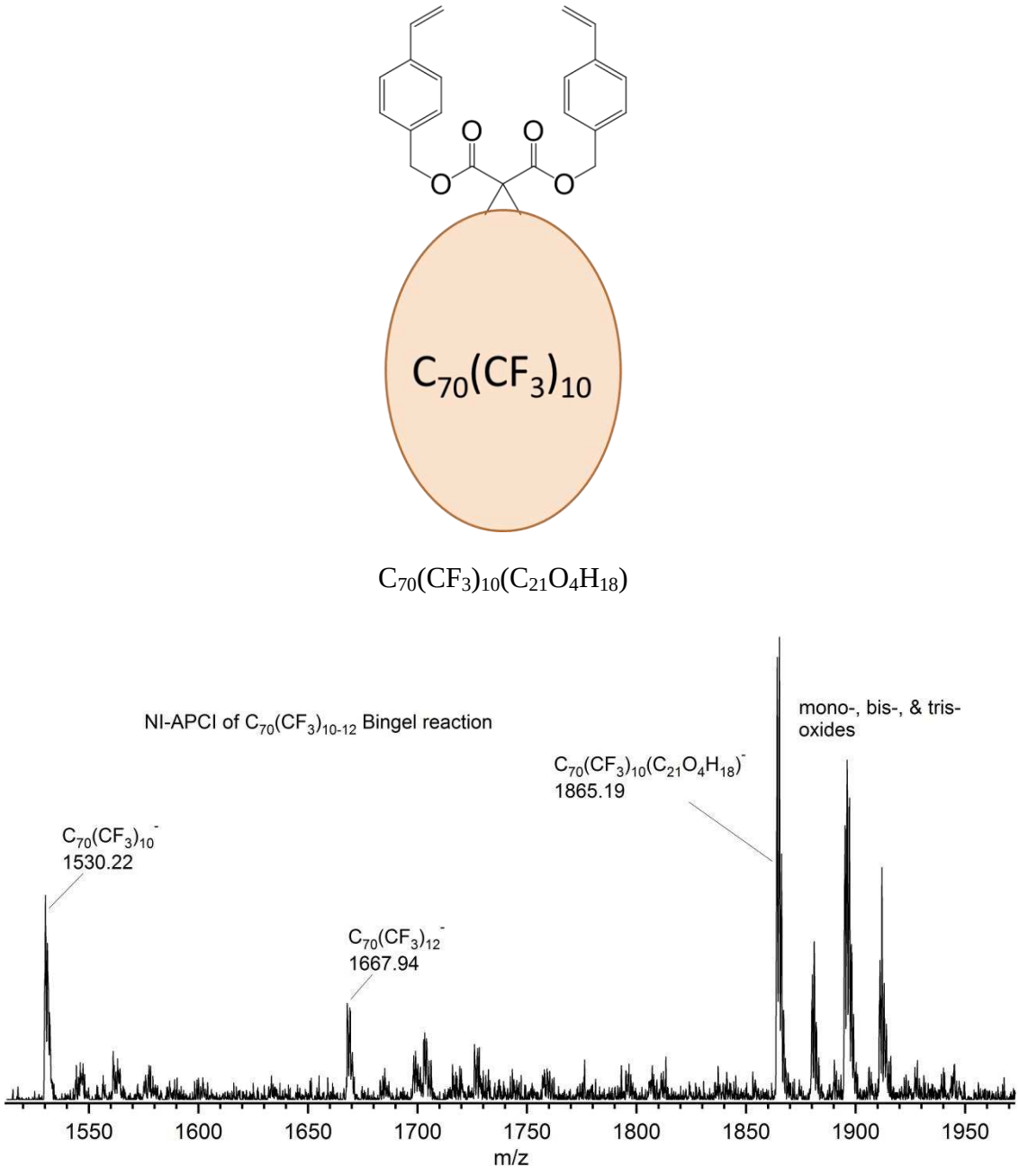

Figure 1.39. NI-APCI mass spectrum of the modified Bingel reaction with $C_{70}(CF_3)_{10\text{-}12}$. The peak at 1865.19 m/z corresponds to the mono malonate addition to $C_{70}(CF_3)_{10}$.

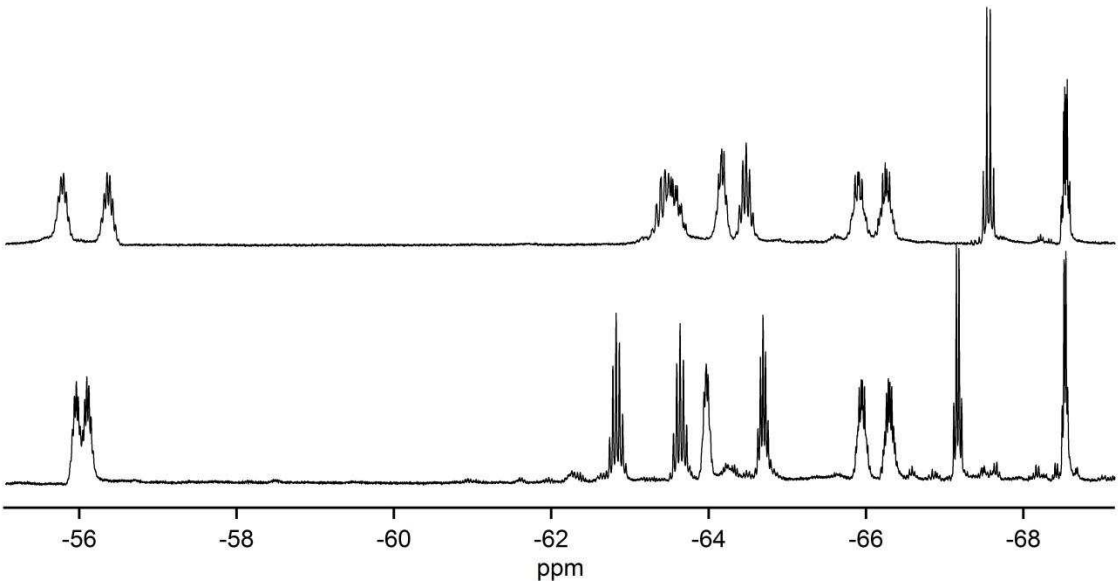

Figure 1.40. Fluorine-19 NMR spectra of **60-10-3** (bottom) and HPLC purified **(60-10-3)(phosphonic ester)** in $CDCl_3$. C_6F_6 external standard $\delta = -161.4$ ppm.

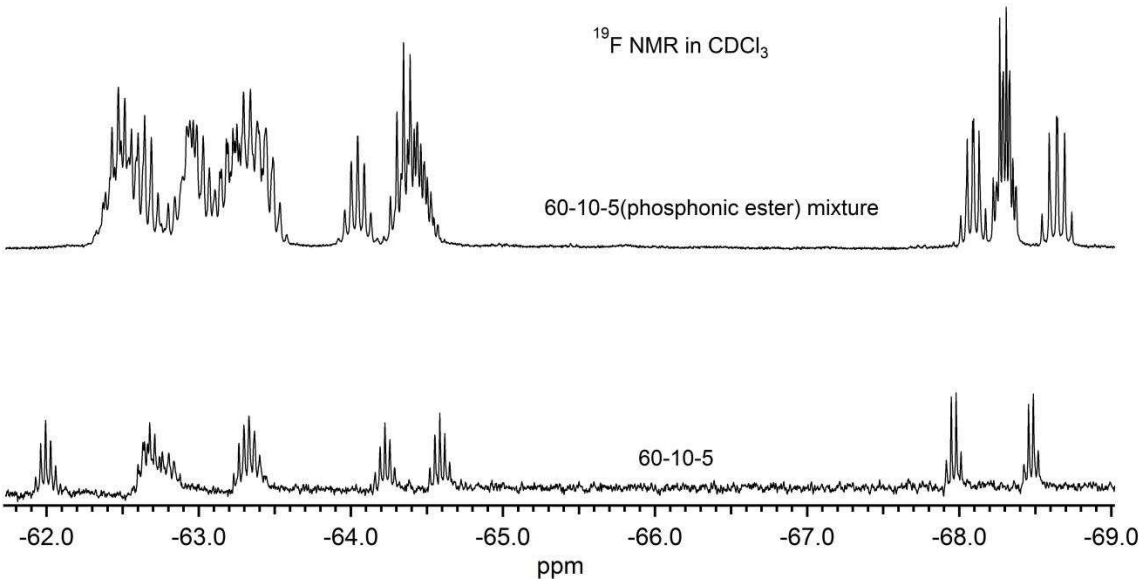

Figure 1.41. Fluorine-19 NMR spectra of **60-10-5** (bottom) and two isomers of **(60-10-5)(phosphonic ester)** in $CDCl_3$. C_6F_6 external standard $\delta = -161.4$ ppm.

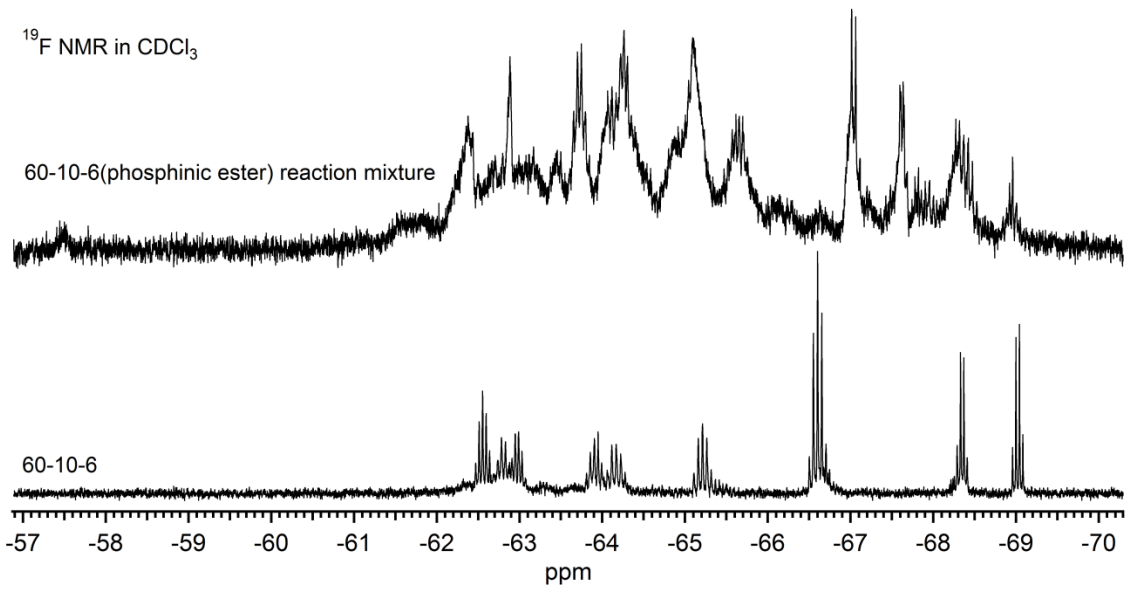

Figure 1.42. Fluorine-19 NMR spectra of **60-10-6** (bottom) and crude mixture of **(60-10-6)(phosphonic ester)** products in $CDCl_3$. C_6F_6 external standard $\delta = -161.4$ ppm.

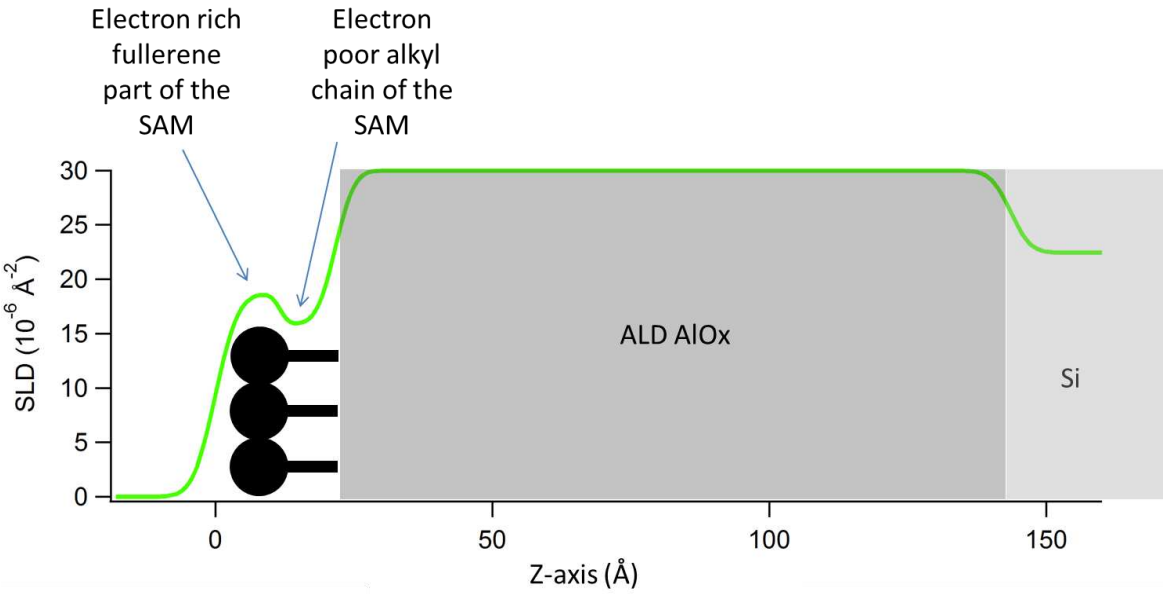

Figure 1.43. The vertical electron density profile of **(60-10-3)(phosphonic acid)**-SAMs on ALD AlO_x plotted over a representative cartoon of the layers.

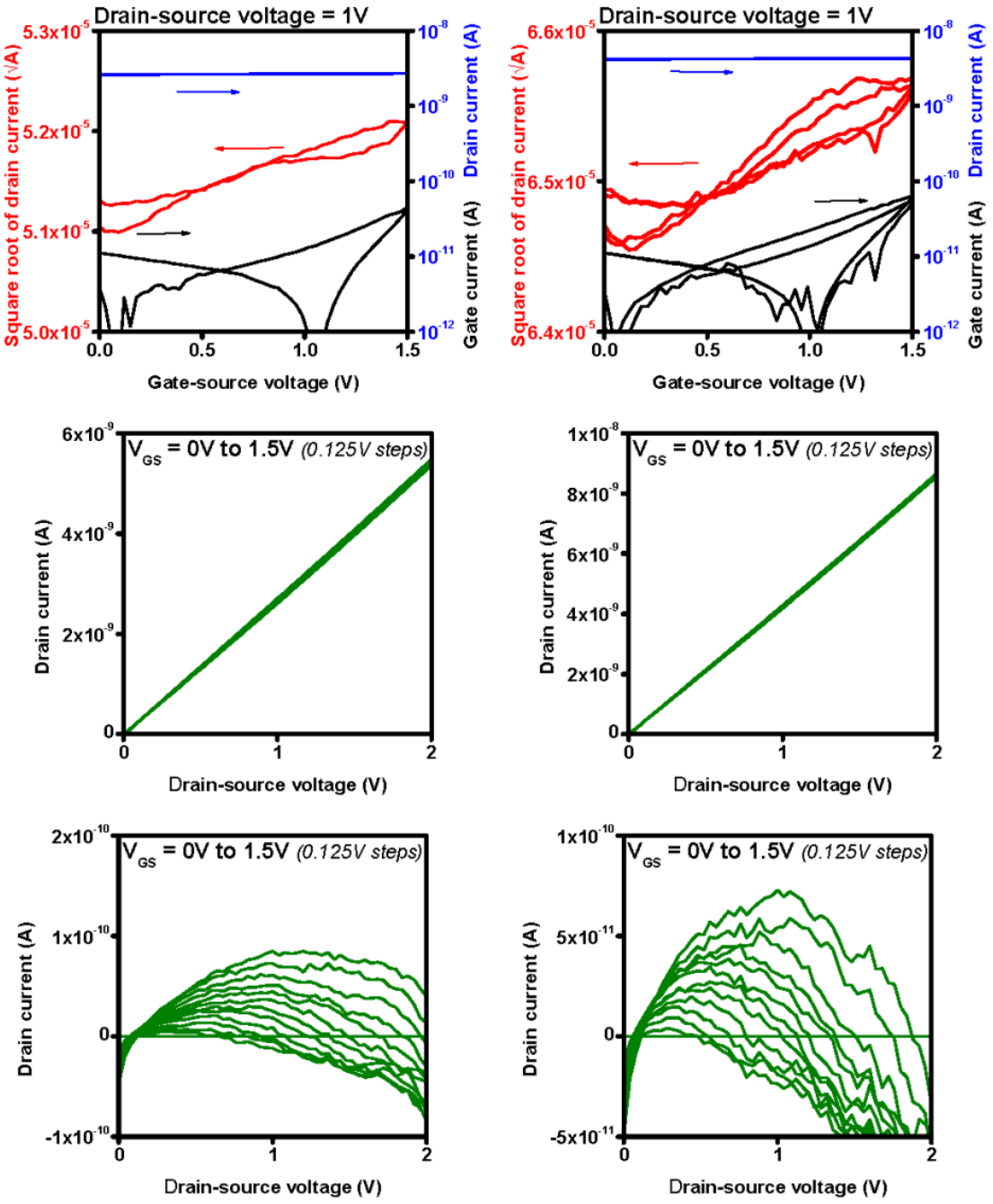

Figure 1.44. Transfer (top), output (middle), and corrected output curves (bottom) of pure **(60-10-3)(phosphonic acid)**-SAMFETs (left column) and $C_{10}F_{17}$-(carboxylic acid) SAMFETs that were exchanged with **(60-10-3)(phosphonic acid)**-SAMs (right column)

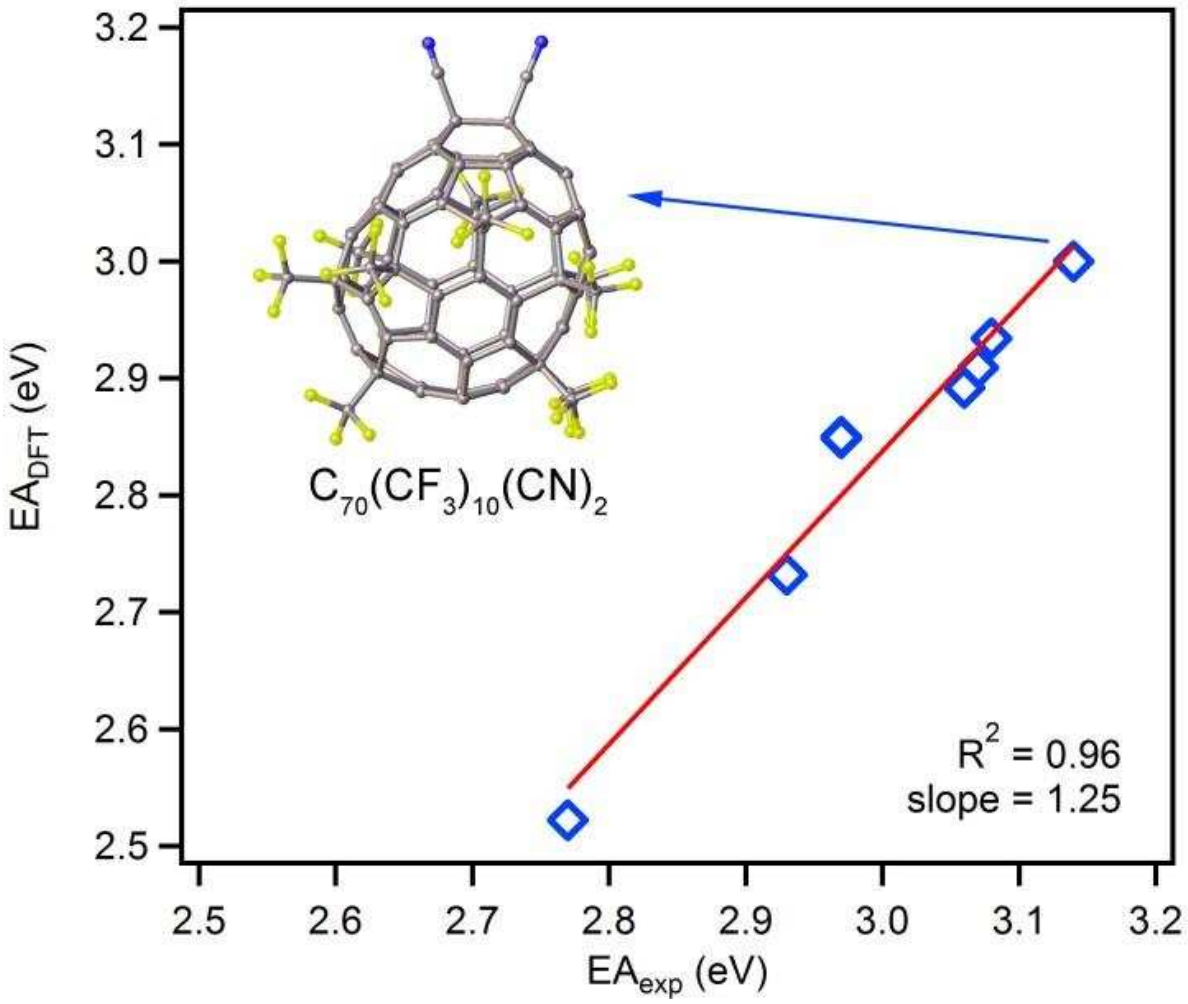

Figure 1.45. Correlation of DFT calculated and experimental electron affinities for $C_{70}(CF_3)_x(CN)_y$ studied in this work. A 3D model of the fullerene with the highest electron affinity, **(70-10-1)$(CN)_2$**, is shown.

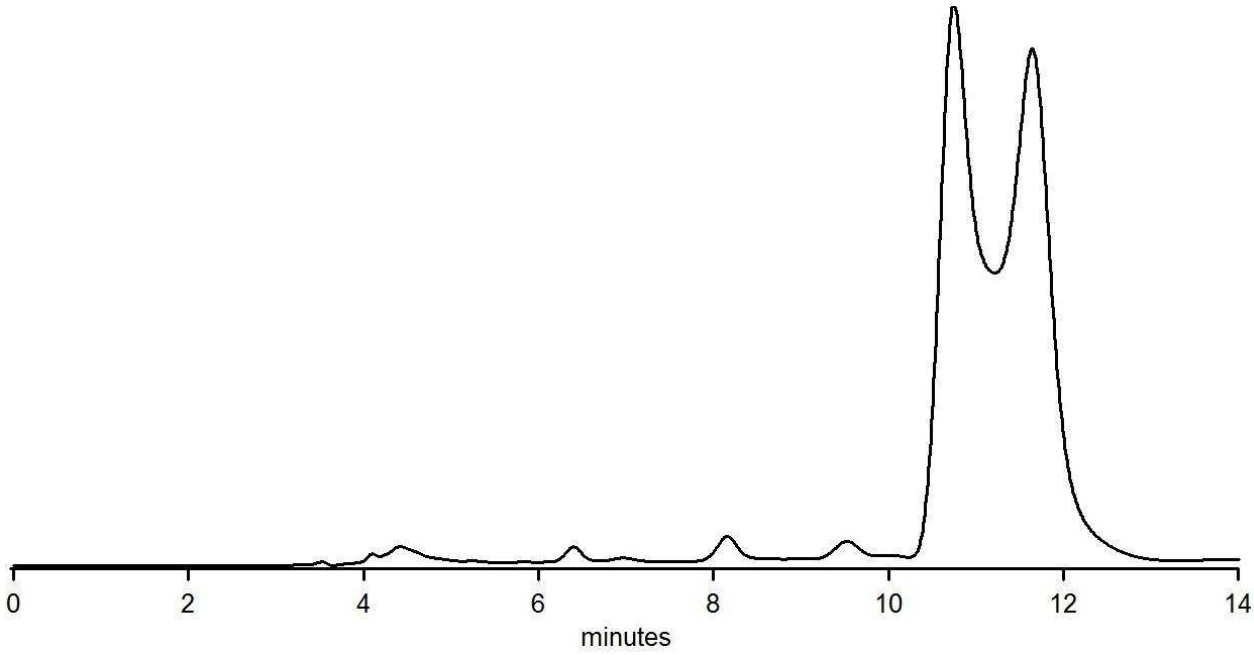

Figure 1.46. HPLC of the **(60-2-1)(CN)(CH_3)** reaction mixture ($PhCH_3$ eluent), showing two predominant isomers in a ca. 3:2 ratio (this ratio also matches the ^{19}F NMR spectrum).

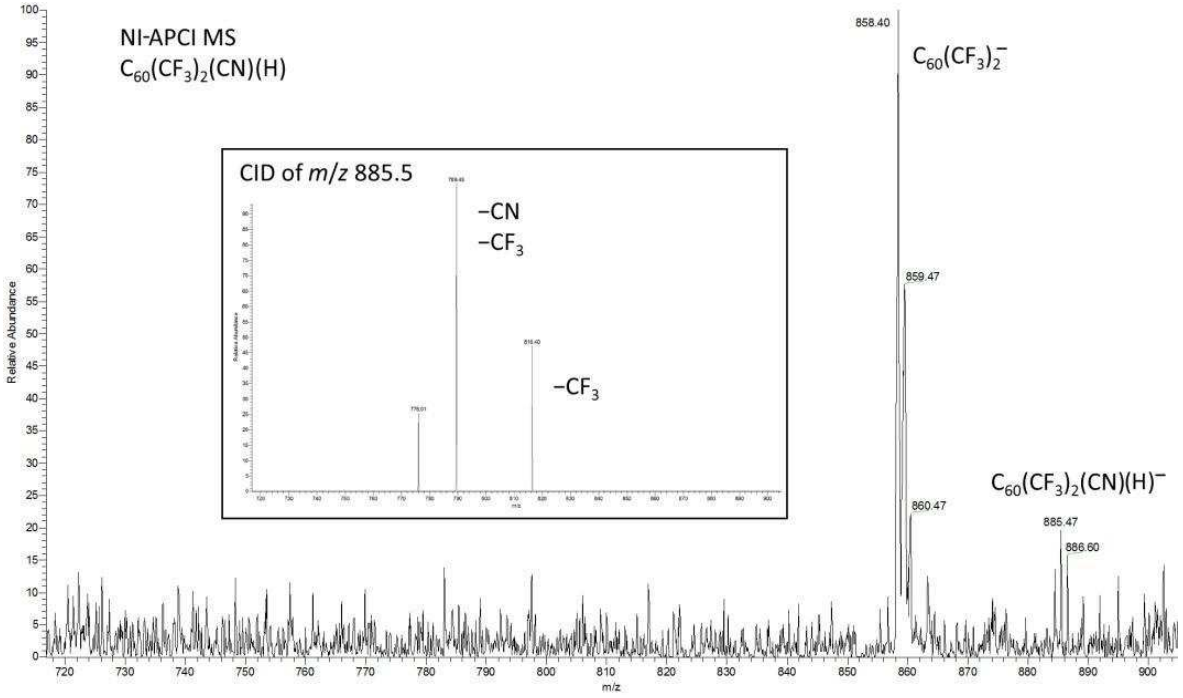

Figure 1.47. Negative-ion APCI mass spectrum of the **(60-2-1)(CN)(H)** reaction mixture (calc. *m*/*z* = 885.7) and the CID spectrum of the *m*/*z* 885.5 peak.

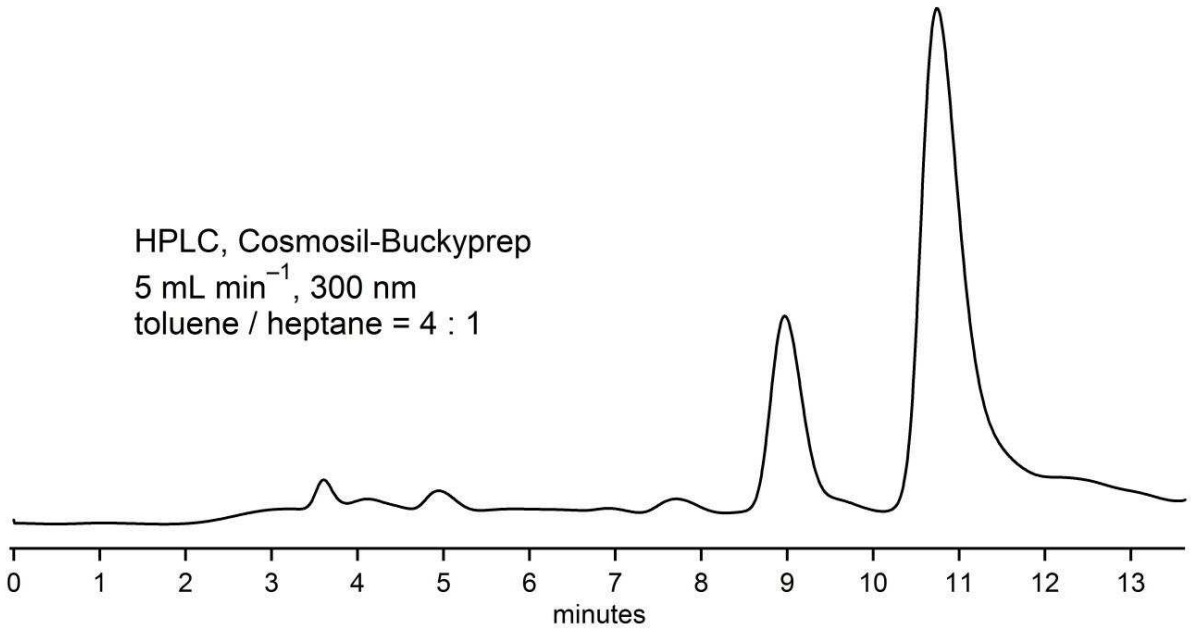

Figure 1.48. HPLC of the crude reaction mixture of compound $C_{60}(CF_3)_4(CN)H$ (**(60-4-2)(CN)H**). The desired product (**(60-4-2)(CN)H**, retention time = 10.9 min.) was separated from unreacted $C_{60}(CF_3)_4O$ (retention time = 9.0 min) and byproducts.

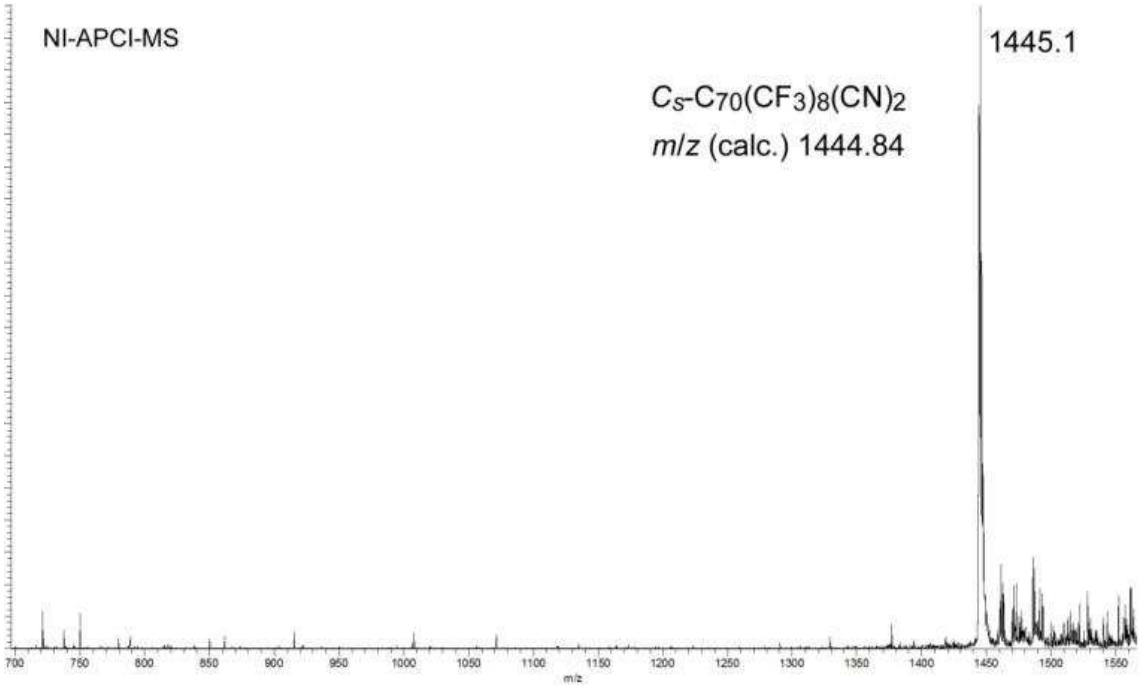

Figure 1.49. Negative-ion APCI mass spectrum of an HPLC purified sample of the major isomer C_s-p^9o(loop)-$C_{70}(CF_3)_8(CN)_2$ ***C*$_s$-(70-8-1)(CN)$_2$.**

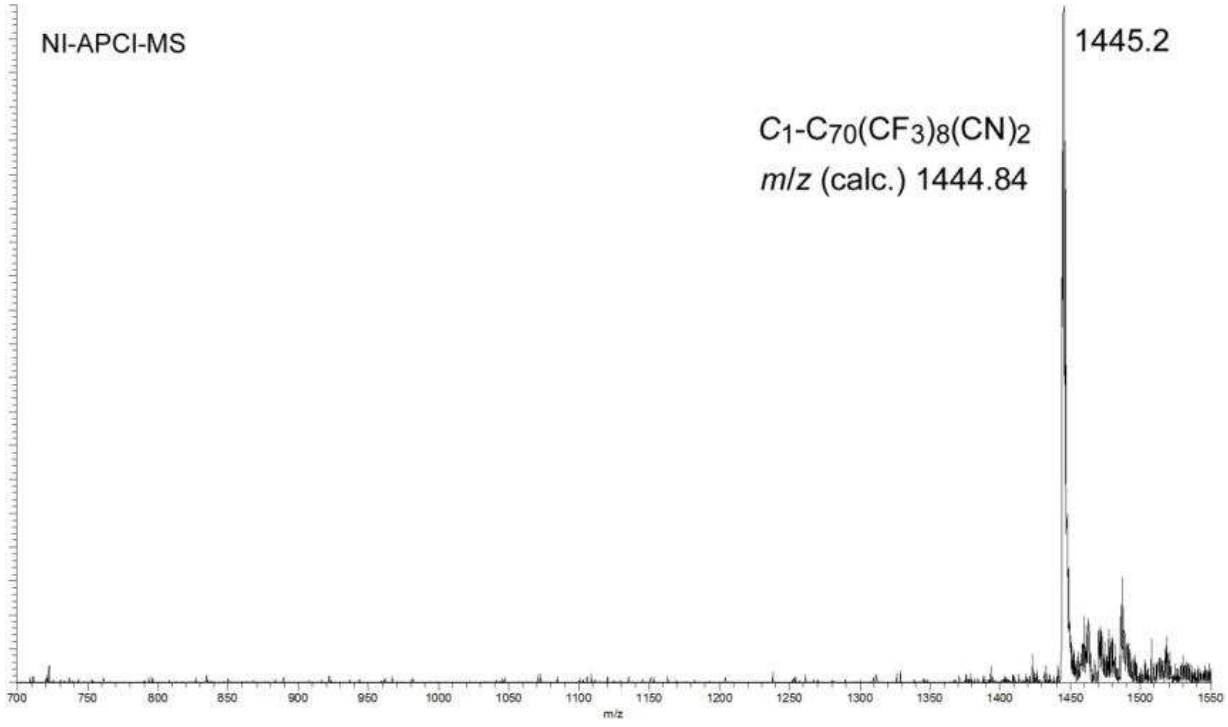

Figure 1.50. Negative-ion APCI mass spectrum of an HPLC purified sample of the minor isomer C_1-$C_{70}(CF_3)_8(CN)_2$, ***C*$_1$-(70-8-1)(CN)$_2$**.

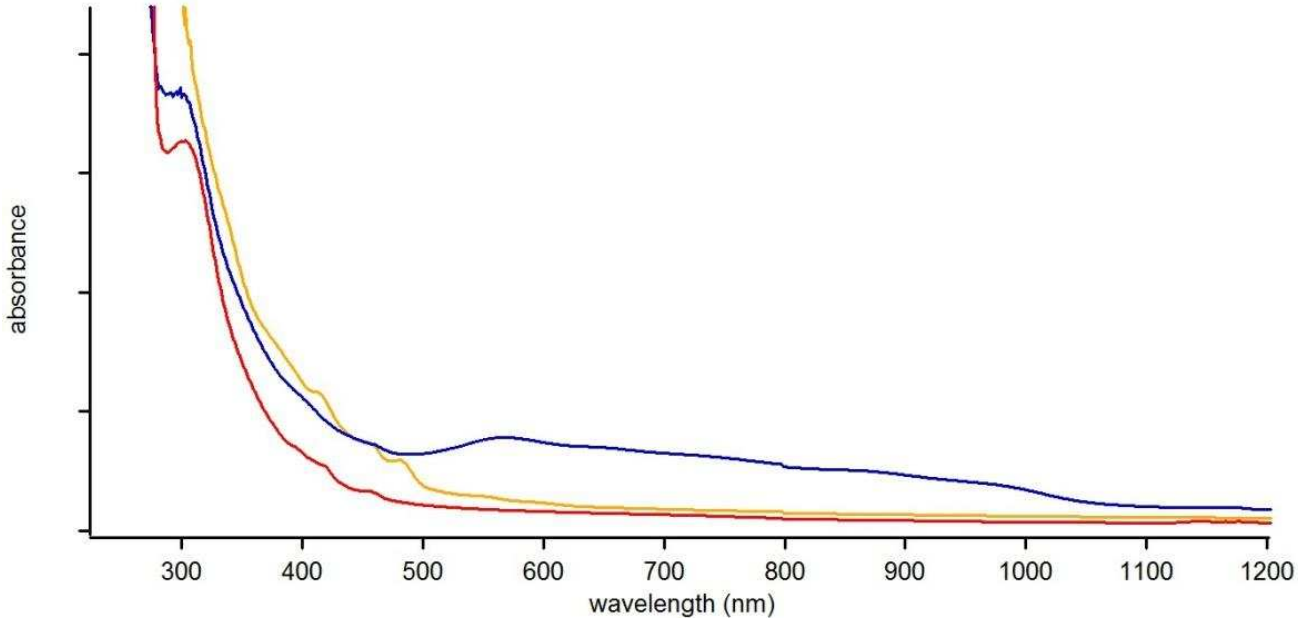

Figure 1.51. UV-Vis spectra of C_s-p^7-$C_{70}(CF_3)_8$ (**70-8-1**; yellow trace; C_6D_6), the $\boldsymbol{C_1}$**-(70-8-1)(CN)**$^-$ intermediate (blue trace; 20:3:2 C_6D_6:$PhCH_3$:ACN), and an purified sample of the major C_s-p^9o(loop)-(70-8-1)$(CN)_2$ isomer ($\boldsymbol{C_s}$**-(70-8-1)(CN)$_2$**, red trace; 7:1 C_6D_6:ACN).

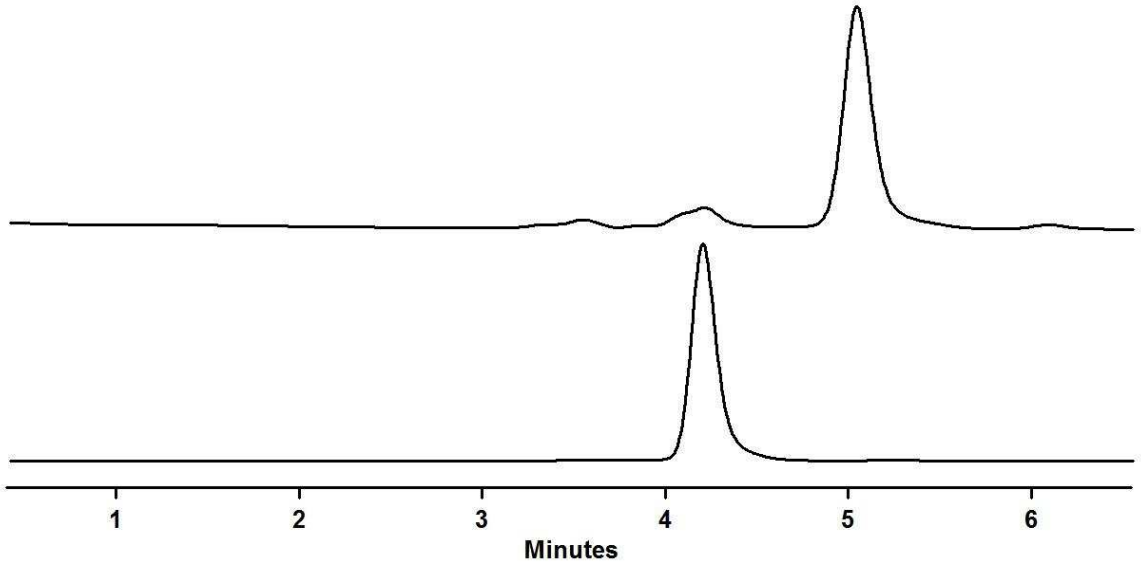

Figure 1.52. HPLC of the p^7mp-$C_{70}(CF_3)_{10}$ (**70-10-**1) starting material (bottom) and the $C_{70}(CF_3)_{10}(CN)(CH_3)$ (**(70-10-1)(CN)(CH_3)**) reaction mixture (top). Toluene was the eluent.

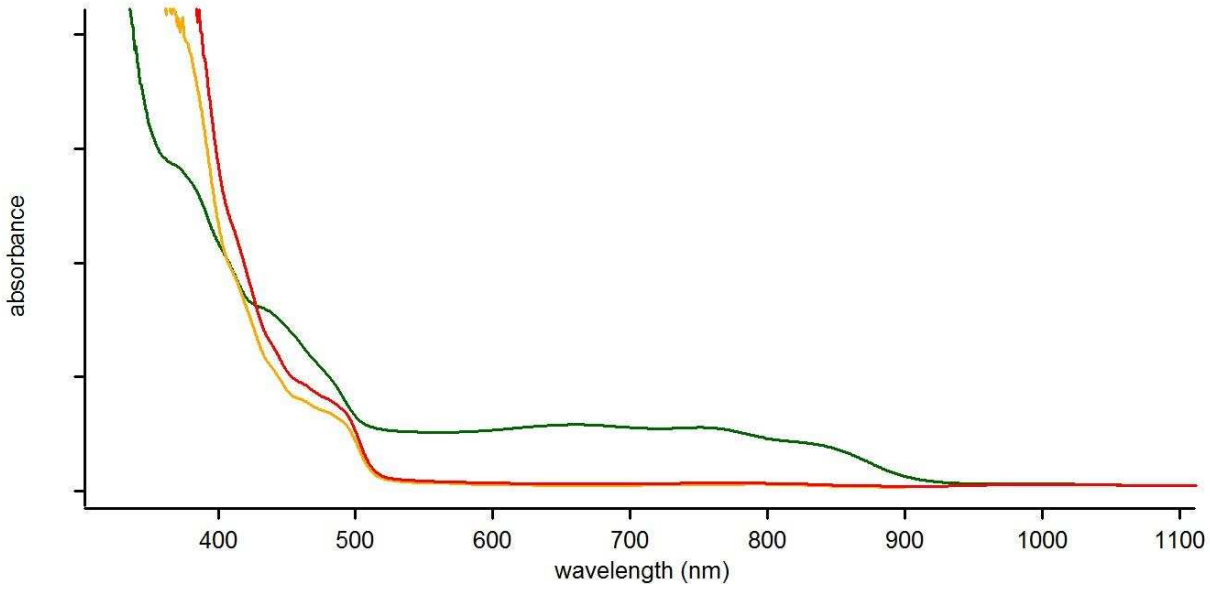

Figure 1.53. UV-Vis spectra of the p^7mp-$C_{70}(CF_3)_{10}$ starting material (yellow trace; $PhCH_3$), the $C_{70}(CF_3)_{10}(CN)^-$ intermediate (green trace; 5:1 $PhCH_3$:ACN), and an HPLC purified sample of the neutral product $C_{70}(CF_3)_{10}(CN)(CH_3)$ (red trace; $PhCH_3$).

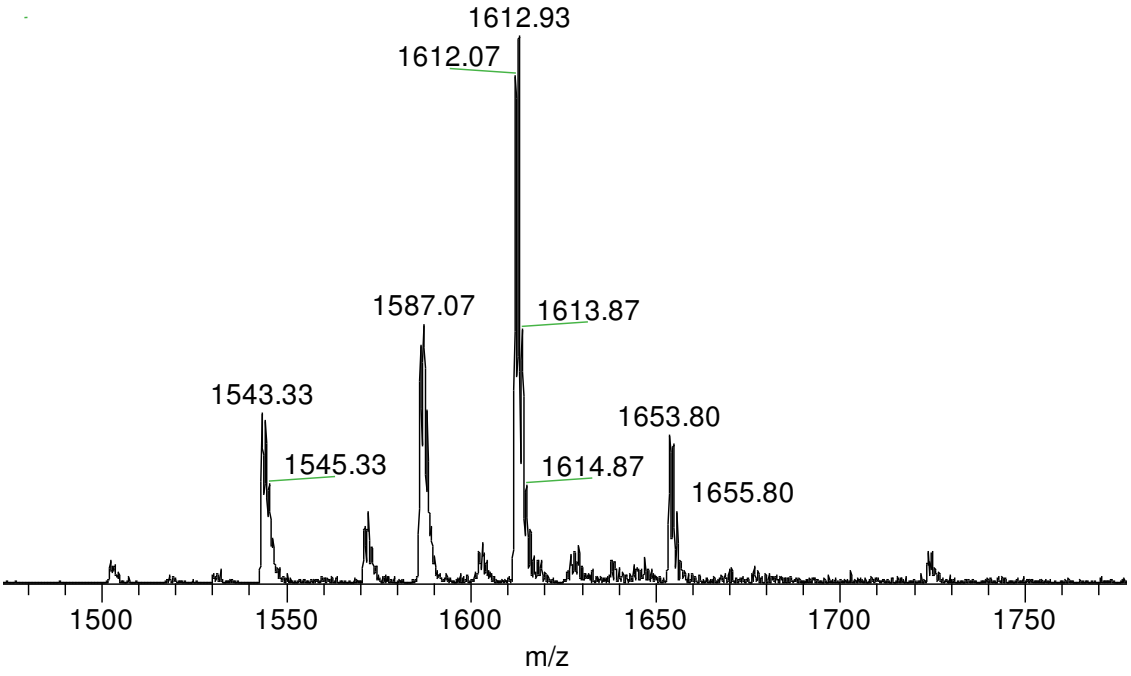

Figure 1.54. APCI mass spectrum of the major $C_{70}(CF_3)_{10}(CH_3)_2(CN)_2$ isomer (***C*$_1$-$C_{70}(CF_3)_{10}$(34,44-CH_3)$_2$(23,33-CN)$_2$**) in acetonitrile.

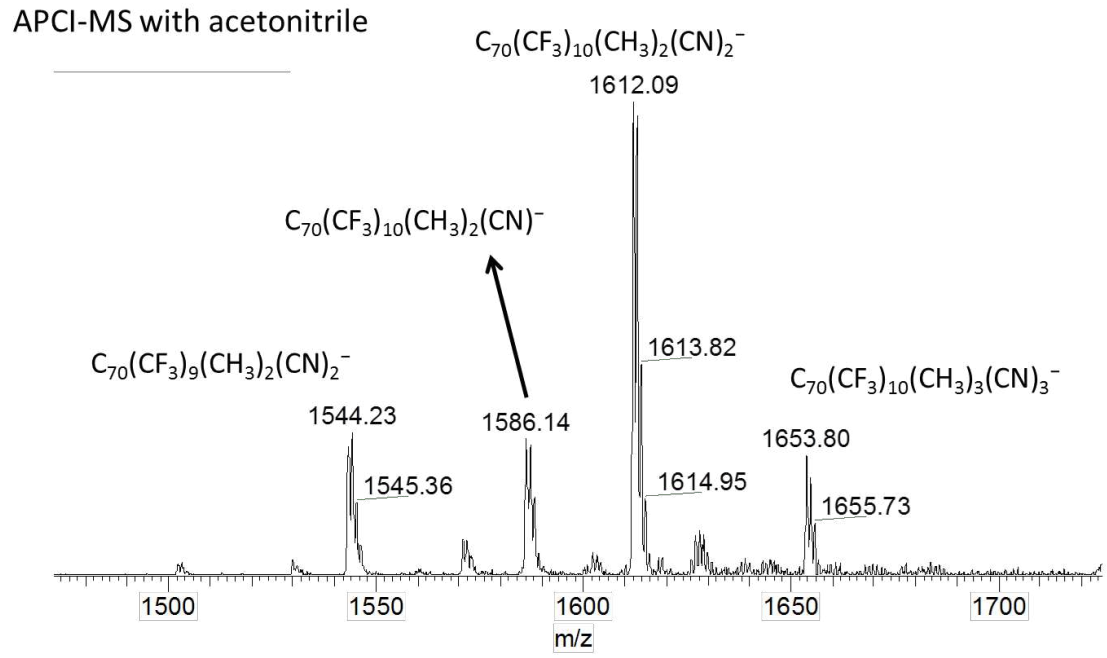

Figure 1.55. APCI mass spectrum of the minor $C_{70}(CF_3)_{10}(CH_3)_2(CN)_2$ isomer (***C*$_1$-$C_{70}(CF_3)_{10}$(33,44-CH_3)$_2$(23,34-CN)$_2$**) in acetonitrile. The proposed formulas for the major species are shown (the peaks at ca. m/z 1654 are due to addition of acetonitrile to the parent ion; this was demonstrated by the absence of these peaks when the solvent was isopropanol).

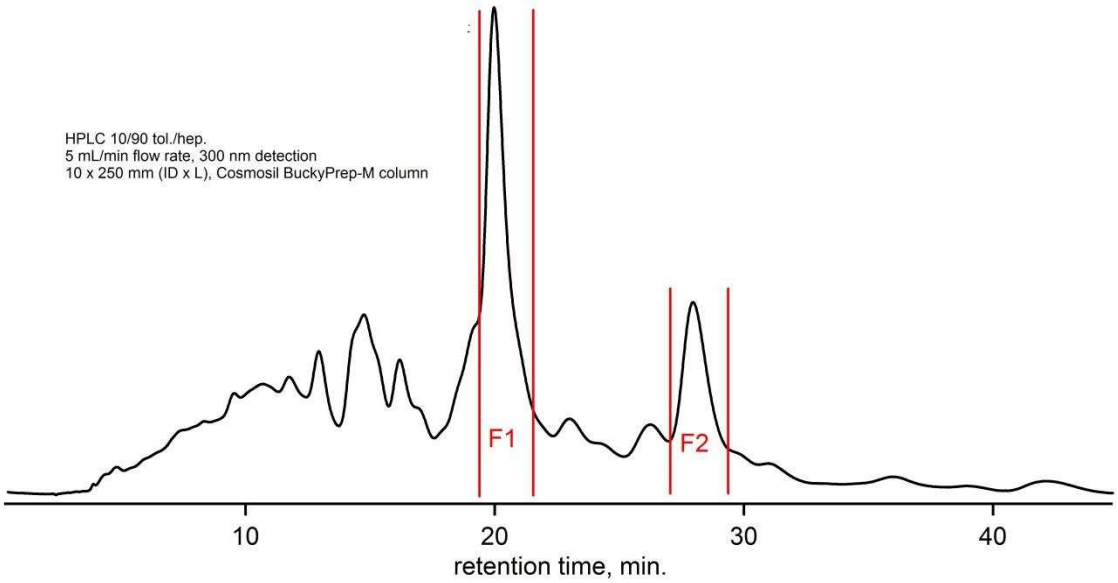

Figure 1.56. HPLC separation of **(70-10-1)$(CH_3)_2(CN)_2$** isomers in 10/90 toluene/heptane, 5 mL min^{-1}, Cosmosil BuckyPrep-M column, 300 nm detection. Major isomer = F1, minor isomer = F2.

Table 1.1. DFT-predicted relative energies (kJ mol^{-1}) of selected $C_{60}(CF_3)_2(CN)^-$ anions and neutral $C_{60}(CF_3)_2(CN)(X)$ compounds (X = CH_3, H, CN)[a]

CN locant	Δ*E* (anion)	X locant	Δ*E* (neutral)		
			CH_3	H	CN
11	0.0	10	0.0	0.0	0.0
11		8	19.1	0.4	9.4
11		27	19.2	32.1	14.5
11		24	21.7	33.2	15.3
28	13.4				
17	19.5	16			25.9
10	22.5				
15	24.7		119.4	99.0	
27	25.7	26			24.9

[a] The locants refer to the numbered Schlegel diagram in Figure 1.13.

Table 1.2. DFT-predicted relative energies (kJ mol^{-1}) of selected $C_{70}(CF_3)_8(CN)^-$ anions and neutral $C_{70}(CF_3)_8(CN)_2$ compounds[a]

CN locant	ΔE (anion)	2nd CN locant	ΔE (neutral)[c]
11	0.0	29	0.0
11		31	44.9
11		48	56.9
11		30	220.5
25	7.6	10	42.6
9	13.5		
34	20.3		
23	25.8		

[a] The locants refer to the numbered Schlegel diagram in Figure 1.19.

Table 1.3. DFT-predicted relative energies (kJ mol^{-1}) of selected $C_{70}(CF_3)_{10}(CN)^-$ anions and neutral $C_{70}(CF_3)_{10}(CN)(CH_3)$ compounds[a]

CN locant	Δ*E* (anion)	CH_3 locant	Δ*E* (neutral)
34	0.0	33	0.0
34		15	46.6
34		52	49.0
34		13	80.9
34		31	92.2
53	6.6	33	30.7
16	7.8	33	32.7
33	9.5	34	1.0
33		53	30.9
33		16	32.6
37	13.3		
11	14.1		
15	14.5		
44	15.1	23	12.0
56	15.6		
29	16.7		
52	16.8		

[a] The locants refer to the numbered Schlegel diagram in Figure 1.19.

Table 1.4. DFT-predicted relative energies (kJ mol^{-1}) of selected $C_{70}(CF_3)_{10}(CH_3)_2^{2-}$ dianions and neutral $C_{70}(CF_3)_{10}(CH_3)_2(CN)_2$ compounds[a]

CH_3 locants	ΔE (dianion)	CN locants	ΔE (neutral)
34,44	0.0	23,33	0.8
33,44	4.1	23,34	0.0
33,23	37.7	52	2.5
33,34	75.7	—	—

[a] The locants refer to the numbered Schlegel diagram in Figure 1.19.

Table 1.5. Experimental and DFT calculated EAs (eV), $E_{1/2}$(V, vs. $C_{60}^{0/-}$) and E_{LUMO} (eV, vs. C_{60}) values of some closed-shell TMFs.

Name	Fullerene	EA(exp)	EA(DFT)[a,b]	$E_{1/2}$(exp)[48]	$E_{1/2}$(DFT)[48c]	E_{LUMO}[48d]
	C_{60}	2.68(1)[88]	2.64[a]	0	0	0
60-2-1	$C_{60}(CF_3)_2$	2.92(1)[20]	2.77[a,20]	0.11	0.09	−0.213
60-4-2	p^3-$C_{60}(CF_3)_4$	**3.21(1)**	3.10[a]	(irrev.)	0.29	−0.460
60-4-1	*pmp*-$C_{60}(CF_3)_4$	-	2.96[b,48]	0.17	0.17	−0.303
	S_6-$C_{60}(CF_3)_{12}$	2.57(17)[85]	2.65[b,85]	−0.16	−0.21	0.101

[a] B3LYP/def2-TZVP//PBE/TZ2P level; [b] B3LYP/6-311G*//PBE/TZ2P level; [c] estimated based on the linear correlation found between PBE-derived LUMO energies and experimentally measured redox potentials; [d] PPE/TZ2P level; $E_{1/2}$ and E_{LUMO} are referred to C_{60} values.

Table 1.6. Experimental and DFT Electron Affinities, EAs (eV) of $C_{60}X_5$ radicals and NICS values in $C_{60}X_5^-$ anions.[a]

Name	$C_{60}X_5$	EA(exp)	EA(DFT)	NICS(Cp)	NICS(center)	NICS(cage)
	$C_{60}(CH_3)_5$		2.76	−5.8	−11.9	12.2
	$C_{60}H_5$		2.79	−12.8	−12.0	10.4
	$C_{60}(Ph)_5$		3.07	−5.2	−12.3	11.5
(60-4-2)H	$C_{60}(CF_3)_4H$	3.96(1)	3.73	−10.2	−12.9	11.0
	$C_{60}(CF_3)_5$		3.99	−10.0	−13.1	10.7
	$C_{60}(C_2F_5)_5$		4.02	−9.0	−13.2	10.9
(60-4-2)(CN)	$C_{60}(CF_3)_4CN$	4.28(1)	4.07	−10.2	−13.3	10.8
	$C_{60}(CN)_5$		4.47	−11.7	−13.6	10.7

[a] EA computed at B3LYP/def2-TZVP level, NICS – at the PBE/Λ2 level, coordinates are optimized at the PBE/TZ2P level.

Table 1.7 Experimental and DFT-calculated electron affinities (EA) of fullerene compounds from this work

Compound	Abbreviation	Experimental EA (eV)[a]	DFT EA (eV)
C_{70}	C_{70}	2.765(1)[b], 2.72(5)[c]	2.522
C_s-$C_{70}(CF_3)_8$	**70-8-1**	3.08	2.934
C_2-$C_{70}(CF_3)_8$	**70-8-2**	not measured	3.224
C_s-$C_{70}(CF_3)_8(CN)_2$	***C*$_s$-(70-8-1)(CN)$_2$**	3.06	2.892
C_1-$C_{70}(CF_3)_8(CN)_2$	***C*$_1$-(70-8-1)(CN)$_2$**	3.07	2.909
C_1-$C_{70}(CF_3)_8(CN)_2$-th	***C*$_1$-(70-8-1)(CN)$_2$-th**	n/a	3.147
C_1-$C_{70}(CF_3)_{10}$	**70-10-1**	2.93	2.732
C_2- $C_{70}(CF_3)_{10}$	**70-10-2**	not measured	2.952
C_1-$C_{70}(CF_3)_{10}(CN)_2$	**(70-10-1)(CN)$_2$**	3.14	3.000
C_1-$C_{70}(CF_3)_{10}$(34,44-$CH_3)_2$(23,33-$CN)_2$	**(70-10-1)(34,44-CH$_3$)$_2$(23,33-CN)$_2$**	2.97	2.849
C_1-$C_{70}(CF_3)_{10}$(33,44-$CH_3)_2$(23,34-$CN)_2$	**(70-10-1)(33,44-CH$_3$)$_2$(23,34-CN)$_2$**	2.97	2.850

a – uncertainty is ±10 meV ; b) see ref.[72] c) see ref.[107]

Table 1.8. Crystallographic data and refinement parameters for three PFAFs.

Compound	**60-8-3**	**60-10-14**	**60-12-X**
CCDC number	n/a	n/a	n/a
Formula	$C_{68}F_{24}$, CH_2Cl_2	$C_{70}F_{30}$	$C_{72}F_{36}$
Formula weight	1357.61	1410.70	1548.72
Habit, color	block, red	block, red	rhomb, red
Crystal system	monoclinic	monoclinic	triclinic
Space group	*Cc*	$P2_1/c$	$P\bar{1}$
a (Å)	20.5504(6)	20.5157(8)	12.3253(7)
b (Å)	13.7754(4)	12.1614(5)	20.9546(12)
c (Å)	16.5197(5)	20.1763(8)	21.6419(13)
α (°)	90	90	64.0871(10)
β (°)	104.3160(15)	114.3613(8)	81.5919(11)
γ (°)	90	90	81.4823(11)
V (Å^3)	4531.3(2)	4585.8(3)	4951.2(5)
Z	4	4	4
T (K)	120(2)	100(2)	100(2)
ρ_{calc} (g cm^{-3})	1.990	2.043	2.078
R(F) (*I*>2σ(*I*))[a]	0.0372	0.0523	0.0673
wR(F^2) [all data][a]	0.0974	0.1535	0.1673
Goodness of Fit	1.017	1.029	0.938
Source	$Mo_{K\alpha}$	0.41328 Å	0.41328 Å

[a] $R(F) = \Sigma \left| |F_o| - |F_c| \right| / \Sigma |F_o|$; $wR(F^2) = (\Sigma[w(F_o^2 - F_c^2)^2 / \Sigma[w(F_o^2)^2])^{1/2}$

Table 1.9. Crystallographic data and refinement parameters for two cyano-modified PFAFs.

Compound	***C*$_s$-(70-8-1)(CN)$_2$**	***C*$_1$-C$_{70}$(CF$_3$)$_{10}$(33,44-CH$_3$)$_2$(23,34-CN)$_2$**
CCDC number	841565	902699
Formula	$C_{80}F_{24}N_2$,$(CCl_{2.32})_2$	$C_{85}H_8Cl_2F_{30}N_2$
Formula weight	1633.42	1697.83
Habit, color	plate, yellow	rectangular, orange
Crystal system	orthorhombic	triclinic
Space group	*Pbcm*	$P\bar{1}$
a (Å)	11.271(1)	12.7507(16)
b (Å)	19.520(2)	12.7605(17)
c (Å)	26.346(3)	19.956(2)
α (°)	90	81.693(7)
β (°)	90	81.693(7)
γ (°)	90	89.437(7)
V (Å^3)	5796(1)	3175.9(7)
Z	4	2
T (K)	100(2)	120(2)
ρ_{calc} (g cm^{-3})	1.872	1.775
R(F) (*I*>2σ(*I*))[a]	0.0781	0.0767
wR(F^2) [all data][a]	0.1971	0.2075
Goodness of Fit	1.078	1.032
Source	0.41328 Å	$Mo_{K\alpha}$

[a] $R(F) = \Sigma \big| |F_o| - |F_c| \big| / \Sigma |F_o|$; $wR(F^2) = (\Sigma[w(F_o^2 - F_c^2)^2 / \Sigma[w(F_o^2)^2])^{1/2}$

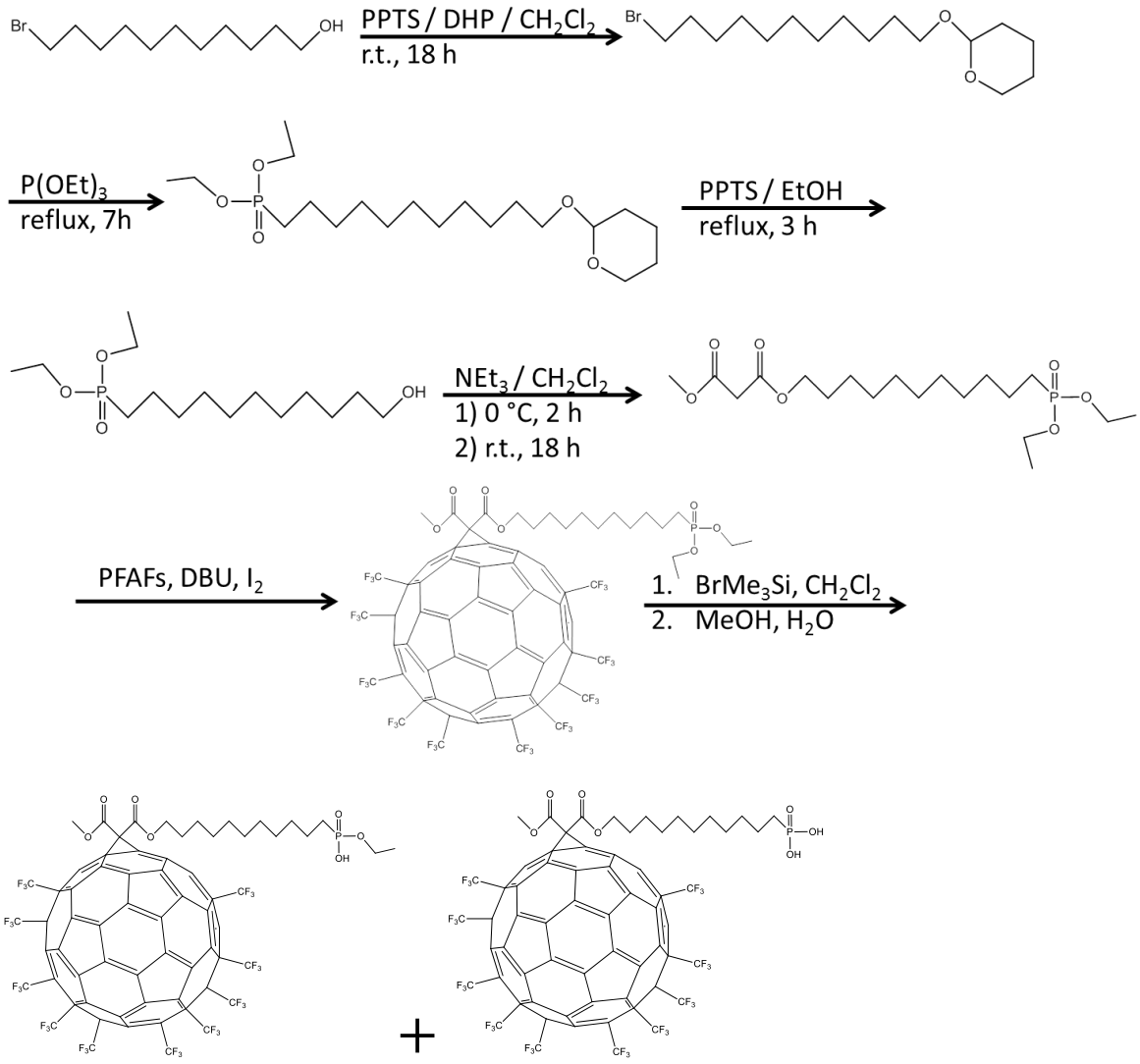

Scheme 1.1. Synthesis of PFAF(phosphonic acid)

CHAPTER 2. Synthesis and Properties of Poly(trifluoromethyl)azulenes and Solid-state Packing of PAH(R_F)$_n$ where R_F = CF_3, Bn_F, or C_4F_8

2.1 Introduction

Introducing EWGs to molecular substrates used as n-type semiconductors, such as azulene and other PAHs, is a method that is used to alter electron-withdrawing strengths, but it can also affect solubility and solid-state packing by disrupting intermolecular interactions.[108] Understanding charge transport through n-type semiconductors used in OPV active layers, FETs, and OLEDs is important when designing new and efficient semiconductors. A DFT study on several PAH$(CF_3)_n$ derivatives demonstrated that electron transport was predominately influenced by intermolecular hydrogen bonding interactions and hole transport was dominated by π-stacking interactions.[109] Other theoretical calculations on the distance and slip displacement of interfacial π-stacking interactions have shown that they have a strong influence on charge transfer and electronic coupling within a crystal.[110] Directly measuring and understanding these distances and interactions is a key step in designing new semiconducting molecules.

This work involves the synthesis and characterization of six new trifluoromethyl derivatives of azulene (**AZUL**), three isomers of AZUL$(CF_3)_3$ and three isomers of AZUL$(CF_3)_4$. Azulene is a non-alternant, non-benzenoid aromatic hydrocarbon with an intense blue color, a dipole moment of 1.0 D,[111] positive electron affinity, and an "anomalous" emission from the second excited state in violation of Kasha's rule.[112,113] Azulene's unique properties have potential uses in molecular switches,[114,115] molecular diodes,[116] organic photovoltaics,[117] and charge-transfer complexes.[118-122] Introduction of electron-withdrawing groups to the azulenic core, such as CN,[118,123,124] halogens,[125-129] and CF_3,[25,130] can enhance certain electrical and photophysical properties. Azulene$(CF_3)_5$ exhibited the highest gas-phase electron affinity of all

PAH(CF_3)$_n$ derivatives synthesized by the Strauss/Boltalina group prior to 2013, which warranted additional trifluoromethylation studies.[25]

One of the most powerful experimental tools used to discover idealized intermolecular interactions within a pristine semiconducting material is single crystal XRD. Determining packing motifs in a perfect crystal can show close intermolecular interactions and charge transport pathways, which could possibly be translated to less idealized packing situations that often arise in the particular applications. Three crystal structures with AZUL(CF_3)$_n$ were studied in this work, including the first X-ray structure of a π-stacked donor-acceptor complex of a trifluoromethyl azulene with donor pyrene. Additionally, colleagues in the Strauss/Boltalina research group have substituted various PAHs with EWGs (CF_3, Bn_F, and C_4F_8) with the intention of changing electronic energy levels and intermolecular interactions. Single crystal X-ray structures of several of these compounds were collected and analyzed in this body of work to help ascertain interesting substitution and intermolecular packing motifs.

This chapter involves work that has been reproduced from *Chem. Comm.* **2014**, *50*, 6263-6266 and *Chem. Eur. J.* **2015**, *21*, 9488-9492 along with work from three recently submitted papers: Rippy, K. C.; Bukovsky, E. V.; Clikeman, T. T.; Chen Y.-S.; Hou, G.; Wang, X. -B.; Popov, A. A.; Boltalina, O. V.; Strauss, S. H *Chem. Eur. J.,* **2015,** San, L. K.; Clikeman, T. T.; Chen Y.-S; Strauss, S. H.; Boltalina, O. V. *Chem. Comm.* **2015**, and Castro, K. P.; Clikeman, T. T.; DeWeerd, N. J.; Bukovsky, E. V.; Rippy, K. C.; Kuvychko, I. V.; Chen Y.-S; Wang, X. -B.; Strauss, S. H.; Boltalina, O. V. *Angew. Chem., Int. Ed.*, **2015** with permission from John Wiley and Sons and The Royal Society of Chemistry. Tyler Clikeman performed the synthesis and characterization of all azulene derivatives, and the synthesis, isolation, and crystal growth of the other PAH derivatives were performed by Igor Kuvychko, Long San, Kerry Rippy, or Karlee

Castro. Xue-Bin Wang and coworkers performed LT PES experiments, crystals of AZUL-5-1/pyrene were grown by Igor Kuvychko and he performed the XRD data collection and refinement experiments, Eric Bukovsky collected the XRD data set for AZUL-4-1 and he performed the refinement with the help of Natalia Shustova and Dimitry Peryshkov, Yu-Sheng Chen collected the data set for CORA(Bn_F)$_5$, Eric Bukovsky collected and refined the data for PHNZ-4-2, data for PHNZ-6-1 were collected at the 2014 American Crystallographic Association Summer Course in Chemical Crystallography at the University of Notre Dame, and all other XRD experiments, refinements, and analyses were primarily performed by Tyler Clikeman.

2.2 Poly(trifluoromethyl)azulene Derivatives

2.2.1 Synthesis and Isolation of Poly(trifluoromethyl)azulene

In sharp contrast to the commonly applied multi-step, solution-based methods of hydrogen substitutions in azulene with electron withdrawing groups, such as CN[118,123,124] or Hal,[125-129] in this work, all AZUL(CF_3)$_n$ compounds were prepared in a rapid single-step reaction carried out in the gas phase. Azulene and CF_3I gas were loaded into a sealed glass ampoule and heated in a furnace to 300 °C for 15 minutes to produce mostly a mixture of azulene(CF_3)$_n$ (n = 3-5), as shown by negative-ion atmospheric-pressure chemical ionization mass spectrometry (APCI-MS). The crude reaction mixture also contained small amounts of $C_{10}H_2(CF_3)_6$, and dimers ($C_{20}H_{16-(n+1)}(CF_3)_{n=7,8,9}$). Formation of the thermally stable dimeric azulene species in such high-temperature reactions has not been previously reported and deserves further studies, particularly due to the relatively high electrical conductivity observed for polymeric AZUL$_n$.[131,132] Doubling the reaction time resulted in more selective formation of **AZUL-5-1**.[25] The crude reaction mixture of the 15-minute reaction was separated by HPLC (Figure 2.1),

yielding seven AZUL$(CF_3)_n$ derivatives, i.e., three isomers of AZUL$(CF_3)_3$, three isomers of AZUL$(CF_3)_4$, and one isomer of AZUL$(CF_3)_5$ (see Scheme 2.1 for isomer notations).

Structural assignments for the new compounds were done based on negative-ion APCI-MS and the ^{1}H NMR and ^{19}F NMR spectral analysis (see Figures 2.2 and 2.3). Structural assignments for three compounds were confirmed by single crystal XRD, which will be discussed in Section 2.3.1. The ^{19}F NMR spectra were obtained in $CDCl_3$ and are shown in Figure 2.2. Multiplets corresponding to each CF_3 group appear in two distinct regions consistent to whether they are bonded to the five-membered ring (between −53.5 and −58.5 ppm) or the seven-membered ring of azulene (between −64.4 and −66.5 ppm). Through-space F–F coupling is observed between CF_3 groups bonded to adjacent carbon atoms of the azulene core resulting in quartets and apparent septets and no F–H coupling is observed. In some cases, CF_3 groups substitute the three possible C atoms of the five-membered ring, whereas CF_3 groups bonded to adjacent carbon atoms of the seven-membered ring were not observed.

2.2.2 Electronic Properties of Azulene$(CF_3)_n$

The UV-vis absorption spectra of the seven isolated poly(trifluoromethyl)azulene derivatives were obtained in hexanes and dichloromethane (see Table 2.1 and Figures 2.4–2.8). Unlike azulene, where the S_1 states become more refined in hexanes vs. dichloromethane (Figure 2.8), the solvent choice had little or no effect on the absorption spectra of the trifluoromethyl substituted derivatives.[128] The extinction coefficients for absorption maxima are less than parent azulene and comparable to other azulene derivatives (see Table 2.1).[18] Theoretical and experimental studies by Liu and coworkers showed that electron withdrawing groups on odd-numbered carbon atoms blue-shift the S_1 maxima by lowering the HOMO energy while the LUMO energy remains relatively unchanged.[128] Indeed, the absorption maxima in the S_1 band

for all seven of the trifluoromethyl azulenes are blue shifted by 24-57 nm (see Table 2.1). All seven derivatives have CF_3 substituents at the C1 and C3 positions, which play a large part in blue-shifting the maxima. Two compounds (**AZUL-3-2** and **AZUL-4-3**) have a CF_3 group bonded to an even-numbered C6 atom, which likely causes smaller blue shifts (24 and 27 nm), and is in agreement with the earlier prediction that electron withdrawing groups on even-numbered carbon atoms lower the LUMO energy.[128] Electron withdrawing groups should lower the HOMO and LUMO+1 energy by nearly the same amount since the electron distributions of the HOMO and LUMO+1 are virtually identical, so shifts in the absorption maxima in the S_2 region are not expected to be as pronounced as the S_1 region. Absorption maxima shifts in comparison to azulene in the S_2 region are, in fact, very minor and even slightly red-shifted for one compound, **AZUL-4-1**.

The gas-phase electron affinity (EA) was measured experimentally by LT PES for two new isomers of AZUL$(CF_3)_4$ and compared to electron affinity of the parent azulene, 0.790(8),[133] and **AZUL-5-1**, 2.850(15)[25,134] (Figure 2.9). Two AZUL$(CF_3)_4$ isomers exhibit very close EA values, 2.495(10) and 2.485(10). A plot of EA vs. number of CF_3 groups reveals a remarkable linear correlation, with a slope of 0.42 eV per CF_3 group (Figure 2.9). An extrapolation to AZUL$(CF_3)_6$ (that was observed by mass-spectrometry in the crude product as noted above) yields an estimated EA value of 3.3 eV.

No experimental data are available in the literature on EA values for any azulene derivatives for comparison. The electrochemical potentials in solution were reported for some derivatives.[118,123,135] Coincidentally, a similar linear correlation with the same slope was observed in the half-wave reduction potentials of a series of cyano azulenes, AZUL$(CN)_{2\text{-}4}$, where the $E_{1/2}^{0/-}$ became more positive by 0.42 V per one CN substitution.[118] Cyclic

voltammetry in DME using TBAP electrolyte has been performed in this work (with help from Long San) for the most abundant compounds, and pseudoreversible electrochemical behaviour was only observed in the case of **AZUL-4-1**, $E_{1/2}^{0/-} = -1.05$ V vs. $FeCp_2^{+/0}$ (Figure 2.10). Comparison with the reduction potentials of $AZUL(CN)_4$ shows the latter to be a stronger acceptor in solution than $AZUL(CF_3)_4$, in agreement with the theoretical predictions reported earlier for other polycyclic aromatic molecules,[6] including recent work on the substituted corannulene derivatives by the Strauss/Boltalina research group.[99] Consistent with gas-phase electron affinity measurements of azulene and napthalene (**NAPH**),[25] isomeric $NAPH(CF_3)_4$ is a weaker electron acceptor than $AZUL(CF_3)_4$ in dimethoxyethane.[136]

2.3 Molecular Structures and Solid-state Packing of Select $PAH(R_F)_n$ Based on X-ray Crystallography

2.3.1 Crystal Structures of $AZUL(CF_3)_n$

The structures of the two most abundant $AZUL(CF_3)_4$ isomers, **AZUL-4-1** and **AZUL-4-2** were confirmed by single-crystal X-ray diffraction (Scheme 2.1); the crystals were grown by slow evaporation from dichloromethane and hexane solutions, respectively. The collection and refinement of **AZUL-4-1** was completed with significant help from Eric Bukovsky, Natalia Shustova, and Dimitry Peryshkov. **AZUL-4-1** crystallizes in the $P\bar{1}$ space group with three molecules per unit cell. One molecule is ordered while the other two molecules are disordered, adopting opposite orientations at a given site. This disorder is typical and has been observed for azulene[137] and azulene derivatives.[138] **AZUL-4-1** packs in planes of parallel molecules that have no π-π overlap between or within the planes. Disorder in the azulenic core is not observed in the structure of **AZUL-4-2**; however, the fluorine atoms of the CF_3 group attached to C5 are rotationally disordered around the attached carbon atom. One type of parallel π-π overlap exists between **AZUL-4-2** molecules (Figure 2.12). The pentagon subunit of one molecule and

heptagon subunit of the adjacent molecule are partially overlapped and are 3.86 Å apart. Having two molecules with similar electronic energy levels, but different charge transport pathways, could be useful when selecting azulene derivatives for application purposes.

Varying the degree of CF_3 substitution allows for the selection of an electron-accepting azulene derivative to match with a proper donor to form a charge-transfer complex. The increased EA of **AZUL-5-1** was exploited to form a charge-transfer complex with pyrene as the donor molecule. Dark red-purple crystalline rods of the charge-transfer complex between pyrene and **AZUL-5-1** were grown by the slow evaporation from a dichloromethane solution at 2 °C. Columns of alternating **AZUL-5-1** and pyrene were formed in a pseudo hexagonal close-packed formation (Figure 2.13A) with intermolecular, donor-acceptor distances of 3.58 and 3.61 Å (Figure 2.13B). These distances are significantly closer than the intermolecular distances and exhibit more overlap than in the structure of **AZUL-4-2**, described above. The charge-transfer between **AZUL-5-1** and pyrene possibly prevents **AZUL-5-1** from adopting opposite orientations within its position and there was no disorder observed in the azulene core as was observed in the structure of **AZUL-4-1**. Solutions with varying ratios of **AZUL-5-1**:pyrene were made in DCM. All solutions remained the deep purple color of **AZUL-5-1** and no new absorption bands were observed in UV-vis absorption measurements at different concentrations, even when **AZUL-5-1**:pyrene = 50:50 (the same ratio that formed the single-crystal charge-transfer complex). The absence of charge-transfer bands has also been observed with other azulene charge-transfer complexes,[119] but charge-transfer bands from pyrene have been observed in other pyrene:oligomer complexes.[120]

2.3.2 Crystal Structure of CORA(Bn_F)$_5$

Crystals of **CORA(Bn_F)$_5$** were grown by Long San and data were collected by Yu-Sheng Chen at APS. Structure refinement and analyses were performed by Tyler Clikeman. Slow evaporation of an acetonitrile solution of **CORA(Bn_F)$_5$** afforded thin, pale yellow needles suitable for X-ray diffraction study, which confirmed the C_5-symmetry.[139] It crystallizes with $P2_1/c$ symmetry and contains one toluene molecule per **CORA(Bn_F)$_5$** (most likely solvent trapped after HPLC separation). One disordered toluene molecule packs with **CORA(Bn_F)$_5$** in columns along the *c* axis and the other toluene molecule lies in a void between the columns having no π-π or hydrogen bonding interactions with **CORA(Bn_F)$_5$** (Figure 2.14). All **CORA(Bn_F)$_5$** exhibit the same bowl direction within each column. The disordered toluene centroid between two **CORA(Bn_F)$_5$** molecules lies 3.65 Å from the centroid of one **CORA(Bn_F)$_5$** pentagon hub. The shortest distance between hub centroids is 3.72 Å. Two different conformers of **CORA(Bn_F)$_5$** are present in the crystal structure which is likely influenced by the inclusion of toluene within the crystal. In one conformer, A, four Bn_F blades point perpendicularly "down" and one blade points "parallel" to the hub plane; and in the other conformer, B, all five blades point "parallel". The A and B conformers also exhibit two significantly different bowl depths, 0.65 and 0.82 Å, respectively, compared to 0.870(8) Å for **CORA**.[140] Such a significant difference in bowl depth of 0.17 Å for two **CORA** conformers within the same crystal structure has not been observed before. For comparison, "down" and "up" conformers within the crystal structure of an imide-fused CORA derivative exhibit only a slight difference of 0.04 Å in bowl depths (0.67 and 0.63 Å, respectively).[141] It is, however, not uncommon that significant variations in bowl depth may occur upon exhaustive hydrogen substitution of **CORA** with various organic functional groups,[142-144] or by varying composition of alkali metal ion **CORA** complexes; in the latter case bowl depths vary by as much as 0.62

Å.[145] Such effective chemical control of **CORA** bowl depth may be utilized in material designs for energy storage.[146]

Corannulene was also substituted with CF_3 groups by Igor Kuvychko. Several single crystal XRD data sets of isolated CORA$(CF_3)_n$ (n = 4,5,7) were collected, but only two were of sufficient quality for publication (see Figures 2.15 and 2.16, **CORA-5-1** was published previously[99] and **CORA-7-1** was studied in this work). Inversion of the **CORA** core, rotation of the molecule within the crystal structure, and CF_3 disorder led towards multiple enantiomers and disordered molecules within certain unpublishable structures. These poor quality structures were sometimes used to confirm substitution patterns or packing motifs, but bond distances could not be measured accurately. The bowl depth of **CORA** derivatives typically decrease upon substitution, which depends on the type and amount of substituents. For example, it can range from 0.870(8) Å for **CORA**[140] to 0.72 Å for CORA$(t\text{Bu})_5$[144] to 0.51 Å for CORA$(\text{Cl})_{10}$[147] and can even vary within the same crystal for two different conformers of **CORA($\mathbf{Bn_F}$)$_5$** as described above. Following this trend, the bowl depths of **CORA-5-1** and **CORA-7-1** are 0.788 and 0.594 Å, respectively.[99] Decreasing the bowl depth allows for less strain during bowl inversion, which is why disorder via bowl inversion is observed in many of the CORA$(CF_3)_7$ structures. Bowl inversion plus 1/10th of a rotation allows for the presence of two enantiomers within the structure of **CORA-7-1** that occupy the same space, see Figure 2.15. This inversion and rotation allows for the CF_3 groups to also occupy similar positions. The presence of the second enantiomer was modeled to be present only 15% of the time.

With only four or five CF_3 substitutions, the molecules pack in columns that resemble stacks of bowls. **CORA-4-1** packs in columns where the bowl direction is the same for all molecules within each column and for adjacent columns. The bowl direction is the same within

the columns of **CORA-5-1**, but adjacent columns point in opposite directions. The presence of repulsive CF_3 groups likely causes a disruption of this columnar packing and isomers of CORA$(CF_3)_7$ packed in a more herringbone fashion. No bowl stacking or columnar packing was observed in the structure of **CORA-7-1**. The only π-π interaction between adjacent **CORA-7-1** molecules is between two hexagon units of the main enantiomer: the mean planes of nearest hexagons are parallel and 3.74 Å apart, and the closest C atom-to-hexagon plane distance is 3.68 Å. Closer hexagon-hexagon distances were observed when the bowls were stacked, such as in CORA-5-1 (3.5–3.6 Å).[99] Pairs of **CORA-7-3** pack in a herringbone fashion where the pentagons in each pair point towards each other and the rims point away.

Substituting **CORA** with CF_3 groups can affect crystallographic packing by flattening the **CORA** bowl or by disrupting bowl stacking. Flatter bowls lead to more disorder within pure crystals, which causes difficulty when refining the crystal structures. For future experiments, mixing the highly substituted **CORA** derivatives with electron donors could help reduce this disorder by aligning the molecules in charge transfer complexes.

2.3.3 Crystal Structures of PHNZ$(CF_3)_n$

A series of PHNZ$(CF_3)_n$ were purified by Karlee Castro and several crystal structures were collected and analyzed in this body of work (Figure 2.17). Introducing repulsive CF_3 groups is expected to reduce **PHNZ** core interactions between adjacent molecules. Indeed, PHNZ$(CF_3)_{2,3}$ derivatives stack in columns that exhibit significant core overlap while PHNZ$(CF_3)_{4,5,6}$ derivatives exhibit no core overlap (Figure 2.18). Adjacent molecules of **PHNZ-3-1** and **PHNZ-3-2** adopt opposite orientations within the columns, but adjacent molecules of **PHNZ-2-1** are all oriented the same direction within columns. The average perpendicular distances between mean planes of neighboring **PHNZ** core atoms are 3.56, 3.44, and 3.55 Å in

PHNZ-2-1, **PHNZ-3-1**, and **PHNZ-3-2**, respectively. For comparison, the interplanar distances between **PHNZ** and 1,2,4-trifluoro-6,8-dimethyl-3-trifluoromethylphenazine cores are 3.49 and 3.48 Å, respectively.[148] Repulsive CF_3 groups in *both* the C1 and C5 positions cause less favorable stacking interactions in **PHNZ-2-1** and **PHNZ-3-2** compared to when CF_3 groups are at C1 and C3 as in **PHNZ-3-1**, which actually packs closer than bare **PHNZ** (Figure 2.19). Having two isomers with different packing distances allows for a means of choosing molecules with the same electron-withdrawing strength, but with potentially different charge transport pathways. Some core planes in the crystal structures of **PHNZ-4-2** and **PHNZ-5-1** are also parallel to adjacent molecules (perpendicular distances are 4.00 and 4.09 Å, respectively), but the bulky CF_3 groups cause such a shift that there is actually no core overlap. In the most extreme case, **PHNZ-6-1**, all molecules pack in a herringbone fashion where no cores are parallel to the nearest neighbors.

2.3.4 Crystal Structures of TRPH(C_4F_8)$_n$

A series of TRPH(C_4F_8)$_n$ derivatives were synthesized and isolated by Kerry Rippy and several crystal structures were collected and analyzed in this body of work (Figure 2.20). **1,2-TRPH(C_4F_8)** crystallizes in $P\bar{1}$ with two unique conformers that have slightly different twisted **TRPH** cores. The repulsive F–C12 interactions shown in Figure 2.20 are undoubtedly the cause of the severely non-planar "twisted" structure of the C(sp^2) **TRPH** core. The root mean square distances (RMSD) for the **TRPH** core planes of each conformer are 0.178 and 0.215 Å and the torsion angles of the most twisted bays (C1–C14–C13–C12) are 20.86 and 22.87°, respectively. These differences must arise from the solid-state packing, which also causes slightly different F–C12 distances as depicted in Figure 2.20. There is still some C(sp^2) overlap despite the twisted cores, which is as close as 3.36 Å. This twisting is slightly less in the case of **1,2;10,11-**

TRPH(C_4F_8)$_2$, but is even more twisted when there are two repulsive F–C interactions as in the case of **1,2;5,6;10,11-TRPH(C_4F_8)$_3$**. The closest F–C12 distances are 2.65 and 2.96 Å, the F–C4 distances are 2.86 and 2.93 Å, the C1–C14–C13–C12 torsion angle is 19.22°, and the RMSD of the **TRPH** core plane is 0.168 for **1,2;10,11-TRPH(C_4F_8)$_2$**. The closest F–C12 distances are 2.66 and 2.89 Å, the C1–C14–C13–C12 torsion angle is 32.94°, the C4–C15–C16–C15 torsion angle is 27.74° and the RMSD of the **TRPH** core plane is 0.365 for **1,2;5,6;10,11-TRPH(C_4F_8)$_3$**. As expected, the intermolecular distances between neighboring molecules increases as more C_4F_8 groups are introduced. The closest overlapping C(sp^2) atoms to benzene subunits are 3.36, 3.46, and 3.66 Å for **1,2-TRPH(C_4F_8)**, **1,2;10,11-TRPH(C_4F_8)$_2$**, and **1,2;5,6;10,11-TRPH(C_4F_8)$_3$**, respectively. The high degree of twisting for **1,2;5,6;10,11-TRPH(C_4F_8)$_3$** results in very little core overlap between adjacent molecules. Benzene subunits of neighboring molecules are perfectly parallel, but contain only one overlapping C atom, Figure 2.22.

Symmetric **2,3-TRPH(C_4F_8)** crystallizes in the monoclinic space group, *C*2/*c*. The C_4F_8 moiety in **2,3-TRPH(C_4F_8)** was modeled with 9% disorder (Figure 2.23). In this case, there are no repulsive F–C interactions, so the **TRPH** core is much more planar than in **1,2-TRPH(C_4F_8)**. The RMSD of the **TRPH** plane is only 0.039 Å and the largest bay torsion angle is only 3.65°. The molecules pack parallel to nearest neighbors with partially overlapping cores 3.32 Å apart and C_4F_8 moieties pointing in opposite directions. Even though **2,3;6,7-TRPH(C_4F_8)$_2$** does not contain any repulsive F–C interactions from 1,2-(C_4F_8) substitutions, the **TRPH** core is more twisted than in **2,3-TRPH(C_4F_8)**. It crystallizes in $P\bar{1}$ with four unique molecules that have slightly different core twisting (RMSD of **TRPH** cores range from 0.088–0.132 Å and bay torsion angles range from 1.83–14.20°). Only one C_4F_8 moiety had the same disorder found in

2,3-TRPH(C_4F_8) which was modeled with 42% disorder. Similar to the set of highly twisted 1,2 derivatives described above, the intermolecular overlap decreases as more C_4F_8 groups are introduced. The closest overlapping C(sp^2) atoms to benzene subunits is 3.41 Å and the twisted cores cause some non-parallel overlap.

2.3.5 Crystal Structures of ANTH(Bn_F)$_n$

Several PAHs studied in this dissertation were synthesized with the intention of having strong π–π intermolecular interactions for increased charge transport in OPV applications. However, one criterion hypothesized for the development of an efficient blue emitter for OLED application calls for solid-state packing with limited π–π intermolecular interactions, which could suppress fluorescence self-quenching.[149] Not only will bulky substituents disrupt this interaction, they may provide chemical stability and prevent photo-oxidation.[150] Furthermore, fluorinated substituents have been predicted by DFT[151] and shown experimentally[25] to improve device air stability by increasing the electron affinities of organic semiconductors. With these criteria in mind, Long San synthesized **ANTH** derivatives with bulky, electron-withdrawing Bn_F groups.

Off-white plates **of 9,10-ANTH(Bn_F)$_2$** that were suitable for X-ray diffraction studies were grown by Long San from the slow evaporation of a CH_2Cl_2 solution at 2 °C. From the top view (Figure 2.24, top panel), two distinct columns are shown in orange and black that are skewed by 31.2°. At first glance on the top view, there appears to be a significant π-π overlap from the tail of one column and the head of the next column, but there is virtually no π-π overlap as shown from the side view (Figure 2.24, bottom panel). In fact, the two hexagons that appear to overlap are separated by 4.154 Å and are tilted by 21.6° from each other. The columns of **ANTH** cores are insulated along the *b* axis by the Bn_F groups (shown in grey), which can be observed by viewing down the long **ANTH** axis (Figure 2.25). This insulation further inhibits any electronic

coupling between columns. Having zero π-π overlap results in reduced electronic communication between molecules and can be seen as beneficial for OLED applications due to the increased chances of an excited molecule to relax via fluorescence.[150]

Other **ANTH** derivatives are produced in the process of synthesizing **9,10-ANTH(Bn_F)$_2$**, including **9-ANTH(Bn_F)**. As a consequence of the high temperature radical reaction and the highly reactive C10 position on **9-ANTH(Bn_F)**, dimerization can occur and break aromaticity. This can then form **[9-ANTH*(Bn_F)]$_2$**. X-ray diffraction quality single-crystals of **[9-ANTH*(Bn_F)]$_2$** were grown by Long San from the slow evaporation from solution. Similar to the solid-state packing of **9,10-ANTH(Bn_F)$_2$** described above, these dimers pack in columns that are insulated by the Bn_F groups on two sides (Figure 2.26). On the other hand, and despite the broken π system, there are close intermolecular π–π interactions between adjacent benzene subunits (Figure 2.27). The parallel mean planes of the hexagon subunits are partially overlapped and only separated by 3.56 Å. The **ANTH*** core is bent in center at the sp^3 carbon atoms causing a doming angle of 146.3° and the dimers are slip-stacked from each other which prevents further core overlap. Reducing electronic communication between and within dimers by breaking aromaticity can be another way to tune **ANTH** molecules for OLED applications.

2.4 Conclusions

An efficient trifluoromethylation method for azulene was developed that yields a mixture of seven readily separable poly(trifluoromethyl)azulenes. Low-temperature photoelectron spectroscopy revealed a linear increase in gas-phase electron affinity of 0.42 eV per CF_3 group. Symmetric **AZUL-4-1** is disordered in the single-crystal structure and exhibits no π-π overlap, whereas asymmetric **AZUL-4-2** exhibits no core disorder and forms better charge transport pathways through close π-π interactions. Strong acceptor properties of the new compounds were

utilized in the first example of a charge-transfer complex with pyrene that exhibits regular columnar packing and strong π-π interactions between the aromatic cores of the donor and acceptor. Elucidating oligomeric poly(trifluoromethyl)azulene and AZUL(CF_3)$_6$ species will result in even stronger electron acceptors and could lead to charge-transfer complexes with unique packing motifs and unusual electronic properties.

Single crystal XRD was used to determine interesting packing motifs of other PAH families modified with various EWGs. Introducing bulky EWGs was expected to influence intermolecular packing, but some other interesting effects were discovered upon analyses of various crystal structures. Flexible and bulky Bn_F groups attached to **CORA** allowed for two different conformers in the crystal structure. These conformers exhibited significantly different bowl depths, which could be utilized in energy storage applications. Core overlap in PHNZ(CF_3)$_n$ compounds was dependent on amount and placement of CF_3 groups. Derivatives with less CF_3 groups and less substitutions on the long **PHNZ** axis were more likely to exhibit close π-π overlap, which could affect solid-state charge transport. One striking example was that molecules of **PHNZ-3-2** could actually pack closer than pristine **PHNZ**. Repulsive F–C interactions across the bay regions of **1,2-TRPH(C_4F_8)** derivatives causes significant core twisting. Surprisingly, modest core twisting was also observed in a derivative without 1,2-(C_4F_8) substitution, **2,3;6,7-TRPH(C_4F_8)$_2$**. Twisting of the core results in less parallel π–π interactions which could hinder intermolecular charge transfer in TRPH(C_4F_8)$_n$ crystals. Furthermore, introducing more C_4F_8 substituents also causes reduced π–π interactions. Substituting **ANTH** with bulky Bn_F groups was shown to eliminate π-π stacking and disrupt aromaticity, which could be useful in OLED applications. These electron-withdrawing substituents can tune the electronic properties of PAHs, but can hinder charge transfer pathways in the solid state. Choosing the

optimal derivative to balance electronic levels and charge transport is necessary and possible when synthesizing new PAH compounds for each application.

2.5 Experimental Details

2.5.1 General information

All reagents and solvents were reagent grade or better. ACS Grade dichloromethane (Fisher Scientific), HPLC Grade acetonitrile (Fisher Scientific), ACS Grade hexanes (Fisher Scientific), sodium thiosulfate crystals (Mallinckrodt), trifluoromethyl iodide (Synquest Labs), chloroform-D (Cambridge Isotopes Laboratories), and hexafluorobenzene (Oakwood Products) were used as received. HPLC analysis and separation was done using a Shimadzu liquid chromatography instrument (CBM-20A control module, SPDA UV detector set to 300 or 275 nm detection wavelength, LC-6AD pump, manual injector valve) equipped with semipreparative 10 mm I.D. × 250 nm COSMOSIL Buckyprep column (Nacalai Tesque, Inc.) or analytical 4.6 mm I.D. × 150 nm FluoroFlash PF-C8 100 Å 5 µm column (Fluorous Technologies, Inc.). The atmospheric-pressure chemical ionization (APCI) mass spectra were recorded on a 2000 Finnigan LCQ-DUO mass-spectrometer (acetonitrile carrier solvent, 0.3 $mL \cdot min^{-1}$ flow rate, analyte samples injected as solutions in dichloromethane or acetonitrile). All NMR spectra were recorded on Varian INOVA 400 instrument in $CDCl_3$ solution. The ^{1}H and ^{19}F frequencies were 400 and 376 MHz, respectively. The ^{19}F chemical shifts were determined using hexafluorobenzene as an internal standard (δ −164.9). The ^{1}H chemical shifts were determined using the resonance of the residual $CHCl_3$ in $CDCl_3$ as an internal standard (δ 7.26). UV-vis absorption spectra were recorded by using a Cary 500 spectrophotometer with a resolution of 1 nm. Cyclic voltammetry measurements were carried out on PAR 263 potentiostat/galvanostat in anaerobic conditions using 0.1 M $N(n\text{Bu})_4ClO_4$ in dimethoxyethane; platinum working and

counter electrodes; silver wire quasi-reference electrode; 500 $mV \cdot s^{-1}$; ferrocene internal standard. X-ray diffraction experiments are described in Section 2.5.4.

2.5.2 Trifluoromethylation of azulene

Azulene$(CF_3)_n$ was prepared according a modified literature procedure. Azulene (50 mg, 0.39 mmol, blue solid) was placed into a glass ampoule (327 mL) and the ampoule was cooled with liquid nitrogen and evacuated using a vacuum line equipped with a pressure gauge and a calibrated volume (51.7 mL). Using the calibrated volume and pressure gauge, CF_3I gas was measured (11.7 mmol, 30 equiv.), and then the measured CF_3I gas was condensed into the cooled ampoule containing azulene. The ampoule was then flame-sealed and warmed to room temperature. **DANGER! High pressure can be generated within the ampoule leading to explosive ampoule failure. The maximum pressure inside the ampoule at high temperature has to be calculated using ideal gas law. Depending on the size and wall thickness of the ampoule the maximum allowable pressure changes, so a conservative limit of 2-3 bar must be set. The burst pressure for the glass ampoule is largely determined by the quality of the seal, so care must be taken during the sealing step. Use shields and personal protection at all times. Only experienced personnel should perform these operations.** The sealed ampoule was then placed in a heating furnace and heated at 10 °C min^{-1} to 300 °C. When the formation of purple iodine gas was observed at 285 °C, the ampoule was heated for another 15 min. up to 300 °C before cooling to room temperature. After cooling to room temperature, the ampoule was cooled in liquid nitrogen and opened (lower than ambient pressure inside). Excess CF_3I gas was boiled off upon warming to room temperature and then the soluble products were dissolved in dichloromethane. The purple dichloromethane solution was washed twice with a saturated sodium thiosulfate solution (aq) to remove I_2 until color was no longer observed in the aqueous

layer. The dichloromethane was removed by rotovap and the remaining solid was dissolved and filtered in acetonitrile (purple solution). The desired products were then purified by HPLC as described below. Care must be taken when rotovapping the crude mixture since some of the products are rather volatile. Total conversion of azulene to isolated products = 25 mol%.

AZUL-5-1, 1,2,3,5,7-azulene(CF_3)$_5$: Purple solid. Co-crystals of **AZUL-5-1**/pyrene (dark red-purple rods) were grown from the slow evaporation of a dichloromethane solution (**AZUL-5-1**:pyrene = 1:1) at 2 °C. 16.6 mg, 9.0 mol% yield based on azulene. ^{19}F NMR: δ −54.35 (q, J = 12.3 Hz, 2CF_3, $CF_3^{1,3}$); −58.02 (sept, J = 12.0 Hz, 1CF_3, CF_3^{2}); −65.46 (s, 2CF_3, $CF_3^{5,7}$). ^{1}H NMR: δ 9.50 (s, 2H, $H^{4,8}$); 8.63 (s, 1H, H^6). UV-vis (hexane, λ_{nm} (log ε): 276 (4.40), 282 (4.43), 299 (3.46), 327 (3.32), 338 (3.45), 353 (3.28), 536 (2.36), 570 (2.33), 632 (1.88). NI-APCI mass spec: 468.41 *m*/*z*. Calc. 468.00.

AZUL-4-1, 1,3,5,7-azulene(CF_3)$_4$: Purple solid. Single crystals (purple plates) were grown by the slow evaporation from a dichloromethane solution. 14.7 mg, 9.5 mol% yield based on azulene. ^{19}F NMR: δ −58.41 (s, 2CF_3, $CF_3^{1,3}$); −65.19 (s, 2CF_3, $CF_3^{5,7}$). ^{1}H NMR: δ 9.12 (s, 2H, $H^{4,8}$); 8.51 (s, 1H, $H^{2\text{ or }6}$); 8.49 (s, 1H, $H^{2\text{ or }6}$). UV-vis (hexane, λ_{nm} (log ε): 273 (4.13), 281 (4.15), 301 (3.41), 330 (3.12), 342 (3.28), 359 (3.29), 532 (2.01), 574 (1.94), 629 (1.60). NI-APCI mass spec: 400.40 *m*/*z*. Calc: 400.01.

AZUL-4-2, 1,2,3,5-azulene(CF_3)$_4$: Purple solid. Single crystals (thin purple plates) were grown by the slow evaporation from a dichloromethane solution. 4.6 mg, 3.1 mol% yield based on azulene. ^{19}F NMR: δ −54.02 (q, J = 12.3 Hz, 1CF_3, $CF_3^{1\text{ or }3}$); −54.07 (q, J = 11.8 Hz, 1CF_3, $CF_3^{1\text{ or }3}$); −57.71 (sept, J = 12.0 Hz, 1CF_3, CF_3^{2}); −65.20 (s, 1CF_3, CF_3^{5}). ^{1}H NMR: δ 9.41 (s, 1H, H^4); 9.28 (d, $^3J_{HH}$ = 10.6 Hz, 1H, H^8); 8.41 (d, $^3J_{HH}$ = 10.6 Hz, 1H, H^6); 7.90 (t, $^3J_{HH}$ = 10.4 Hz, 1H,

H^7). UV-vis (hexane, λ_{nm} (log ε): 276 (3.59), 281 (3.58), 321 (2.67), 334 (2.72), 348 (2.49), 531 (1.71), 562 (1.69), 613 (1.39). NI-APCI mass spec: 400.40 *m*/*z*. Calc: 400.01.

AZUL-4-3, 1,2,3,6-azulene(CF_3)$_4$: Purple solid. 1.1 mg, 0.7 mol% yield based on azulene. ^{19}F NMR: δ −54.06 (q, *J* = 11.8 Hz, 2CF_3, $CF_3^{1,3}$); −57.82 (sept, *J* = 12.0 Hz, 1CF_3, CF_3^2); −66.46 (s, 1CF_3, CF_3^6). ^{1}H NMR: δ 9.28 (d, $^3J_{HH}$ = 11 Hz, 2H, $H^{4,8}$); 8.05 (d, $^3J_{HH}$ = 11 Hz, 2H, $H^{5,7}$). UV-vis (hexane, λ_{nm} (log ε): 259 (3.21), 275 (3.44), 283 (3.39), 331 (2.58), 344 (2.25), 503 (1.72), 552 (1.79), 583 (1.78), 664 (1.54). NI-APCI mass spec: 400.40 *m*/*z*. Calc: 400.01.

AZUL-4-4, 1,2,5,7-azulene(CF_3)$_4$: Purple. This isomer was isolated by HPLC, but was lost during work-up due to volatility. The ^{19}F NMR spectrum of a crude sample is shown in Figure 2.28.

AZUL-3-1, 1,3,5-azulene(CF_3)$_3$: Purple solid. 2.1 mg, 1.6 mol% yield based on azulene. ^{19}F NMR: δ −58.17 (s, 1CF_3, $CF_3^{1 \text{ or } 3}$); −58.21 (s, 1CF_3, $CF_3^{1 \text{ or } 3}$); −64.89 (s, 1CF_3, CF_3^5). ^{1}H NMR: δ 9.03 (s, 1H, H^4); 8.91 (d, $^3J_{HH}$ = 9.8 Hz, 1H, H^8); 8.37 (s, 1H, H^2); 8.27 (d, $^3J_{HH}$ = 10.6 Hz, 1H, H^6); 7.77 (t, $^3J_{HH}$ = 10.4 Hz, 1H, H^7). UV-vis (hexane, λ_{nm} (log ε): 276 (4.40), 281 (4.39), 297 (3.54), 330 (3.37), 338 (3.46), 354 (3.43), 533 (2.32), 569 (2.28), 620 (1.91). NI-APCI mass spec: 332.40 *m*/*z*. calc: 332.02.

AZUL-3-2, 1,3,6-azulene(CF_3)$_3$: Purple solid. 0.8 mg, 0.6 mol% yield based on azulene. ^{19}F NMR: δ −58.21 (s, 2CF_3, $CF_3^{1,3}$); −65.98 (s, 1CF_3, CF_3^6). ^{1}H NMR: δ 8.90 (d, $^3J_{HH}$ = 10.2 Hz, 2H, $H^{4,8}$); 8.40 (s, 1H, H^2); 7.95 (d, $^3J_{HH}$ = 11 Hz, 2H, $H^{5,7}$). UV-vis (hexane, λ_{nm} (log ε): 275 (3.95), 280 (3.95), 312 (2.81), 320 (2.91), 327 (3.00), 334 (3.05), 350 (2.87), 555 (2.06), 595 (2.00), 653 (1.62). NI-APCI mass spec: 332.40 *m*/*z*. calc: 332.02.

AZUL-3-3, 1,2,3-azulene$(CF_3)_3$: Pink solid. 0.7 mg, 0.5 mol% yield based on azulene. ^{19}F NMR: δ −53.71 (q, J = 11.8 Hz, 2CF_3, $CF_3^{1,3}$); −57.38 (sept, J = 12.0, 1CF_3, CF_3^{2}). ^{1}H NMR: δ 9.17 (d, $^{3}J_{HH}$ = 10.2 Hz, 2H, $H^{4,8}$); 8.17 (t, $^{3}J_{HH}$ = 10.0 Hz, 1H, H^{6}); 7.81 (t, $^{3}J_{HH}$ = 10.4 Hz, 2H, $H^{5,7}$). UV-vis (hexane, λ_{nm} (log ε): 275 (3.91), 284 (3.90), 310 (2.94), 329 (3.06), 341 (2.66), 522 (2.14), 555 (2.15), 601 (1.82). NI-APCI mass spec: 332.27 *m*/*z*. calc: 332.02.

2.5.3 HPLC purifications of azulene$(CF_3)_n$

The first HPLC separation of the azulene$(CF_3)_n$ crude samples was done using semipreparative COSMOSIL Buckyprep HPLC column, acetonitrile eluent, flow rate of 5.0 mL·min^{-1}, 300 nm detection. Three different fractions 4.3–5.0 min (**I**), 5.0–5.8 min (**II**), and 5.9–6.7 min (**III**) were isolated for further separation using analytical FluoroFlash column, flow rate of 2.0 mL·min^{-1}. Second stage separation of **I** (acetonitrile/H_2O = 90:10, 300 nm detection) resulted in two more fractions: 3.4–5 min. (**IV**) and 5.9–7.3 min (**AZUL-4-1**). Fraction **IV** was further separated (acetonitrile/H_2O = 60:40, 275 nm detection) and resulted in two fractions: 20–21.6 min (**AZUL-3-2**) and 21.6–24.0 min (**AZUL-3-1**). Second stage separation of **II** (acetonitrile/H_2O = 80:20, 275 nm detection) resulted in one predominant fraction collected from 4.0–6.4 min (**AZUL-3-3**) and contained a volatile fraction collected from 8.5–10.5 min (**AZUL-4-4**) which was lost due to volatility before further characterization (see Figure 2.26 for ^{19}F NMR spectrum). Second stage separation of **III** (acetonitrile/H_2O = 95:5, 300 nm detection) resulted in two more fractions: 3.3–4.6 min (**V**) and 4.6–6.0 min (**AZUL-5-1**). Fraction **V** was further separated (acetonitrile/H_2O = 80:20, 300 nm detection) and resulted in two fractions: 6.8–7.8 min (**AZUL-4-3**) and 7.8–9.4 min (**AZUL-4-2**). The HPLC solvent mixtures could not easily be removed by rotovap due to the volatility of the compounds. Acetonitrile/H_2O mixtures were cooled in a freezer until purple acetonitrile solutions remained on top of colorless $H_2O_{(s)}$. The

acetonitrile solutions were decanted from $H_2O_{(s)}$ and the solvent was carefully removed via rotovap until a concentrated purple solution remained. Dichloromethane was then added to the purple solution and all of the solvent was dried down in air.

2.5.4 X-ray Diffraction Details

Data for **AZUL-4-2**, **CORA(Bn_F)$_5$**, **CORA-5-1**, **PHNZ-3-2**, **PHNZ-5-1**, **9-10-ANTH(Bn_F)$_2$**, **[9-ANTH*(Bn_F)]$_2$**, **1,2-TRPH(C_4F_8)**, **2,3-TRPH(C_4F_8)**, **1,2;5,6-TRPH(C_4F_8)$_2$**, **1,2;5,6;10,11-TRPH(C_4F_8)$_3$**, and **2,3;6,7-TRPH(C_4F_8)$_2$** were collected at ChemMatCARS sector 15ID-B at the Advanced Photon Source (Argonne National Laboratory). The data sets were collected at 100(2) K using a diamond (111) crystal monochromator, Bruker D8 goniometer a wavelength of 0.41328 Å (0.40651 Å for **PHNZ-3-2 and PHNZ-5-1**), and a Bruker CCD detector. Data for **AZUL-4-1** and **AZUL-5-1/pyrene PHNZ-2-1 and PHNZ-3-1** were collected using a Bruker Kappa APEX II CCD diffractometer employing Mo Kα radiation and a graphite monochromator.

Unit cell parameters were obtained from least-squares fits to the angular coordinates of all reflections, and intensities were integrated from a series of frames (ω and ϕ rotation) covering more than a hemisphere of reciprocal space. Absorption and other corrections were applied using SCALE.[103] The structures were solved using direct methods and refined (on F^2, using all data) by a full-matrix, weighted least-squares process. Standard Bruker control and integration software (APEX II) was employed,[104] and Bruker SHELXTL software was used with Olex2 for structure solution, refinement, and molecular graphics.[105,106]

Data for **PHNZ-6-1** were collected during the 2014 American Crystallographic Association Summer Course in Chemical Crystallography at the University of Notre Dame using

a Bruker Kappa APEX II CCD diffractometer employing $Cu_{K\alpha}$ radiation and a graphite monochromator. Unit cell parameters were obtained from least-squares fits to the angular coordinates of all reflections, and intensities were integrated from a series of frames (ω and ϕ rotation) covering more than a hemisphere of reciprocal space. The data were indexed with three twin components and absorption and other corrections were applied using TWINABS.[152] The structure was solved using direct methods and refined (on F^2, using all data) by a full-matrix, weighted least-squares process. Standard Bruker control and integration software (APEX II) was employed,[104] and Bruker SHELXTL software was used with Olex2 for structure solution, refinement, and molecular graphics.[105,106] A small amount of additional twinning was accounted for by modeling disorder near one F atom.

Crystal data for **AZUL-4-1**: Data collection, solving, and refining were performed with extensive help from Eric Bukovsky, Natalia Shustova, and Dimitry Peryshkov. Crystal data for **AZUL-5-1**/pyrene were collected by Dr. Igor Kuvychko. Final refinements and analyses were performed by Tyler Clikeman.

Additional crystallographic data and refinement parameters can be found in Tables 2.2–2.6.

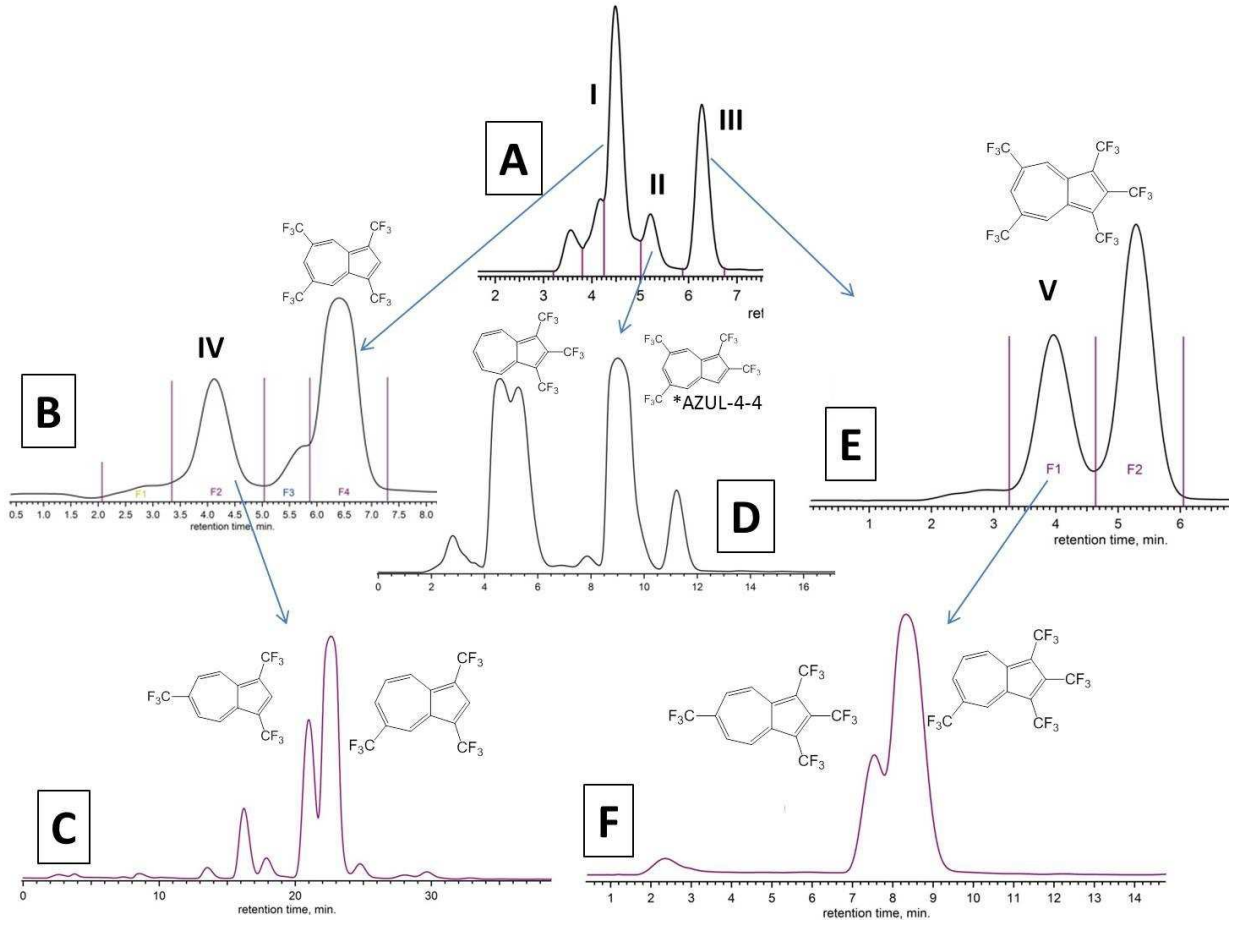

Figure 2.1. HPLC separation scheme of AZUL$(CF_3)_n$ compounds. A) semi-preparative COSMOSIL Buckyprep HPLC column, acetonitrile eluent, 5.0 mL·min^{-1}, 300 nm detection; B–F) analytical FluoroFlash column, 2.0 mL·min^{-1}, B) acetonitrile/H_2O = 90/10, 300 nm detection; C) acetonitrile/H_2O = 60/40, 275 nm detection; D) acetonitrile/H_2O = 80/20, 275 nm detection; E) acetonitrile/H_2O = 95/5, 300 nm detection; F) acetonitrile/H_2O = 80/20, 300 nm detection.

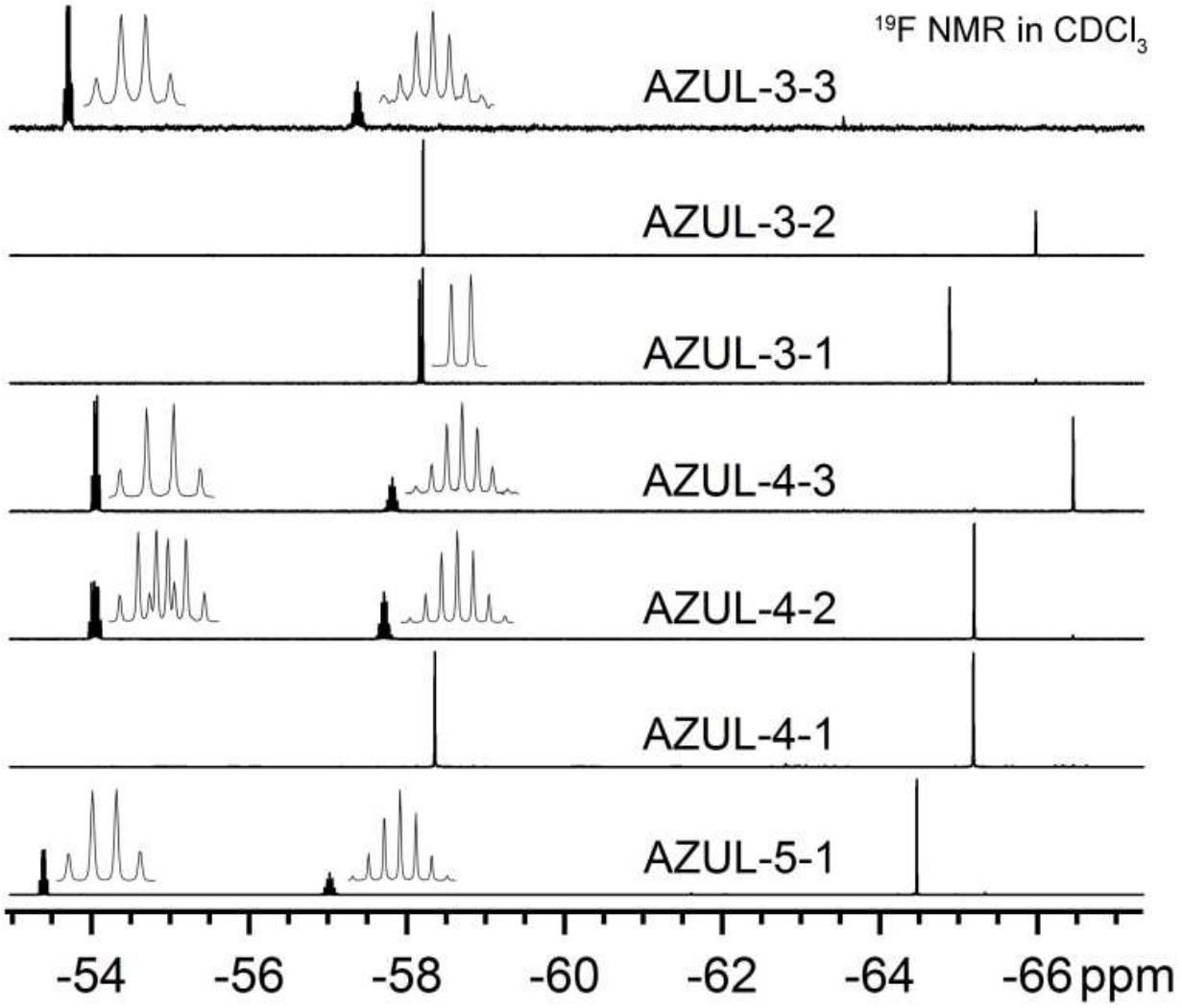

Figure 2.2. ^{19}F NMR spectra ($CDCl_3$, 376.5 MHz, $\delta(C_6F_6) = -164.9$ ppm) showing the CF_3 multiplets and singlets of the seven azulene derivatives. Regions where peaks are in close proximity are shown as insets for clarity. Coupling constants can be found in the experimental section.

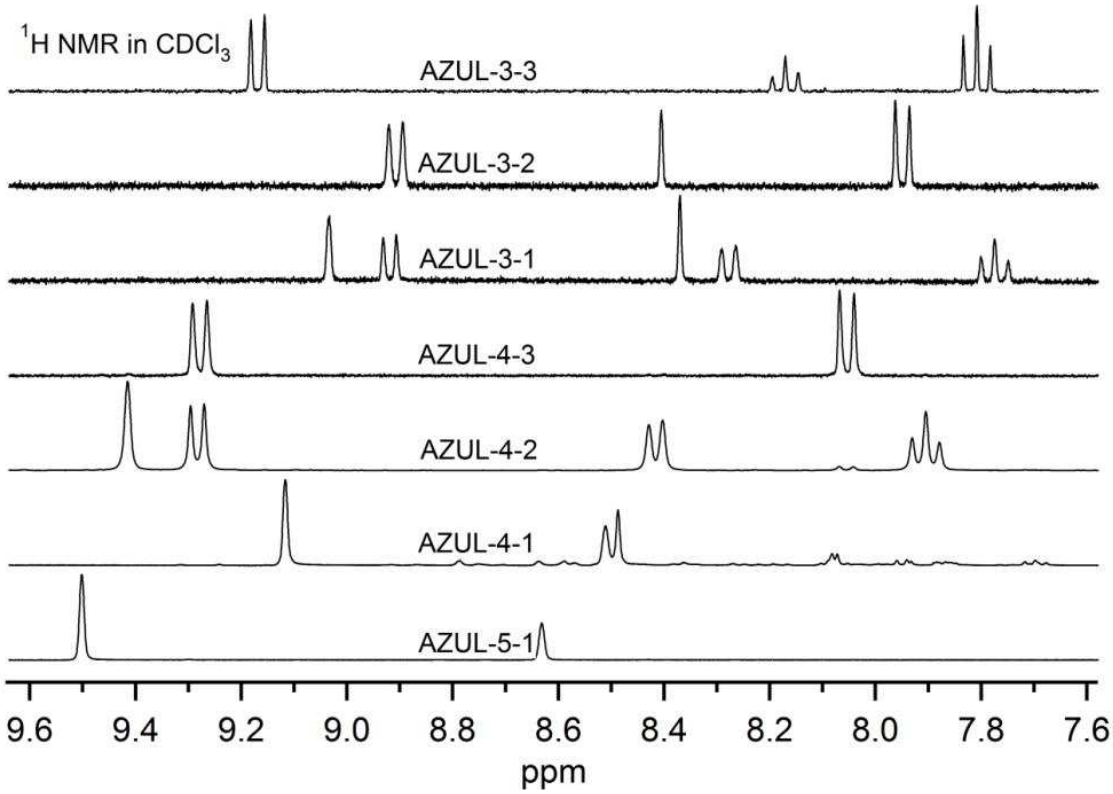

Figure 2.3. Proton NMR of the seven azulene derivatives in $CDCl_3$. Some residual solvents are present (acetonitrile, water, dichloromethane, toluene, hexane), which cannot be easily removed due to the volatility of the compounds, and may cause different chemical shifts. **AZUL-4-2** contains a 3% impurity of **AZUL-4-3**. **AZUL-4-1** contains ca. 5% impurities of other $AZUL(CF_3)_4$ derivatives.

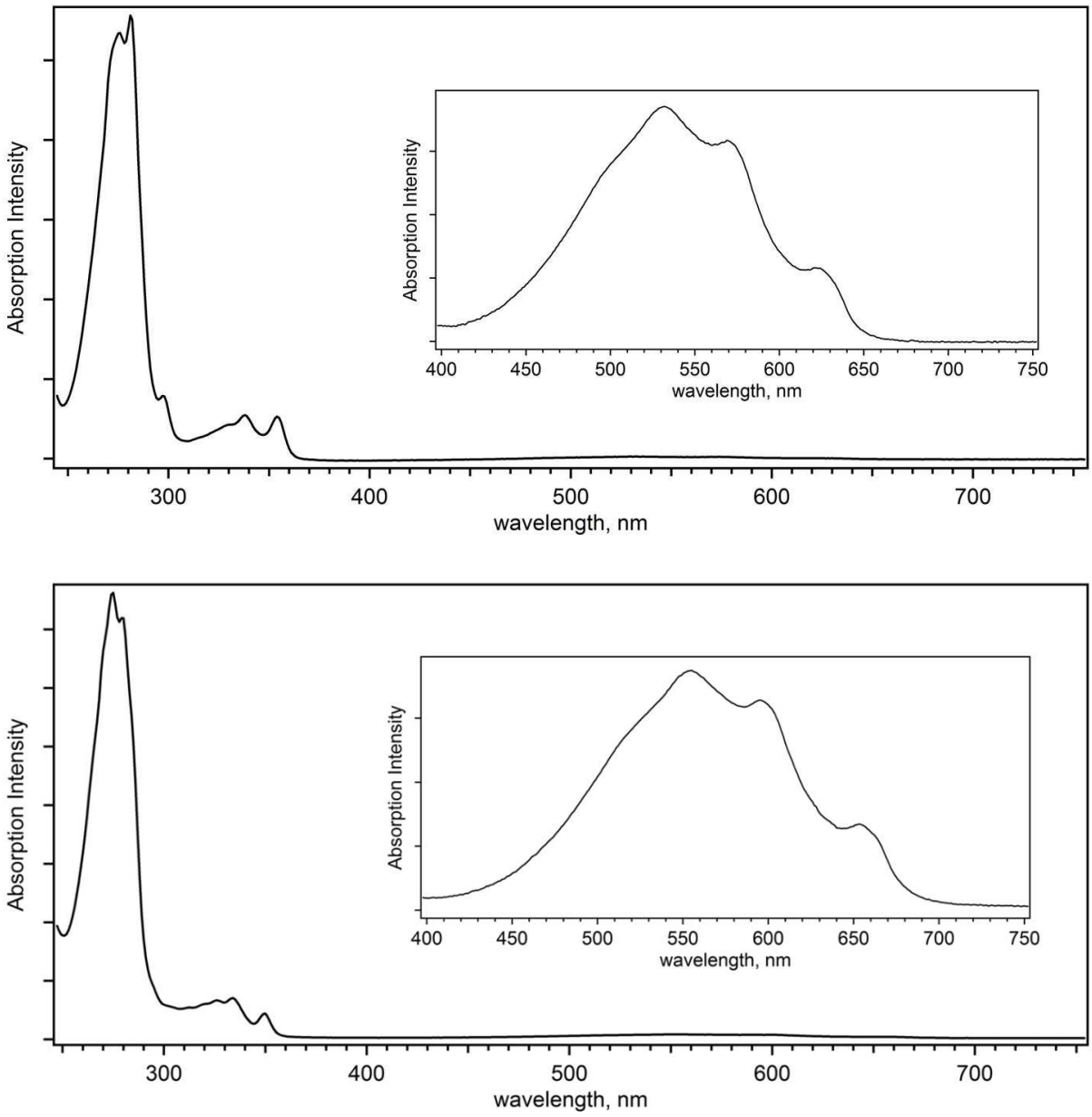

Figure 2.4. UV-vis spectra of **AZUL-3-1** (top) and **AZUL-3-2** (bottom) in hexanes. The insets show a zoomed in view of the S_1 band.

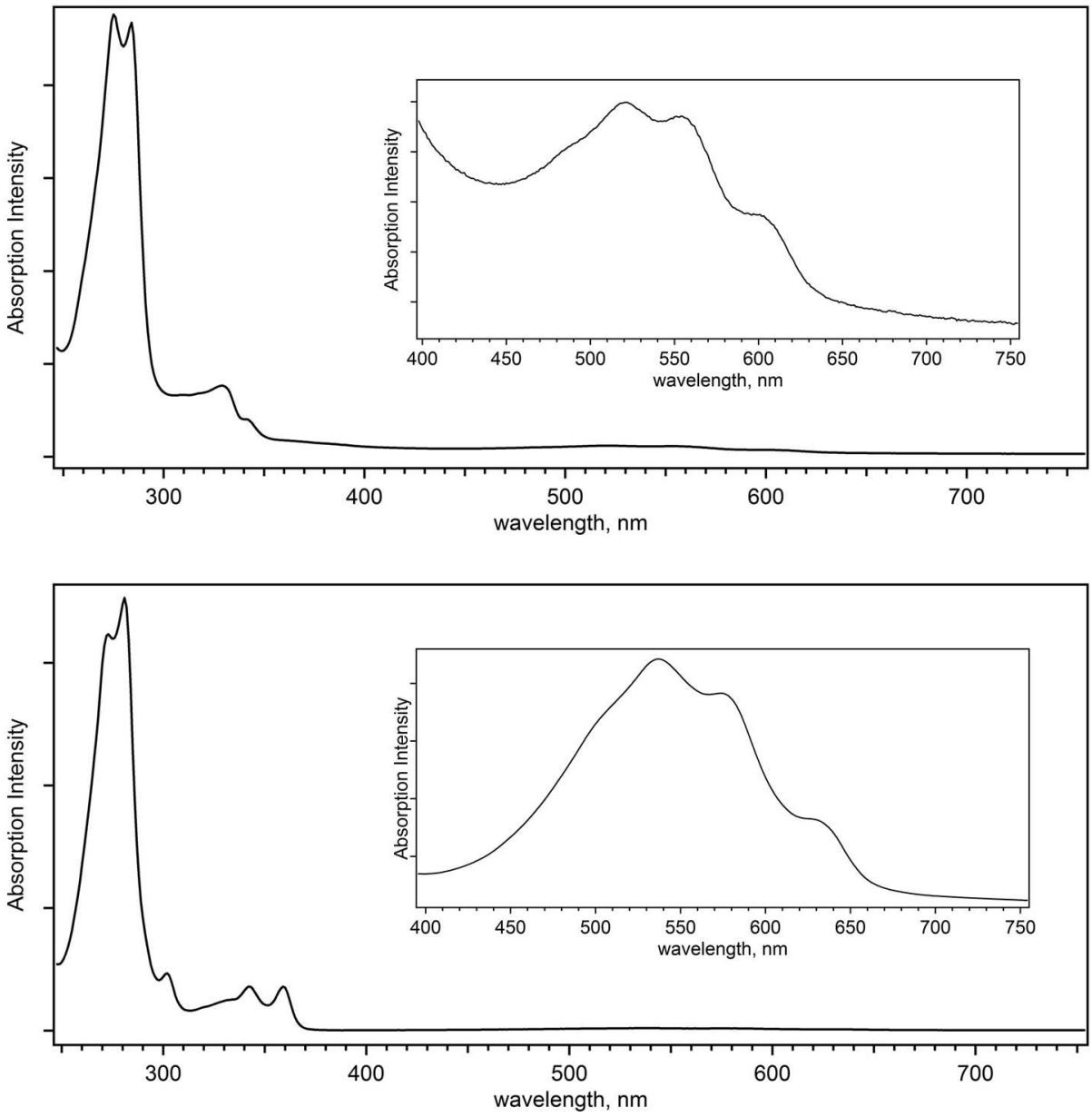

Figure 2.5. UV-vis spectra of **AZUL-3-3** (top) and **AZUL-4-1** (bottom) in hexanes. The insets show a zoomed in view of the S_1 band.

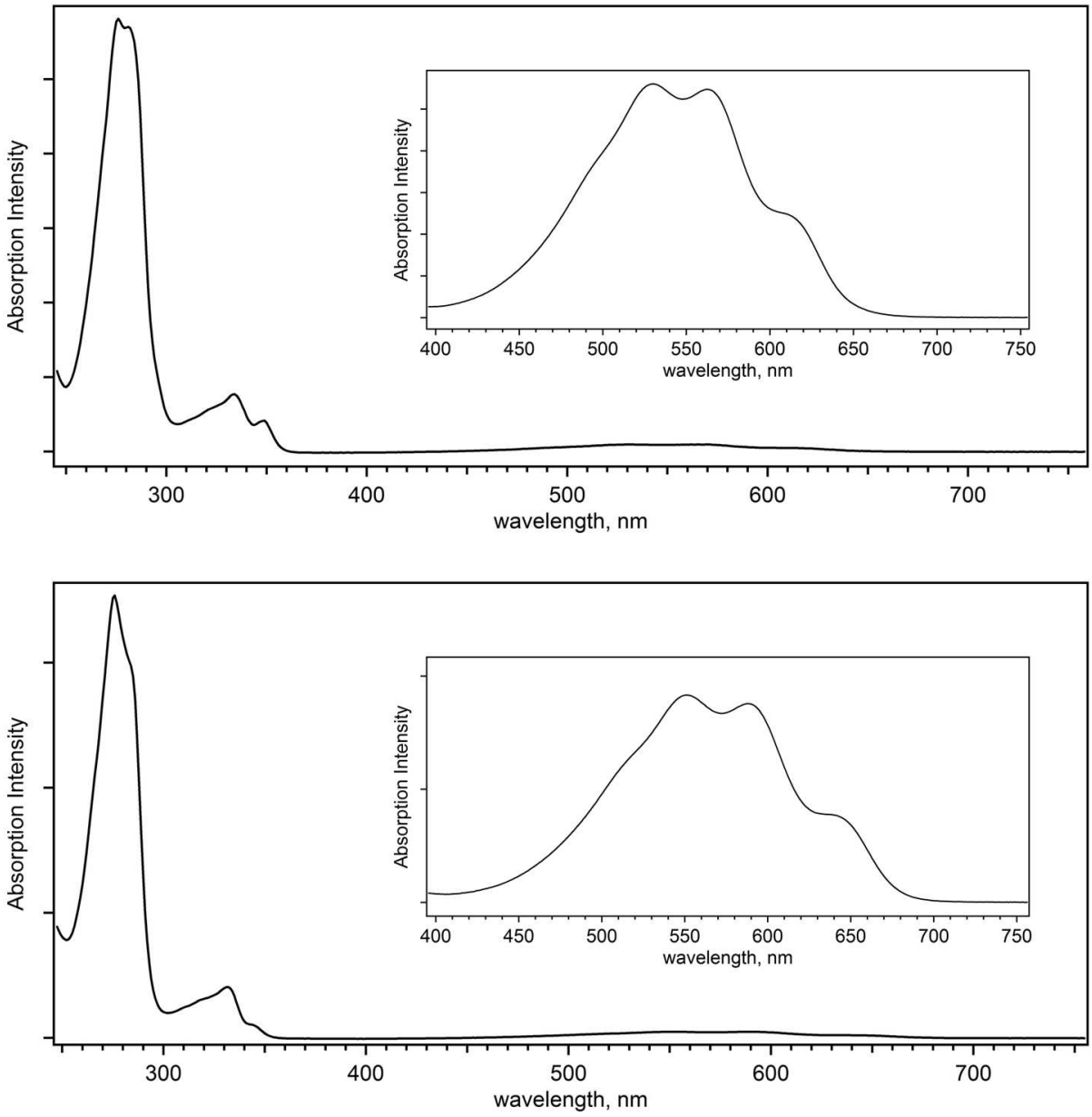

Figure 2.6. UV-vis spectra of **AZUL-4-2** (top) and **AZUL-4-3** (bottom) in hexanes. The insets show a zoomed in view of the S_1 band.

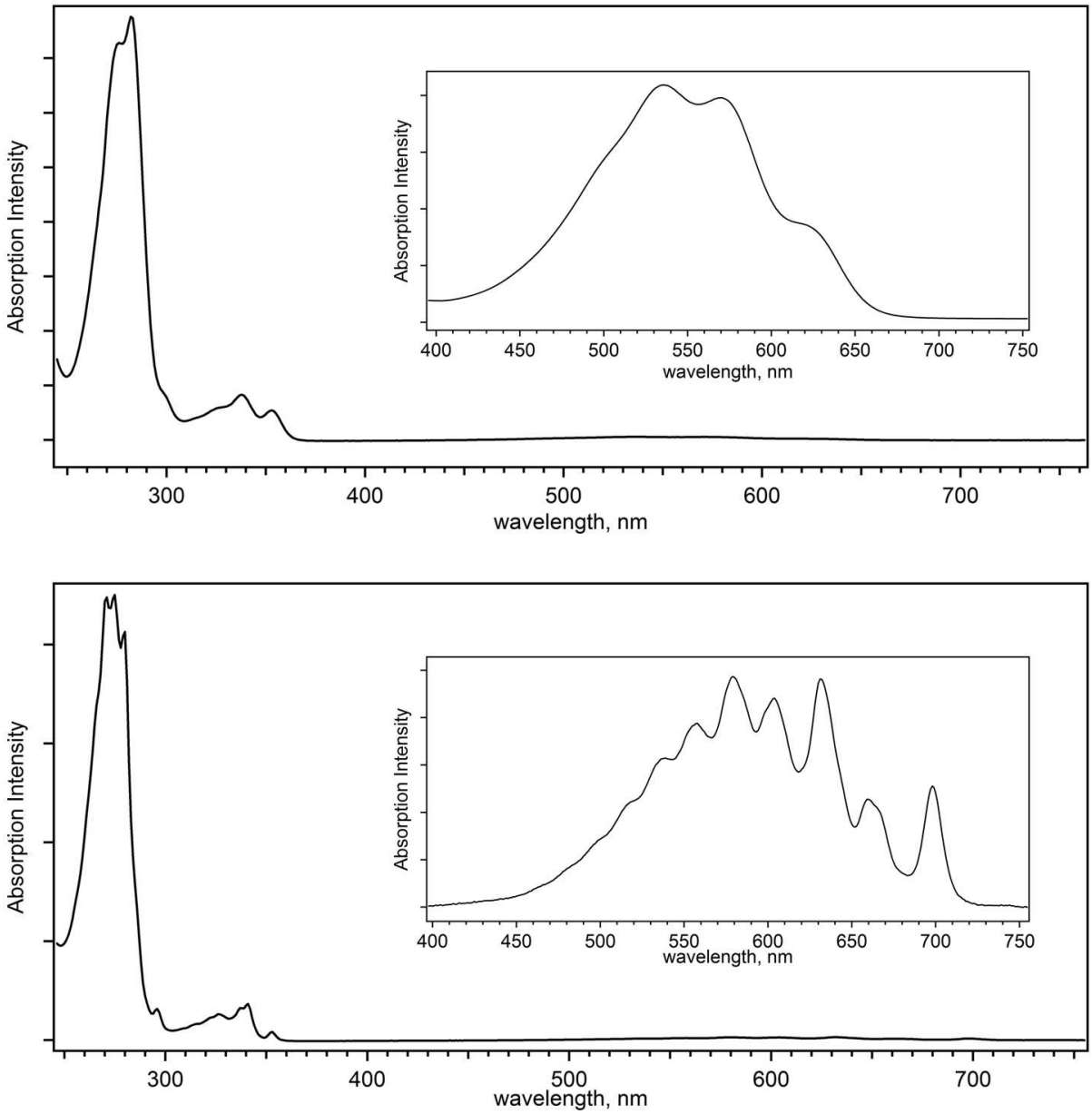

Figure 2.7. UV-vis spectra of **AZUL-5-1** (top) and **AZUL** (bottom) in hexanes. The insets show a zoomed in view of the S_1 band.

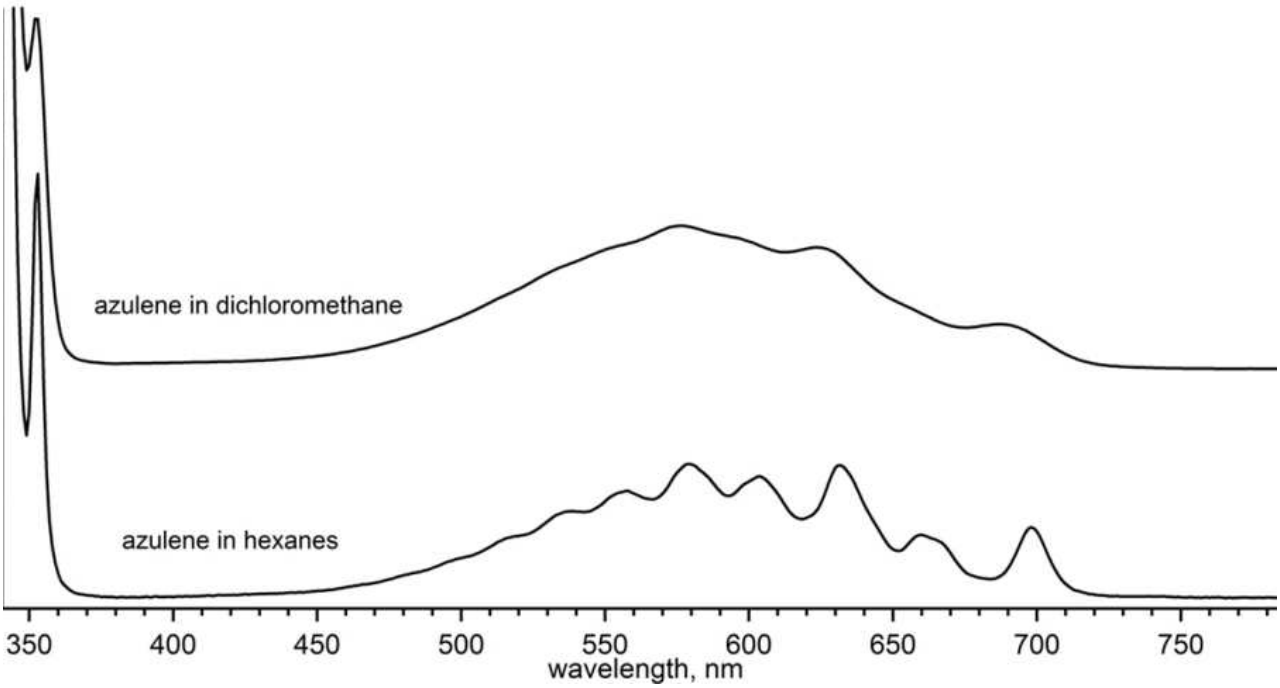

Figure 2.8. UV-vis absorption spectra of azulene in dichloromethane and hexanes, showing the difference in S_1 band structure between solvents.

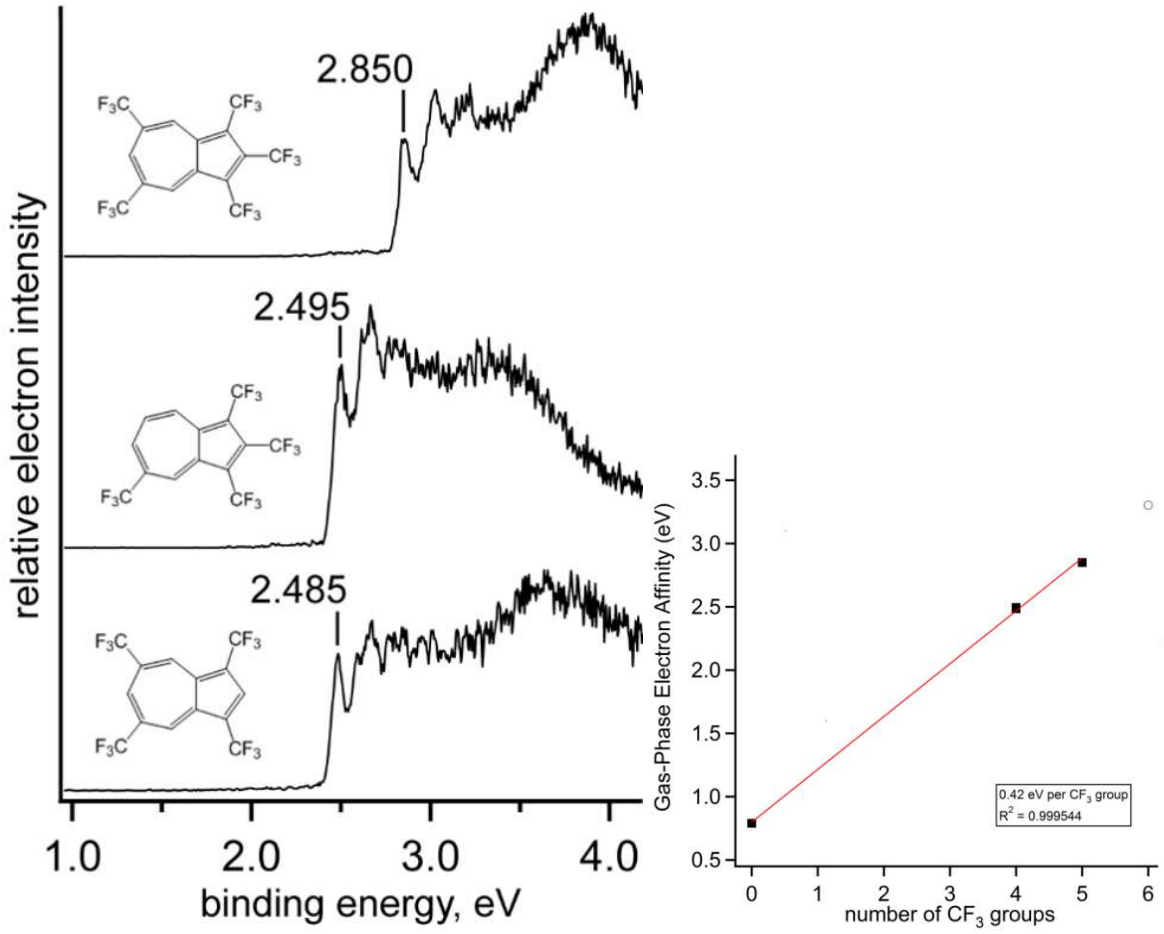

Figure 2.9. Left) The low-temperature (12 K) photoelectron spectrum at 266 nm of **AZUL-5-1** (top), **AZUL-4-2** (middle), and **AZUL-4-1** (bottom). Right) Plot of the experimentally measured gas-phase EA values of **AZUL**, **AZUL-4-1**, **AZUL-4-2**, and **AZUL-5-1** (black squares) including extrapolation to the estimated EA value for the experimentally observed azulene$(CF_3)_6$.

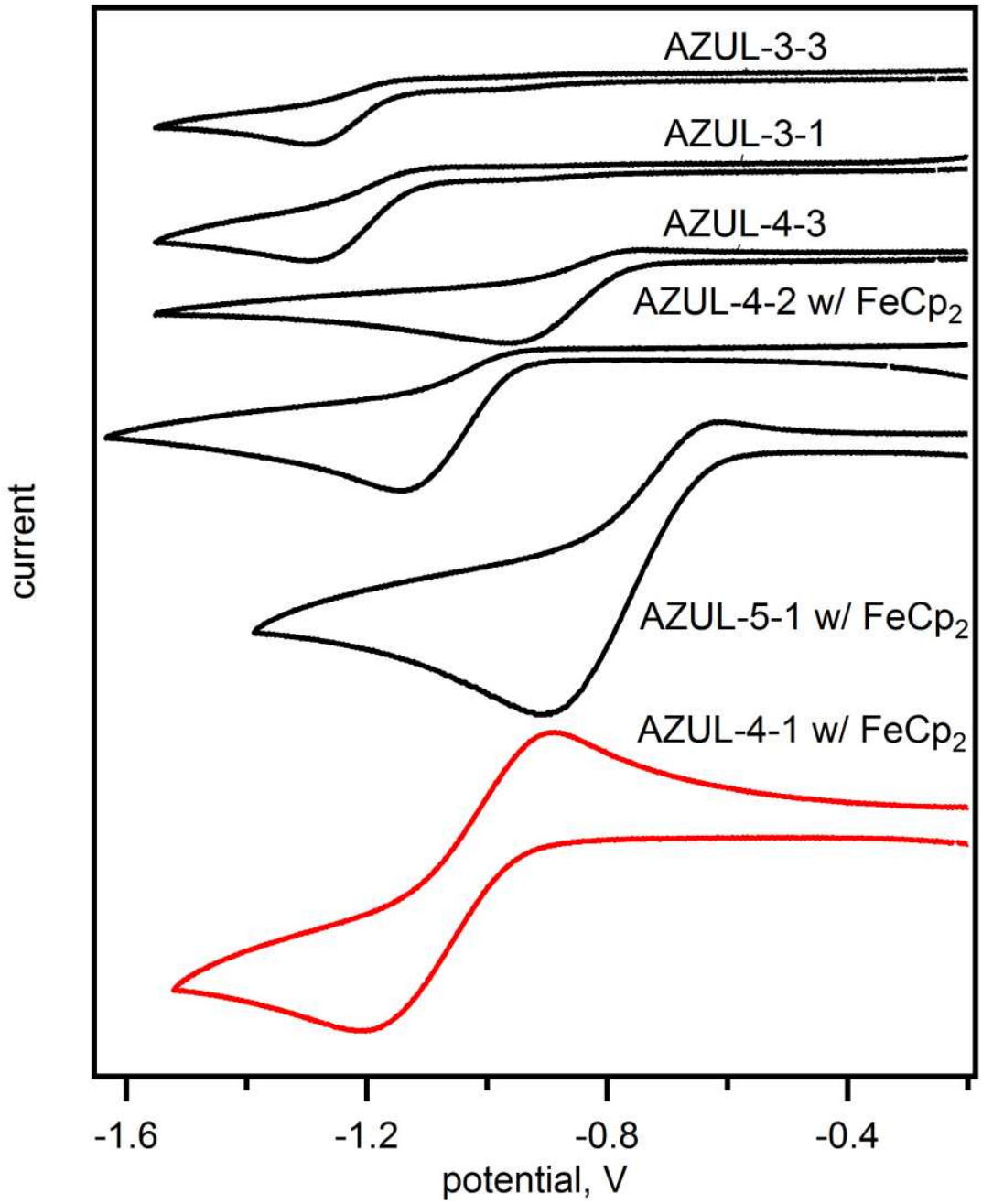

Figure 2.10. Cyclic voltammograms (0.1 M $N(nBu)_4ClO_4$ in dimethoxyethane, 500 $mV \cdot s^{-1}$) of $AZUL(CF_3)_n$ derivatives comparing the reversibility of **AZUL-4-1** (red) versus the other derivatives (black). Measurements without $FeCp_2$ internal standard are offset using an average of $FeCp_2$ external standard measurements; otherwise the values are reported versus $FeCp_2^{+/0}$ internal standard. **AZUL-3-2** was lost due to volatility and was not measured.

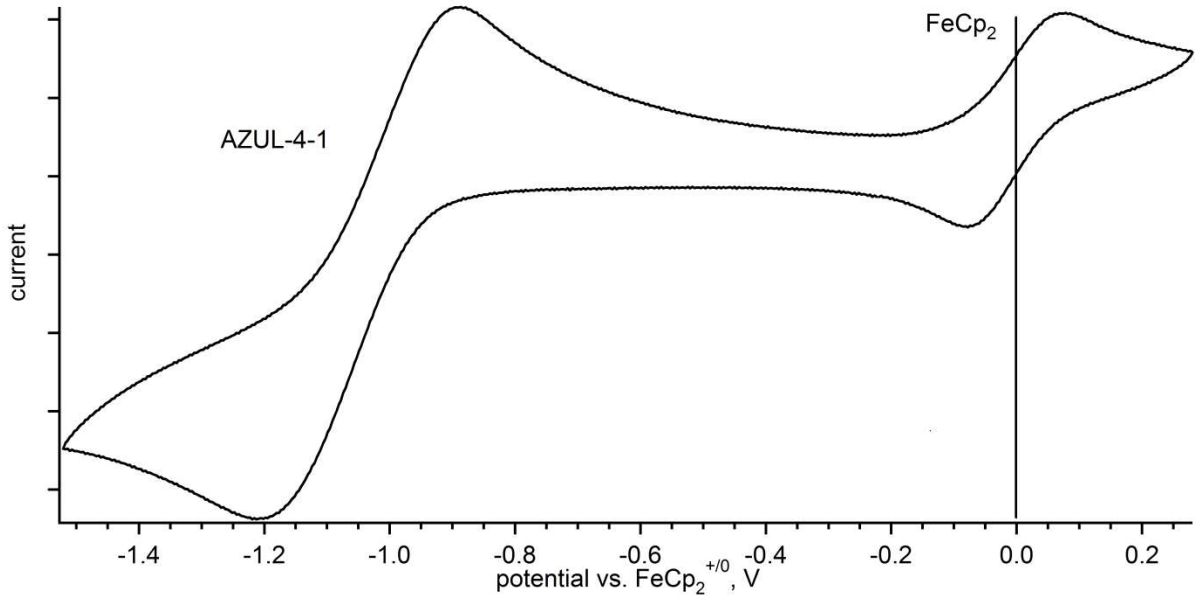

Figure 2.11. Cyclic voltammogram (0.1 м $N(nBu)_4ClO_4$ in dimethoxyethane, 500 $mV \cdot s^{-1}$) of **AZUL-4-1** with $FeCp_2^{+/0}$ internal standard.

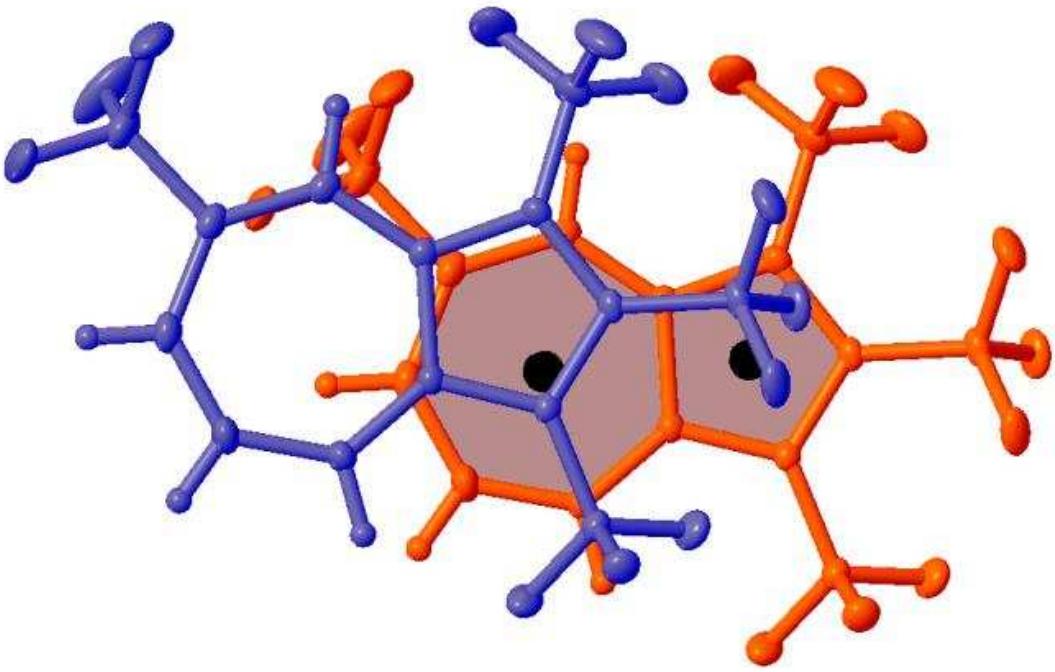

Figure 2.12. Packing diagram of two molecules of **AZUL-4-2**. The mean planes of heptagon and pentagon subunits are shown for the bottom molecule.

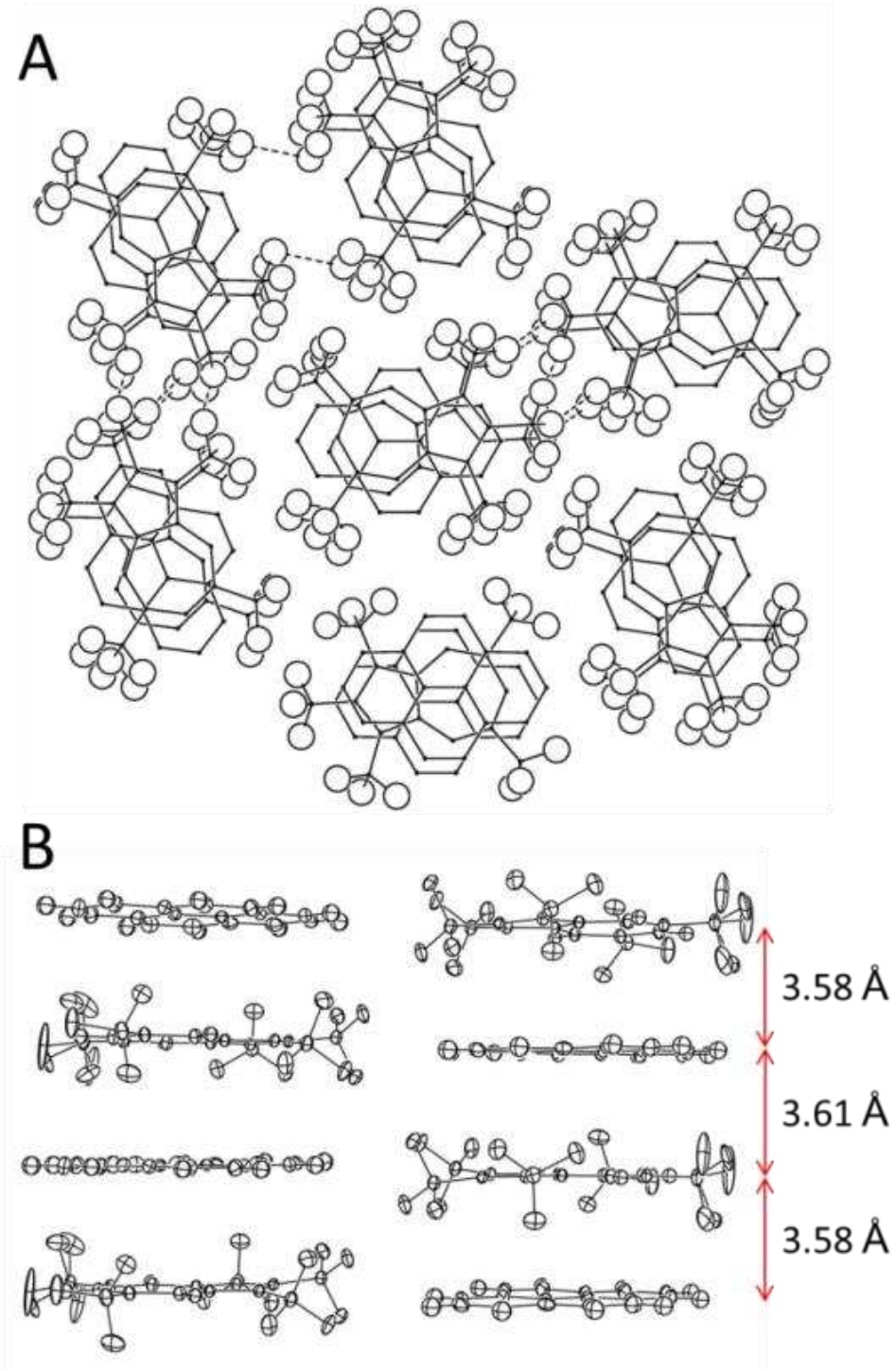

Figure 2.13. Showing the packing of **AZUL-5-1**/pyrene columns from the top down (A) and a view of two columns from the side (B). Distances between **AZUL-5-1** core plane and pyrene core planes are given.

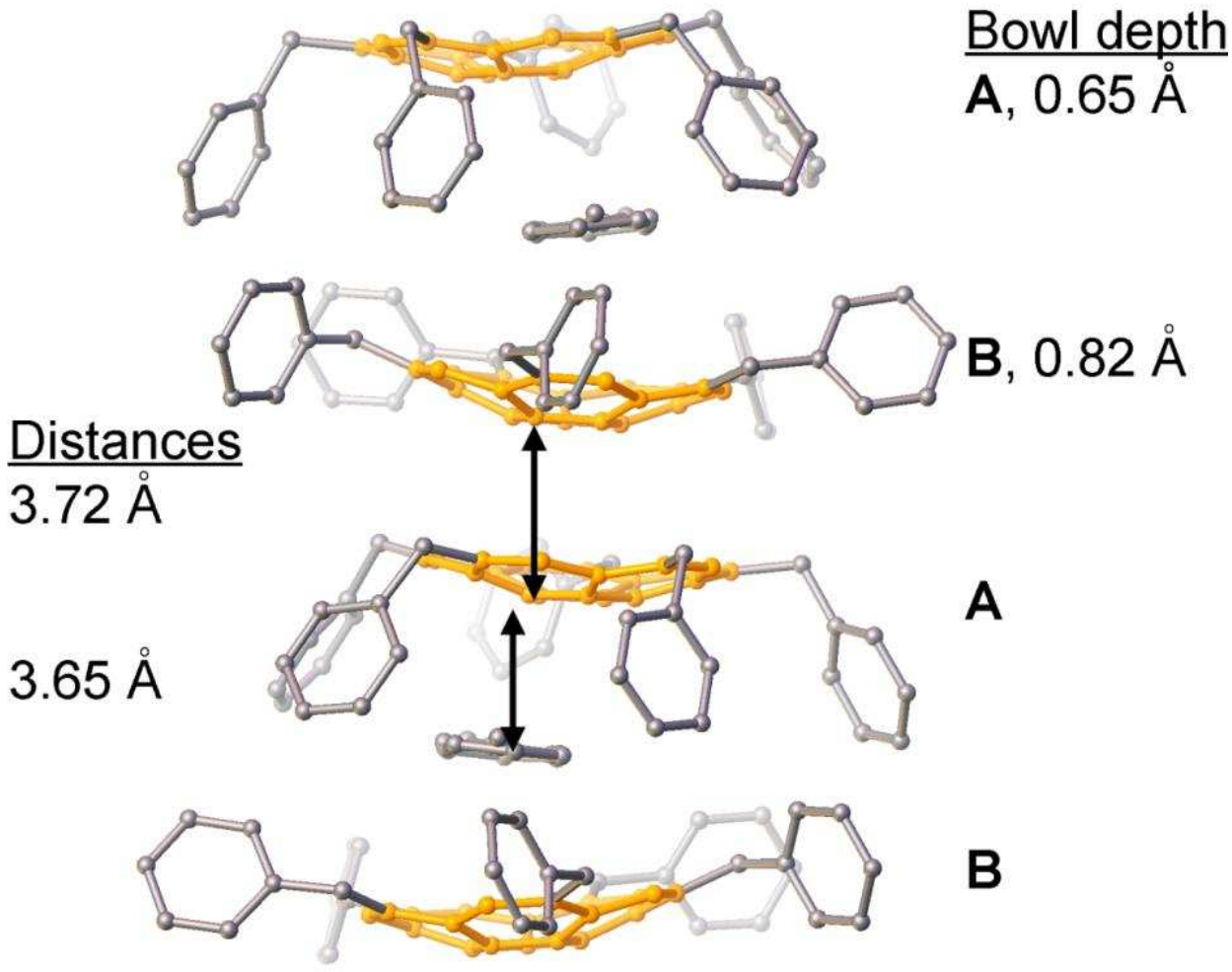

Figure 2.14. Crystal packing of one column of **CORA(Bn$_F$)$_5$** viewed along the *a* axis. Conformer names, selected distances, and bowl depths are given. Orange represents the CORA core carbon atoms. Fluorine and hydrogen atoms and the second toluene molecule are removed for clarity.

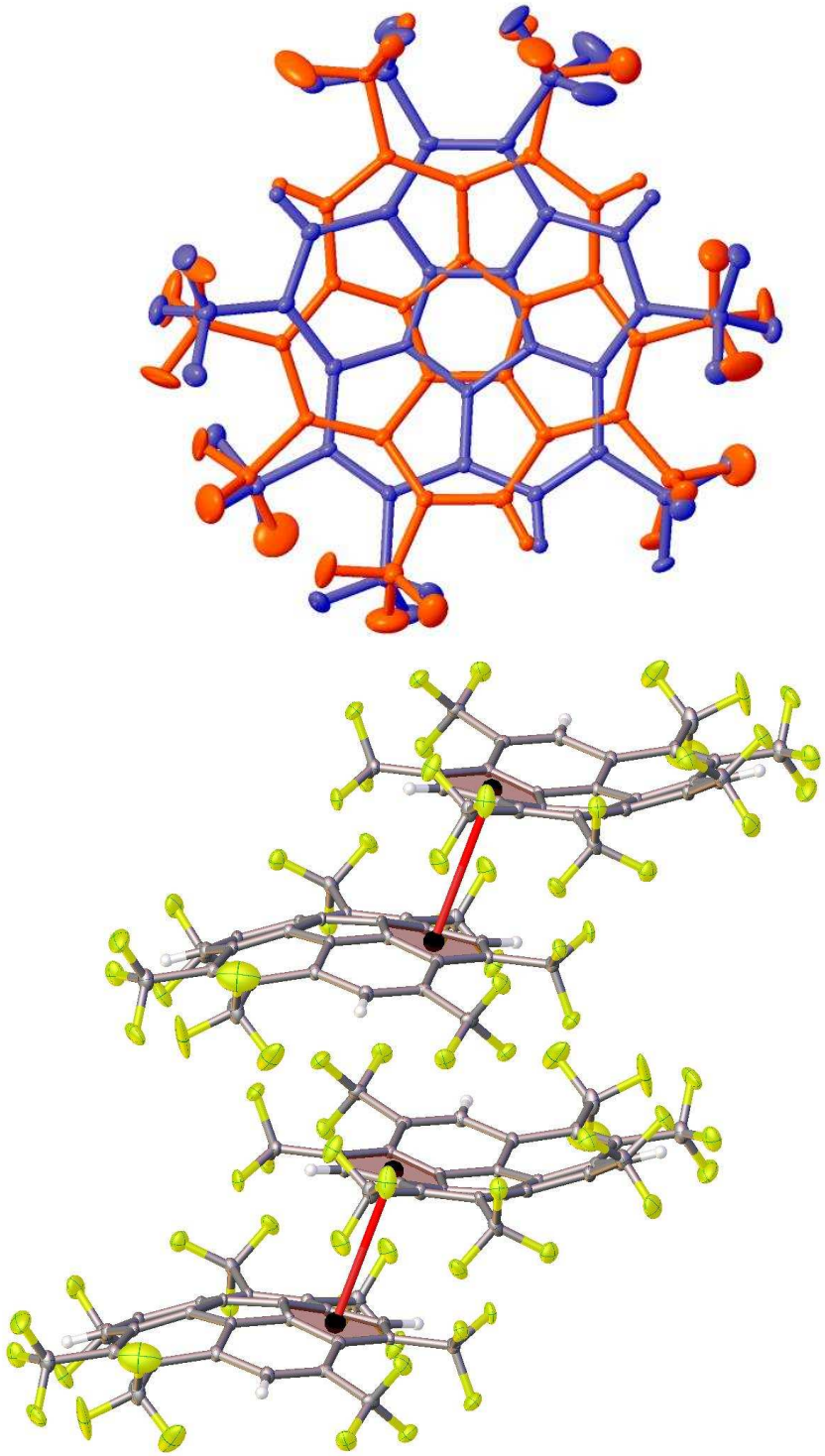

Figure 2.15. Thermal ellipsoid plots of CORA-7-1 showing both enantiomers (top) and the packing of four molecules of the predominant enantiomer (bottom). Red lines in the packing figure represent the close overlapping hexagons.

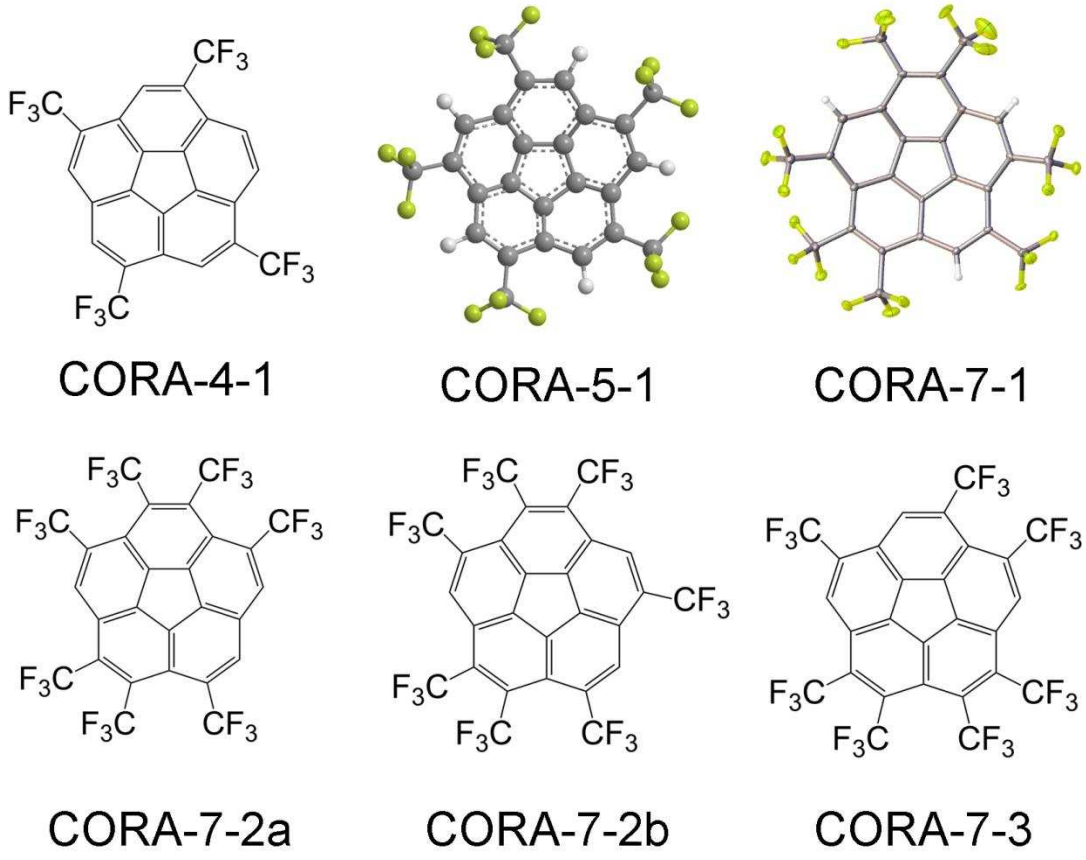

Figure 2.16. Molecular drawings from preliminary crystal structures and from two higher quality crystal structures. CORA-5-1 comes from ref [99], CORA-7-1 comes from this work, and the rest are from preliminary structures that were of sufficient quality to determine the substitution pattern. CORA-7-2a(b) were two different isomers that crystallized together.

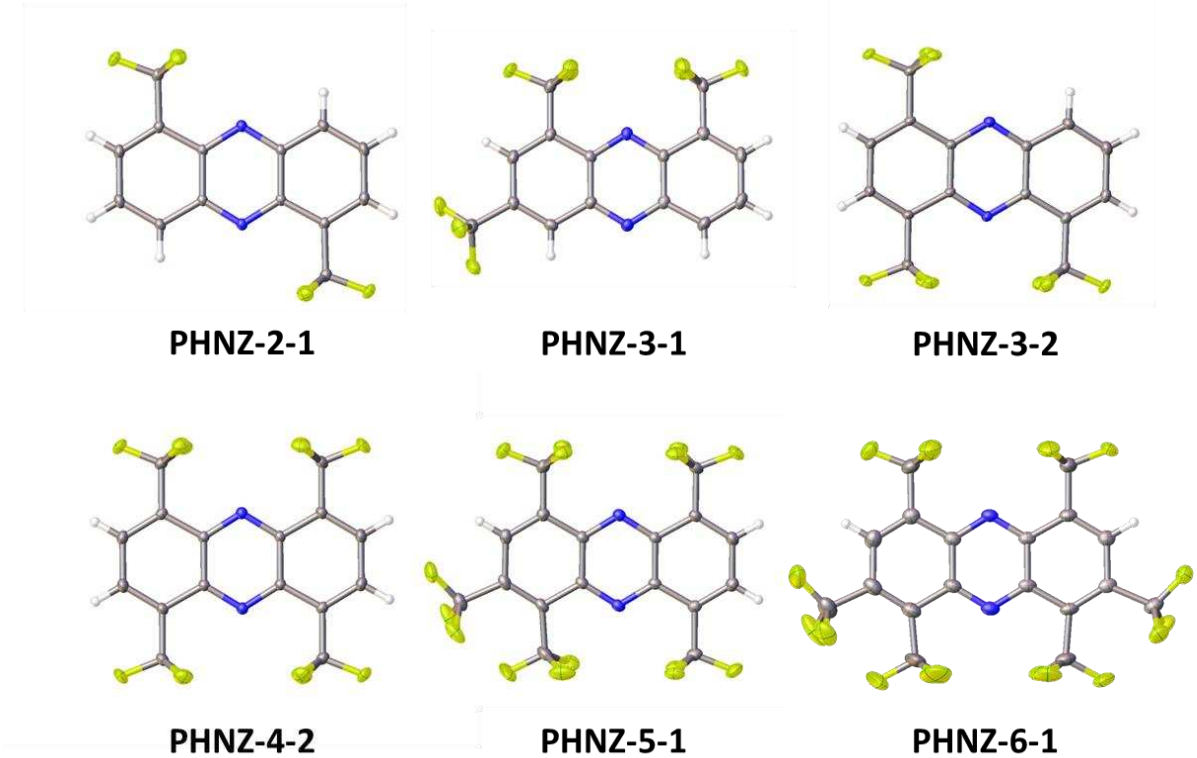

Figure 2.17. Thermal ellipsoid plots (50% probability ellipsoids except for H atoms, F atoms are yellow, N atoms are blue) of PHNZ$(CF_3)_n$ compounds studied by XRD in this work.

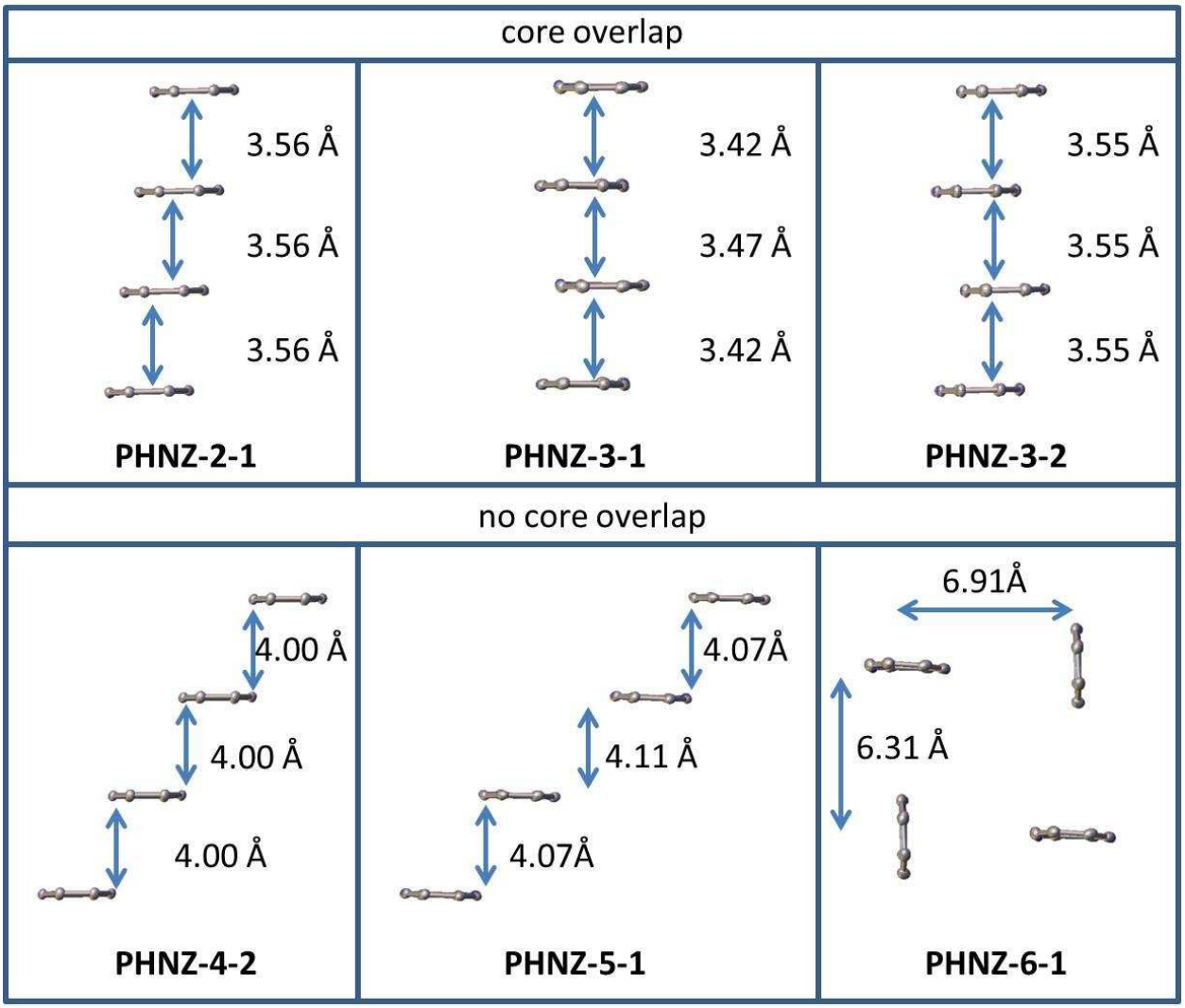

Figure 2.18. Molecular packing of four molecular cores of PHNZ$(CF_3)_n$ (n = 2–6) viewed down the long axis of the PHNZ core. Distances between nearest parallel cores are given. H atoms and CF_3 groups are removed for clarity.

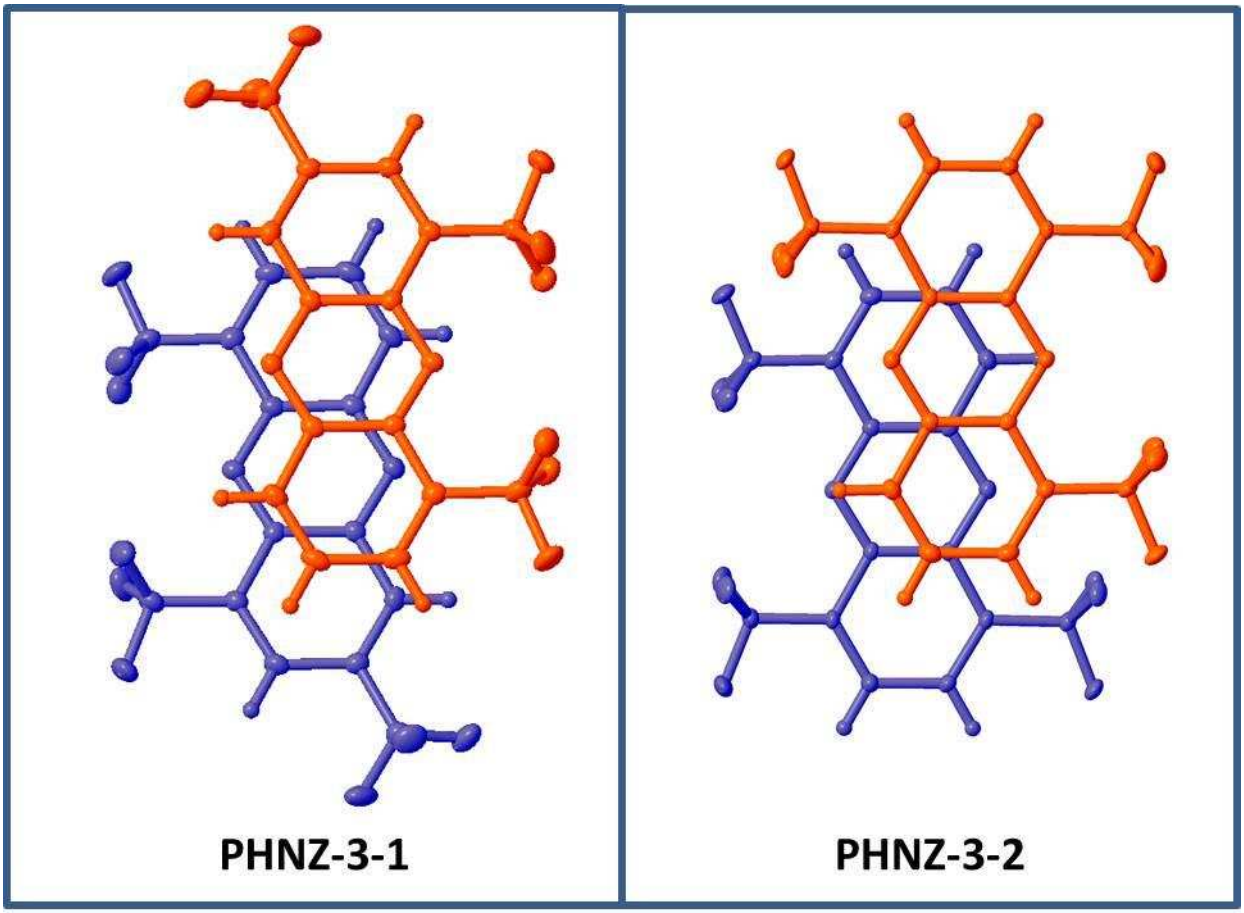

Figure 2.19. Crystallographic packing of two molecules of **PHNZ-3-1** and **PHNZ-3-2** both showing opposite orientations within columns. Note that **PHNZ-3-1** molecules are more overlapped than **PHNZ-3-2**.

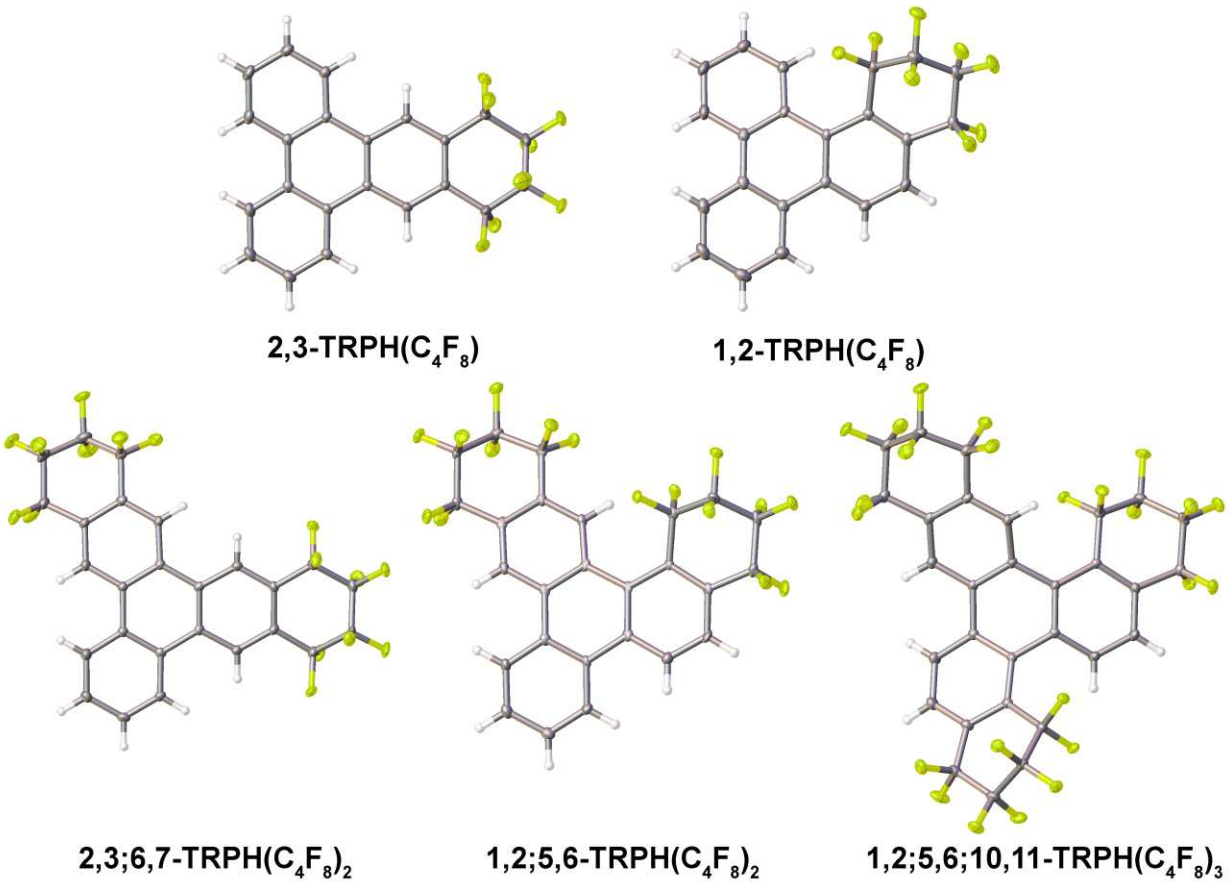

Figure 2.20. Thermal ellipsoid plots (50% probability ellipsoids except for H atoms, F atoms are yellow) of TRPH$(C_4F_8)_n$ compounds studied by XRD in this work.

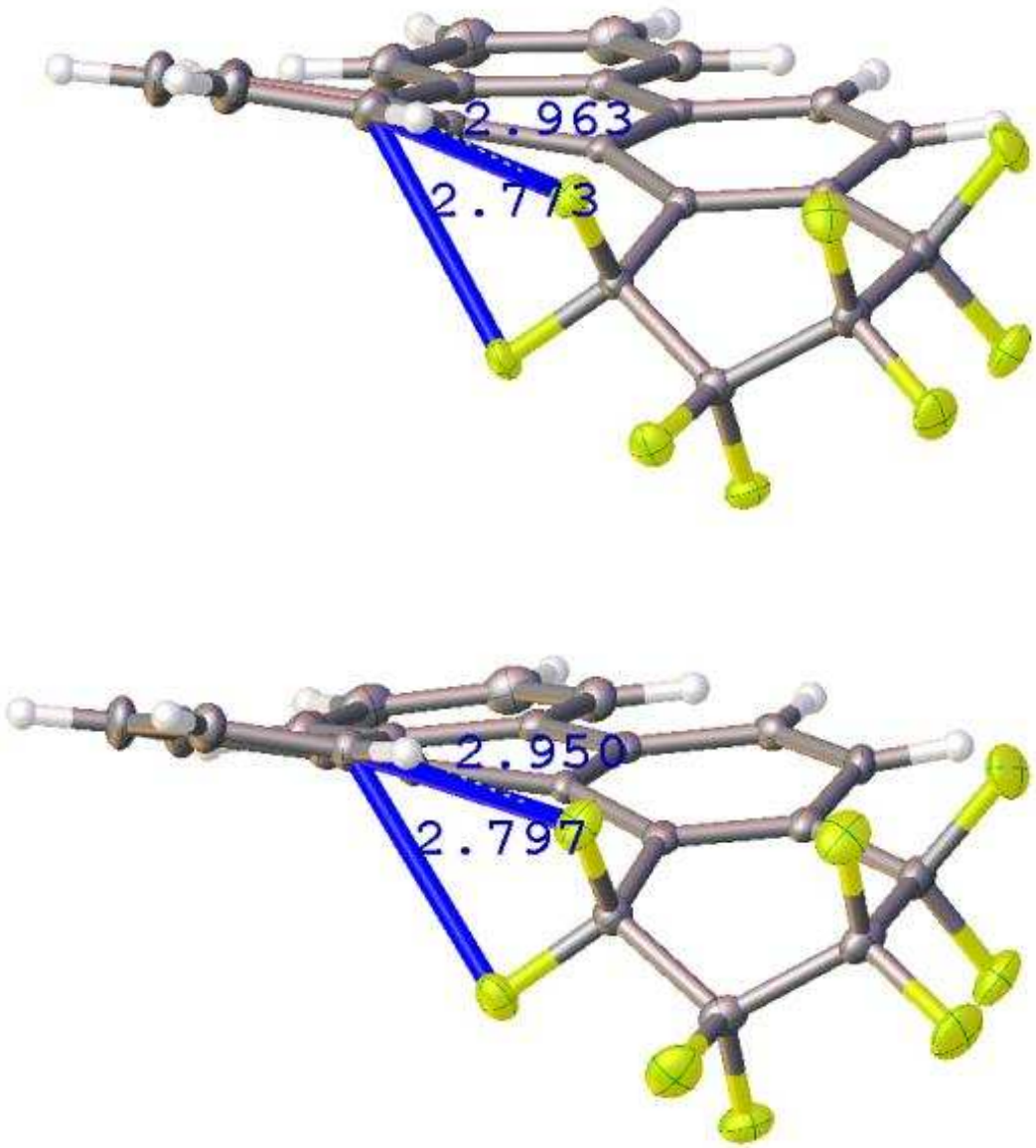

Figure 2.20. The X-ray structure of **1,2-TRPH(C_4F_8)** (50% probability ellipsoids except for H atoms) showing the twisted core of each conformer. The closest F–C12 distances are 2.77 and 2.96 Å, the C1–C14–C13–C12 torsion angle is 20.86°, and the RMSD of the TRPH core plane is 0.178 for the conformer on the top. The closest F–C12 distances are 2.80 and 2.95 Å, the C1–C14–C13–C12 torsion angle is 22.87°, and the RMSD of the TRPH core plane is 0.215 for the conformer on the bottom.

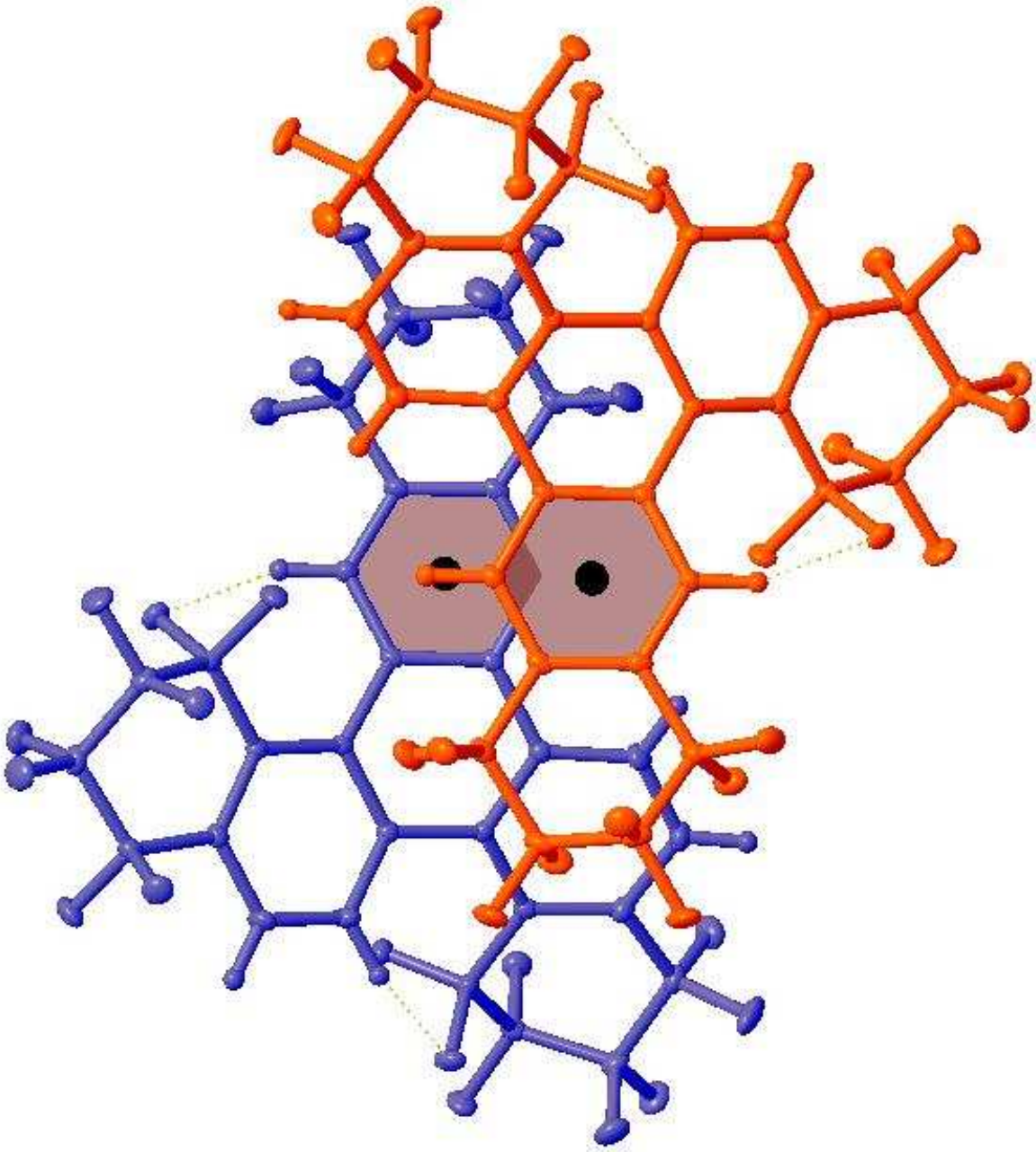

Figure 2.22. The X-ray structure of **1,2;5,6;10,11-TRPH(C_4F_8)$_3$** (50% probability ellipsoids except for H atoms) showing two neighboring molecules. The partially overlapping parallel benzene subunits that are 3.66 Å apart are highlighted.

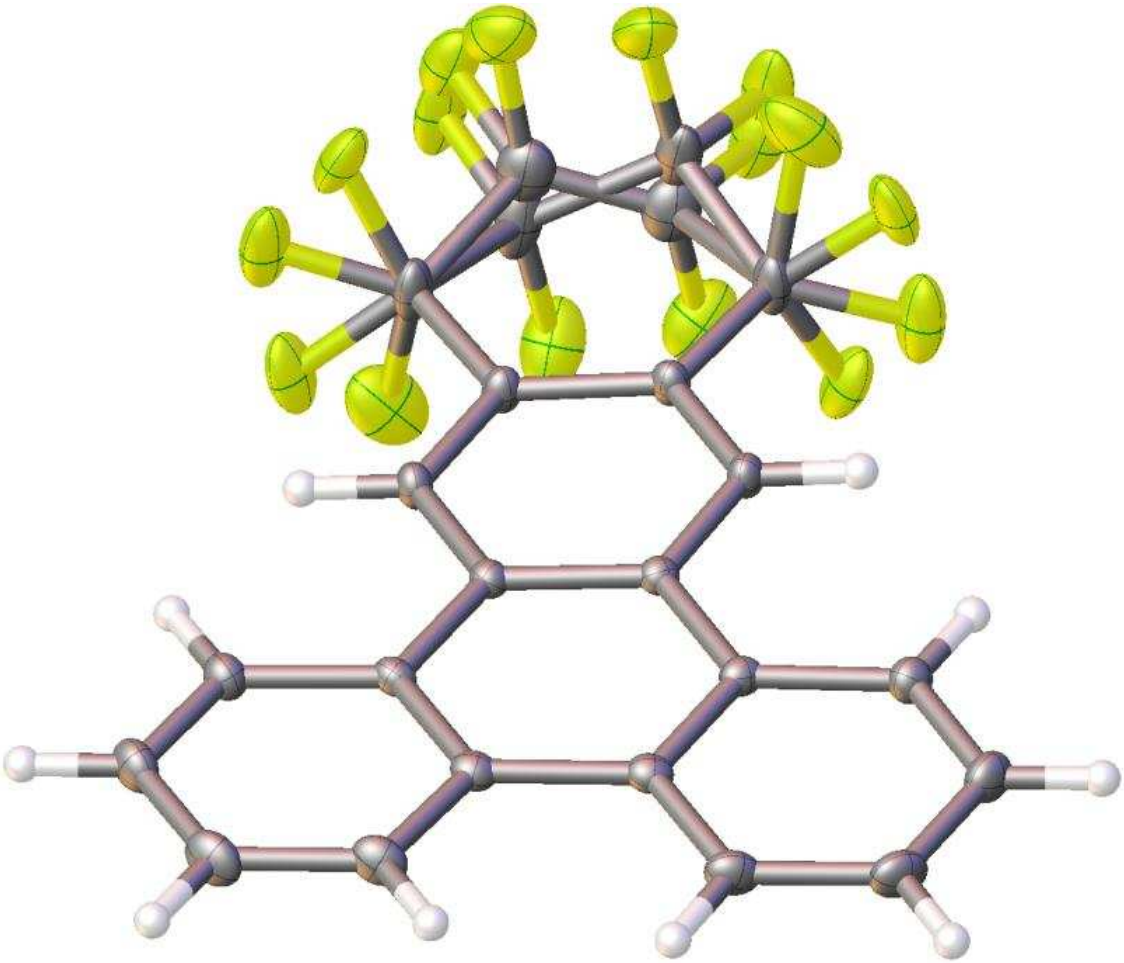

Figure 2.23. The X-ray structure of **2,3-TRPH(C_4F_8)** (50% probability ellipsoids except for H atoms) showing both disordered C_4F_8 parts.

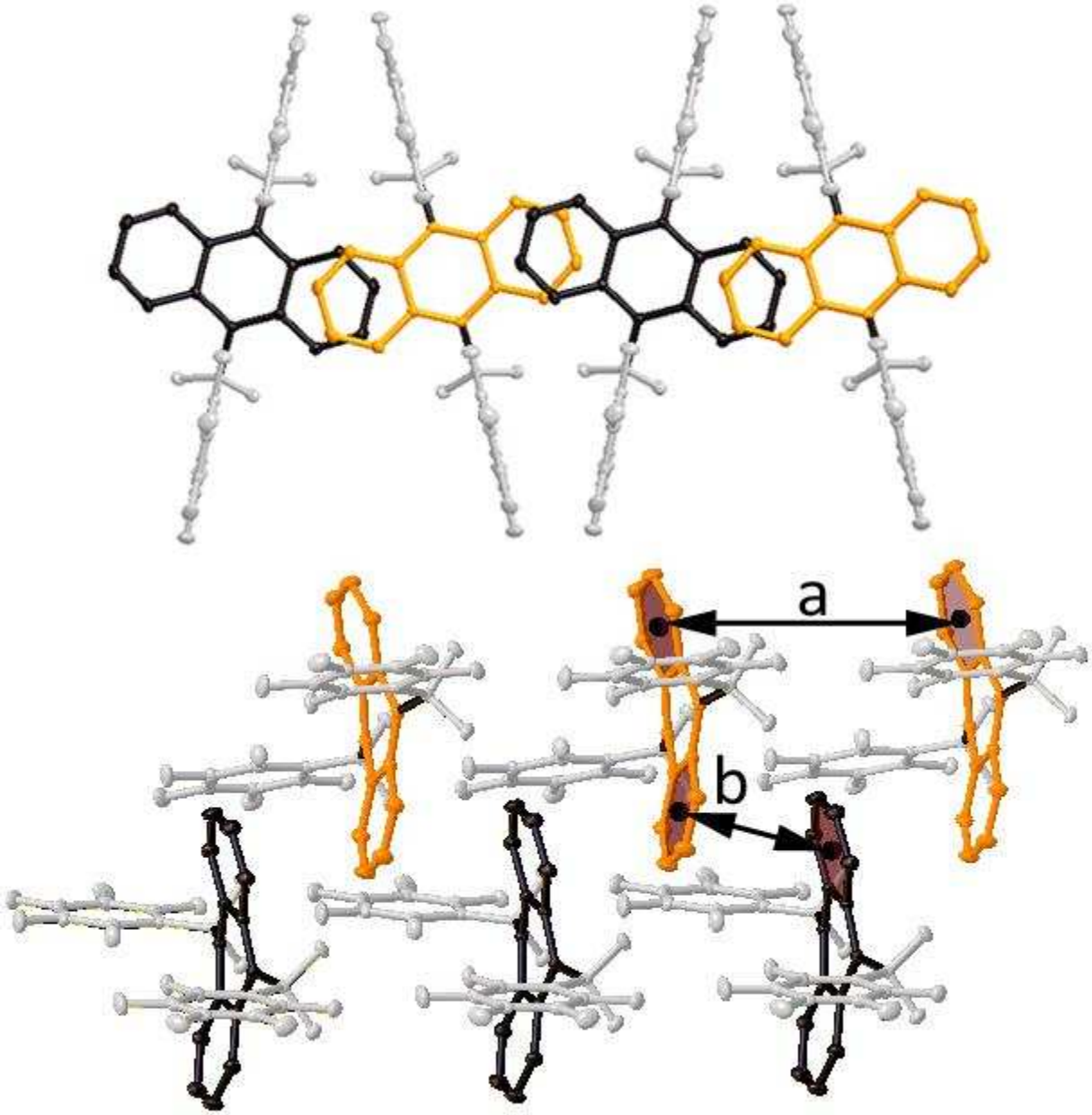

Figure 2.24. Top view down the *c* axis (top panel) and side view (bottom panel) of the **9,10-ANTH(Bn_F)$_2$** columns in the solid-state packing. Two different stacked columns are colored in orange and black, and the Bn_F groups are colored in grey. Distances between centroids a = 8.028 Å and b = 4.154 Å. Hydrogen atoms are omitted for clarity.

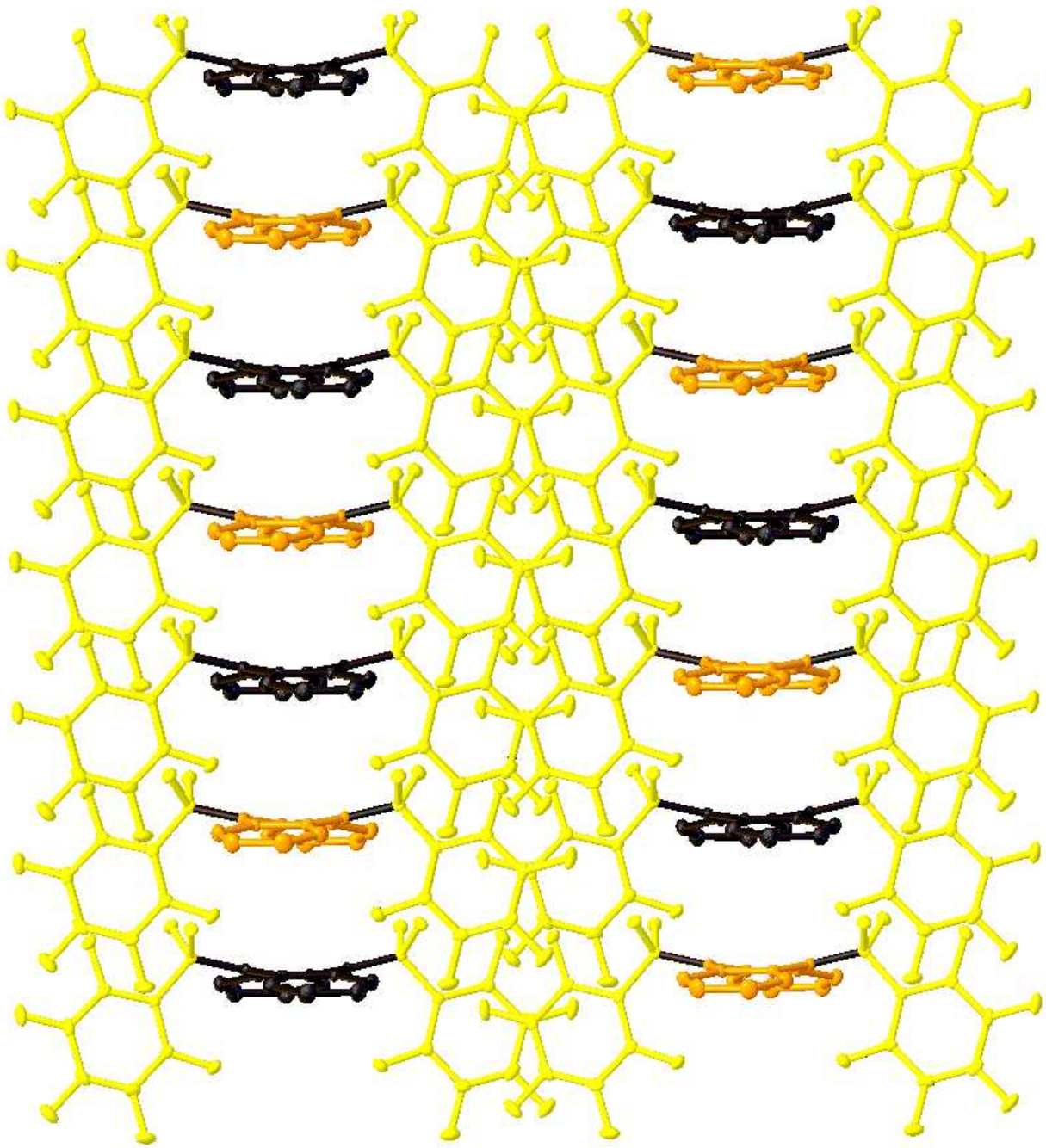

Figure 2.25. Solid-state packing of **9,10-ANTH(Bn_F)$_2$** viewed along the major axis of ANTH core. Two different stacked columns are colored in orange and black, and the Bn_F groups are colored in yellow. The Bn_F groups are shown to insulate the ANTH core. Hydrogen atoms are omitted for clarity.

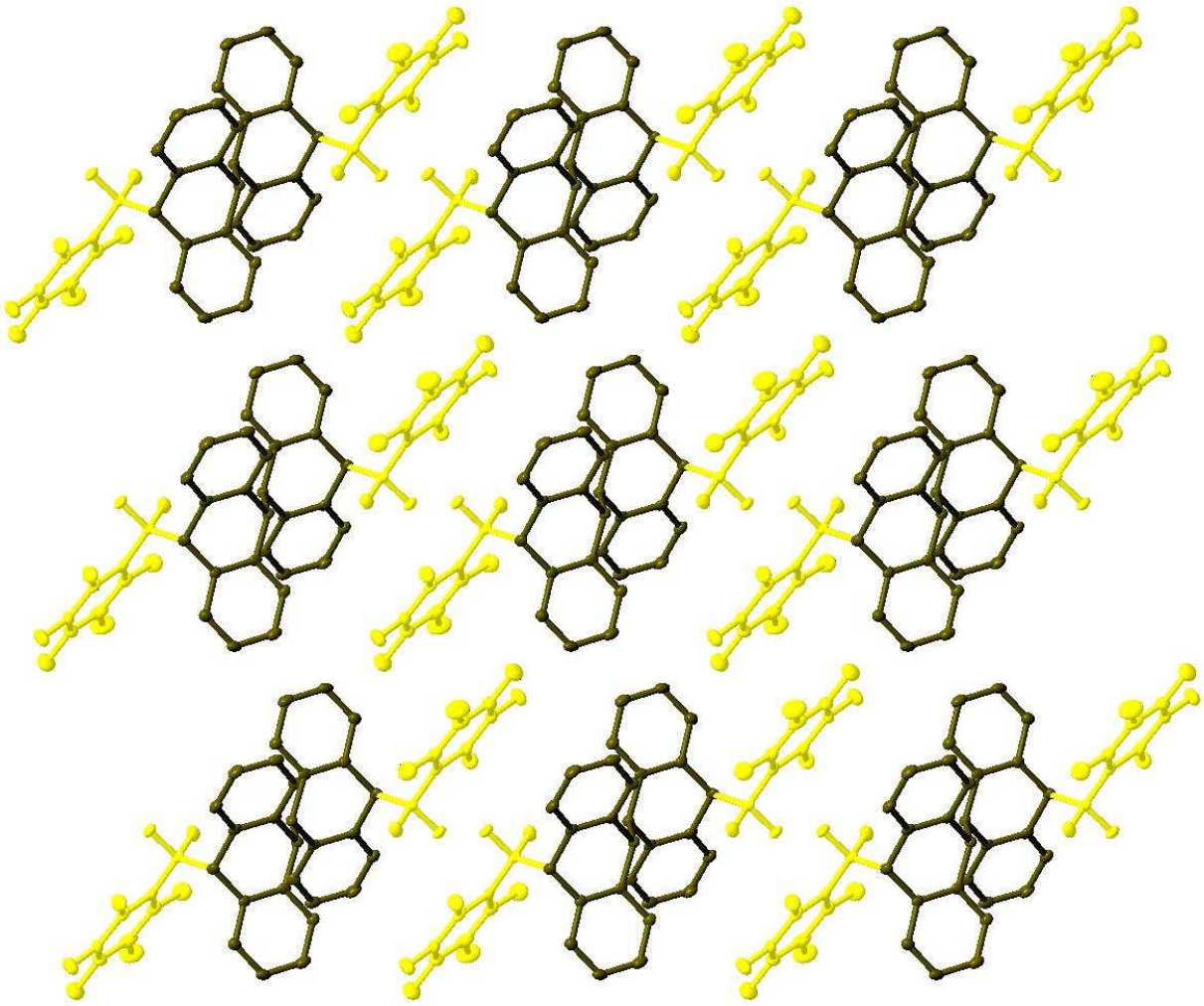

Figure 2.26. Crystallographic packing of **[9-ANTH*(Bn$_F$)]$_2$** viewed down the *a*-axis. Columns of ANTH* cores (black) are separated by insulating Bn$_F$ groups (yellow) along the *b*-axis. H atoms are omitted for clarity.

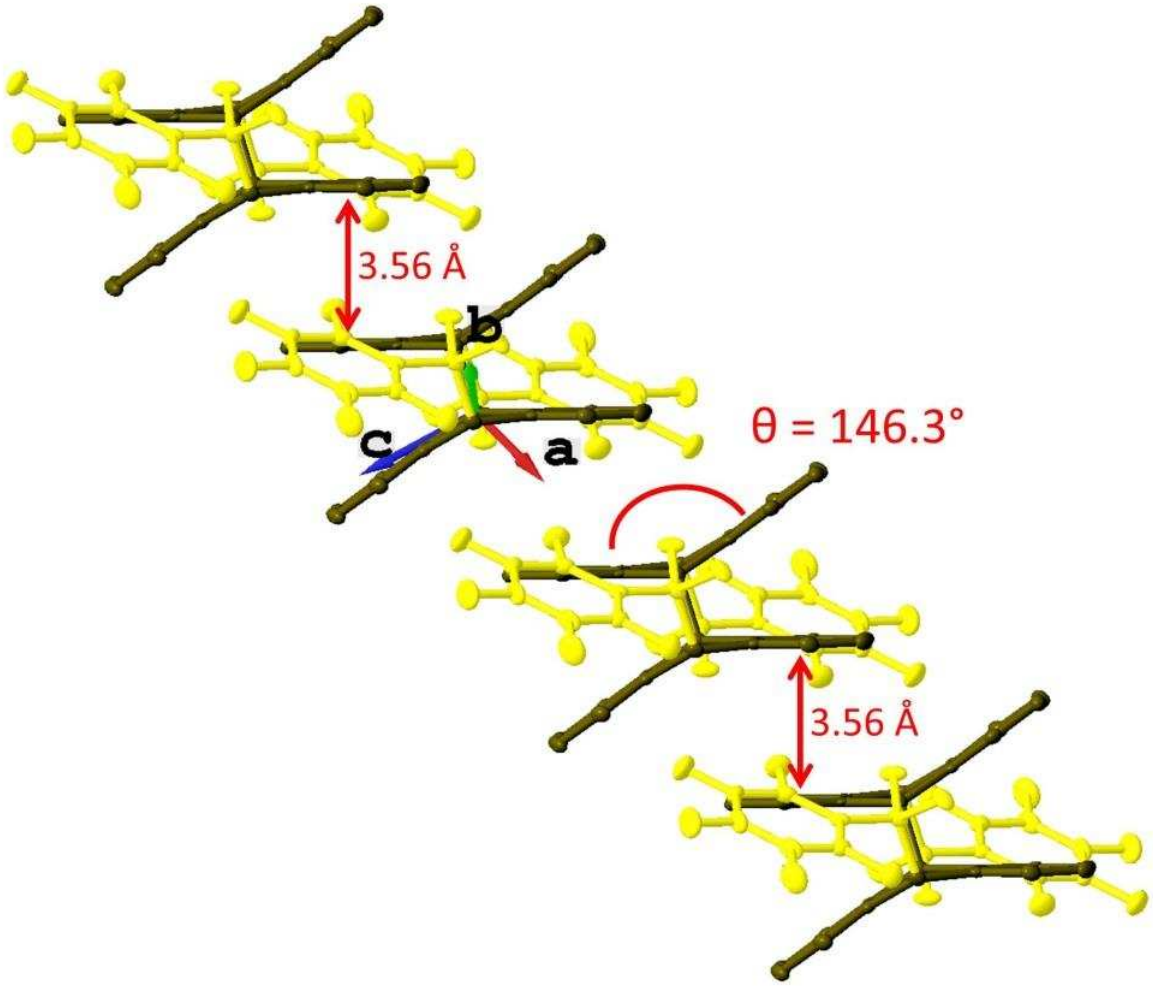

Figure 2.27. Four **[9-ANTH*(Bn_F)]$_2$** molecules from one column viewed along the short ANTH* axis showing the distances between parallel, partially overlapped benzene subunits and the angle of domed ANTH* cores (black). H atoms removed for clarity, Bn_F groups are yellow.

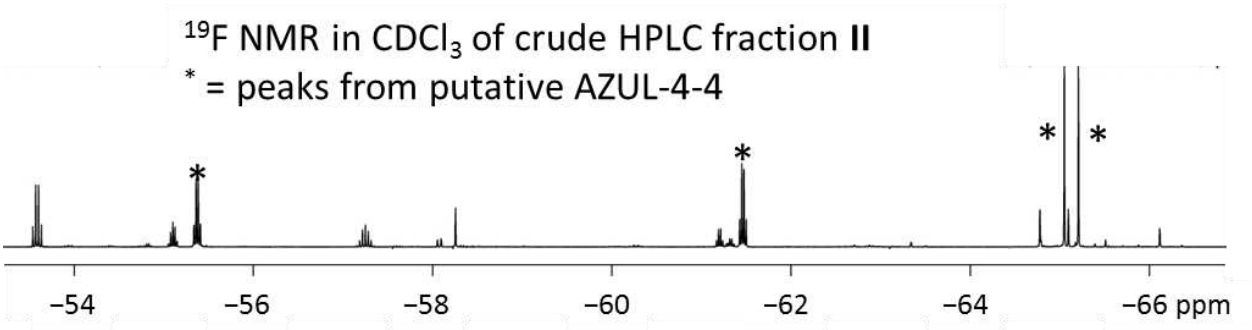

Figure 2.28. Fluorine-19 NMR of crude HPLC fraction **II** from Figure 2.1 in $CDCl_3$ showing the peaks from **AZUL-4-4**, which was lost due to volatility.

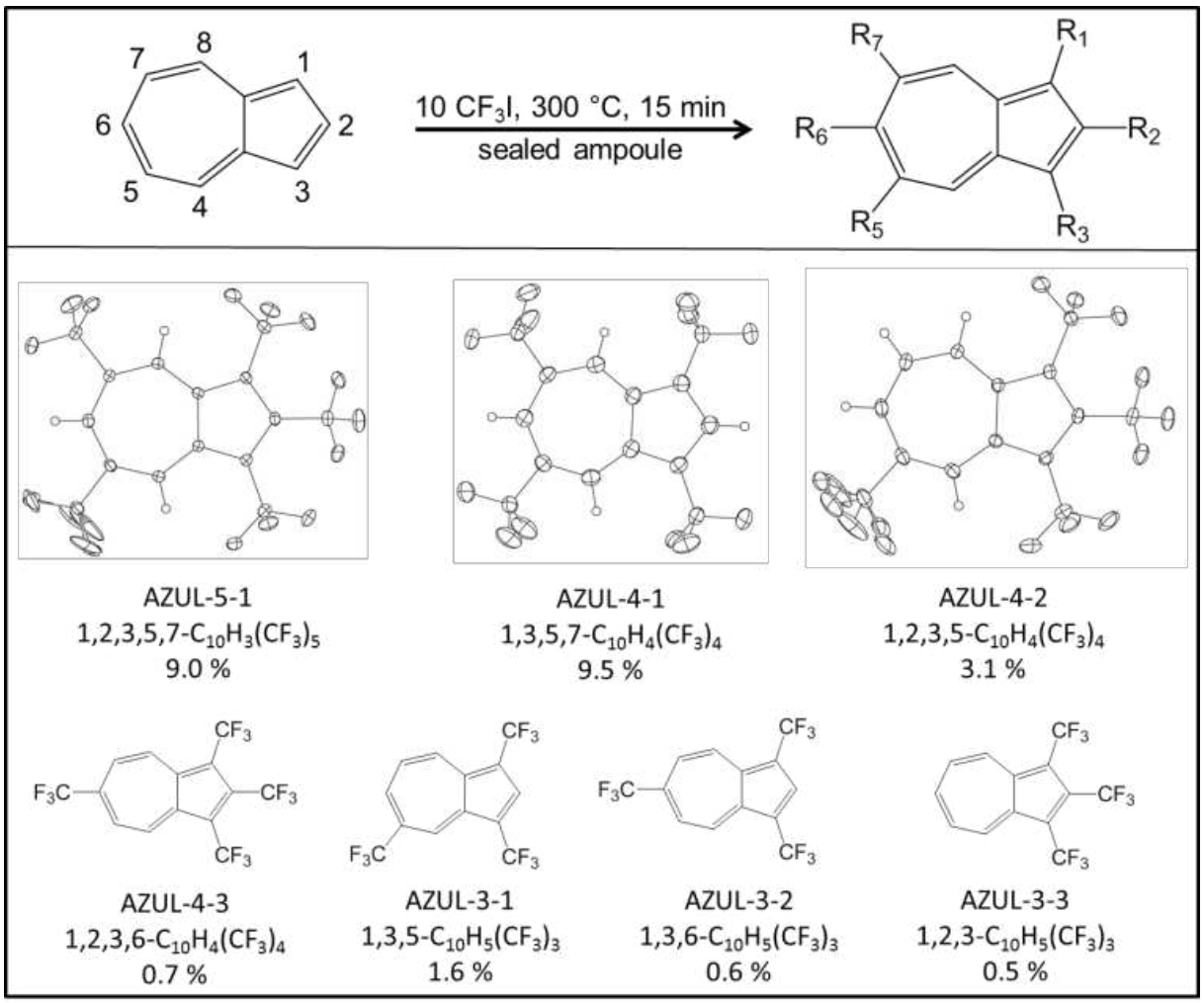

Scheme 2.1. Synthesis of AZUL$(CF_3)_{3\text{-}5}$. Abbreviations, formulas, and isolated yields are given. The X-ray structures of **AZUL-5-1**, **AZUL-4-1**, **AZUL-4-2**, are shown with thermal ellipsoids at the 50 % probability level. Overall yield = 25%.

Table 2.1. Absorption maxima for azulene$(CF_3)_n$ derivatives in hexanes (nm).

Compound	$\lambda_{max}(S_0\text{-}S_2)$	$\Delta\lambda_{max}$	$\lambda_{max}(S_0\text{-}S_1)$	$\Delta\lambda_{max}$
AZUL	341		579	
AZUL-3-1	338	−3	533	−46
AZUL-3-2	334	−7	555	−24
AZUL-3-3	329	−12	522	−57
AZUL-4-1	342	+1	537	−42
AZUL-4-2	334	−7	531	−48
AZUL-4-3	331	−10	552	−27
AZUL-5-1	338	−3	536	−43

Table 2.2. Crystallographic data and refinement parameters for three azulene$(CF_3)_n$ derivatives.

Compound	**AZUL-4-1**	**AZUL-4-2**	**AZUL-5-1**/pyrene
CCDC number	980904	980900	980901
Formula	$C_{14}H_4F_{12}$	$C_{14}H_4F_{12}$	$C_{31}H_{13}F_{15}$
Formula weight	400.17	400.17	670.41
Habit, color	plate, purple	plate, purple	rod, purple
Crystal system	triclinic	monoclinic	monoclinic
Space group	$P\bar{1}$	Cc	$P2_1/n$
a (Å)	8.9064(4)	4.8939(3)	7.2226(7)
b (Å)	9.5245(4)	32.3450(18)	16.1783(17)
c (Å)	13.4137(6)	8.6013(5)	21.334(2)
α (°)	105.240(2)	90	90
β (°)	101.240(2)	94.4396(11)	92.461(5)
γ (°)	101.091(2)	90	90
V (Å^3)	1040.70(8)	1357.44(14)	2490.6(4)
Z	3	4	4
T (K)	120(2)	100(2)	120(2)
ρ_{calc} (g cm^{-3})	1.916	1.958	1.788
$R(F)$ ($I>2\sigma(I)$)[a]	0.0497	0.0369	0.0396
$wR(F^2)$ [all data][a]	0.1173	0.0963	0.1056
Goodness of Fit	1.045	1.194	1.024
Source	$Mo_{K\alpha}$	0.41328 Å	$Mo_{K\alpha}$

[a] $R(F) = \Sigma \big| |F_o| - |F_c| \big| / \Sigma |F_o|$; $wR(F^2) = (\Sigma[w(F_o^2 - F_c^2)^2 / \Sigma[w(F_o^2)^2])^{1/2}$

Table 2.3. Crystallographic data and refinement parameters for **CORA(Bn_F)$_5$**.

Compound	**CORA(Bn_F)$_5$**	**CORA-7-1**
CCDC number	1034107	n/a
Formula	$C_{62}H_{13}F_{35}$	$C_{27}H_3F_{21}$
Formula weight	1422.72	726.29
Habit, color	needle, yellow	rhomb, colorless
Crystal system	monoclinic	triclinic
Space group	$P2_1/c$	$P\bar{1}$
a (Å)	18.1806(14)	8.9755(5)
b (Å)	25.501(2)	12.3423(7)
c (Å)	22.0827(16)	12.4101(7)
α (°)	90	104.3540(10)
β (°)	90.9790(10)	106.4830(10)
γ (°)	90	108.2000(10)
V (Å^3)	10236.5(13)	1163.73(11)
Z	8	2
T (K)	106(2)	100(2)
ρ_{calc} (g cm^{-3})	1.846	2.073
R(F) (*I*>2σ(*I*))[a]	0.0507	0.0477
wR(F^2) [all data][a]	0.1244	0.1120
Goodness of Fit	1.044	1.086
Source	0.41328 Å	0.41328 Å

[a] $R(F) = \Sigma \left| |F_o| - |F_c| \right| / \Sigma |F_o|$; $wR(F^2) = (\Sigma[w(F_o^2 - F_c^2)^2 / \Sigma[w(F_o^2)^2])^{1/2}$

Table 2.4. Crystallographic data and refinement parameters for 5 PHNZ compounds.

Compound	**PHNZ-2-1**	**PHNZ-3-1**	**PHNZ-3-2**
CCDC number	1429940	1429941	1429942
Formula	$C_{14}H_6F_6N_2$	$C_{15}H_5F_9N_2$	$C_{15}H_5F_9N_2$
Formula weight	316.21	384.21	384.21
Habit, color	plate, yellow	needle, yellow	needle, yellow
Crystal system	monoclinic	monoclinic	orthorhombic
Space group	$P2_1/n$	$P2_1/n$	*Pnma*
a (Å)	10.3419(9)	7.2537(4)	11.7529(4)
b (Å)	4.7503(4)	15.3070(8)	7.0963(2)
c (Å)	11.9705(11)	12.8472(7)	16.7040(5)
α (°)	90	90	90
β (°)	100.941(4)	102.374(3)	90
γ (°)	90	90	90
V (Å^3)	577.39(9)	1393.32	1393.15(7)
Z	2	4	4
T (K)	120(2)	120(2)	100(2)
ρ_{calc} (g cm^{-3})	1.819	1.832	1.832
R(F) (*I*>2σ(*I*))[a]	0.0365	0.0442	0.0323
wR(F^2) [all data][a]	0.1040	0.0936	0.0923
Goodness of Fit	1.051	1.034	1.059
Source	$Mo_{K\alpha}$	$Mo_{K\alpha}$	0.40651 Å

Compound	**PHNZ-4-2**	**PHNZ-5-1**	**PHNZ-6-1**
CCDC number	1429202	1429943	1429944
Formula	$C_{16}H_4F_{12}N_2$	$C_{17}H_3F_{15}N_2$	$C_{18}H_2F_{18}N_2$
Formula weight	452.21	520.21	588.22
Habit, color	prism, yellow	needle, yellow	plate, yellow
Crystal system	monoclinic	monoclinic	orthorhombic
Space group	$P2_1/c$	$P2_1/n$	$Pca2_1$
a (Å)	5.4811(3)	12.0626(5)	9.1825(4)
b (Å)	15.8196(8)	11.3398(5)	22.1387(10)
c (Å)	9.3584(4)	13.0857(6)	9.7101(4)
α (°)	90	90	90
β (°)	102.978(2)	98.974(1)	90
γ (°)	90	90	
V (Å^3)	790.73(7)	1768.05(13)	1973.95(15)
Z	2	4	4
T (K)	120(2)	100(2)	120(2)
ρ_{calc} (g cm^{-3})	1.899	1.954	1.979
R(F) (*I*>2σ(*I*))[a]	0.0328	0.0437	0.0350
wR(F^2) [all data][a]	0.0912	0.1195	0.0978
Goodness of Fit	1.054	1.080	1.122
Source	$Mo_{K\alpha}$	0.40651 Å	$Cu_{K\alpha}$

[a] $R(F) = \Sigma \left| |F_o| - |F_c| \right| / \Sigma |F_o|$; $wR(F^2) = (\Sigma[w(F_o^2 - F_c^2)^2 / \Sigma[w(F_o^2)^2])^{1/2}$

Table 2.5. Crystallographic data and refinement parameters for ANTH and ANTH* compounds.

Compound	**9,10-ANTH(Bn_F)$_2$**	**[9-ANTH*(Bn_F)]$_2$**
CCDC number	1407453	n/a
Formula	$C_{28}H_8F_{14}$	$C_{42}H_{20}F_{14}$
Formula weight	610.34	790.58
Habit, color	plate, off-white	plate, colorless
Crystal system	orthorhombic	triclinic
Space group	*Aba*2	$P\bar{1}$
a (Å)	11.5338(4)	7.4018(11)
b (Å)	24.6701(9)	10.6440(15)
c (Å)	8.0275(3)	10.7240(15)
α (°)	90	94.667(3)
β (°)	90	104.049(3)
γ (°)	90	90.993(4)
V (Å^3)	2284.15	816.3(2)
Z	4	1
T (K)	100(2)	100(2)
ρ_{calc} (g cm^{-3})	1.775	1.608
R(F) ($I>2\sigma(I)$)[a]	0.0241	0.0419
wR(F^2) [all data][a]	0.0613	0.1044
Goodness of Fit	1.054	1.083
Source	0.41328 Å	0.41328 Å

[a] $R(F) = \Sigma \left| |F_o| - |F_c| \right| / \Sigma |F_o|$; $wR(F^2) = (\Sigma[w(F_o^2 - F_c^2)^2 / \Sigma[w(F_o^2)^2])^{1/2}$

Table 2.6. Crystallographic data and refinement parameters for five TRPH compounds.

Compound	**1,2-TRPH(C_4F_8)**	**2,3-TRPH(C_4F_8)**	**1,2;5,6-TRPH(C_4F_8)$_2$**
CCDC number	1412573	1412575	n/a
Formula	$C_{22}H_{10}F_8$	$C_{22}H_{10}F_8$	$C_{26}H_8F_{16}$
Formula weight	426.30	426.30	624.32
Habit, color	needle, colorless	rod, white	plate, colorless
Crystal system	triclinic	monoclinic	orthorhombic
Space group	$P\bar{1}$	$C2/c$	$Pbca$
a (Å)	11.5700(4)	14.7137(9)	7.644(3)
b (Å)	12.5953(5)	16.5769(9)	23.271(10)
c (Å)	13.6440(5)	7.1777(4)	23.611(10)
α (°)	66.2175(8)	90	90
β (°)	69.3626(7)	107.2763(16)	90
γ (°)	77.8561(7)	90	90
V (Å^3)	1697.30(11)	1671.71(16)	4200(3)
Z	4	4	8
T (K)	100(2)	100(2)	100(2)
ρ_{calc} (g cm^{-3})	1.668	1.694	1.975
$R(F)$ ($I>2\sigma(I)$)[a]	0.0414	0.0481	0.0653
$wR(F^2)$ [all data][a]	0.0983	0.1193	0.1229
Goodness of Fit	1.027	1.026	1.198
Source	0.41328 Å	0.41328 Å	0.41328 Å

Compound	**1,2;5,6;10,11-TRPH(C_4F_8)$_3$**	**2,3;6,7-TRPH(C_4F_8)$_2$**
CCDC number	n/a	n/a
Formula	$C_{30}H_6F_{24}$	$C_{26}H_8F_{16}$
Formula weight	822.35	624.32
Habit, color	rhomb, colorless	plate, colorless
Crystal system	monoclinic	triclinic
Space group	$C2/c$	$P\bar{1}$
a (Å)	24.3822(10)	11.9435(4)
b (Å)	9.1812(4)	14.9914(5)
c (Å)	23.8682(11)	25.3126(10)
α (°)	90	79.8990(10)
β (°)	93.2387(11)	85.8210(11)
γ (°)	90	79.1420(11)
V (Å^3)	5334.6(4)	4378.4(3)
Z	8	8
T (K)	100(2)	100(2)
ρ_{calc} (g cm^{-3})	2.048	1.894
$R(F)$ ($I>2\sigma(I)$)[a]	0.0346	0.0450
$wR(F^2)$ [all data][a]	0.0882	0.1184
Goodness of Fit	1.028	1.025
Source	0.41328 Å	0.41328 Å

[a] $R(F) = \Sigma \left| |F_o| - |F_c| \right| / \Sigma |F_o|$; $wR(F^2) = (\Sigma[w(F_o^2 - F_c^2)^2 / \Sigma[w(F_o^2)^2])^{1/2}$

CHAPTER 3: Trifluoromethyl Substituted Perylenediimides: Synthesis, Isolation, X-Ray Structures, Optical and Electronic Properties, and Use in OPV Active Layers

3.1 Introduction

Recent research on synthetic derivatization of perylene diimides (PDIs) has resulted in the development of new methods targeting incorporation into advanced electronics,[153] such as organic transistors[6,154] and photovoltaics.[155,156] Figure 3.1 shows three locations (imide, bay, and *ortho* positions) on a PDI molecule where chemical modifications can be carried out using one of the many chemical reactions developed in the past decades. Judicious modifications at all three PDI positions can finely tune the physical, optical, and electronic properties of PDIs. Historically, imide substitutions were first developed, followed by core substitutions in the bay region (1, 6, 7, and 12) predominately beginning with dibromo perylenedianhydride (PDA-Br_2, see Scheme 1 for abbreviation method).[157] More recently, regioselective substitution at *ortho* positions (2, 5, 8, and 11) using ruthenium catalysis has enabled core modification without the significant core twisting observed in most bay-substituted PDIs.[155,158-161]

Due to different reactivities at bay and ortho positions, each substitution typically requires specific reaction conditions. The synthesis of octachloro PDI is the only literature example where both the bay and *ortho* region were simultaneously substituted.[162-164] In 2014, Wang and coworkers published two papers on PDIs substituted at the bay and *ortho* positions starting from bay-substituted tetrachloro PDIs.[165,166] This method was utilized by Wüthner and coworkers to synthesize the most electron-withdrawing PDI derivative, PDI(F7Bu)-1,6,7,12-Cl_4-2,5,8,11-$(CN)_4$.[167] There has yet to be a synthetic procedure to substitute at the bay and *ortho* positions where all four bay positions were not substituted with chlorine atoms and only one example of simultaneous bay and *ortho* substitutions.

The first example of perfluoroalkyl core modification of PDIs by Wang and coworkers via copper-mediated reactions of 1,7-dibromo PDIs with perfluorobutyl iodide and perfluorooctyl iodide in 2008 had yields as high as 90%.[168] Field effect transistors made with these compounds were measured and the highest field effect mobility in ambient air was 0.052 $cm^2\ V^{-1}\ s^{-1}$ with PDI(F7Bu)-1,7-$(C_8F_{17})_2$.[168] At nearly the same time, Qian and coworkers released a patent on PDI perfluoroalkylation,[169] and in 2009, they introduced CF_3 substituents to the PTCDA core by synthesizing a mixture of PDA-1,6-$(CF_3)_2$ and PDA-1,7-$(CF_3)_2$ in a three step process from soluble 3,4,9,10-tetra(*n*-butyoxy-carbonyl)-perylene.[170] The same group then used the mixture of PDA-$(CF_3)_2$ isomers and analogous PDA-1-(C_8F_{19}) and PDA-$(C_8F_{19})_2$ to create perfluoroalkyl PDIs with a variety of imide substituents.[171] More recently, Wasielewski and coworkers synthesized three trifluoromethyl perylene imides and diimides via bromine substitution.[172] Thus, the current family of core-perfluoroalkylated PDIs is limited to the above mentioned compounds, and the existing syntheses are limited to substitution at the bay region.

Progress in fundamental understanding of charge transport properties of crystalline PDIs as a function of solid-state packing, electronic coupling, and molecular electronic properties has been made in recent years, and molecular design guidelines have been proposed.[6,164,173,174] In particular, analysis of thin-film organic transistors made of modified PDIs and other organic semiconductors showed that compounds with an increased gas-phase electron affinity ($EA_{(g)}$ > 2.8 eV) exhibited consistently improved air-stability and higher electron mobility.[6] To further the progress in the design of next-generation, efficient, and functional PDI based materials, it is important to determine, understand and, if possible, reliably predict effects of chemical substitutions on the electronic properties of PDIs.

The quantitative measures of electron withdrawing effects can be experimentally obtained from solution reduction potential (and then deriving E_{LUMO} energy), gas-phase electron affinity, or solid-state electron affinity.[175] Complementary results can also be estimated from theoretical calculations. Among experimental methods, inverse photoelectron spectroscopy (IPES) has been established as a technique for determination of the solid-state EAs, and measurements have been reported for several PDIs [PDI(F7Bu)-1,6,7,12-Cl_4, PDI(F7Bu)-1,7-F_2, PDI(F7Bu), PDI(dipp), PDI(CH_3), and PDI(H)].[176-178] However, insufficient instrument resolution (±0.1-0.3 eV) currently hampers accurate comparisons of organic acceptor materials with close EAs. A highly precise method of photoelectron spectroscopy for gas-phase anions has been applied to determine EAs for many parent PAHs and some of the derivatives,[25,179] but not for any PDI molecules.

By far, the most common and convenient experimental technique applicable to soluble PDIs is cyclic voltammetry. Table 3.1 contains an extensive compilation of electrochemical data for core-derivatized PDIs with more positive reduction potentials than corresponding core-unsubstituted PDIs. Reported values span nearly 1200 mV, an impressive expansion of the PDI acceptor library since 2011 when Wüthner and Stolte reviewed electron-poor PDIs with ca. 800 mV range.[154] After a brief survey of Table 3.1, it became apparent that direct and accurate comparison of the electrochemical potentials is possible in many, but not all, cases due to similar experimental parameters and conditions used by researchers from different groups. Some reported E_{LUMO} values exhibit significant discrepancies due to inconsistencies in the methods of their calculations. These problems in E_{LUMO} estimations will be further addressed in this dissertation; they are not unique for PDIs, and were noted earlier for other systems such as donor polymers and fullerene acceptors.[68,180,181]

In this work, a method to directly (poly)trifluoromethylate PTCDA in one step with CF_3I at elevated temperatures and without solvent or catalysts to produce a mixture of PDA-$(CF_3)_{2\text{-}4}$ has been developed. The mixture can then easily be converted to corresponding PDI(R)-$(CF_3)_{2\text{-}4}$ by typical imidization procedures and isolated by HPLC to isomeric purity. These are the first examples of: (i) more than two perfluoroalkyl groups being substituted on the PDI core; (ii) successful isolation of multiple PDI(R)-$(CF_3)_n$ isomers; (iii) solvent-free core substitution of PTCDA; and (iv) introducing the same substituents at *both* the bay and *ortho* positions of a PDI core without full chlorine substitution at the bay region. This approach involves direct trifluoromethylation of the perylene core at high temperatures without the need for also synthesizing or purchasing high-cost commercial samples of halogenated PDI precursors. While the synthesis is not selective towards one product, the effective chromatographic separation method allows for straightforward isolation of several single-isomer components from a crude mixture for fundamental studies.

This series of structurally characterized compounds appears to be a particularly attractive candidate to study electronic effects in PDIs: (i) they form a set of molecules with a gradually increased substitution degree, PDI(R)-$(CF_3)_{0\text{-}4}$; (ii) two different isomers for most compositions were isolated allowing the study of substitution position effects; (iii) in one case, a CF_3 group was replaced with a CN group permitting direct comparison of substituent electron withdrawing effects; and (iv) electronic trends determined for these (poly)trifluoromethyl compounds could be compared and correlated with the available literature data on other electron-poor PDIs and the examples of bay-substituted bis-perfluoroalkyl PDIs among them.

To study electronic properties of the new PDIs, two experimental techniques were chosen: cyclic voltammetry for reduction potentials in solution and LT PES for gas-phase EAs.

While the former technique is commonly employed due to its simplicity and high precision, the LT PES method is considerably more sophisticated and requires specific expertise,[83] hence it is more rarely used. At the same time, LT PES may provide absolute values of adiabatic electron affinity in the gas phase with high precision, which is the fundamental quantity characterizing the ability of a molecule to accept an electron. This characteristic does not depend on the solvation or polarization energies, and thus it is the best to be used to validate theoretical gas-phase EA calculations.

The goals of this work are (i) to describe the synthesis, isolation, molecular structures, solid-state packing and electronic properties of a new family of twelve (poly)trifluoromethylated PDIs and a cyano derivative; (ii) quantitatively determine electronic effects of CF_3 and CN EWGs in solution for these new compounds; (iii) determine electronic effects of CF_3 in the gas-phase; (iv) compare these effects to other EWGs, and determine general trends in PDI acceptor electronic properties based on compiled literature data and new data from this study; and (v) study charge transfer characteristics between conjugated polymer donors and PDIs.

This chapter involves work that has been reproduced from *Eur. J. Org. Chem.* **2015**, DOI: 10.1002/ejoc.201501024 with permission from John Wiley and Sons. The LT PES experiments were performed by Xue-Bin Wang and coworkers, Eric Bukovsky helped collect and refine the XRD data sets of PDIs with $Mo_{K\alpha}$, and Hilary Marsh helped collect powder XRD data. Tyler Clikeman primarily performed all syntheses and spectroscopic characterization, cyclic voltammetry, thin film and TRMC experiments, and most single crystal XRD collections, refinements, and analyses.

3.2 Synthesis of Perylene Diimides

In a typical synthesis, PTCDA and CF_3I gas were heated at 400 °C in a gradient-temperature gas-solid (GTGS) hot plate reactor[28] for 4.5 h to produce a mixture of PDA-$(CF_3)_{2\text{-}4}$ (Scheme 1, see experimental section for a detailed experimental procedure). An alternative flow-tube method was also employed for the synthesis of PDA-$(CF_3)_{2\text{-}4}$, yielding similar products, but with less economical use of CF_3I reagent. Most of the product and a small amount of PTCDA sublimed from the hot zone of the reactor and condensed at the cold zone using either reaction method; no decomposition was detected in the sublimed material indicating high thermal stability. The products were easily separated from unreacted PTCDA since the product mixture was readily soluble in organic solvents such as dichloromethane and toluene. Unreacted PTCDA was successfully used in subsequent reactions to produce similar product mixtures with comparable yields. The soluble product mixture underwent subsequent imidization reactions in solution. In these reactions, the mixtures of PDA-$(CF_3)_{2\text{-}4}$ were heated to reflux in propionic acid with primary amines, *n*-butylamine or 1H,1H-perfluorobutylamine, according to standard literature procedures[26,182] to form mixtures of PDI(Bu)-$(CF_3)_{2\text{-}4}$ and PDI(F7Bu)-$(CF_3)_{2\text{-}4}$, respectively (Scheme 1, see experimental section for a more detailed experimental procedure). The trifluoromethylation and imidization reactions were monitored with ^{19}F NMR, see Figures 3.2 and 3.3.

The PDIs were then purified by flash chromatography to remove monoimides and excess reagents and then separated further by HPLC with a Cosmosil Buckyprep column (see Figure 3.4). Two predominant isomers of PDI(Bu)-$(CF_3)_2$, PDI(Bu)-$(CF_3)_3$, and PDI(Bu)-$(CF_3)_4$ were isolated by HPLC. The analogous isomers of PDI(F7Bu)-$(CF_3)_2$, PDI(F7Bu)-$(CF_3)_3$, and only the

major isomer of PDI(F7Bu)-$(CF_3)_4$ were also separated. Other minor isomers of PDI(R)-$(CF_3)_2$ and PDI(R)-$(CF_3)_3$ were observed in the mixtures, but will not be discussed further.

For comparison, unsubstituted PDI(Bu) and PDI(F7Bu) were also synthesized according to literature procedures.[174,183,184] Preliminary experiments to substitute PDI(Bu) without solvent were also performed using the GTGS reactor. A single peak in the ^{19}F NMR spectrum of the crude reaction mixture indicated CF_3 substitution in the bay region and most likely the presence of the mono adduct, PDI(Bu)-1-(CF_3), which was confirmed with NI-APCI MS analysis. This single perfluoroalkylation was also observed by Li et al. when PDIs were reacted in DMSO with $C_nF_{2n+1}I$ (n = 4 and 8).[185] Their main product was the selective monoaddition in the bay region with 60% yields and secondary products were 1,7- and 1,6-bis adducts.

At room temperature, the solubility of PDI(Bu)-1,7-$(CF_3)_2$ was 11 mM and 16 mM in toluene and dichloromethane, respectively. In hot toluene, the solubility increased to 15 mM. Increasing the alkyl chain length of the imide substituent is known to increase the solubility of PDIs. For example, the solubility of a mixture of PDI(C_8H_{17})-1,7-$(CF_3)_2$ and PDI(C_8H_{17})-1,6-$(CF_3)_2$ was reported to be 15× greater than a mixture of PDI(Bu)-1,7-$(CF_3)_2$ and PDI(Bu)-1,6-$(CF_3)_2$ in dichloromethane.[171]

The substitution patterns and compositions of all PDIs were determined by ^{19}F and ^{1}H NMR, negative-ion atmospheric pressure chemical ionization (NI-APCI) mass spectrometry, and UV-visible spectroscopy (see experimental section for more details). Singlets with chemical shifts between −58.5 and −59.5 ppm in ^{19}F NMR spectra correspond to CF_3 groups in the bay region and the singlets between −63 and −64 ppm correspond to CF_3 groups attached at the *ortho*

positions (Figures 3.5 and 3.6). Similarly, the singlets corresponding to H atoms in the bay region were more shielded than ^{1}H signals originating from the *ortho* H atoms.

A new method to selectively substitute at the *ortho* positions in bis-trifluoromethyl PDIs was applied involving nucleophilic hydrogen substitution with cyanide; this method was adopted from earlier published cyanation reactions for other substrates.[64,124] Tetraethylammonium cyanide was added to PDI(Bu)-1,7-$(CF_3)_2$ in dichloromethane solution and then quenched with *p*-chloranil (Scheme 2). The symmetrically equivalent core carbon atoms, C5 and C11, are the core carbon atoms that are least sterically hindered by the two CF_3 groups in PDI(Bu)-1,7-$(CF_3)_2$ and are likely candidates for nucleophilic attack. Mass spectrometry showed an increase of 25 *m/z* in the molecular anion mass due to substitution of hydrogen with one CN group, and the ^{19}F NMR spectrum exhibited two singlets, collectively indicating the substitution of one H atom with CN to form a new asymmetric PDI derivative, PDI(Bu)-1,7-$(CF_3)_2$-5-(CN). Proton NMR peaks from PDI(Bu)-1,7-$(CF_3)_2$-5-(CN) resemble the ^{1}H signals from PDI(Bu)-1,7,5-$(CF_3)_3$ (Figure 3.7). One ^{1}H singlet from the perylene core was more shielded with respect to the same H6 atom in PDI(Bu)-1,7,5-$(CF_3)_3$ while the other ^{1}H peaks had very similar chemical shifts. Shifting of this singlet proton resonance upfield suggested that the proton was near a stronger electron-withdrawing substituent in PDI(Bu)-1,7-$(CF_3)_2$-5-(CN) compared to PDI(Bu)-1,7,5-$(CF_3)_3$. A similar upfield trend in other PAHs with varying strength of electron-withdrawing groups has been observed previously.[25,136,179] Nucleophilic substitution with a cyano group on C5 was expected from steric reasons and also had the largest influence on the ^{1}H resonance of H6, indicating that PDI(Bu)-1,7-$(CF_3)_2$-5-(CN) has the same substitution pattern as PDI(Bu)-1,7,5-$(CF_3)_3$, which was later confirmed by single-crystal XRD experiments. Straightforward HPLC

separation of PDI(Bu)-1,7-$(CF_3)_2$-5-(CN) from PDI(Bu)-1,7-$(CF_3)_2$ showed that the versatile Cosmosil Buckyprep column could be useful for PDIs with core substituents other than CF_3.

Preliminary cyanation experiments with PDI(F7Bu) were also conducted to see if CN could be substituted on a core-unsubstituted PDI without the use of more expensive halogenated precursors as was done in the previous reports on PDI cyanation.[26] Tetraethylammonium cyanide was added to PDI(F7Bu) in dichloromethane solution, quenched with *p*-chloranil, and the product mixture was isolated with flash chromatography. Mass spectrometry experiments revealed the addition of up to three CN moieties, see Figure 3.8. This reaction could be further optimized and utilized to introduce CN before CF_3 in order to minimize core twisting and enhance intermolecular PDI core interactions.

3.3 Optical Properties

The absorption and emission spectra of the new PDIs were obtained in DCM and are shown in the Figures 3.9–3.12; the absorption and emission maxima are given in Table 2. The CF_3 groups in the bay region appear to have the largest influence on absorption maxima, whereas the additional CF_3 or CN groups on *ortho* positions have negligible influence. All 12 core-substituted PDIs studied have absorption maxima blue-shifted by 13-18 nm from parent PDI(R). Twisting of the perylene core is similar for this PDI series (see X-ray section) and is hypothesized to cause the blue-shift.[171] Substitution at the 1,6 position leads to broadening of the peaks and the absorption event near 446 nm is barely distinguishable as compared with the 1,7 isomers and parent PDI(R). Partial fluorination of the butyl imide groups has very little influence on the absorption spectra which was also observed for other core-perfluoroalkyl-substituted PDIs.[168] The imide group has a minimal effect on the absorption and emission spectra because of HOMO and LUMO orbitals nodes at the imide position.[186,187] All 1,6 isomers

exhibited larger Stokes shifts than the corresponding 1,7 isomers, which is consistent with other PDI series.[171,188] Absorption and emission spectra broadening for 1,6 isomers with respect to corresponding 1,7 isomers has been observed in some derivatives,[182,189] but was not always the case with the isomeric pairs.[190,191]

Time-resolved photoluminescence (TRPL) studies with several PDIs were performed using dilute dichloromethane solutions to obtain emission lifetimes. All solutions were excited at 488 nm and the emission was detected at 530 nm. The PDIs exhibited decays that were fitted with monoexponential functions to extract excited state lifetimes, see Table 2. The lifetimes of core-modified PDIs are all longer than PDI(Bu) and the lifetimes of 1,6 derivatives are all longer than the 1,7 derivatives. Conversely, in a series of diaryl-substituted PDIs, the 1,7 isomers had longer lifetimes than corresponding 1,6 isomers. [188] In another study, PDI(C_8H_{17})-1,6-(2,4-bis(*t*-Bu)-Phenyl)$_2$ had a longer lifetime than the 1,7 isomer in three different solvents by ca. 0.5 ns, but in the same study, PDI(C_8H_{17})-1,6-(dipyrrolidinyl)$_2$ exhibited shorter lifetimes than the 1,7 isomer (1.27 vs. 6.08 ns in hexane).[182] Apparently, the excited state lifetime trends among different isomers are highly dependent on the core substituents.

3.4 Molecular Structures and Solid State Packing

Intermolecular interactions in the solid state will undoubtedly have profound effects on solid-state charge mobility. Progress in the fundamental understanding of charge transport properties of crystalline PDIs as a function of solid-state packing, electronic coupling, and molecular electronic properties has been made in recent years, and molecular design guidelines have been proposed.[6,164,173,174] For this reason, several PDI derivatives were analyzed with single crystal XRD to study possible charge transport pathways via close intermolecular interactions.

The slow evaporation of DCM or toluene solutions at room temperature or at 2 °C in air resulted in single crystals of ten compounds suitable for single crystal XRD (see experimental section for more details). Six structures included solvent molecules and four structures were solvent free (see Table 3). Steric effects from CF_3 groups in the bay region and packing motifs led to asymmetric twisting of the perylene core with an average torsion angle of 24.3°, ranging from 20.8° to 27.8° (see Table 3 for all torsion angles). The reported torsion angles are the torsion angles of two inner bay carbon atoms with C1 and C12 or C6 and C7. Substitution at the *ortho* positions had little influence on the torsion angles compared to bay substitution and packing motifs. Owing to the twisted π -system, atropo-enantiomers (*P*- and *M*-enantiomers) were observed in the solid state for all 10 PDI structures regardless of solvent inclusion. The presence of conformational chirality is typical for PDI derivatives and the enantiomers can even be separated in some cases.[192] Close π-π interactions were observed in the solid state for these PDIs despite having twisted cores, bulky fluorinated groups, and solvent inclusion.

Two molecules with the same core substitution pattern, PDI(Bu)-1,7,5-$(CF_3)_3$ and PDI(F7Bu)-1,7,5-$(CF_3)_3$, crystallized in the monoclinic space group $P2_1/n$ (Figure 3.13). They both pack in *PM*-enantiomer pairs that are arranged in a "herringbone" fashion. They were both crystallized from the slow evaporation from toluene solutions, but PDI(Bu)-1,7,5-$(CF_3)_3$ contains two toluene molecules between each enantiomer pair and PDI(F7Bu)-1,7,5-$(CF_3)_3$ is solvent free. It appears that two toluene molecules in the PDI(Bu)-1,7,5-$(CF_3)_3$ structure fill the void near butyl chains that is occupied by bulkier fluorinated butyl chains in the PDI(F7Bu)-1,7,5-$(CF_3)_3$ structure. PDI molecules are offset along the long PDI axis resulting in only one type of π-π interaction from partial naphthalene subunit overlap. The least-squares planes of the naphthalene subunits are parallel to each other and 3.40 Å apart with PDI(F7Bu)-1,7,5-$(CF_3)_3$ molecules,

which is closer than 3.43 Å observed in the PDI(Bu)-1,7,5-$(CF_3)_3$/toluene structure. This closer interaction appears to result from PDI(F7Bu)-1,7,5-$(CF_3)_3$ having a less twisted perylene core. Bay torsion angles for PDI(F7Bu)-1,7,5-$(CF_3)_3$ are 22.8° and 24.8°, which are less than 23.7° and 25.7° observed for PDI(Bu)-1,7,5-$(CF_3)_3$. Different torsion angles for trifluoromethyl PDIs with the same substitution pattern most likely arise from interactions with intercalated toluene. The toluene molecule in PDI(Bu)-1,7,5-$(CF_3)_3$ is rotated with respect to the nearest naphthalene subunit by 7.4° and the closest toluene C atom overlapping the naphthalene plane is 3.34 Å.

Eight other PDIs crystallized in the triclinic space group $P\bar{1}$. PDI(Bu)-1,7-$(CF_3)_2$ and PDI(F7Bu)-1,7-$(CF_3)_2$ crystallized without solvent inclusion and pack in columns consisting of alternating *P*- and *M*-enantiomers that are offset from one another which leads to two types of π-π interactions in each structure (Figure 3.14). All least-squares planes of overlapping naphthalene subunits in the structure of PDI(Bu)-1,7-$(CF_3)_2$ are essentially parallel. In the *P*- over *M*-enantiomer pair for PDI(Bu)-1,7-$(CF_3)_2$ depicted in Figure 3.14A, there are six out of ten naphthalene atoms in the *M*-enantiomer that lie under the *P*-enantiomer naphthalene fragment. The perpendicular distance of the *M*-enantiomer to the least-squares plane of the *P*-enantiomer fragment is 3.68 Å. In the *M*- over *P*-enantiomer pair shown on Figure 3.14, there are only two naphthalene subunit atoms that overlap, but the distance between the mean planes is only 3.33 Å.

In one intermolecular interaction from PDI(F7Bu)-1,7-$(CF_3)_2$, the *M*- over *P*-enantiomer pair depicted on Figure 3.14B, the two enantiomers are offset mostly along the long PDI axis where one naphthalene subunit of one enantiomer is partially overlapped with the naphthalene subunit of the other enantiomer. The mean planes of these naphthalene subunits are essentially parallel and 3.98 Å apart. In the other interaction, *P*- over *M*-enantiomers are offset from each other mostly along the short PDI axis and there is very little overlap of the perylene core.

Furthermore, the naphthalene subunits have opposite tilts and the mean planes of overlapping naphthalene subunits are not parallel, but tilted by 28.2°. The closest overlapping naphthalene C atom from this interaction is 3.42 Å from the adjacent naphthalene subunit.

Similarly, PDI(Bu)-1,7,5,11-$(CF_3)_4$ crystallized in $P\bar{1}$ with no solvent. The PDI molecules are more shifted on the long PDI axis than PDI(Bu)-1,7-$(CF_3)_2$ and PDI(F7Bu)-1,7-$(CF_3)_2$, presumably due to the presence of four bulky CF_3 groups, which results in only one type of naphthalene subunit overlap. Only three naphthalene C atoms overlap and the distance between the mean planes of the naphthalene subunits is 3.69 Å. This distance is comparable to one of the interactions observed with PDI(Bu)-1,7-$(CF_3)_2$ despite the presence of two more CF_3 substituents.

Bay torsion angles in PDI(Bu)-1,7-$(CF_3)_2$ are 23.0° and 22.1° and more varied with PDI(F7Bu)-1,7-$(CF_3)_2$, 26.2° and 20.8°. These two PDIs exhibit similar packing to the only other published trifluoromethyl PDI crystal structure, PDI(Cy)-1,7-$(CF_3)_2$.[172] The intermolecular naphthalene subunit plane distances in the PDI(Cy)-1,7-$(CF_3)_2$ structure are 3.56 and 3.70 Å, which are in between the distances measured for PDI(Bu)-1,7-$(CF_3)_2$ and PDI(F7Bu)-1,7-$(CF_3)_2$. The size and shape of the imide substituent clearly influences the packing arrangements of PDIs that have the same core substitution. The torsion angles are slightly larger on average in PDI(Cy)-1,7-$(CF_3)_2$, 24.2° and 26.6°. Crystal structures of PDI(Bu)-1,7-$(C_4F_9)_2$ and PDI(F7Bu)-1,7-$(C_4F_9)_2$ demonstrate that the torsion angles are even larger with longer R_F core substituents, ranging from 25.0° to 29.5°.[168] Only one parallel naphthalene subunit overlap exists in each of the two C_4F_9 structures and the Bu structure has shorter overlap distances than the F7Bu structure (3.59 and 3.77 Å, respectively), which is comparable with the CF_3 derivatives presented here.

PDI(F7Bu)-1,6-$(CF_3)_2$, PDI(F7Bu)-1,6,8-$(CF_3)_3$, and PDI(F7Bu)-1,7,5,11-$(CF_3)_4$ all crystallized in a similar fashion with two toluene molecules per PDI (Figure 3.15). The structure of PDI(F7Bu)-1,6-$(CF_3)_2$ is of low quality, but the core substitution pattern, unit cell dimensions, and solid state packing motif are not in question (see Table 3.4). A plot of unit cell volumes vs. number of CF_3 substitutions revealed a linear relationship with an increase in volume = 75.5 $Å^3$ per CF_3 group (Figure 3.16, R^2 = 0.99963). There are no PDI-PDI core interactions in these structures because the PDIs are separated by two toluene molecules, one over each naphthalene subunit. They pack in columns along the *a*-axis with alternating PDI and toluene layers in a pseudo hexagonal-close-packed array. Each column consists of only one enantiomer and the columns stack in rows along the *b*-axis with only one type of enantiomer in each row. Parallel PDI(F7Bu)-1,6,8-$(CF_3)_3$ are separated by two toluene molecules rotated 3.4° and 5.1° from nearest naphthalene subunits. The closest overlapping toluene C atoms to naphthalene planes are 3.46 and 3.36 Å for the toluene rotated 3.4° and 3.47 and 3.49 Å for the toluene rotated 5.1°. Parallel PDI(F7Bu)-1,7,5,11-$(CF_3)_4$ molecules are separated by two toluene molecules rotated 3.4° and 4.2° with respect to mean planes of naphthalene subunits. The toluene rotated 3.4° only overlaps one naphthalene subunit and the closest toluene C atom to naphthalene mean plane distance is 3.48 Å. The other toluene partially overlaps two naphthalene subunits and the closest distances are 3.51 and 3.50 Å.

Single crystals of PDI(Bu)-1,6-$(CF_3)_2$ were grown by slow evaporation of a dichloromethane solution. It crystallized with one dichloromethane per two PDI(Bu)-1,6-$(CF_3)_2$ molecules in the triclinic space group $P\bar{1}$. It contained two unique *P*-enantiomers in the asymmetric unit that stacked in parallel columns in a pseudo hexagonal-close-packed array with dichloromethane between columns. Four different bay torsion angles exist from two different

PDI(Bu)-1,6-$(CF_3)_2$ molecules in the asymmetric unit, 21.9° and 22.9° in one molecule and 25.1° and 24.5° in the other molecule. Four types of molecules are present within the columns, since both enantiomers are present in the asymmetric unit with $P\bar{1}$ symmetry. The molecules stack in repeating *PP* and *MM* enantiomer pairs offset within a slanted column. Enantiomerically pure planes are formed by adjacent *PP* or MM pairs in the *a*-*c* plane. Four types of molecules lead to three types of π-π interactions, (*PP(MM), PM* and *MP* overlap; *PP* and *MM* pairs are symmetrically equivalent) with the most core overlap between *P*- over *M*- shown in Figure 3.17 (red over blue). The mean planes of the overlapping naphthalene subunits in the *P*- over *M*- pair are essentially parallel and are separated by 3.84 Å. The *PP* and symmetrically equivalent *MM* pairs only have some core overlap. In this case, the naphthalene subunit planes are not parallel, but at angles of 9.2° and 11.5° to each other and the closest carbon atom distances of one naphthalene subunit to the mean plane of the naphthalene subunit of the adjacent molecules are 3.16 and 3.58 Å. In the third pair, *M*- over *P*-, there is essentially no core overlap and the naphthalene subunits planes are tilted by 23.4°.

Single crystals of PDI(Bu)-1,7-$(CF_3)_2$-5-(CN) were grown by slow evaporation of a toluene solution. It crystallized with two PDI molecules and one disordered toluene molecule (disordered about a special position) in the triclinic space group, $P\bar{1}$. The disordered toluene is centered between the central hexagons of two PDI molecules and has no π overlap with the nearest naphthalene subunits (Figure 3.18). Only one type of naphthalene subunit overlap exists. The two overlapping subunits each contain the CN group and the mean planes are separated by 3.66 Å. The two torsion angles of the PDI core are 25.6° and 27.8°, the latter being the largest PDI torsion angle studied in this work.

3.5 Electronic Properties of Perylene Diimides

3.5.1 Reduction Potentials

Electrochemical measurements of the purified compounds were performed using 0.1 M $TBAPF_6$ in DCM at a scan rate of 100 $mV \cdot s^{-1}$ with $FeCp_2^{+/0}$ as an internal standard (see Tables 3.1 and 3.2). The measured reduction potential of PDI(Bu) (−1.08 V) is close to the value reported earlier in THF (Table 3.1, entry 4); for PDI(F7Bu) the $E_{1/2}^{0/-}$ value of −0.95 V measured here is the same as the value reported by Würthner et al. (Table 3.1, entry 12). However, this value differs by 0.14 V from another reported value (Table 3.1, entry 15), the reasons of such deviation are unclear at this time.

All new compounds exhibited two reversible reduction events and no oxidation events were observed within the solvent window; see Figure 3.19 for representative cyclic voltammograms and Figures 3.20–3.22 for all spectra. A plot showing the linear correlations of $E_{1/2}$ values for the series of PDI(Bu)-$(CF_3)_n$ and PDI(F7Bu)-$(CF_3)_n$ compounds versus n is given in Figure 3.10. Such a linear correlation suggests that CF_3 substituents have virtually the same electron withdrawing effect whether they are attached to the bay or *ortho* regions. The first reduction becomes more positive by 0.14 V per CF_3 group for both series of compounds; a slope of 0.14 V is found for each series whether or not the $E_{1/2}^{0/-}$ of PDI(R) is included. A similar increase in the first reduction potential of 0.15 V per CF_3 substitution for perylene$(CF_3)_{4\text{-}6}$ has been observed by the Strauss group.[25] Comparing PDI(dipp)-$(C_nF_{2n+1})_{1,2}$ (n = 4 and 8) (Table 3.1, entries 87, 88, 91, 97, 98, and 101) shows the same value of 0.14 V per R_F and indicates that the chain length of the core perfluoroalkyl group may not affect the reduction potential.[185] The second reduction only changes by 0.10 V per CF_3 group for PDI(Bu)-$(CF_3)_n$ and PDI(F7Bu)-$(CF_3)_n$ (n = 0-4). Smaller increases in reduction potentials for the second reduction event versus

the first reduction has also been observed in other PDI series.[165] Substitution of both Bu imide groups for F7Bu has nearly the same effect on $E_{1/2}^{0/-}$ as substitution of one H atom for CF_3 at the core. In some studies it was believed that the imide chain did not affect the electronic properties because of the node in the HOMO and LUMO orbitals at the imide group.[156,173,182,186,188,193] However, other studies have clearly demonstrated that the imide chain does have an effect on the electrochemical behavior, [6,26] which is consistent with the series of compounds studied in this work and literature discussion below.

Substituting a hydrogen atom for CN at the *ortho* position resulted in a simple and controlled method to further tune the reduction potentials. Introduction of one CN group increased $E_{1/2}^{0/-}$ by 0.21 V, which is 1.5 times larger than adding a third CF_3 group on PDI(Bu)-1,7-$(CF_3)_2$. This increase per CN is the same as observed by Perrin and Hudhomme when introducing two CN groups to the bay region to PDI(C_5H_{11}).[194] Substitution with CN at *ortho* positions of PDI(Bu)-1,6,7,12-Cl_4 or PDI($C_{15}H_{31}$) increased the first reduction by an average 0.15 V per CN in both studies.[165,195]

3.5.2 Gas-Phase Electron Affinity of PDI(Bu)-$(CF_3)_{2,3,4}$

In 2013, the Strauss group reported that $E_{1/2}^{0/-}$ increases linearly by 0.73 V eV^{-1} with respect to gas-phase EA for a series of PAH and PAH$(CF_3)_n$ derivatives.[64] In this work, the gas-phase electron affinity of 3 PDIs (PDI(Bu)-1,7-$(CF_3)_2$, PDI(Bu)-1,7,5-$(CF_3)_3$, and PDI(Bu)-1,7,5,11-$(CF_3)_4$) using LT PES was measured by collaborators at PNNL,[83] Figure 3.11. Gas-phase electron affinity has not been measured for any PDIs prior to this work. In agreement with the trend observed for reduction potentials measured in solution for these compounds, the EA linearly increases with the degree of trifluoromethylation. Importantly, the absolute EA values of each of these three PDIs are significantly higher than those of fullerenes C_{60} and C_{70},[71,196] and

any poly(trifluoromethyl)PAH previously measured using the same method.[64,179,197] A plot of $E_{1/2}^{0/-}$ vs. EA reveals that $E_{1/2}^{0/-}$ increases linearly by 0.76 V eV^{-1} with respect to EA, Figure 3.12. This linear relationship was then used to predict the EA for the other trifluoromethyl PDIs prepared in this work. The predicted EA values span 0.88 eV from PDI(Bu) (2.66 eV) to PDI(F7Bu)-1,7,5,11-$(CF_3)_4$ (3.54 eV), see Figure 3.13. Electron affinities of PDI(Bu)-1,7-$(CF_3)_2$ and other electron-poor PDIs were calculated in 2010 by Chang et al.[6] Depending on the basis set, their DFT calculations either overestimate by +0.134 eV (B3LYP/6-31+G*) or by +0.161 eV (B3LYP/6-311+G**) or underestimate by −0.294 eV (B3LYP/6-31G**) the experimental gas-phase EA of PDI(Bu)-1,7-$(CF_3)_2$ (3.00 eV) measured for this work. At the same time, relative EA changes between different PDI acceptors were correlated well with the new experimental findings. For example, strong electronic effects of imide substitutions with electron withdrawing groups were correctly predicted.[6]

3.5.3 General Trends in Electronic Properties of PDIs with Electron-Withdrawing Core Substituents

To investigate the influence of core derivatization with electron-withdrawing groups, the electrochemical data from previously characterized PDIs containing electron-withdrawing groups at the bay and/or *ortho* core positions have been summarized. These data are presented in Table 3.1 and Figures 8, 9, and S11–S14. The selected PDIs are from papers in which cyclic voltammetry data were reported. Only PDIs with symmetric diimide substituents were included. Direct comparison of $E_{1/2}^{0/-}$ is not always possible due to different electrochemical conditions, references, and variations between different research groups, so the change in $E_{1/2}^{0/-}$ per one substituent ($\Delta E_{1/2}^{0/-}$) was calculated by comparing measurements performed within the same research groups.

It is apparent that the electron-withdrawing effect of a given substituent is not constant in different PDI derivatives. For instance, cyanation can shift the first reduction potential by as little as 0.09 V and as much as 0.22 V (Table 3.1, entries 102–123) and bromination effect varies from 0.02 to 0.08 V (Table 3.1, entries 52–71). With chlorination and bromination it appears that introducing four groups to the bay positions has a slightly larger influence on $E_{1/2}^{0/-}$ than four groups at the *ortho* positions. Chlorination(bromination) at all four bay positions shifts $E_{1/2}^{0/-}$ by 0.05 to 0.07 V(0.063 V) and only by 0.038 V(0.02 V) per Cl(Br) at the *ortho* positions. On the other hand, the largest effects from F, CF_3, and CN groups were at the *ortho* positions of bay-substituted PDIs. Also notice that the first bay substitution had a greater effect than the second substitution in two cases (NO_2 and C_8F_{17}), but it was the opposite in the case of Br derivatives. Two F or Br substituents in the bay positions had a smaller influence than the next two F or Br substituents in the bay when comparing PDI(R)-1,7-X_2 with PDI(R)-1,6,7,12-X_4 ($\Delta E_{1/2}^{0/-}$ = 0.015-0.02 vs 0.025-0.045 V for F and 0.035-0.05 vs. 0.07 V for Br). It appears that the positional effect is different for each compound and most likely influenced by more than just the electron-withdrawing nature of the substituent, such as solvation, symmetry, and steric effects of the substituents that cause varying degrees of distortions in the polycyclic aromatic framework of PDIs.

Choosing the proper imide group is important for increased solubility and packing effects when designing new PDI acceptors, but it can also serve as a tool for fine-tuning the molecular energy levels. The effect of imide groups on $E_{1/2}^{0/-}$ was ascertained for PDI molecules with the same substitution patterns. For four derivatives of PDI(R)-1,7-$(CN)_2$, the $E_{1/2}$ can change by 0.22 V from R = Cy to R = F7Bu, Figure 3.15. Even two different alkyl groups exhibit significant differences. Comparison of four PDI($C_{15}H_{31}$)-2,5,8,11-X_4 derivatives shows that precise tuning

of $E_{1/2}^{0/-}$ can be accomplished by using halogens or *p*-(CN)-phenyl and larger increases are possible with cyanation, Figure 3.16. The $E_{1/2}^{0/-}$ of electron-withdrawing PDIs can be tuned by 0.42 and 0.47 V when only two core substituents are altered in PDI(Bu)-1,7-X_2 and PDI(F7Bu)-1,7-X_2, respectively, Figure 3.17. In PDI(Bu)-1,7-X_2 derivatives with X = perfluoroalkyl, C_4F_9 has the strongest electron-withdrawing effect compared to CF_3 and C_8F_{17}. On the other hand, Wang et al. demonstrated that C_4F_9 and C_8F_{17} had the same electron withdrawing effects when incorporated into PDI(dipp)-1,6-X_2 or PDI(dipp)-1,7-X_2.[185] The longer perfluoroalkyl chains (R_F) had a greater influence on $E_{1/2}^{0/-}$ for poly(perfluoroalkyl)naphthalene derivatives,[136] but they were not markedly different from shorter R_F groups in a series of $C_{60}(R_F)_2$.[20] These contrasts in the electron-withdrawing effects of perfluoroalkyl groups are due to the different nature of C-C(R_F) bonding and different solvation energies presumably play a lesser role: in PAHs, core carbon atoms are sp^2 hybridized whereas in fullerenes, cage C atoms are sp^3. Figure 3.17 provides another clear example of the partially fluorinated butyl chain contributing to stronger electron-withdrawing effects than *n*-alkyl chains as imide substituents.

Despite the relatively linear increase in $E_{1/2}^{0/-}$ from CF_3 substitutions depicted in Figure 3.10, the change per CF_3 group can differ by 40 mV when comparing consecutive substitutions. Introduction of a third CF_3 group to PDI(Bu)-1,7-$(CF_3)_2$ or PDI(Bu)-1,6-$(CF_3)_2$ increases $E_{1/2}^{0/-}$ by 0.16 V and 0.12 V, respectively. This difference might come from dipole effects along the long PDI axis. The symmetry of PDI(Bu)-1,7-$(CF_3)_2$ is lost when a third CF_3 group is introduced, leading to a more polar molecule and a larger increase in $E_{1/2}^{0/-}$. Trifluoromethyl groups in PDI(Bu)-1,6-$(CF_3)_2$ already cause a dipole towards one side of the molecule and a third CF_3 group will only help to balance this dipole, so the $E_{1/2}^{0/-}$ value does not increase as much. A similar trend was observed with cyanation of PDI(R)-1,6,7,12-Cl_4-2-(CN) (Table 3.1, entries 110

and 119) despite a seemingly linear correlation. Cyanation led to three different isomers of PDI(R)-1,6,7,12-Cl_4-$(CN)_2$ and the largest increase in $E_{1/2}^{0/-}$ was for the derivative with two CN groups on the same naphthalene subunit, i.e. the most polar isomer along the long axis.

Combining all three substitution methods expands the $E_{1/2}^{0/-}$ range to an impressive 1200 mV, and yet allows for fine tuning the electron-withdrawing capabilities of PDI acceptors, see Figure 3.18. This range could be extended even further when considering core-substitution with electron donating groups. The majority of reduction potentials gathered in Table 3.1 were reported in the same solvent and electrolyte system versus $FeCp_2^{+/0}$ and only these values are plotted in Figure 3.18. This diverse set of PDI acceptors spans from core-unsubstituted PDIs to the highly substituted PDI(F7Bu)-1,6,7,12-Cl_4-2,5,8,11-$(CN)_2$. Several PDIs with different substituents have nearly identical reduction potentials, which could enable researchers to choose molecules with desirable substituents (and hence specific solid-state morphologies, and physical properties) while keeping the reduction potentials constant.

Care must be taken when comparing $E_{1/2}^{0/-}$ among different research groups since different electrochemistry conditions (solvent, electrolyte, standard, electrochemical cell, atmospheric and solvent purity, etc.) may cause discrepancies.[180] In some cases, different values for the same molecules can even be observed between laboratories when nearly identical conditions are used. For example, reported $E_{1/2}^{0/-}$ vs. $FeCp_2^{+/0}$ for PDI(F7Bu) differ by 0.14 V (Table 3.1, entries 12 and 15). Additional caution is warranted when using E_{LUMO} from multiple sources since different conversions from comparable cyclic voltammetry measurements are often used without proper justification.[180,181] Recently the Strauss group reported on the rampant inconsistencies of reported electrochemical potentials and E_{LUMO} estimates for [6,6]-phenyl-C_{61}-butyric acid methyl ester (PCBM).[68] Molecules can appear to be stronger electron acceptors than

others when comparing E_{LUMO} even when the comparable $E_{1/2}^{0/-}$ results suggest otherwise. For example, cyclic voltammetry measurements of PDI(F7Bu)-1,7-Br_2 suggest that it is a stronger electron acceptor than PDI(Bu)-1,7-$(C_8F_{17})_2$ in DCM with 0.1 M $TBAPF_6$ vs. $FeCp_2^{+/0}$ by 0.10 V (Figure 3.17 and Table 3.1, entries 59 and 100). Conversely, comparing reported E_{LUMO} that were converted from these precise cyclic voltammetry measurements suggests that PDI(Bu)-1,7-$(C_8F_{17})_2$ is the stronger electron acceptor by 0.06 eV, simply because different $E_{1/2}^{0/-}$ to E_{LUMO} conversions were used.

3.6 Perylene Diimides in OPV Active Layers

3.6.1 Measuring Photoinduced Electron Transfer Between Isolated PDIs and TFB with TRMC

The formation of free and separated charge carriers at a Type II heterojunction between polymer electron donors and molecular acceptors is predicated upon an exergonic thermodynamic driving force (ΔG_{PET}) for exciton dissociation (Figure 3.33).[198] In an OPV device, this initial charge separation and light absorption occur at a heterojunction within an OPV active layer. Therefore, understanding factors that contribute to the initial charge separation is essential when designing an efficient OPV device. Most experimental techniques require an entire device (active layer, electron and hole blocking layers, electrodes, electrical contacts, etc.), which makes it difficult to precisely understand where successes and failures occur within the device. Device operation may be hampered by poor charge extraction for some donor/acceptor combinations, for example due to morphology considerations,[199] even for appropriately tuned interfacial energetics of the active layer and charge-selective contacts. Time-resolved microwave conductivity (TRMC) provides an electrodeless approach to directly observe free charge generation in an OPV active layer without the need for electrical contacts or additional layers. TRMC has been utilized as a sensitive probe of charge generation yields and recombination

dynamics for a variety of donor/acceptor systems.[200-204] This electrodeless approach is advantageous since it can study charges in an OPV active layer while eliminating several uncertainties that can arise with charge extraction in a full OPV device, such as long-range mobility and poor contact interactions.

Active layers are further complicated by different charge transfer and mobility dynamics from irregular film morphology. Charge transfer and mobility are most certainly different between distinctive interactions between crystalline or amorphous donor and acceptor regimes.[205] For example, acceptor molecules within large aggregates will not have efficient charge transfer between donor polymers, but they will contribute more to charge mobility compared to acceptor molecules that are isolated within the donor regime. TRMC experiments on films containing only isolated acceptors molecules in a polymer host helps to eliminate some uncertainties arising from irregular film morphology in the acceptor region. Furthermore, isolating each acceptor molecule eliminates electron mobility, which eliminates another variable inherent to TRMC experiments.

By tracking the photoinduced change in microwave conductance (ΔG_{photo}) as a function of time in an OPV active layer after excitation, TRMC experiments can measure the yield (φ) of photoinduced carriers at particular times after excitation (particularly at the start (t = 0) or end of laser pulse (EOP), see Figure 3.35), as shown in Equation 3.1.[202]

$$G_{photo} = eI_0F_A \qquad \text{(Equation 3.1)}$$

In Equation 3.1, β is related to the dimensions of the waveguide cross-section, e is the elementary charge, I_0 is the flux of the incident photons, F_A is the fraction of light absorbed by the sample, and $\Sigma\mu$ is the sum of charge mobilities. Since a pair of photoinduced carriers is

produced by dissociation of each exciton, then the yield of both holes and electrons are equivalent and $\Sigma\mu$ is the sum of the high-frequency (~9 GHz in this study) hole and electron mobilities. The electron mobility can be eliminated from the equation by only using isolated acceptor molecules in the polymer hosts, i.e. the dilute acceptor regime.[7] This ensures that the microwave absorbance is only due to mobile holes in the polymer regime and the measured $\varphi\Sigma\mu$ becomes $\varphi\mu_h$. For a specific polymer with unchanging film fabrication, μ_h will be the same for each sample, allowing for relative differences in φ to be inferred for the specific polymer and acceptors used.

An essential aspect of the dilute regime experiment requires a polymer donor that is transparent where the acceptor can selectively absorb so that only one pathway for charge transfer exists. All PDI(R)-$(CF_3)_{2\text{-}4}$ acceptors developed in this work have absorption maxima near 510 nm when isolated (Table 3.2), so selective excitation in active layer blends is possible if the polymer donor does not absorb light at wavelengths greater than 500 nm. The selective excitation of isolated PDIs surrounded by the polymer host guarantees that exciton generation occurs at a donor/acceptor interface and ensures that only one charge transfer pathway is active (pathway 2 in Figure 3.33). The polyfluorene-based polymer, poly[(9,9-dioctylfluorenyl-2,7-diyl)-co-(N,N'-diphenyl)-N,N'-di(p-butylphenyl)-1,4-diamino-benzene)] (TFB), is transparent at wavelengths greater than 450 nm and could be used for dilute regime experiments, see Figure 3.34 and Scheme 3.3. Furthermore, TFB has a high IP_D (5.50 eV), which could match well with the high EA_A of PDI(R)-$(CF_3)_{2\text{-}4}$.[206] Thick films are desirable for TRMC measurements when in the dilute regime so that the small amount of isolated PDIs can absorb a significant amount of laser flux. By using the entire solution, drop-casting makes thick films compared to other film deposition techniques (blade coating, spin-casting, etc.). For these reasons, TFB films with 2

mol% (based on monomer repeat unit of polymer) of two isomers of PDI(F7Bu)-$(CF_3)_{2,3,4}$ isomers, one isomer of each PDI(Bu)-$(CF_3)_{2,3,4}$, and Lumogen Orange and Red (see Scheme 3.4 for molecular drawings of Lumogen PDIs) were drop-cast onto quartz substrates from toluene solutions containing 2 mol% PDI and constant polymer concentration. Low molar ratios in these thick drop-cast films offered sufficient absorption (see Figure 3.34) while being adequately dilute to contain isolated PDIs.

In a typical TRMC experiment, TFB films containing isolated PDI acceptors were first placed in a cavity with a standing microwave field. Then ΔG_{photo} was monitored as a function of time upon selective photoexcitation of the PDI with a 5 ns laser pulse (510 nm). No ΔG_{photo} was observed when pristine polymer or PDI films were used. The measured ΔG_{photo} transients were then converted to $\varphi\Sigma\mu$ using Equation 3.1 (select $\varphi\Sigma\mu$ transients as a function of time are shown in Figure 3.35). Hole transfer from the PDI to TFB occurs upon photoinduced exciton generation in the PDI and $\varphi\Sigma\mu$ is initially high during the laser pulse. The $\varphi\Sigma\mu$ decrease after the laser pulse because of charge recombination and trapping at early times at donor/acceptor interfaces without additional charge generation. This charge recombination is strongly influenced by the polymer morphology since the polymer constitutes most of the film and the entire TRMC signal is from mobile holes in the polymer. For the four experiments shown in Figure 3.35, the transients can be fitted with a biexponential function, which indicates that at least two mechanisms contribute to free charge loss (i.e. trapping and recombination). Initially the $\varphi\Sigma\mu$ decays quickly, but is still present at long times (500 ns) due to some long-lived charges. This trend in transient shape and decay lifetimes holds constant for all TFB films regardless of PDI used. The $\varphi\Sigma\mu$ can then be compared between different TFB/PDI combinations by deconvoluting the loss of $\varphi\Sigma\mu$ during the 5 ns laser pulse using the biexponential fits and extrapolating to the value at the beginning of the

laser pulse (t = 0) or by using the peak $\varphi\Sigma\mu$ at the end-of-pulse (EOP), see Figure 3.35. Either value (t = 0 or EOP) will provide the same relative differences between samples when the transient shapes and decay dynamics are virtually identical. From $\varphi\Sigma\mu$ at t = 0, the $\varphi\mu_h$ can then be extracted or each sample as a function of laser fluence (Figure 3.35) by tuning several combinations of optical filters to change the laser fluence for each sample. Employing a previously developed empirical fit[207] to extrapolate $\varphi\mu_h$ to low fluence (~1-sun conditions) allows for relevant extraction of yield without complication by higher order recombination processes such as Auger recombination dynamics.[200] As discussed above, the hole mobility is expected to remain constant, allowing direct correlation of the relative yield of PET from $\varphi\Sigma\mu$ at the low fluence saturation value. If μ_h in the polyfluorene regimes[208] is ca. 4×10^{-4} $cm^2V^{-1}s^{-1}$ and μ_e is negligent, then φ at low fluence is equal to the extrapolated low fluence values divided by 4×10^{-4} $cm^2V^{-1}s^{-1}$. Figure 3.35 shows how $\varphi\Sigma\mu$ at low fluence changes for four different PDIs within the same polymer. If these values are divided by 4×10^{-4} $cm^2V^{-1}s^{-1}$, then φ ranges from ca. 2 to 9% for the four experiments. Since the relative differences for $\varphi\Sigma\mu$ and φ are the same and μ_h could differ between polymers, the $\varphi\Sigma\mu$ values will be depicted throughout the rest of this text and figures.

A recent publication by Coffey et al. showed that free carrier yield from photoinduced electron transfer in dilute acceptor regime films consisting of fullerene acceptors in polyfluorene-based polymer donors was dependent on the accepting strength of the fullerene when the polymer was held constant.[7] In other words, there appeared to be an optimal driving force for photoinduced electron transfer (ΔG_{PET}) between isolated fullerenes and polymers. Data from TRMC measurements along with Marcus formalisms indicated that this optimal driving force existed at specific ΔG_{PET} for each polymer. In Marcus formalisms, the rate of electron transfer

from an initial state to a final state depends on ΔG_{PET} and the reorganization energy, λ, associated with the energy needed to arrange the initial state into the configuration of the final state. The formalism predicts an increasing rate of charge transfer as $|\Delta G_{PET}|$ increases (normal region) up to a certain point where ΔG_{PET} becomes too large compared to λ and the rate begins to decrease (inverted region). If the yields measured via TRMC are dominated by this rate of initial charge transfer, then Marcus formalisms could be used to the optimal ΔG_{PET} for optimal yield of charge transfer.

The polymer/fullerene study used a few commercially available fullerenes along with a series of PFAFs that differed by the number and placement of trifluoromethyl groups on the fullerene cage. Comparing these calculated yields to the relative ΔG_{PET} (essentially the difference in HOMO levels between donor and acceptor in Figure 3.33) allowed for the Marcus trends to be observed. Perhaps these trends hold true with non-fullerene acceptors such as PDIs. Is the use of a fullerene as important as the relative driving force? Will PDIs that have the same electron accepting strength in solution as the PFAFs generate the same yield of free carriers and will they follow similar trends? To mimic the previous study, the series of PDI(R)-$(CF_3)_{0\text{-}4}$ that have similar electron accepting strength in solution, yet vastly different molecular structures, as the PFAFs were studied.

Equation 3.2 is used to estimate ΔG_{PET} between donors and acceptors.[7]

$$G_{PET} = \left(IP_D \quad EA_A\right) \quad E_{Exciton} \quad \text{(Equation 3.2)}$$

Here ΔG_{PET} is the change in Gibbs energy (thermodynamic driving force) of PET, IP_D is the ionization potential of the donor polymer, EA_A is the electron affinity of the PDI acceptor, and $E_{exciton}$ is the energy of the photoexcited exciton. Solid state PES from Kahn and coworkers was

used to determine IP_D for TFB.[206] The cyclic voltammetry measurements of isolated PDIs in dichloromethane described in Section 3.5 were used to estimate EA_A using $EA_A = E_{1/2}$(vs. $FeCp_2^{+/0}$) + 4.8 eV. Although this is only an estimate of EA_A, and is inherent to errors that were described in Section 3.5,[180] it is an accurate method for comparing the relative changes in electron accepting ability of isolated molecules in solution. The averages from absorption and emission maxima of isolated PDIs in dichloromethane were used to estimate $E_{exciton}$.[7,181] These solution measurements of isolated PDIs in solution were generalized for isolated solid-state PDIs in polymer hosts with the assumption that the relative changes would be constant for all PDIs. The main variable used in Equation 3.2 for this series is EA_A, derived from solution $E_{1/2}$. The subtle differences in $E_{exciton}$ will cause the isomers to only have slightly different driving forces for charge transfer despite having the same EA_A. In this series, $E_{exciton}$ are much larger than in the PFAF series, so there will be a larger ΔG_{PET} between acceptor/donor HOMO levels than between acceptor/donor LUMO levels for PFAFs and PDIs with the same solution reduction potentials. The relevant electronic energy levels and ΔG_{PET} between polymers and PDIs can be found in Table 3.3.

The PFAF series chosen by Coffey et al. were predominantly spherical and exhibited an $E_{exciton}$ range of ca. 0.5 eV, broad and dissimilar absorption features with small extinction coefficients, and very different π-systems that were dependent on the number and placement of CF_3 groups.[7] On the other hand, PDI(R)-$(CF_3)_{0\text{-}4}$ chosen for this work are more planar, have a more narrow $E_{exciton}$ range ($\Delta E_{exciton}$ = 0.07 eV), more defined, intense, and consistent absorption spectra, and unchanged π-systems upon CF_3 substitution.[173] Even though the two series have a similar range in solution reduction potentials, the fullerene system has a wider range in estimated HOMO values due to the wider range in $E_{exciton}$, which will lead to a wider range of measurable

driving forces. However, the consistent $E_{exciton}$, absorption, and π-system in the PDI series makes for less variables in charge transfer studies despite a narrower driving force range compared to the fullerene system.

Films of dilute PDIs in TFB for the 11 combinations described above were measured with TRMC; transient for four examples are shown in Figure 3.34. The transient appearance was rather uniform regardless of the PDI used. Transients were fit to biexponential functions and the t = 0 values of $\varphi\Sigma\mu$ were extracted and plotted vs. I_0F_A so that $\varphi\Sigma\mu$ at lower light intensities could be extracted from empirical fits.[207] These low fluence values for each combination are plotted in Figure 3.36; two identical films were measured for four PDIs to test measurement consistency. A gradual decrease in $\varphi\Sigma\mu$ was observed as ΔG_{PET} became more negative. This trend remained the same if EOP values were used to determine $\varphi\Sigma\mu$ instead of t = 0 values. This trend could be indicative of an inverted Marcus region that is quite broad. Perhaps the optimal ΔG_{PET} between HOMOs of PDIs and TFB is more positive than –0.6 eV and could be near –0.2 where Lumogen Red lies. For comparison, optimal driving forces between fullerenes and F8T2, F8BT, and PFO were near –0.7, –0.6, and –0.4 eV, respectively.[7]

If the TFB/PDI system is actually in a broad inverted Marcus region, then it is strange that the normal Marcus region is not observed as ΔG_{PET} approaches 0 eV. One likely explanation is that the values used in Equation 3.2 lead to a poor estimation ΔG_{PET}. The TRMC experiments are all conducted in the solid state, so it would be ideal to have all measurements that contribute to Equation 3.2 to also be conducted in the solid state. However, conducting these experiments is not straightforward. The most common way for directly measuring EA_A of solid state samples is IPES.[209] This method would require thick films of PDIs that would undoubtedly have large aggregates, so measuring isolated molecules would not be possible. The LT PES experiments

described in Section 3.5 measure gas-phase *EA* of isolated molecules, but it could also have similar problems when converting to solid-state *EA* as the solution measurements. Converting $E_{1/2}$ to EA_A by adding 4.8 eV is commonly used in the literature, but many assumptions from a limited number of examples are needed for these conversions to be valid and correlations between $E_{1/2}$ and *EA* are poorly understood.[180] If the relative differences in $E_{1/2}$ and *EA* are constant for this PDI series, then using a different conversion (such as adding 5.1 instead of 4.8 eV)[180] could change the absolute values ΔG_{PET} while keeping relative differences equal, which could leave more room for the normal Marcus region near 0 eV. Using a different literature measurement of IP_D could also change the absolute values of ΔG_{PET} while keeping relative differences the same. Changing the absolute values of EA_A and IP_D would only shift ΔG_{PET} and still wouldn't account for a broad inverted region. Perhaps a different method for calculating $E_{exciton}$ would create larger differences in ΔG_{PET}. However, the electron-hole pair binding energy is ignored when using the optical gap[181] and measuring the optical gap in the solid state gives similar results as solution measurements, since PDIs diluted in an inert polymer such as polystyrene (PS) have identical absorption/emission spectra as dilute PDIs in dichloromethane. Perhaps cyclic voltammetry measurements in a different solvent could measure the first oxidation and this could be used to estimate the IP_A.[181] Then the difference in *IP* between donor and acceptor could be used to estimate ΔG_{PET}.

Another possibility is that Equation 3.2 is too simple to describe ΔG_{PET}. The Rehm-Weller equation attempts to account for many of the problems in converting solution measurements to solid-state measurements by adding a coulomb term to Equation 3.2.[210-212] This extra term is influenced by the distance between separated charges, the dielectric constant within the film, and dielectric constant of the solvent that was used in the cyclic voltammetry

measurements. Relative differences in ΔG_{PET} will not change when incorporating the coulomb term since these variables will all be the same throughout the TFB/PDI series, but this term could shift the absolute values of ΔG_{PET} towards more negative values. Using this term with other polymer/PDI systems was shown to shift ΔG_{PET} by nearly 0.5 eV.[210] This correction would leave more space for a broad normal Marcus region in the TFB/PDI system.

No matter how ΔG_{PET} is estimated, it appears that this TFB/PDI(R)-$(CF_3)_{2-4}$ system is not in the right range for efficient charge transfer. Increasing EA_A by fluorination does not improve φ and these PDIs appear to be in the inverted Marcus region with TFB. A different donor with different IP_D will be necessary to better match the electronic levels in this PDI series.

3.6.2 Isolating PDIs in Solution, TFB, and PS

Additional spectroscopy and TRMC experiments were conducted to assure that 2 mol% PDIs were actually isolated in TFB films. The dilute regime will be where the absorption and emission of PDIs in a wide bandgap polymer (i.e. photophysically inert polymer) resembles solution measurements. Some PDIs in inert PS were first studied with absorption and emission experiments to determine where the dilute regime lies in the solid state. Also, $\varphi\Sigma\mu$ from TRMC experiments is expected to remain unchanged in the dilute regime as the amount of PDI loading changes within a polymer donor and will likely have similar dilution as PDI/PS films.[7]

It is important to know how much light can be absorbed by each PDI since the TRMC signal will be directly affected by F_A in each film. Absorption measurements of TFB films with 2 mol% PDIs showed that the amount of light absorbed by each PDI was different even though the same molar amounts were added to each film. This indicated that the molar extinction coefficients in the solid-state differed across the PDI series for different isomers and for different

compositions. This result is consistent with the difference in extinction coefficients in dichloromethane shown in Table 3.2. The extinction coefficients in solution can differ by as much as 30%, so some 2 mol% films will be able to absorb more light and, as a result, use lower laser fluences in the TRMC experiment. In all cases, the isomers with CF_3 groups on C1 and C7 all have larger extinction coefficients than the isomer pair with CF_3 groups on C1 and C6.

Next, a series with varying amounts of PDI(Bu)-1,7-$(CF_3)_2$ in films of PS were prepared by drop-casting from toluene to investigate the behavior of isolated and aggregated PDI in an inert polymer. The absorption and emission spectra in solution are shown in Figure 3.37 (black lines) and the excitation and emission spectra of a film of 0.03 mol% PDI(Bu)-1,7-$(CF_3)_2$ in PS are also shown (red lines). Steady-state excitation and emission spectra of 0.2 wt% PDI(Bu)-1,7-$(CF_3)_2$ in PS resemble absorption and emission spectra of PDI(Bu)-1,7-$(CF_3)_2$ in DCM. These similarities indicate that the PDI molecules are isolated in PS like in DCM, which is also observed for 0.2 and 0.4 mol% films. Note that 0.4 mol% in PS is the same PDI mass loading as 12 mol% in TFB because the difference in monomer repeat unit molecular weights and amount of polymer used. A significant shift in emission spectra and loss of vibrational structure is observed with higher PDI loadings (Figure 3.37, blue lines). Also, the excitation spectra of higher loading films are broadened and red-shifted. It appears that the excitation spectra of high loading films are an overlay of features from isolated PDIs and aggregated PDIs.

All PDI(Bu)-1,7-$(CF_3)_2$/PS films exhibit less monoexponential TRPL decay behavior than solution measurements (Figure 3.38). However, the primary decay component in PS films with less than 0.4 mol% PDI(Bu)-1,7-$(CF_3)_2$ resembles the primary decay component from the solution spectrum. Since the major component in the dilute films has a similar lifetime to the PDI in solution and the long-lived component is significantly less prominent than in PS films with

higher PDI loading, it appears that PDI(Bu)-1,7-$(CF_3)_2$/PS films with less than 0.4 mol% PDI(Bu)-1,7-$(CF_3)_2$ contain predominately isolated PDI molecules. The aggregated PDIs in higher loading films exhibit both shorter- and longer-lived components compared to the isolated molecules.

A series of TFB films with varying amounts of PDI(Bu)-1,7-$(CF_3)_2$ were prepared to investigate behavior of isolated and aggregated PDI in the electron-donating polymer. The fraction of light absorbed by PDI(Bu)-1,7-$(CF_3)_2$ increases linearly from 1–4 mol% PDI. Broadening and red-shifted absorption features are prominent with PDI loading from 8–64% and the peak PDI absorption does not increase linearly with PDI concentration, both of which are indicative of PDI aggregation (Figure 3.39). When selectively exciting the PDI, steady-state emission of PDI(Bu)-1,7-$(CF_3)_2$ in TFB was quenched below 4 mol% PDI loadings and resembled aggregated PDI(Bu)-1,7-$(CF_3)_2$ in PS at higher PDI loadings (Figure 3.39). Apparently, there is efficient charge transfer between isolated PDI(Bu)-1,7-$(CF_3)_2$ and TFB whereas PDI(Bu)-1,7-$(CF_3)_2$ within large aggregates exhibit less efficient charge transfer since emission is not completely quenched.

Excitation spectra of high loading PDI(Bu)-1,7-$(CF_3)_2$/TFB films do not resemble the solution absorption spectrum and only a broadened, red-shifted spectrum was observed (Figure 3.40). It appears that this is the species that is overlaid with isolated PDIs in the excitation spectra of high loading PS films shown in Figures 3.37 and 3.40. It also appears that all isolated PDI(Bu)-1,7-$(CF_3)_2$ in the high loading films are quenched by charge transfer to TFB and only the aggregate species are emitting and observed in excitation spectra. By subtracting the excitation spectrum of isolated PDI(Bu)-1,7-$(CF_3)_2$ in PS from a concentrated PDI(Bu)-1,7-$(CF_3)_2$/PS excitation spectrum, a new spectrum that closely resembles the excitation spectrum of

concentrated PDI(Bu)-1,7-$(CF_3)_2$ in TFB is produced, see Figure 3.40. This new spectrum helps show that all isolated PDI in TFB do not contribute to excitation as a result of a quenching mechanism and that the excitation spectrum from concentrated PDI(Bu)-1,7-$(CF_3)_2$ in TFB must only be from the same aggregated species observed in PS films. Therefore, some molecules in more concentrated films do not contribute to the yield of free carriers because they are emitting from large aggregates instead.

The same series of TFB films with varying amounts of PDI(Bu)-1,7-$(CF_3)_2$ was used for TRMC experiments. The purpose of using the same films in TRMC experiments was to determine if electron mobility turns on at the same time as the formation of PDI aggregates, as determined by absorption/emission data. A sharp increase in $\varphi\sum\mu$ due to the turn on of electron mobility from acceptor aggregates was observed in similar experiments with fullerenes.[7] As shown in Figure 3.41, the $\varphi\sum\mu$ remained essentially constant from 1% to 64% PDI(Bu)-1,7-$(CF_3)_2$ loading in TFB and no sharp increase was observed. Since PDIs within aggregates do not participate in charge transfer (as indicated by emission spectra), then the φ per PDI(Bu)-1,7-$(CF_3)_2$ would be expected to decrease with increased aggregation. Since $\varphi\sum\mu$ remained constant with increased aggregation, then $\sum\mu$ must have increased to offset the decreased yield. Therefore, it is likely that there is electron mobility within the PDI(Bu)-1,7-$(CF_3)_2$ aggregates, which happens to be inversely proportional to the loss of yield from molecules within the aggregates.

Another possibility is that only the isolated molecules in the aggregated films are being measured by the integrating sphere and TRMC. It is likely that the extinction coefficient of isolated PDI(Bu)-1,7-$(CF_3)_2$ is higher than for aggregated PDI(Bu)-1,7-$(CF_3)_2$. This would mean that the isolated molecules are primarily being measured in the integrating sphere experiments

and primarily absorbing light in the TRMC experiment. The $\varphi\sum\mu$ from TRMC is dependent on the F_A, so these measurements could also be favoring isolated molecules with higher extinction coefficients. In this case, observing no discernable rise in $\varphi\sum\mu$ as a function of PDI(Bu)-1,7-$(CF_3)_2$ could be from the fact that isolated molecules are primarily being measured and the aggregated species contribute very little or not at all to φ or F_A. In either case, these TRMC results cannot be used to determine at which loadings the dilute regime begins or ends, so the dilute regime can only be assumed from a combination of absorption and emission measurements in PS and TFB.

3.6.3 Measuring Photoinduced Electron Transfer Between Isolated PDIs and PFB with TRMC

Another polyfluorene-based polymer with a lower IP_D was used in TRMC experiments to assure that polymer/PDI(R)-$(CF_3)_n$ pairs with highly negative ΔG_{PET} were well within the inverted region. The polymer, poly[(9,9-dioctylfluorenyl-2,7-diyl)-co-(4,4'-(N-(p-butylphenyl))diphenylamine)] (PFB), has similar solubility and absorption features as TFB, but its IP_D is 5.35 eV (see Scheme 3.3 for molecular drawing).[206] This difference in IP_D will cause ΔG_{PET} to be 0.15 eV more negative than TFB/PDI pairs. Toluene solutions of PFB were spin-cast and drop-cast to first investigate different methods of film fabrication. Both methods produced visually uniform films with drop-cast films appearing thicker. The absorption of each film was measured using an integrating sphere to account for scattering and proved that the drop-cast films could absorb more light in both the polymer and PDI regions. Pure PFB films were transparent and had smooth baselines at wavelengths above 470 nm, therefore only PDIs would be excited at 510 nm in subsequent TRMC experiments. Since both methods produced uniform films, the more desirable thick films from drop-casting were chosen for further studies. This was also consistent with drop-cast TFB films.

Films of PFB with two isomers of each PDI(Bu)-$(CF_3)_{2,3,4}$ and PDI(F7Bu)-$(CF_3)_{2,3,4}$ composition were drop-cast from toluene using 2 mol% PDI and constant polymer concentration. Longer transient lifetimes were observed in PFB films compared to TFB films and essentially no intensity dependences on transient shapes were observed for either polymer, see Figure 3.42 for typical PFB transients. The $\varphi\sum\mu$ transients were then fit to biexponential functions and $\varphi\sum\mu$ from t = 0 was plotted versus laser fluence. An empirical fit was then employed and extrapolated $\varphi\sum\mu$ from low laser fluence were plotted versus ΔG_{PET}, Figure 3.42. More constant $\varphi\sum\mu$ as a function of ΔG_{PET} was observed for PFB films than in the TFB experiments. Having no increasing trend in $\varphi\sum\mu$ as ΔG_{PET} becomes more positive is consistent with this system being in the far extreme of the inverted Marcus region. This confirmed that a polymer with a higher IP_D than TFB was needed for efficient charge transfer to PDI(R)-$(CF_3)_{2,3,4}$. Strong electron donating groups, rather than electron withdrawing CF_3, on PDIs are necessary to explore more positive ΔG_{PET} with PFB.

3.6.4 Measuring Photoinduced Electron Transfer Between Isolated PDIs and PFO

One way to increase IP_D compared to TFB and PFB is to remove the solubilizing, electron-donating phenylamino groups. The IP_D of poly(9,9-di-*n*-octylfluorenyl-2,7-diyl) (PFO) is 5.75 eV, which will cause ΔG_{PET} to be 0.25 eV more positive than TFB/PDI pairs and could be ideal for electron transfer (see Scheme 3.3 for molecular drawing).[206] Furthermore, PFO is also one of the donor polymers used in the previous polymer/fullerene study by Coffey et al.[7] Experiments in this work revealed that removing the solubilizing groups causes problems during film fabrication. These problems in film fabrication were not explored in the polymer/fullerene study, but they have profound effects on TRMC and absorption behavior, which will briefly be described in this section.

The solubility of PFO was tested in dichloromethane, chloroform, toluene, chlorobenzene, and *o*-dichloro-benzene. The highest solubility was found in chloroform (ca. 10 mg/mL, 26 mM based on monomer repeat unit). The solubilizing, electron-withdrawing groups attached to fluorene in TFB and PFB cause these two polymers to be much more soluble than PFO. Solubility in toluene was measured for all three polymers and significant differences in solubility were observed with PFB having the highest solubility and PFO having the lowest solubility (in toluene: PFB = 24 mg mL^{-1}, 26 mM; TFB = 12 mg mL^{-1}, 19 mM; and PFO = 2.3 mg mL^{-1}, 5.8 mM based on monomer repeat unit). The higher solubility of PFB and TFB compared to PFO allowed for thicker films to be made from the typical 100 µL of solution used for drop-casting or spin-casting.

Films of PFO deposited from toluene or chlorobenzene were fairly uniform, but too thin for TRMC measurements. On the other hand, films deposited from chloroform were thicker but too inconsistent. For this reason, 10% chlorobenzene was added to the chloroform solutions in order to fabricate uniform films from the more concentrated solutions. This solution mixture was also used for all polymers in the previous polymer/fullerene study.[7] Films of PFO were fabricated from chloroform/chlorobenzene = 90/10 v/v solutions by drop-casting, spin-coating, or blade-coating. Drop-cast films produced desirably thick films, but were of poor optical quality. The slow evaporation of drop-cast films can lead to some domains of the film drying slower and becoming thicker than the rest of the film. As this happens, the less soluble polymer may precipitate from the solution earlier than the more soluble PDI. Selective crashing out of PFO during solvent evaporation leads to a solution that is no longer dilute in acceptor loading. The PDI can then agglomerate in one particular area of the substrate and not actually be diluted across the whole film. Furthermore, the polymer morphology can be inconsistent across the area

of the film. Consistent polymer morphology and PDI isolation are necessary for the driving force experiments to work properly, since hole and electron mobility could change drastically in different environments. Spin-coating and blade-coating both resulted in much more uniform albeit very thin films that were nearly optically transparent. This trade off in film thickness might be exactly what is needed to avoid agglomeration of donors or acceptors and improve uniformity of the active layer films.

Powder XRD of three films with or without 3 mol% PDI (drop-cast PDI(Bu)-1,7,5,11-$(CF_3)_4$ in PFO, drop-cast PFO, and spin-cast PDI(Bu)-1,7,5,11-$(CF_3)_4$ in PFO) were measured in order to probe polymer aggregation within the films. The two drop-cast films have nearly identical XRD patterns that indicate the presence of semi-crystalline β-phase of PFO,[213,214] and no peaks were observed in the spin-cast film (Figure 3.43). In both cases, no peaks were observed that indicate the presence of PDI(Bu)-1,7,5,11-$(CF_3)_4$ aggregates, which could mean that no PDI(Bu)-1,7,5,11-$(CF_3)_4$ aggregates are formed or that they are too small to be detected in the XRD experiment. Also, the presence of PDI(Bu)-1,7,5,11-$(CF_3)_4$ in drop-cast PFO films had no significant influence on the d-spacing of PFO aggregates.

Since the dilute regime turn-on or turn-off was not observed by TRMC with PDI(Bu)-1,7-$(CF_3)_2$/TFB films, the same study was repeated with PDI(Bu)-1,7-$(CF_3)_2$/PFO films. Spin-cast and drop-cast films using varying amounts of PDI(Bu)-1,7-$(CF_3)_2$ in 10 mg mL^{-1} solutions of PFO were both fabricated. Spin-cast films sacrifice thickness, but are much more uniform compared to the drop-cast films. Less light is absorbed with the thin films, which results in larger errors in absorption measurements using an integrating sphere and limits the amount of practical laser fluences in TRMC experiments. However, the increased uniformity of the films allows for

more consistent absorption throughout the film, reduces the likelihood of PDI agglomeration, and produces more consistent polymer morphology.

As shown in Figure 3.44, a more consistent $\varphi\sum\mu$ was observed for the spin-cast films vs. the drop-cast films as the amount of PDI(Bu)-1,7-$(CF_3)_2$ was changed at low loadings. Larger variations in $\varphi\sum\mu$ with drop-cast films, presumably due to PDI and polymer agglomeration or from poor absorption measurements, cause difficulty in determining at which point a constant $\varphi\sum\mu$ occurs. On the other hand, it is clear that $\varphi\sum\mu$ remains relatively constant below 10 mol% PDI(Bu)-1,7-$(CF_3)_2$ and increases sharply at higher acceptor loadings for spin-cast films. Thus, it was determined that agglomeration and electron mobility becomes negligent below 10 mol% PDI(Bu)-1,7-$(CF_3)_2$ and the dilute regime can be achieved for PDI(Bu)-1,7-$(CF_3)_2$ immersed in PFO films when solutions with less than 10 mol% PDI are spin-cast onto TRMC substrates. The increase in $\varphi\sum\mu$ at higher loadings indicates that μ_e within PDI(Bu)-1,7-$(CF_3)_2$ aggregates is larger than the loss of φ from within the aggregates. One reason why this increase is larger for spin-cast than drop-cast films or TFB films could be that smaller aggregates are formed in quickly fabricated spin-cast films. These smaller aggregates could be small enough for most of the molecules to participate in charge transfer, yet large enough for some μ_e to turn on. On the other hand, drop-cast films probably have aggregates that are too large for efficient charge transfer from deep within the aggregates.

Spin-cast films of dilute PDIs in PFO for PDI(R)-$(CF_3)_{2–4}$ and drop-cast films of PDI(Bu)-1,7-$(CF_3)_2$ and PDI(Bu)-1,7,5,11-$(CF_3)_4$ were fabricated and studied with TRMC. The spin-cast and drop-cast films behaved very different optically and in the TRMC experiments (Figure 3.45). Spin-casting made very thin, clear, and uniform films that exhibited very short-lived transients in TRMC, whereas drop-cast films were thick and cloudy with varying thickness

across the substrate and exhibited long-lived transients. One reason for such drastic differences in decay rates could be from aggregation within the films. Aggregation of particles, from PFO or PDIs, could result in the cloudiness seen in drop-cast films. Potentially, the semi-crystalline regions of PFO in drop-cast films measured by XRD (see Figure 3.43) could account for the long-lived transients. Controlling film microstructure by increasing crystallinity within polythiophene regimes is known to increase TRMC transient lifetimes due to increased charge delocalization.[215] Charges in the semi-crystalline regions of PFO are more likely to be delocalized throughout different polymer chains, which would allow for further separation from recombination sites and could explain the increased TRMC transient lifetimes for drop-cast films. Another hypothesis for why spin-cast films demonstrate faster free carrier recombination than the drop-cast films is that the thin films are more influenced by surface effects. It is well known that free carriers can be quenched at the surface of films in contact with the quartz substrate or in contact with the air boundary.[202] This surface quenching will have a larger influence on the thin films whereas the thick films will be more influenced by bulk properties of the film that are not near surface boundaries.

The fraction of light absorbed by PDIs in drop-cast films is also much higher than in spin-cast films, ca. 80% vs. 10%. Higher light absorption is better, since more laser fluences can be measured with TRMC and a more accurate absorption measurement should be obtained. However, scattering effects due to polymer aggregate formation in the drop-cast films influence the absorption measurement in an unpredictable way and cause errors that could be as great as 20%. These errors could also arise from the non-uniform nature of the drop-cast films across the substrate. This problem is persistent when using two different integrating sphere instruments. On the other hand, the absorption of the uniform spin-cast films without PFO aggregates could be

measured and no scattering affects were observed. For this reason, spin-cast PFO films were preferred over drop-cast films. Solutions with 3 mol% PDI(R)-$(CF_3)_{2–4}$ were spin-cast onto TRMC substrates. This amount of PDI was chosen since it is well below the turnoff of the dilute regime and 3% PDIs allow for enough light absorption to use several laser fluences with TRMC.

A measurable TRMC signal was observed for all of the 3% PDI films in PFO when exciting at 510 nm, but was not observed in pristine PFO spin-cast films. This shows that charge transfer occurs between each PDI and PFO. End of pulse $\varphi\sum\mu$ values were compared for all PDI/PFO films and no significant trends were observed, see Figure 3.42. No Marcus behavior was observed, 1,6 isomers did not outperform 1,7 isomers and vice versa, and the amount of CF_3 groups did not have profound influences on $\varphi\sum\mu$. The best performing PDI only outperformed the worst by a factor of two, so they all have relatively similar $\varphi\sum\mu$ in PFO. The difference of a factor of two could merely be from the errors in measurements, which is most likely a combination of absorption measurements, lack of measured laser fluences, and loss of measurable signal due to rapid decay of the free carriers. These possible errors and lack of significant changes in $\varphi\sum\mu$ warrant no longer using spin-cast films of PDIs in PFO to measure $\varphi\sum\mu$ as a function of driving force. However, the drastic difference in the transient lifetimes has warranted further studies on PFO morphology and how it affects charge transfer in the solid state, which are currently underway by other members of the Rumbles group.

3.6.5 Measuring Photoinduced Electron Transfer Between Isolated PDIs and P3HT

In additional experiments, isolated PDIs were incorporated into regioregular-poly(3-hexylthiophene-2,5-diyl) (rr-P3HT) films; IP_D = 5.0 eV and EA_D = 3.1 eV (see Scheme 3.3 for molecular drawing).[216,217] Absorption maxima of PDIs and rr-P3HT are both in the same range, so these experiments are slightly different from the previously studied polymers. Since rr-P3HT

and the PDIs both absorb light at the wavelength used in the TRMC experiments (510 nm) there are two pathways for charge transfer as shown in Figure 3.33. These pathways could be in competition depending on the rate constants for charge transfer. However, more light absorption will be from the rr-P3HT domains since they are much more prominent than the dilute PDIs. If the rate constants for charge transfer are similar for both pathways and all PDIs, then pathway 1 will dominate and the ΔG_{PET} can be estimated as the difference in LUMO energy levels. Absorption can take place across the entire films, but charge transfer will only occur at donor/acceptor interfaces. This is in contrast to the previous polymers where absorption always occurs at donor/acceptor interfaces since it only occurred at isolated acceptors. In both experiments, the acceptors are isolated, so electron mobility should be negligible and the TRMC signal will only be from charges in the rr-P3HT region.

A series of rr-P3HT films were fabricated by spin-coating toluene solutions of rr-P3HT with 2 mol% PDI(R)-$(CF_3)_{2–4}$ or Lumogen Orange. The films were excited at 510 nm in TRMC experiments and $\varphi\sum\mu$ values were extracted from the peak value at EOP. As shown in Figure 3.46, the $\varphi\sum\mu$ showed no trend as driving force changed among the PDI(R)-$(CF_3)_n$ series ($–1.3 \leq \Delta G_{PET} \leq –0.9$ eV) and was significantly decreased for the Lumogen Orange film ($\Delta G_{PET} = –0.7$ eV). As described earlier, the extinction coefficients in the PDI series are not constant, so PDI absorption might be more prevalent in some 2 mol% PDI films. In this case, pathway 2 could turn on more in some films. If the rate constants for charge transfer in pathway 2 are actually faster than pathway 1, then pathway 2 could start to become dominant. These competing pathways may change among the PDI series and could explain the lack of a trend in $\varphi\sum\mu$ versus driving force.

3.7 Conclusions

For the first time, a direct substitution in PTCDA with strong EWGs such as CF_3, has been synthetically realized in solvent free reactions without requiring the use of more expensive halogenated derivatives, as in the previously reported syntheses. Furthermore, this approach allowed simultaneous introduction of as many as four CF_3 groups in the core in a single reaction step. Direct introduction of cyano groups in PDI(F7Bu) and PDI(Bu)-1,7-$(CF_3)_2$ demonstrated an efficient and simple route towards molecules with even stronger electron withdrawing groups than CF_3. Efficient chromatographic separation yields single isomer compounds. These new PDI materials are air-stable, soluble in organic solvents, and thermally robust allowing for vapor deposition as well as solution processing. Different packing arrangements and intermolecular distances observed for PDIs of the same composition in this work demonstrate that PDI isomers exhibit different morphologies in the solid state, and could have varying transport properties.

This work reports, for the first time, solution- and gas-phase electronic properties for a new family of a dozen PDI acceptors with linearly modulated electronic properties, as determined by their measured reduction potentials in solution and gas-phase electron affinities. The gas-phase electron affinities can be used as a foundation for subsequent calculations and conversions of solution-phase reduction potentials. A thorough literature analysis of electron-poor PDIs, together with new results from this work, demonstrate that molecular design of PDIs are not limited by derivatization of only one position at a time, but PDI electronic properties can be finely tuned by a combination of imide, bay, and *ortho* substitutions. Researchers can synthesize molecules with precise energy levels, predictable morphologies, and desired transport properties by carefully selecting electron-withdrawing groups. The different strengths of electron-withdrawing substituents can also be related by comparing $\Delta E_{1/2}{}^{0/-}$ rather than $E_{1/2}{}^{0/-}$ or

calculated LUMO values. The new synthetic work contributed to the plethora of PDI syntheses already developed in the past two decades and illustrates the possibility of tuning PDI energy levels at all three positions with fluorinated core and imide substituents and core cyano groups to achieve a range in reduction potentials of nearly 800 mV.

Active layer blends with PDIs and conducting polymer donors were fabricated. Isolation of PDIs occurs at low blending ratios with less than 5 mol% PDI per polymer monomer repeat unit. Higher PDI loading leads to aggregate emission as revealed by steady-state and time-resolved emission studies. Photoinduced electron transfer was observed in TRMC studies with all of the PDIs and four different polymers. Broad, inverted Marcus behavior was observed with TFB films as a result of a thermodynamic driving force for charge separation that was too large for the small delocalization energy within the system. The electron accepting strength of the PDI series appeared to be too extreme for PFB films and the blends were at the onset of the inverted Marcus region. Charge delocalization in semi-crystalline β-phase regions of PFO films revealed interesting, long-lived recombination behavior. The ability to tune the excited state lifetimes of free charges by fine-tuning the amount of β-phase regions is a new method for controlling charge delocalization and has prompted further exploration within the Rumbles group.

3.8 Experimental Section

Abbreviations of PDIs: PDA = perylene dianhydride; PDI(R) = perylene diimide; R = imide substituent; positions of core substituents are given beginning with the bay substituent positions. No positions are given with mixtures and unknown compositions. Additional abbreviations of substituents for literature compounds can be found in Figure 3.32.

PDI(Bu): *N*,*N*'-bis(*n*-butyl)-perylene-3,4:9,10-tetracarboxylic acid diimide

PDI(Bu)-1,7-(CF_3)$_2$: *N*,*N*'-bis(*n*-butyl)-1,7-bis(trifluoromethyl)perylene-3,4:9,10-tetracarboxylic acid diimide

PDI(Bu)-1,6-(CF_3)$_2$: *N*,*N*'-bis(*n*-butyl)-1,6-bis(trifluoromethyl)perylene-3,4:9,10-tetracarboxylic acid diimide

PDI(Bu)-1,7,5-(CF_3)$_3$: *N*,*N*'-bis(*n*-butyl)-1,5,7-tris(trifluoromethyl)perylene-3,4:9,10-tetracarboxylic acid diimide

PDI(Bu)-1,6,8-(CF_3)$_3$: *N*,*N*'-bis(*n*-butyl)-1,6,8-tris(trifluoromethyl)perylene-3,4:9,10-tetracarboxylic acid diimide

PDI(Bu)-1,7,5,11-(CF_3)$_4$: *N*,*N*'-bis(*n*-butyl)-1,5,7,11-tetrakis(trifluoromethyl)perylene-3,4:9,10-tetracarboxylic acid diimide

PDI(Bu)-1,6,8,11-(CF_3)$_4$: *N*,*N*'-bis(*n*-butyl)-1,6,8,11-tetrakis(trifluoromethyl)perylene-3,4:9,10-tetracarboxylic acid diimide

PDI(F7Bu): *N*,*N*'-bis(heptafluorobutyl)-perylene-3,4:9,10-tetracarboxylic acid diimide

PDI(F7Bu)-1,7-(CF_3)$_2$: *N*,*N*'-bis(heptafluorobutyl)-1,7-bis(trifluoromethyl)perylene-3,4:9,10-tetracarboxylic acid diimide

PDI(F7Bu)-1,6-(CF_3)$_2$: *N*,*N*'-bis(heptafluorobutyl)-1,6-bis(trifluoromethyl)perylene-3,4:9,10-tetracarboxylic acid diimide

PDI(F7Bu)-1,7,5-(CF_3)$_3$: *N*,*N*'-bis(heptafluorobutyl)-1,5,7-tris(trifluoromethyl)perylene-3,4:9,10-tetracarboxylic acid diimide

PDI(F7Bu)-1,6,8-(CF_3)$_3$: *N*,*N*'-bis(heptafluorobutyl)-1,6,8-tris(trifluoromethyl)perylene-3,4:9,10-tetracarboxylic acid diimide

PDI(F7Bu)-1,7,5,11-(CF_3)$_4$: *N*,*N*'-bis(heptafluorobutyl)-1,5,7,11-tetrakis(trifluoromethyl)perylene-3,4:9,10-tetracarboxylic acid diimide

PDI(Bu)-1,7-(CF_3)$_2$-5-CN: *N*,*N*'-bis(*n*-butyl)-1,7-bis(trifluoromethyl)-5-cyanoperylene-3,4:9,10-tetracarboxylic acid diimide

General information: HPLC grade acetonitrile (Fisher Scientific), ACS grade hexanes, toluene, chloroform, 2-propanol, ethyl acetate, hydrochloric acid, and dichloromethane (Fisher Scientific), trifluoromethyl iodide (Synquest Labs), chloroform-D (Cambridge Isotopes Laboratories), ACS grade 1-methyl-2-pyrrolidinone (Sigma), propionic acid (Sigma, 99.5%), tetraethylammonium cyanide (Aldrich), perylene-3,4,9,10-tetracarboxylic dianhydride (Aldrich, 97%), 2,2,3,3,4,4,4-perfluorobutyl amine (Matrix), tetrachloro-1,4-benzoquinone (Aldrich), *n*-butylamine (Sigma-Aldrich), Cu powder (Strem Chemicals, 99%), silica gel (Sigma, 60 Å, 70-230 mesh), and hexafluorobenzene (Oakwood Products) were used as received. HPLC analysis and separation were done using Shimadzu liquid chromatography instrument (CBM-20A control

module, SPDA UV detector set to 514 nm detection wavelength, LC-6AD pump, manual injector valve) equipped with semipreparative 10 mm I.D. × 250 nm or preparative 25 mm I.D. × 250 nm COSMOSIL Buckyprep column (Nacalai Tesque, Inc.). The atmospheric-pressure chemical ionization (APCI) and electrospray ionization (ESI) mass spectra were recorded on 2000 Finnigan LCQ-DUO mass-spectrometer (acetonitrile carrier solvent, 0.3 $mL \cdot min^{-1}$ flow rate, analyte samples injected as solutions in dichloromethane). NMR spectra were recorded on Varian INOVA 400 or 500 instruments in $CDCl_3$ solution. The ^{1}H and ^{19}F frequencies were 400 and 376.5 MHz, respectively and the ^{13}C frequency was 100.52 or 125.78 MHz depending on which instrument was used. The ^{19}F chemical shifts were determined using hexafluorobenzene as an internal standard (δ −164.9). The ^{1}H chemical shifts were determined using the resonance of the residual $CHCl_3$ in $CDCl_3$ as an internal standard (δ 7.26). UV-vis absorption spectra were recorded by using a Cary 500 spectrophotometer with a resolution of 1 nm. Emission spectra were recorded by using a Horiba-Jovin-Yvon Fluorolog 3 spectrofluorometer equipped with a CCD detector using 430 nm excitation. Optical densities of excitation wavelengths were approximately 0.1 and the wavelengths were corrected using a correction function. Emission spectra were collected with different excitation wavelengths and the excitation wavelength made no significant difference on wavelength position of emission peaks. Emission lifetimes were measured using the time-correlated single-photon counting (TCSPC) technique. Excitation at 488 nm was afforded by a supercontinuum fiber laser (Fianium, SC-450-PP) operating at a repetition rate of 5 MHz and emission at 530 nm was collected by a short focal length Czerny-Turner spectrometer)Horiba Jobin-Yvon, TBX 850) and processed using a single-photon counting electronics module (Becker & Hickl, SPC-130). The instrument response function was measured by collection of the scattering of the excitation at 488 nm and was deconvoluted from

the measured data. Dichloromethane was dried over 3 Å molecular sieves prior to electrochemistry experiments. Ferrocene ($FeCp_2$, Acros Organics, 98%) and tetrabutylammonium hexafluorophosphate ($TBAPF_6$, Sigma-Aldrich, >99%) were used as received. Cyclic voltammetry measurements were carried out on PAR 263 potentiostat/galvanostat in anaerobic conditions using 0.1 M $N(n\text{-}Bu)_4PF_6$ in dichloromethane; platinum working and counter electrodes; silver wire quasi-reference electrode; 100 $mV \cdot s^{-1}$; ferrocene internal standard. Low-temperature photoelectron spectroscopy measurements and procedures were described earlier.[83]

Synthesis of PDA-$(CF_3)_n$ using hot plate reactor. In a typical reaction, PTCDA (420 mg, 1.07 mmol) is loaded into the GTGS reactor (reactor specifications reported elsewhere).[28] Glass wool (prewashed in DCM) is wrapped around the cold finger to prevent a large amount of sublimable material from escaping into the upper region of the GTGS reactor. The sample is then heated under dynamic vacuum for about 10 min. until the temperature of the hot plate reaches 390 °C, before PTCDA begins subliming, at which point $CF_3I_{(g)}$ (630 torr, ca. 16.8 mmol) is added. The temperature of the hot plate is then increased to 500 °C (temperature at the reaction site is ca. 410 °C). After 2 h the hot plate is removed for ca. 5 min., the gas is removed by vacuum, fresh $CF_3I_{(g)}$ (630 torr) is added, and the hot plate is reapplied to T = 500 °C. The heat must be removed before vacuum is applied or the more easily sublimable products will be removed. Fresh $CF_3I_{(g)}$ (630 torr) is added 2-3 times in order to assure that enough active CF_3 radicals were present to react with a substantial amount of PTCDA. The heat is removed after 4.5 h, excess gas is removed by vacuum upon cooling, and the soluble products are collected with DCM into a round bottom flask. The DCM and iodine are then removed from the desired products via rotovap. To promote the removal of $I_{2(s)}$, ca. 20 mL toluene is added to the flask and removed via

rotovap ca. five times until no $I_{2(s)}$ is seen in the receiving flask. After all $I_{2(s)}$ is removed, the crude mixture is then filtered in DCM to remove a red solid, which is mostly unreacted PTCDA. The soluble material is then dried down and analyzed by NMR in $CDCl_3$ and by NI-APCI mass spectrometry. The crude mixture is soluble in organic solvents such as toluene, DCM, and chloroform. Mass of soluble material = 224 mg. A yield can only be estimated because the exact composition of the products is not known. Assuming that the soluble material ranges from all PDA-$(CF_3)_2$ to all PDA-$(CF_3)_4$, then 0.42–0.34 mmols of product were extracted with an estimated yield of 32–40%.

If the hot plate temperature is increased during the reaction, even by 20 °C, the insoluble material will look darker than PTCDA. This darker color is attributed to larger PAHs or anhydrides with or without CF_3 substituents that are formed at higher temperatures. The reaction will still work at the higher temperatures (T_{HP} = 520-600 °C) and produce similar yields and product composition (determined by NMR), but the insoluble material will appear darker. Some amount of reaction was observed at lower temperatures (T_{HP} = 400 °C), but the highest yields for the synthesis of PDA-$(CF_3)_{2\text{-}4}$ were obtained at T_{HP} = 500 °C with the temperature at the reaction site ca. 410 °C.

The crude PDA-$(CF_3)_{2\text{-}4}$ mixture cannot be separated by flash chromatography or by HPLC, because they will react with the columns. The dianhydrides must be converted to diimides (PDI-$(CF_3)_{2\text{-}4}$) before a safe separation can commence. An alternative synthesis of PDI(Bu)-$(CF_3)_{2\text{-}4}$ was attempted by reversing the steps, i.e., by first creating PDI(Bu) and then attaching CF_3 groups using the GTGS reactor. This reaction scheme is not as good because two purification steps are needed (after imidization and after trifluoromethylation) and the addition of more than one CF_3 group was not observed by NI-APCI mass spectrometry. A single peak in the

^{19}F NMR spectrum of the crude reaction mixture indicated CF_3 substitution in the bay region and most likely the presence of the mono adduct, PDI(Bu)-1-(CF_3). This single perfluoroalkylation was also observed by Li et al. when PDIs were reacted in DMSO with $C_nF_{2n+1}I$ (n = 4 and 8).[185] Their main product was the selective monoaddition in the bay region with 60 % yields and secondary products were 1,7- and 1,6-bis adducts. Perhaps this method could be optimized to selectively form PDI(R)-1-(CF_3) if desired.

Synthesis of PDI(Bu)-$(CF_3)_{2-4}$ mixture from crude PDA-$(CF_3)_{2-4}$. An excess of *n*-butylamine (1.0 mL, 10 mmol) and a red, dark green fluorescent mixture of PDA-$(CF_3)_{2-4}$ (476 mg, at most 0.902 mmol; calculated as if the entire mixture was PDA-$(CF_3)_2$) was heated to reflux in propionic acid (95 mL) for 3 hours. Upon cooling, H_2O (100 mL) was added and the reaction mixture was filtered. The precipitate was collected into a round bottom flask via DCM, the DCM was removed by rotovap, and the solid was heated in an oven overnight to remove any residual solvents. The diimides were then separated from monoimides and other byproducts by flash chromatography on silica gel. The crude mixture has poor solubility in hexanes, so it was loaded on the column with a mixture of DCM/hexanes = 30/70. The mixture was then separated with a gradient from hexane to DCM. Small amounts of byproducts were removed with hexane mixtures and the desired diimides eluted with 100% DCM. In general, flash chromatography in DCM separates PDI(R)-$(CF_3)_{2-4}$ by composition, but HPLC is required for separation of isomers. Flash chromatography fractions containing only diimides (observed by NI-APCI mass spectrometry) were then further purified by HPLC (Cosmosil Buckyprep prep column, toluene/*i*-PrOH = 80/20, 16 mL·min^{-1}, 514 nm detection). The composition and purity (> 95%) of each product was determined by NI-APCI mass spec and ^{19}F and ^{1}H NMR. PDI impurities are due to different PDI compositions with similar elution times. Absolute yields cannot be determined

accurately since the composition of the starting PDA-$(CF_3)_{2\text{-}4}$ was not accurately known. Isolated amounts after HPLC and estimated isolated yields based on a conservative estimate of starting material = 0.902 mmol: PDI(Bu)-1,7-$(CF_3)_2$ = 122.5 mg (21 %), PDI(Bu)-1,6-$(CF_3)_2$ = 38.2 mg (6.7 %), PDI(Bu)-1,7,5-$(CF_3)_3$ = 19.0 mg (3.0%), PDI(Bu)-1,6,8-$(CF_3)_3$ = 12.1 mg (1.9%), PDI(Bu)-1,7,5,11-$(CF_3)_4$ = 12.7 mg (1.8%), and PDI(Bu)-1,6,8,11-$(CF_3)_4$ = 3.8 mg (0.5%).

PDI(Bu)-1,7-$(CF_3)_2$. ^{1}H NMR (400 MHz, $CDCl_3$, δ($CHCl_3$) = 7.26): δ = 9.06 (s, 2H), 8.80 (d, $^3J_{H,H}$ = 7.8 Hz, 2H), 8.56 (d, $^3J_{H,H}$ = 8.2 Hz, 2H), 4.27 (t, $^3J_{H,H}$ = 8.0 Hz, 4H), 1.79 (m, 4H), 1.52 (m, 4H), 1.04 (t, $^3J_{H,H}$ = 7.4 Hz, 4H) ppm; ^{19}F NMR (376.5 MHz, $CDCl_3$, δ(C_6F_6) = −164.9): δ = −58.48 (s, $2CF_3$) ppm; ^{13}C NMR (125.78 MHz, $CDCl_3$, δ($CHCl_3$) = 77.16): 162.9, 162.7, 134.0, 132.8, 132.0, 131.9, 130.3, 128.7, 128.0, 127.5, 125.3, 123.9, 123.4, 123.2, 40.8, 30.4, 20.5, 14.0 ppm. Mp 285–286 °C. NI-APCI mass spec: 638.53 *m/z*. Calcd for $C_{34}H_{24}F_6N_2O_4$ 638.16.

PDI(Bu)-1,6-$(CF_3)_2$. ^{1}H NMR (400 MHz, $CDCl_3$, δ($CHCl_3$) = 7.26): δ = 9.12 (s, 2H), 8.74 (d, $^3J_{H,H}$ = 8.2 Hz, 2H), 8.62 (d, $^3J_{H,H}$ = 7.8 Hz, 2H), 4.25 (m, 4H), 1.77 (m, 4H), 1.48 (m, 4H), 1.01 (t, $^3J_{H,H}$ = 7.4 Hz, 6H) ppm; ^{19}F NMR (376.5 MHz, $CDCl_3$, δ(C_6F_6) = −164.9): δ = −58.55 (s, $2CF_3$) ppm; ^{13}C NMR (100.52 MHz, $CDCl_3$, δ($CHCl_3$) = 77.16): 163.2, 162.4, 135.9, 131.7, 130.5, 130.2, 129.9, 129.3, 128.1, 127.8, 127.3, 126.6, 125.5, 124.9, 122.7, 122.5, 40.9, 40.8, 30.4, 30.3, 20.5, 20.5, 14.0, 14.0 ppm. Mp 255–258 °C. NI-ESI mass spec: 638.33 *m/z*. Calcd for $C_{34}H_{24}F_6N_2O_4$ 638.16.

PDI(Bu)-1,7,5-$(CF_3)_3$. ^{1}H NMR (400 MHz, $CDCl_3$, δ($CHCl_3$) = 7.26): δ = 9.15 (s, 1H), 9.10 (s, 1H), 8.93 (s, 1H), 8.83 (d, $^3J_{H,H}$ = 7.8 Hz, 1H), 8.60 (d, $^3J_{H,H}$ = 8.2 Hz, 1H), 4.26 (m, 4H), 1.78 (m, 4H), 1.50 (m, 4H), 1.02 (t, $^3J_{H,H}$ = 7.2 Hz, 6H) ppm; ^{19}F NMR (376.5 MHz, $CDCl_3$, δ(C_6F_6) = −164.9): δ = −58.70 (s, $1CF_3$), −59.12 (s, $1CF_3$), −63.43 (s, $1CF_3$) ppm; ^{13}C NMR (100.52

MHz, $CDCl_3$, δ($CHCl_3$) = 77.16): 162.6, 162.4, 161.6, 160.2, 133.8, 133.5, 133.1, 133.0, 132.8, 132.5, 132.2, 132.1, 131.4, 130.2, 129.9, 129.6, 129.3, 128.9, 128.6, 128.5, 128.1, 127.8, 124.3, 124.2, 124.0, 122.5, 41.4, 40.9, 30.3, 30.2, 20.5, 13.9 ppm. Mp 235–237 °C. NI-ESI mass spec: 706.33 *m/z*. Calcd for $C_{35}H_{23}F_9N_2O_4$ 706.15.

PDI(Bu)-1,6,8-(CF_3)$_3$. ^{1}H NMR (400 MHz, $CDCl_3$, δ($CHCl_3$) = 7.26): δ = 9.16 (s, 1H), 9.15 (s, 1H), 9.00 (s, 1H), 8.88 (d, $^3J_{H,H}$ = 8.2 Hz, 1H), 8.71 (d, $^3J_{H,H}$ = 7.8 Hz, 1H), 4.27 (m, 4H), 1.79 (m, 4H), 1.52 (m, 4H), 1.03 (m, 6H) ppm; ^{19}F NMR (376.5 MHz, $CDCl_3$, δ(C_6F_6) = −164.9): δ = −58.59 (s, 1CF_3), −59.74 (s, 1CF_3), −63.23 (s, 1CF_3) ppm; ^{13}C NMR (100.52 MHz, $CDCl_3$, δ($CHCl_3$) = 77.16): 162.1, 160.4, 135.3, 134.6, 132.9, 131.9, 131.7, 130.6, 130.4, 129.8, 129.4, 129.1, 128.2, 128.0, 125.4, 123.6, 123.3, 123.0, 41.3, 41.0, 30.3, 20.6, 20.5, 14.0 ppm. Mp 195–200 °C. NI-ESI mass spec: 706.33 *m/z*. Calcd for $C_{35}H_{23}F_9N_2O_4$ 706.15.

PDI(Bu)-1,7,5,11-(CF_3)$_4$. ^{1}H NMR (400 MHz, $CDCl_3$, δ($CHCl_3$) = 7.26): δ = 9.19 (s, 2H), 8.97 (s, 2H), 4.28 (t, $^3J_{H,H}$ = 8.0 Hz, 4H), 1.80 (m, 4H), 1.52 (m, 4H), 1.04 (t, $^3J_{H,H}$ = 7.2 Hz, 6H) ppm; ^{19}F NMR (376.5 MHz, $CDCl_3$, δ(C_6F_6) = −164.9): δ = −59.29 (s, 2CF_3), −63.42 (s, 2CF_3) ppm; ^{13}C NMR (125.78 MHz, $CDCl_3$, δ($CHCl_3$) = 77.16): 161.4, 159.9, 133.7, 133.5, 132.6, 132.4, 131.3, 130.4, 129.5, 129.1, 124.9, 123.0, 41.5, 30.2, 20.5, 13.9 ppm. Mp 206–210 °C. NI-ESI mass spec: 774.17 *m/z*. Calcd for $C_{36}H_{22}F_{12}N_2O_4$ 774.14.

PDI(Bu)-1,6,8,11-(CF_3)$_4$. ^{1}H NMR (400 MHz, $CDCl_3$, δ($CHCl_3$) = 7.26): δ = 9.17 (s, 2H), 9.04 (s, 2H), 4.26 (m, 4H), 1.77 (m, 4H), 1.49 (m, 4H), 1.01 (m, 6H) ppm; ^{19}F NMR (376.5 MHz, $CDCl_3$, δ(C_6F_6) = −164.9): δ = −58.82 (s, 2CF_3), −62.93 (s, 2CF_3) ppm; ^{13}C NMR (125.78 MHz, $CDCl_3$, δ($CHCl_3$) = 77.16): 161.9, 159.7, 134.1, 131.8, 130.9, 130.4, 129.8, 128.9, 124.6, 123.8,

41.8, 41.1, 31.2, 20.5, 20.5, 13.9 ppm. Mp 245–250 °C. NI-APCI mass spec: 774.70 *m/z*. Calcd for $C_{36}H_{22}F_{12}N_2O_4$ 774.14.

Synthesis of PDI(F7Bu)-$(CF_3)_{2\text{-}4}$ mixture from crude PDA-$(CF_3)_{2\text{-}4}$. An excess of 1H,1H-heptafluorobutylamine (1.70 mL, 12.7 mmol) and a dark green mixture of PDA-$(CF_3)_{2\text{-}4}$ (337 mg, at most 0.638 mmol; calculated as if the entire mixture was PDA-$(CF_3)_2$) was heated to reflux in propionic acid (25 mL) for 4 hours. The reaction progress was monitored by NI-APCI mass spec and was considered finished when no monoimide was observed. After 4 h of reflux, the solvent and excess heptafluorobutylamine were removed by heating under reduced pressure. The diimides were then separated by flash chromatography on silica. The crude mixture has poor solubility in hexanes, so it was loaded on the column with a mixture of DCM/hexanes = 30/70. The mixture was then separated with a gradient from hexane to DCM. Small amounts of byproducts were removed with hexane mixtures and the desired diimides eluted with 100% DCM. A fraction containing only PDI(F7Bu)-$(CF_3)_{2\text{-}4}$ according to mass spectra was then further purified by HPLC (Cosmosil Buckyprep prep column, toluene/*i*-PrOH = 80/20, 16 mL·min^{-1}, 512 nm detection). In some cases, the HPLC fractions were purified further using Cosmosil Buckyprep semiprep column, toluene/*i*-PrOH = 80/20 or 65/35, 5 mL·min^{-1}, 512 nm detection). The composition and purity (> 90%) of each product was determined by NI-APCI mass spec and ^{19}F and ^{1}H NMR. PDI impurities are due to different PDI compositions with similar elution times. Absolute yields cannot be determined accurately since the composition of the starting PDA-$(CF_3)_{2\text{-}4}$ was not accurately known. Isolated amounts after HPLC and estimated isolated yields based on a conservative estimate of starting material = 0.638 mmol: PDI(F7Bu)-1,7-$(CF_3)_2$ = 47.4 mg (8.3%), PDI(F7Bu)-1,6-$(CF_3)_2$ = 31.0 mg (5.5%), PDI(F7Bu)-1,7,5-$(CF_3)_3$ =

63.7 mg (10%), PDI(F7Bu)-1,6,8-$(CF_3)_3$ = 27.9 mg (4.6%), and PDI(F7Bu)-1,7,5,11-$(CF_3)_4$ = 7.0 mg (1.1%).

Separation of PDI(F7Bu)-$(CF_3)_{2\text{-}4}$ mixture from crude PDI(F7Bu)-$(CF_3)_{2\text{-}4}$. The separation of PDI(F7Bu)-$(CF_3)_{2\text{-}4}$ was not as straightforward as the separation of PDI(Bu)-$(CF_3)_{2\text{-}4}$. Compositions could be separated by flash chromatography in 100% DCM from crude PDI(Bu)-$(CF_3)_{2\text{-}4}$, whereas almost all PDI(F7Bu)-$(CF_3)_{2\text{-}4}$ compounds eluted together. Both sets of compounds follow similar trends in HPLC and have similar elution times (see Figure 3.4). In general, the compounds elute as follows: PDI(F7Bu)-1,7-$(CF_3)_2$, PDI(F7Bu)-1,7,5-$(CF_3)_3$, PDI(F7Bu)-1,7,5,11-$(CF_3)_4$, PDI(F7Bu)-1,6-$(CF_3)_2$, and then PDI(F7Bu)-1,6,8-$(CF_3)_3$. Non-chromatographic separations have not been successful at this time for the isolation of different PDI(R)-$(CF_3)_n$ isomers. Any anhydride that is present can be detrimental the HPLC column. A small amount of monoanhydride will stick to the column and elutes with CH_3CN if at all. The anhydride can also react with the column or stick very strongly to the column and only elute after many hours of flushing with multiple solvents.

PDI(F7Bu)-1,7-$(CF_3)_2$. ^{1}H NMR (400 MHz, $CDCl_3$, δ($CHCl_3$) = 7.26): δ = 9.13 (s, 2H), 8.87 (d, $^3J_{H,H}$ = 7.8 Hz, 2H), 8.62 (d, $^3J_{H,H}$ = 8.2 Hz, 2H), 5.06 (t, $^3J_{H,F}$ = 15.5 Hz, 4H) ppm; ^{19}F NMR (376.5 MHz, $CDCl_3$, δ(C_6F_6) = −164.9): δ = −58.55 (s, $2CF_3$), −83.60 (t, *J* = 9.5 MHz, 6F), −119.08 (m, 4F), −130.84 (m, 4F) ppm; ^{13}C NMR (125.78 MHz, $CDCl_3$, δ($CHCl_3$) = 77.16): 162.4, 162.3, 134.5, 133.3, 132.7, 132.2, 131.0, 128.8, 128.3, 128.2, 123.1, 122.9, 122.8, 38.7 ppm. Mp 258–260 °C. NI-APCI mass spec: 890.53 *m/z*. Calcd for $C_{34}H_{10}F_{20}N_2O_4$ 890.03.

PDI(F7Bu)-1,6-$(CF_3)_2$. ^{1}H NMR (400 MHz, $CDCl_3$, δ($CHCl_3$) = 7.26): δ = 9.19 (s, 2H), 8.83 (d, $^3J_{H,H}$ = 8.2 Hz, 2H), 8.69 (d, $^3J_{H,H}$ = 8.2 Hz, 2H), 5.07 (m, 4H) ppm; ^{19}F NMR (376.5 MHz,

$CDCl_3$, δ(C_6F_6) = −164.9): δ = −58.54 (s, 2CF_3), −83.59 (t, *J* = 9.5 MHz, 6F), −119.07 (m, 4F), −130.82 (m, 4F) ppm; ^{13}C NMR (100.52 MHz, $CDCl_3$, δ($CHCl_3$) = 77.16): 162.8, 162.0, 136.4, 132.4, 131.9, 131.1, 131.0, 130.1, 129.5, 128.6, 128.3, 128.0, 127.5, 126.8, 125.3, 124.2, 122.5, 121.8, 38.8 ppm Mp 255–258 °C. NI-APCI mass spec: 890.53 *m/z*. Calcd for $C_{34}H_{10}F_{20}N_2O_4$ 890.03.

PDI(F7Bu)-1,7,5-(CF_3)$_3$. ^{1}H NMR (400 MHz, $CDCl_3$, δ($CHCl_3$) = 7.26): δ = 9.22 (s, 1H), 9.16 (s, 1H), 8.98 (s, 1H), 8.91 (d, $^3J_{H,H}$ = 7.8 Hz, 1H), 8.66 (d, $^3J_{H,H}$ = 7.8 Hz, 1H), 5.08 (m, 4H) ppm; ^{19}F NMR (376.5 MHz, $CDCl_3$, δ(C_6F_6) = −164.9): δ = −58.70 (s, 1CF_3), −59.13 (s, 1CF_3), −63.70 (s, 1CF_3), −83.58 (t, *J* = 8.9 MHz, 6F), −119.13 (m, 4F), −130.76 (m, 4F) ppm; ^{13}C NMR (125.78 MHz, $CDCl_3$, δ($CHCl_3$) = 77.16): 162.2, 162.0, 161.3, 159.6, 134.4, 134.0, 133.5, 133.3, 132.9, 132.7, 132.2, 131.0, 130.2, 129.7, 129.5, 128.7, 128.0, 123.6, 123.4, 121.7, 38.8 ppm. Mp 236–239 °C. NI-ESI mass spec: 958.08 *m/z*. Calcd for $C_{35}H_9F_{23}N_2O_4$ 958.02.

PDI(F7Bu)-1,6,8-(CF_3)$_3$. ^{1}H NMR (400 MHz, $CDCl_3$, δ($CHCl_3$) = 7.26): δ = 9.23 (s, 1H), 9.22 (s, 1H), 9.05 (s, 1H), 8.96 (d, $^3J_{H,H}$ = 7.8 Hz, 1H), 8.77 (d, $^3J_{H,H}$ = 7.8 Hz, 1H), 5.09 (m, 4H) ppm; ^{19}F NMR (376.5 MHz, $CDCl_3$, δ(C_6F_6) = −164.9): δ = −58.60 (s, 1CF_3), −59.73 (s, 1CF_3), −63.51 (s, 1CF_3), −83.57 (t, *J* = 9.5 MHz, 6F), −119.12 (m, 4F), −130.71 (m, 4F) ppm; ^{13}C NMR (125.78 MHz, $CDCl_3$, δ($CHCl_3$) = 77.16): 161.8, 161.7, 159.9, 135.8, 133.2, 132.6, 132.5, 131.1, 130.9, 130.0, 129.7, 129.3, 128.4, 128.1, 124.6, 122.6, 122.3, 38.7 ppm. Mp 205–210 °C. NI-APCI mass spec: 958.73 *m/z*. Calcd for $C_{35}H_9F_{23}N_2O_4$ 958.02.

PDI(F7Bu)-1,7,5,11-(CF_3)$_4$. ^{1}H NMR (400 MHz, $CDCl_3$, δ($CHCl_3$) = 7.26): δ = 9.25 (s, 2H), 9.00 (s, 2H), 5.09 (t, $^3J_{H,F}$ = 15.1 Hz, 4H) ppm; ^{19}F NMR (376.5 MHz, $CDCl_3$, δ(C_6F_6) = −164.9): δ = −59.31 (s, 2CF_3), −63.73 (s, 2CF_3) , −83.59 (t, *J* = 9.5 MHz, 6F), −119.22 (m, 4F),

−130.73 (m, 4F) ppm; ^{13}C NMR (125.78 MHz, $CDCl_3$, δ($CHCl_3$) = 77.16): 161.1, 159.4, 133.1, 132.9, 132.1, 130.6, 130.1, 129.6, 129.3, 124.2, 38.9 ppm. Mp 231–234 °C. NI-APCI mass spec: 1026.08 *m/z*. Calcd for $C_{36}H_8F_{26}N_2O_4$ 1026.08.

Synthesis of PDI(Bu): Adapted from literature procedures.[183,184] A 4-fold excess of *n*-butylamine (66 µL, 0.66 mmol) and PTCDA (65 mg, 0.17 mmol) were heated to reflux in N-methylpyrrolidone (3 mL) for 1 hour. Upon cooling, $HCl_{(aq)}$ (25 mL, 4 M) was added and the reaction mixture was filtered. Some solid dissolved into a red orange solution after soaking and sonicating in DCM. The DCM solution was then filtered and separated by flash chromatography on silica gel with a mixture of DCM/EtOAc = 10/1 v/v. The composition of the fraction containing PDI(Bu) was confirmed by NI-APCI mass spec and ^{1}H NMR.

PDI(Bu). ^{1}H NMR (400 MHz, $CDCl_3$, δ($CHCl_3$) = 7.26): δ = 8.71 (d, $^3J_{H,H}$ = 8.0 Hz, 4H), 8.65 (d, $^3J_{H,H}$ = 8.0 Hz, 4H), 4.23 (m, 4H), 1.75 (m, 4H), 1.49 (m, 4H), 1.01 (t, $^3J_{H,H}$ = 7.4 Hz, 6H) ppm.

Synthesis of PDI(F7Bu): Synthesized according to literature procedure.[174]

PDI(F7Bu). ^{1}H NMR (400 MHz, $CDCl_3$, δ($CHCl_3$) = 7.26): δ = 8.78 (m, 4H), 8.72 (m, 4H); 5.05 (t, $^3J_{H,F}$ = 15.5 Hz, 4H) ppm; ^{19}F NMR (376.5 MHz, $CDCl_3$, δ(C_6F_6) = −164.9): δ = −83.60 (t, *J* = 9.5 MHz, 6F), −119.01 (m, 4F), −130.86 (m, 4F) ppm.

Synthesis of PDI(Bu)-1,7-$(CF_3)_2$-5-(CN) from PDI(Bu)-1,7-$(CF_3)_2$. In a typical synthesis, an aliquot of a solution of NEt_4CN in CH_2Cl_2 (0.20 mL, 35 mM, 6.9 µmol, 1.3 equiv. CN^-) was added to an orange solution of PDI(Bu)-1,7-$(CF_3)_2$ in CH_2Cl_2 (3.4 mg, 5.3 µmol, 1.5 mL CH_2Cl_2) at 23(2) °C and the mixture instantly turned dark green and became blue within 20 minutes. After 1 h the solution was treated with *p*-chloranil (0.86 mL, 19 mM, 16 µmol, 3 equiv.

p-chloranil) and the solution instantly turned dark orange with green fluorescence. After 1 hour the solution was exposed to air and subjected to flash chromatography on silica. A mixture of PDI(Bu)-1,7-$(CF_3)_2$ and PDI(Bu)-1,7-$(CF_3)_2$-5-(CN) was eluted in a mixture of DCM and EtOAc which was further purified by HPLC to obtain unreacted PDI(Bu)-1,7-$(CF_3)_2$ and pure PDI(Bu)-1,7-$(CF_3)_2$-5-(CN). HPLC: Cosmosil Buckyprep column, 5 mL min^{-1}, toluene/*i*-PrOH = 65/35, 512 nm detection, unreacted PDI(Bu)-1,7-$(CF_3)_2$ at 4.5 min, PDI(Bu)-1,7-$(CF_3)_2$-5-(CN) at 9.6 min.

PDI(Bu)-1,7-$(CF_3)_2$-5-(CN). ^{1}H NMR (400 MHz, $CDCl_3$, δ($CHCl_3$) = 7.26): δ = 9.14 (s, 1H), 9.10 (s, 1H), 8.84 (d, $^3J_{H,H}$ = 7.8 Hz, 1H), 8.72 (s, 1H), 8.59 (d, $^3J_{H,H}$ = 7.8 Hz, 1H), 4.26 (m, 4H), 1.77 (m, 4H), 1.49 (m, 4H), 1.01 (t, $^3J_{HH}$ = 7.4 Hz, 6H) ppm; ^{19}F NMR (376.5 MHz, $CDCl_3$, δ(C_6F_6) = −164.9): δ = −58.70 (s, 1CF_3), −59.12 (s, 1CF_3), −63.43 (s, 1CF_3) ppm; ^{13}C NMR (125.78 MHz, $CDCl_3$, δ($CHCl_3$) = 77.16): 162.5, 162.3, 161.4, 160.6, 135.0, 134.2, 133.2, 132.7, 132.2, 131.9, 131.7, 130.2, 129.2, 128.6, 127.7, 125.4, 124.6, 124.5, 123.5, 116.7, 115.5, 41.4, 41.0, 30.3, 30.2, 20.5, 14.0, 13.9 ppm. Mp 268–270 °C. NI-ESI mass spec: 663.33 *m/z*. Calcd for $C_{35}H_{25}F_6N_3O_4$ 663.16.

Thin-film sample fabrication. Polymer solutions (150 µL of 13 mg mL^{-1} TFB in toluene, 15 mg mL^{-1} PFB in toluene, 10 mg mL^{-1} PFO in a mixture of chloroform/chlorobenzene = 9/1 by volume, 13 mg mL^{-1} PS in toluene, or 15 mg mL^{-1} rr-P3HT in toluene) were added to solid PDI to make polymer/PDI solution mixtures. These mixtures (100 µL) were then drop-cast (TFB, PFB, PFO, and PS) or spin-cast (P3HT and PFO) onto quartz substrates so that a constant polymer amount was deposited within each polymer series. Thin-film absorption was measured using a Cary6000 integrating sphere and averaged over multiple locations covering the entire sample to account for variations in film thickness.

TRMC measurement details have been described previously.[218-221] Measurements were made in air or nitrogen. Select measurements made in nitrogen showed no difference in the resulting values for PFO and TFB films. P3HT films were always measured under nitrogen. To determine film photoconductivities, the following procedure is followed: (1) TRMC data of the sample series are taken over a range of illumination intensities to ensure that the response is linearly correlated with light intensity, (2) these traces are fit to a double exponential function and deconvoluted from the ca. 5 ns cavity response for t = 0 value or the maximum signal is used for end of pulse values,[33] (3) the resulting peak value (t = 0 or end of pulse) is normalized by the film absorption.

NMR spectra of PDI derivatives synthesized for this work: Relaxation times of core protons and aliphatic protons may be different which could interfere with integration comparisons from ^{1}H signals between core and aliphatic protons. Similar integration ratios have been observed with PDI(Bu)-$(CF_3)_2$ in the literature.[171] The presence of solvents may also interfere with integration of aliphatic proton signals. Water (1.56), toluene (2.36, and 7.17-7.30), DCM (5.30), and *i*PrOH are present in small amounts.

Single-crystal XRD. Data were collected on the Advanced Photon Source synchrotron instrument at Argonne National Laboratory, Argonne IL, on beamline 15ID-B with a wavelength of 0.41328 Å, employing a diamond 1 1 1 monochromator and Bruker D8 goniometer or using a Bruker Kappa APEX II CCD diffractometer employing $Mo_{K\alpha}$ radiation and a graphite monochromator Unit cell parameters were obtained from least-squares fits to the angular coordinates of all reflections, and intensities were integrated from a series of frames ω and ϕ rotation scans. Absorption and other corrections were applied using SCALE.[103] The structures

were solved using direct methods and refined (on F^2, using all data) by a full-matrix, weighted least-squares process. Standard Bruker control and integration software (APEX II) was employed,[104] and Bruker SHELXTL software was used with Olex 2 for structure solution, refinement, and molecular graphics.[105,106] Additional diffraction data and refinement parameters can be found in Tables 3.4 and 3.5.

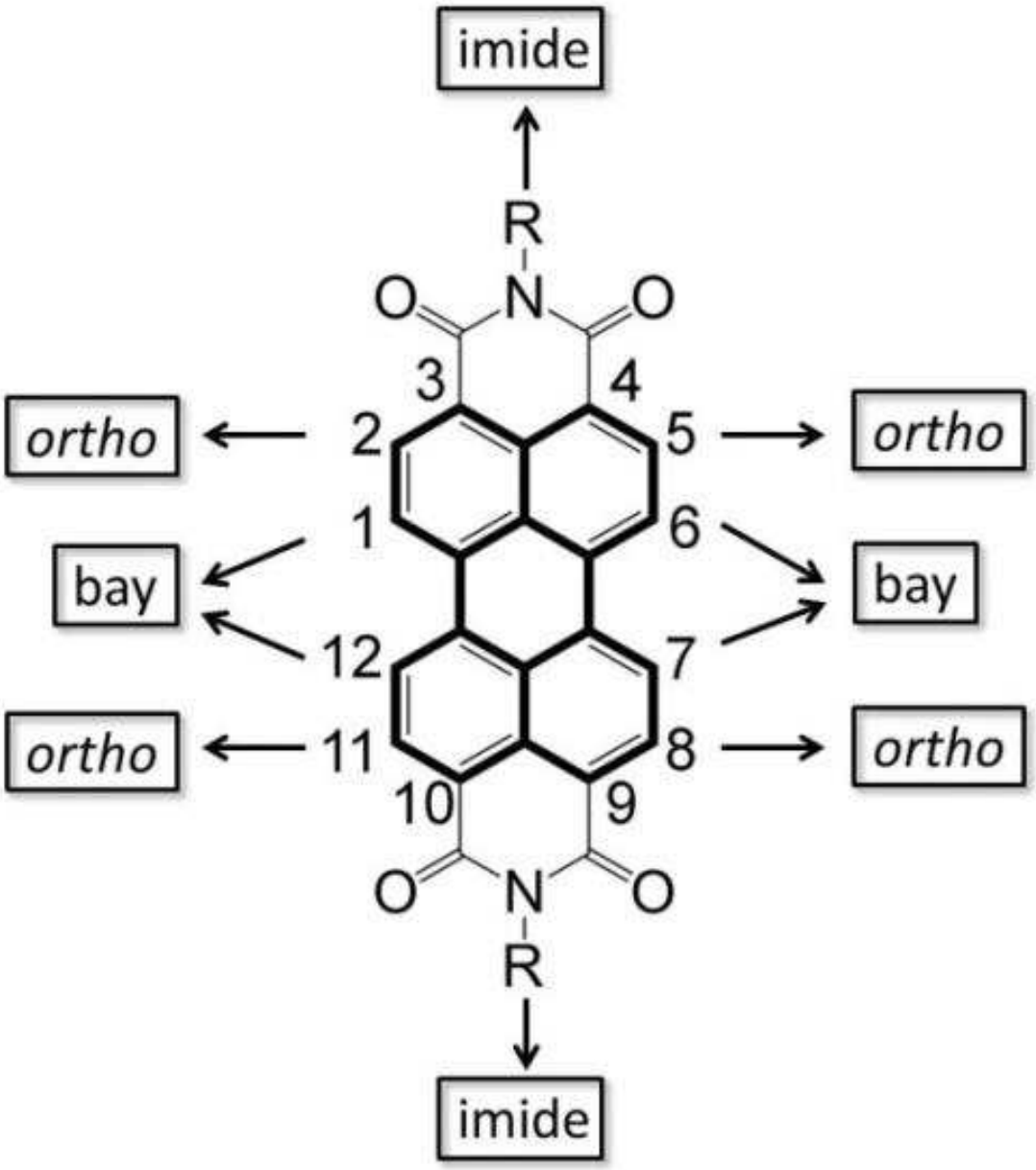

Figure 3.1. Naming and numbering scheme of PDI(R).

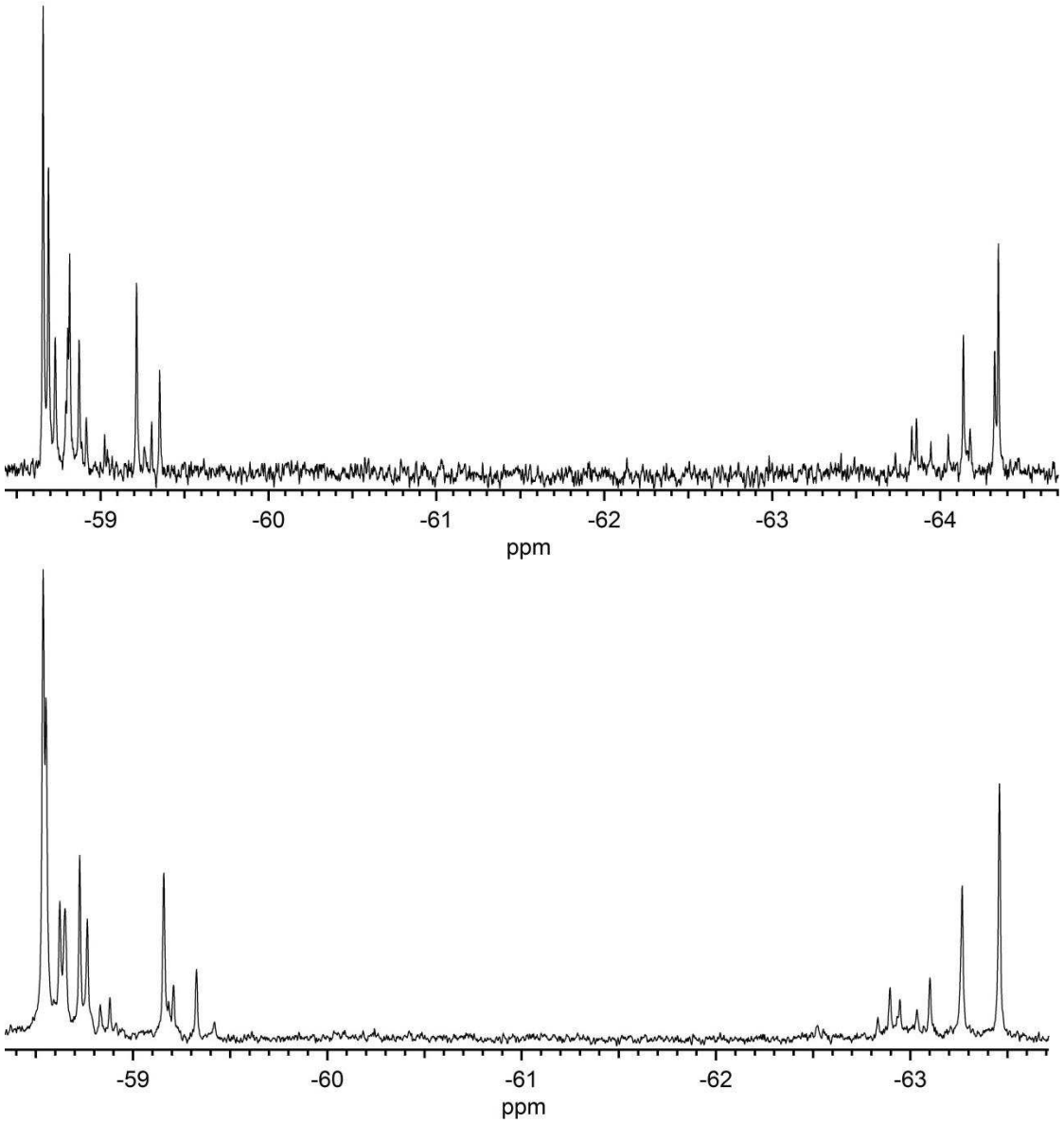

Figure 3.2. Fluorine–19 NMR spectra in $CDCl_3$ of crude PDA-$(CF_3)_{2\text{-}4}$ (top) and crude PDI(Bu)-$(CF_3)_{2\text{-}4}$ (bottom) before flash chromatography. The signals near −59 correspond to CF_3 groups in the bay region and the signals near −64 correspond to CF3 groups in the ortho region.

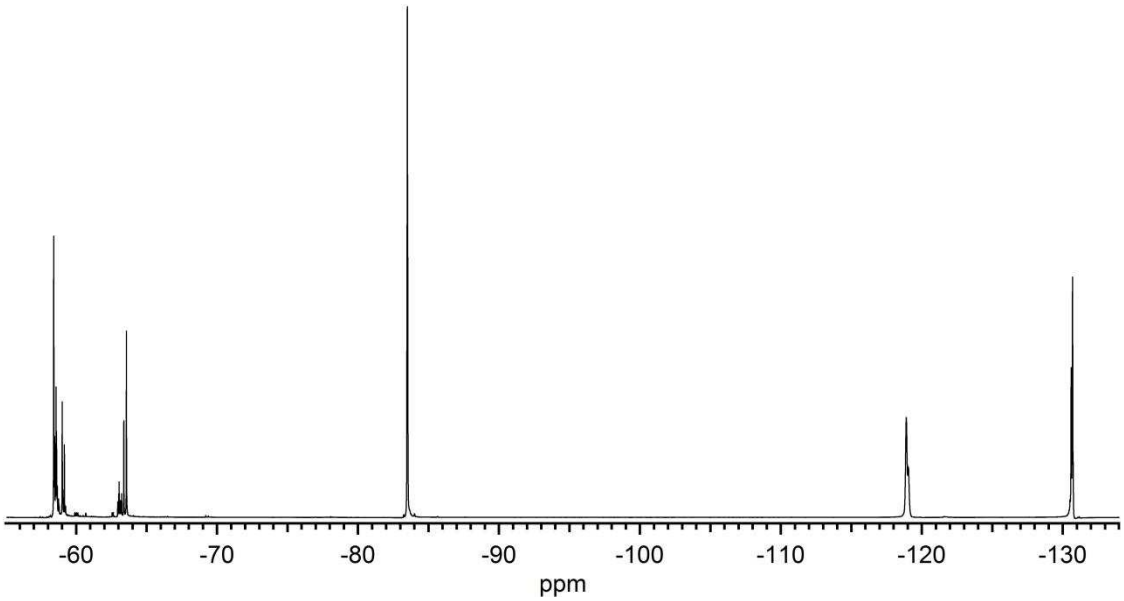

Figure 3.3. Fluorine-19 NMR spectrum in $CDCl_3$ of crude PDI(F7Bu)-$(CF_3)_{2\text{-}4}$ after flash chromatography.

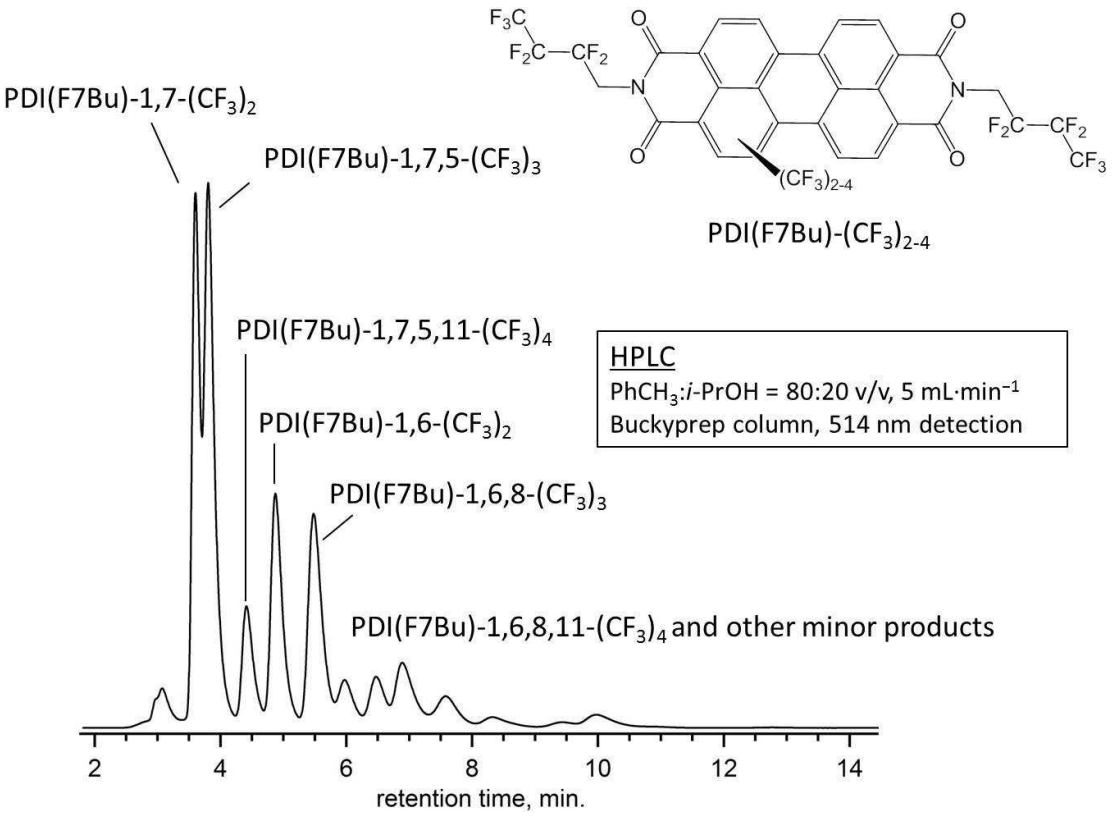

Figure 3.4. HPLC of a mixture of PDI(F7Bu)-$(CF_3)_{2\text{-}4}$ derivatives, 80-20 tol-iPrOH, 514 nm detection, BuckyPrep semiprep column, 5 mL·min−1.

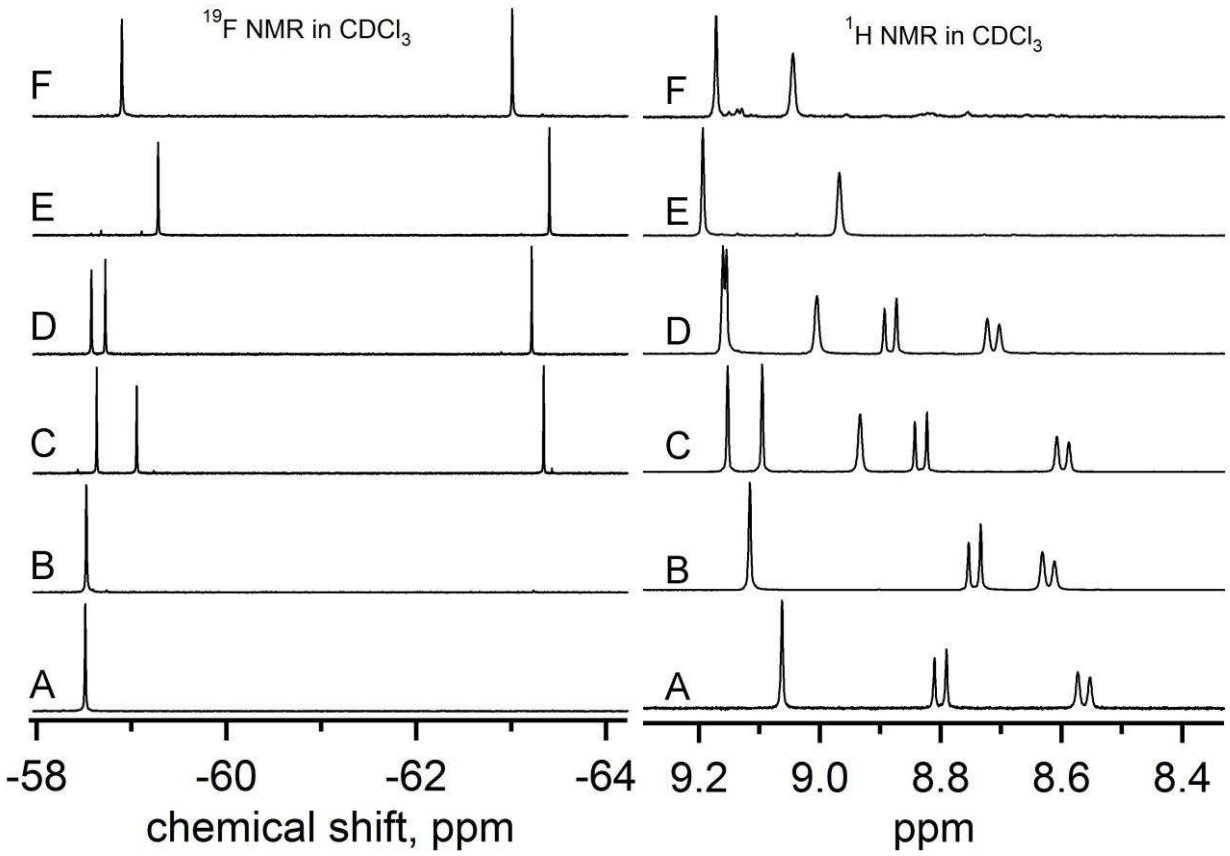

Figure 3.5. ^{19}F (left) and ^{1}H NMR (right) in $CDCl_3$ of: A) PDI(Bu)-1,7-$(CF_3)_2$, B) PDI(Bu)-1,6-$(CF_3)_2$, C) PDI(Bu)-1,7,5-$(CF_3)_3$, D) PDI(Bu)-1,6,8-$(CF_3)_3$, E) PDI(Bu)-1,7,5,11-$(CF_3)_4$, and F) PDI(Bu)-1,6,8,11-$(CF_3)_4$. Only the signals from CF_3 groups and core H are shown. See experimental section for chemical shifts from other H atoms.

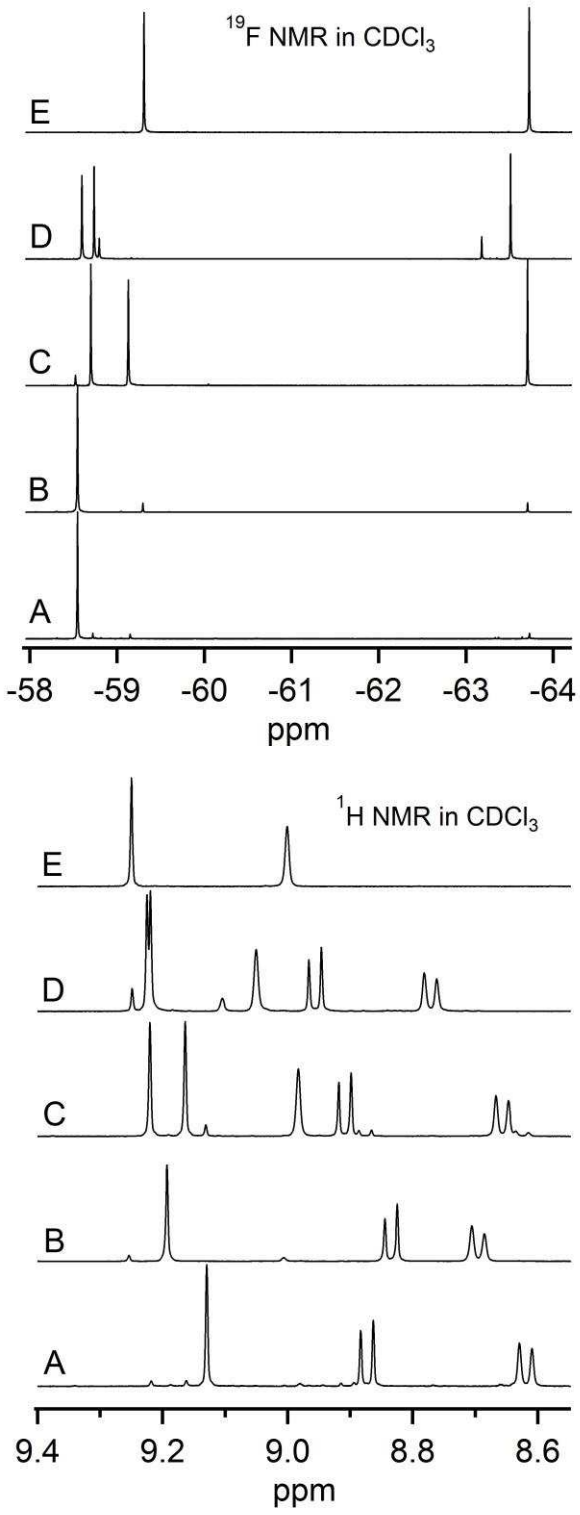

Figure 3.6. ^{19}F (top) and ^{1}H NMR (bottom) in $CDCl_3$ of: A) PDI(F7Bu)-1,7-$(CF_3)_2$, B) PDI(F7Bu)-1,6-$(CF_3)_2$, C) PDI(F7Bu)-1,7,5-$(CF_3)_3$, D) PDI(F7Bu)-1,6,8-$(CF_3)_3$, and E) PDI(F7Bu)-1,7,5,11-$(CF_3)_4$. Only the signals from CF_3 groups and core H are shown. See experimental section for chemical shifts from other F and H atoms.

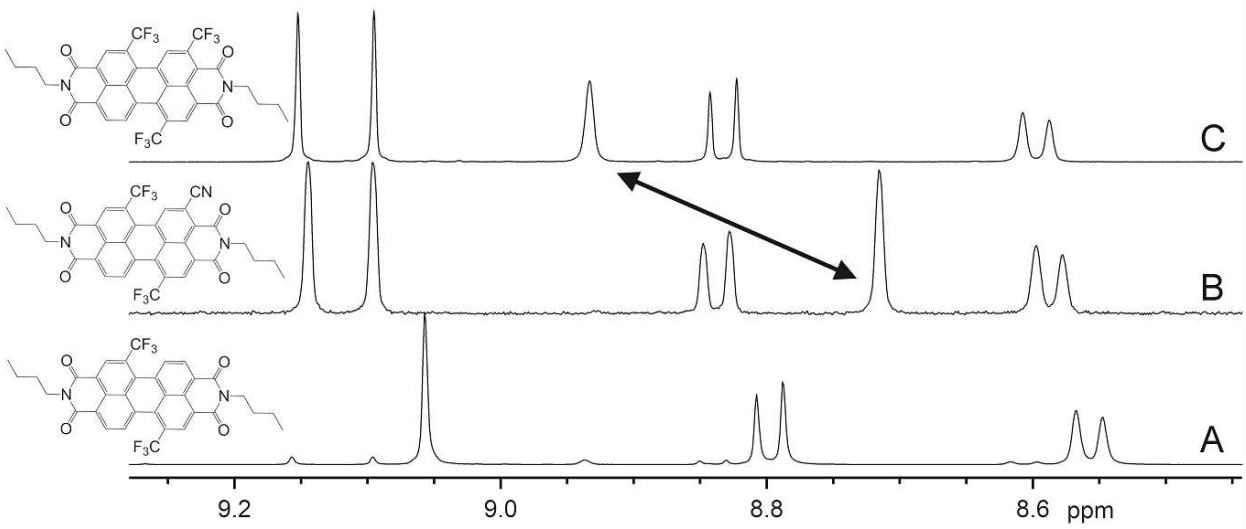

Figure 3.7. Proton NMR spectra showing the core ^{1}H signals from PDI(Bu)-1,7-$(CF_3)_2$ (A), PDI(Bu)-1,7-$(CF_3)_2$-5-(CN) (B), and PDI(Bu)-1,7,5-$(CF_3)_3$ (C). The arrow shows the shift of the singlet corresponding to H6. The spectrum of PDI(Bu)-1,7-$(CF_3)_2$ contains a small impurity of PDI(Bu)-1,7,5-$(CF_3)_3$.

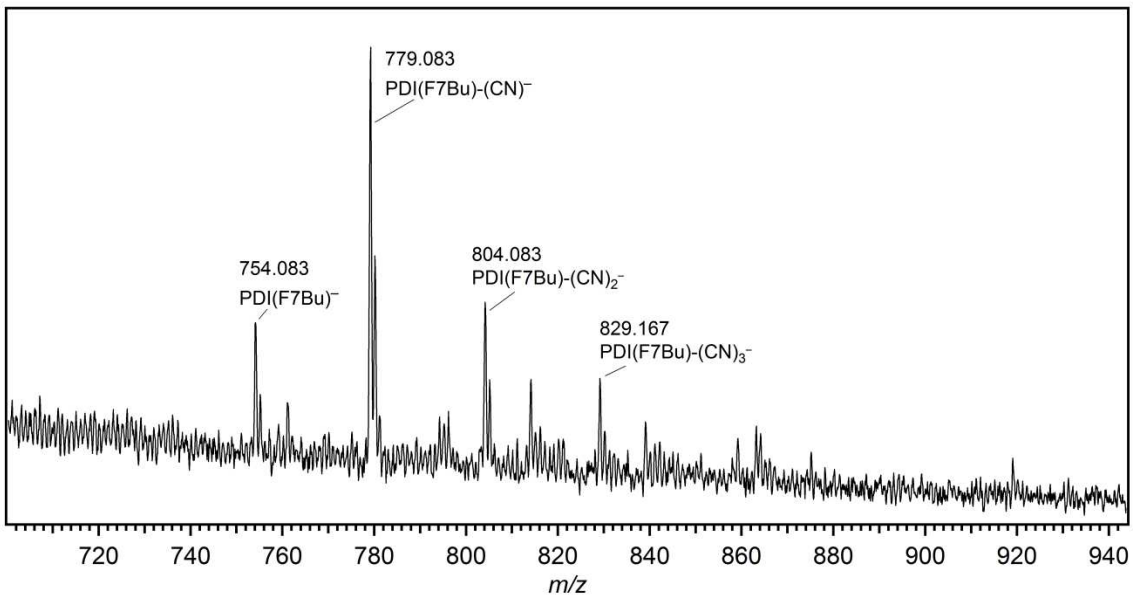

Figure 3.8. Negative-ion ESI mass spectrum showing up to three CN substitutions on PDI(F7Bu).

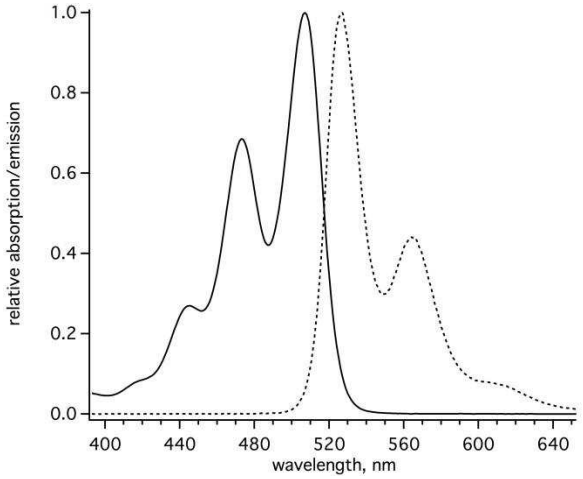

PDI(Bu)-1,7-$(CF_3)_2$

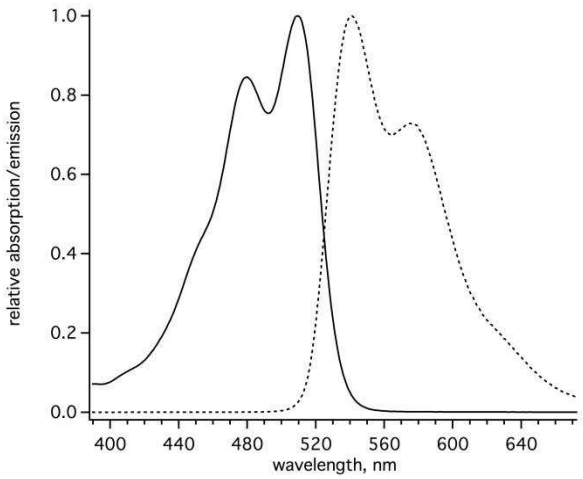

PDI(Bu)-1,6-$(CF_3)_2$

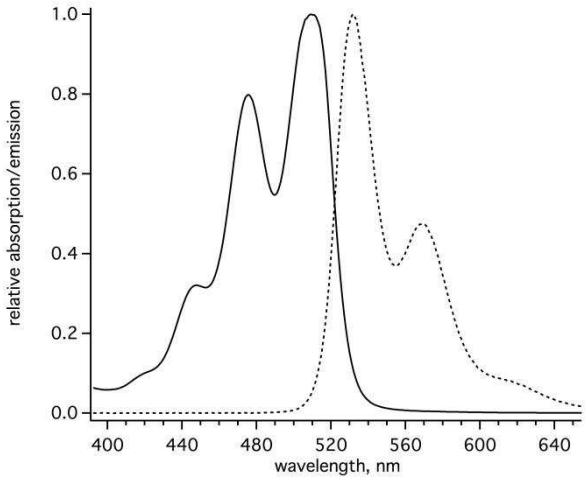

PDI(Bu)-1,7,5-$(CF_3)_3$

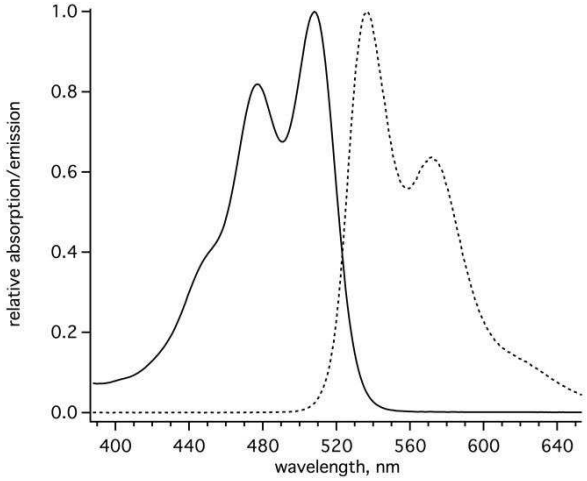

PDI(Bu)-1,6,8-$(CF_3)_3$

Figure 3.9. Absorption and emission spectra of four PDI derivatives in DCM. Solid trace = absorption, dotted trace = emission. The emission spectra shown are from 430 nm excitations.

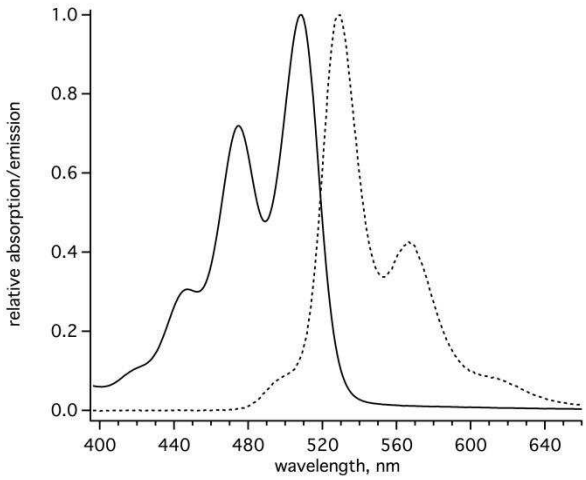

PDI(Bu)-1,7,5,11-$(CF_3)_4$

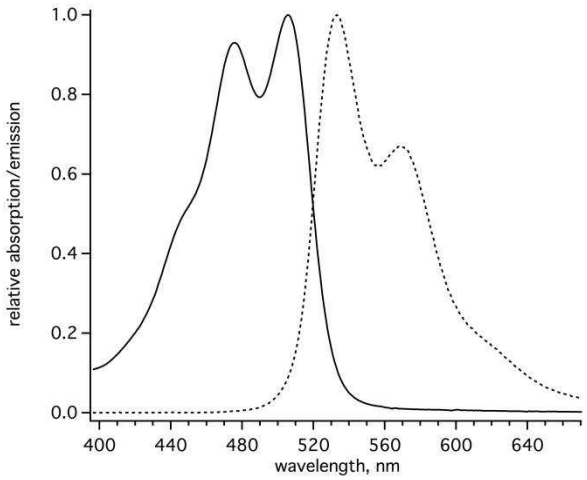

PDI(Bu)-1,6,8,11-$(CF_3)_4$

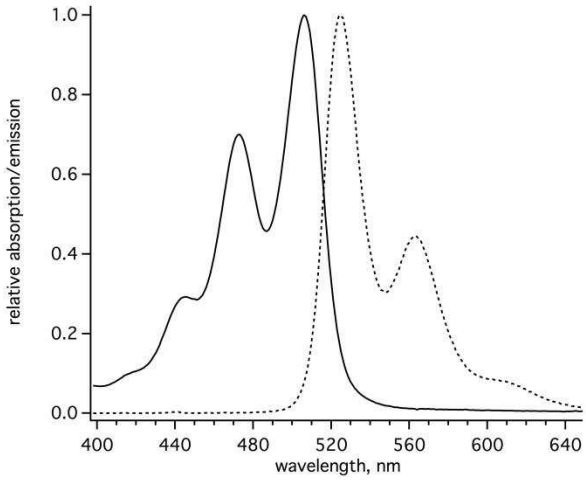

PDI(F7Bu)-1,7-$(CF_3)_2$

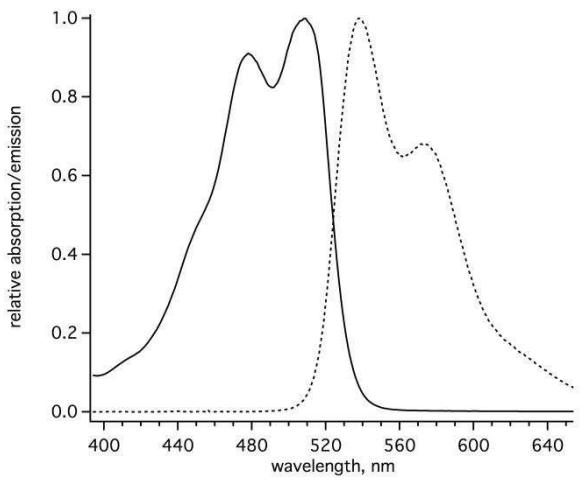

PDI(F7Bu)-1,6-$(CF_3)_2$

Figure 3.10. Absorption and emission spectra of four PDI derivatives in DCM. Solid trace = absorption, dotted trace = emission. The emission spectra shown are from 430 nm excitations.

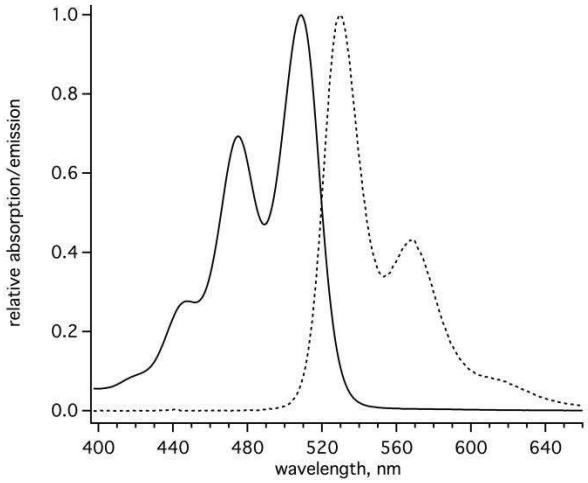

PDI(F7Bu)-1,7,5-$(CF_3)_3$

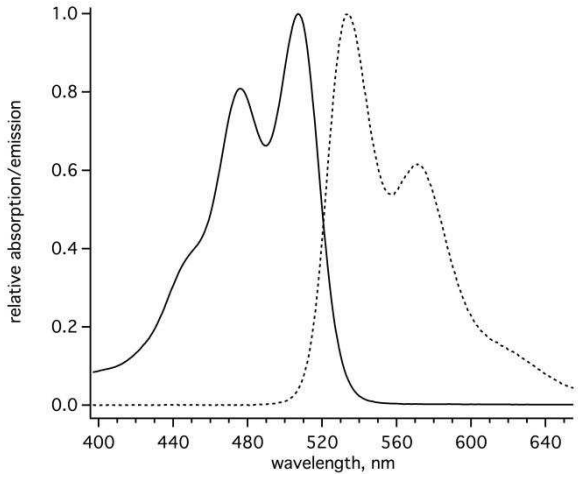

PDI(F7Bu)-1,6,8-$(CF_3)_3$

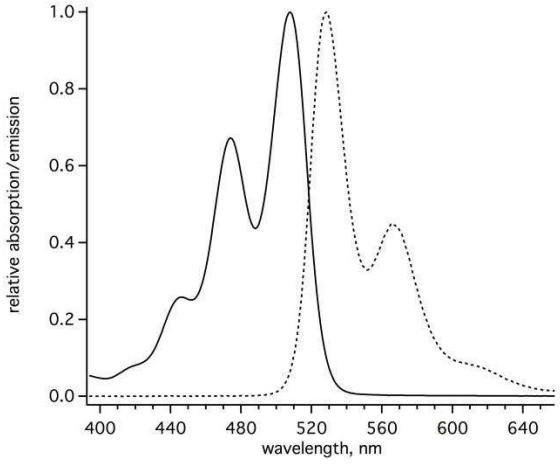

PDI(F7Bu)-1,7,5,11-$(CF_3)_4$

Figure 3.11. Absorption and emission spectra of three PDI derivatives in DCM. Solid trace = absorption, dotted trace = emission. The emission spectra shown are from 430 nm excitations.

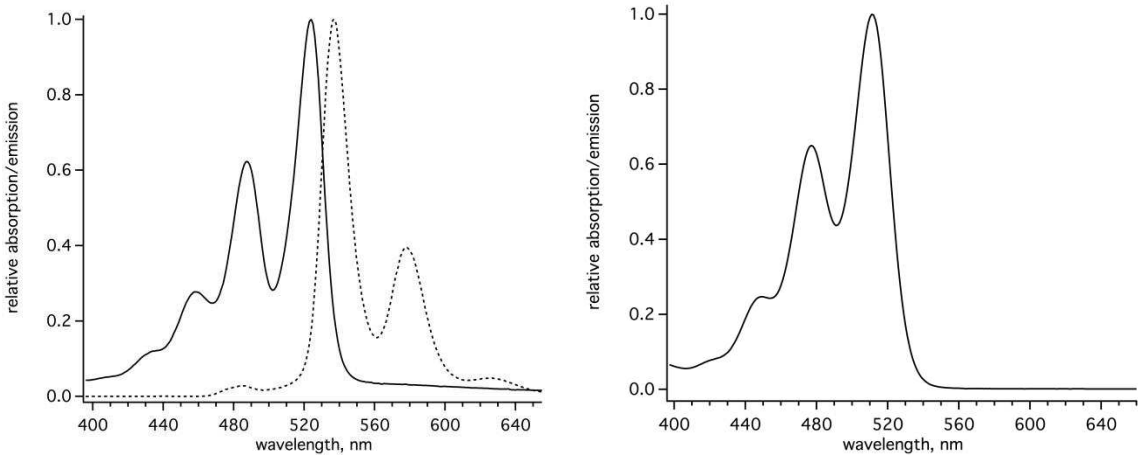

PDI(Bu) PDI(Bu)-1,7-$(CF_3)_2$-5-(CN)

Figure 3.12. Absorption and emission spectra of two PDI derivatives in DCM. Solid trace = absorption, dotted trace = emission. The emission spectra shown are from 430 nm excitations.

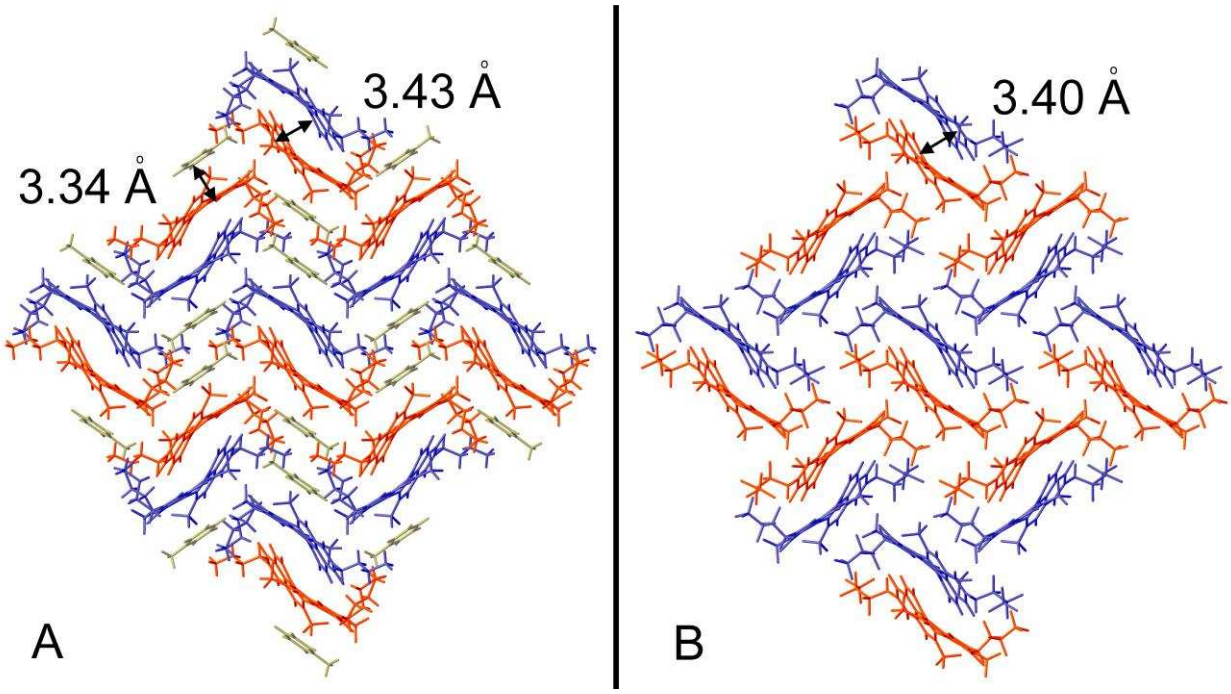

Figure 3.13. Crystallographic packing observed down the *a*-axis in the monoclinic space group $P2_1/n$ for A) PDI(Bu)-1,7,5-$(CF_3)_3$ with toluene and B) PDI(F7Bu)-1,7,5-$(CF_3)_3$ with no solvent. Red = *P*-enantiomers, blue = *M*-enantiomers, and grey = toluene.

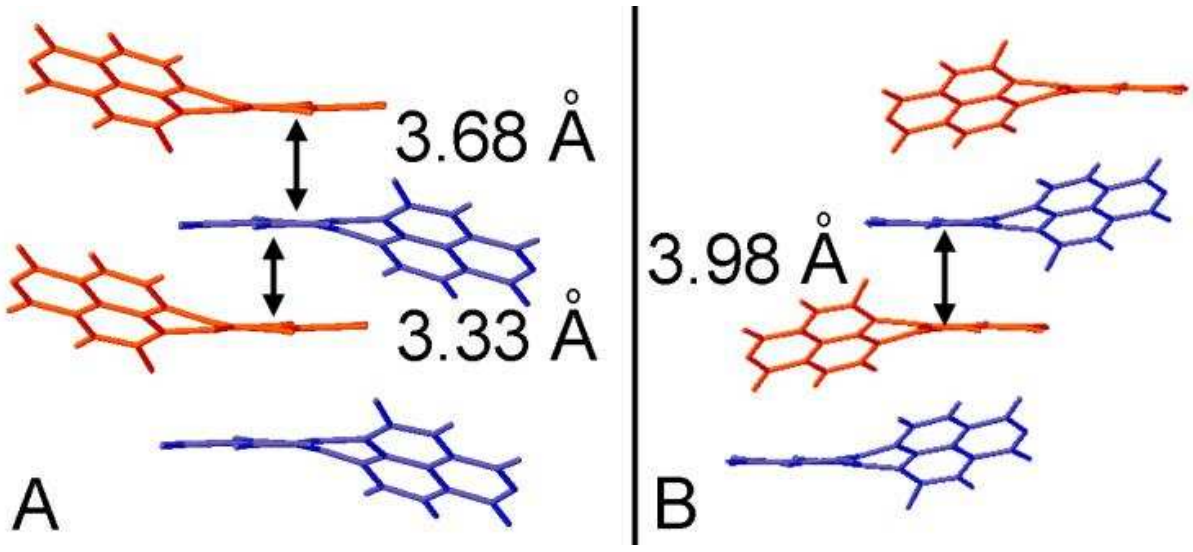

Figure 3.14. Crystallographic packing observed in columns of solvent free structures of A) PDI(Bu)-1,7-$(CF_3)_2$ and B) PDI(F7Bu)-1,7-$(CF_3)_2$. Red = *P*-enantiomers, blue = *M*-enantiomers. Fluorine atoms and imide chains were removed for clarity.

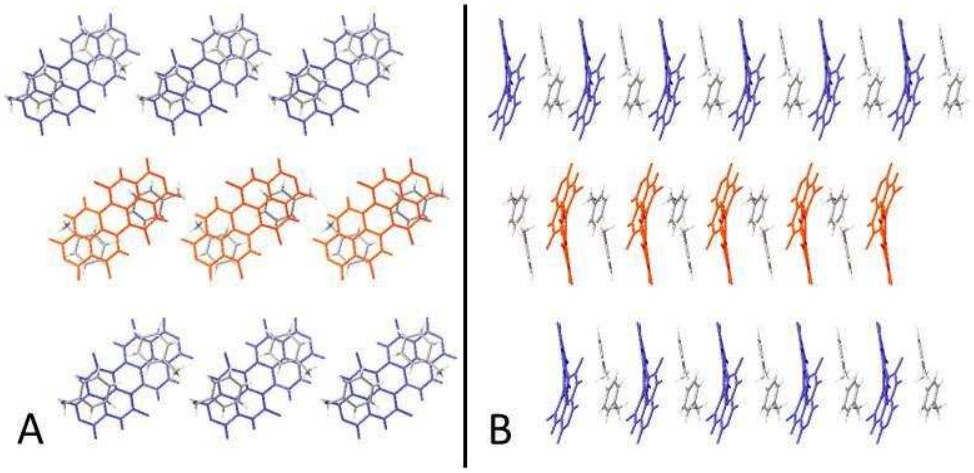

Figure 3.15. Solid-state packing of PDI(F7Bu)-1,6,8-$(CF_3)_3$ with toluene viewed down the *a*-axis (A) and down the *b*-axis (B). Red = *P*-enantiomers, blue = *M*-enantiomers, and grey = toluene. Fluorine atoms and imide chains were removed for clarity.

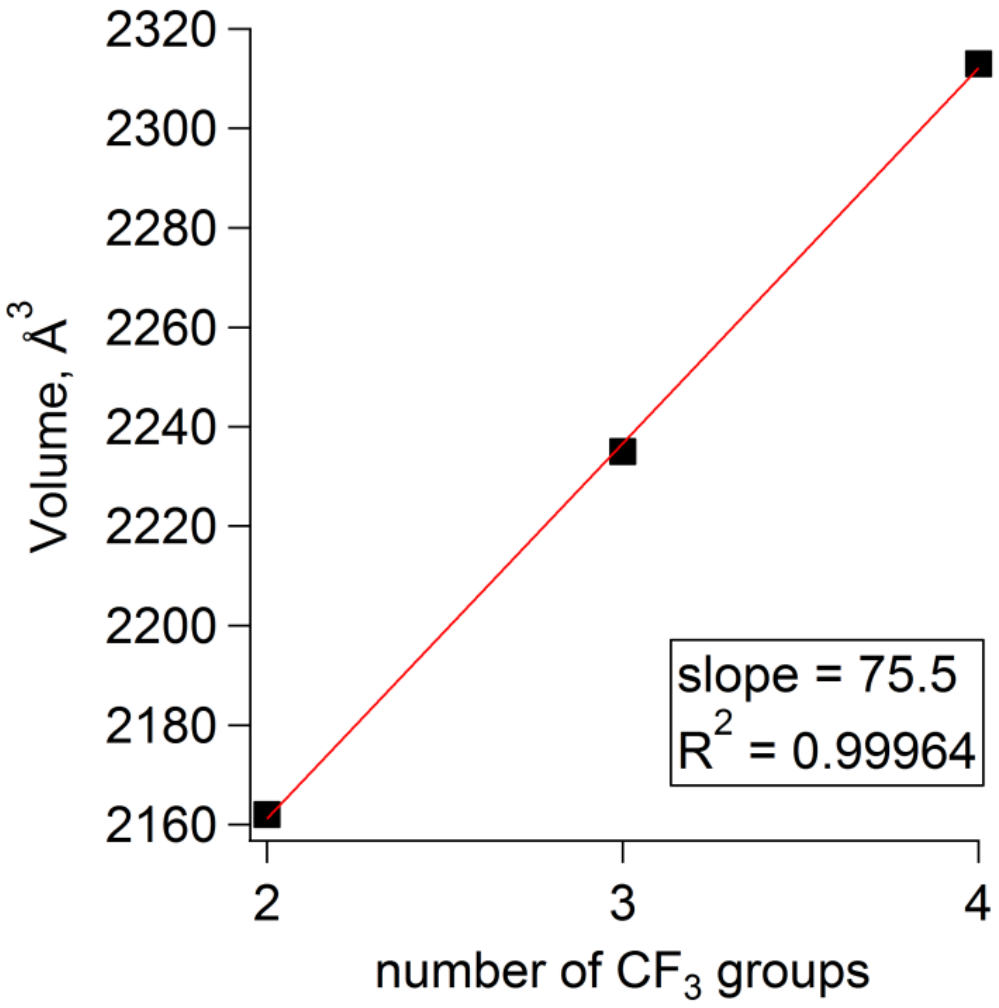

Figure 3.16. Unit cell volumes of PDI(F7Bu)-1,6-$(CF_3)_2$, PDI(F7Bu)-1,6,8-$(CF_3)_3$, and PDI(F7Bu)-1,6,8,11-$(CF_3)_4$ vs number of CF_3 groups.

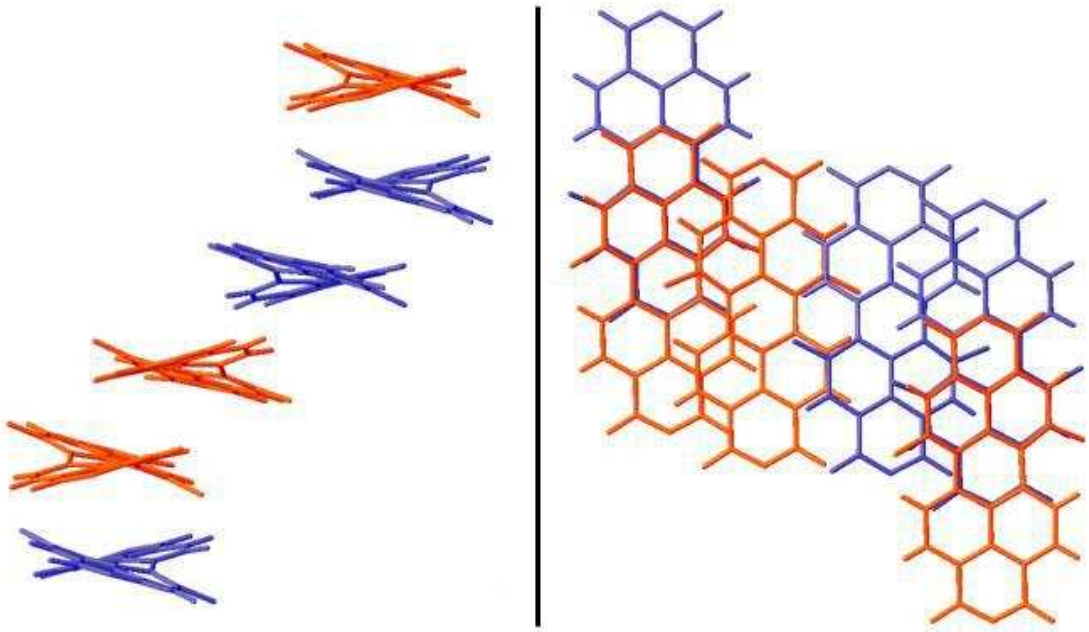

Figure 3.17. Solid-state packing of six molecules of PDI(Bu)-1,6-$(CF_3)_2$ in a column viewed from two different angles. Red = *P*-enantiomers, blue = *M*-enantiomers. Dichloromethane, fluorine atoms, and imide chains were removed for clarity.

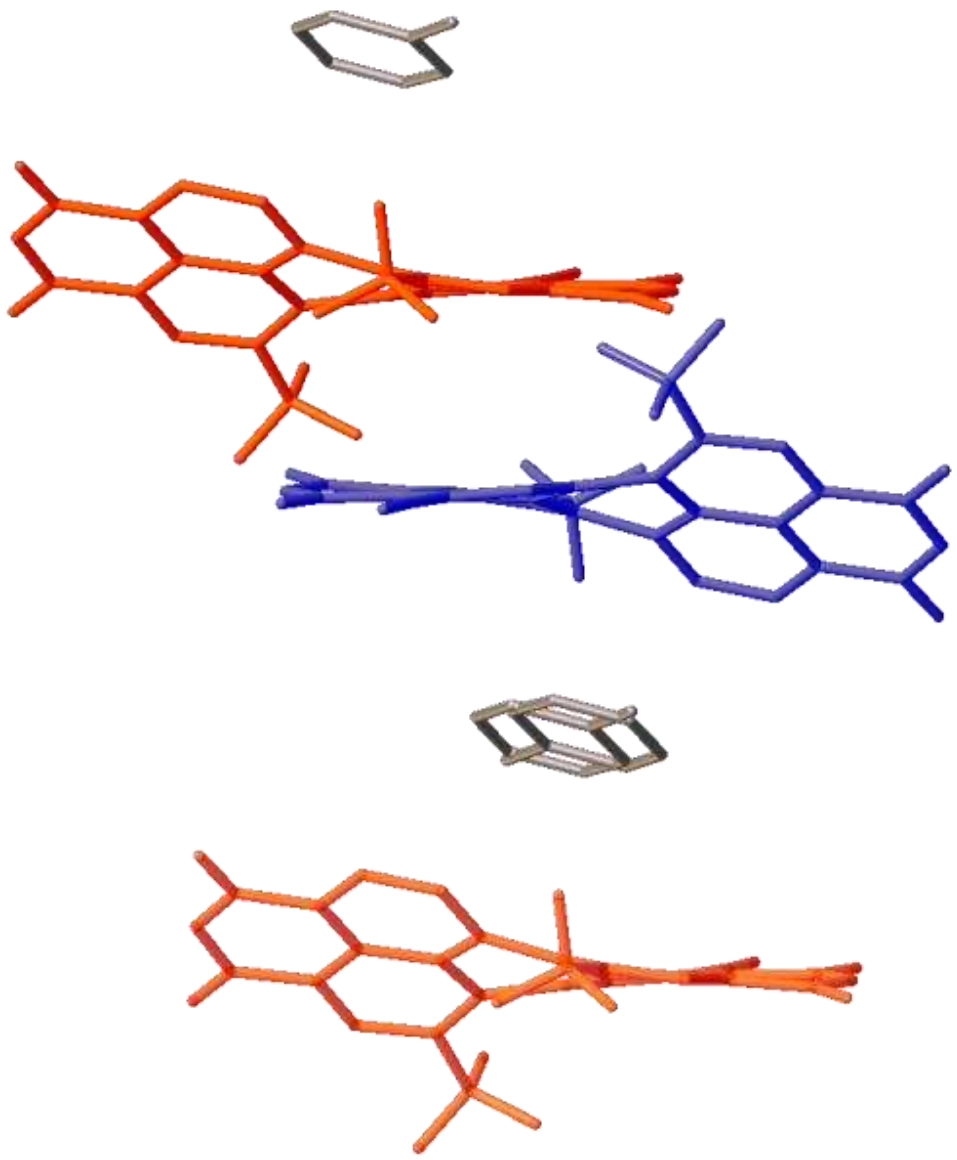

Figure 3.18. Packing of three molecules of PDI(Bu)-1,7-$(CF_3)_2$-5-(CN) with disordered toluene. Blue = M-enantiomer, red = P-enantiomer, and grey = toluene.

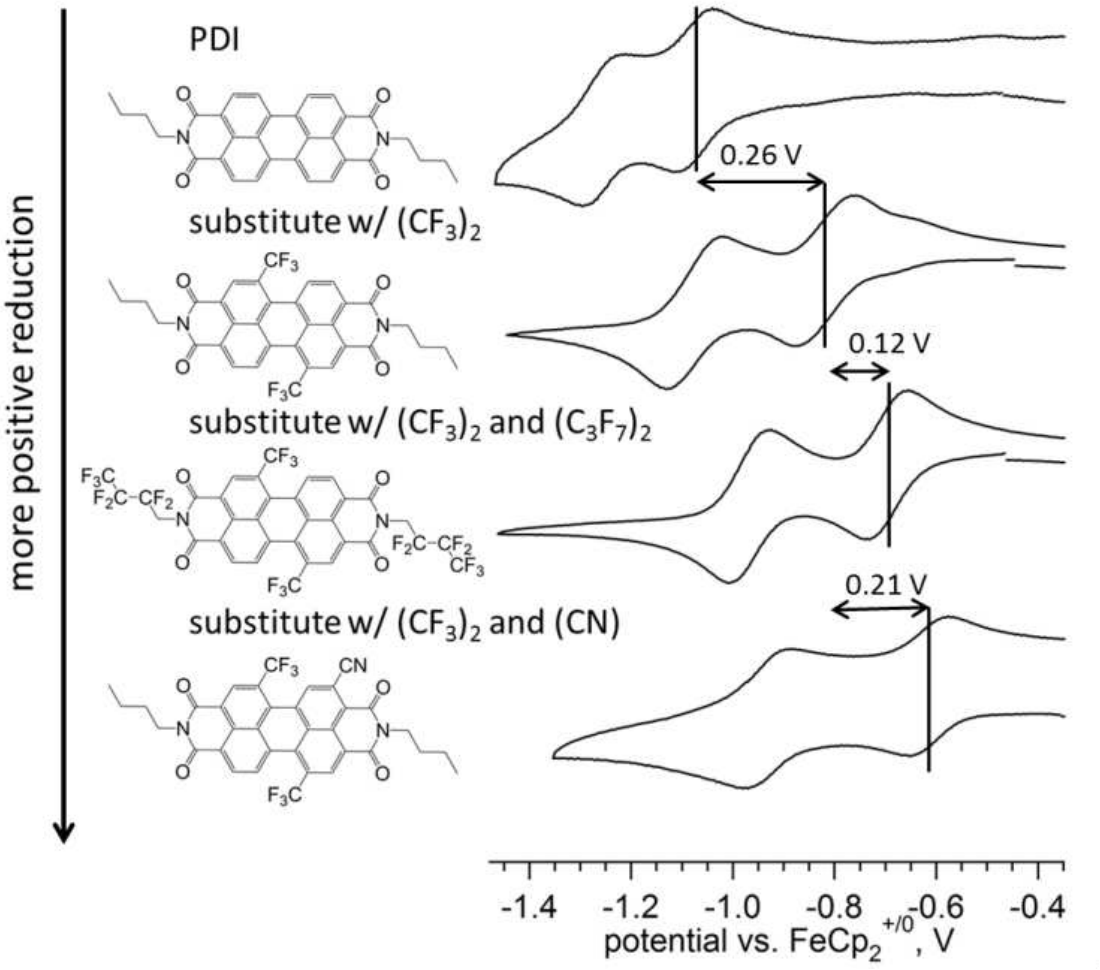

Figure 3.19. Representative cyclic voltammograms using 0.1 M $TBAPF_6$ in DCM at a scan rate of 100 $mV \cdot s^{-1}$ with $FeCp_2^{+/0}$ as an internal standard. $E_{1/2}^{0/-}$ are illustrated with vertical lines and selected differences in $E_{1/2}^{0/-}$ between molecules are given.

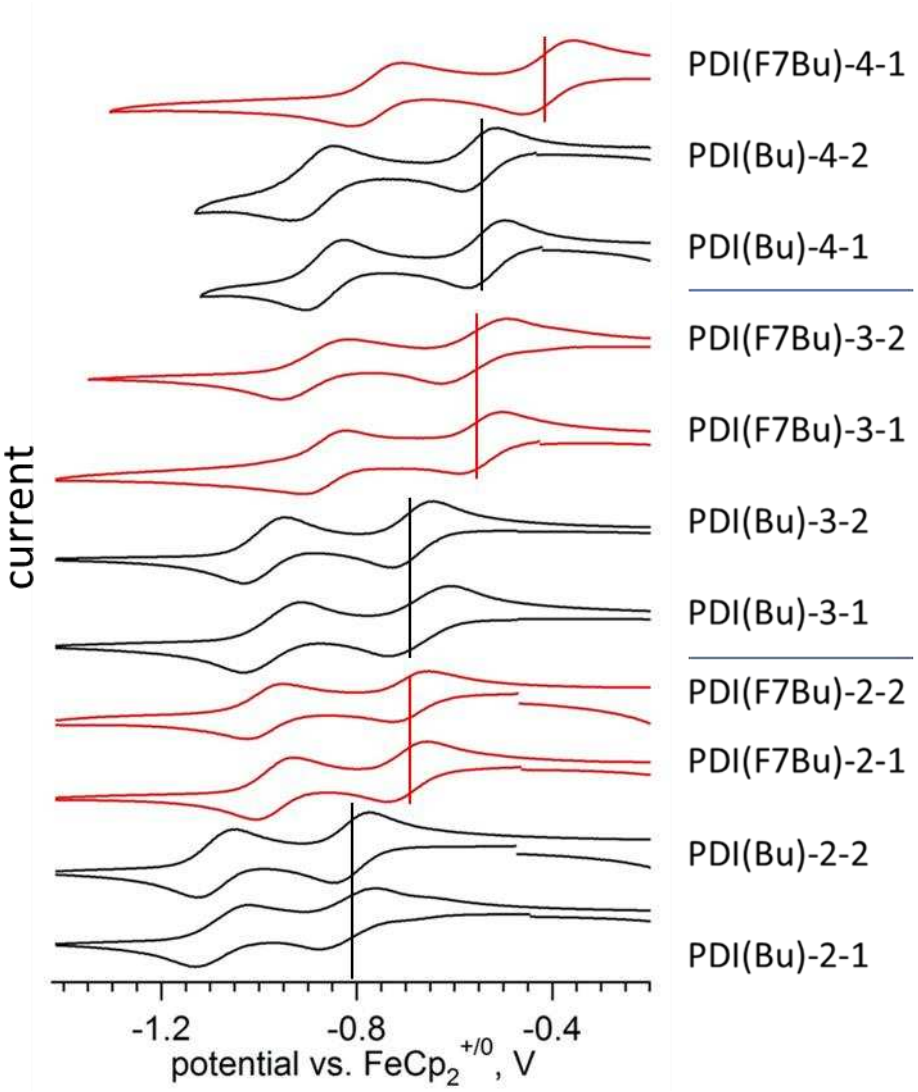

Figure 3.20. Cyclic voltammograms of PDI(Bu)-$(CF_3)_n$ and PDI(F7Bu)-$(CF_3)_n$ in dichloromethane with 0.1 M $TBAPF_6$ and $FeCp_2$ as an internal standard (not shown), 100 $mV \cdot s^{-1}$. Vertical lines are roughly in the position of $E_{1/2}{}^{0/-}$ for each set of isomers in order to guide the eye.

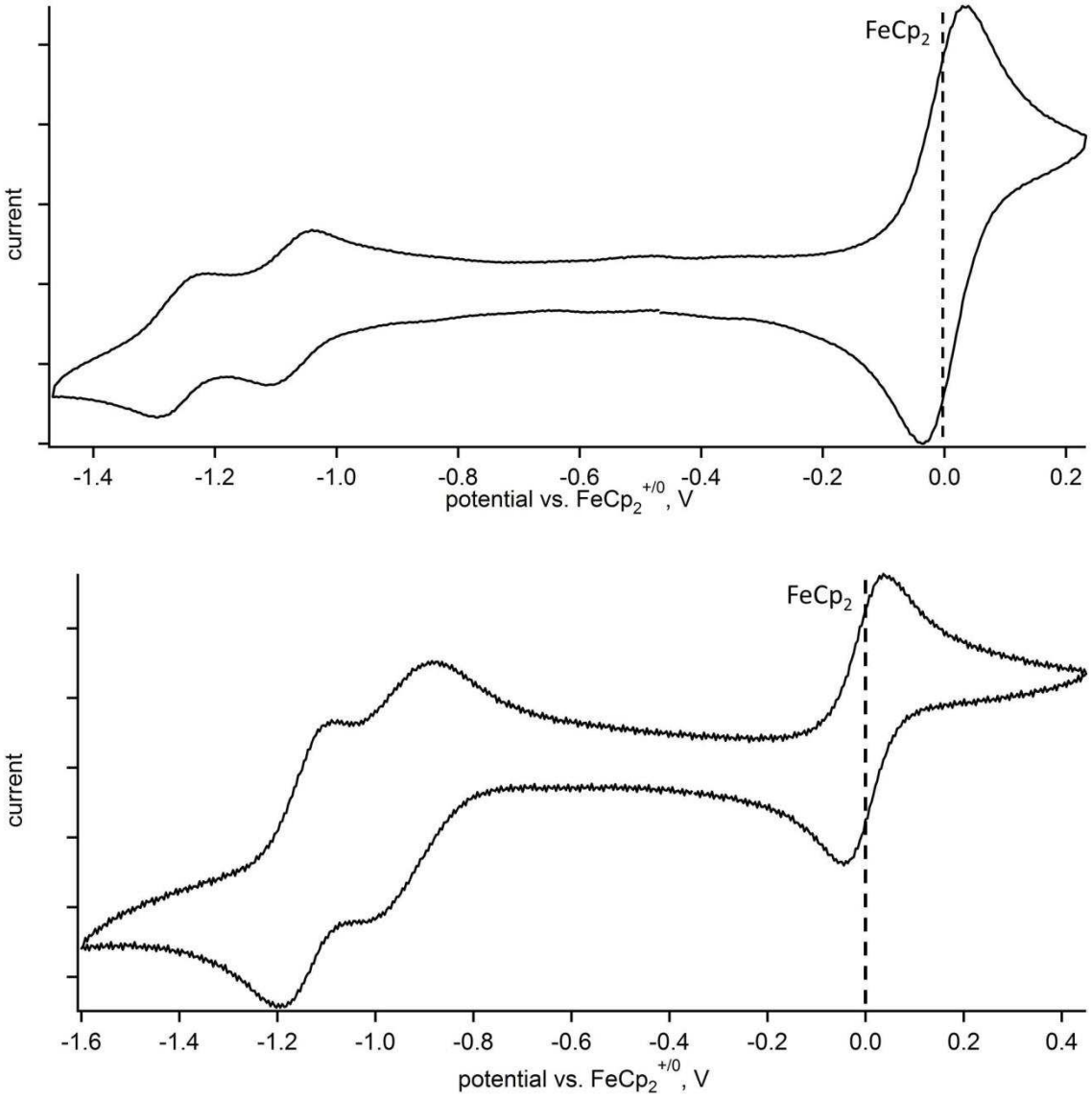

Figure 3.21. Cyclic Voltammograms of PDI(Bu) (top) and PDI(F7Bu) (bottom) in dichloromethane with 0.1 M $TBAPF_6$ and $FeCp_2$ as an internal standard, 100 $mV \cdot s^{-1}$.

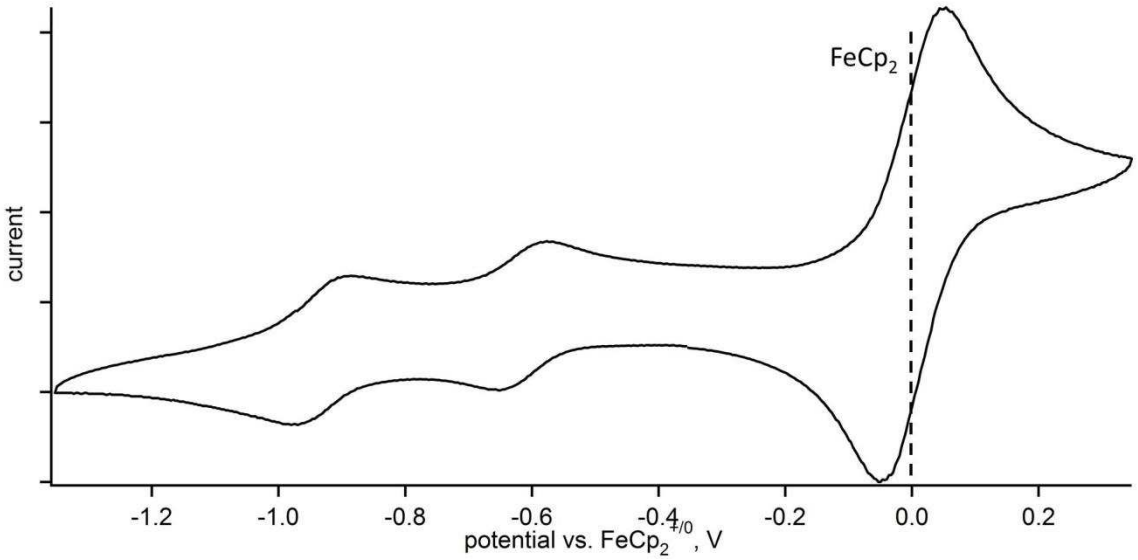

Figure 3.22. Cyclic Voltammogram of PDI(Bu)-1,7-$(CF_3)_2$-5-(CN) in dichloromethane with 0.1 M $TBAPF_6$ and $FeCp_2$ as an internal standard, 100 $mV \cdot s^{-1}$.

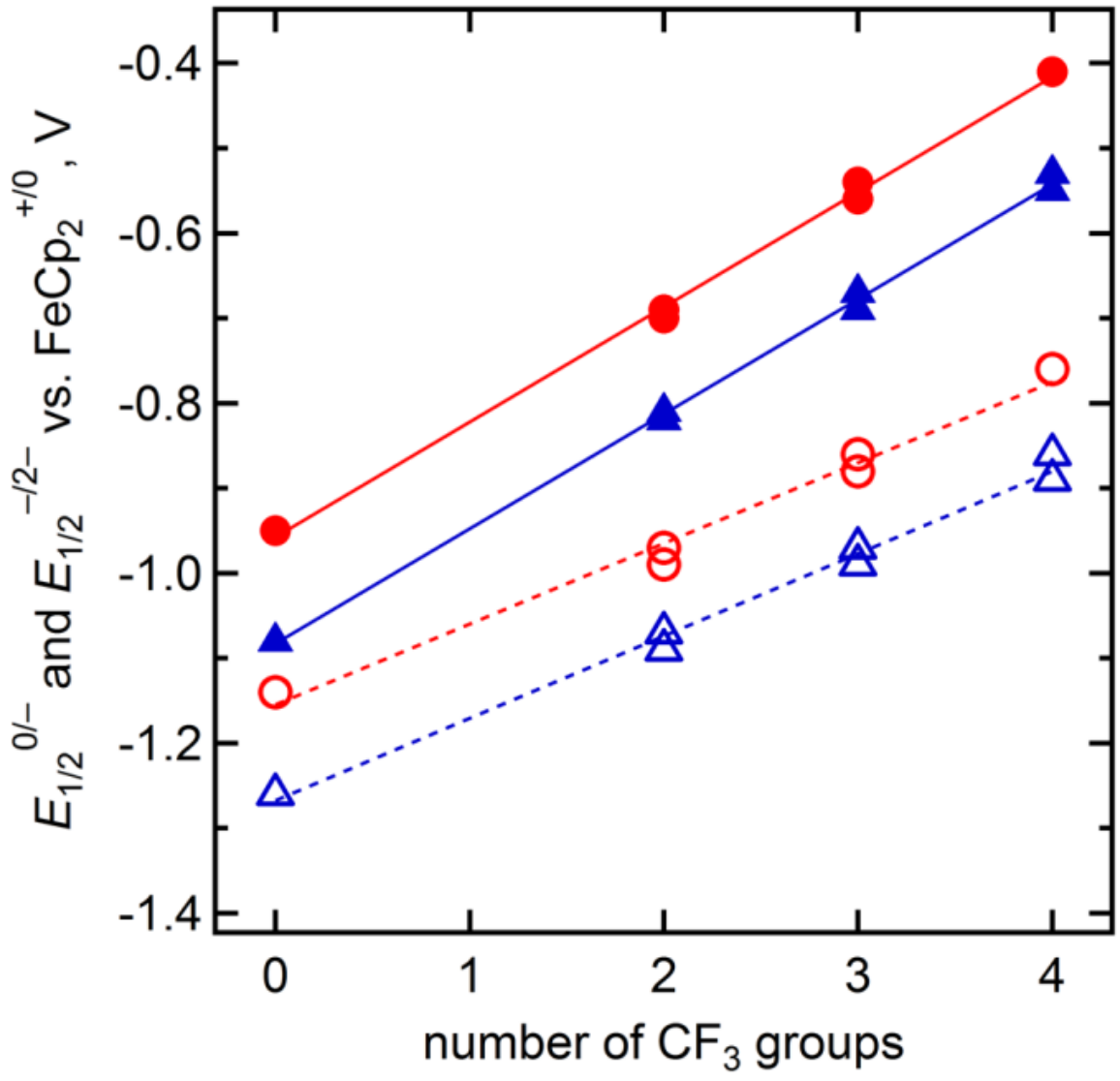

Figure 3.23. Reduction potentials of PDI(F7Bu)-$(CF_3)_{2\text{-}4}$ (red circles) and PDI(Bu)-$(CF_3)_{0\text{-}4}$ (blue triangles) using 0.1 M $TBAPF_6$ in DCM with $FeCp_2$ as an internal standard and a scan rate of 100 $mV \cdot s^{-1}$. Filled symbols and solid lines represent $E_{1/2}{}^{0/-}$, open symbols and dashed lines represent $E_{1/2}{}^{-/2-}$. For PDI(Bu)-$(CF_3)_n$: $E_{1/2}{}^{0/-} = 0.14n - 1.08$ ($R^2 = 0.998$), $E_{1/2}{}^{-/2-} = 0.10n - 1.27$ ($R^2 = 0.990$) and for PDI(F7Bu)-$(CF_3)_n$: $E_{1/2}{}^{0/-} = 0.14n - 0.96$ ($R^2 = 0.997$), $E_{1/2}{}^{-/2-} = 0.10n - 1.16$ ($R^2 = 0.985$).

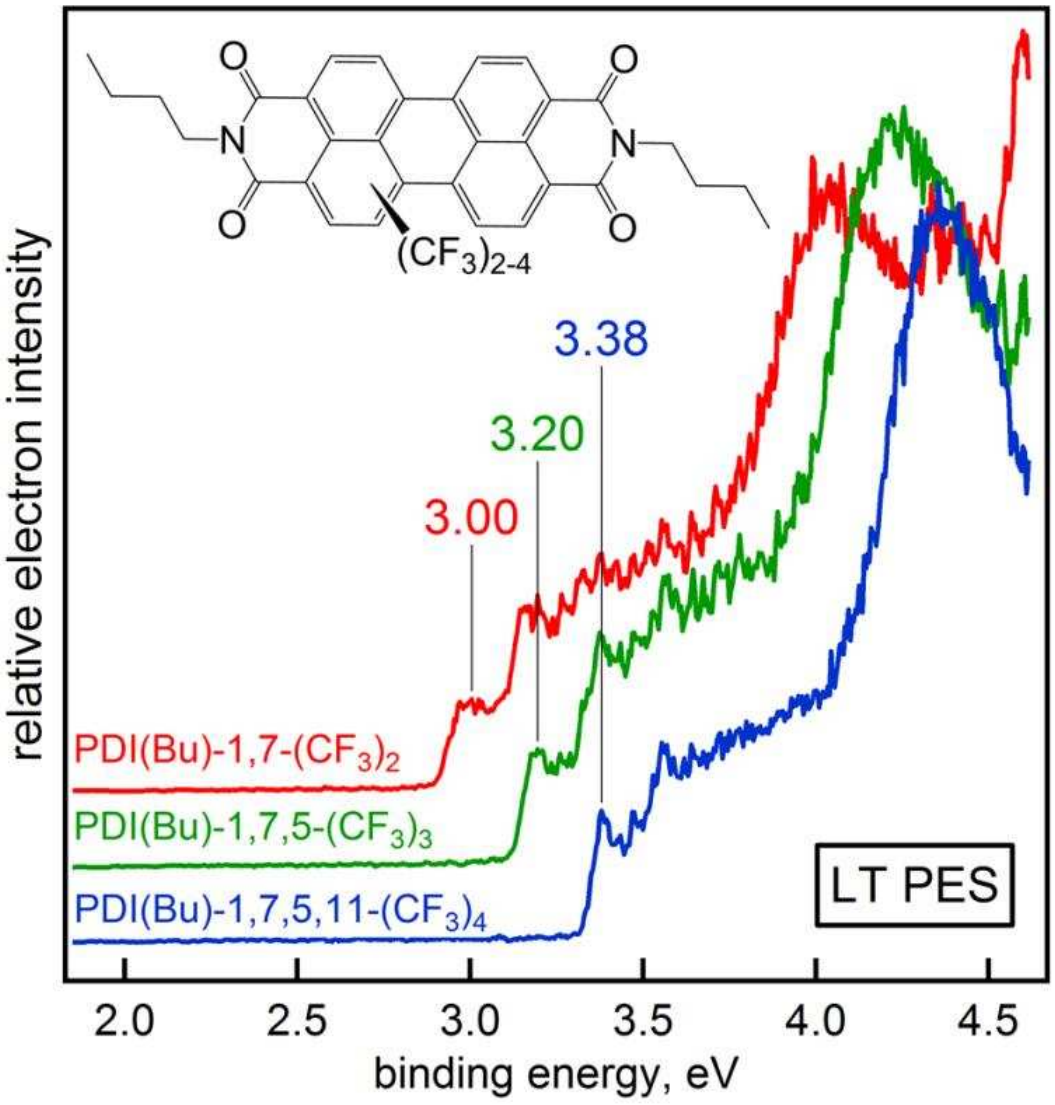

Figure 3.24. Low-temperature photoelectron spectra of three trifluoromethyl PDIs. EA = 3.00(2), 3.20(2), and 3.38(2) eV for PDI(Bu)-1,7-$(CF_3)_2$, PDI(Bu)-1,7,5-$(CF_3)_3$, and PDI(Bu)-1,7,5,11-$(CF_3)_4$, respectively

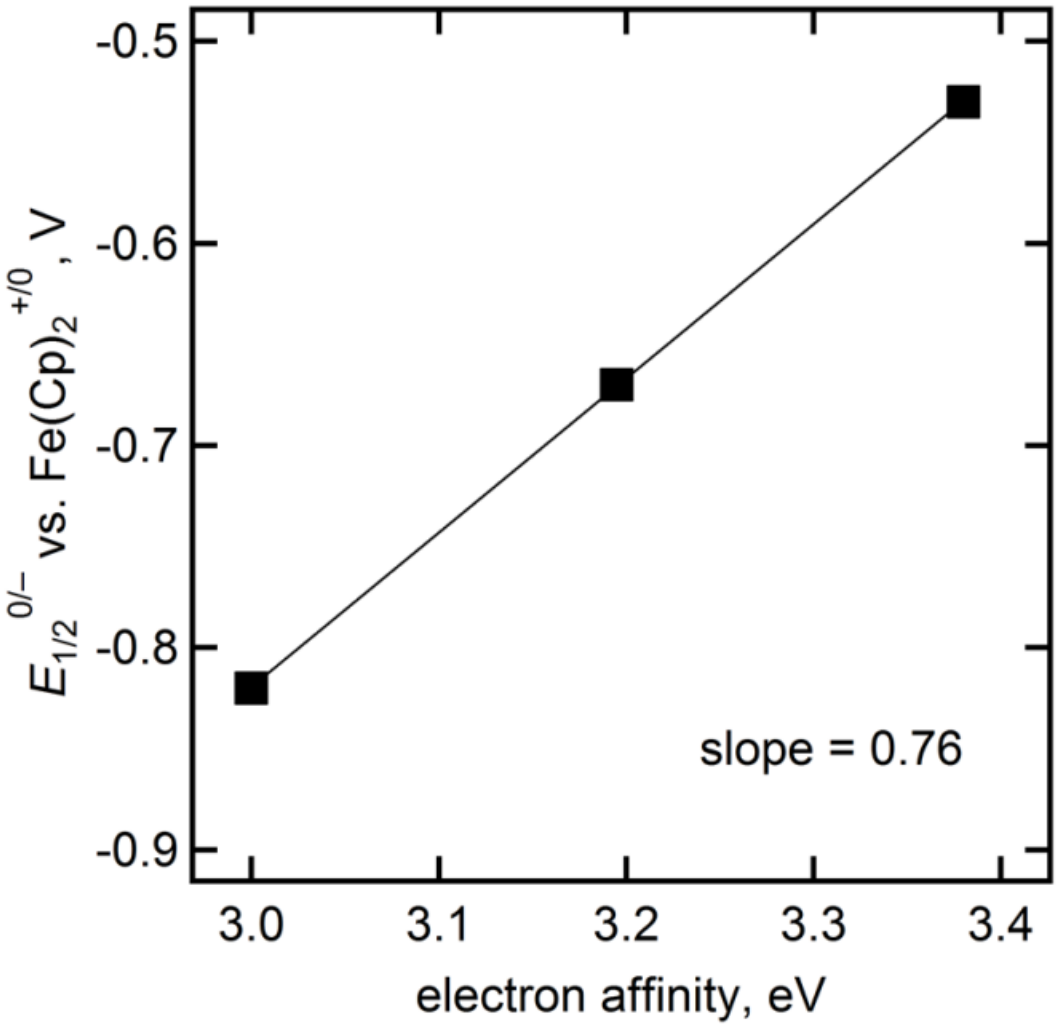

Figure 3.25. $E_{1/2}{}^{0/-}$ vs. EA for three trifluoromethyl PDIs.

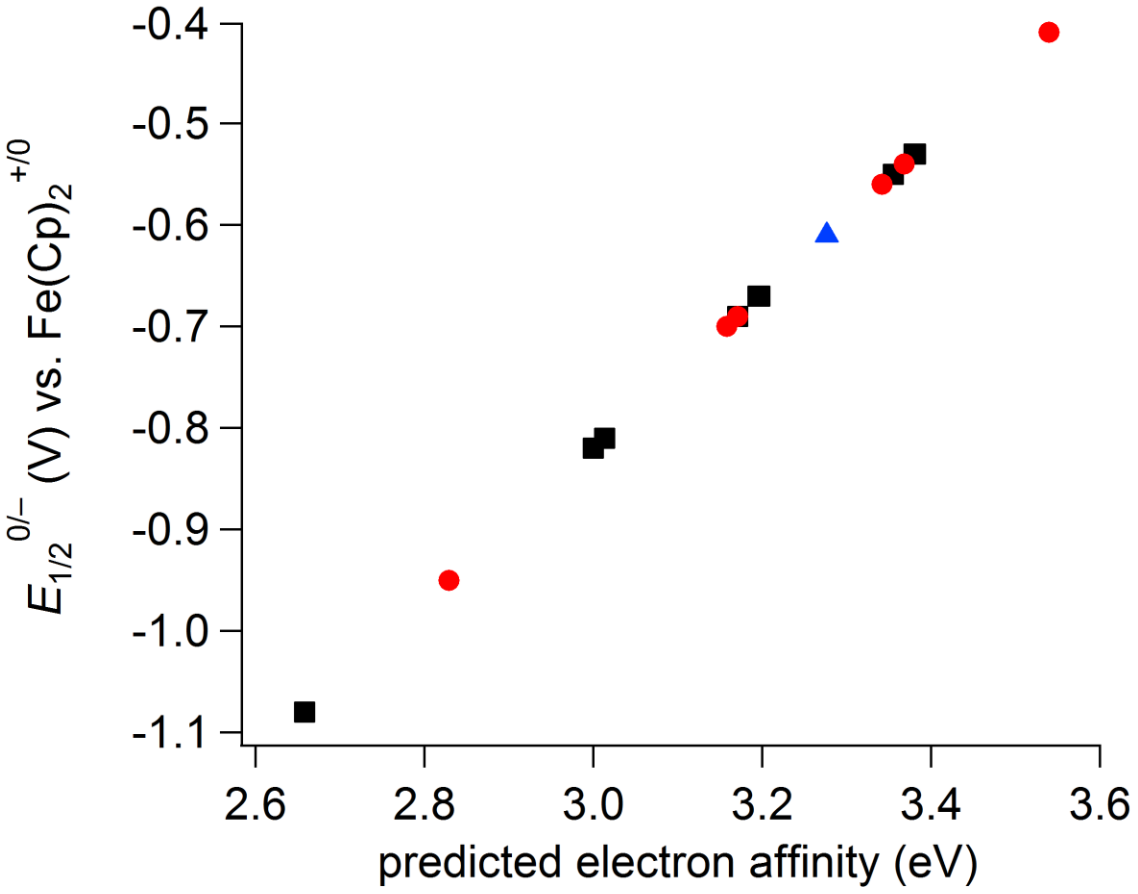

Figure 3.26. $E_{1/2}^{0/-}$ vs. predicted EA of PDI(Bu)-$(CF_3)_n$ (black squares), PDI(F7Bu)-$(CF_3)_n$ (red circles), and PDI(Bu)-1,7-$(CF_3)_2$-5-(CN) (blue triangle). The equation $E_{1/2}^{0/-}$ = 0.76X – 3.1 was derived from the three measured EA values (see Figure 3.12) and was used to calculate the predicted electron affinities of the remaining PDIs. The predicted EA of PDI(Bu) (2.66 eV) is similar to the DFT calculated EA of PDI(H) (2.74 eV).[Heimel, et al. *Nature Chem.* **2013**, *5*, 187.]

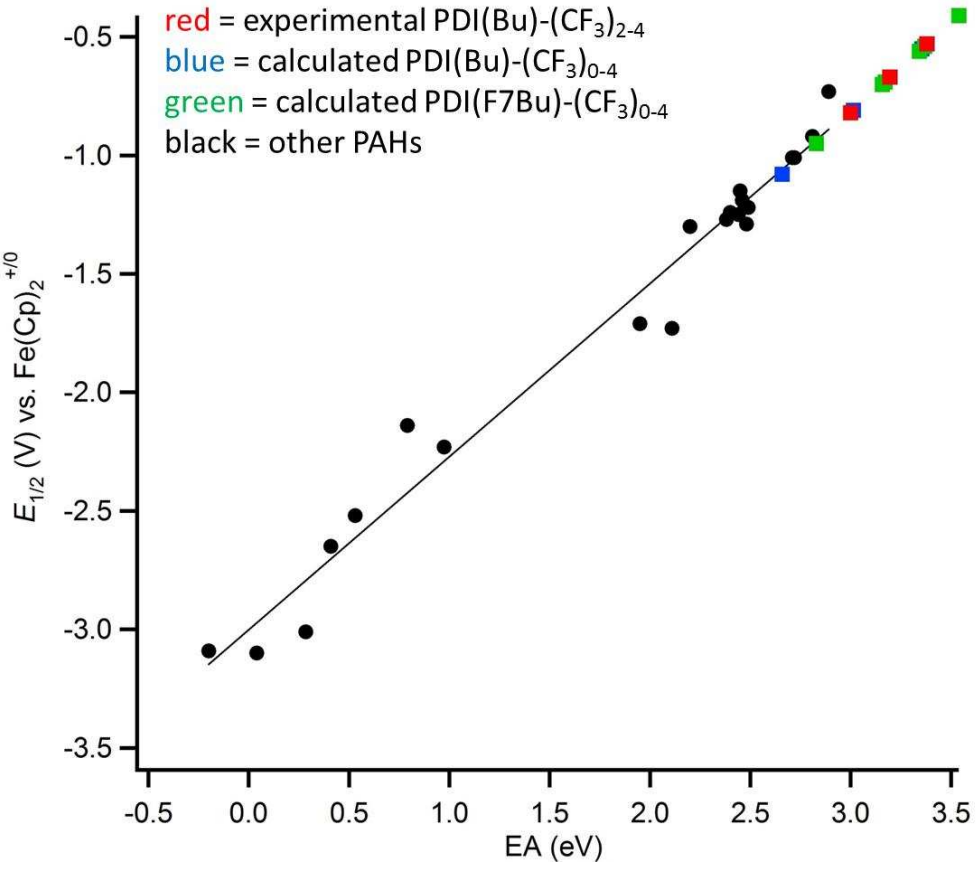

Figure 3.27. Reduction potential versus electron affinity of PAHs[25] and PDIs. The black line represents a linear fit of only the literature PAH values (black points).

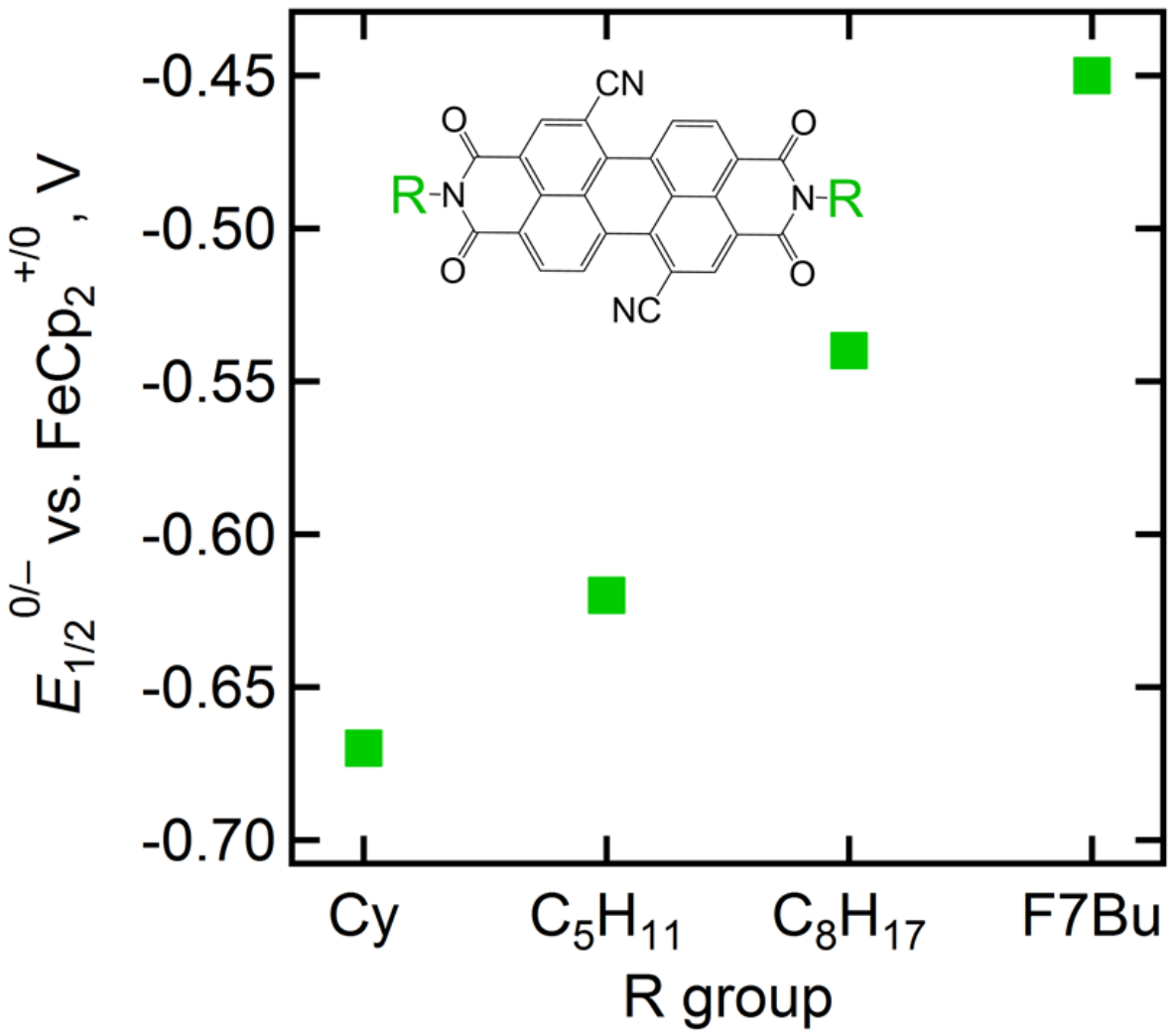

Figure 3.28. Plot of the reduction potential vs. imide substituent for different R in PDI(R)-1,7-$(CN)_2$.

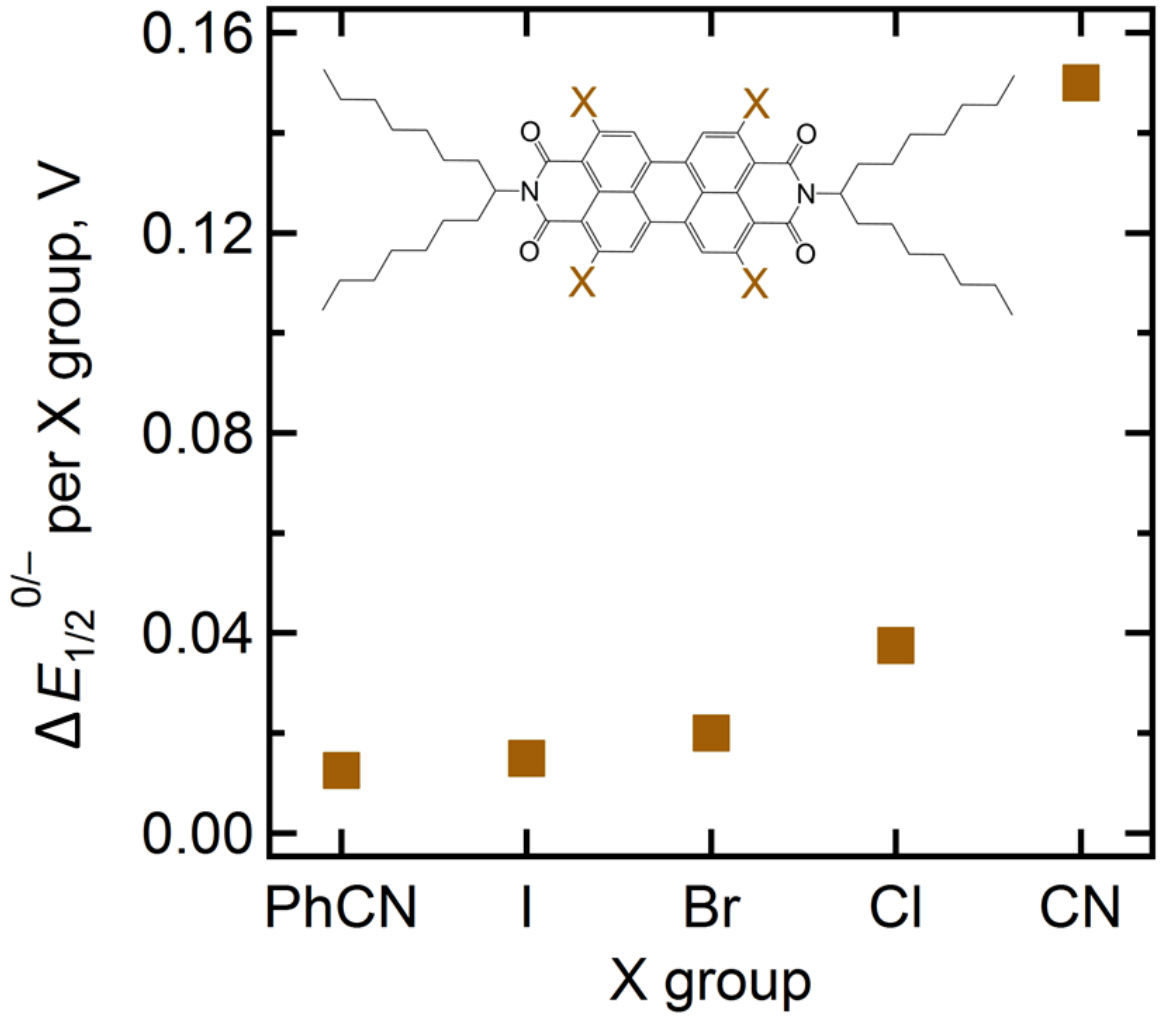

Figure 3.29. Plot of the change in reduction potential ($\Delta E_{1/2}{}^{0/-}$) vs. *ortho* substituent for constant PDI substitution pattern = PDI($C_{15}H_{31}$)-2,5,8,11-X_4.

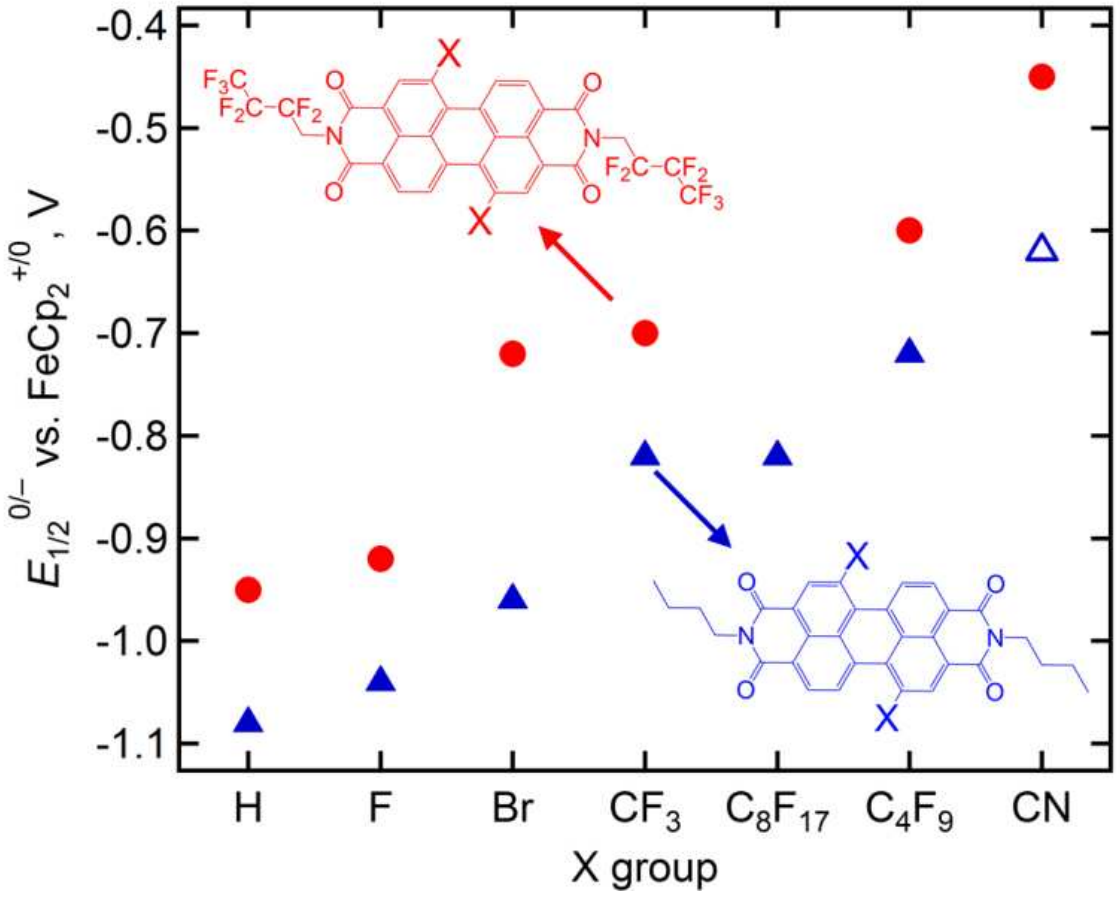

Figure 3.30. First reduction potential versus $FeCp_2^{+/0}$ in dichloromethane with $TBAPF_6$ electrolyte vs core substituent, X, in PDI(R)-1,7-X_2 derivatives. Red circles = PDI(F7Bu)-1,7-X_2, solid blue triangles = PDI(Bu)-1,7-X_2, and open blue triangle = PDI(C_5H_{11})-1,7-X_2.

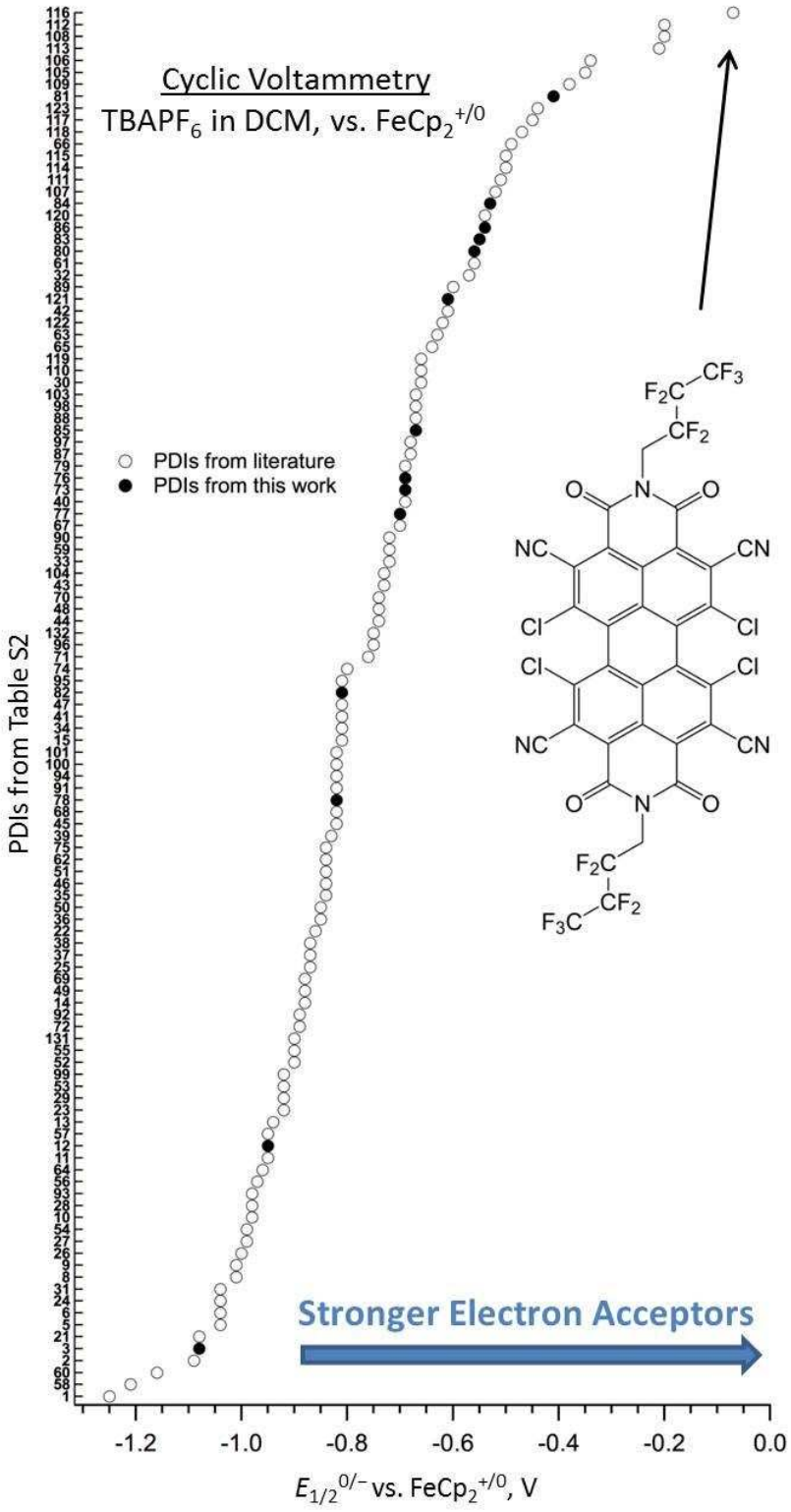

Figure 3.31. Reduction potentials of PDIs from Table 3.1 that were reported in DCM with $TBAPF_6$ vs. $FeCp_2^{+/0}$. See Figure 3.32 and Table 3.1 for more details.

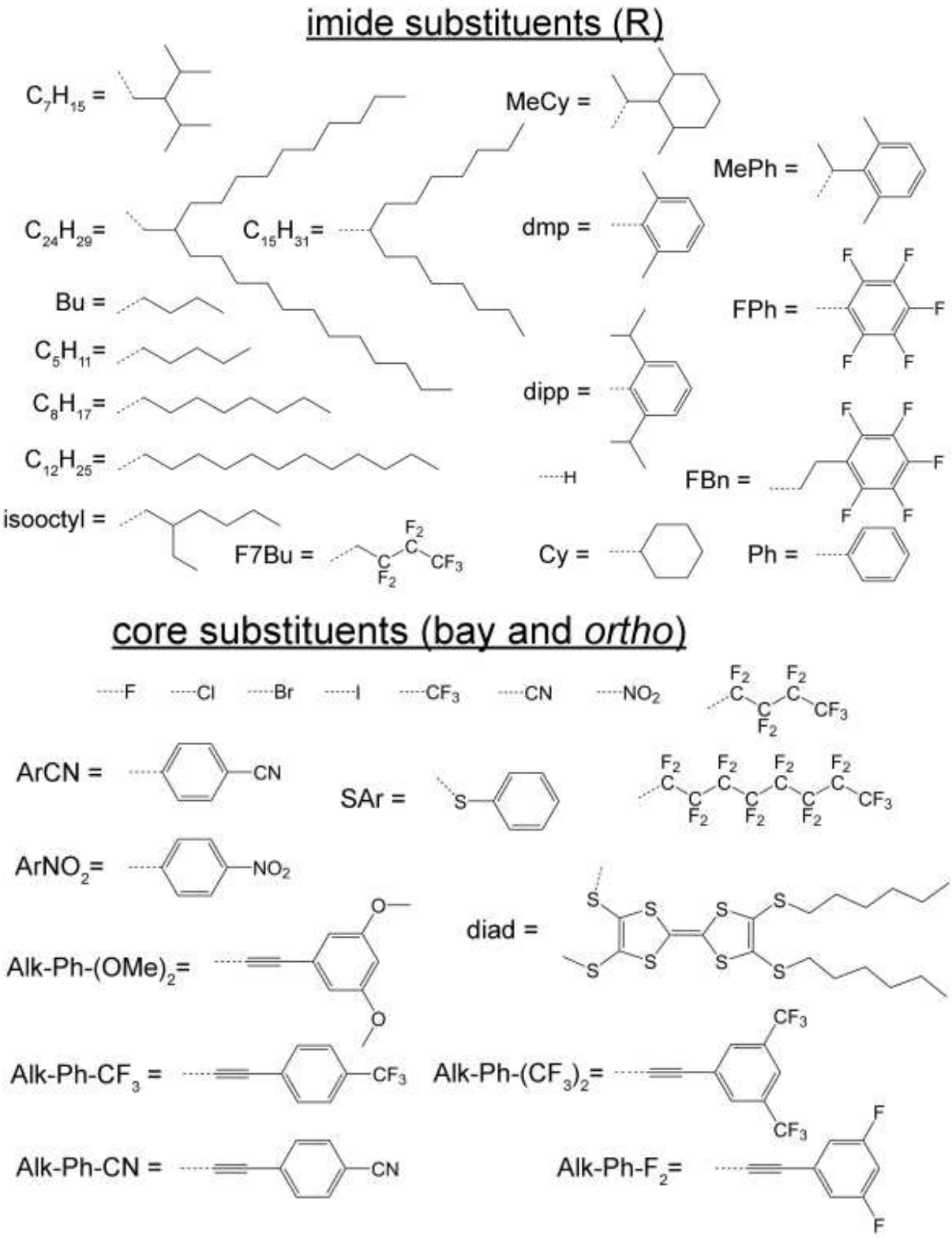

Figure 3.32. Imide substituents, R (top); and electron-withdrawing core substituents (bottom) in PDI derivatives from Table 3.1. See Scheme 3.1 caption for abbreviation method of core-substituted PDIs in this text.

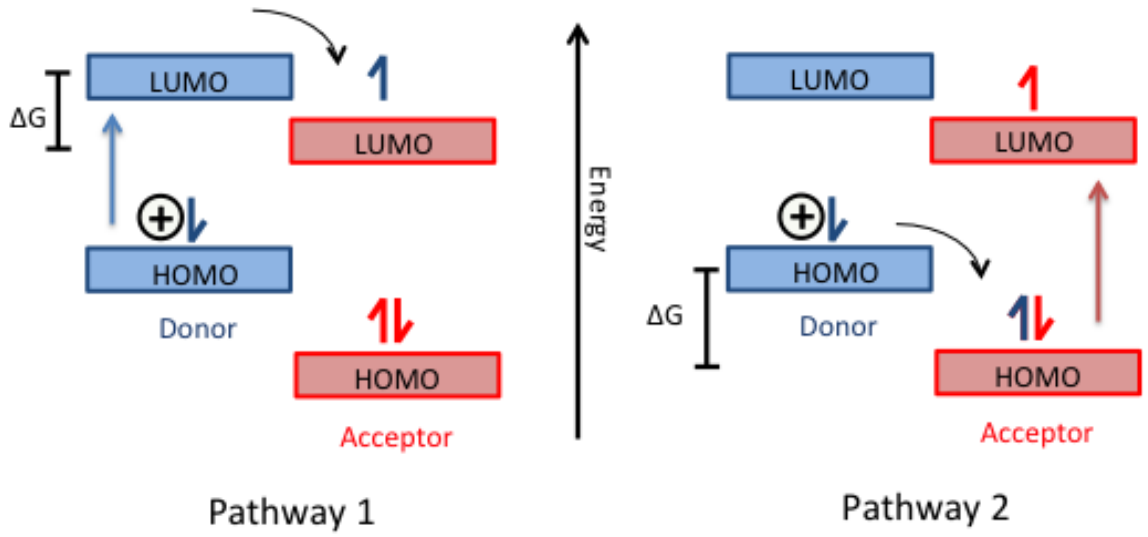

Figure 3.33. Schematic representation of the driving force for charge transfer (ΔG_{PET}) when selectively exciting the donor (pathway 1) or the acceptor (pathway 2) in a Type II heterojunction.

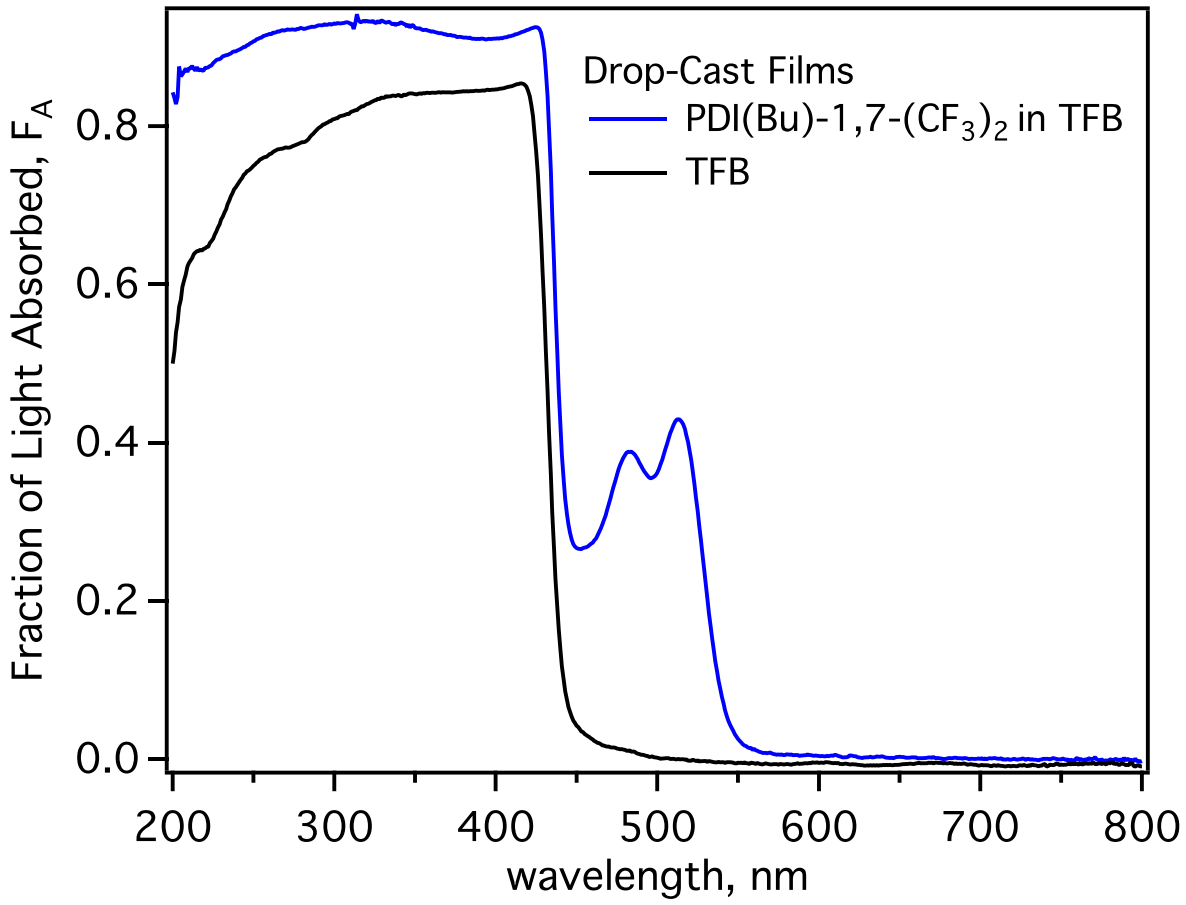

Figure 3.34. Fraction of light absorbed in drop-cast films of 2 mol% PDI(Bu)-1,7-$(CF_3)_2$ in TFB (blue) and pristine TFB (black) from integrating sphere measurements.

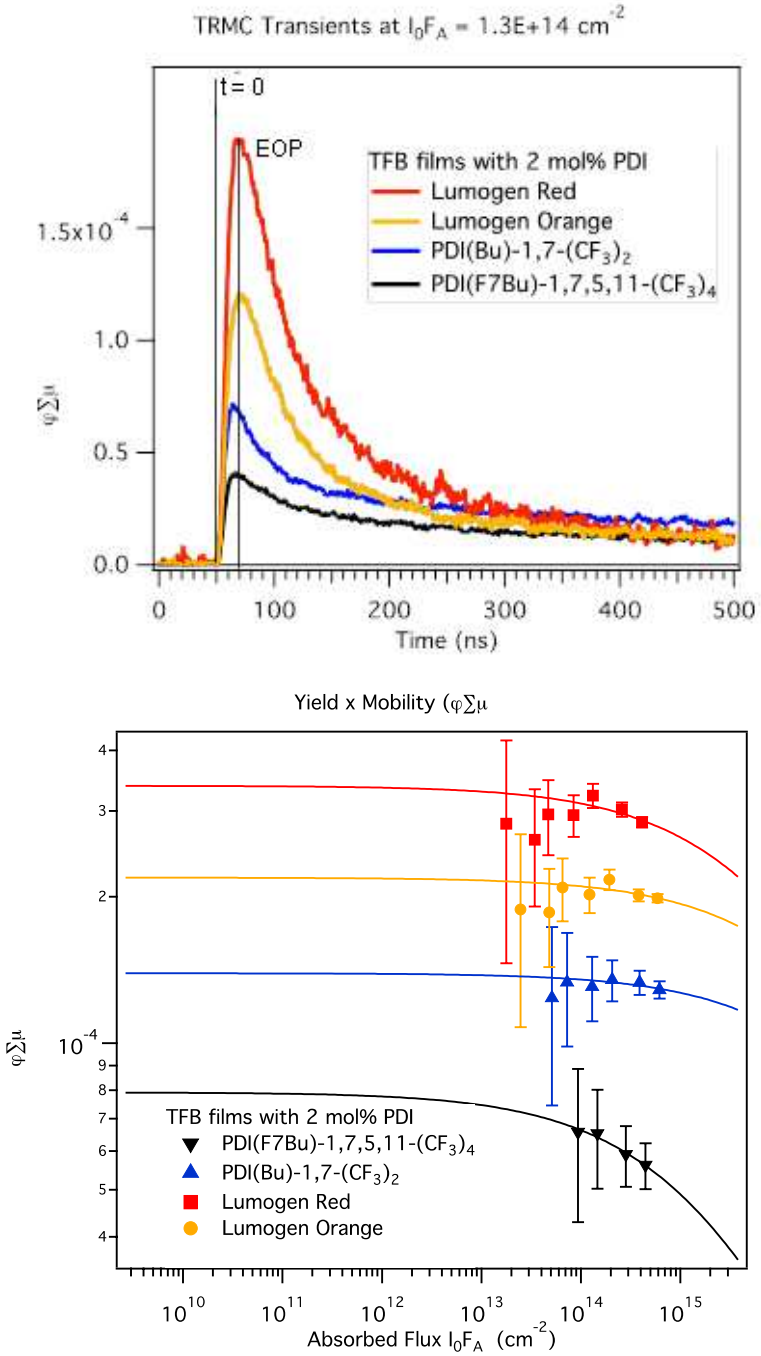

Figure 3.35. TRMC photoconductance transients at I_0F_A = 1.3x10^{14} cm^{-2} (top) and $\varphi\sum\mu$ at t = 0 from biexponential fits of photoconductance transients versus absorbed flux (bottom) for TFB films with 2 mol% of four different PDIs. Solid lines show empirical fits to the data (see ref. [207]) to extrapolate the yield to low fluence. Error bars represent standard deviation from the mean signal to account for random fluctuations in the microwave power and the laser pulse energy.

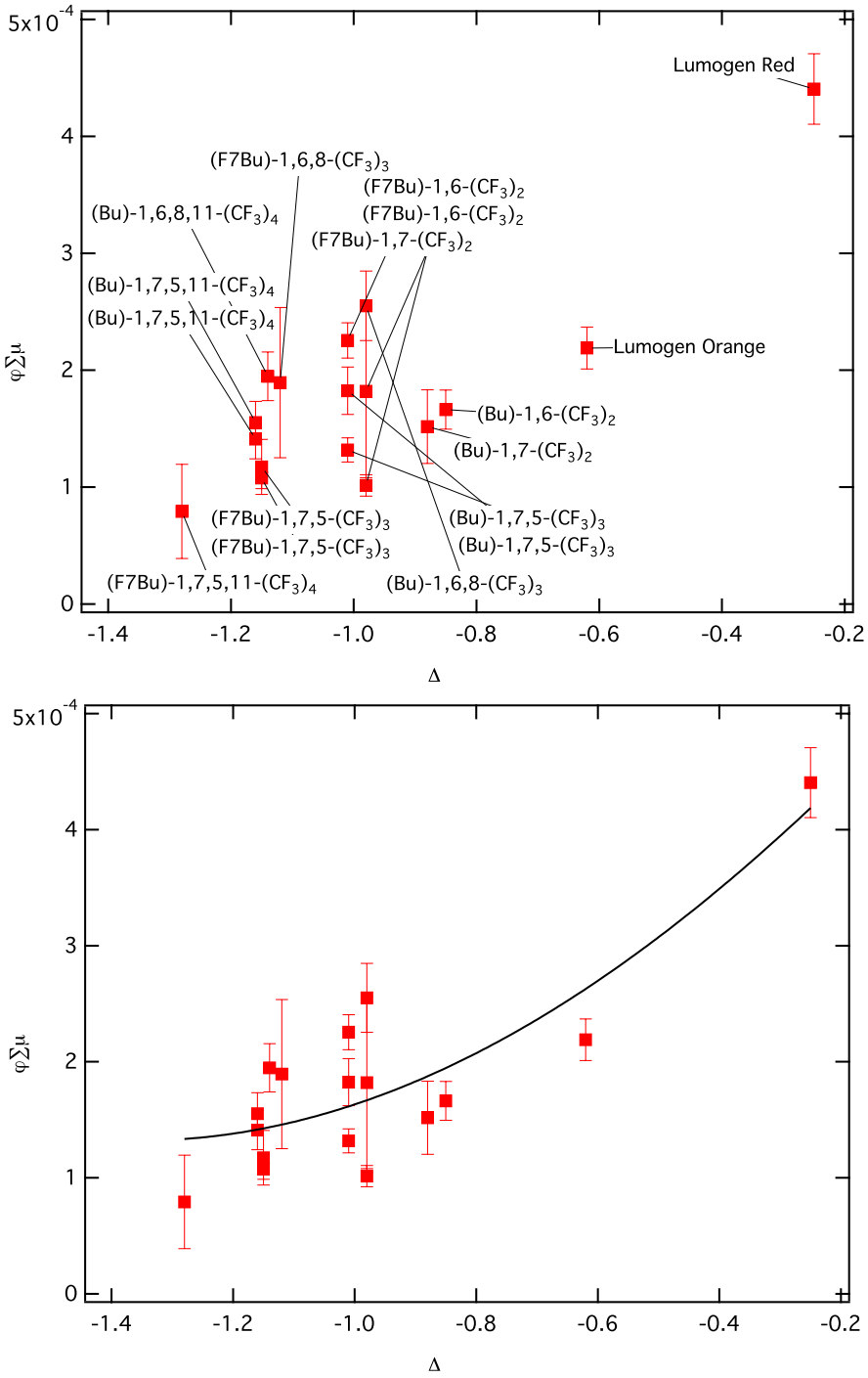

Figure 3.36. $\varphi\sum\mu$ at low fluence from t = 0 values versus ΔG_{PET} for PDIs in TFB. Both graphs show the same data. The top graph includes PDI labels, and the bottom graph includes a Gaussian fit to the data to guide the eye. Two identical films were measured for 4 different PDIs. Error bars represent standard deviation from the mean signal to account for random fluctuations in the microwave power and the laser pulse energy.

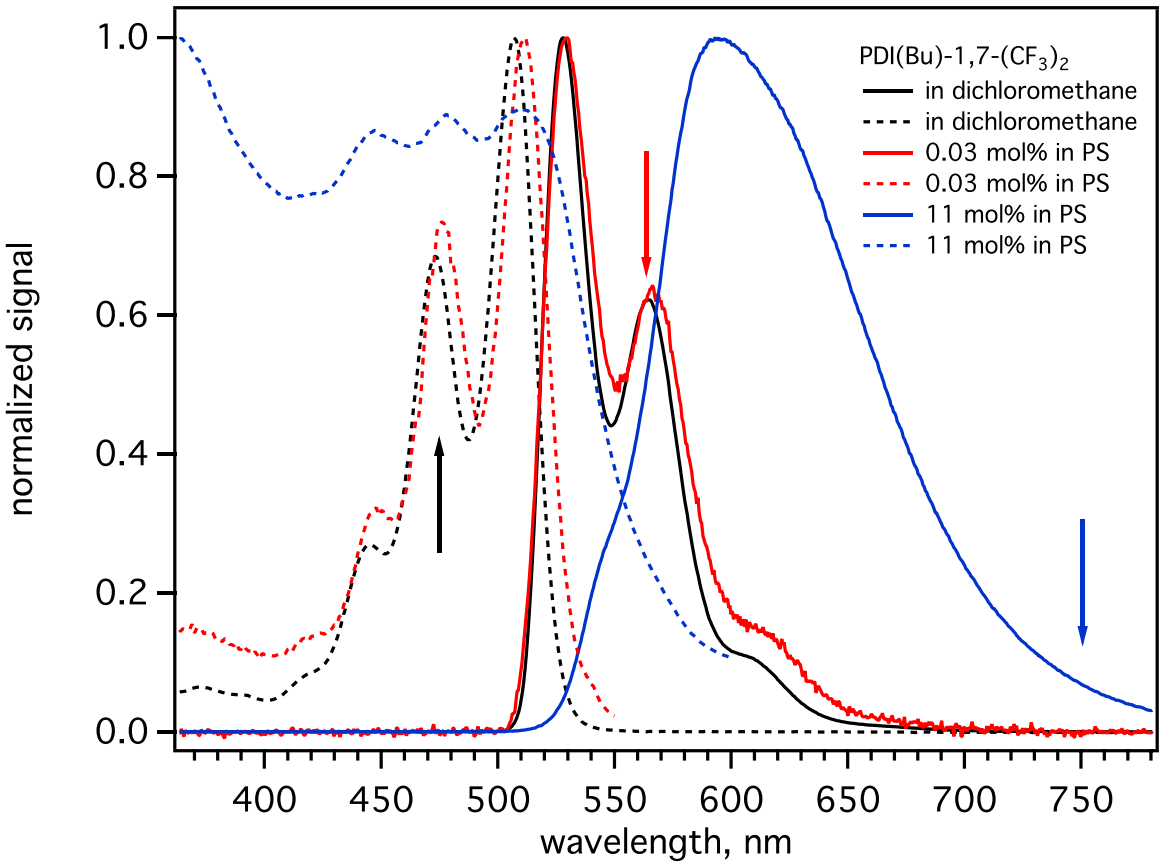

Figure 3.37. Emission spectra of PDI(Bu)-1,7-$(CF_3)_2$ in dichloromethane (black), diluted in polystyrene (red), and concentrated in polystyrene (blue) all excited at 475 nm (black arrow). The absorption spectrum of PDI(Bu)-1,7-$(CF_3)_2$ in dichloromethane (dotted black) is shown as a reference for the excitation spectra of dilute PDI(Bu)-1,7-$(CF_3)_2$ in PS (dotted red, $\lambda_{emission}$ = 565 nm) and concentrated PDI(Bu)-1,7-$(CF_3)_2$ in PS (dotted blue, $\lambda_{emission}$ = 750 nm).

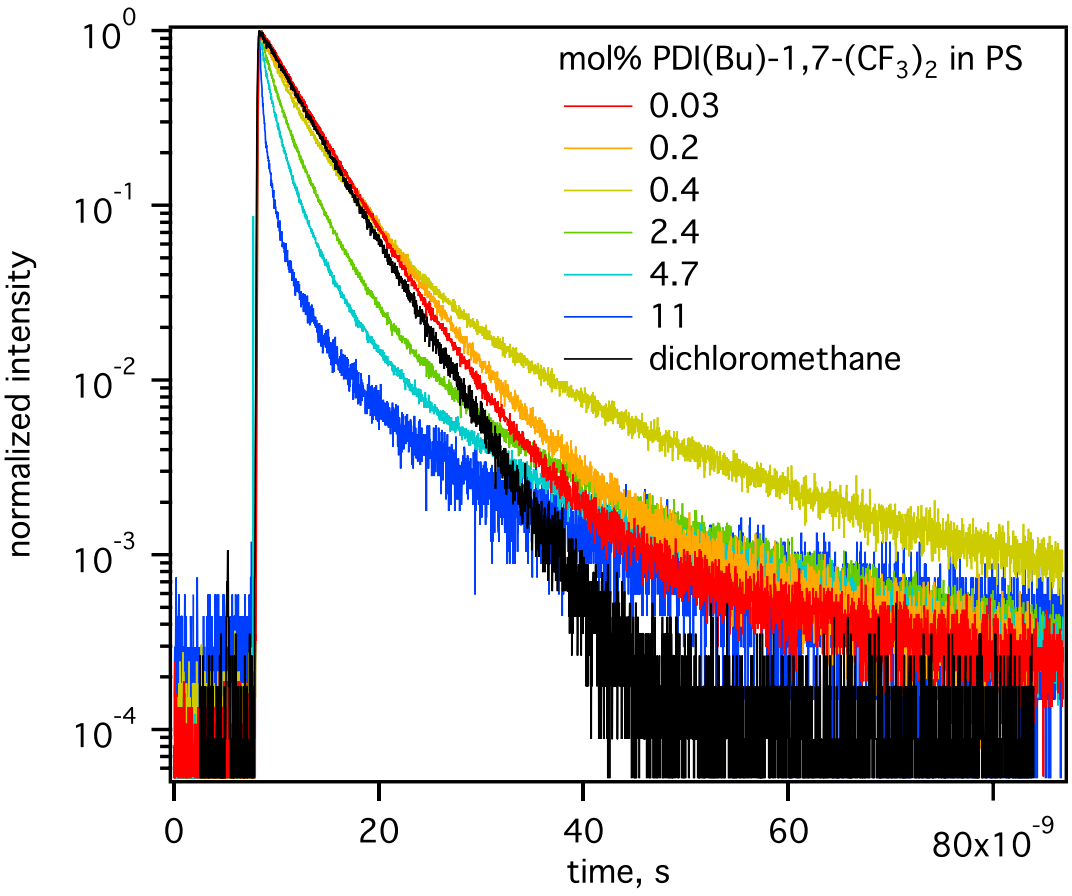

Figure 3.38. TRPL of dilute PDI(Bu)-1,7-$(CF_3)_2$ in DCM (black) and with different loadings in polystyrene (colored).

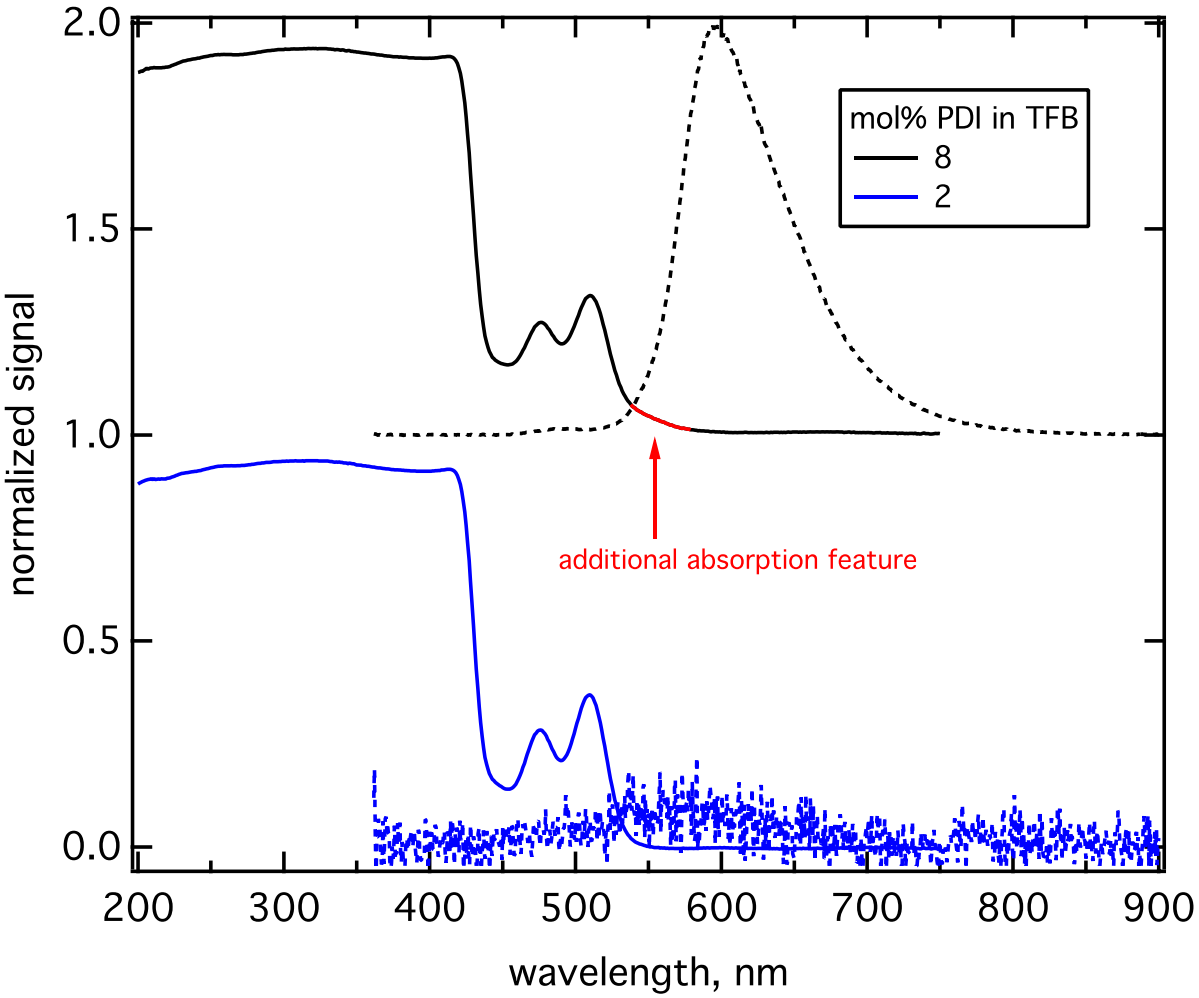

Figure 3.39. Normalized fraction of light absorbed during integrating sphere experiments (solid lines) and steady-state emission spectra (dashed lines) of 2 and 8 mol% PDI(Bu)-1,7-$(CF_3)_2$ in TFB. The emission in 2 mol% film was completely quenched. $\lambda_{excitation}$ = 450 nm. Broadened absorption along with an additional absorption feature were observed in the 8 mol% film and higher loading films.

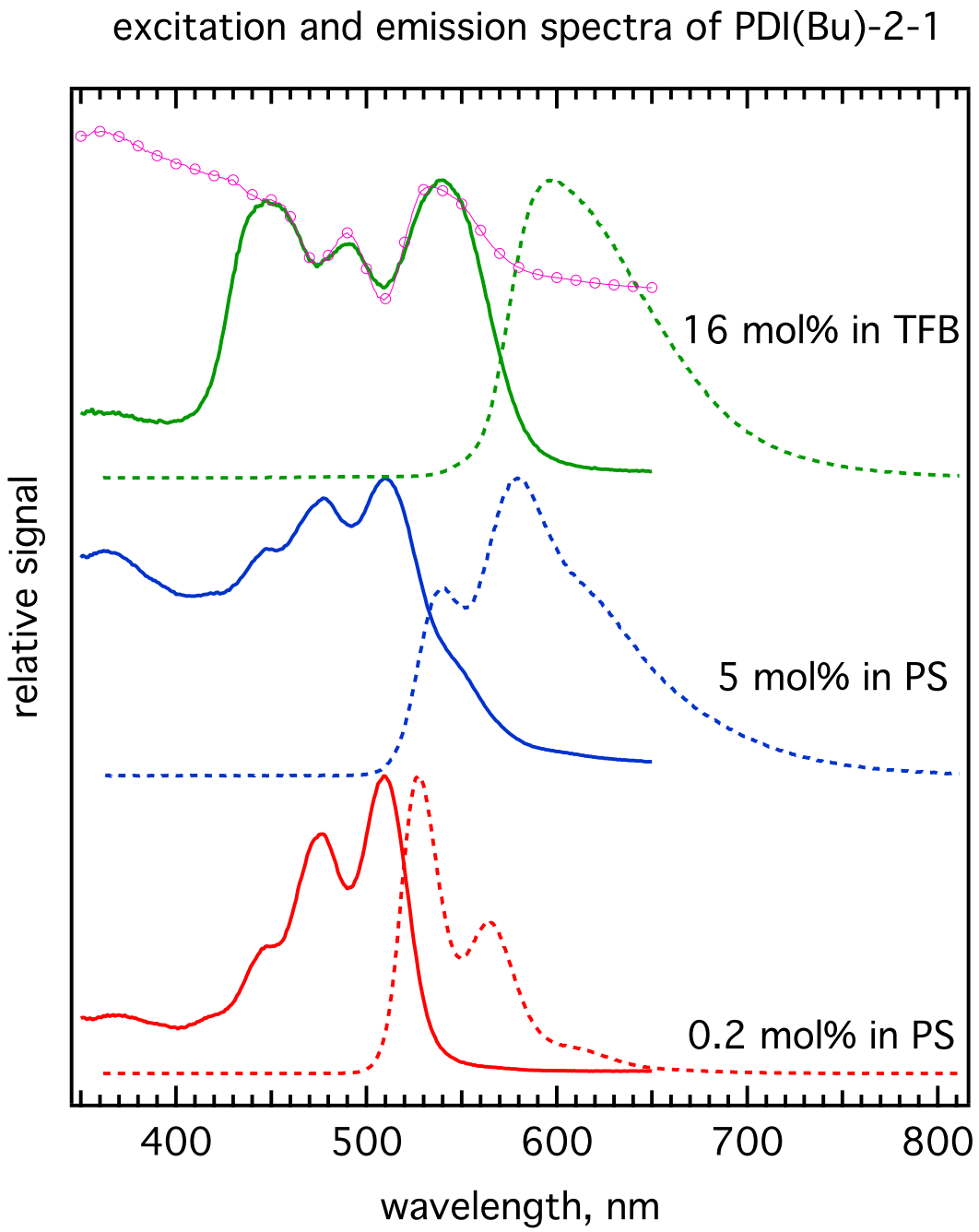

Figure 3.40. Excitation (solid lines) and emission (dashed lines) spectra of PDI(Bu)-1,7-$(CF_3)_2$ diluted in PS (red), more concentrated in PS (Blue), and concentrated in TFB (green); for emission spectra, $\lambda_{excitation}$ = 450 nm and for excitation spectra, $\lambda_{emission}$ = 750 nm. The pink circle line is a result of subtracting the normalized 0.2 mol% excitation spectrum from the normalized 5 mol% excitation spectrum. Note that the excitation spectrum of PDI(Bu)-1,7-$(CF_3)_2$ diluted in PS resembles the spectrum of PDI(Bu)-1,7-$(CF_3)_2$ diluted in DCM.

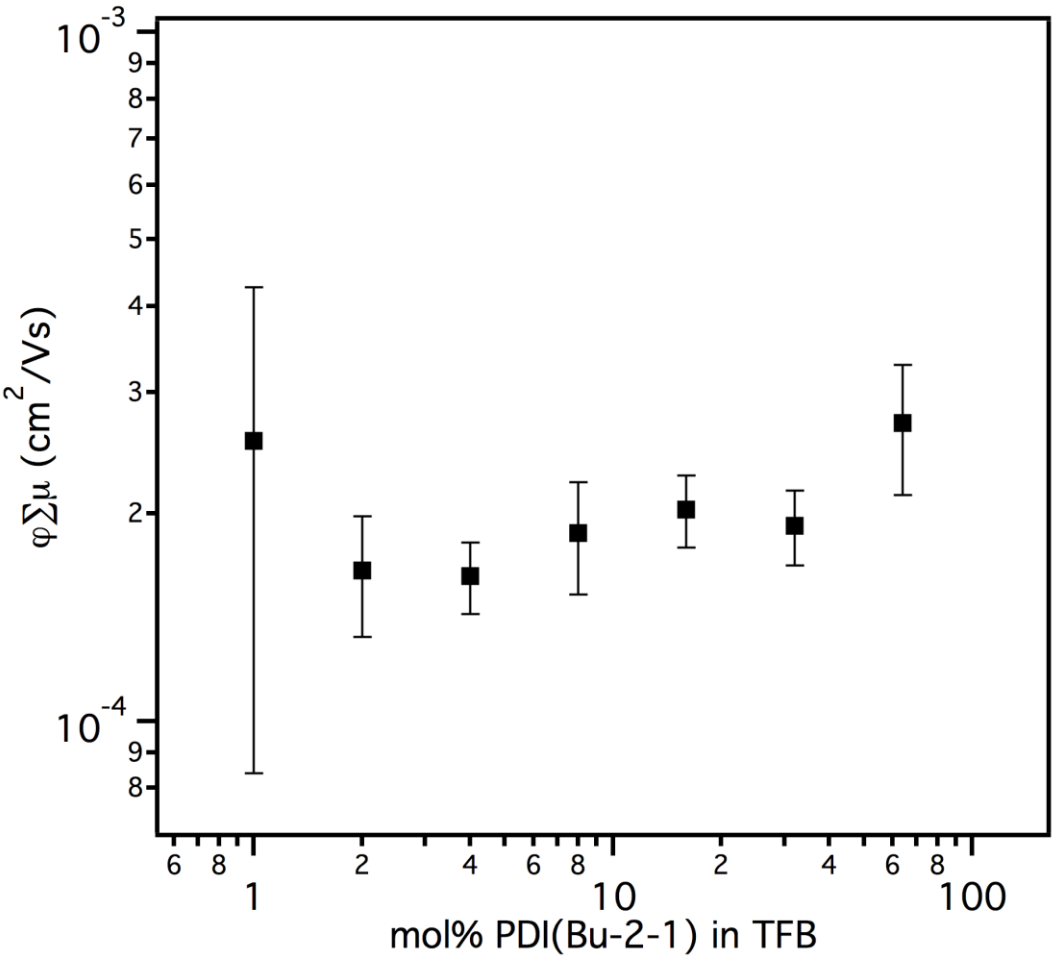

Figure 3.41. $\varphi\sum\mu$ from TRMC transients versus PDI(Bu)-1,7-$(CF_3)_2$ loading in TFB. Error bars represent standard deviation from the mean signal to account for random fluctuations in the microwave power and the laser pulse energy.

PFB

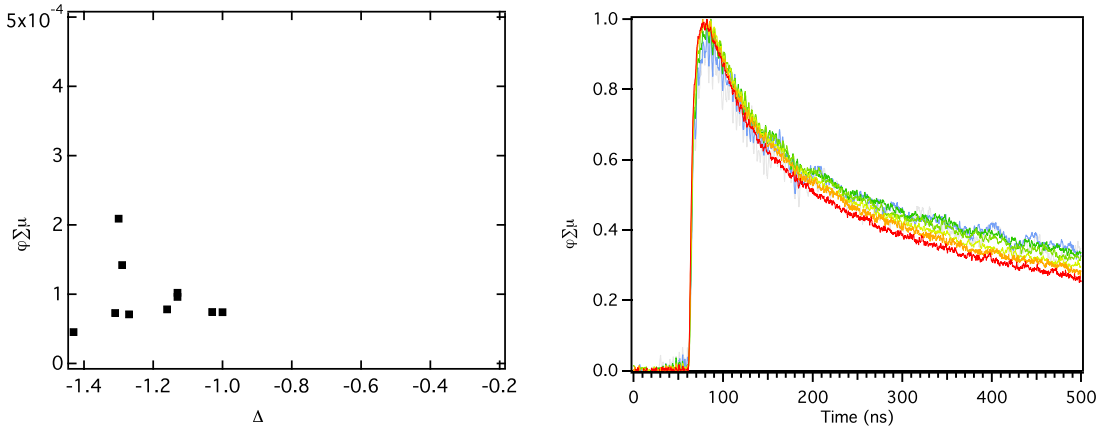

PFO

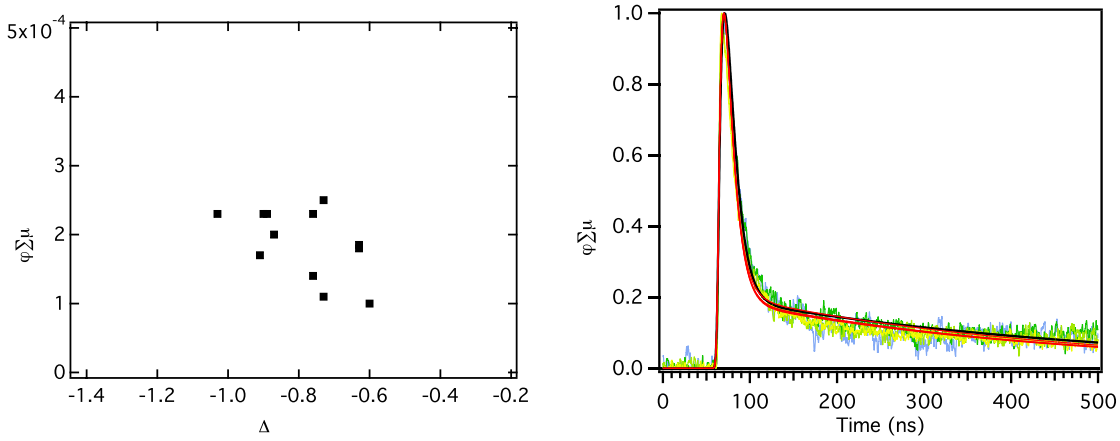

Figure 3.42. $\varphi\sum\mu$ as a function of driving force for 2 mol% PDI(R)-$(CF_3)_{2–4}$ drop-cast in PFB (top) and spin-cast in PFO (bottom). Normalized $\varphi\sum\mu$ transients at several laser intensities for typical samples of each polymer are shown for comparison of transient shape.

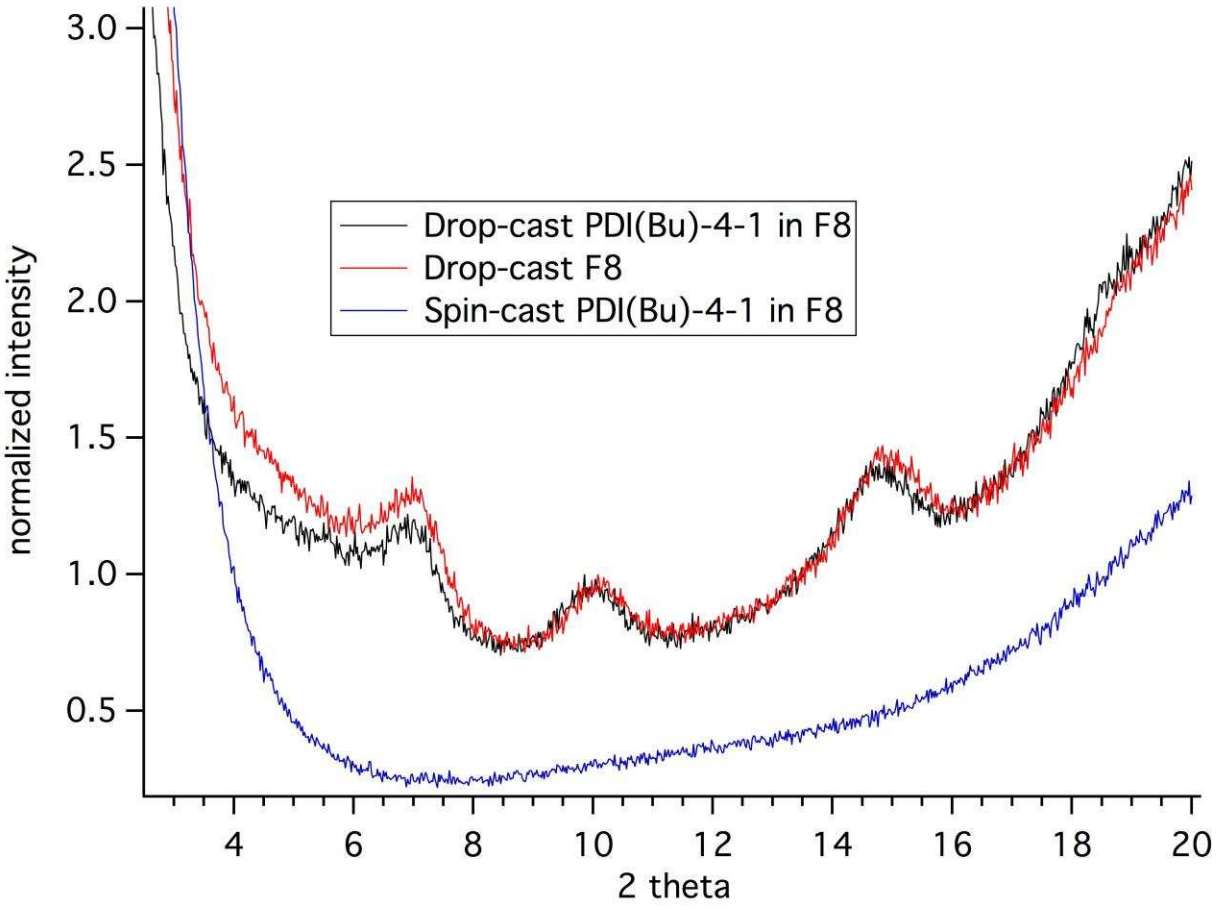

Figure 3.43. Powder X-ray diffraction patterns of drop-cast PDI(Bu)-1,7,5,11-$(CF_3)_4$ in PFO (black), drop-cast PFO (red), and spin-cast PDI(Bu)-1,7,5,11-$(CF_3)_4$ in PFO (blue).

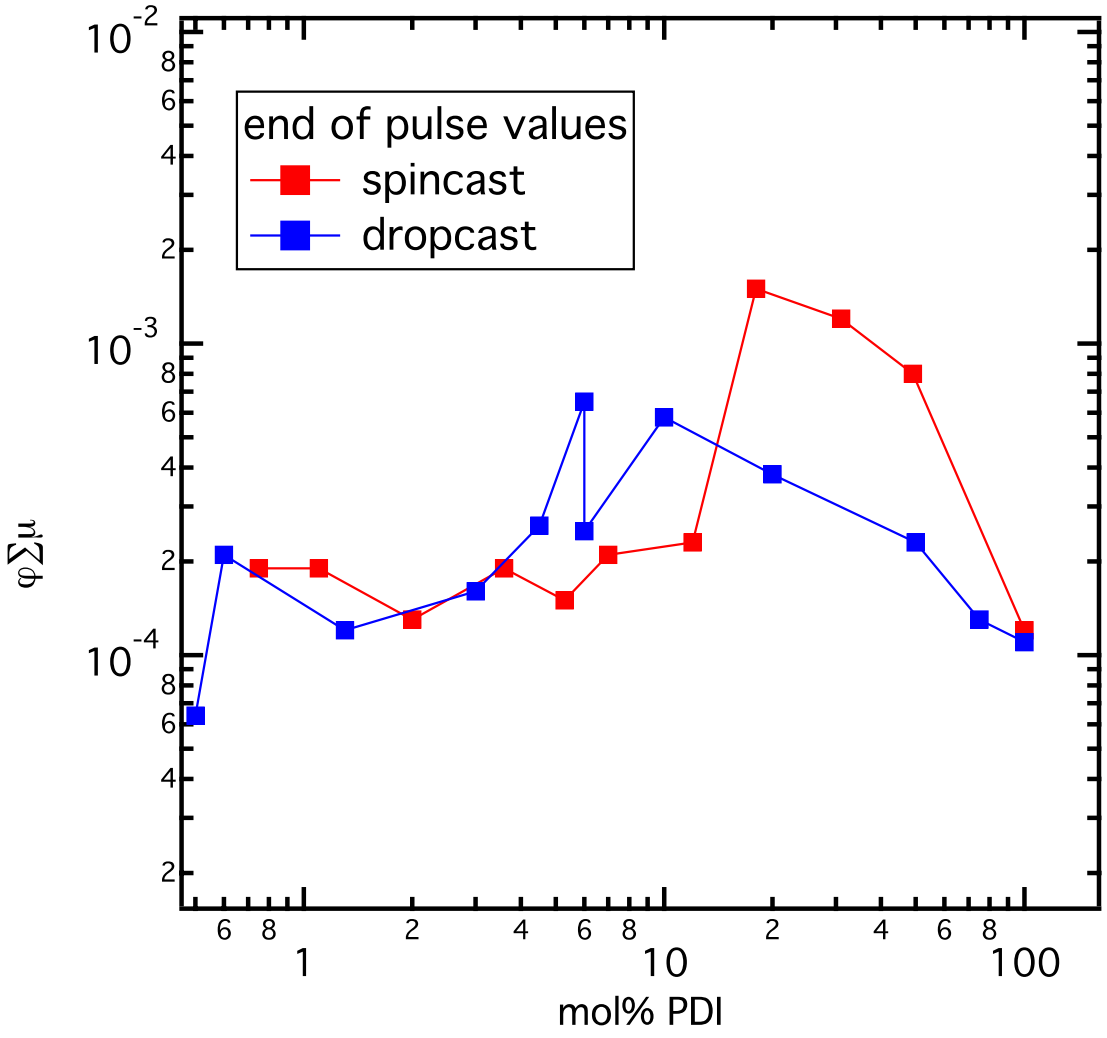

Figure 3.44. $\varphi\sum\mu$ of the spin-cast (black circles) and drop-cast (red squares) series with different PDI(Bu)-1,7-$(CF_3)_2$ loadings. The $\varphi\sum\mu$ below 10 mol% and 4 mol% PDI(Bu)-1,7-$(CF_3)_2$ remains relatively constant for spin-cast films and drop-cast films, respectively, which is indicative of the dilute acceptor regime.

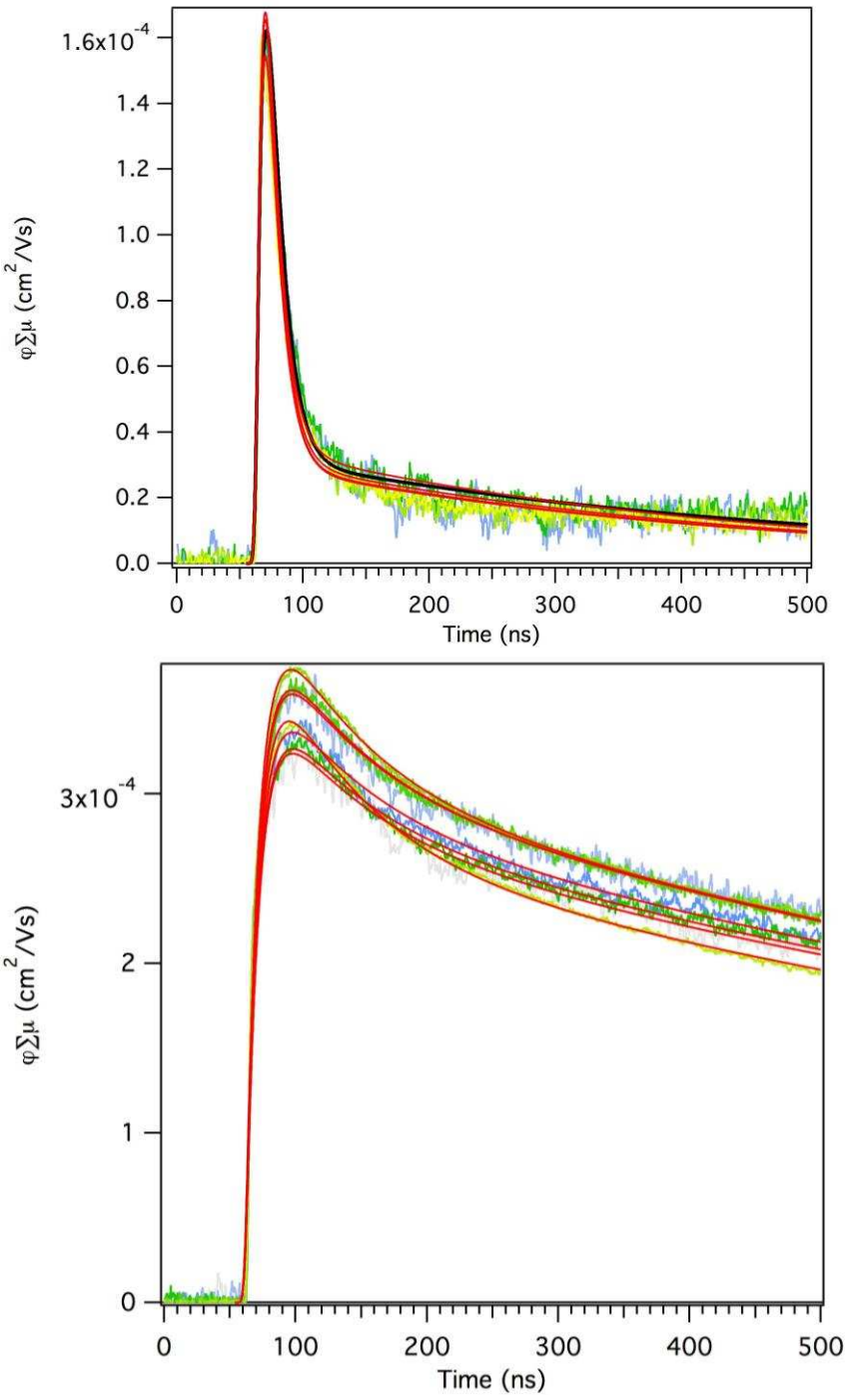

Figure 3.45. $\varphi\sum\mu$ transients and biexponential fits from spin-cast PDI(Bu)-1,7,5,11-$(CF_3)_4$ in PFO (top) and drop-cast PDI(Bu)-1,7,5,11-$(CF_3)_4$ in PFO (bottom). Significant differences in transient shapes due to different decay times are clearly observed.

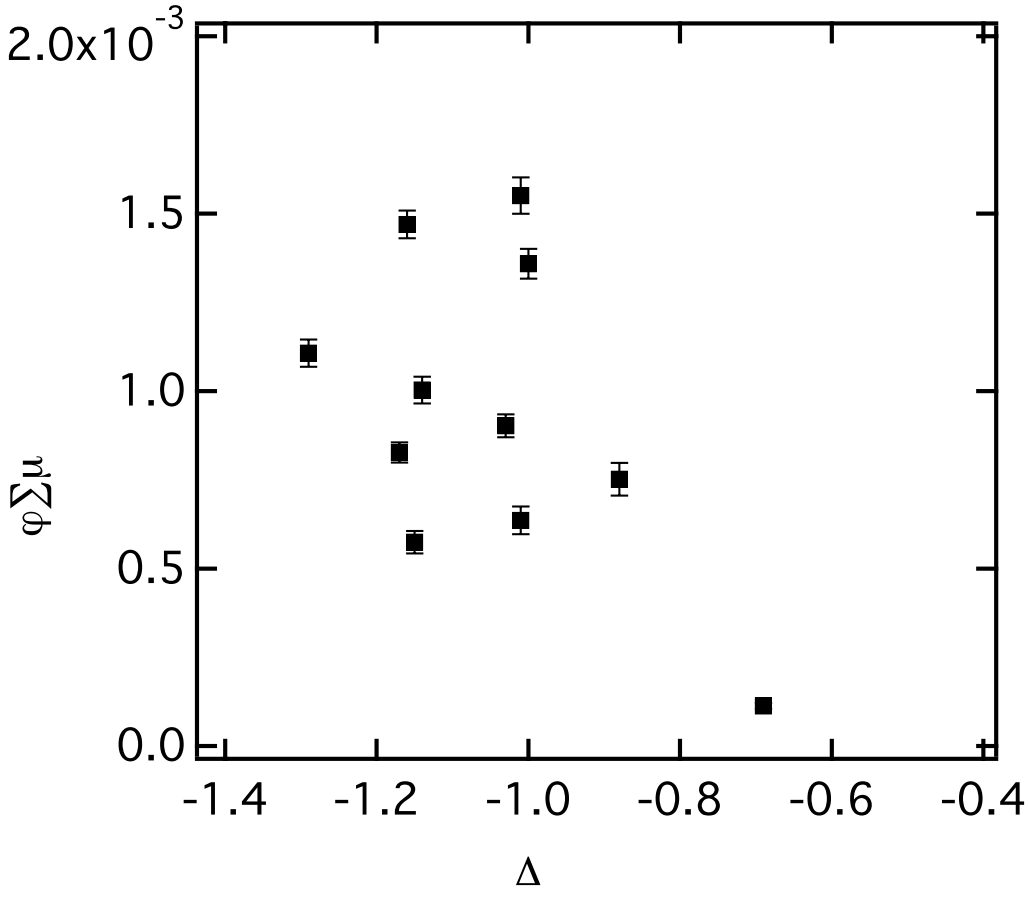

Figure 3.46. $\varphi\sum\mu$ vs. ΔG_{PET} between LUMOs of PDIs and rr-P3HT.

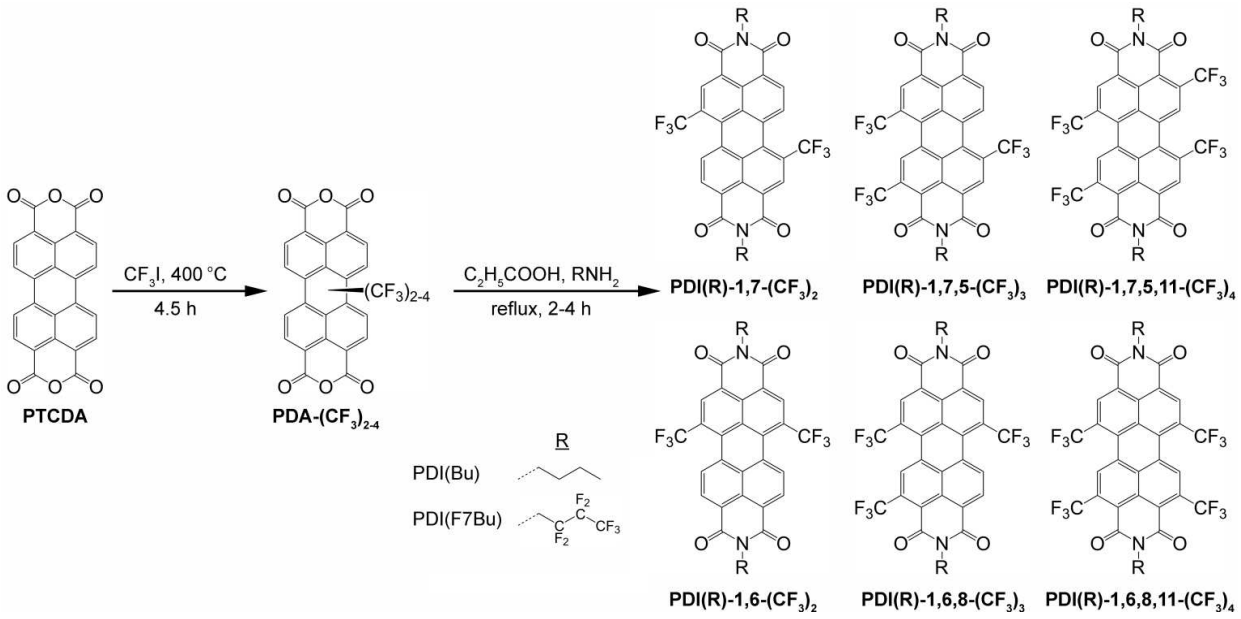

SCHEME 3.1. Synthesis of PDI(R)-$(CF_3)_n$ from PTCDA. PTCDA = 3,4,9,10-oxylic dianhydride; PDA = perylene dianhydride; PDI = perylene diimide; R = imide substituent; positions of core substituents are given beginning with the bay substituent positions. No positions are given with mixtures and unknown compositions. Additional abbreviations of substituents for literature compounds can be found in Figure 3.32.

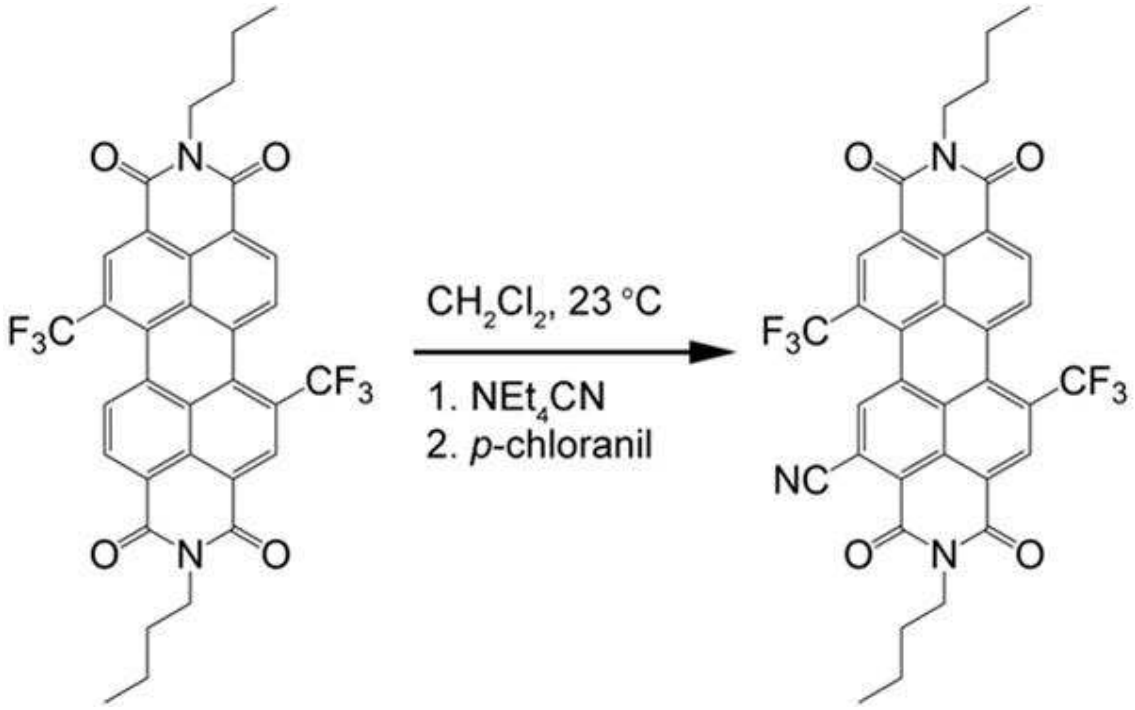

Scheme 3.2. Synthesis of PDI(Bu)-1,7-$(CF_3)_2$-5-(CN) from PDI(Bu)-1,7-$(CF_3)_2$.

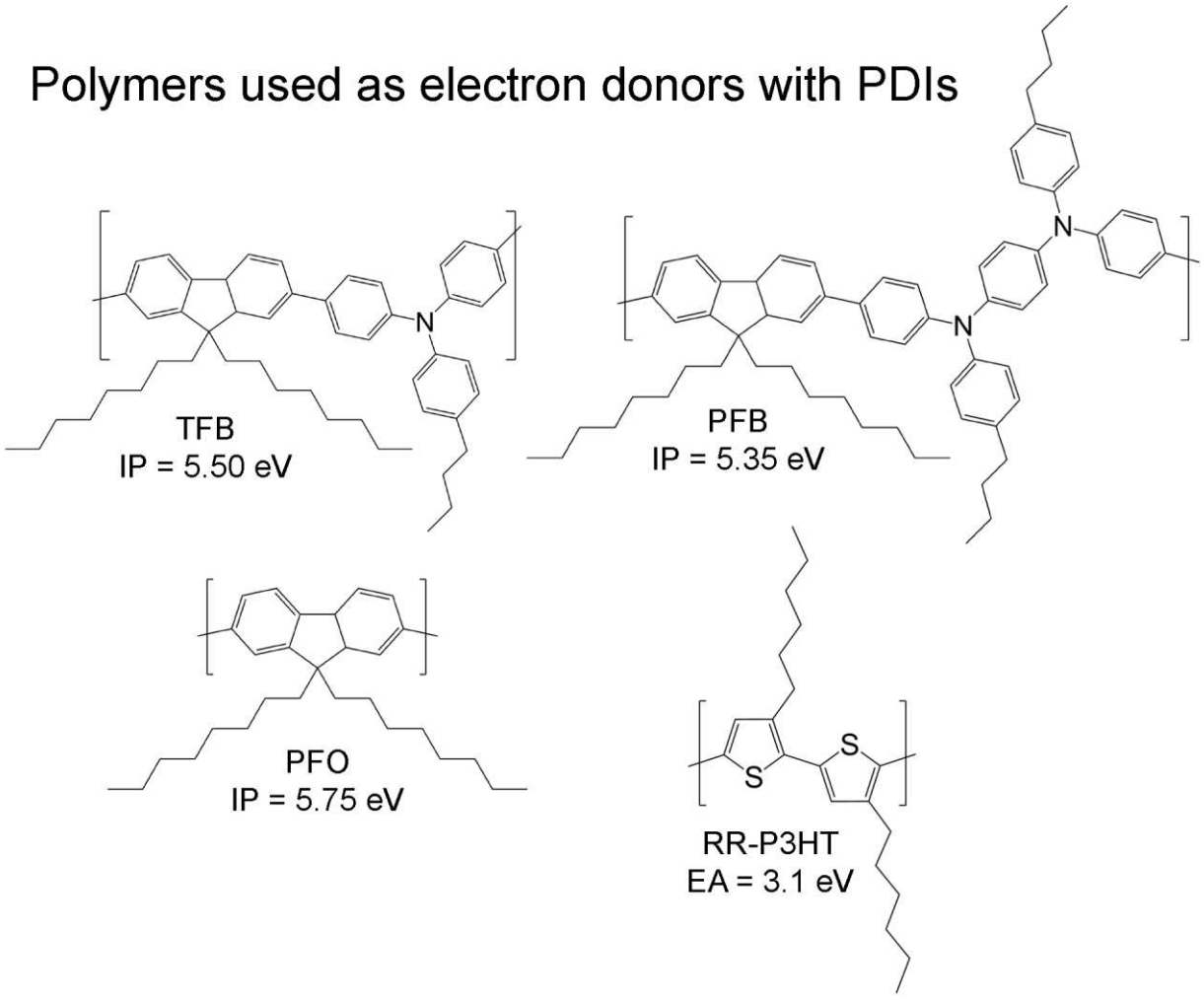

Scheme 3.3. Molecular drawings of polymers that were used for TRMC experiments with PDIs along with IP_D from reference [206] and EA from reference [217].

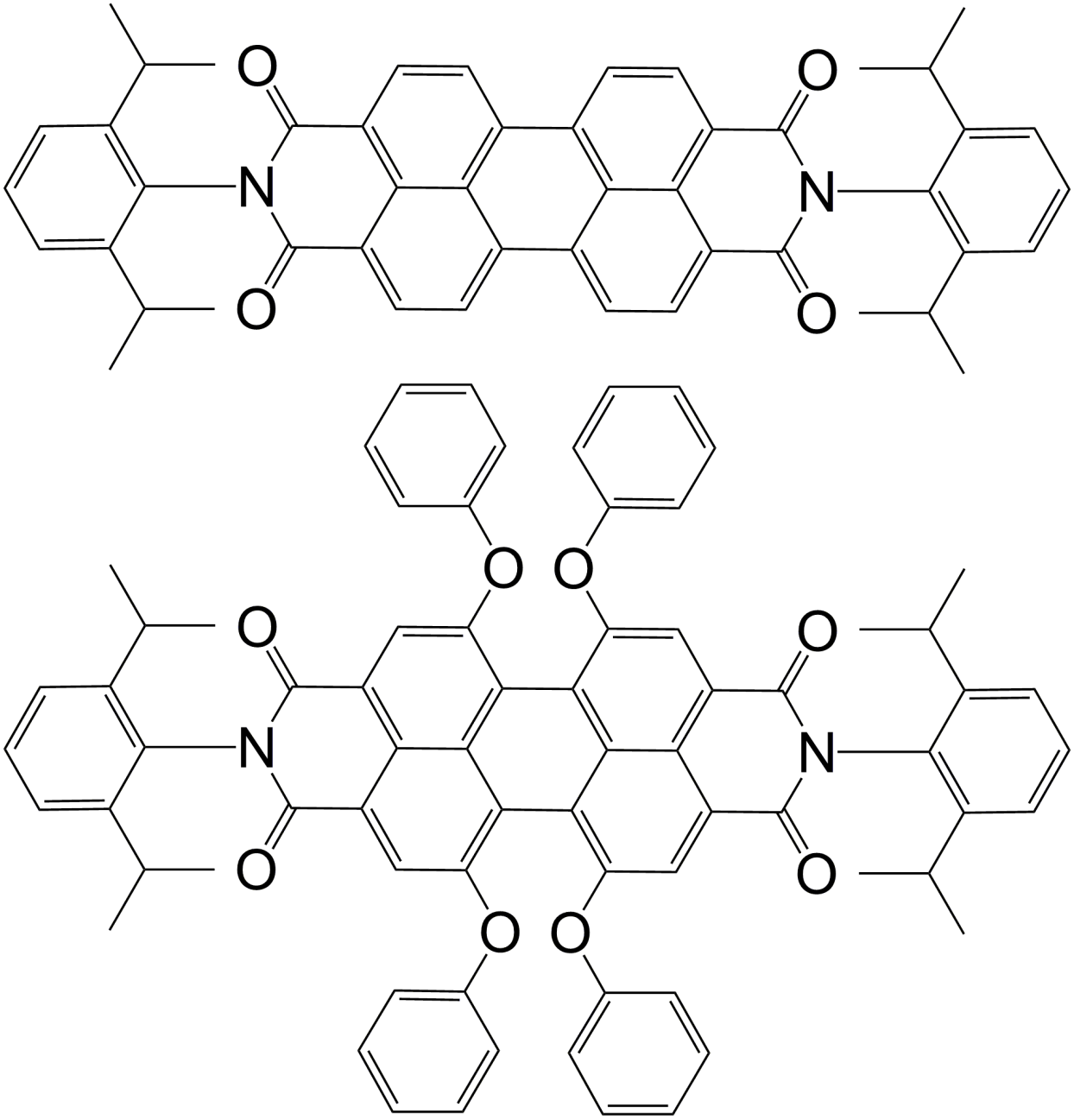

Scheme 3.4. Molecular drawings of commercially available PDIs, Lumogen Orange (top) and Lumogen Red (bottom).

Table 3.1. Compilation of the data on the electrochemical potentials, conditions of the cyclic voltammetry experiments, and E_{LUMO} estimates for PDIs.

General abbreviation in this text = PDI(R)-positions-(substituents) where: PDI = perylene diimide; R = imide substituent; and positions of core substituents are given beginning with the bay substituent positions and no positions are given with mixtures and unknown compositions. Abbreviations of substituents can be found in Figure 3.32.

PDIs with no core substituents are arranged by $E_{1/2}^{0/-}$ vs. $FeCp_2^{+/0}$ when applicable. The other sections are arranged first by "$\Delta E_{1/2}$ from 'precursor'" and then "$\Delta E_{1/2}$ from entries 1–18" taking preference to the value with no asterisk (*). An * means that $\Delta E_{1/2}$ is referenced to a PDI from a different paper or research group. Blank spaces in"$\Delta E_{1/2}$ from entries 1–18" and "$\Delta E_{1/2}$ from 'precursor'" sections are because no suitable parent PDI or precursor were reported with the same electrochemical conditions. More core-unsubstituted PDIs have been reported that are not relevant to core-substituted PDIs in this table.

entry	PDI	solvent, electrolyte, reference	$E_{1/2}^{0-}$, V	$\Delta E_{1/2}$ from entries 1–20	$\Delta E_{1/2}$ from 'precursor'	'precursor'	E_{LUMO} from $E_{1/2}$[a]	LUMO conversion	ref.
	PDIs with no core substituents								
1	PDI($C_{24}H_{49}$)	DCM, $TBAPF_6$, $FeCp_2^{+/0}$	−1.25[b]				−3.55	−($E_{1/2}$+4.8)	222
2	PDI(isooctyl)	DCM, $TBAPF_6$, $FeCp_2^{+/0}$	−1.09				−3.99	−($E_{1/2}$+5.08)	171
3	PDI(Bu)	DCM, $TBAPF_6$, $FeCp_2^{+/0}$	−1.08						tw
4	PDI(Bu)	THF, $TBABF_4$, $FeCp_2^{+/0}$	−1.04						223
5	PDI(dipp)	DCM, $TBAPF_6$, $FeCp_2^{+/0}$	−1.04				−3.76	−($E_{1/2}$+4.8)	176
6	PDI(C_5H_{11})	DCM, $TBAPF_6$, $FeCp_2^{+/0}$	−1.04						194
7	PDI(C_8H_{17})	PhCN, $TBABF_4$, $FeCp_2^{+/0}$	−1.02				−3.78	−($E_{1/2}$+4.8)	188
8	PDI(dipp)	DCM, $TBAPF_6$, $FeCp_2^{+/0}$	−1.01						224
9	PDI(F5Bn)	DCM, $TBAPF_6$, $FeCp_2^{+/0}$	−1.01				−3.79	−($E_{1/2}$+4.8)	174
10	PDI($C_{15}H_{31}$)	DCM, $TBAPF_6$, $FeCp_2^{+/0}$	−0.98				−3.82	−($E_{1/2}$+4.8)	195
11	PDI($C_{15}H_{31}$)	DCM, $TBAPF_6$, $FeCp_2^{+/0}$	−0.95				−3.85	−($E_{1/2}$+4.8)	160
12	PDI(F7Bu)	DCM, $TBAPF_6$, $FeCp_2^{+/0}$	−0.95				−3.85	−($E_{1/2}$+4.8)	tw, 174, 176

13	PDI(C_8H_{17})	DCM, $TBAPF_6$, SCE	−0.46 [−0.94][d]				−3.9	−($E_{1/2}$+4.4)	225
14	PDI(FPh)	DCM, $TBAPF_6$, $FeCp_2^{+/0}$	−0.88				−3.96	−($E_{1/2}$+4.8)	174
15	PDI(F7Bu)	DCM, $TBAPF_6$, SCE	−0.33 [−0.81][d]				−4.1	−($E_{1/2}$+4.4)	225
16	PDI(C_7H_{15})	DCM, $TBAPF_6$, SCE	−0.70						226
17	PDI(Bu)	DCM, $TBAPF_6$, AgCl/Ag	−0.60						184
18	PDI(Cy)	DCM, $TBAPF_6$, SCE[e]	−0.46				−3.98	−4.88−(E_{oxd}−$E_{FeCp_2^{+/o}}$)+E_g	189,227
19	PDI(Cy)	THF, $TBAPF_6$, SCE	−0.46				−3.98	−($E_{1/2}$+4.44)	228
20	PDI(C_8H_{17})	THF, $TBAPF_6$, SCE	−0.45				−3.99	−($E_{1/2}$+4.44)	228
	Effect of F Substitution								
21	PDI(Cy)-1,7-F_2	DCM, $TBAPF_6$, $FeCp_2^{+/0}$	−1.08						229
22	PDI(FPh)-1,7-F_2	DCM, $TBAPF_6$, $FeCp_2^{+/0}$	−0.86	0.01			−3.94	−($E_{1/2}$+4.8)	174
23	PDI(F7Bu)-1,7-F_2	DCM, $TBAPF_6$, $FeCp_2^{+/0}$	−0.92	0.015			−3.88	−($E_{1/2}$+4.8)	174,176
24	PDI(Bu)-1,7-F_2	DCM, $TBAPF_6$, $FeCp_2^{+/0}$	−1.04	0.02*			−3.76	−($E_{1/2}$+4.8)	174
25	PDI(F7Bu)-1,6,7,12-F_4	DCM, $TBAPF_6$, $FeCp_2^{+/0}$	−0.87	0.02			−3.93	−($E_{1/2}$+4.8)	174
26	PDI(C_5H_{11})-1,7-F_2	DCM, $TBAPF_6$, $FeCp_2^{+/0}$	−1.00	0.02					194
27	PDI(dipp)-1,7-F_2	DCM, $TBAPF_6$, $FeCp_2^{+/0}$	−0.99	0.025		PDI(dipp) entry 5			229
28	PDI(C_8H_{17})-1,6,7,12-F_4	DCM, $TBAPF_6$, $FeCp_2^{+/0}$	−0.98	0.01*	0.03	PDI(C_8H_{17})-1,7-F_2			229
29	PDI(dipp)-1,6,7,12-F_4	DCM, $TBAPF_6$, $FeCp_2^{+/0}$	−0.92	0.06	0.035	PDI(dipp)-1,7-F_2			229
30	PDI(C_8H_{17})- 1,6,7,12-Cl_4-2,5,8,11-F_4	DCM, $TBAPF_6$, $FeCp_2^{+/0}$	−0.66		0.045	PDI(C_8H_{17})-1,6,7,12-Cl_4	−4.21	−($E_{red\ on}$+4.8)	166

31	PDI(C_8H_{17})-1,7-F_2	DCM, $TBAPF_6$, $FeCp_2^{+/0}$	−1.04	0.05*					229
	Effect of Cl Substitution								
32	PDI(H)-Cl_8	DCM, $TBAPF_6$, $FeCp_2^{+/0}$	−0.57				−4.23	−($E_{1/2}$+4.8)	164
33	PDI(dmp)-1,6,7,12-Cl_4	DCM, $TBAPF_6$, $FeCp_2^{+/0}$	−0.72				−4.08	−($E_{1/2}$+4.8)	230
34	PDI(MeBn)-1,6,7,12-Cl_4	DCM, $TBAPF_6$, $FeCp_2^{+/0}$	−0.81				−3.99	−($E_{1/2}$+4.8)	230
35	PDI(MeCy)-1,6,7,12-Cl_4	DCM, $TBAPF_6$, $FeCp_2^{+/0}$	−0.84				−3.96	−($E_{1/2}$+4.8)	230
36	PDI($C_{12}H_{25}$)-1,6,7,12-Cl_4	DCM, $TBAPF_6$, $FeCp_2^{+/0}$	−0.85[c]				−4.00	from $E_{red\ on}$	165
37	PDI($C_{12}H_{25}$)-1,6,7,12-Cl_4	DCM, $TBAPF_6$, $FeCp_2^{+/0}$	−0.87				−3.9	−($E_{1/2}$+4.8)	231
38	PDI(Cy)-1,6,7,12-Cl_4	DCM, $TBAPF_6$, $FeCp_2^{+/0}$	−0.87				−3.93	−($E_{1/2}$+4.8)	230
39	PDI($C_{15}H_{31}$)-2,5,8,11-Cl_4	DCM, $TBAPF_6$, $FeCp_2^{+/0}$	−0.83	0.038		PDI($C_{15}H_{31}$) entry 10	−3.97	−($E_{1/2}$+4.8)	195
40	PDI(FPh)-1,6,7,12-Cl_4	DCM, $TBAPF_6$, $FeCp_2^{+/0}$	−0.69	0.048			−4.11	−($E_{1/2}$+4.8)	174
41	PDI(F5Bn)-1,6,7,12-Cl_4	DCM, $TBAPF_6$, $FeCp_2^{+/0}$	−0.81	0.05			−3.99	−($E_{1/2}$+4.8)	174
42	PDI(F7Bu)-1,6,7,12-Cl_4	DCM, $TBAPF_6$, SCE	−0.13 [−0.61][d]	0.05			−4.3	−($E_{1/2}$+4.4)	225
43	PDI(C_8H_{17})-1,6,7,12-Cl_4	DCM, $TBAPF_6$, SCE	−0.25 [−0.73][d]	0.053			−4.2	−($E_{1/2}$+4.4)	225
44	PDI(F7Bu)-1,6,7,12-Cl_4	DCM, $TBAPF_6$, $FeCp_2^{+/0}$	−0.74	0.053			−4.06	−($E_{1/2}$+4.8)	174,176
45	PDI(C_5H_{11})- 1,6,7,12-Cl_4	DCM, $TBAPF_6$, $FeCp_2^{+/0}$	−0.82	0.055					194
46	PDI(Bu)-1,6,7,12-Cl_4	DCM, $TBAPF_6$, $FeCp_2^{+/0}$	−0.84	0.06*			−3.96	−($E_{1/2}$+4.8)	230
47	PDI(Bu)-1,6,7,12-Cl_4	DCM, $TBAPF_6$, $FeCp_2^{+/0}$	−0.81	0.068*			−4.06	from $E_{red\ on}$	165
48	PDI(dipp)-1,6,7,12-Cl_4	DCM, $TBAPF_6$, $FeCp_2^{+/0}$	−0.74	0.08*	0.07	PDI(dipp)-1,12-Cl_2	−4.06	−($E_{1/2}$+4.8)	232

49	PDI(dipp)-1,12-Cl_2	DCM, TBAPF$_6$, $FeCp_2^{+/0}$	−0.88	0.09*			−3.92	−($E_{1/2}$+4.8)	232
50	PDI(C_8H_{17})-1,6,7,12-Cl_4	DCM, TBAPF$_6$, $FeCp_2^{+/0}$	−0.85	0.085*			−3.95	−($E_{1/2}$+4.8)	232
51	PDI(C_8H_{17})-1,6,7,12-Cl_4	DCM, TBAPF$_6$, $FeCp_2^{+/0}$	−0.84	0.09*			−4.13	−($E_{red\ on}$+4.8)	166
	Effect of Br Substitution								
52	PDI(dmp)-1,7-Br_2	DCM, TBAPF$_6$, $FeCp_2^{+/0}$	−0.90				−3.90	−($E_{1/2}$+4.8)	230
53	PDI(MeCy)-1,7-Br_2	DCM, TBAPF$_6$, $FeCp_2^{+/0}$	−0.92				−3.88	−($E_{1/2}$+4.8)	230
54	PDI(Cy)-1,7-Br_2	DCM, TBAPF$_6$, $FeCp_2^{+/0}$	−0.99				−3.81	−($E_{1/2}$+4.8)	230
55	PDI($C_{15}H_{31}$)-2,5,8,11-Br_4	DCM, TBAPF$_6$, $FeCp_2^{+/0}$	−0.90	0.02		PDI($C_{15}H_{31}$) entry 10	−3.90	−($E_{1/2}$+4.8)	195
56	PDI(C_5H_{11})-1,7-Br_2	DCM, TBAPF$_6$, $FeCp_2^{+/0}$	−0.97	0.035					194
57	PDI(C_8H_{17})-1,7-Br_2	DCM, TBAPF$_6$, $FeCp_2^{+/0}$	−0.95	0.035*			−3.85	−($E_{1/2}$+4.8)	232
58	PDI($C_{24}H_{49}$)-1-Br	DCM, TBAPF$_6$, $FeCp_2^{+/0}$	−1.21[b]	0.04			−3.59	−($E_{1/2}$+4.8)	222
59	PDI(F7Bu)-1,7-Br_2	DCM, TBAPF$_6$, SCE	−0.24 [−0.72][d]	0.045			−4.2	−($E_{1/2}$+4.4)	225
60	PDI($C_{24}H_{49}$)-1,7-Br_2	DCM, TBAPF$_6$, $FeCp_2^{+/0}$	−1.16[b]	0.045			−3.64	−($E_{1/2}$+4.8)	222
61	PDI(dipp)-1,6,7,12-Cl_4-2,5,8,11-Br_4	DCM, TBAPF$_6$, $FeCp_2^{+/0}$	−0.56		0.045*	PDI(dipp)-1,6,7,12-Cl_4 1,6,7,12-Cl_4	−4.24	−($E_{red\ on}$+4.8)	166
62	PDI(C_8H_{17})-1,7-Br_2	DCM, TBAPF$_6$, SCE	−0.36 [−0.84][d]	0.05			−4.0	−($E_{1/2}$+4.4)	225
63	PDI(C_8H_{17})-1,6,7,12-Cl_4-2,5,8,11-Br_4	DCM, TBAPF$_6$, $FeCp_2^{+/0}$	−0.63		0.053	PDI(C_8H_{17})-1,6,7,12-Cl_4	−4.24	−($E_{red\ on}$+4.8)	166
64	PDI(Bu)-1,7-Br_2	DCM, TBAPF$_6$, $FeCp_2^{+/0}$	−0.96	0.06*			−3.84	−($E_{1/2}$+4.8)	230
65	PDI(FPh)-1,6,7,12-Br_4	DCM, TBAPF$_6$, $FeCp_2^{+/0}$	−0.64	0.06			−4.16	−($E_{1/2}$+4.8)	174

66	PDI(F7Bu)-1,6,7,12-Cl_4-2,5,8,11-Br_4	DCM, $TBAPF_6$, $FeCp_2^{+/0}$	−0.49		0.063	PDI(F7Bu)-1,6,7,12-Cl_4	−4.31	−($E_{1/2}$+4.8)	[167]
67	PDI(F7Bu)-1,6,7,12-Br_4	DCM, $TBAPF_6$, $FeCp_2^{+/0}$	−0.70	0.063			−4.10	−($E_{1/2}$+4.8)	[174]
68	PDI(Bu)-1,6,7,12-Br_4	DCM, $TBAPF_6$, $FeCp_2^{+/0}$	−0.82	0.065*	0.07	PDI(Bu)-1,7-Br_2	−3.98	−($E_{1/2}$+4.8)	[230]
69	PDI(dipp)-1,7-Br_2	DCM, $TBAPF_6$, $FeCp_2^{+/0}$	−0.88	0.08*			−3.92	−($E_{1/2}$+4.8)	[232]
70	PDI(dmp)-1,6,7,12-Br_4	DCM, $TBAPF_6$, $FeCp_2^{+/0}$	−0.74		0.08	PDI(dmp)-1,7-Br_2	−4.06	−($E_{1/2}$+4.8)	[230]
71	PDI(MeCy)-1,6,7,12-Br_4	DCM, $TBAPF_6$, $FeCp_2^{+/0}$	−0.76		0.08	PDI(MeCy)-1,7-Br_2	−4.06	−($E_{1/2}$+4.8)	[230]
	Effect of I Substitution								
72	PDI($C_{15}H_{31}$)- 2,5,8,11-I_4	DCM, $TBAPF_6$, $FeCp_2^{+/0}$	−0.89	0.015		PDI($C_{15}H_{31}$) entry 11	−3.91	−($E_{1/2}$+4.8)	[160]
	Effect of CF_3 Substitution								
73	PDI(Cy)-1,7-$(CF_3)_2$	DMF, $TBAPF_6$, SCE	−0.21 [−0.69][d]						[172]
74	PDI(C_8H_{17})-1,7&1,6-$(CF_3)_2$	DCM, $TBAPF_6$, $FeCp_2^{+/0}$	−0.80	0.12*			−4.28	−($E_{1/2}$+5.08)	[171]
75	PDI(Bu)-1,7&1,6-$(CF_3)_2$	DCM, $TBAPF_6$, $FeCp_2^{+/0}$	−0.84	0.12*			−4.24	−($E_{1/2}$+5.08)	[171]
76	PDI(Bu)-1,6,8-$(CF_3)_3$	DCM, $TBAPF_6$, $FeCp_2^{+/0}$	−0.69	0.13	0.12	PDI(Bu)-1,6-$(CF_3)_2$			tw
77	PDI(F7Bu)-1,7-$(CF_3)_2$	DCM, $TBAPF_6$, $FeCp_2^{+/0}$	−0.70	0.13					tw
78	PDI(Bu)-1,7-$(CF_3)_2$	DCM, $TBAPF_6$, $FeCp_2^{+/0}$	−0.82	0.13					tw
79	PDI(F7Bu)-1,6-$(CF_3)_2$	DCM, $TBAPF_6$, $FeCp_2^{+/0}$	−0.69	0.13					tw
80	PDI(F7Bu)-1,6,8-$(CF_3)_3$	DCM, $TBAPF_6$, $FeCp_2^{+/0}$	−0.56	0.13	0.13	PDI(F7Bu)-1,6-$(CF_3)_2$			tw
81	PDI(F7Bu)-1,7,5,11-$(CF_3)_4$	DCM, $TBAPF_6$, $FeCp_2^{+/0}$	−0.41	0.14	0.13	PDI(F7Bu)-1,7,5-$(CF_3)_2$			tw
82	PDI(Bu)-1,6-$(CF_3)_2$	DCM, $TBAPF_6$, $FeCp_2^{+/0}$	−0.81	0.14					tw
83	PDI(Bu)-1,6,8,11-$(CF_3)_4$	DCM, $TBAPF_6$, $FeCp_2^{+/0}$	−0.55	0.13	0.14	PDI(Bu)-1,6,8-$(CF_3)_2$			tw

84	PDI(Bu)-1,7,5,11-$(CF_3)_4$	DCM, $TBAPF_6$, $FeCp_2^{+/0}$	−0.53	0.14	0.14	PDI(Bu)-1,7,5-$(CF_3)_2$			tw
85	PDI(Bu)-1,7,5-$(CF_3)_3$	DCM, $TBAPF_6$, $FeCp_2^{+/0}$	−0.67	0.14	0.15	PDI(Bu)-1,7-$(CF_3)_2$			tw
86	PDI(F7Bu)-1,7,5-$(CF_3)_3$	DCM, $TBAPF_6$, $FeCp_2^{+/0}$	−0.54	0.14	0.16	PDI(F7Bu)-1,7-$(CF_3)_2$			tw
	Effect of C_4F_9 Substitution								
87	PDI(dipp)-1,6-$(C_4F_9)_2$	DCM, $TBAPF_6$, $FeCp_2^{+/0}$	−0.68	0.18*	0.14	PDI(dipp)-1-C_4F_9			185
88	PDI(dipp)-1,7-$(C_4F_9)_2$	DCM, $TBAPF_6$, $FeCp_2^{+/0}$	−0.67	0.19*	0.15	PDI(dipp)-1-C_4F_9			185
89	PDI(F7Bu)-1,7-$(C_4F_9)_2$	DCM, $TBAPF_6$, $FeCp_2^{+/0}$	−0.60	0.18*					168
90	PDI(Bu)-1,7-$(C_4F_9)_2$	DCM, $TBAPF_6$, $FeCp_2^{+/0}$	−0.72	0.18*					168
91	PDI(dipp)-1-(C_4F_9)	DCM, $TBAPF_6$, $FeCp_2^{+/0}$	−0.82	0.22*					185
	Effect of C_8F_{17} Substitution								
92	PDI(Ph)-1-(C_8F_{17})	DCM, $TBAPF_6$, $FeCp_2^{+/0}$	−0.89				−4.19	−($E_{1/2}$+5.08)	171
93	PDI(Bu)-1-(C_8F_{17})	DCM, $TBAPF_6$, $FeCp_2^{+/0}$	−0.98	0.10*			−4.10	−($E_{1/2}$+5.08)	171
94	PDI(isooctyl)-1,6-$(C_8F_{17})_2$	DCM, $TBAPF_6$, $FeCp_2^{+/0}$	−0.82	0.14	0.10	PDI(isooctyl)-1-(C_8F_{17})	−4.26	−($E_{1/2}$+5.08)	171
95	PDI(isooctyl)-1,7-$(C_8F_{17})_2$	DCM, $TBAPF_6$, $FeCp_2^{+/0}$	−0.81	0.14	0.11	PDI(isooctyl)-1-(C_8F_{17})	−4.27	−($E_{1/2}$+5.08)	171
96	PDI(Ph)-1,7-$(C_8F_{17})_2$	DCM, $TBAPF_6$, $FeCp_2^{+/0}$	−0.75		0.14	PDI(Ph)-1-(C_8F_{17})	−4.33	−($E_{1/2}$+5.08)	171
97	PDI(dipp)-1,6-$(C_8F_{17})_2$	DCM, $TBAPF_6$, $FeCp_2^{+/0}$	−0.68	0.18*	0.14	PDI(dipp)-1-C_8F_{17}			185
98	PDI(dipp)-1,7-$(C_8F_{17})_2$	DCM, $TBAPF_6$, $FeCp_2^{+/0}$	−0.67	0.19*	0.15	PDI(dipp)-1-C_8F_{17}			168,185
99	PDI(isooctyl)-1-(C_8F_{17})	DCM, $TBAPF_6$, $FeCp_2^{+/0}$	−0.92	0.16			−4.16	−($E_{1/2}$+5.08)	171
100	PDI(Bu)-1,7-$(C_8F_{17})_2$	DCM, $TBAPF_6$, $FeCp_2^{+/0}$	−0.82	0.13*	0.16	PDI(Bu)-1-(C_8F_{17})	−4.26	−($E_{1/2}$+5.08)	171
101	PDI(dipp)-1-(C_8F_{17})	DCM, $TBAPF_6$, $FeCp_2^{+/0}$	−0.82	0.22*					185
	Effect of CN Substitution								
102	PDI(Cy)-1,7-$(CN)_2$	Butyronitrile, $TBAClO_4$, SCE	−0.07						233
103	PDI(Cy)-1,7-$(CN)_2$	DCM, $TBAPF_6$, $FeCp_2^{+/0}$	−0.67				−4.13	−($E_{1/2}$+4.8)	230

104	PDI(Cy)-1,7-$(CN)_2$	DCM, $TBAPF_6$, $FeCp_2^{+/0}$	−0.73				−4.07	−($E_{1/2}$+4.8)	[234]
105	PDI($C_{12}H_{25}$)-1,6,7,12-Cl_4-2,5,8-$(CN)_3$	DCM, $TBAPF_6$, $FeCp_2^{+/0}$	−0.35		0.09-0.15[f]	PDI($C_{12}H_{25}$)-1,6,7,12-Cl_4-$(CN)_2$ (**114, 115, 123**)	−4.41	from $E_{red\ on}$	[165]
106	PDI(Bu)-1,6,7,12-Cl_4-2,5,8-$(CN)_3$	DCM, $TBAPF_6$, $FeCp_2^{+/0}$	−0.34		0.13-0.18[f]	PDI(Bu)-1,6,7,12-Cl_4-$(CN)_2$ (**107, 111, 118**)	−4.52	from $E_{red\ on}$	[165]
107	PDI(Bu)-1,6,7,12-Cl_4-2,8-$(CN)_2$	DCM, $TBAPF_6$, $FeCp_2^{+/0}$	−0.52		0.14	PDI(Bu)-1,6,7,12-Cl_4-2-(CN)	−4.34	from $E_{red\ on}$	[165]
108	PDI(Bu)-1,6,7,12-Cl_4-2,5,8,11-$(CN)_4$	DCM, $TBAPF_6$, $FeCp_2^{+/0}$	−0.20		0.14	PDI(Bu)-1,6,7,12-Cl_4-2,5,8-$(CN)_3$	−4.64	from $E_{red\ on}$	[165]
109	PDI($C_{15}H_{31}$)-2,5,8,11- $(CN)_4$	DCM, $TBAPF_6$, $FeCp_2^{+/0}$	−0.38	0.15		PDI($C_{15}H_{31}$) entry 10	−4.42	−($E_{1/2}$+4.8)	[195]
110	PDI(Bu)-1,6,7,12-Cl_4-2-(CN)	DCM, $TBAPF_6$, $FeCp_2^{+/0}$	−0.66		0.15	PDI(Bu)-1,6,7,12-Cl_4	−4.21	from $E_{red\ on}$	[165]
111	PDI(Bu)-1,6,7,12-Cl_4-2,11-$(CN)_2$	DCM, $TBAPF_6$, $FeCp_2^{+/0}$	−0.51		0.15	PDI(Bu)-1,6,7,12-Cl_4-2-(CN)	−4.35	from $E_{red\ on}$	[165]
112	PDI($C_{12}H_{25}$)-1,6,7,12-Cl_4-2,5,8,11-$(CN)_4$	DCM, $TBAPF_6$, $FeCp_2^{+/0}$	−0.20		0.15	PDI($C_{12}H_{25}$)-1,6,7,12-Cl_4-2,5,8-$(CN)_3$	−4.41	from $E_{red\ on}$	[165]
113	PDI(C_8H_{17})-1,6,7,12-Cl_4-2,5,8,11-$(CN)_4$	DCM, $TBAPF_6$, $FeCp_2^{+/0}$	−0.21		0.16	PDI(C_8H_{17})-1,6,7,12-Cl_4	−4.65	−($E_{red\ on}$+4.8)	[166]
114	PDI($C_{12}H_{25}$)-1,6,7,12-Cl_4-2,8-$(CN)_2$	DCM, $TBAPF_6$, $FeCp_2^{+/0}$	−0.50		0.16	PDI($C_{12}H_{25}$)-1,6,7,12-Cl_4-2-(CN)	−4.35	from $E_{red\ on}$	[165]
115	PDI($C_{12}H_{25}$)-1,6,7,12-Cl_4-2,11-$(CN)_2$	DCM, $TBAPF_6$, $FeCp_2^{+/0}$	−0.50		0.16	PDI($C_{12}H_{25}$)-1,6,7,12-Cl_4-2-(CN)	−4.36	from $E_{red\ on}$	[165]
116	PDI(F7Bu)-1,6,7,12-Cl_4-2,5,8,11-$(CN)_4$	DCM, $TBAPF_6$, $FeCp_2^{+/0}$	−0.07[g]		0.17	PDI(F7Bu)-1,6,7,12-Cl_4	−4.73	−($E_{red\ on}$+4.8)	[167]
117	PDI(F7Bu)-1,7-$(CN)_2$	DCM, $TBAPF_6$, SCE	0.03 [−0.45][d]	0.18			−4.5	−($E_{1/2}$+4.4)	[225]
118	PDI(Bu)-1,6,7,12-Cl_4-2,5-$(CN)_2$	DCM, $TBAPF_6$, $FeCp_2^{+/0}$	−0.47		0.19	PDI(Bu)-1,6,7,12-Cl_4-2-(CN)	−4.39	from $E_{red\ on}$	[165]
119	PDI($C_{12}H_{25}$)-1,6,7,12-Cl_4-2-(CN)	DCM, $TBAPF_6$, $FeCp_2^{+/0}$	−0.66		0.19	PDI($C_{12}H_{25}$)-1,6,7,12-Cl_4	−4.21	from $E_{red\ on}$	[165]

120	PDI(C_8H_{17})-1,7($CN)_2$	DCM, $TBAPF_6$, SCE	−0.06 [−0.54][d]	0.20			−4.3	−($E_{1/2}$+4.4)	225
121	PDI(Bu)-1,7-($CF_3)_2$-5-(CN)	DCM, $TBAPF_6$, $FeCp_2^{+/0}$	−0.61		0.21	PDI(Bu)-1,7-CF_3			tw
122	PDI(C_5H_{11})-1,7-$(CN)_2$	DCM, $TBAPF_6$, $FeCp_2^{+/0}$	−0.62	0.21					194
123	PDI($C_{12}H_{25}$)-1,6,7,12-Cl_4-2,5-$(CN)_2$	DCM, $TBAPF_6$, $FeCp_2^{+/0}$	−0.44		0.22	PDI($C_{12}H_{25}$)-1,6,7,12-Cl_4-2-(CN)	−4.41	from $E_{\text{red on}}$	165
	Effect of NO_2 Substitution								
124	PDI(Cy)-1,6-$(NO_2)_2$	DCM, $TBAPF_6$, SCE[e]	−0.11	0.18	0.08	PDI(Cy)-1-NO_2	−4.33	$-4.88-(E_{\text{oxd}}-E_{FeCp_2^{+/0}})+E_g$	189
125	PDI(C_8H_{17})-1,7-$(NO_2)_2$	THF, $TBAPF_6$, SCE	−0.09	0.18	0.09	PDI(C_8H_{17})-1-(NO_2)	−4.35	−($E_{1/2}$+4.44)	228
126	PDI(Cy)-1,7-$(NO_2)_2$	THF, $TBAPF_6$, SCE[e]	−0.09	0.19	0.10	PDI(Cy)-1-(NO_2)	−4.35	−($E_{1/2}$+4.44)	228
127	PDI(Cy)-1,7-$(NO_2)_2$	DCM, $TBAPF_6$, SCE[e]	−0.09	0.19	0.10	PDI(Cy)-1-(NO_2)	−4.35	$-4.88-(E_{\text{oxd}}-E_{FeCp_2^{+/0}})+E_g$	189
128	PDI(C_8H_{17})-1-(NO_2)	THF, $TBAPF_6$, SCE	−0.18	0.27			−4.26	−($E_{1/2}$+4.44)	228
129	PDI(Cy)-1-(NO_2)	THF, $TBAPF_6$, SCE	−0.19	0.27		PDI(Cy) entry 19	−4.25	−($E_{1/2}$+4.44)	228
130	PDI(Cy)-1-(NO_2)	DCM, $TBAPF_6$, SCE[e]	−0.19	0.27		PDI(Cy) entry 18	−4.25	$-4.88-(E_{\text{oxd}}-E_{FeCp_2^{+/0}})+E_g$	189,227
	Effect of Aryl Substitution[h]								
131	PDI($C_{15}H_{31}$)-2,5,8,11-$(PhCN)_4$	DCM, $TBAPF_6$, $FeCp_2^{+/0}$	−0.90	0.013		PDI($C_{15}H_{31}$) entry 11	−3.90	−($E_{1/2}$+4.8)	160
132	PDI(C_8H_{17})-1,6,7,12-Cl_4-2,5,8,11-$(SAr)_4$	DCM, $TBAPF_6$, $FeCp_2^{+/0}$	−0.75		0.023	PDI(C_8H_{17})-1,6,7,12-Cl_4	−4.11	−($E_{\text{red on}}$+4.8)	166
133	PDI(C_8H_{17})-1,6-$(PhCN)_2$	PhCN, $TBABF_4$, $FeCp_2^{+/0}$	−0.96	0.03			−3.84	−($E_{1/2}$+4.8)	188
134	PDI(C_8H_{17})-1,6-$(ArNO_2)_2$	PhCN, $TBABF_4$, $FeCp_2^{+/0}$	−0.94	0.04			−3.86	−($E_{1/2}$+4.8)	188

135	PDI(C_8H_{17})-1,7-($PhCN)_2$	PhCN, $TBABF_4$, $FeCp_2^{+/0}$	−0.94	0.04		−3.86	−($E_{1/2}$+4.8)	188
136	PDI(Bu)-1,7-$(dyad)_2$	DCM, $TBAPF_6$, AgCl/Ag	−0.50	0.05				184
137	PDI(C_7H_{15})-1-(Alk-Ph)	DCM, $TBAPF_6$, SCE	−0.65	0.05				226
138	PDI(C_7H_{15})-1-(Alk-Ph-$(OMe)_2$)	DCM, $TBAPF_6$, SCE	−0.65	0.05				226
139	PDI(C_8H_{17})-1,7-$(ArNO_2)_2$	PhCN, $TBABF_4$, $FeCp_2^{+/0}$	−0.91	0.055		−3.89	−($E_{1/2}$+4.8)	188
140	PDI(C_7H_{15})-1-(Alk-Ph-CF_3)	DCM, $TBAPF_6$, SCE	−0.64	0.06				226
141	PDI(C_7H_{15})-1-(Alk-Ph-CN)	DCM, $TBAPF_6$, SCE	−0.62	0.08				226
142	PDI(C_7H_{15})-1-(Alk-Ph-F_2)	DCM, $TBAPF_6$, SCE	−0.62	0.08				226
143	PDI(C_7H_{15})-1-(Alk-Ph-$(CF_3)_2$)	DCM, $TBAPF_6$, SCE	−0.61	0.09				226

[a] In some cases, reported E_{LUMO} were converted to negative values for consistency. [b] $E_{1/2}$ values were extracted from reported E_{LUMO} values by subtracting 4.8 according to the corresponding supplemental information. [c] $E_{1/2}$ for this compound may come from the onset. [d] $FeCp_2^{+/0}$ = 0.475 vs. SCE according to source paper. [e] No conversion from ferrocenium/ferrocene to SCE is given $\Delta E_{1/2}$ from 'precursor' PDI(R)-1,6,7,12-Cl_4-$(CN)_3$ could arise from 3 different PDI(R)-1,6,7,12-Cl_4-$(CN)_2$ isomers. [g] Electrochemistry of this PDI was reported in various solvents and became more positive with decreasing polarity of the solvent. [h] Additional aryl substituted PDIs exist and only a small amount are presented for comparison with smaller groups; see ref [232] for more examples.

Table 3.2. Absorption maxima (λ_{max}) and molar extinction coeficients (ε), change in absorption maxima from PDI(R) ($\Delta_{PDI(R)}$), emission maxima (λ_F), change in emission maxima from PDI(R) ($\Delta_{PDI(R)}$), Stokes shifts, optical bandgaps ($E_{exciton}$), emission lifetimes (τ_F), and reduction potentials ($E_{1/2}^{0/-}$ and $E_{1/2}^{-/2-}$) vs $FeCp_2^{+/0}$ from cyclic voltammetry with 0.1 M $TBAPF_6$, 100 $mV \cdot s^{-1}$. All measurements were performed in dichloromethane solutions.

compound	λ_{max}, nm (ε, M^{-1} cm^{-1})	$\Delta_{PDI(R)}$, nm	λ_F, nm	$\Delta_{PDI(R)}$, nm	Stokes shift, cm^{-1}	$E_{exciton}$, eV	τ_F, ns	$E_{1/2}^{0/-}$ vs $FeCp_2^{+/0}$, V	$E_{1/2}^{-/2-}$ vs $FeCp_2^{+/0}$, V
PDI(Bu)	524(58000)[a]		537		462	2.34	4.05	−1.08	−1.25
PDI(Bu)-1,7-$(CF_3)_2$	507(58500)	−17	527	−10	749	2.40	4.17	−0.82	−1.07
PDI(Bu)-1,6-$(CF_3)_2$	509(46100)	−15	541	4	1160	2.36	4.85	−0.81	−1.09
PDI(Bu)-1,7,5-$(CF_3)_3$	509(48200)	−15	532	−5	849	2.38	4.23	−0.67	−0.97
PDI(Bu)-1,6,8-$(CF_3)_3$	508(40200)	−16	537	0	1060	2.37	4.80	−0.69	−0.99
PDI(Bu)-1,7,5,11-$(CF_3)_4$	508(44200)	−16	530	−7	817	2.39	4.21	−0.53	−0.86
PDI(Bu)-1,6,8,11-$(CF_3)_4$	506(14700)	−18	533	−4	1000	2.39	4.89	−0.55	−0.89
PDI(F7Bu)	524(85200)[b]		532[b]		287[b]	2.35	---	−0.95	−1.14
PDI(F7Bu)-1,7-$(CF_3)_2$	506(56900)	−18	524	−8	679	2.41	4.19	−0.70	−0.97
PDI(F7Bu)-1,6-$(CF_3)_2$	509(41800)	−15	538	6	1060	2.39	4.79	−0.69	−0.99
PDI(F7Bu)-1,7,5-$(CF_3)_3$	509(53600)	−15	530	−2	778	2.39	4.37	−0.54	−0.86
PDI(F7Bu)-1,6,8-$(CF_3)_3$	507(41900)	−17	534	2	850	2.38	4.80	−0.56	−0.88
PDI(F7Bu)-1,7,5,11-$(CF_3)_4$	508(51900)	−16	529	−3	247	2.39	4.23	−0.41	−0.76
PDI(Bu)-1,7-$(CF_3)_2$-5-(CN)	511(52500)	−13	---	---	---	---	---	−0.61	−0.93

[a] ε = 75900 in $CHCl_3$.[183] The reasons for these differences are unclear at this time. [b] values obtained from ref[225]

Table 3.3. Reduction potentials ($E_{1/2}^{0/-}$)[a], optical bandgap ($E_{exciton}$)[b], estimated EA_A,[c] and driving force (ΔG_{PET})[d,e] of charge transfer for PDIs studied in this work.

compound	$E_{1/2}^{0/-}$, V	$E_{exciton}$, eV	EA_A, eV	ΔG_{TFB}, eV	ΔG_{PFB}, eV	ΔG_{PFO}, eV	ΔG_{P3HT}, eV
PDI(Bu)-1,7-$(CF_3)_2$	-0.82	2.40	3.98	-0.88	-1.03	-0.63	-0.88
PDI(Bu)-1,6-$(CF_3)_2$	-0.81	2.36	3.99	-0.85	-1.00	-0.60	-0.89
PDI(Bu)-1,7,5-$(CF_3)_3$	-0.67	2.38	4.13	-1.01	-1.16	-0.76	-1.03
PDI(Bu)-1,5,8-$(CF_3)_3$	-0.69	2.37	4.11	-0.98	-1.13	-0.73	-1.01
PDI(Bu)-1,7,5,11-$(CF_3)_4$	-0.53	2.39	4.27	-1.16	-1.31	-0.91	-1.17
PDI(Bu)-1,6,8,11-$(CF_3)_4$	-0.55	2.39	4.25	-1.14	-1.29	-0.89	-1.15
PDI(F7Bu)-1,7-$(CF_3)_2$	-0.70	2.41	4.10	-1.01	-1.16	-0.76	-1.00
PDI(F7Bu)-1,6-$(CF_3)_2$	-0.69	2.37	4.11	-0.98	-1.13	-0.73	-1.01
PDI(F7Bu)-1,7,5-$(CF_3)_3$	-0.54	2.39	4.26	-1.15	-1.30	-0.90	-1.16
PDI(F7Bu)-1,6,8-$(CF_3)_3$	-0.56	2.38	4.24	-1.12	-1.27	-0.87	-1.14
PDI(F7Bu)-1,7,5,11-$(CF_3)_4$	-0.41	2.39	4.39	-1.28	-1.43	-1.03	-1.29
Lumogen Orange	-1.01	2.33	3.79	-0.62	-0.77	-0.37	-0.69
Lumogen Red	-1.13	2.08	3.67	-0.25	-0.40	0.00	-0.57

a) vs $FeCp_2^{+/0}$ from cyclic voltammetry with 0.1 M $TBAPF_6$, 100 $mV \cdot s^{-1}$, b) optical bandgap, c) $E_{1/2}^{0/-}$ + 4.8 eV, d) $\Delta G_{PET} = IP_D - EA_A - E_{exciton}$, IP_D = 5.35, 5.50, and 5.75 eV for PFB, TFB, and PFO, respectively,[206] e) $\Delta G_{PET} = EA_D - EA_A$, EA_D(P3HT) = 3.1 eV (ref [217])

Table 3.4. Select XRD information

compound	**solvent**	**torsion angles, °**	**PDI-PDI core overlap?**
PDI(Bu)-1,7-$(CF_3)_2$	no	23.0, 22.1	yes
PDI(Bu)-1,6-$(CF_3)_2$	CH_2Cl_2	21.9, 22.9 and 25.1, 24.5	yes
PDI(Bu)-1,7,5-$(CF_3)_3$	toluene	23.7, 25.7	yes
PDI(Bu)-1,7,5,11-$(CF_3)_4$	no	23.4, 24.2	yes
PDI(F7Bu)-1,7-$(CF_3)_2$	no	26.2, 20.8	yes
PDI(F7Bu)-1,6-$(CF_3)_2$	toluene		no
PDI(F7Bu)-1,7,5-$(CF_3)_3$	no	24.8, 22.8	yes
PDI(F7Bu)-1,6,8-$(CF_3)_3$	toluene	23.9, 26.6	no
PDI(F7Bu)-1,7,5,11-$(CF_3)_4$	toluene	24.9, 25.7	no
PDI(Bu)-1,7-$(CF_3)_2$-5-(CN)	toluene	25.6, 27.8	yes

Table 3.5. Crystallographic data and refinement parameters for ten PDI derivatives.

Compound	PDI(Bu)-1,7-$(CF_3)_2$	PDI(Bu)-1,6-$(CF_3)_2$	PDI(Bu)-1,7,5-$(CF_3)_3$
CCDC number	1053169	1053170	1053171
Formula	$C_{34}H_{24}F_6N_2O_4$	$C_{69}H_{50}Cl_2F_{12}N_4O_8$	$C_{42}H_{31}F_9N_2O_4$
Formula weight	638.55	1362.03	798.69
Habit, color	prism, orange	rhomb, orange	rod, red
Crystal system	triclinic	triclinic	monoclinic
Space group	$P\bar{1}$	$P\bar{1}$	$P2_1/n$
a (Å)	8.2658(7)	12.3437(3)	12.4462(6)
b (Å)	11.4034(10)	15.8240(5)	16.2113(8)
c (Å)	15.0623(14)	17.2377(5)	17.4281(8)
α (°)	86.532(5)	96.556(2)	90
β (°)	79.225(4)	109.2850(10)	97.664(3)
γ (°)	80.425(4)	109.9170(10)	90
V (Å^3)	1374.7(2)	2888.84(14)	3485.0(3)
Z	2	2	4
T (K)	120(2)	120(2)	120(2)
ρ_{calc} (g cm^{-3})	1.543	1.566	1.522
$R(F)$ ($I>2\sigma(I)$)[a]	0.0554	0.0449	0.0550
$wR(F^2)$ [all data][a]	0.1389	0.1201	0.1728
Goodness of Fit	1.015	1.027	1.041
Source	$Mo_{K\alpha}$	$Mo_{K\alpha}$	$Mo_{K\alpha}$

Compound	PDI(Bu)-1,7,5,11-$(CF_3)_4$	PDI(F7Bu)-1,7-$(CF_3)_2$	PDI(F7Bu)-1,6-$(CF_3)_2$
CCDC number	1053172	1053173	1053174
Formula	$C_{36}H_{22}F_{12}N_2O_4$	$C_{34}H_{10}F_{20}N_2O_4$	$C_{48}H_{26}F_{20}N_2O_4$
Formula weight	774.55	890.44	1074.71
Habit, color	rhomb, orange	rhomb, orange	plate, orange
Crystal system	triclinic	triclinic	triclinic
Space group	$P\bar{1}$	$P\bar{1}$	$P\bar{1}$
a (Å)	9.9448(4)	10.4925(9)	7.2312(4)
b (Å)	12.4938(5)	12.5528(11)	11.8115(7)
c (Å)	14.4595(5)	13.2123(11)	26.0726(15)
α (°)	74.8900(10)	108.438(5)	79.7710(12)
β (°)	69.9490(10)	96.582(5)	86.8404(13)
γ (°)	72.7920(10)	107.634(5)	80.7836(12)
V (Å^3)	1586.54(11)	1530.1(2)	2162.4(2)
Z	2	2	2
T (K)	100(2)	120(2)	100(2)
ρ_{calc} (g cm^{-3})	1.621	1.933	1.651
$R(F)$ ($I>2\sigma(I)$)[a]	0.0604	0.0506	0.1298
$wR(F^2)$ [all data][a]	0.1800	0.1218	0.2734
Goodness of Fit	1.042	1.027	1.316
Source	0.41328 Å	$Mo_{K\alpha}$	0.41328 Å

Compound	PDI(F7Bu)-1,7,5-$(CF_3)_3$	PDI(F7Bu)-1,6,8-$(CF_3)_3$	PDI(F7Bu)-1,7,5,11-$(CF_3)_4$
CCDC number	1053175	1053176	1053177
Formula	$C_{35}H_9F_{23}N_2O_4$	$C_{49}H_{25}F_{23}N_2O_4$	$C_{50}H_{24}F_{26}N_2O_4$
Formula weight	958.44	1142.71	1210.71
Habit, color	rhomb, orange	plate, orange	rod, orange
Crystal system	monoclinic	triclinic	triclinic
Space group	$P2_1/n$	$P\bar{1}$	$P\bar{1}$
a (Å)	12.3786(5)	7.2063(2)	7.7312(9)
b (Å)	15.6968(7)	11.8412(4)	14.0811(17)
c (Å)	18.1259(8)	27.0829(9)	21.717(3)
α (°)	90	99.4130(8)	80.887(2)
β (°)	97.0251(10)	92.3469(8)	84.589(3)
γ (°)	90	100.5917(8)	83.839(3)
V (Å^3)	3495.5(3)	2235.04(12)	2313.7(5)
Z	4	2	2
T (K)	100(2)	100(2)	100(2)
ρ_{calc} (g cm^{-3})	1.821	1.698	1.738
R(F) ($I>2\sigma(I)$)[a]	0.0595	0.0410	0.0612
wR(F^2) [all data][a]	0.1668	0.1154	0.1799
Goodness of Fit	1.021	1.031	1.028
Source	0.41328 Å	0.41328 Å	0.41328 Å

Compound	PDI(Bu)-1,7-$(CF_3)_2$-5-(CN)
CCDC number	1053168
Formula	$C_{38.5}H_{27}F_6N_3O_4$
Formula weight	958.44
Habit, color	rhomb, orange
Crystal system	triclinic
Space group	$P\bar{1}$
a (Å)	11.2630(3)
b (Å)	11.4003(3)
c (Å)	14.3874(4)
α (°)	107.9800(10)
β (°)	94.3410(10)
γ (°)	114.4940(10)
V (Å^3)	1554.11(7)
Z	2
T (K)	120(2)
ρ_{calc} (g cm^{-3})	1.516
R(F) ($I>2\sigma(I)$)[a]	0.0406
wR(F^2) [all data][a]	0.1045
Goodness of Fit	1.020
Source	$Mo_{K\alpha}$

[a] $R(F) = \Sigma \left| |F_o| - |F_c| \right| / \Sigma |F_o|$; $wR(F^2) = (\Sigma[w(F_o^2 - F_c^2)^2 / \Sigma[w(F_o^2)^2])^{1/2}$

SUMMARY

Trifluoromethylation of C_{60}, C_{70}, and $M_3N@C_{80}$ was explored using a hot plate reactor and crystal structures were used to confirm the CF_3 addition patterns of three previously unexplored PFAFs. It appears that the reaction conditions do not simply translate from using hollow cage fullerenes to EMFs, so new reaction conditions must first be developed to synthesize $M_3N@C_{80}(CF_3)_n$ compounds in more quantitative amounts. Regioselective sequential nucleophilic and electrophilic additions were used to determine which carbon atoms on a variety of PFAFs were most reactive. These newly developed PFAF reactions were used to regioselectively add electron-withdrawing CN to several C_{60} and C_{70} PFAFs. Especially reactive carbon atoms gave insight into why some PFAFs exhibit irreversible reductions in cyclic voltammetry. The electronic effects of nucleophiles, CN and CF_3, and electrophile CH_3 in specific positions on the fullerene core were studied with a combination of cyclic voltammetry, LT PES, and DFT. Modified Bingel-Hirsch reactions on some of the same PFAFs showed that cycloadditions were typically not as regioselective as a single nucleophilic CN addition. These studies will give insight when deliberately synthesizing new fullerenes for specific electronic applications. Such derivatives of PFAFs may become increasingly important building blocks in the molecular and supramolecular designs of the electroactive functional materials.

A new family of poly(trifluoromethyl)azulene derivatives was synthesized and characterized. Trifluoromethyl substitution on the azulenic core incrementally increased gas phase electron affinity by 0.42 eV per substitution and effectively created stronger electron acceptors. One of the highly substituted azulene derivatives and strongly electron withdrawing derivatives was utilized in a charge transfer complex with pyrene. Elucidating oligomeric

poly(trifluoromethyl)azulene and AZUL(CF_3)$_6$ species will result in even stronger electron acceptors and could lead to charge-transfer complexes with unique packing motifs and unusual electronic properties. Solid-state packing motifs were also investigated for two azulene(CF_3)$_4$ isomers along with four other families of PAH acceptors. In some cases, close intermolecular interactions were still present with high degrees of substitution as long as only specific locations participated in substitution. These electron-withdrawing substituents can tune the electronic properties of PAHs, but can hinder or enhance charge transfer pathways in the solid state. Choosing the optimal derivative to balance electronic levels and charge transport is necessary and possible when synthesizing new PAH compounds for each application.

A new family of poly(trifluoromethyl)peryelene diimide acceptors was also synthesized, isolated, and studied. Substitution at bay positions had a greater influence on absorption and emission behavior than substitution at *ortho* positions. Crystallographic data for these PDIs along with a cyano derivative were compared to elucidate the influence of core and imide substitution on close intermolecular interactions and packing motifs. Trifluoromethyl substitution at either location of the core linearly increased solution-phase reduction potentials and gas-phase electron affinities. The effects of specific electron-withdrawing substituents at specific locations on reduction potentials were compared with an extensive set of literature compounds. The tunable reduction potentials within this series of poly(trifluoromethyl)peryelene diimide acceptors was utilized in fundamental studies of charge transport within OPV active layers. These studies were instrumental in discovering when PDIs aggregate in polymer films and determining solid-state charge transfer characteristics from polymer donors to PDI acceptors with a large thermodynamic driving force for charge transfer.

REFERENCES

(1) http://energyinformative.org/potential-of-solar-energy/ *accessed on October 1, 2015*.

(2) Janssen, R. A. J.; Nelson, J. *Adv. Mater.* **2013**, *25*, 1847.

(3) http://energy.gov/eere/sunshot/organic-photovoltaics-research *accessed on October 1, 2015*.

(4) Lopez, A. M.; Mateo-Alonso, A.; Prato, M. *J. Mater. Chem.* **2011**, *21*, 1305.

(5) Tang, M. L.; Bao, Z. A. *Chem. Mater.* **2011**, *23*, 446.

(6) Chang, Y. C.; Kuo, M. Y.; Chen, C. P.; Lu, H. F.; Chao, I. *J. Phys. Chem. C* **2010**, *114*, 11595.

(7) Coffey, D. C.; Larson, B. W.; Hains, A. W.; Whitaker, J. B.; Kopidakis, N.; Boltalina, O. V.; Strauss, S. H.; Rumbles, G. *J. Phys. Chem. C* **2012**, *116*, 8916.

(8) Boltalina, O. V.; Popov, A. A.; Kuvychko, I. V.; Shustova, N. B.; Strauss, S. H. *Chem. Rev.* **2015**, *115*, 1051.

(9) Boltalina, O. V.; Kuvychko, I. V.; Shustova, N. B.; Strauss, S. H. In *Handbook of Carbon Materials, Volume 1, Syntheses and Supramolecular Systems*; Desouza, F., Kadish, K. M., Eds.; World Scientific: Singapore, **2010**, p pp 101.

(10) Shustova, N. B.; Kuvychko, I. V.; Bolskar, R. D.; Seppelt, K.; Strauss, S. H.; Popov, A. A.; Boltalina, O. V. *J. Am. Chem. Soc.* **2006**, *128*, 15793.

(11) Kareev, I. E.; Popov, A. A.; Kuvychko, I. V.; Shustova, N. B.; Lebedkin, S. F.; Bubnov, V. P.; Anderson, O. P.; Seppelt, K.; Strauss, S. H.; Boltalina, O. V. *J. Am. Chem. Soc.* **2008**, *130*, 13471.

(12) Troyanov, S. I.; Tamm, N. B. *Crystallogr. Rep.* **2009**, *54*, 598.

(13) Troyanov, S., I.; Tamm, N. B. *Chem. Commun.* **2009**, 6035.

(14) Troyanov, S., I.; Tamm, N. B. *Crystallogr. Rep.* **2010**, *55*, 432.

(15) Shustova, N. B.; Peryshkov, D. V.; Kuvychko, I. V.; Chen, Y. S.; Mackey, M. A.; Coumbe, C.; Heaps, D. T.; Confait, B. S.; Heine, T.; Phillips, J. P.; Stevenson, S.; Dunsch, L.; Popov, A. A.; Strauss Steven, H.; Boltalina, O. V. *J. Am. Chem. Soc.* **2010**, *133*, 2672.

(16) Shustova, N. B.; Kuvychko, I. V.; Popov, A. A.; von Delius, M.; Dunsch, L.; Anderson, O. P.; Hirsch, A.; Strauss, S. H.; Boltalina, O. V. *Angew. Chem. Int. Ed.* **2011**, *50*, 5537.

(17) Ovchinnikova, N. S.; Ignat'eva, D. V.; Tamm, N. B.; Avdoshenko, S. M.; Goryunkov, A. A.; Loffe, I. N.; Markov, V. Y.; Troyanov, S. I.; Sidorov, L. N.; Yurovskaya, M. A.; Kemnitz, E. *New J. Chem.* **2008**, *32*, 89.

(18) Takano, Y.; Ángeles Herranz, M.; Kareev, I. E.; Strauss, S. H.; Boltalina, O. V.; Akasaka, T.; Martín, N. *J. Org. Chem.* **2009**, *74*, 6902.

(19) Takano, Y.; Ángeles Herranz, M.; Kareev, I. E.; Strauss, S. H.; Boltalina, O. V.; Akasaka, T.; Martín, N. *Chem. Eur. J.* **2010**, *16*, 5343.

(20) Kuvychko, I. V.; Whitaker, J. B.; Larson, B. W.; Folsom, T. C.; Shustova, N. B.; Avdoshenko, S. M.; Chen, Y.-S.; Wen, H.; Wang, X.-B.; Dunsch, L.; Popov, A. A.; Boltalina, O. V.; Strauss, S. H. *Chem. Sci.* **2012**, *3*, 1399.

(21) Zhang, X.; Zhan, C.; Yao, J. *Chem. Mater.* **2015**, *27*, 166.

(22) Hartnett, P. E.; Timalsina, A.; Matte, H. S. S. R.; Zhou, N.; Guo, X.; Zhao, W.; Facchetti, A.; Chang, R. P. H.; Hersam, M. C.; Wasielewski, M. R.; Marks, T. J. *J. Am. Chem. Soc.* **2014**.

(23) Singh, R.; Aluicio-Sarduy, E.; Kan, Z.; Ye, T.; MacKenzie, R. C. I.; Keivanidis, P. E. *J. Mater. Chem. A* **2014**, *2*, 14348.

(24) Sirringhaus, H. *Adv. Mater.* **2014**, *26*, 1319.

(25) Kuvychko, I. V.; Castro, K. P.; Deng, S. H. M.; Wang, X.-B.; Strauss, S. H.; Boltalina, O. V. *Angew. Chem. Int. Ed.* **2013**, *52*, 4871.

(26) Jones, B. A.; Ahrens, M. J.; Yoon, M.-H.; Facchetti, A.; Marks, T. J.; Wasielewski, M. R. *Angew. Chem. Int. Ed.* **2004**, *43*, 6363.

(27) Klauk, H.; Halik, M.; Zschieschang, U.; Schmid, G.; Radlik, W.; Weber, W. *J. Appl. Phys.* **2002**, *92*, 5259.

(28) Kuvychko, I. V.; Whitaker, J. B.; Larson, B. W.; Raguindin, R. S.; Suhr, K. J.; Strauss, S. H.; Boltalina, O. V. *J. Fluorine Chem.* **2011**, *132*, 679.

(29) Ovchinnikova, N. S.; Goryunkov, A. A.; Khavrel, P. A.; Belov, N. M.; Apenova, M. G.; Ioffe, I. N.; Yurovskaya, M. A.; Troyanov, S. I.; Sidorov, L. N.; Kemnitz, E. *Dalton Trans.* **2011**, *40*, 959.

(30) Goryunkov, A. A.; Samokhvalova, N. A.; Khavrel, P. A.; Belov, N. M.; Markov, V. Y.; Sidorov, L. N.; Troyanov, S. I. *New J. Chem.* **2011**, *35*, 32.

(31) Troyanov, S. I.; Kemnitz, E. *Mendeleev Commun.* **2008**, *18*, 27.

(32) Kareev, I. E.; Kuvychko, I. V.; Lebedkin, S. F.; Miller, S. M.; Anderson, O. P.; Seppelt, K.; Strauss, S. H.; Boltalina, O. V. *J. Am. Chem. Soc.* **2005**, *127*, 8362.

(33) Kareev, I. E.; Santiso-Quinones, G.; Kuvychko, I. V.; Ioffe, I. N.; Goldt, I. V.; Lebedkin, S. F.; Seppelt, K.; Strauss, S. H.; Boltalina, O. V. *J. Am. Chem. Soc.* **2005**, *127*, 11497.

(34) Kareev, I. E.; Kuvychko, I. V.; Shustova, N. B.; Lebedkin, S. F.; Bubnov, V. P.; Anderson, O. P.; Popov, A. A.; Strauss, S. H.; Boltalina, O. V. *Angew. Chem. Int. Ed.* **2008**, *47*, 6204.

(35) Diederich, F.; Kessinger, R. *Accounts Chem. Res.* **1999**, 537.

(36) Hirsch, A.; Brettreich, M. *Fullerenes - Chemistry and Reactions*; Wiley-VCH: Weinheim, 2005.

(37) Thilgen, C.; Diederich, F. *Chem. Rev.* **2006**, *106*, 5049.

(38) Herrmann, A.; Diederich, F.; Thilgen, C.; Ter Meer, H.-U.; Muller, W. H. *Helv. Chim. Acta* **1994**, *77*, 1689.

(39) Thilgen, C.; Diederich, F. *Top. Curr. Chem.* **1999**, *199*, 135.

(40) Keshavarz-K, M.; Knight, B.; Srdanov, G.; Wudl, F. *J. Am. Chem. Soc.* **1995**, *117*, 11371.

(41) Jousselme, B.; Sonmez, G.; Wudl, F. *J. Mater. Chem.* **2006**, *16*, 3478.

(42) Khairallah, G.; Peel, J. B. *Chem. Commun.* **1997**, 253.

(43) Khairallah, G.; Peel, J. B. *J. Phys. Chem. A* **1997**, *101*, 6770.

(44) Khairallah, G.; Peel, J. B. *Int. J. Mass Spectrom.* **2000**, *194*, 115.

(45) Braunecker, W. O., S.; Owczarczyk, Z.; Larsen, R.; Larson, B.; Ginley, David; Boltalina, O.; Strauss, S.; Kopidakis, N.; Olson, D. *Macromol.* **2013**, *46*, 3367.

(46) Koppolu, V. R.; Gupta, M. C.; Scudiero, L. *Sol. Energy Mater. Sol. Cells* **2011**, *95*, 1111.

(47) Abe, Y.; Hata, R.; Matsuo, Y. *Chem. Lett.* **2013**, *42*, 1525.

(48) Popov, A. A.; Kareev, I. E.; Shustova, N. B.; Stukalin, E. B.; Lebedkin, S. F.; Seppelt, K.; Strauss, S. H.; Boltalina, O. V.; Dunsch, L. *J. Am. Chem. Soc.* **2007**, *129*, 11551.

(49) Popov, A. A.; Kareev, I. E.; Shustova, N. B.; Lebedkin, S. F.; Strauss, S. H.; Boltalina, O. V.; Dunsch, L. *Chem. Eur. J.* **2008**, *14*, 107.

(50) Clikeman, T. T.; Deng, S. H. M.; Avdoshenko, S.; Wang, X.-B.; Popov , A. A.; Strauss, S. H.; Boltalina, O. V. *Chem.-Eur. J.* **2013**, *19*, 15404.

(51) Dorozhkin, E. I.; Ignat'eva, D. V.; Tamm, N. B.; Goryunkov, A. A.; Khavrel, P. A.; Ioffe, I. N.; Popov, A. A.; Kuvychko, I. V.; Streletskiy, A. V.; Markov, V. Y.; Spandl, J.; Strauss, S. H.; Boltalina, O. V. *Chem. Eur. J.* **2006**, *12*, 3876.

(52) Mas-Torrent, M.; Rovira, C. *Chem. Rev.* **2011**, *111*, 4833.

(53) Sun, B.; Sirringhaus, H. *Nano Lett.* **2005**, *5*, 2408.

(54) Rumpel, A.; Novak, M.; Walter, J.; Braunschweig, B.; Halik, M.; Peukert, W. *Langmuir* **2011**, *27*, 15016.

(55) Burkhardt, M.; Jedaa, A.; Novak, M.; Ebel, A.; Voitchovsky, K.; Stellacci, F.; Hirsch, A.; Halik, M. *Adv. Mater.* **2010**, *22*, 2525.

(56) Voigt, M.; Klaumunzer, M.; Ebel, A.; Werner, F.; Yang, G.; Marczak, R.; Spiecker, E.; Guldi, D. M.; Hirsch, A.; Peukert, W. *J. Phys. Chem. C* **2011**, *115*, 5561.

(57) Niinomi, T.; Matsuo, Y.; Hashiguchi, M.; Sato, Y.; Nakamura, E. *J. Mater. Chem.* **2009**, *19*, 5804.

(58) Matsuo, Y.; Iwashita, A.; Nakamura, E. *Organometallics* **2008**, *27*, 4611.

(59) Matsuo, Y.; Morita, K.; Nakamura, E. *Chem.-Asian J.* **2008**, *3*, 1350.

(60) Matsuo, Y.; Tahara, K.; Nakamura, E. *Chem. Lett.* **2005**, *34*, 1078.

(61) Okada, S.; Arita, R.; Matsuo, Y.; Nakamura, E.; Oshiyama, A.; Aoki, H. *Chem. Phys. Lett.* **2004**, *399*, 157.

(62) Whitaker, J. B.; Kuvychko, I. V.; Shustova, N. B.; Chen, Y.-S.; Strauss, S. H.; Boltalina, O. V. *Chem. Commun.* **2014**, *50*, 1205.

(63) Troyanov, S. I.; Popov, A. A.; Denisenko, N. I.; Boltalina, O. V.; Sidorov, L. N.; Kemnitz, E. *Angew. Chem. Int. Ed.* **2003**, *42*, 2395.

(64) Clikeman, T. T.; Kuvychko, I. V.; Shustova, N. B.; Chen, Y.-S.; Popov, A. A.; Boltalina, O. V.; Strauss, S. H. *Chem.-Eur. J.* **2013**, *19*, 5070.

(65) Xiao, Z.; Wang, F. D.; Huang, S. H.; Gan, L. B.; Zhou, J.; Yuan, G.; Lu, M. J.; Pan, J. Q. *J. Org. Chem.* **2005**, *70*, 2060.

(66) Kareev, I. E.; Kuvychko, I. V.; Popov, A. A.; Lebedkin, S. F.; Miller, S. M.; Anderson, O. P.; Strauss, S. H.; Boltalina, O. V. *Angew. Chem. Int. Ed.* **2005**, *44*, 7984.

(67) Takano, Y.; Herranz, M. A.; Kareev, I. E.; Strauss, S. H.; Boltalina, O. V.; Akasaka, T.; Martin, N. *J. Org. Chem.* **2009**, *74*, 6902.

(68) Larson, B. W.; Whitaker, J. B.; Wang, X.-B.; Popov, A. A.; Rumbles, G.; Kopidakis, N.; Strauss, S. H.; Boltalina, O. V. *J. Phys. Chem. C* **2013**, *117*, 14958.

(69) Han, W.; Yoshida, H.; Ueno, N.; Kera, S. *Appl. Phys. Lett.* **2013**, *103*, 123303.

(70) Yoshida, H. *Anal. and Bioanal. Chem.* **2014**, *406*, 2231.

(71) Huang, D.-L.; Dau, P. D.; Liu, H.-T.; Wang, L.-S. *J. Chem. Phys.* **2014**, *140*, 224315.

(72) Wang, X.-B.; Woo, H.-K.; Huang, X.; Kappes, M. M.; Wang, L.-S. *Phys. Rev. Lett.* **2006**, *96*, 143002.

(73) Iikura, H.; Mori, S.; Sawamura, M.; Nakamura, E. *J. Org. Chem.* **1997**, *62*, 7912.

(74) Sawamura, M.; Kuninobu, Y.; Toganoh, M.; Matsuo, Y.; Yamanaka, M.; Nakamura, E. *J. Amer. Chem. Soc.* **2002**, *124*, 9354.

(75) Sawamura, M.; Nagahama, N.; Toganoh, M.; Hackler, U. E.; Isobe, H.; Nakamura, E.; Zhou, S. Q.; Chu, B. *Chem. Lett.* **2000**, 1098.

(76) Kuninobu, Y.; Matsuo, Y.; Toganoh, M.; Sawamura, M.; Nakamura, E. *Organometallics* **2004**, *23*, 3259.

(77) Matsuo, Y.; Kuninobu, Y.; Ito, S.; Nakamura, E. *Chem. Lett.* **2004**, *33*, 68.

(78) Kareev, I. E.; Shustova, N. B.; Kuvychko, I. V.; Lebedkin, S. F.; Miller, S. M.; Anderson, O. P.; Popov, A. A.; Strauss, S. H.; Boltalina, O. V. *J. Am. Chem. Soc.* **2006**, *128*, 12268.

(79) Kuvychko, I. V.; Shustova, N. B.; Avdoshenko, S. M.; Popov, A. A.; Strauss, S. H.; Boltalina, O. V. *Chem.-Eur. J.* **2011**, *17*, 8799.

(80) Troshin, P. A.; Khakina, E. A.; Peregudov, A. S.; Konarev, D. V.; Soulimenkov, I. V.; Peregudova, S. M.; Lyubovskaya, R. N. *Eur. J. Org. Chem.* **2010**.

(81) Avent, A. G.; Birkett, P. R.; Crane, J. D.; Darwish, A. D.; Langley, G. J.; Kroto, H. W.; Taylor, R.; Walton, D. R. M. *J. Chem. Soc.-Chem. Commun.* **1994**, 1463.

(82) Birkett, P. R.; Avent, A. G.; Darwish, A. D.; Kroto, H. W.; Taylor, R.; Walton, D. R. M. *J. Chem. Soc.-Chem. Commun.* **1993**, 1230.

(83) Wang, X. B.; Wang, L. S. *Rev. Sci. Instrum.* **2008**, *79*, 073108/1.

(84) Wang, X.-B.; Chi, C.; Zhou, M.; Kuvychko, I. V.; Seppelt, K.; Popov, A. A.; Strauss, S. H.; Boltalina, O. V.; Wang, L.-S. *J. Phys. Chem. A* **2010**, *114*, 1756.

(85) Gruzinskaya, N. I. A., V. E. Borshchevskii, A. Ya. Sidorov, L. N. *J. Anal. Chem.* **2010**, *65*, 1328.

(86) Markov, V. Y.; Aleshina, V. E.; Borschevskiy, A. Y.; Khatymov, R. V.; Tuktarov, R. F.; Pogulay, A. V.; Maximov, A. L.; Kardashev, S. V.; Ioffe, I. N.; Avdoshenko, S. M.; Dorozhkin, E. I.; Goryunkov, A. A.; Ignat'eva, D. V.; Gruzinskaya, N. I.; Sidorov, L. N. *International Journal of Mass Spectrometry* **2006**, *251*, 16.

(87) Borshchevskii, A. Y.; Aleshina, V. E.; Markov, V. Y.; Dorozhkin, E. I.; Sidorov, L. N. *Inorg. Mater.* **2005**, *41*, 1318.

(88) Wang, X. B.; Woo, H. K.; Wang, L. S. *J. Chem. Phys.* **2005**, *123*, 051106/1.

(89) Ioffe, I. N.; Avdoshenko, S. M.; Boltalina, O. V.; Sidorov, L. N.; Berndt, K.; Weber, J. M. *Int. J. Mass Spectrom.* **2005**, *243*, 223.

(90) Zalibera, M.; Machata, P.; Clikeman, T. T.; Rosenkranz, M.; Strauss, S. H.; Boltalina, O. V.; Popov, A. A. *Analyst* **2015**.

(91) Chen, E. C. M.; Wentworth, W. E. *J. Chem. Phys.* **1975**, *63*, 3183.

(92) Paolucci, D.; Paolucci, F.; Marcaccio, M.; Carano, M.; Taylor, R. *Chem. Phys. Lett.* **2004**, *400*, 389.

(93) Meerheim, R.; Olthof, S.; Hermenau, M.; Scholz, S.; Petrich, A.; Tessler, N.; Solomeshch, O.; Lüssem, B.; Riede, M.; Leo, K. *J. Appl. Phys.* **2011**, *109*, 103102.

(94) Sque, S.; Jones, R.; Goss, J.; Briddon, P.; Öberg, S. *J. Phys.: Condens. Matter* **2005**, *17*, L21.

(95) Tietze, M. L.; Burtone, L.; Riede, M.; Lüssem, B.; Leo, K. *Phys. Rev. B* **2012**, *86*, 035320.

(96) Ristein, J. *J. Phys. D: Appl. Phys.* **2006**, *39*, R71.

(97) Avent, A. G.; Ala'a, K.; Clare, B. W.; Kepert, D. L.; Street, J. M.; Taylor, R. *Org. Biomol. Chem.* **2003**, *1*, 1026.

(98) Holloway, J.; Hope, E.; Street, J. *J. Chem. Soc.Perkin Trans. 2* **1998**, 1845.

(99) Kuvychko, I. V.; Spisak, S. N.; Chen, Y. S.; Popov, A. A.; Petrukhina, M. A.; Strauss, S. H.; Boltalina, O. V. *Angew. Chem. Int. Ed.* **2012**, *51*, 4939.

(100) Zhang, X.; Sieval, A. B.; Hummelen, J. C.; Hessen, B. *Chem. Commun.* **2005**, *0*, 1616.

(101) Pinzón, J. R.; Zuo, T.; Echegoyen, L. *Chem.-Eur. J.* **2010**, *16*, 4864.

(102) Clikeman, T. T.; Deng, S. H. M.; Popov, A. A.; Wang, X.-B.; Strauss, S. H.; Boltalina, O. V. *Phys. Chem. Chem. Phys.* **2015**, *17*, 551.

(103) Sheldrick, G. M. *SADABS - A program for area detector absorption corrections* **2004**.

(104) Sheldrick, G. M. *Crystallography Program APEX2, v. 2.0-2* **2006**.

(105) Sheldrick, G. M. *Crystallography Software Package SHELXTL, v. 6.12 UNIX* **2001**.

(106) G. M. Dolomanov, L. J. B., R. J. Gildea, J. A. K. Howard, H. Puschmann *J. Appl. Cryst.* **2009**, *42*, 339.

(107) Boltalina, O. V.; Sidorov, L. N.; Borchshevskii, A. Y.; Sukhanova, E. V.; Skokan, E. V. *Rapid Comm. Mass. Spectrom.* **1993**, *7*, 1009.

(108) Mottishaw, J. D.; Sun, H. *J. Phys. Chem. A* **2013**, *117*, 7970.

(109) Liu, L.; Yang, G.; Duan, Y.; Geng, Y.; Wu, Y.; Su, Z. *Org. Electron.* **2014**, *15*, 1896.

(110) Coropceanu, V.; Cornil, J.; da Silva Filho, D. A.; Olivier, Y.; Silbey, R.; Brédas, J.-L. *Chem. Rev.* **2007**, *107*, 926.

(111) Wheland, G. W.; Mann, D. E. *J. Chem. Phys.* **1949**, *17*, 264.

(112) Kasha, M. *Faraday Discuss.* **1950**, *9*, 14.

(113) Viswanath, G.; Kasha, M. *J. Chem. Phys.* **1956**, *24*, 574.

(114) Feringa, B. L.; van Delden, R. A.; Koumura, N.; Geertsema, E. M. *Chem. Rev.* **2000**, *100*, 1789.

(115) Förster, S.; Hahn, T.; Loose, C.; Röder, C.; Liebing, S.; Seichter, W.; Eißmann, F.; Kortus, J.; Weber, E. *J. Phys. Org. Chem.* **2012**, *25*, 856.

(116) Zhou, K.-G.; Zhang, Y.-H.; Wang, L.-J.; Xie, K.-F.; Xiong, Y.-Q.; Zhang, H.-L.; Wang, C.-W. *Phys. Chem. Chem. Phys.* **2011**, *13*, 15882.

(117) Noll, G.; Daub, J.; Lutz, M.; Rurack, K. *J. Org. Chem.* **2011**, *76*, 4859.

(118) Schmitt, S.; Baumgarten, M.; Simon, J.; Hafner, K. *Angew. Chem. Int. Ed.* **1998**, *37*, 1077.

(119) Barnes, J. C.; Juríček, M.; Strutt, N. L.; Frasconi, M.; Sampath, S.; Giesener, M. A.; McGrier, P. L.; Bruns, C. J.; Stern, C. L.; Sarjeant, A. A.; Stoddart, J. F. *J. Am. Chem. Soc.* **2012**, *135*, 183.

(120) Li, F.; Song, Q.; Yang, L.; Wu, G.; Zhang, X. *Chem. Commun.* **2013**, *49*, 1808.

(121) Lambert, C.; Noll, G.; Zabel, M.; Hampel, F.; Schmalzlin, E.; Brauchle, C.; Meerholz, K. *Chem.-Eur. J.* **2003**, *9*, 4232.

(122) Nakatsuji, S. I.; Mizumoto, M.; Takai, A.; Akutsu, H.; Yamada, J.-I.; Kawamura, H.; Schmitt, S.; Hafner, K. *Mol. Cryst. Liq. Cryst.* **2000**, *348*, 1.

(123) Ohki, S.; Yosuke, K.; Yoshihiro, S.; Sachiko, Y.; Josuke, T.; Yong Zhe, Y.; Akira, M.; Hitoshi, T.; Tetsuo, N. *Chem. Lett.* **2000**, *32*, 1078.

(124) Mąkosza, M.; Kędziorek, M.; Ostrowski, S. *Synthesis* **2002**, *2002*, 2517.

(125) Sato, O.; Sato, M.; Sugimoto, H.; Kuramochi, T.; Shirahata, T.; Takahashi, K. *J. Sulfur Chem.* **2009**, *30*, 360.

(126) Ukita, T.; Miyazaki, M.; Watanabe, H. *Pharm. Bull.* **1955**, *3*, 199.

(127) Lou, Y.; Chang, J.; Jorgensen, J.; Lemal, D. M. *J. Am. Chem. Soc.* **2002**, *124*, 15302.

(128) Shevyakov, S. V.; Li, H.; Muthyala, R.; Asato, A. E.; Croney, J. C.; Jameson, D. M.; Liu, R. S. H. *J. Phys. Chem. A* **2003**, *107*, 3295.

(129) Muthyala, R. S.; Liu, R. S. H. *J. Fluor. Chem.* **1998**, *89*, 173.

(130) Le, V.; Wells, P. *Aust. J. Chem.* **1992**, *45*, 1057.

(131) Bargon, J.; Mohmand, S.; Waltman, R. J. *Mol. Cryst. Liq. Cryst.* **1983**, *93*, 279.

(132) Naoi, K.; Ueyama, K.; Osaka, T. *J. Electrochem. Soc.* **1989**, *136*, 2444.

(133) Schiedt, J.; Knott, W. J.; Le Barbu, K.; Schlag, E. W.; Weinkauf, R. *J. Chem. Phys.* **2000**, *113*, 9470.

(134) Previously the EA of AZUL-5-1 was incorrectly reported as 2.890(5) eV in *Angew. Chem. Int. Ed.* **2013**, *52*, 4871.

(135) Saitoh, M.; Yano, J.; Nakazawa, T.; Sugihara, Y.; Hashimoto, K. *J. Electroanal. Chem.* **1996**, *418*, 139.

(136) San, L. K.; Bukovsky, E. V.; Kuvychko, I. V.; Popov, A. A.; Strauss, S. H.; Boltalina, O. V. *Chem.-Eur. J.* **2014**, *20*, 4373.

(137) Shearer, H. M. M.; Robertson, J. M.; Sim, G. A.; Watson, D. G. *Acta Cryst.* **1962**, *15*, 1.

(138) Churchill, M. R. In *Progress in Inorganic Chemistry*; John Wiley & Sons, Inc.: **2007**, p 53.

(139) San, L. K.; Clikeman, T. T.; Dubceac, C.; Popov, A. A.; Chen, Y.-S.; Petrukhina, M. A.; Strauss, S. H.; Boltalina, O. V. *Chem.-Eur. J.* **2015**, *21*, 9488.

(140) Steinberg, B. D.; Jackson, E. A.; Filatov, A. S.; Wakamiya, A.; Petrukhina, M. A.; Scott, L. T. *J. Am. Chem. Soc.* **2009**, *131*, 10537.

(141) Shi, K.; Lei, T.; Wang, X.-Y.; Wang, J.-Y.; Pei, J. *Chem. Sci.* **2014**, *5*, 1041.

(142) Seiders, T. J.; Baldridge, K. K.; Grube, G. H.; Siegel, J. S. *J. Am. Chem. Soc.* **2001**, *123*, 517.

(143) Zhang, Q.; Kawasumi, K.; Segawa, Y.; Itami, K.; Scott, L. T. *J. Am. Chem. Soc.* **2012**, *134*, 15664.

(144) Sevryugina, Y.; Rogachev, A. Y.; Jackson, E. A.; Scott, L. T.; Petrukhina, M. A. *J. Org. Chem.* **2006**, *71*, 6615.

(145) Filatov, A. S.; Zabula, A. V.; Spisak, S. N.; Rogachev, A. Y.; Petrukhina, M. A. *Angew. Chem. Int. Ed.* **2014**, *53*, 140.

(146) Sygula, A. *Eur. J. Org. Chem.* **2011**, 1611.

(147) Samdal, S.; Hedberg, L.; Hedberg, K.; Richardson, A. D.; Bancu, M.; Scott, L. T. *J. Phys. Chem. A* **2003**, *107*, 411.

(148) Wozniak, K.; Kariuki, B.; Jones, W. *Acta Cryst. Sect. C: Struct. Chem.* **1991**, *47*, 1113.

(149) Munkholm, C.; Parkinson, D.-R.; Walt, D. R. *J. Am. Chem. Soc.* **1990**, *112*, 2608.

(150) Zhu, M.; Yang, C. *Chem. Soc. Rev.* **2012**, *42*, 4963.

(151) Sun, H.; Putta, A.; Billion, M. *J. Phys. Chem. A* **2012**, *116*, 8015.

(152) Sheldrick, G. *TWINABS v. 2012/1* **2012**.

(153) Zhan, X.; Facchetti, A.; Barlow, S.; Marks, T. J.; Ratner, M. A.; Wasielewski, M. R.; Marder, S. R. *Adv. Mater.* **2011**, *23*, 268.

(154) Wurthner, F.; Stolte, M. *Chem. Commun.* **2011**, *47*, 5109.

(155) Li, C.; Wonneberger, H. *Adv. Mater.* **2012**, *24*, 613.

(156) Huang, C.; Barlow, S.; Marder, S. R. *J. Org. Chem.* **2011**, *76*, 2386.

(157) Boehm, A. D.; Arms, H.; Henning, G. D.; Blaschka, P. B. A.; German Pat. DE 19547209 A1: **1997** [*Chem. Abstr.* **1997**, *127*, 96569g].

(158) Nakazono, S.; Imazaki, Y.; Yoo, H.; Yang, J.; Sasamori, T.; Tokitoh, N.; Cédric, T.; Kageyama, H.; Kim, D.; Shinokubo, H.; Osuka, A. *Chem.-Eur. J.* **2009**, *15*, 7530.

(159) Nakazono, S.; Easwaramoorthi, S.; Kim, D.; Shinokubo, H.; Osuka, A. *Org. Lett.* **2009**, *11*, 5426.

(160) Battagliarin, G.; Li, C.; Enkelmann, V.; Müllen, K. *Org. Lett.* **2011**, *13*, 3012.

(161) Teraoka, T.; Hiroto, S.; Shinokubo, H. *Org. Lett.* **2011**, *13*, 2532.

(162) Sadrai, M.; Bird, G. R.; Potenza, J. A.; Schugar, H. J. *Acta Cryst. Sect. C: Struct. Chem.* **1990**, *46*, 637.

(163) Sadrai, M.; Hadel, L.; Sauers, R. R.; Husain, S.; Kroghjespersen, K.; Westbrook, J. D.; Bird, G. R. *J. Phys. Chem.* **1992**, *96*, 7988.

(164) Gsanger, M.; Oh, J. H.; Konemann, M.; Hoffken, H. W.; Krause, A. M.; Bao, Z.; Würthner, F. *Angew. Chem. Int. Ed.* **2010**, *49*, 740.

(165) Gao, J.; Xiao, C.; Jiang, W.; Wang, Z. *Org. Lett.* **2014**, *16*, 394.

(166) Yue, W.; Jiang, W.; Boeckmann, M.; Doltsinis, N. L.; Wang, Z. *Chem.-Eur. J.* **2014**, *20*, 5209.

(167) Seifert, S.; Schmidt, D.; Würthner, F. *Chem. Sci.* **2015**, 1663.

(168) Li, Y.; Tan, L.; Wang, Z.; Qian, H.; Shi, Y.; Hu, W. *Org. Lett.* **2008**, *10*, 529.

(169) Xiao, Y.; Yuan, Z. In *Chinese Patent*; Patent, C., Ed. China, **2007**; Vol. CN200710012728, p CN200710012728.

(170) Yuan, Z.; Xiao, Y.; Li, Z.; Qian, X. *Org. Lett.* **2009**, *11*, 2808.

(171) Yuan, Z.; Li, J.; Xiao, Y.; Li, Z.; Qian, X. *J. Org. Chem.* **2010**, *75*, 3007.

(172) Roznyatovskiy, V. V.; Gardner, D. M.; Eaton, S. W.; Wasielewski, M. R. *Org. Lett.* **2014**, *16*, 696.

(173) Delgado, M. C. R.; Kim, E.-G.; Filho, D. A. d. S.; Bredas, J.-L. *J. Am. Chem. Soc.* **2010**, *132*, 3375.

(174) Schmidt, R. d.; Oh, J. H.; Sun, Y.-S.; Deppisch, M.; Krause, A.-M.; Radacki, K.; Braunschweig, H.; Könemann, M.; Erk, P.; Bao, Z.; Würthner, F. *J. Am. Chem. Soc.* **2009**, *131*, 6215.

(175) Djurovich, P. I.; Mayo, E. I.; Forrest, S. R.; Thompson, M. E. *Org. Electron.* **2009**, *10*, 515.

(176) Arantes, C.; Scholz, M.; Schmidt, R.; Dehm, V.; Rocco, M. L. M.; Schoell, A.; Reinert, F.; Würthner, F. *Appl. Phys. A: Mater. Sci. Process.* **2012**, *108*, 629.

(177) Sato, N.; Yoshida, H.; Tsutsumi, K. *J. Electron Spectrosc. Relat. Phenom.* **1998**, *88*, 861.

(178) Zahn, D. R. T.; Gavrila, G. N.; Gorgoi, M. *Chem. Phys.* **2006**, *325*, 99.

(179) Kuvychko, I. V.; Dubceac, C.; Deng, S. H. M.; Wang, X.-B.; Granovsky, A. A.; Popov, A. A.; Petrukhina, M. A.; Strauss, S. H.; Boltalina, O. V. *Angew. Chem.* **2013**, *125*, 7653.

(180) Cardona, C. M.; Li, W.; Kaifer, A. E.; Stockdale, D.; Bazan, G. C. *Adv. Mater.* **2011**, *23*, 2367.

(181) Bredas, J. L. *Mater. Horizons* **2014**, *1*, 17.
(182) Dubey, R. K.; Efimov, A.; Lemmetyinen, H. *Chem. Mater.* **2011**, *23*, 778.
(183) Deyama, K.; Tomoda, H.; Muramatsu, H.; Matsui, M. *Dyes and Pigments* **1996**, *30*, 73.
(184) Zhang, Y.; Cai, L.-Z.; Wang, C.-Y.; Lai, G.-Q.; Shen, Y.-J. *New J. Chem.* **2008**, *32*, 1968.
(185) Li, Y.; Li, C.; Yue, W.; Jiang, W.; Kopecek, R.; Qu, J.; Wang, Z. *Org. Lett.* **2010**, *12*, 2374.
(186) Langhals, H.; Demmig, S.; Huber, H. *Spectrochim. Acta, Part A: Mol. Spec.* **1988**, *44*, 1189.
(187) Pichierri, F. *J. Molecular Struct.: THEOCHEM* **2004**, *686*, 57.
(188) Dey, S.; Efimov, A.; Lemmetyinen, H. *Eur. J. Org. Chem.* **2012**, 2367.
(189) Tsai, H.-Y.; Chang, C.-W.; Chen, K.-Y. *Tetrahedron Lett.* **2014**, *55*, 884.
(190) Handa, N. V.; Shirtcliff, L. D.; Lavine, B. K.; Powell, D. R.; Berlin, K. D. *Phosphorus, Sulfur Silicon Relat. Elem.* **2014**, *189*, 738.
(191) Handa, N. V.; Mendoza, K. D.; Shirtcliff, L. D. *Org. Lett.* **2011**, *13*, 4724.
(192) Osswald, P.; Würthner, F. *J. Am. Chem. Soc.* **2007**, *129*, 14319.
(193) Würthner, F.; Stepanenko, V.; Chen, Z. J.; Saha-Moller, C. R.; Kocher, N.; Stalke, D. *J. Org. Chem.* **2004**, *69*, 7933.
(194) Perrin, L.; Hudhomme, P. *Eur. J. Org. Chem.* **2011**, *2011*, 5427.
(195) Battagliarin, G.; Zhao, Y.; Li, C.; Müllen, K. *Org. Lett.* **2011**, *13*, 3399.
(196) Brink, C.; Andersen, L. H.; Hvelplund, P.; Mathur, D.; Voldstad, J. D. *Chem. Phys. Lett.* **1995**, *233*, 52.
(197) Clikeman, T. T.; Bukovsky, E. V.; Kuvychko, I. V.; San, L. K.; Deng, S. H. M.; Wang, X.-B.; Chen, Y.-S.; Strauss, S. H.; Boltalina, O. V. *Chem. Commun.* **2014**, *50*, 6263.
(198) Cao, W.; Xue, J. *Energy Environ. Sci.* **2014**, *7*, 2123.
(199) Nardes, A. M.; Ferguson, A. J.; Whitaker, J. B.; Larson, B. W.; Larsen, R. E.; Maturova, K.; Graf, P. A.; Boltalina, O. V.; Strauss, S. H.; Kopidakis, N. *Adv. Funct. Mater.* **2012**, *22*, 4115.
(200) Bindl, D. J.; Ferguson, A. J.; Wu, M.-Y.; Kopidakis, N.; Blackburn, J. L.; Arnold, M. S. *J. Phys. Chem. Lett.* **2013**, *4*, 3550.
(201) Ferguson, A. J.; Blackburn, J. L.; Holt, J. M.; Kopidakis, N.; Tenent, R. C.; Barnes, T. M.; Heben, M. J.; Rumbles, G. *J. Phys. Chem. Lett.* **2010**, *1*, 2406.
(202) Ferguson, A. J.; Blackburn, J. L.; Kopidakis, N. *Mater. Lett.* **2013**, *90*, 115.
(203) Ferguson, A. J.; Kopidakis, N.; Shaheen, S. E.; Rumbles, G. *J. Phys. Chem. C* **2011**, *115*, 23134.
(204) Holt, J. M.; Ferguson, A. J.; Kopidakis, N.; Larsen, B. A.; Bult, J.; Rumbles, G.; Blackburn, J. L. *Nano Lett.* **2010**, *10*, 4627.
(205) He, M.; Wang, M.; Lin, C.; Lin, Z. *Nanoscale* **2014**, *6*, 3984.
(206) Hwang, J.; Kim, E.-G.; Liu, J.; Brédas, J.-L.; Duggal, A.; Kahn, A. *J. Phys. Chem. C* **2007**, *111*, 1378.
(207) Dicker, G.; de Haas, M. P.; Siebbeles, L. D. A.; Warman, J. M. *Phys. Rev. B* **2004**, *70*, 045203.
(208) Redecker, M.; Bradley, D. D. C.; Inbasekaran, M.; Woo, E. P. *Appl. Phys. Lett.* **1998**, *73*, 1565.
(209) Braun, S.; Salaneck, W. R.; Fahlman, M. *Adv. Mater.* **2009**, *21*, 1450.

(210) Hartnett, P. E.; Dyar, S. M.; Margulies, E. A.; Shoer, L. E.; Cook, A. W.; Eaton, S. W.; Marks, T. J.; Wasielewski, M. R. *Chem. Sci.* **2015**, *6*, 402.

(211) Bao, D.; Ramu, S.; Contreras, A.; Upadhyayula, S.; Vasquez, J. M.; Beran, G.; Vullev, V. I. *J. Phys. Chem. B* **2010**, *114*, 14467.

(212) Veldman, D.; Meskers, S. C. J.; Janssen, R. A. J. *Adv. Funct. Mater.* **2009**, *19*, 1939.

(213) Chen, S. H.; Su, A. C.; Chen, S. A. *J. Phys. Chem. B* **2005**, *109*, 10067.

(214) Chen, S. H.; Su, A. C.; Su, C. H.; Chen, S. A. *Macromol.* **2005**, *38*, 379.

(215) Marsh, H. S.; Reid, O. G.; Barnes, G.; Heeney, M.; Stingelin, N.; Rumbles, G. *J. Polym. Sci. B: Polym. Phys.* **2014**, *52*, 700.

(216) Irwin, M. D.; Buchholz, D. B.; Hains, A. W.; Chang, R. P. H.; Marks, T. J. *Proc. Nat. Acad. Sci. U.S.A.* **2008**, *105*, 2783.

(217) Huang, F.; Yip, H. L.; Cao, Y. *Polymer Photovoltaics : Materials, Physics, and Device Engineering*; Royal Society of Chemistry, **2015**.

(218) Ferguson, A. J.; Kopidakis, N.; Shaheen, S. E.; Rumbles, G. *J. Phys. Chem. C* **2008**, *112*, 9865.

(219) Kroeze, J. E.; Savenije, T. J.; Vermeulen, M. J. W.; Warman, J. M. *J. Phys. Chem. B* **2003**, *107*, 7696.

(220) Savenije, T. J.; Kroeze, J. E.; Wienk, M. M.; Kroon, J. M.; Warman, J. M. *Phys. Rev. B* **2004**, *69*, 155205.

(221) Savenije, T. J.; Ferguson, A. J.; Kopidakis, N.; Rumbles, G. *J. Phys. Chem. C* **2013**, *117*, 24085.

(222) Shoaee, S.; Clarke, T. M.; Huang, C.; Barlow, S.; Marder, S. R.; Heeney, M.; McCulloch, I.; Durrant, J. R. *J. Am. Chem. Soc.* **2010**, *132*, 12919.

(223) Allwright, E.; Berg, D. M.; Djemour, R.; Steichen, M.; Dale, P. J.; Robertson, N. *J. Mater. Chem. C* **2014**, *2*, 7232.

(224) An, Z.; Odom, S. A.; Kelley, R. F.; Huang, C.; Zhang, X.; Barlow, S.; Padilha, L. A.; Fu, J.; Webster, S.; Hagan, D. J.; Van Stryland, E. W.; Wasielewski, M. R.; Marder, S. R. *J. Phys. Chem. A* **2009**, *113*, 5585.

(225) Jones, B. A.; Facchetti, A.; Wasielewski, M. R.; Marks, T. J. *J. Am. Chem. Soc.* **2007**, *129*, 15259.

(226) Mishra, R.; Lim, J. M.; Son, M.; Panini, P.; Kim, D.; Sankar, J. *Chem.-Eur. J.* **2014**, *20*, 5776.

(227) Chang, C.-W.; Tsai, H.-Y.; Chen, K.-Y. *Mater.* **2014**, *7*, 5488.

(228) Chen, K.-Y.; Chow, T. J. *Tetrahedron Lett.* **2010**, *51*, 5959.

(229) Wuerthner, F.; Osswald, P.; Schmidt, R.; Kaiser, T. E.; Mansikkamaeki, H.; Koenemann, M. *Org. Lett.* **2006**, *8*, 3765.

(230) Queste, M.; Cadiou, C.; Pagoaga, B.; Giraudet, L.; Hoffmann, N. *New J. Chem.* **2010**, *34*, 2537.

(231) Chen, Z. J.; Debije, M. G.; Debaerdemaeker, T.; Osswald, P.; Würthner, F. *ChemPhysChem* **2004**, *5*, 137.

(232) Pagoaga, B.; Giraudet, L.; Hoffmann, N. *Eur. J. Org. Chem.* **2014**, *2014*, 5178.

(233) Ahrens, M. J.; Fuller, M. J.; Wasielewski, M. R. *Chem. Mater.* **2003**, *15*, 2684.

(234) Shin, W. S.; Jeong, H.-H.; Kim, M.-K.; Jin, S.-H.; Kim, M.-R.; Lee, J.-K.; Lee, J. W.; Gal, Y.-S. *J. Mater. Chem.* **2006**, *16*, 384.

LIST OF ACRONYMS AND ABBREVIATIONS

acronym/abbreviation	full name
60-*x*-*y*	$C_{60}(CF_3)_x$, 60 = C_{60}, *x* = number of CF_3 addends, *y* = arbitrary isomer number
70-*x*-*y*	$C_{70}(CF_3)_x$, 70 = C_{70}, *x* = number of CF_3 addends, *y* = arbitrary isomer number
ACRD	acridine
ALD	atomic layer deposition
ANTH	anthracene
APS	Advanced Photon Source
as	apparent septet
AZUL	azulene
BnF	$CF_2C_6F_5$
CORA	corannulene
CSU	Colorado State University
CV	cyclic voltammetry
DBU	1,8-diazabicycloundec-7-ene
DCM	dichloromethane
DFT	density functional theory
$E_{1/2}$	reduction potential
$E_{exciton}$	exciton energy from optical bandgap
E_{LUMO}	LUMO energy
EA	electron affinity
EDG	electron-donating group
EMF	endometallofullerene
EMPFAF	perfluoroalkyl endometallofullerene
ESP	electrostatic potential
EWG	electron-withdrawing group
F4-TCNQ	2,3,5,6-tetrafluoro-7,7,8,8-tetracyanoquinodimethane
FET	field-effect transistor
GID	grazing incidence x-ray diffraction
HCP	hexagonal close-packed
HOMO	highest occupied molecular orbital
HPLC	high performance liquid chromatography
IPES	inverse photoelectron spectroscopy
LT PES	low temperature photoelectron spectroscopy
LUMO	lowest unoccupied molecular orbital
NAPH	naphthalene
NI APCI MS	negative ion atmospheric pressure chemical ionization mass spectrometry
NI ESI MS	negative ion electrospray ionization mass spectrometry
NICS	nucleus-independent chemical shift

NMR	nuclear magnetic resonance
NREL	National Renewable Energy Laboratry
o-DCB	1,2-dichlorobenzene
OLED	organic light-emitting diode
omp	*ortho-meta-para*
OPV	organic photovoltaic
OTF	trifluoromethanesulfonate
p-TsCN	*p*-toluenesulfonyl cyanide
P3HT	poly-3-hexylthiophene
PA	phosphonic acid
PAH	polycyclic aromatic hydrocarbon
PCBM	phenyl-C_{61}-butryic acid methyl ester
PDA	substituted perylene dianhydride
PDI	perylene diimide
PDI(R)-*n*,*n*-(X)	perylene diimide, R = imide substituent, *n* = core carbon position of X substituent
PE	phosphonic ester
PFAF	perfluoroalkylfullerene
PFB	poly[(9,9-dioctylfluorenyl-2,7-diyl)-co-(4,4'-(N-(p-butylphenyl))diphenylamine)]
PFO	poly(9,9-di-*n*-octylfluorenyl-2,7-diyl)
$PhCH_3$	toluene
PHNZ	phenazine
PNNL	Pacific Northwest National Laboratory
proton sponge	1,8-bis(dimethylamino)naphthalene, $C_{14}H_{18}N_2$
PS	polystyrene
PTCDA	3,4,9,10-perylene tetracarboxylic dianhydride
SAM	self-assembled monolayer
SCA	static-contact angle
SPP	skew pentagonal pyramid
TBA	tetrabutylammonium
TBAP	tetrabutylammonium perchlorate
TETR	tetracene
TFB	poly[(9,9-dioctylfluorenyl-2,7-diyl)-co-(N,N'-diphenyl)-N,N'-di(p-butylphenyl)-1,4-diamino-benzene)]
TMF	trifluoromethylfullerene
TRMC	time resolved microwave conductivity
TRPH	triphenylene
UV-vis	ultraviolet-visible
XRR	x-ray reflectivity